

Understanding Movement and its Influence on Tribology of the Human Hip

Robin B. Layton

Submitted in accordance with the requirements for the degree of Doctor of
Philosophy

The University of Leeds
Institute of Medical and Biological Engineering
School of Mechanical Engineering

Supervisors:

Dr. Todd Stewart

Dr. Neil Messenger

April 2020

The candidate confirms that the work submitted is his own and that appropriate credit has been given where reference has been made to the work of others.

This copy has been supplied on the understanding that it is copyright material and that no quotation from the thesis may be published without proper acknowledgement.

Acknowledgements

I would like to thank my supervisors, Dr. Todd Stewart and Dr. Neil Messenger, for this opportunity and for their guidance throughout the project. Their creativity, optimism and technical expertise has been invaluable. A second thanks is extended to the participants who generously offered up their time to take part in this study. Without their selflessness, this body of work would not have been possible.

I would like to acknowledge the financial support received from the Engineering and Physical Sciences Research Council (EPSRC). Further to this, I would like to acknowledge the high-class facilities and support provided by the Institute of Medical and Biological Engineering (iMBE) and the School of Biomedical Sciences, within the University of Leeds.

Most of all, I would like to thank my family and friends. Thank you to Nicholas Hales, for his compelling advice on scientific and engineering principles. I am forever grateful to my girlfriend Emma, for her constant support and motivation over the past three and a half years. Finally, I would like to dedicate this thesis to my parents, Nick and Claire, thank you for everything.

Abstract

Total hip arthroplasty is one of the most successful and innovative medical procedures developed during the 20th century. Success post-op has been shown to decrease for younger, more active patients when compared to those who are older and less active, raising concerns surrounding the reasons behind the increased risk of prosthesis failure for some individuals. Sliding distance, cross-shear, load and edge loading are important factors when determining potential wear rates at the hip.

Global and local hip biomechanics were calculated for eighteen healthy subjects, completing thirteen common daily activities. Results showed variation in cross-shear motion and hip reaction forces between individuals and across activities. Variation in motion paths and loading, between and within activities, suggested variation in the fluid film thickness and corresponding lubrication regimes at the joint. Walking tasks showed high levels of cross-shear and the potential for excessive wear both at initial contact and heel-off. More linear activities, such as sitting and standing, showed low cross-shear alongside a potential risk of posterior edge loading. Tribological discrepancies were shown between hip simulator input data (ISO) and measured walking data, with the ISO cycle potentially underestimating cross-shear wear at initial contact, during walking.

Results provide detailed data that may facilitate improvements in the reliability of pre-clinical testing for hip prostheses and tissue engineered cartilage substitution. The data indicates that durability testing standards should consider incorporating a range of activities, rather than just walking, and aim to represent the variability shown between individuals. Results also provide evidence for determining the appropriateness of specific activities/ rehabilitation for post-operative total hip replacement patients.

Key Words: hip replacement, biomechanics, gait analysis, hip reaction force, cross shear.

Contents

Acknowledgements	1
Abstract	2
Contents	3
List of Tables	4
List of Figures	5
List of Publications and Presentations	1
Abbreviations	2
Introduction	3
Thesis Outline	4
1. Literature Review	5
1.1. Biomechanics of the Hip.....	5
1.1.1. Anatomy	5
1.1.2. Mechanics.....	6
1.2. Articular Cartilage Degradation	7
1.2.1. Cartilage Lubrication.....	7
1.2.2. Cartilage Wear	8
1.2.3. Tissue Engineered Cartilage	9
1.2.4. Summary	9
1.3. Total Hip Replacement Theory and Development	11
1.3.1. Material Development.....	13
1.3.2. Femoral Head Size	16
1.3.3. Fixation.....	16
1.3.4. Implant Position and Orientation	17
1.3.5. Summary	20
1.4. Gait Cycle.....	22
1.4.1. Natural Walking.....	22
1.4.2. Simulated Walking.....	25
1.4.3. Summary	27
1.5. Tribology of the Joint.....	28
1.5.1. Lubrication	28
1.5.2. Wear	32
1.5.3. Motion Path Trajectories	37
1.5.4. Edge Loading.....	47
1.5.5. Summary	50
1.6. Hip Replacement and Physical Activity.....	52
1.6.1. Physical Activity Levels.....	52
1.6.2. Physical Activity and Wear	57

1.6.3.	Post-operative Functionality	60
1.6.4.	Summary	65
2.	Aim and Objectives.....	66
3.	Overview	67
3.1.	Methods.....	67
3.2.	Results.....	68
3.3.	Discussion	71
3.4.	Conclusion.....	71
4.	Movement Analysis.....	72
4.1.	Introduction	72
4.2.	Methods.....	72
4.2.1.	Patient Activity Questionnaire.....	72
4.2.2.	Ethics for Data Collection	73
4.2.3.	Lab Set-up	74
4.2.4.	Participant Information.....	76
4.2.5.	Participant Set-up.....	77
4.2.6.	Data Collection	80
4.2.7.	Data Processing.....	83
4.2.8.	Statistical Analysis.....	100
4.3.	Results.....	101
4.3.1.	Hip Joint Kinematics.....	101
4.3.1.1.	Walk	103
4.3.1.2.	Walk Turn.....	106
4.3.1.3.	Incline Walk.....	108
4.3.1.4.	Decline Walk	111
4.3.1.5.	Stand to Sit.....	113
4.3.1.6.	Sit to Stand.....	115
4.3.1.7.	Sit Cross Legged	117
4.3.1.8.	Squat.....	119
4.3.1.9.	Stand Reach	121
4.3.1.10.	Kneel Reach	123
4.3.1.11.	Lunge.....	125
4.3.1.12.	Golf Swing.....	128
4.3.1.13.	Cycle.....	131
4.3.2.	Range of Motion	133
4.3.3.	Peak Hip Angles	134
4.3.4.	Kinematic Variation	135
4.3.5.	Peak Hip Velocities.....	137
4.3.6.	Variation and Age.....	138

4.3.7.	Variation and Gender	142
4.3.8.	Summary	146
4.4.	Discussion	147
4.4.1.	Walk	148
4.4.2.	Walk Turn.....	149
4.4.3.	Incline and Decline Walk	150
4.4.4.	Stand to Sit and Sit to Stand	151
4.4.5.	Sit Cross Legged.....	152
4.4.6.	Squat.....	153
4.4.7.	Stand Reach	154
4.4.8.	Kneel Reach.....	154
4.4.9.	Lunge.....	155
4.4.10.	Golf Swing.....	155
4.4.11.	Cycle.....	156
4.4.12.	Kinematic Variation	157
4.4.13.	Movement Times	157
4.4.14.	Overall Discussion	158
4.4.15.	Summary.....	161
4.5.	Conclusion.....	162
5.	Musculoskeletal Simulations	162
5.1.	Introduction	162
5.2.	Methods.....	162
5.2.1.	Model Calculations	163
5.2.2.	Model Adaptations.....	165
5.2.3.	Python Macro Script	166
5.2.4.	Joint Reaction Forces: Resultant Force and Impulse	166
5.3.	Results.....	167
5.3.1.	Mean Ground Reaction Force.....	167
5.3.2.	Hip Moments	168
5.3.3.	Mean Hip Reaction Force.....	169
5.3.4.	Resultant Hip Reaction Forces.....	179
5.3.5.	Hip Reaction Impulse.....	183
5.3.6.	Variation and Age	185
5.3.7.	Variation and Gender	187
5.3.8.	Summary	189
5.4.	Discussion	190
5.4.1.	Walk	191
5.4.2.	Walk Turn.....	193
5.4.3.	Stand to Sit and Sit to Stand	193

5.4.4.	Squat.....	195
5.4.5.	Stand Reach	195
5.4.6.	Kneel Reach.....	196
5.4.7.	Lunge.....	196
5.4.8.	Golf Swing.....	196
5.4.9.	Variation and Age	197
5.4.10.	Variation and Gender	197
5.4.11.	Overall Discussion	199
5.5.	Conclusion.....	201
6.	Tribology.....	202
6.1.	Introduction	202
6.2.	Methods.....	202
6.2.1.	Motion Path Calculations	202
6.2.2.	Visual3D Method.....	206
6.2.3.	Motion Path Differentiation and Lubrication Calculations	208
6.2.4.	Edge Loading Analysis	211
6.2.5.	Hertz Contact Area Analysis	211
6.2.6.	SolidWorks Visualisation Model.....	212
6.3.	Results.....	215
6.3.1.	Motion Paths.....	215
6.3.2.	Motion Path Aspect Ratios	231
6.3.3.	Sliding Distances	234
6.3.4.	Sliding Velocity and Acceleration	234
6.3.5.	Variation and Age	264
6.3.6.	Variation and Gender	265
6.3.7.	Edge Loading.....	266
6.4.	Discussion	279
6.4.1.	Method Development – Novel Cross-shear Calculation	279
6.4.2.	Motion Paths – Detailed Hip Contact Mechanics	281
6.4.3.	Edge Loading.....	298
6.5.	Conclusion.....	304
7.	Overall Discussion	305
7.1.	Synthesis of Results.....	307
7.2.	Implications	319
7.2.1.	Pre-clinical Testing	319
7.2.2.	Cartilage Testing.....	320
7.2.3.	Activity Risk.....	320
7.2.4.	Hip Wear Analysis Tool.....	321
7.3.	Limitations	323

7.3.1.	Data Collection	323
7.3.2.	Data Analysis.....	323
7.4.	Future Work	326
7.4.1.	Pre-clinical Testing	326
7.4.2.	Control Comparison.....	326
7.4.3.	Knee Cross-shear	326
8.	Conclusion.....	327
9.	References	328
10.	Appendix.....	345
10.1.	Joint Replacement and Physical Activity Questionnaire.....	346
10.2.	Ethics Documentation	353
10.2.1.	Recruitment Poster	353
10.2.3.	Participant Information.....	354
10.2.4.	Screening Questionnaire and Consent Form.....	356
10.2.5.	Risk Assessment Details.....	357
10.3.	Python Macro Script	358
10.4.	Sliding Velocity and Acceleration Graphs	359
10.4.1.	Walk	360
10.4.2.	Walk Turn.....	361
10.4.3.	Incline Walk.....	362
10.4.4.	Decline Walk	363
10.4.5.	Stand to Sit.....	364
10.4.6.	Sit to Stand.....	365
10.4.7.	Sit Cross Legged	366
10.4.8.	Squat.....	367
10.4.9.	Stand Reach	368
10.4.10.	Kneel Reach.....	369
10.4.11.	Lunge.....	370
10.4.12.	Golf Swing.....	371
10.4.13.	Cycle.....	372
10.5.	Hip Reaction Force, Sliding Velocity and Sliding Acceleration Scatter Plots	373
10.5.1.	Stand to Sit.....	374
10.5.2.	Squat.....	374
10.5.3.	Stand Reach	375
10.5.4.	Kneel Reach.....	375
10.6.	Ground Reaction Forces and Hip Moments	377
10.6.1.	Walk	378
10.6.2.	Walk Turn.....	381
10.6.3.	Stand to Sit and Sit to Stand	383

10.6.4.	Squat.....	388
10.6.5.	Stand Reach	390
10.6.6.	Kneel Reach.....	392
10.6.7.	Lunge.....	394
10.6.8.	Golf Swing.....	397
10.6.9.	Peak Forces	400
10.6.10.	Discussion.....	402
10.6.11.	Conclusion.....	402

List of Tables

Table 1. Results of the Hip Society survey. Activities are compared between 1999 and 2005 meetings, meaning some removed/ added activities may not be included. Adapted from Healy et al. (2008).	59
Table 2. Demographics for the eighteen healthy subjects who completed thirteen common daily activities within a movement analysis laboratory.....	69
Table 3. Activities completed and corresponding variables that were calculated. The number of subjects (n) are shown in brackets for each activity and variable. Note that in some cases, subject numbers were reduced due to an inability to process the data reliably. This occurred due to the subject's inability to complete the activity successfully, excessive marker drop-out or excessive noise within the data. The cross (✱) represents activities in which a force platform could not be used.	70
Table 4. Subject demographics for subjects who participated in the movement analysis.	77
Table 5. Location of external skin markers. Co-ordinate system 'A' refers to the anatomical markers and 'T' to the tracking markers. Those with both 'A' and 'T' were used to define both anatomical and technical co-ordinate systems. Markers were mirrored on the left and right side (excluding sternum and vertebra markers).....	79
Table 6. Mean range of motion for hip angular rotation about three axes (X: flexion-extension; Y: abduction-adduction; Z: internal-external rotation). Data are presented for thirteen activities. Peak values for each axis are highlighted in bold.	133
Table 7. Peak hip angles (degrees) in each axis (flexion-extension, abduction-adduction and internal-external rotation). The highest peak angles, across activities, are highlighted in bold.	134
Table 8. Average and peak standard deviation for activities. Inter-subject variation is shown in three axes of motion (flexion-extension (F-E), abduction-adduction (Ab-Ad) and internal-external rotation (I-E)). Peak values within each column are highlighted in bold.	136
Table 9. Peak hip angular velocity (degrees per second) in each axis (flexion-extension, abduction-adduction and internal-external rotation). Maximum peak velocities, across activities, are highlighted in bold.....	137
Table 10. Peak hip reaction forces normalised to proportion of body weight (<i>p</i> BWT). Resultant vectors are calculated from the anterior-posterior, medial-lateral and proximal-distal force. Resultant hip reaction force magnitudes (bold), standard deviations (SD) and angles (italics) are shown. Angles reported are the relative rotational values between a vertical vector and the resultant vector. Rotations are about the medial (X), anterior (Y) and superior (Z) axes.	180
Table 11. Average and peak standard deviation for hip reaction forces. Inter-subject variation is shown for loading in three planes (Anterior-Posterior (A-P), Medial-Lateral (M-L) and Proximal-Distal (P-D)). The highest variation, by activity, is highlighted within each column (bold).....	182

Table 12. Total hip impulse reaction force (proportion of body weight seconds: $pBWT \cdot s$) occurring at anterior, medial and proximal positions on the femoral head. Maximum impulse values are highlighted in bold.	183
Table 13. Mean peak resultant hip reaction forces for under and over 55 year olds, normalised to proportion of body weight ($pBWT$). Differences between age groups is shown, with discrepancies over one $pBWT$ in bold.	185
Table 14. Mean peak resultant hip reaction forces for males and females, normalised to proportion of body weight ($pBWT$). Differences between genders is shown, with discrepancies over one $pBWT$ in bold.	187
Table 15. Twenty equally spaced points were defined on the femoral head surface (28 mm diameter). The position of each point, relative to the femoral head centre (0.0 mm, 0.0 mm, 0.0 mm) are shown.	204
Table 16. Average error and standard deviation between the sliding distances predicted from the Visual3D method and the MATLAB method, for calculating motion paths. Average error and standard deviations, for level walking and sitting down, across twenty points on the femoral head (M-L: Medial-lateral; A-P: Anterior-posterior; I-S: Inferior-Superior).	208
Table 17. Input variables, symbols, values and units for the calculation of fluid film thickness between components of a total hip replacement.	210
Table 18. Variables required for Hertz contact area analysis of a metal-on-polyethylene hip replacement (Equation 11 to 13). Symbols, values and units are shown for each variable.	211
Table 19. Coordinate positions of twenty equally spaced points on the femoral head (mm). Positions are in 3D, relative to the coordinate system of a 28 mm diameter femoral head (0.0 mm defines the hip centre). Points 1 to 11 run along the anterior-posterior arc, whereas points 11 to 20 run along the medial-lateral arc.	216
Table 20. Mean aspect ratio of motion path trajectories, for groups under and over 55 years of age. The difference between groups is reported, with discrepancies more than 1 highlighted in bold. Significance is reported from an equal variance, two-tailed T-test, with a confidence limit of 0.05.	264
Table 21 Mean motion path aspect ratios, for male and female groups. The difference between groups is reported, with discrepancies more than 1 highlighted in bold. Significance is reported from an equal variance, two-tailed T-test, with a confidence limit of 0.05.	265
Table 22. Peak resultant hip reaction force (proportional to body weight) and vector orientation (relative to X: medial-lateral; Y: anterior-posterior; Z: proximal-distal axes) are shown for activities. Corresponding hip angle and time within the movement cycle are also shown.	267
Table 23. Motion path aspect ratio (AR), sliding distance, sliding velocity, sliding acceleration and hip contact force (proportional to body weight: $pBWT$) for 13 activities and the Leeds Prosim hip wear simulator. Aspect ratios are shown both for the average	

across the femoral head and for Point 7 (Located anteriorly and at the approximate position of femoral head loading: Medial: 0 mm; Anterior: 7 mm; Distal: 12 mm).... 308

Table 24. Peak vertical ground reaction forces (vGRF), average and mean standard deviations (SD) for common daily activities. Data is normalised to proportion of body weight..... 400

Table 25. Peak hip joint moments (flexion-extension) and average and mean standard deviations for common daily activities. Data is normalised to body weight (Nm/kg). Maximum values, between activities, are highlighted in bold. 401

List of Figures

- Figure 1. Exploded view of the modular components of a metal-on-polyethylene total hip replacement (left), combined components (centre) and the device fitted at the hip (right). Adapted from <https://orthoinfo.aaos.org/en/treatment/total-hip-replacement...> 12
- Figure 2. Acetabular cup inclination angle (I) measured on anterior-posterior pelvic radiograph. Adapted from Jolles and Zangger (2002). 18
- Figure 3. Acetabular cup anteversion angle measured on anterior-posterior pelvic radiograph. d: short axis of the ellipse of the acetabular component. D: long axis of the ellipse of the acetabular component. Anteversion (A) angle can be calculated as:
 $A = \sin^{-1} (d/D)$. Adapted from Abdel et al. (2016b). 18
- Figure 4. Number of patients who dislocated within the Lewinnek ‘safe zone’, categorised by surgical approach. Adapted from Abdel et al. (2016b). 20
- Figure 5. Hip flexion-extension and internal-external rotation angle for physiological motion (Paul, 1966) and hip simulator motion (Leeds ProSim hip wear simulator). 24
- Figure 6. Hip load during physiological motion and the hip simulator cycle (Leeds ProSim hip wear simulator). 24
- Figure 7. Stribeck curve demonstrating the general relationship between the coefficient of friction, fluid dynamic viscosity (ν), sliding velocity (s) and load (L) between two surfaces. The curve shows the transition of friction from high (boundary lubrication) to low (fluid-film lubrication). 29
- Figure 8. Schematic of fluid entrainment, in which relative motion between surfaces drags fluid into contact ($U = \text{Velocity}$). Adapted from Stewart (2010). 30
- Figure 9. Schematic of squeeze film formation for a cylinder on a soft flat layer ($W = \text{Load}$). Lubricant is trapped between the sudden contact of surfaces and slowly leaks out over time. Adapted from Stewart (2010). 31
- Figure 10. Comparison of wear factors for five different rectangular motion path patterns and linear tracking. Adapted from Turell et al. (2003). 35
- Figure 11. Multiple overlapping hip motion paths are shown for one walking gait cycle from first initial contact (black) to second initial contact (blue) (left). The crossing of motion path vectors are magnified within the red box (right) and demonstrate the point at which the polyethylene liner would experience high cross-shear. 38
- Figure 12. Quantification of a walking motion path, through dividing length/height (L) by the perpendicular width (W), thus resulting the aspect ratio. 39
- Figure 13. Anterioposterior view of a generic femoral stem, indicating important landmarks on the femoral head (left). View from the apex of the femoral head, showing 10 points running on a semi-circle from superior to inferior and 10 points running from posterior to anterior. The 20 points seen within the adapted image, represent locations where motion paths were calculated by Ramamurti et al. (1996). It is noteworthy that in the current study, although the same point locations were used, ‘inferior-superior’ was referred to as ‘medial-lateral’ and points were numbered differently. 42

Figure 14. Computed motion paths at the point of resultant loading. Trajectories are presented for different simulators and for ISO walk data from Paul (1966). Square indicates heel strike and arrow indicates direction of sliding. Adapted from Calonius and Saikko (2003).....	44
Figure 15. (A) The stripe on this retrieved alumina ceramic head has been coloured with felt pen for analysis. (B) The stripe on this retrieved alumina ceramic liner has been coloured with graphite pencil for photography. Adapted from Walter et al. (2004).	48
Figure 16. Example of Talysurf traces and photographs of femoral head and acetabular cup components demonstrating stripe wear. Wear depth and area is shown in micrometres (μ). Adapted from Al-Hajjar et al. (2013).....	49
Figure 17. Posterior edge loading. In this adapted illustration, an anteverted stem and an anteverted cup are seen. With the hip flexed to approximately 90° , such as when the patient rises from a chair or climbs a high step, the load is directed approximately posteriorly. Therefore, the posterior edge of the liner produces a line of contact on the superior surface of the head, which is highly retroverted with respect to a line of latitude on the head and remote from the equator. This fits the wear pattern seen in nine patients within the study by Walter et al. (2004).....	50
Figure 38. Workflow demonstrating the movement of data between software in order to assess hip tribology.....	68
Figure 18. Total time spent per week engaging in activities by total hip replacement patients (n=9). Activities were only included if the collective group engaged for over 2 hours per week.....	73
Figure 19. Movement analysis lab space (10 x 10 m) is shown on the left, surrounded by thirteen Qualisys Oqus cameras and containing two AMTI force platforms (blue). The calibrated movement volume surrounds the force platforms. Qualisys Oqus cameras surrounded the movement area and were fixed to a rail running 3 m above the ground (right).	75
Figure 20. L-shaped reference structure and a T-shaped calibration wand required for Qualisys calibration.	76
Figure 21. Four-marker semi-rigid thermoplastic shell used as tracking markers during kinematic data collection.....	78
Figure 22. Static trial within Qualisys Track Manager, containing 54 reflective markers.	80
Figure 23. Schemata illustrating the right hand rule used for 3D analysis using a vertical axis (Z), horizontal axis (X) and perpendicular axis (Y) (C-Motion, 2018).....	85
Figure 24. An example of residual analysis for inferior-superior motion of the greater trochanter marker during walking. The root mean square (RMS) of residual is the total error between the raw and filtered signal. The dotted trend-line (intersect) runs from the 20 Hz cut-off frequency to the y-axis. The red line runs horizontally from the x-axis intersect to the RMS curve and then vertically down to the y-axis: this estimates the cut-off frequency.	87

Figure 25. Qualisys marker template, showing from left to right: trajectory name, fill level (drop-out), movement range, signal type and marker coordinates (X: medial-lateral; Y: anterior-posterior; Z: inferior-superior).....	90
Figure 26. Displacement of the right ASIS (ASIS) and virtual ASIS (ASIS _v) markers during a golf swing. Displacements are in the medial (-) lateral (+) (X), anterior (+) posterior (-) (Y) and proximal (-) distal (+) (Z) directions.	93
Figure 27. Displacement of the right ASIS (ASIS) and virtual ASIS (ASIS _v) markers during a stand to sit. Displacements are in the medial (-) lateral (+) (X), anterior (+) posterior (-) (Y) and proximal (-) distal (+) (Z) directions.	93
Figure 28. Composite pelvis showing the origin of the pelvis between the mid-ASIS and mid-PSIS. The local coordinate system of the pelvis is shown by X (Medial-Lateral), Y (Anterior-Posterior) and Z (Inferior-Superior) axes (C-Motion, 2018).....	95
Figure 29. Mean right vertical ground reaction force during one gait cycle for a level walk. The raw data (Newtons) is compared to the normalised data (proportional to body weight or <i>p</i> BWT). Standard deviations above and below the mean are shown as shaded error bars.	98
Figure 30. Mean right vertical ground reaction force during one movement cycle for a lunge. The raw data (Newtons) is compared to the normalised data (proportional to body weight or <i>p</i> BWT). Standard deviations above and below the mean are shown as shaded error bars.....	98
Figure 39. Mean movement time in seconds (s) for thirteen activities. Standard deviations are shown as error bars.....	101
Figure 40. Walking model within Visual3D showing a walking gait cycle from start (left) to finish (right).	103
Figure 41. Mean right hip angle during one gait cycle for a level walk. Standard deviation above and below the mean are shown as shaded error bars (n=17).	103
Figure 42. Mean right hip angular velocity during one gait cycle for a level walk. Standard deviation above and below the mean are shown as shaded error bars (n=17).	104
Figure 43. Walking model within Visual3D showing a walk turn gait cycle from start (left) to end (right).	106
Figure 44. Mean right hip angle during one gait cycle for a walk turn. Standard deviation above and below the mean are shown as shaded error bars (n=18).	106
Figure 45. Mean right hip angular velocity during one gait cycle for a walk turn. Standard deviation above and below the mean are shown as shaded error bars (n=18).	107
Figure 46. Walking model within Visual3D showing an incline walk gait cycle from start (left) to end (right).....	108

Figure 47. Mean right hip angle during one gait cycle for an incline walk (1:12 ramp). Standard deviation above and below the mean are shown as shaded error bars (n=18).	109
Figure 48. Mean right hip angular velocity during one gait cycle for an incline walk (1:12 ramp). Standard deviation above and below the mean are shown as shaded error bars (n=18).	109
Figure 49. Walking model within Visual3D showing a decline walk gait cycle from start (left) to end (right).	111
Figure 50. Mean right hip angle during one gait cycle for a decline walk (1:12 ramp). Standard deviation above and below the mean are shown as shaded error bars (n=18).	111
Figure 51. Mean right hip angular velocity during one gait cycle for a decline walk (1:12 ramp). Standard deviation above and below the mean are shown as shaded error bars (n=18).	112
Figure 52. Walking model within Visual3D showing a stand to sit cycle from start (left) to end (right).	113
Figure 53. Mean right hip angle during one movement cycle for a stand to sit (chair height: 47 cm). Standard deviation above and below the mean are shown as shaded error bars (n=8).	113
Figure 54. Mean right hip angular velocity during one movement cycle for a stand to sit (chair height: 47 cm). Standard deviation above and below the mean are shown as shaded error bars (n=8).	114
Figure 55. Walking model within Visual3D showing a sit to stand cycle from start (left) to end (right).	115
Figure 56. Mean right hip angle during one movement cycle for a sit to stand (chair height: 47 cm). Standard deviation above and below the mean are shown as shaded error bars (n=8).	115
Figure 57. Mean right hip angular velocity during one movement cycle for a sit to stand (chair height: 47 cm). Standard deviation above and below the mean are shown as shaded error bars (n=8).	116
Figure 58. Walking model within Visual3D showing a sit cross legged cycle from start (left) to end (right).	117
Figure 59. Mean right hip angle during one movement cycle for sitting and crossing legs (right crossed over left) (chair height: 47 cm). Standard deviation above and below the mean are shown as shaded error bars (n=14).	117
Figure 60. Mean right hip angular velocity during one movement cycle for sitting and crossing legs (right crossed over left) (chair height: 47 cm). Standard deviation above and below the mean are shown as shaded error bars (n=14).	118
Figure 61. Walking model within Visual3D showing a squat cycle from start (left) to end (right).	119

Figure 62. Mean right hip angle during one movement cycle for a squat. Standard deviation above and below the mean are shown as shaded error bars (n=13).	119
Figure 63. Mean right hip angular velocity during one movement cycle for a squat. Standard deviation above and below the mean are shown as shaded error bars (n=13).	120
Figure 64. Walking model within Visual3D showing a stand reach cycle from start (left) to end (right).	121
Figure 65. Mean right hip angle during one movement cycle for standing and reaching down to the floor. Standard deviation above and below the mean are shown as shaded error bars (n=12).	121
Figure 66. Mean right hip angular velocity during one movement cycle for standing and reaching down to the floor. Standard deviation above and below the mean are shown as shaded error bars (n=12).	122
Figure 67. Walking model within Visual3D showing a kneeling reach cycle from start (left) to end (right).	123
Figure 68. Mean right hip angle during one movement cycle for kneeling and reaching forwards. Standard deviation above and below the mean are shown as shaded error bars (n=13).	123
Figure 69. Mean right hip angular velocity during one movement cycle for kneeling and reaching forwards. Standard deviation above and below the mean are shown as shaded error bars (n=13).	124
Figure 70. Walking model within Visual3D showing a lunge cycle from start (left) to end (right).	125
Figure 71. Mean right hip angle during one movement cycle for a right footed lunge. Standard deviation above and below the mean are shown as shaded error bars (n=17).	125
Figure 72. Mean right hip angular velocity during one movement cycle for a right footed lunge. Standard deviation above and below the mean are shown as shaded error bars (n=17).	126
Figure 73. Walking model within Visual3D showing a golf cycle from start (Left) to end (Right).	128
Figure 74. Mean right hip angle during one movement cycle for a golf swing. Standard deviation above and below the mean are shown as shaded error bars (n=18).	128
Figure 75. Mean right hip angular velocity during one movement cycle for a golf swing. Standard deviation above and below the mean are shown as shaded error bars (n=18).	129
Figure 76. Walking model within Visual3D showing a cycle from start (Left) to end (Right).	131
Figure 77. Mean right hip angle during one movement cycle for cycling. Standard deviation above and below the mean are shown as shaded error bars (n=10).	131

Figure 78. Mean right hip angular velocity during one movement cycle for cycling. Standard deviation above and below the mean are shown as shaded error bars (n=10).	132
Figure 158. Mean right hip angle during one gait cycle for a stand to sit. Flexion-extension (blue), abduction-adduction (red) and internal-external rotation (green) is presented. Mean data is shown for groups under (solid line) (n=7) and over (dotted line) (n=1) 55 years of age.	138
Figure 159. Mean right hip angle during one gait cycle for a sit to stand. Flexion-extension (blue), abduction-adduction (red) and internal-external rotation (green) is presented. Mean data is shown for groups under (solid line) (n=7) and over (dotted line) (n=1) 55 years of age.	139
Figure 160. Mean right hip angle during one gait cycle for a stand reach. Flexion-extension (blue), abduction-adduction (red) and internal-external rotation (green) is presented. Mean data is shown for groups under (solid line) (n=9) and over (dotted line) (n=1) 55 years of age.	140
Figure 161. Mean right hip angle during one gait cycle for a cycle. Flexion-extension (blue), abduction-adduction (red) and internal-external rotation (green) is presented. Mean data is shown for groups under (solid line) (n=8) and over (dotted line) (n=2) 55 years of age.....	141
Figure 163. Mean right hip angle during one gait cycle for a sit to stand. Flexion-extension (blue), abduction-adduction (red) and internal-external rotation (green) is presented. Mean data is shown for male (solid line) (n=3) and female (dotted line) (n=5) groups.....	142
Figure 164. Mean right hip angle during one gait cycle for a squat. Flexion-extension (blue), abduction-adduction (red) and internal-external rotation (green) is presented. Mean data is shown for male (solid line) (n=4) and female (dotted line) (n=7) groups.	143
Figure 165. Mean right hip angle during one gait cycle for a kneel reach. Flexion-extension (blue), abduction-adduction (red) and internal-external rotation (green) is presented. Mean data is shown for male (solid line) (n=6) and female (n=7) (dotted line) groups.....	144
Figure 166. Mean right hip angle during one gait cycle for a lunge. Flexion-extension (blue), abduction-adduction (red) and internal-external rotation (green) is presented. Mean data is shown for male (solid line) (n=9) and female (dotted line) (n=8) groups.	145
Figure 169. Average hip angular range of motion, in three axes, for thirteen common activities (n=18).....	159
Figure 170. The relationship between hip flexion velocity and fluid film thickness at a total hip replacement (metal-on-polyethylene). The load was standardised at 1000 N for all activities, therefore the linear trend-line indicates a positive relationship between sliding distance and wear. The fluid entrainment calculations were taken from Hamrock and Dowson (1978).....	159

Figure 31. Anterior (left) and posterior (right) view of the Twente Lower Extremity Model (TLEM).	163
Figure 32. Flow chart of the processes involved in the musculoskeletal lower body model. White sequences represent input parameters and boundary conditions, whereas blue sequences represent processes executed within the AnyBody software. Outputs are shown in italics.	164
Figure 33. Kinematic analysis model (left) and inverse dynamic analysis model (right) from AnyBody. Experimental markers (blue) and AnyBody segment nodes (red) are shown alongside two AMTI force platforms.	165
Figure 137. Mean right hip reaction force during one gait cycle for a level walk. Standard deviation above and below the mean are shown as shaded error bars (n=16).	170
Figure 138. Mean right hip reaction force during one gait cycle for a walk turn. Standard deviation above and below the mean are shown as shaded error bars (n=17).	171
Figure 139. Mean right hip reaction force during one movement cycle for a stand to sit (chair height: 47 cm). Standard deviation above and below the mean are shown as shaded error bars (n=7).	172
Figure 140. Mean right hip reaction force during one movement cycle for a sit to stand (chair height: 47 cm). Standard deviation above and below the mean are shown as shaded error bars (n=7).	173
Figure 141. Mean right hip reaction force during one movement cycle for a squat. Standard deviation above and below the mean are shown as shaded error bars (n=11).	174
Figure 142. Mean right hip reaction force during one movement cycle for standing and reaching down to the floor. Standard deviation above and below the mean are shown as shaded error bars (n=12).	175
Figure 143. Mean right hip reaction force during one movement cycle for kneeling and reaching forwards. Standard deviation above and below the mean are shown as shaded error bars (n=10).	176
Figure 144. Mean right hip reaction force during one movement cycle for a right footed lunge. Standard deviation above and below the mean are shown as shaded error bars (n=13).	177
Figure 145. Mean right hip reaction force during one movement cycle for a golf swing. Standard deviation above and below the mean are shown as shaded error bars (n=16).	178
Figure 146. Mean resultant hip reaction forces during one movement cycle for activities, proportional to body weight (<i>p</i> BWT).	179
Figure 147. Peak resultant hip reaction force (proportional to body weight, <i>p</i> BWT) with standard deviation shown as error bars.	181

Figure 148. Resultant hip reaction impulse (proportion of body weight seconds, $pBWT \cdot s$).....	184
Figure 162. Mean resultant hip reaction force for a golf swing. Under 55 year olds (<55 y: solid line) (n=10) and over 55 year olds (>55 y: dashed line) (n=6) are compared.	186
Figure 167. Mean resultant hip reaction force for a squat. Male (solid line) (n=3) and female (dashed line) (n=6) groups are compared.	188
Figure 168. Mean resultant hip reaction force for a golf swing. Male (solid line) (n=9) and female (dashed line) (n=7) groups are compared.....	188
Figure 175. Theoretical representation of the relationship between hip loading and relative wear. The linear trend-line indicates a positive relationship between the two variables, when considered independently.....	200
Figure 176. The relationship between hip reaction force and fluid film thickness at a total hip replacement (metal-on-polyethylene). The sliding velocity was standardised to 3 radians per second for all activities, therefore the linear trend-line indicates an inverse relationship between hip reaction force and wear. The fluid entrainment calculations were taken from Hamrock and Dowson (1978).	200
Figure 34. Visual representation of the twenty equally defined points, on the surface of the femoral head, as shown in Table 4. Ten points run from posterior (1) to anterior (10) and ten points from medial (11) to lateral (20).....	205
Figure 35. Motion paths plotted at twenty equally spaced locations on a 28 mm femoral head, within MATLAB (left). Visual representation of the calculation of a motion path aspect ratio, whereby the length (L) is divided by the perpendicular width (W) (right).	205
Figure 36. A full body model with 54 markers (grey) is shown (left), alongside the hip centre (yellow) (right) surrounded by twenty equally spaced landmarks (blue). As the thigh segment rotates, landmarks are displaced, thus resulting relative motion paths occurring between bearing surfaces at the hip.	207
Figure 37. Anterior view of the cup (blue) and femoral component (red) assembly within SolidWorks. Force vector orientation is represented as a green, dotted line. Axis directions are shown as X (lateral) and Z (superior). The cup is fixed to a position of 45° inclination and 20° anteversion.	214
Figure 79. Motion path trajectories throughout a walk cycle, defined at 20 positions on the femoral head. Paths run clockwise from initial contact (black) to second initial contact (blue) (n=17).....	217
Figure 80. Motion path trajectories throughout a walk turn cycle, defined at 20 positions on the femoral head. Paths run clockwise from initial contact (black) to second initial contact (blue) (n=18).....	218
Figure 81. Motion path trajectories throughout an incline walk cycle, defined at 20 positions on the femoral head. Paths run from initial contact (black) to second initial contact (blue) (n=18).....	219

Figure 82. Motion path trajectories throughout a decline walk cycle, defined at 20 positions on the femoral head. Paths run from initial contact (black) to second initial contact (blue) (n=17).....	220
Figure 83. Motion path trajectories throughout a stand to sit cycle, defined at 20 positions on the femoral head. Paths run from initial contact (black) to second initial contact (blue) (n=8).	221
Figure 84. Motion path trajectories throughout a sit to stand cycle, defined at 20 positions on the femoral head. Paths run from initial contact (black) to second initial contact (blue) (n=8).	222
Figure 85. Motion path trajectories throughout a sit cross legged cycle, defined at 20 positions on the femoral head. Paths run from initial contact (black) to second initial contact (blue) (n=14).....	223
Figure 86. Motion path trajectories throughout a squat cycle, defined at 20 positions on the femoral head. Paths run from initial contact (black) to second initial contact (blue) (n=11).....	224
Figure 87. Motion path trajectories throughout a stand reach cycle, defined at 20 positions on the femoral head. Paths run from initial contact (black) to second initial contact (blue) (n=12).....	225
Figure 88. Motion path trajectories throughout a kneeling reach cycle, defined at 20 positions on the femoral head. Paths run from initial contact (black) to second initial contact (blue) (n=13).....	226
Figure 89. Motion path trajectories throughout a lunge cycle, defined at 20 positions on the femoral head. Paths run from initial contact (black) to second initial contact (blue) (n=17).....	227
Figure 90. Motion path trajectories throughout a golf swing cycle, defined at 20 positions on the femoral head. Paths run from initial contact (black) to second initial contact (blue) (n=18).....	228
Figure 91. Motion path trajectories throughout a cycle, defined at 20 positions on the femoral head. Paths run from initial contact (black) to second initial contact (blue) (n=10).....	229
Figure 92. Mean aspect ratios (length/width) for twenty motion path trajectories across the femoral head. Variation between subjects is shown by standard deviations (error bars).....	231
Figure 93. Minimum, mean aspect ratio (height/width) between subjects.	232
Figure 94. Minimum aspect ratios (height/width) within subjects, when considering twenty motion path trajectories across the femoral head.	232
Figure 95. Mean sliding distances for twenty motion path trajectories across the femoral head. Variation between subjects is shown by standard deviations (error bars).	234
Figure 96. Example of a displacement and velocity curve. Red dashed line shows the point at which the displacement curve changes direction.	235

Figure 97. Point 7 (X, Y, Z : 0 mm, 7 mm, 12 mm) for an average walking cycle, showing sliding displacement in anterior-posterior (blue), medial-lateral (red), proximal-distal (green) axes ($n=17$).	237
Figure 98. Point 7 (X, Y, Z : 0 mm, 7 mm, 12 mm) for an average walking cycle, showing sliding velocity in anterior-posterior (blue), medial-lateral (red), proximal-distal (green) axes (dotted lines). Resultant sliding velocity is shown in black. The corresponding motion path trajectory is shown in the top right corner, with an arrow showing the direction of motion at movement initiation.	238
Figure 99. Point 7 (X, Y, Z : 0 mm, 7 mm, 12 mm) for an average walking cycle, showing resultant sliding acceleration. The corresponding motion path trajectory is shown in the top right corner, with an arrow showing the direction of motion at movement initiation.	238
Figure 100. Point 7 (X, Y, Z : 0 mm, 7 mm, 12 mm) for an average walk turn cycle, showing sliding displacement in anterior-posterior (blue), medial-lateral (red), proximal-distal (green) axes ($n=18$).	239
Figure 101. Point 7 (X, Y, Z : 0 mm, 7 mm, 12 mm) for an average walk turn cycle, showing sliding velocity in anterior-posterior (blue), medial-lateral (red), proximal-distal (green) axes (dotted lines). Resultant sliding velocity is shown in black. The corresponding motion path trajectory is shown in the top right corner, with an arrow showing the direction of motion at movement initiation.	240
Figure 102. Point 7 (X, Y, Z : 0 mm, 7 mm, 12 mm) for an average walk turn cycle, showing resultant sliding acceleration. The corresponding motion path trajectory is shown in the top right corner, with an arrow showing the direction of motion at movement initiation.	240
Figure 103. Point 7 (X, Y, Z : 0 mm, 7 mm, 12 mm) for an average incline walk cycle, showing sliding displacement in anterior-posterior (blue), medial-lateral (red), proximal-distal (green) axes ($n=18$).	241
Figure 104. Point 7 (X, Y, Z : 0 mm, 7 mm, 12 mm) for an average incline walk cycle, showing sliding velocity in anterior-posterior (blue), medial-lateral (red), proximal-distal (green) axes (dotted lines). Resultant sliding velocity is shown in black. The corresponding motion path trajectory is shown in the top right corner, with an arrow showing the direction of motion at movement initiation.	242
Figure 105. Point 7 (X, Y, Z : 0 mm, 7 mm, 12 mm) for an average incline walk cycle, showing resultant sliding acceleration. The corresponding motion path trajectory is shown in the top right corner, with an arrow showing the direction of motion at movement initiation.	242
Figure 106. Point 7 (X, Y, Z : 0 mm, 7 mm, 12 mm) for an average decline walk cycle, showing sliding displacement in anterior-posterior (blue), medial-lateral (red), proximal-distal (green) axes ($n=18$).	243
Figure 107. Point 7 (X, Y, Z : 0 mm, 7 mm, 12 mm) for an average decline walk cycle, showing sliding velocity in anterior-posterior (blue), medial-lateral (red), proximal-distal (green) axes (dotted lines). Resultant sliding velocity is shown in black. The	

corresponding motion path trajectory is shown in the top right corner, with an arrow showing the direction of motion at movement initiation.	244
Figure 108. Point 7 (X, Y, Z: 0 mm, 7 mm, 12 mm) for an average decline walk cycle, showing resultant sliding acceleration. The corresponding motion path trajectory is shown in the top right corner, with an arrow showing the direction of motion at movement initiation.	244
Figure 109. Point 7 (X, Y, Z: 0 mm, 7 mm, 12 mm) for an average stand to sit cycle, showing sliding displacement in anterior-posterior (blue), medial-lateral (red), proximal-distal (green) axes (n=18).	245
Figure 110. Point 7 (X, Y, Z: 0 mm, 7 mm, 12 mm) for an average stand to sit cycle, showing sliding velocity in anterior-posterior (blue), medial-lateral (red), proximal-distal (green) axes (dotted lines). Resultant sliding velocity is shown in black. The corresponding motion path trajectory is shown in the top right corner, with an arrow showing the direction of motion at movement initiation.	246
Figure 111. Point 7 (X, Y, Z: 0 mm, 7 mm, 12 mm) for an average stand to sit cycle, showing resultant sliding acceleration. The corresponding motion path trajectory is shown in the top right corner, with an arrow showing the direction of motion at movement initiation.	246
Figure 112. Point 7 (X, Y, Z: 0 mm, 7 mm, 12 mm) for an average sit to stand cycle, showing sliding displacement in anterior-posterior (blue), medial-lateral (red), proximal-distal (green) axes (n=18).	247
Figure 113. Point 7 (X, Y, Z: 0 mm, 7 mm, 12 mm) for an average sit to stand cycle, showing sliding velocity in anterior-posterior (blue), medial-lateral (red), proximal-distal (green) axes (dotted lines). Resultant sliding velocity is shown in black. The corresponding motion path trajectory is shown in the top right corner, with an arrow showing the direction of motion at movement initiation.	248
Figure 114. Point 7 (X, Y, Z: 0 mm, 7 mm, 12 mm) for an average sit to stand cycle, showing resultant sliding acceleration. The corresponding motion path trajectory is shown in the top right corner, with an arrow showing the direction of motion at movement initiation.	248
Figure 115. Point 7 (X, Y, Z: 0 mm, 7 mm, 12 mm) for an average sit cross legged cycle, showing sliding displacement in anterior-posterior (blue), medial-lateral (red), proximal-distal (green) axes (n=14).	249
Figure 116. Point 7 (X, Y, Z: 0 mm, 7 mm, 12 mm) for an average sit cross legged cycle, showing sliding velocity in anterior-posterior (blue), medial-lateral (red), proximal-distal (green) axes (dotted lines). Resultant sliding velocity is shown in black. The corresponding motion path trajectory is shown in the top right corner, with an arrow showing the direction of motion at movement initiation.	250
Figure 117. Point 7 (X, Y, Z: 0 mm, 7 mm, 12 mm) for an average sit cross legged cycle, showing resultant sliding acceleration. The corresponding motion path trajectory is shown in the top right corner, with an arrow showing the direction of motion at movement initiation.	250

Figure 118. Point 7 (X, Y, Z : 0 mm, 7 mm, 12 mm) for an average squat cycle, showing sliding displacement in anterior-posterior (blue), medial-lateral (red), proximal-distal (green) axes ($n=11$).....	251
Figure 119. Point 7 (X, Y, Z : 0 mm, 7 mm, 12 mm) for an average squat cycle, showing sliding velocity in anterior-posterior (blue), medial-lateral (red), proximal-distal (green) axes (dotted lines). Resultant sliding velocity is shown in black. The corresponding motion path trajectory is shown in the top right corner, with an arrow showing the direction of motion at movement initiation.....	252
Figure 120. Point 7 (X, Y, Z : 0 mm, 7 mm, 12 mm) for an average squat cycle, showing resultant sliding acceleration. The corresponding motion path trajectory is shown in the top right corner, with an arrow showing the direction of motion at movement initiation.	252
Figure 121. Point 7 (X, Y, Z : 0 mm, 7 mm, 12 mm) for an average stand reach cycle, showing sliding displacement in anterior-posterior (blue), medial-lateral (red), proximal-distal (green) axes ($n=11$).	253
Figure 122. Point 7 (X, Y, Z : 0 mm, 7 mm, 12 mm) for an average stand reach cycle, showing sliding velocity in anterior-posterior (blue), medial-lateral (red), proximal-distal (green) axes (dotted lines). Resultant sliding velocity is shown in black. The corresponding motion path trajectory is shown in the top right corner, with an arrow showing the direction of motion at movement initiation.	254
Figure 123. Point 7 (X, Y, Z : 0 mm, 7 mm, 12 mm) for an average stand reach cycle, showing resultant sliding acceleration. The corresponding motion path trajectory is shown in the top right corner, with an arrow showing the direction of motion at movement initiation.	254
Figure 124. Point 7 (X, Y, Z : 0 mm, 7 mm, 12 mm) for an average kneel reach cycle, showing sliding displacement in anterior-posterior (blue), medial-lateral (red), proximal-distal (green) axes ($n=13$).	255
Figure 125. Point 7 (X, Y, Z : 0 mm, 7 mm, 12 mm) for an average kneel reach cycle, showing sliding velocity in anterior-posterior (blue), medial-lateral (red), proximal-distal (green) axes (dotted lines). Resultant sliding velocity is shown in black. The corresponding motion path trajectory is shown in the top right corner, with an arrow showing the direction of motion at movement initiation.	256
Figure 126. Point 7 (X, Y, Z : 0 mm, 7 mm, 12 mm) for an average kneel reach cycle, showing resultant sliding acceleration. The corresponding motion path trajectory is shown in the top right corner, with an arrow showing the direction of motion at movement initiation.	256
Figure 127. Point 7 (X, Y, Z : 0 mm, 7 mm, 12 mm) for an average lunge cycle, showing sliding displacement in anterior-posterior (blue), medial-lateral (red), proximal-distal (green) axes ($n=17$).....	257
Figure 128. Point 7 (X, Y, Z : 0 mm, 7 mm, 12 mm) for an average lunge cycle, showing sliding velocity in anterior-posterior (blue), medial-lateral (red), proximal-distal (green) axes (dotted lines). Resultant sliding velocity is shown in black. The corresponding	

motion path trajectory is shown in the top right corner, with an arrow showing the direction of motion at movement initiation.....	258
Figure 129. Point 7 (X, Y, Z: 0 mm, 7 mm, 12 mm) for an average lunge cycle, showing resultant sliding acceleration. The corresponding motion path trajectory is shown in the top right corner, with an arrow showing the direction of motion at movement initiation.	258
Figure 130. Point 7 (X, Y, Z: 0 mm, 7 mm, 12 mm) for an average golf swing, showing sliding displacement in anterior-posterior (blue), medial-lateral (red), proximal-distal (green) axes (n=18).....	259
Figure 131. Point 7 (X, Y, Z: 0 mm, 7 mm, 12 mm) for an average golf swing cycle, showing sliding velocity in anterior-posterior (blue), medial-lateral (red), proximal-distal (green) axes (dotted lines). Resultant sliding velocity is shown in black. The corresponding motion path trajectory is shown in the top right corner, with an arrow showing the direction of motion at movement initiation.	260
Figure 132. Point 7 (X, Y, Z: 0 mm, 7 mm, 12 mm) for an average golf cycle, showing resultant sliding acceleration. The corresponding motion path trajectory is shown in the top right corner, with an arrow showing the direction of motion at movement initiation.	260
Figure 133. Point 7 (X, Y, Z: 0 mm, 7 mm, 12 mm) for an average cycle, showing sliding displacement in anterior-posterior (blue), medial-lateral (red), proximal-distal (green) axes (n=10).....	261
Figure 134. Point 7 (X, Y, Z: 0 mm, 7 mm, 12 mm) for an average cycle, showing resultant sliding acceleration. The corresponding motion path trajectory is shown in the top right corner, with an arrow showing the direction of motion at movement initiation.	262
Figure 135. Point 7 (X, Y, Z: 0 mm, 7 mm, 12 mm) for an average cycle, showing sliding velocity in anterior-posterior (blue), medial-lateral (red), proximal-distal (green) axes (dotted lines). Resultant sliding velocity is shown in black. The corresponding motion path trajectory is shown in the top right corner, with an arrow showing the direction of motion at movement initiation.....	262
Figure 136. Peak sliding accelerations, between bearing surfaces at the hip, for a range of activities.	263
Figure 149. Femoral head (red) and cup (blue) rotated to the angular position of peak hip reaction force for a walk. Contact loci of the force vector is shown as a green circle and the orientation of the vector is represented by a green cylinder. Axis directions are shown as X (lateral), Y (anterior) and Z (superior). Posterior (A), medial (B), superior (C) and lateral cross-section (D) views are displayed.	269
Figure 150. Femoral head (red) and cup (blue) rotated to the angular position of peak hip reaction force for a walk turn. Contact loci of the force vector is shown as a green circle and the orientation of the vector is represented by a green cylinder. Axis directions are shown as X (lateral), Y (anterior) and Z (superior). Posterior (A), medial (B), superior (C) and lateral cross-section (D) views are displayed.....	270

Figure 151. Femoral head (red) and cup (blue) rotated to the angular position of peak hip reaction force for a stand to sit. Contact loci of the force vector is shown as a green circle and the orientation of the vector is represented by a green cylinder. Axis directions are shown as X (lateral), Y (anterior) and Z (superior). Posterior (A), medial (B), superior (C) and lateral cross-section (D) views are displayed.....	271
Figure 152. Femoral head (red) and cup (blue) rotated to the angular position of peak hip reaction force for a sit to stand. Contact loci of the force vector is shown as a green circle and the orientation of the vector is represented by a green cylinder. Axis directions are shown as X (lateral), Y (anterior) and Z (superior). Posterior (A), medial (B), superior (C) and lateral cross-section (D) views are displayed.....	272
Figure 153. Femoral head (red) and cup (blue) rotated to the angular position of peak hip reaction force for a squat. Contact loci of the force vector is shown as a green circle and the orientation of the vector is represented by a green cylinder. Axis directions are shown as X (lateral), Y (anterior) and Z (superior). Posterior (A), medial (B), superior (C) and lateral cross-section (D) views are displayed.	273
Figure 154. Femoral head (red) and cup (blue) rotated to the angular position of peak hip reaction force for a stand reach. Contact loci of the force vector is shown as a green circle and the orientation of the vector is represented by a green cylinder. Axis directions are shown as X (lateral), Y (anterior) and Z (superior). Posterior (A), medial (B), superior (C) and lateral cross-section (D) views are displayed.....	274
Figure 155. Femoral head (red) and cup (blue) rotated to the angular position of peak hip reaction force for a kneel reach. Contact loci of the force vector is shown as a green circle and the orientation of the vector is represented by a green cylinder. Axis directions are shown as X (lateral), Y (anterior) and Z (superior). Posterior (A), medial (B), superior (C) and lateral cross-section (D) views are displayed.....	275
Figure 156. Femoral head (red) and cup (blue) rotated to the angular position of peak hip reaction force for a lunge. Contact loci of the force vector is shown as a green circle and the orientation of the vector is represented by a green cylinder. Axis directions are shown as X (lateral), Y (anterior) and Z (superior). Posterior (A), medial (B), superior (C) and lateral cross-section (D) views are displayed.	276
Figure 157. Femoral head (red) and cup (blue) rotated to the angular position of peak hip reaction force for a golf swing. Contact loci of the force vector is shown as a green circle and the orientation of the vector is represented by a green cylinder. Axis directions are shown as X (lateral), Y (anterior) and Z (superior). Posterior (A), medial (B), superior (C) and lateral cross-section (D) views are displayed.....	277
Figure 171. Twenty landmarks equally spaced in a hemisphere, around the hip joint centre. Anterior, posterior, medial and lateral directions are labelled.	282
Figure 172. Mean motion path for thirteen common activities. Mean aspect ratio (AR) (motion path height divided by perpendicular width) is shown above each individual graph.....	292

Figure 173. Theoretical representation of the relationship between total sliding distance and relative wear. The linear trend-line indicates a positive relationship between the two variables, as reported in work by Saikko (2014).	294
Figure 174. Theoretical representation of the relationship between aspect ratio (motion path height divided by perpendicular width) and relative wear. The linear trend-line indicates an inverse relationship between the two variables, as shown in work by Turell et al. (2003).	294
Figure 177. Anterior view of the cup (blue) and femoral component (red) assembly within SolidWorks. Force vector orientation is represented as a green, dotted line. Axis directions are shown as X (lateral) and Z (superior). The cup is fixed to a position of 45° inclination and 20° anteversion.	298
Figure 178. Hip reaction force (proportional to body weight or <i>pBWT</i>) is shown alongside the corresponding sliding velocity and sliding acceleration for a walk turn motion path. The motion path is located at femoral head ‘Point 7’ (<i>Medial, Anterior, Distal</i> ; 0 mm, 7 mm, 12 mm).	310
Figure 179. Hip reaction force (proportional to body weight or <i>pBWT</i>) is shown alongside the corresponding sliding velocity and sliding acceleration for a sit to stand motion path. The motion path is located at femoral head ‘Point 7’ (<i>Medial, Anterior, Distal</i> ; 0 mm, 7 mm, 12 mm).	311
Figure 180. Hip reaction force (proportional to body weight or <i>pBWT</i>) is shown alongside the corresponding sliding velocity and sliding acceleration for a lunge motion path. The motion path is located at femoral head ‘Point 7’ (<i>Medial, Anterior, Distal</i> ; 0 mm, 7 mm, 12 mm).	313
Figure 181. Hip reaction force (proportional to body weight or <i>pBWT</i>) is shown alongside the corresponding sliding velocity and sliding acceleration for a golf swing motion path. The motion path is located at femoral head ‘point 7’ (<i>Medial, Anterior, Distal</i> ; 0 mm, 7 mm, 12 mm).	314
Figure 182. Hip reaction force (proportional to body weight or <i>pBWT</i>) is shown alongside the corresponding sliding velocity and sliding acceleration for a walk motion path. The motion path is located at femoral head ‘Point 7’ (<i>Medial, Anterior, Distal</i> ; 0 mm, 7 mm, 12 mm).	316
Figure 183. Hip reaction force (proportional to body weight or <i>pBWT</i>) is shown alongside the corresponding sliding velocity and sliding acceleration for a Leeds Prosim motion path input. The motion path is located at femoral head ‘Point 7’ (<i>Medial, Anterior, Distal</i> ; 0 mm, 7 mm, 12 mm).	316
Figure 184. The recruitment poster for healthy participants to be involved in the movement analysis data collection.	353
Figure 185. Screening questionnaire and consent form that were completed by participants prior to data collection.	357
Figure 186. Summary of the risk assessment for data collection within the movement analysis laboratory.	357

Figure 187. AnyBody Macro written within the Python add on, AnyPyTools. The macro runs the kinematic optimisation and inverse dynamics for a given C3D file (MoCap_LowerBody.main_S1 in this case). MedioLateral, ProximoDistal and AnteroPosterior hip reaction forces are exported to Python ('dumped'). The data was then written to a text file and formatted to remove unwanted empty lines and commas.	358
Figure 188. Sliding displacement shown in each axis for a mean walk. From left to right, femoral head points 1 (0, -14, 0), 11 (-14, 0, 0) and 17 (7, 0, 12) are shown.	360
Figure 189. Sliding velocity shown in each axis for a mean walk. Resultant sliding velocity is shown in black. From left to right, femoral head points 1 (0, -14, 0), 11 (-14, 0, 0) and 17 (7, 0, 12) are shown.	360
Figure 190. Sliding acceleration shown for a mean walk. From left to right, femoral head points 1 (0, -14, 0), 11 (-14, 0, 0) and 17 (7, 0, 12) are shown.	360
Figure 191. Sliding displacement shown in each axis for a mean walk turn. From left to right, femoral head points 1 (0, -14, 0), 11 (-14, 0, 0) and 17 (7, 0, 12) are shown.	361
Figure 192. Sliding velocity shown in each axis for a mean walk turn. Resultant sliding velocity is shown in black. From left to right, femoral head points 1 (0, -14, 0), 11 (-14, 0, 0) and 17 (7, 0, 12) are shown.	361
Figure 193. Sliding acceleration shown for a mean walk turn. From left to right, femoral head points 1 (0, -14, 0), 11 (-14, 0, 0) and 17 (7, 0, 12) are shown.	361
Figure 194. Sliding displacement shown in each axis for a mean incline walk. From left to right, femoral head points 1 (0, -14, 0), 11 (-14, 0, 0) and 17 (7, 0, 12) are shown.	362
Figure 195. Sliding velocity shown in each axis for a mean incline walk. Resultant sliding velocity is shown in black. From left to right, femoral head points 1 (0, -14, 0), 11 (-14, 0, 0) and 17 (7, 0, 12) are shown.	362
Figure 196. Sliding acceleration shown for a mean incline walk. From left to right, femoral head points 1 (0, -14, 0), 11 (-14, 0, 0) and 17 (7, 0, 12) are shown.	362
Figure 197. Sliding displacement shown in each axis for a mean decline walk. From left to right, femoral head points 1 (0, -14, 0), 11 (-14, 0, 0) and 17 (7, 0, 12) are shown.	363
Figure 198. Sliding velocity shown in each axis for a mean decline walk. Resultant sliding velocity is shown in black. From left to right, femoral head points 1 (0, -14, 0), 11 (-14, 0, 0) and 17 (7, 0, 12) are shown.	363
Figure 199. Sliding acceleration shown for a mean decline walk. From left to right, femoral head points 1 (0, -14, 0), 11 (-14, 0, 0) and 17 (7, 0, 12) are shown.	363
Figure 200. Sliding displacement shown in each axis for a mean stand to sit. From left to right, femoral head points 1 (0, -14, 0), 11 (-14, 0, 0) and 17 (7, 0, 12) are shown.	364
Figure 201. Sliding velocity shown in each axis for a mean stand to sit. Resultant sliding velocity is shown in black. From left to right, femoral head points 1 (0, -14, 0), 11 (-14, 0, 0) and 17 (7, 0, 12) are shown.	364

Figure 202. Sliding acceleration shown for a mean stand to sit. From left to right, femoral head points 1 (0, -14, 0), 11 (-14, 0, 0) and 17 (7, 0, 12) are shown.	364
Figure 203. Sliding displacement shown in each axis for a mean sit to stand. From left to right, femoral head points 1 (0, -14, 0), 11 (-14, 0, 0) and 17 (7, 0, 12) are shown.	365
Figure 204. Sliding velocity shown in each axis for a mean sit to stand. Resultant sliding velocity is shown in black. From left to right, femoral head points 1 (0, -14, 0), 11 (-14, 0, 0) and 17 (7, 0, 12) are shown.	365
Figure 205. Sliding acceleration shown for a mean sit to stand. From left to right, femoral head points 1 (0, -14, 0), 11 (-14, 0, 0) and 17 (7, 0, 12) are shown.	365
Figure 206. Sliding displacement shown in each axis for a mean sit cross legged. From left to right, femoral head points 1 (0, -14, 0), 11 (-14, 0, 0) and 17 (7, 0, 12) are shown.	366
Figure 207. Sliding velocity shown in each axis for a mean sit cross legged. Resultant sliding velocity is shown in black. From left to right, femoral head points 1 (0, -14, 0), 11 (-14, 0, 0) and 17 (7, 0, 12) are shown.	366
Figure 208. Sliding acceleration shown for a mean sit cross legged. From left to right, femoral head points 1 (0, -14, 0), 11 (-14, 0, 0) and 17 (7, 0, 12) are shown.	366
Figure 209. Sliding displacement shown in each axis for a mean squat. From left to right, femoral head points 1 (0, -14, 0), 11 (-14, 0, 0) and 17 (7, 0, 12) are shown.	367
Figure 210. Sliding velocity shown in each axis for a mean squat. Resultant sliding velocity is shown in black. From left to right, femoral head points 1 (0, -14, 0), 11 (-14, 0, 0) and 17 (7, 0, 12) are shown.	367
Figure 211. Sliding acceleration shown for a mean squat. From left to right, femoral head points 1 (0, -14, 0), 11 (-14, 0, 0) and 17 (7, 0, 12) are shown.	367
Figure 212. Sliding displacement shown in each axis for a mean stand reach. From left to right, femoral head points 1 (0, -14, 0), 11 (-14, 0, 0) and 17 (7, 0, 12) are shown.	368
Figure 213. Sliding velocity shown in each axis for a mean stand reach. Resultant sliding velocity is shown in black. From left to right, femoral head points 1 (0, -14, 0), 11 (-14, 0, 0) and 17 (7, 0, 12) are shown.	368
Figure 214. Sliding acceleration shown for a mean stand reach. From left to right, femoral head points 1 (0, -14, 0), 11 (-14, 0, 0) and 17 (7, 0, 12) are shown.	368
Figure 215. Sliding displacement shown in each axis for a mean kneel reach. From left to right, femoral head points 1 (0, -14, 0), 11 (-14, 0, 0) and 17 (7, 0, 12) are shown.	369
Figure 216. Sliding velocity shown in each axis for a mean kneel reach. Resultant sliding velocity is shown in black. From left to right, femoral head points 1 (0, -14, 0), 11 (-14, 0, 0) and 17 (7, 0, 12) are shown.	369
Figure 217. Sliding acceleration shown for a mean kneel reach. From left to right, femoral head points 1 (0, -14, 0), 11 (-14, 0, 0) and 17 (7, 0, 12) are shown.	369

Figure 218. Sliding displacement shown in each axis for a mean lunge. From left to right, femoral head points 1 (0, -14, 0), 11 (-14, 0, 0) and 17 (7, 0, 12) are shown.	370
Figure 219. Sliding velocity shown in each axis for a mean lunge. Resultant sliding velocity is shown in black. From left to right, femoral head points 1 (0, -14, 0), 11 (-14, 0, 0) and 17 (7, 0, 12) are shown.	370
Figure 220. Sliding acceleration shown for a mean lunge. From left to right, femoral head points 1 (0, -14, 0), 11 (-14, 0, 0) and 17 (7, 0, 12) are shown.	370
Figure 221. Sliding displacement shown in each axis for a mean golf swing. From left to right, femoral head points 1 (0, -14, 0), 11 (-14, 0, 0) and 17 (7, 0, 12) are shown.	371
Figure 222. Sliding velocity shown in each axis for a mean golf swing. Resultant sliding velocity is shown in black. From left to right, femoral head points 1 (0, -14, 0), 11 (-14, 0, 0) and 17 (7, 0, 12) are shown.	371
Figure 223. Sliding acceleration shown for a mean golf swing. From left to right, femoral head points 1 (0, -14, 0), 11 (-14, 0, 0) and 17 (7, 0, 12) are shown.	371
Figure 224. Sliding displacement shown in each axis for a mean cycle. From left to right, femoral head points 1 (0, -14, 0), 11 (-14, 0, 0) and 17 (7, 0, 12) are shown.	372
Figure 225. Sliding velocity shown in each axis for a mean cycle. Resultant sliding velocity is shown in black. From left to right, femoral head points 1 (0, -14, 0), 11 (-14, 0, 0) and 17 (7, 0, 12) are shown.	372
Figure 226. Sliding acceleration shown for a mean cycle. From left to right, femoral head points 1 (0, -14, 0), 11 (-14, 0, 0) and 17 (7, 0, 12) are shown.	372
Figure 227. Hip reaction force (proportional to body weight or pBWT) is shown alongside the corresponding sliding velocity and sliding acceleration for a stand to sit motion path. The motion path is located at femoral head ‘point 7’ (Medial, Anterior, Distal; 0 mm, 7 mm, 12 mm).	374
Figure 228. Hip reaction force (proportional to body weight or pBWT) is shown alongside the corresponding sliding velocity and sliding acceleration for a squat motion path. The motion path is located at femoral head ‘point 7’ (Medial, Anterior, Distal; 0 mm, 7 mm, 12 mm).....	374
Figure 229. Hip reaction force (proportional to body weight or pBWT) is shown alongside the corresponding sliding velocity and sliding acceleration for a stand reach motion path. The motion path is located at femoral head ‘point 7’ (Medial, Anterior, Distal; 0 mm, 7 mm, 12 mm).	375
Figure 230. Hip reaction force (proportional to body weight or pBWT) is shown alongside the corresponding sliding velocity and sliding acceleration for a kneel reach motion path. The motion path is located at femoral head ‘point 7’ (Medial, Anterior, Distal; 0 mm, 7 mm, 12 mm).	375
Figure 231. Mean right foot, vertical ground reaction force during one gait cycle for a level walk, proportional to body weight (pBWT). Standard deviation above and below the mean are shown as shaded error bars (n=17).....	378

Figure 232. Mean right hip moment during one gait cycle for a level walk. Standard deviation above and below the mean are shown as shaded error bars (n=17).	379
Figure 233. Mean right foot, vertical ground reaction force during one gait cycle for a walk turn, proportional to body weight (<i>p</i> BWT). Standard deviation above and below the mean are shown as shaded error bars (n=17).....	381
Figure 234. Mean right hip moment during one gait cycle for a walk turn. Standard deviation above and below the mean are shown as shaded error bars (n=18).	382
Figure 235. Mean right foot, vertical ground reaction force during one movement cycle for a stand to sit, proportional to body weight (<i>p</i> BWT) (chair height: 47 cm). Standard deviations above and below the mean are shown as shaded error bars (n=8).....	383
Figure 236. Mean right hip moment during one movement cycle for a stand to sit (chair height: 47 cm). Standard deviation above and below the mean are shown as shaded error bars (n=8).	384
Figure 237. Mean right foot, vertical ground reaction force during one movement cycle for a sit to stand, proportional to body weight (<i>p</i> BWT) (chair height: 47 cm). Standard deviation above and below the mean are shown as shaded error bars (n=8).	385
Figure 238. Mean right hip moment during one movement cycle for a sit to stand (chair height: 47 cm). Standard deviation above and below the mean are shown as shaded error bars (n=8).	386
Figure 239. Mean right foot, vertical ground reaction force during one movement cycle for a squat, proportional to body weight (<i>p</i> BWT). Standard deviation above and below the mean are shown as shaded error bars (n=11).....	388
Figure 240. Mean right hip moment during one movement cycle for a squat. Standard deviation above and below the mean are shown as shaded error bars (n=11).	389
Figure 241. Mean right foot, vertical ground reaction force during one movement cycle for standing and reaching down to the floor, proportional to body weight (<i>p</i> BWT). Standard deviation above and below the mean are shown as shaded error bars (n=12).	390
Figure 242. Mean right hip moment during one movement cycle for standing and reaching down to the floor. Standard deviation above and below the mean are shown as shaded error bars (n=12).	391
Figure 243. Mean right foot, vertical ground reaction force during one movement cycle for kneeling and reaching forwards, proportional to body weight (<i>p</i> BWT). Standard deviation above and below the mean are shown as shaded error bars (n=13).	392
Figure 244. Mean right hip moment during one movement cycle for kneeling and reaching forwards. Standard deviation above and below the mean are shown as shaded error bars (n=10).	393
Figure 245. Mean right vertical ground reaction force during one movement cycle for a right footed lunge, proportional to body weight (BWT). Standard deviation above and below the mean are shown as shaded error bars (n=17).	394

Figure 246. Mean right hip moment during one movement cycle for a right footed lunge. Standard deviation above and below the mean are shown as shaded error bars (n=13).....	395
Figure 247. Mean right foot, vertical ground reaction force during one movement cycle for a golf swing, proportional to body weight (p BWT). Standard deviation above and below the mean are shown as shaded error bars (n=18).	397
Figure 248. Mean right hip moment during one movement cycle for a golf swing. Standard deviation above and below the mean are shown as shaded error bars (n=16).	398

List of Publications and Presentations

*Submitted 2020

Layton, R.B., Messenger, N. and Stewart, T.D. 2019. Hip Cross-shear Surface Velocities, Accelerations and Load during Common Activities: Implications for Joint Replacement and Tissue Engineering in Younger Patients. *Journal of Arthroplasty*.*

Layton, R.B., Messenger, N. and Stewart, T.D. 2018. Understanding Movement and its Influence on the Tribology of the Human Hip. *World Congress of Biomechanics*, 2018, Dublin.

Layton, R.B., Messenger, N. and Stewart, T.D. 2018. A Novel Method to Investigate Cross-shear Motion in a Total Hip Replacement. *Computer Methods in Biomechanics and Biomedical Engineering*, 2018, Lisbon.

Lunn, D., Chapman, G., Layton, R.B. and Redmond, A. 2018. Contact Surface Pathways in Total Hip Replacement Patients Stratified by Gender. *Computer Methods in Biomechanics and Biomedical Engineering*, 2018, Lisbon.

Layton, R.B., Messenger, N. and Stewart, T.D. 2018. Understanding Movement and its Influence on the Tribology of the Human Hip. *MeDe Innovation Annual Conference*, 2018, Sheffield.

Kohlhardt, S., Layton, R.B. and Messenger, N. The Difference in Femoral Head Motion Path Kinematics between Walking and Picking Up a Golf Ball. *The British Association of Sport and Exercise Sciences*, 2018, Harrogate.

Layton, R.B., Messenger, N. and Stewart, T.D. 2016. Understanding Movement and its Influence on the Tribology of the Human Hip – A Preliminary Study. *North East Postgraduate Conference*, 2016, Newcastle.

Abbreviations

THR	Total hip replacement
BWT	Body weight
UHMWPE	Ultra-high-molecular-weight polyethylene
NICE	Nation Institute for Health and Care Excellence
NJR	Nation Joint Registry
ISO	International Organization for Standardization
AR	Aspect ratio
LLI	Leg length inequality
LBRU	Leeds Biomedical Research Centre
GCS	Global coordinate system
LCS	Local coordinate system
STA	Soft tissue artefact
RMS	Root mean square
p BWT	Proportional to body weight
v GRF	Vertical ground reaction force
TLEM	Twente lower extremity model
GRF	Ground reaction force
HRF	Hip reaction force
V3D	Visual3D
SV	Sliding velocity
SA	Sliding acceleration
ROM	Range of motion
SD	Standard deviation
StSi	Stand to sit
SiSt	Sit to stand
p BWT·s	Proportional to body weight seconds
F-E	Flexion-Extension
Ab-Ad	Abduction-Adduction
I-E	Internal-External rotation
A-P	Anterior-Posterior
M-L	Medial-Lateral
P-D	Proximal-Distal

Introduction

Total hip arthroplasty is one of the most successful and innovative medical procedures to have been developed during the 20th century. The surgery improves functionality for patients whilst also decreasing pain, meaning that patients will often resume normal activity levels shortly after the operation (Evans et al., 2019; Morlock et al., 2001; NJR, 2018). An increasing demand for total hip replacement (THR) has seen a gradual increase in implantation since 2003, with latest figures indicating 91,698 primary procedures in 2017 (NJR, 2018). Corresponding revision rates have been cited as 7.4% after 14 years (NJR, 2018). This rate, however, has shown an inverse relationship with age (Abdel et al., 2016a; NJR, 2018). Given that the majority of currently implanted hips incorporate a metal-on-polyethylene design, there is a requirement to understand wear mechanisms of the polyethylene cup for a young, active and functional patient group (Kurtz et al., 2009; NJR, 2018). This increased risk for younger patients is believed to be related to patient activity and hip biomechanics (Gschwend et al., 2000; Healy et al., 2008; Morlock et al., 2001; Schmalzried et al., 2000).

Past pre-clinical testing of devices has focused on walking (Paul gait curve), as this was previously considered to be the most representative of daily activities that will promote high relative motion between bearing surfaces at the hip. It is now clear that everyday motion is more complex than the simplified motion curve shown by Paul (1966). Sliding distance (relative sliding between components) (Cooper et al., 1993), cross-shear (Barbour et al., 1999), load (Barbour et al., 1997) and edge loading (contact of the femoral head on the acetabular rim) (Al-Hajjar et al., 2013; Al-Hajjar et al., 2017; Esposito et al., 2012; Hart et al., 2013; Hua et al., 2016; Walter et al., 2004) have been shown to relate directly to polyethylene wear.

Although biomechanical analysis has defined global loads and motions of a number of common activities, there is a gap in the literature for the analysis of localised hip motion and loading, in relation to THR and tissue engineered cartilage wear. Owing to variation in the biomechanical profiles of different movement patterns, it is reasonable to suggest that the cross-shear, and therefore risk of wear, may vary between activities. Assessing the tribological link between hip sliding distance, cross-shear motion, loading and edge loading, for a range of activities and ages, may be crucial to bearing/ tissue longevity. This may also provide information relating to post-operative THR rehabilitation and pre-clinical testing of devices.

Thesis Outline

This thesis begins with a review of the literature (Chapter 1), before outlining the project aim and objectives (Chapter 2). An overview of the thesis is presented in Chapter 3. Chapters 4 (Movement Analysis), 5 (Musculoskeletal Simulations) and 6 (Tribology) represent three distinct studies, each relating to independent biomechanical/ tribological variables. Although Chapter 4 includes information relating to the collection of raw data which was used for all three chapters, the specific processing and analysis of data is independent to each chapter. Chapter 7 – Overall Discussion - brings together Chapters 4, 5 and 6 in order to provide a synthesis of the findings. This includes the implications, limitations and intentions for future work of the thesis. Chapter 8 consists of concluding statements for the thesis and is followed by the list of references (Chapter 9). Finally, the Appendix (Chapter 10) includes relevant forms and supporting data which was not included in the main text.

1. Literature Review

1.1. Biomechanics of the Hip

1.1.1. Anatomy

The hip is a ball-and-socket joint where the femoral head rotates against the concave surface of the acetabular cup, with three degrees of freedom. Both surfaces are lined with articular cartilage and the acetabulum is surrounded by the acetabular labrum, allowing for a deep and stable joint (Hamill and Knutzen, 2006). Forces at the hip have been found to reach up to five times body weight when walking, highlighting the importance of soft tissue support around the joint (Bergmann et al., 1993). Spongy trabecular bone, making up both the femoral head and the acetabulum, absorbs and distributes the load at the hip (Hamill and Knutzen, 2006).

The joint is surrounded by a strong joint capsule which is in turn, supported by ligaments and the tendon of the psoas muscle (Hamill and Knutzen, 2006; Lunn et al., 2016). The joint capsule limits excessive motion of the femoral head on the acetabular cup and thus protects the joint from dislocation (Lunn et al., 2016). Three ligaments support the hip joint: the iliofemoral ligament, pubofemoral ligament and ischiofemoral ligament. The Y-shaped iliofemoral ligament extends from the ilium, to the intertrochanteric line of the femur. It resists extension (hyperextension is prevented), external rotation and to some degree, adduction. The pubofemoral ligament, attached to the obturator crest and superior ramus of the pubis, primarily resists abduction with some resistance to external rotation and extension. The ischiofemoral ligament, originating from the ischium and inserting on the intertrochanteric line of the femur, resists extension, adduction and internal rotation. The three ligaments do not resist hip flexion, hence why this movement shows the greatest range of motion (Hamill and Knutzen, 2006; Lunn et al., 2016). Following total hip replacement (THR) surgery, muscular damage is often ensued at the abductor muscles, specifically the gluteus medius, gluteus minimum, tensor fascia lata and piriformis (Barry et al., 2018; Bremer et al., 2011; Meneghini et al., 2006; Müller et al., 2011; Pfirrmann et al., 2005). This muscular damage has the potential to lead to pain and gait abnormalities (such as Trendelenburg gait) following surgery (Barry et al., 2018; Müller et al., 2011; Pfirrmann et al., 2005).

1.1.2. Mechanics

Mechanics at the hip joint rely on the interaction of bone and soft tissue. This interaction will vary, depending on the type of motion occurring. Both hips support body weight (BWT) when standing. Thus, should a person stand perfectly balanced, the hip abductors would not be required and each hip would be loaded with 0.5 BWT. However, it is unlikely that the body is perfectly balanced, emphasising the importance of the hip abductors (particularly during locomotion) (Lunn et al., 2016).

During dynamic motion, the femoral head will rotate within the acetabular cup. This can be defined as motion of the femur, in relation to the pelvis, about the hip centre. The hip joint allows for a large range of motion about three axes (anterior-posterior, medial-lateral and inferior-superior). The absolute range of motion for the hip joint, before bony impingement, has been reported as 120° flexion/ 10° extension, 45° abduction/ 25° adduction, 15° internal rotation/ 35° external rotation (Buckwalter et al., 2000). Clearly, these are maximum angles that are unlikely to be achieved during human motion.

During walking, the leading leg will step forward, causing a period of single leg stance. At this point, the force from BWT is counteracted by the hip abductors. The additional forces from the abductors increase the overall joint reaction force. This force can reach multiples of body weight. Given that hip motion varies between different activities, muscular recruitment and therefore hip reaction forces will also be altered, in order to balance the system.

1.2. Articular Cartilage Degradation

Articular cartilage is hyaline cartilage found within articulating joints. The tissue is formed from chondrocytes and an extracellular matrix (fine collagen fibres embedded within a gelatinous ground substance) (McConnell and Hull, 2011). The prime function of articular cartilage is to provide protective covering and cushioning between bearing surfaces at the end of bones (McConnell and Hull, 2011).

Cartilage degradation often occurs in the presence of arthritis, trauma or joint disease. Consequentially, treatment is commonly required in order to repair articular cartilage in high load bearing joints, such as the hip (Katta et al., 2008a). Due to the relatively soft structure of cartilage, localised cross-shear forces have the potential to damage the surface. Given the large population affected by arthritis and other joint related conditions (approximately 15% of the population), understanding the biomechanical and tribological function of both healthy and tissue engineered replacement cartilage is crucial (Katta et al., 2008a). Additionally, knowledge surrounding cartilage replacement survivorship is limited, further highlighting the importance of this field of work.

1.2.1. Cartilage Lubrication

A number of classical engineering lubrication theories have been utilised to explore and understand the low friction wear of cartilage, within synovial joints. It is now accepted that a number of lubrication mechanisms act synonymously, to provide the low frictional characteristics of the joint (see section 1.5.1 for more detail) (Katta et al., 2008a). Even under high loads, cartilage-cartilage friction will remain close to zero (Radin and Paul, 1971). Sliding distance and sliding velocity (between hip surfaces) have been highlighted as key variables influencing the amount of cartilage and the time available for rehydration of previously loaded tissue, respectfully (Katta et al., 2008a). Hence, this will influence joint lubrication, friction and potential wear at cartilage surfaces (Katta et al., 2008a). Due to constant relative motion between surfaces and dynamic loading at the hip, it is unlikely that the cartilage fluid load will reach zero. Although a film thickness of up to 1.5 μm has been predicted at the hip (Stewart et al., 1997), when stood still or moving slowly these fluid films can deplete and break down, potentially leading to a boundary lubrication regime (contact of cartilage tissue asperities) (Stewart, 2010). Thus, it is reasonable to postulate that prolonged periods of loading, in static positions, may lead to an increased coefficient of friction, limited lubrication and potential wear at the loaded joint.

1.2.2. Cartilage Wear

Wear refers to the removal of material due to the contact of surfaces and may occur in cartilage by virtue of three mechanisms: adhesion, abrasion and fatigue (Mow and Ateshian, 1997). The soft material will deform when loaded, leading to high contact areas with low contact stress (Stewart et al., 1997). High cyclical stresses and strains may lead to micro-cracks on the articular surface, which can develop into observable damage throughout the tissue (Chahal et al., 2013; Mow et al., 1993). Micro-cracks have been shown to coalesce and lead to delamination of the surface membrane from the cartilage (Chahal et al., 2013; Mow and Ateshian, 1997). Following mechanical damage, chemical processes may exacerbate wear of the tissue (Katta et al., 2008a). With a near zero coefficient of friction between hip surfaces, it is inconceivable for healthy cartilage to become damaged through simple ‘wear and tear’ due to rubbing. When considering the low friction between surfaces for both native and implanted substitute cartilage, there are two possible explanations for wear of the tissue and potential failure. These theories relate to the joint under boundary lubrication conditions, that is, when the femoral head and acetabular cup are in close contact, thus allowing for potential contact of cartilage asperities. During human motion, this is likely to occur when standing still or moving slowly, leading to slow sliding velocities and a break down in the fluid film (Stewart et al., 1997).

Firstly, it is possible that high compressive loads act to squeeze interstitial fluid out from the joint, leaving the tissue vulnerable to temporary high levels of cross-shear (friction). The combination of a high contact stress and a large contact area between surfaces, may limit full fluid entrainment in the joint during motion, thus leading to a break down in the fluid film (Stewart et al., 1997). In addition, should this be accompanied by slow and variable sliding velocities, fluid entrainment during contact may be further reduced, leading to an increased coefficient of friction and potential for wear (Stewart et al., 1997).

A second theory is that a high magnitude of compressive load may cause stress damage to the structure, thus damaging the tissue and altering the tribological conditions of the joint (Radin and Paul, 1971). This however, would still be reliant on a reduction in the fluid film, in order to create a boundary lubrication regime in which stress damage could occur. Ultimately, it is possible that long periods of high uninterrupted loading could drain fluid, increase friction and lead to wear.

1.2.3. Tissue Engineered Cartilage

Small defects in articular cartilage can be repaired using replacement tissue with similar properties to the native tissue (Katta et al., 2008a; Liu et al., 2017; Mollon et al., 2013). Cartilage replacement research has been translated into a clinical setting, with three commonly used surgical procedures: osteochondral autograft transplantation, osteochondral allograft transplantation and autologous chondrocyte implantation (Khanna et al., 2014; Kubo et al., 2015; Maldonado et al., 2018; Oladeji et al., 2018; Thier et al., 2017; Tirico et al., 2018). These methods share a similar commonality, in that they involve implanting healthy cartilage into the damaged joint. This can be achieved using healthy cartilage from another joint of the patient (osteochondral autograft transplantation), healthy cartilage from a donor (osteochondral allograft transplantation) or regenerated cartilage grown from healthy cartilage from the patient (autologous chondrocyte implantation). Engineered cartilage is thought to possess inferior frictional and wear characteristics when compared to native cartilage. However, the presence of a time-dependant response suggests that the tissue demonstrates a biphasic lubrication response that is comparable to native cartilage (Katta et al., 2008a). It is crucial to rigorously test tissue engineered cartilage substitutions, pre-clinically, in order to understand the potential survivorship of the material *in vivo*.

Within *in vitro* studies, increased normal loads, area of contact and relative speed of the opposing surfaces has led to increased wear of cartilage plugs on metal (Lipshitz and Glimcher, 1975; Lipshitz and Glimcher, 1976; Lipshitz et al., 1980). Katta et al. confirmed that an increased load will also lead to increased wear of lubricated cartilage on cartilage (Katta et al., 2008b). Understanding these detailed tribological variables (loads and sliding velocities), for a range of activities, is crucial in order to reliably replicate *in vivo* conditions during tissue engineered cartilage testing.

1.2.4. Summary

Ultimately, the wear of cartilage-on-cartilage can be attributed to a range of interlinked variables, including a reduction in lubricating fluid load (due to static/ constant loading), increased friction (cross-shear), increased joint loading/ contact stress and variation in the sliding velocity of surfaces (low velocities may act to reduce lubrication whereas high velocities will increase wear of contacting surfaces). It is possible that certain individuals and/ or activities are more prone to high cross-shear loading and sliding velocities and are therefore at a higher risk of wear and potential failure of natural and implanted cartilage

tissue. **Understanding realistic magnitude ranges and localised kinematics for these variables, during common activities of daily living, is likely to be beneficial for the reliable testing of tissue engineered cartilage substitution.**

1.3. Total Hip Replacement Theory and Development

The hip joint is a synovial ball-and-socket joint, with a high range of motion and good stability. Pain at the hip, caused by chronic conditions such as arthritis, may lead to a requirement for total hip replacement (THR). Irreversible damage to the joint surface, such as softening and deterioration of the articular cartilage during osteoarthritis, may lead to contact between bone and ultimately increased pain and reduced function (Adams and Hamblen, 2001). The predominant cause of THR is osteoarthritis, with 92% of all cases related to the joint disease (NJR, 2018).

The overall purpose of a THR is to reduce pain (caused by relative motion of contacting bone). THR involves removal of the damaged proximal femur and resurfacing of the pelvic acetabulum. A surgical reamer is used to uncover cancellous bone and the acetabular cup is generally aligned within the 'safe zone', at $40^{\circ}\pm 10^{\circ}$ of inclination and $15^{\circ}\pm 10^{\circ}$ anteversion (Banaszkiewicz, 2014; Lewinnek et al., 1978). The femoral stem is then inserted into the acetabulum. Most commonly, a metal femoral component (steel, cobalt chrome or titanium) is utilised alongside a polyethylene acetabular cup and the components are often fixed with a polymethylmethacrylate cement (Figure 1) (Temple, 2004). A local catheter that pumps pain relief directly into the joint may be applied and patients are often discharged day(s) later without return for approximately 60 days. THRs are now expected to last for 15 to 20 years and the operation is considered to be one of the most successful procedures offered in the NHS (Evans et al., 2019; NHS, 2019).

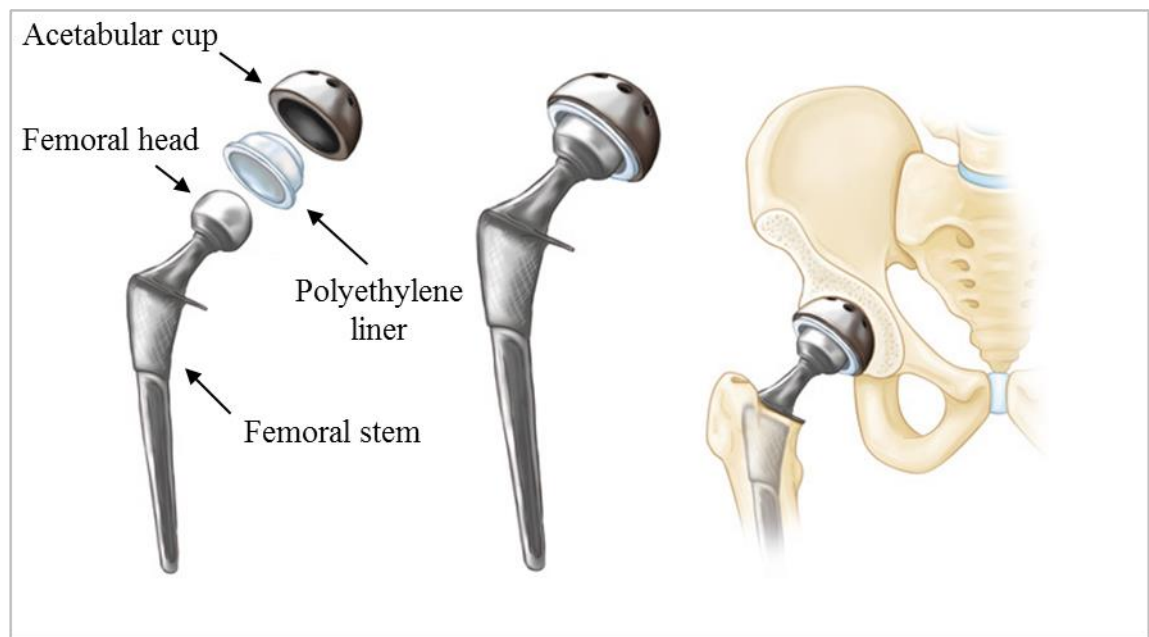


Figure 1. Exploded view of the modular components of a metal-on-polyethylene total hip replacement (left), combined components (centre) and the device fitted at the hip (right). Adapted from <https://orthoinfo.aaos.org/en/treatment/total-hip-replacement>.

The component material/ manufacturer chosen will vary depending on a number of factors, including the age and weight of the patient, as well as the preference of the surgeon (Temple, 2004). Three surgical approaches are commonly used for THR and are ultimately dependent on the training of the surgeon. The direct anterior (DA), direct lateral (DL) and direct posterior (DP) surgical approaches are accepted as successful techniques, although each will present different problems relating to the type of musculoskeletal damage ensued (Jolles and Bogoch, 2003). Generally, the DA approach is thought to be ‘muscle sparing’, in comparison to the DL and DP approaches (Moretti and Post, 2017). Within a cadaver study, the DA approach has shown less damage to the gluteus minimus, compared to the DP approach (10% less surface area damage) (Meneghini et al., 2006). With this being said, the tensor fascia latae (31%) and direct head of the rectus femoris (12%) also showed damaged during the DA approach (Meneghini et al., 2006). The DL approach has received criticism of showing high levels of abductor damage, with weakness found in 4%-20% of post-op patients (Masonis and Bourne, 2002).

Post-operatively, patients are encouraged to return to their normal activity as soon as possible and may undergo a programme of basic rehabilitation (Temple, 2004). Although some activities are advised against due to the range of motion involved, little is known regarding the impact that common daily activities may have on the prosthesis longevity.

Understanding the associated impact of activities on the prosthesis bearing surfaces would provide crucial information relating to the appropriateness of activities for post-operative patients.

1.3.1. Material Development

The theory behind THR procedures was reported as early as the 1930s, however longevity at this point was poor. Early metal-on-metal McKee hip arthroplasty prostheses and Charnley metal-on-polyethylene prostheses were introduced during the 1960s and showed the first signs of long-term success (Charnley, 1970; McKee, 1970). Concerns that the first generation metal-on-metal design caused higher levels of aseptic loosening, were attributed to greater friction compared to the alternative metal-on-polyethylene and lead to the metal-on-metal bearing surface being largely abandoned during the mid-1970s (Vassiliou et al., 2007; Zhou et al., 1997). Although good survival rates have been shown for hard-on-hard bearing combinations *in vitro* (Goldsmith et al., 2000; Schmalzried et al., 1996; Schmidt et al., 1996; Sieber et al., 1999), poor clinical survival rates have meant that metal-on-metal implants are now rarely used (NJR, 2018; Van der Weegen et al., 2011). Ultra-high molecular weight polyethylene (UHMWP) is now the most common bearing material used in hip replacements, owing to its high strength, resistance to impact/abrasion, low surface friction and inert chemical composition (Kurtz, 2009). In the current day, manufacturers DePuy, Stryker, Howmedica, Osteonics and Zimmer distribute the majority of hip replacements, which include a range of designs and material combinations (NJR, 2018).

1.3.1.1. Ultra-high Molecular Weight Polyethylene

Articulation of a highly polished metal/ ceramic head on an UHMWPE cup has been the most commonly used material combination for hip replacements in recent years (Bozic et al., 2010; Cooper et al., 1993; Macdonald et al., 2003; NJR, 2018; Scholes and Unsworth, 2000; Zhou et al., 1997). Both ceramic and metal bearings show similar wear rates when articulating with UHMWPE (Barbour et al., 2000). Wear debris resulting from the UHMWPE component has caused concern over the longevity, with some cases showing inflammatory reactions, bone reabsorption and potentially prosthesis loosening (Livermore et al., 1990).

The increasing numbers of younger hip replacement patients has generated a strong interest into the wear and durability of UHMWPE (Cooper et al., 1993). In particular, research has investigated the influence of cross-shear between bearing surfaces and the

link to polyethylene wear. Cross-shear is influenced by multi-directional relative motion between surfaces and is directly linked to polyethylene wear (Galvin et al., 2006; Kang et al., 2008a; Kang et al., 2008b; Knight et al., 2005). In order to combat potential wear at the acetabular surface, modifications have been made to the traditional metal-on-polyethylene bearings, with the introduction of highly cross-linked polyethylene, which may reduce wear by as much as 50-70% compared to conventional UHMWPE (Dumbleton et al., 2006; Zywiell et al., 2011). The crosslinking of UHMWPE is achieved using gamma irradiation in nitrogen, followed by re-melting at various, high temperatures. This creates more carbon-carbon bonds between molecules, ultimately making the molecules harder to split (Galvin et al., 2006). The material becomes more isotropic, leading to a reduction in the molecular degree of orientation during sliding as well as an increase in the density of carbon-carbon bonds between adjacent molecular chains (Wang, 2001). Cross-shear, multi-directional motion will not effect highly cross-linked polyethylene. However, this type of motion is still a concern given that conventional polyethylene is still the most commonly used material for hip replacements (NJR, 2018). The reintroduction of hard-on-hard bearing combinations of ceramic and metal is a strategy which has been reported, with the aim of reducing wear rates, particularly for younger patients (Zywiell et al., 2011). **Analysis of joint motions, for a range of activities, can advise of localised cross-shear that can influence polyethylene wear rates.**

1.3.1.2. Metal-on-metal

Modern low tolerance metal-on-metal combinations have shown substantially lower wear rates than metal-on-polyethylene implants, largely due to their ability to 'self-polish' resulting in smooth bearing surfaces (Goldsmith et al., 2000; Schmalzried et al., 1996; Schmidt et al., 1996; Sieber et al., 1999). Although the volumetric wear rates are lower, the number of wear particles (nanometre in size) is higher than that of the same volume of wear for a polyethylene cup, due to the smaller mean size of metal wear fragments (Firkins et al., 2001; Goldsmith et al., 2000; Sieber et al., 1999). There are concerns regarding the limited knowledge surrounding the risk associated with the physiological reaction to these metal wear particles (Macdonald et al., 2003; Schmalzried et al., 1996; Smith et al., 2012; Zywiell et al., 2011). Additionally, clinical results have indicated high failure rates with metal-on-metal bearings, particularly when using larger head sizes (Smith et al., 2012). Issues were first publicised in the early 2000s, when the National Institute for Health and Clinical Excellence (NICE) set a revision rate of 10% or less after

10 years for conventional hip replacements (this revision rate requirement has since dropped to 5%). It was at this time when the lack of knowledge surrounding the long term safety of metal implants was highlighted (Mathieson, 2000; NICE, 2002). More recently, a systematic review of 29 hip studies concluded that no metal-on-metal studies achieved the 10 year benchmark set by NICE (Van der Weegen et al., 2011). This is thought to be predominantly due to high levels of edge loading (contact between the femoral head component and the edge of the liner) occurring between bearing surfaces (Underwood et al., 2012). It is generally accepted that metal bearings are the more susceptible to edge loading, but it has not yet been established whether participation in certain activities will also influence this process. Consequently, the use of metal-on-metal implants has gradually decreased over the last ten years and is now rare following publication of failure rates by NICE (Mathieson, 2000; NICE, 2002). Since 2011, $\leq 1\%$ of all primary hip operations have implemented the metal-on-metal hip replacement design (NJR, 2018).

Ceramic-on-ceramic

The combination of ceramic-on-ceramic has been suggested as an alternative hard-on-hard bearing prosthesis to metal (Smith et al., 2012). When compared to UHMWPE, ceramics show higher resistance to wear and therefore potentially higher survivorship rates for the implant (Al-Hajjar et al., 2017; D'antonio et al., 2012; Geduldig et al., 1976; Oonishi et al., 2004). Early literature has questioned this combination (Mahoney, 1990), but with developments in material quality, more recent studies have generally shown successful clinical results (Beaupre et al., 2013; Dorlot, 1992; Hannouche et al., 2016; Kim et al., 2016; Sedel et al., 1990). Some notable issues with ceramic-on-ceramic prostheses include the potential for implant fracture, chipping and squeaking due to the rigidity of the material (Vassiliou et al., 2007; Zywiell et al., 2011). Another issue is that 'stripe wear', a long, thin, peripheral wear zone at risk to high levels of wear, can be seen on some explanted joints. This elliptical shaped zone can generally be seen across one side of the head, following the outside edge of the main wear area and is generally associated with edge loading (edge loading is discussed in more detail within section 1.5.4) (Vassiliou et al., 2007). Ceramic combinations are generally only used for uncemented prostheses and account for approximately 15% of all THRs implanted (NJR, 2018). **Analysis of joint motions for a range of activities, can advise when bearings may be at risk of edge loading.**

1.3.2. Femoral Head Size

The prosthesis femoral head size will have implications for the patient, with stability (Harris, 1995) and surface area (Griffith et al., 1978) two key discussion points. Shaju et al. (2005) assessed the long term performance of two different femoral head sizes against polyethylene (22 mm and 32 mm). X-rays for the 22 mm head resulted higher mean levels of linear wear than the 32 mm head, whereas the 32 mm head demonstrated higher mean volumetric wear levels. The decreased level of volumetric wear for the 22 mm head has been seen previously (Charnley et al., 1969; Galante and Rostoker, 1972; Livermore et al., 1990) and indicates that the 22 mm femoral head is more appropriate than the 32 mm femoral head when articulating on a polyethylene cup. When considering that volume of wear is equal to area ($\pi \text{ radius}^2$) multiplied by penetration, it can be suggested that femoral head size will influence penetration and therefore wear. Larger head sizes are also associated with increased stability, potentially reducing the risk of dislocation (by increasing the arc of movement and the jump distance) (Ritter et al., 1983; Smith et al., 2012). Owing to the reduced wear rates of hard-on-hard bearing surfaces, there is an argument for increasing the femoral head size for these prostheses. That is, the greater sliding distance will lead to a greater velocity and thus, a more desirable lubrication regime with potentially less wear (than a smaller diameter component). However, a larger femoral head size was shown to increase implant failure for metal-on-metal prostheses, but decrease failure for ceramic bearing surfaces (Smith et al., 2012). The National Joint Registry (NJR, 2018) suggested that larger head sizes of 36 mm and above are generally inappropriate for most bearing combinations (metal-on-polyethylene, metal-on-metal and ceramic-on-polyethylene), however 40 mm femoral heads showed the best survival rates for ceramic on ceramic prostheses. It can be concluded that increasing head size, where appropriate, for ceramic-on-ceramic replacements may be beneficial to the implant survival. Considering that femoral head size will influence the surface area contact at the hip joint, it is important to standardise the femoral head diameter for computational and simulator testing when assessing localised cross-shear motion and loading.

1.3.3. Fixation

Hip prostheses may be cemented, cementless or hybrid (cemented stem with a cementless cup) (NJR, 2018). Cemented implants utilise polymethyl methacrylate, in order to mechanically interlock the acetabular cup in place (Learmonth et al., 2007). This method allows minutes for the surgeon to orientate the acetabular cup into the desired position.

Although this is reliant on the technical skill of the surgeon, it is reasonable to suggest that this method has the potential to yield optimum surgical positioning. The cemented THR has shown good clinical results and is well accepted amongst clinicians (Learmonth et al., 2007).

During cementless THR procedures, initial fixation is achieved by press-fit of the acetabular cup, followed by additional support from screws and/or a threaded cup design (Learmonth et al., 2007). Unlike for cemented implants, this technique is completed instantaneously, without time to adjust and re-move the positioning of the cup. The survivorship of cementless implants has been questioned within the literature, with studies indicating poor longevity compared to cemented implants. A high proportion of these acetabular cup failures have been attributed to osteolysis induced wear (Learmonth et al., 2007). It is possible that these high wear rates are due to the difficulty of positioning the implant when using a press-fit, thus leading to potential edge loading (loading of the femoral head on the acetabular cup rim). Ultimately, implant positioning will influence the wear rates for a THR and may therefore be influenced by the fixation method adopted by the surgeon (Bosker et al., 2007).

1.3.4. Implant Position and Orientation

Positioning of the acetabular cup will influence the lifetime of a THR. Dislocation, impingement, edge loading and increased bearing wear/ loosening have all been linked to improper cup positioning (Meftah et al., 2013). In surgery, the cup is positioned at a specific anteversion and inclination angle using bony landmarks, alignment jigs or surgical navigation/ haptic robots (Meftah et al., 2013). Both angles can be calculated from anterior-posterior radiographs as shown in Figure 2 (inclination angle) and Figure 3 (anteversion angle).

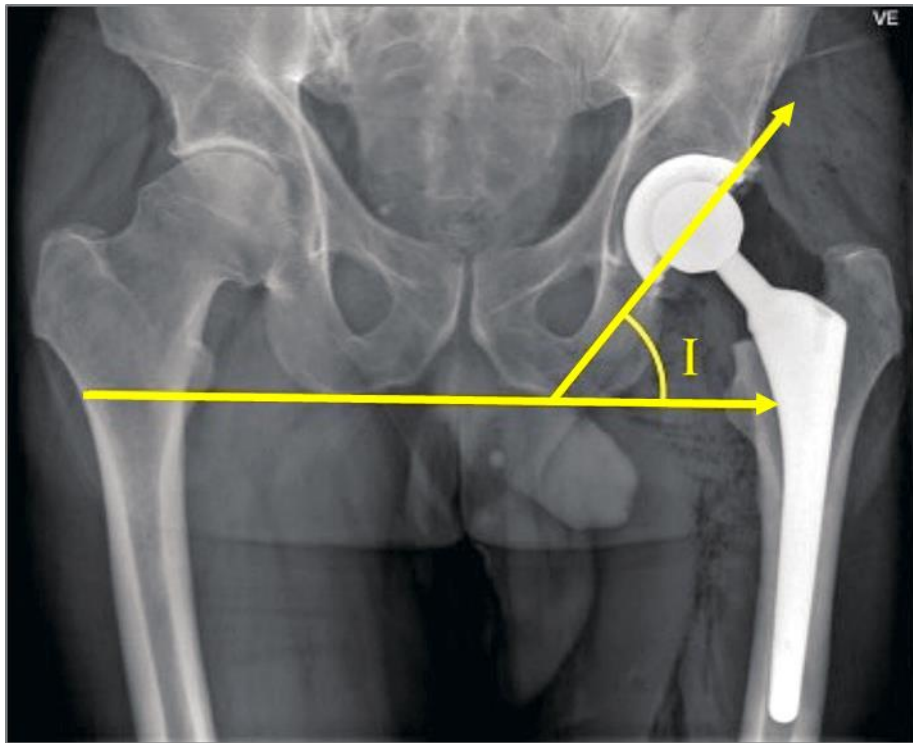


Figure 2. Acetabular cup inclination angle (I) measured on anterior-posterior pelvic radiograph. Adapted from Jolles and Zangger (2002).

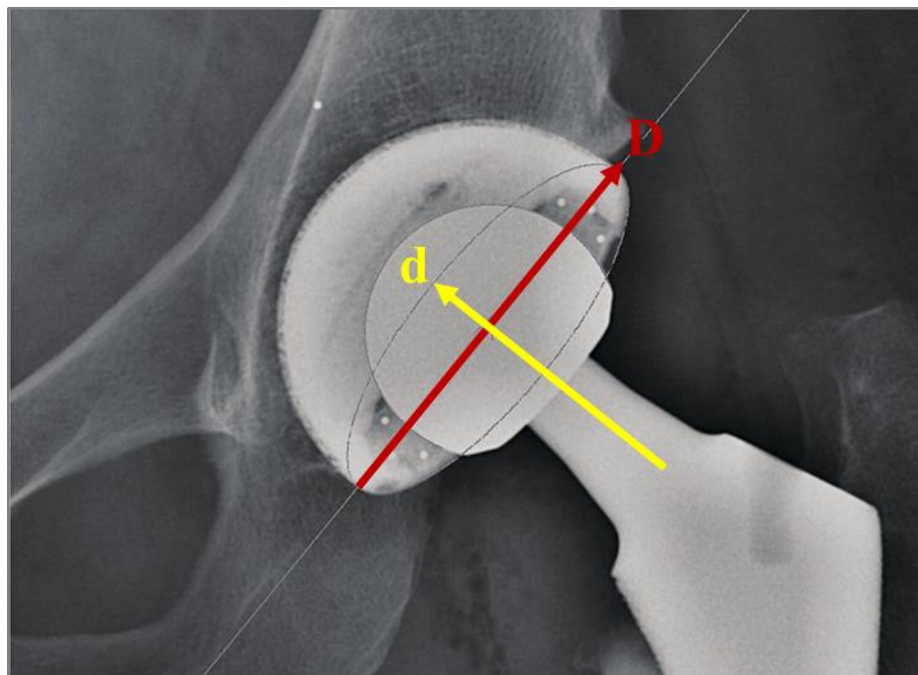


Figure 3. Acetabular cup anteversion angle measured on anterior-posterior pelvic radiograph. d : short axis of the ellipse of the acetabular component. D : long axis of the ellipse of the acetabular component. Anteversion (A) angle can be calculated as: $A = \sin^{-1}(d/D)$. Adapted from Abdel et al. (2016b).

In 1978, a 'safe zone' was proposed by Lewinneck and colleagues (Lewinnek et al., 1978) in which a fourfold reduction in dislocation was reported. The study suggested that an inclination angle of $40^{\circ} \pm 10^{\circ}$ and an anteversion angle of $15^{\circ} \pm 10^{\circ}$ should be accepted as the gold standard. Historically, this has been utilised as a guide. However, the validity of this claim has been questioned and it is now more accepted that dislocation and implant stability is multifactorial (Abdel et al., 2016b; Seagrave et al., 2017). Although the 'safe zone' provides a reasonable range, the ideal cup position is patient specific and may require more advanced analysis for some subgroups (Abdel et al., 2016b).

Abdel and colleagues identified patients who had experienced dislocation between the years of 2003 and 2012. Part of the study involved radiographic analysis of the acetabular component orientation for 206 hips (from 206 patients) (Abdel et al., 2016b). Mean cup inclination was $44^{\circ} \pm 8^{\circ}$ and anteversion was $15^{\circ} \pm 9^{\circ}$. Figure 4 shows that 58% of all hips fell within the 'safe zone' for both inclination and anteversion. It is noticeable that a number of hips were outside of the anteversion 'safe zone', between 0 and 10° (34%) (Abdel et al., 2016b). Findings question the validity of the suggestion of a 'safe zone', whilst confirming the variability in cup positioning across patients.

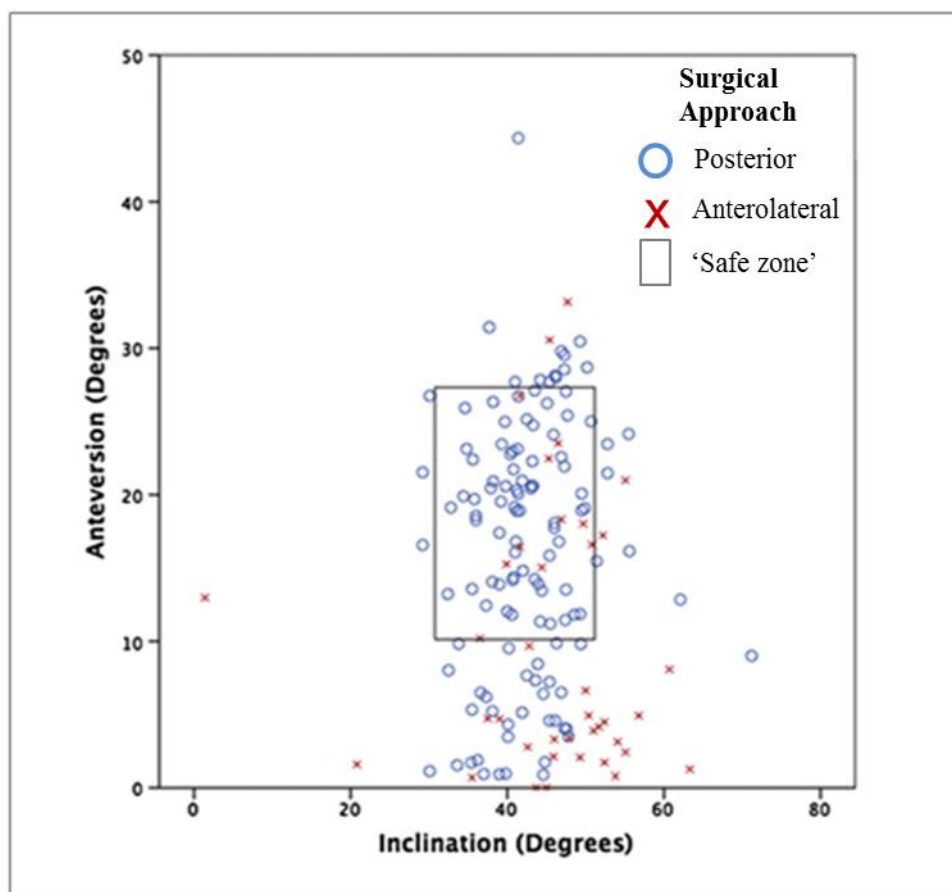


Figure 4. Number of patients who dislocated within the Lewinnek ‘safe zone’, categorised by surgical approach. Adapted from Abdel et al. (2016b).

A systematic review completed by Seagrave and colleagues (Seagrave et al., 2017), assessed 28 studies of cup positioning. The relationship between cup positioning and postoperative dislocation was found to be inconclusive. It was stated that the ideal zone for hip position varies between patients, but targeting a range (such as the ‘safe zone’) may minimize the risk of dislocation (Seagrave et al., 2017). After considering the literature, within the current study, 45° inclination and 20° anteversion was used to standardise cup positioning during analysis.

1.3.5. Summary

Within the literature, it is widely accepted that the metal-on-UHMWPE combination is the most favoured by surgeons (Bozic et al., 2010; Cooper et al., 1993; Macdonald et al., 2003; NJR, 2018; Scholes and Unsworth, 2000; Zhou et al., 1997) and this was supported by figures within the NJR (NJR, 2018). It is noteworthy that hard-on-hard bearing surfaces are more commonly used for younger patients, with the combined percentage for ceramic-on-ceramic and metal-on-metal increasing from 31% (>80 years) to 43% (65 to

69 years) for younger patients (Bozic et al., 2010). With this being said, metal-on-metal combinations have reduced to a point where they are rarely implanted, with 2016 figures lower than 0.05% (NJR, 2018). Femoral head size will influence both stability and penetration. Determining the optimum sized head is dependent on the type of prosthesis and the patient. The ideal implant positioning will vary from patient to patient, but targeting a 'safe zone' (Inclination: $45^{\circ} \pm 10^{\circ}$; Anteversion: $20^{\circ} \pm 10^{\circ}$) may minimise the risk of dislocation (Lewinnek et al., 1978; Seagrave et al., 2017). During biomechanical research, it is crucial to standardise these variables throughout testing.

1.4. Gait Cycle

The longevity of a total hip replacement (THR) design can be assessed within a laboratory, using a hip joint simulator that replicates a smoothed gait cycle. This walking cycle was based on early gait analysis of healthy, asymptomatic individuals, completed by Paul (1966) and is the historical standard to represent activity. This testing is regulated by the ISO testing standard ISO 14242 (ISO, 2014).

1.4.1. Natural Walking

Walking is a cyclical activity in which one gait cycle describes the time between two consecutive, identical events of the same limb, for example from right initial contact to right initial contact. The cycle consists of two steps, where both a stance phase (when the foot is in contact with the ground) and a swing phase (when the foot is not in contact with the ground) can be identified. The stance phase, occurring for approximately 60% of the gait cycle, is comprised of a number of events: initial contact, foot-flat, mid-stance, heel-off and toe-off. The swing phase contributes to approximately 40% of the gait cycle and involves the limb being swung forwards in preparation for the next initial contact (Hamill and Knutzen, 2006; Jacobs et al., 1972). The gait cycle is underpinned by both kinetic and kinematic factors. Kinetic activity is the underlying forces that cause an observed movement. Kinematic information therefore describes the final effect caused by joint forces. The 3D kinematic motion occurring at a joint is therefore related to the magnitude and direction of the resultant joint reaction force. Similarly, when combined with the ground reaction force, kinematics will influence joint moment activity. Further to this, kinematics at the hip (for example) will influence the localised cross-shear occurring at the joint. That is, the relative motion occurring between bearing surfaces. Considering this, it is reasonable to suggest that although kinetics will underpin kinematic motion, the two are intrinsically linked and must be analysed synonymously.

Coronal (flexion-extension), sagittal (abduction-adduction) and transverse (internal-external rotation) plane motion at the hip, knee and ankle allow for the description 3D motion at the lower limb. When considering the hip, during walking, the most obvious motion is observed in the coronal plane. At the point of initial contact, the hip exhibits a net flexion angle. This angular motion continues up to mid-stance, before a change to hip extension occurring at the end of the stance phase (Hamill and Knutzen, 2006). A vertical ground reaction force can be observed during the stance phase and consists of two clear peaks when walking. Each peak is approximately double the magnitude of body weight

and represent the points where the body centre of gravity is at its lowest (Jacobs et al., 1972).

The walking gait cycle was first described by Paul (1966). The Paul gait curve is still used as the ISO standard to determine cyclical motion and loading during hip replacement implant testing (ISO 14242-1) (ISO, 2014). Input data is smoothed prior to testing, in order to ensure that the simulator can run smoothly. In Figure 5, physiological hip angles are compared to the simplified ISO walk curves used for hip simulator testing. The corresponding, simplified loading cycle is shown in Figure 6.

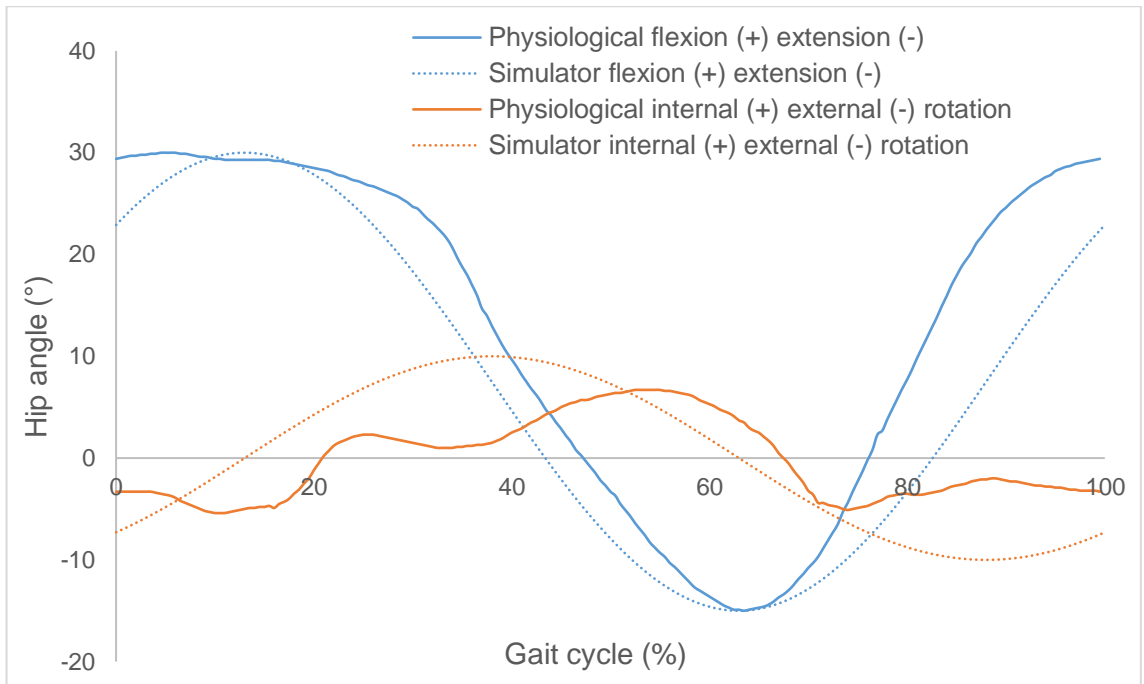


Figure 5. Hip flexion-extension and internal-external rotation angle for physiological motion (Paul, 1966) and hip simulator motion (Leeds ProSim hip wear simulator).

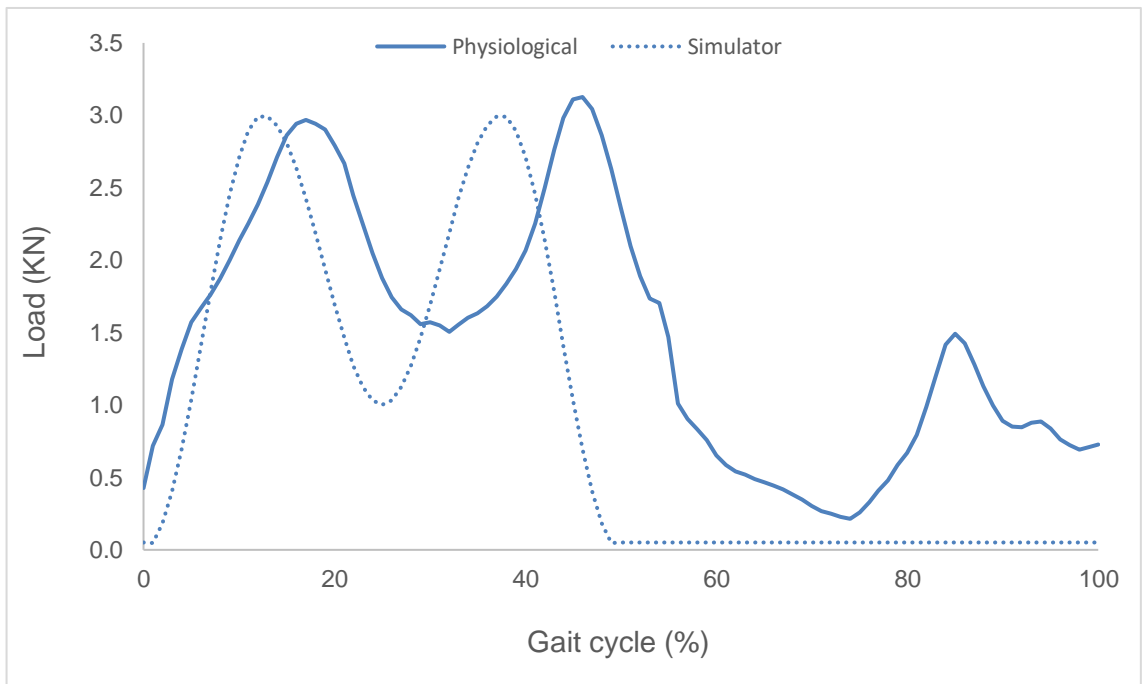


Figure 6. Hip load during physiological motion and the hip simulator cycle (Leeds ProSim hip wear simulator).

1.4.2. Simulated Walking

Historically, preclinical durability testing of hip replacement implants relies on the ability of simulators to reliably reproduce the sliding conditions (relative motion between hip surfaces) and loads occurring during walking. ISO standards (ISO-14242), determined from data for healthy subjects (Paul, 1966), provide inputs for hip simulators (ISO, 2014). Hip simulators have developed over time, with a number of models from different manufacturers described in the literature (Bragdon et al., 1996; Dowson and Jobbins, 1988; Saikko, 1996). Common simulation models include MTS, AMTI, MMED, Leeds Mk I/II, Leeds Prosim and Hut-3 (Barbour et al., 1999). A general principle for most simulators is that three mutually perpendicular loading patterns are applied at three motions of articulation to the joint (6 degrees of freedom) and set to a physiological frequency in a controlled environment (Dowson and Jobbins, 1988). The loading/ motion patterns are approximations of those seen *in vivo* and the joint is usually lubricated with bovine serum in order to replicate the frictional characteristics of the joint (Barbour et al., 1999). However, other lubricants such as distilled water can also be seen in the literature (Saikko, 1996). The type and concentration of lubricant will influence the friction factor, highlighting the need for the standardisation of fluids for wear testing (Scholes and Unsworth, 2000). However, even with the standardisation of lubricants, the relative sliding motion and load between components will influence the lubrication regime (section 1.5.1) (Stewart, 2010; Stewart et al., 1997). This further highlights the importance of accurately replicating *in vivo* joint conditions. The use of bovine serum adds biological proteins and lipids to the environment, which reduce adhesion and recreate a more physiological boundary lubrication regime.

One million cycles is accepted as representing approximately one year *in vivo* (Barbour et al., 1999). Material wear tests generally last for several million cycles at a frequency of 1 Hz, meaning a full test will often last over six months (Saikko, 1996). Wear can be measured volumetrically (a coordinate measurement machine maps the wear surface to compare before and after) or gravimetrically (the cup is removed and weighed to determine changes in mass) (Barbour et al., 1999).

Motion paths describe the relative motion occurring between bearing surfaces at the hip (Barbour et al., 1999; Calonius and Saikko, 2002; Calonius and Saikko, 2003; Ramamurti et al., 1996; Saikko and Calonius, 2002; Turell et al., 2003). The shape of these 3D trajectories will influence the cross-shear occurring between the femoral head and acetabular cup (Kang et al., 2008a; Kang et al., 2008b). Accurately replicating the

relationship between the three global hip motions during gait (flexion-extension, abduction-adduction, internal-external rotation) is crucial in order to successfully reproduce the complex quasi-elliptical motion paths seen on the femoral head from computational work using clinical data (Bennett et al., 2008; Bennett et al., 2002; Bennett et al., 2000; Bragdon et al., 1996; Budenberg et al., 2012).

Smith and Unsworth (2001) argued the case for simplified input motion and loading, using the Mark II Durham Hip Simulator. An elliptical wear path was produced using approximately sinusoidal motion (flexion-extension and internal-external rotation) with dynamic loading approximated to a square wave. This theory is largely accepted in the literature, with Barbour et al. (1999) also producing elliptical wear paths from two axes of rotation (flexion-extension and internal-external rotation) at a phase angle of 90° . The simplification of motion to a single axis has also been explored, however it was concluded that this fundamentally alters the wear rates and therefore cannot be suggested as an alternative method (Smith and Unsworth, 2000). A limitation with the simplification of motion is that slight changes to relative motion paths can influence the instantaneous cross-shear. Although visually, simplified simulator motion paths were found to be similar to measured data, there was no depth to the analysis. In order to truly understand potential differences between measured data and simplified ISO data, motion paths should be quantified into aspect ratios (height/ width) and the sliding distances, velocities and accelerations should all be considered. A number of studies have shown motion paths to vary between manufacturers, with many showing obvious discrepancies when compared to physiological gait cycles (Calonius and Saikko, 2002; Calonius and Saikko, 2003; Saikko and Calonius, 2002). It was suggested that differences in motion paths, by different simulator manufacturers, may go some way to explaining the variation in reported wear values (Calonius and Saikko, 2003). The variation in simulator motion paths is discussed in more detail within section 1.5.3.1..

Hip joint contact forces are another input variable that has been questioned within the literature (Li et al., 2014). Asymptomatic THR patients showed 30% lower peak loads at toe-off and significantly higher stance phase loading than the ISO data. This increased stance phase load coupled with slower walking speeds may have a negative impact on lubrication and wear at the joint (Li et al., 2014). With this being said, it is difficult to determine prosthesis loading on reported data from a small number of patients. It may be more beneficial to analyse a larger group of individuals, of varying age, to begin to understand the variation that might be expected to occur between patients. From this, the

relationship between hip loading and instantaneous cross-shear could be explored, as a combination of the two is likely to lead to excessive wear at the polyethylene liner.

A final criticism of current pre-clinical testing of hips, is that only walking biomechanics are simulated. It is well documented that hip replacement patients are exposed to a wide range of activities of daily living (Morlock et al., 2001). In order to truly replicate the motion and loading between a metal/ ceramic femoral head and a polyethylene liner, a wide range of activities should be incorporated into the simulator cycle. **Detailed tribological information is required, for a range of activities, in order to understand the variation in localised biomechanics between components at the hip.** Once this is understood, material testing should analyse various combinations of activities and the implications for polyethylene wear.

1.4.3. Summary

Walking gait is determined by complex kinetic and kinematic motion, which can be measured biomechanically within a lab environment. Hip simulators aim to replicate these motions in order to assess the influence of factors such as wear, on joint replacement survivorship. Due to the design of joint simulators, motions must be simplified to allow for the execution of smooth cyclical patterns from the machine. An issue with this is that some potentially important parts of walking data may be lost and complex motions other than walking, are difficult to test on many simulators. The introduction of high range of motion simulators which can incorporate realistic joint loading and edge loading may allow for more realistic and reliable testing of hip prostheses. **Understanding hip tribology during a range of common activities, for a range of individuals, may provide crucial information in order to begin incorporating realistic motion and loading into hip simulators.**

1.5. Tribology of the Joint

1.5.1. Lubrication

Tribological principles underpin the understanding of friction, lubrication and wear at the hip joint. The principles of lubrication can be well explained through the Stribeck curve (Figure 7). The Stribeck curve shows the coefficient of friction in relation to the Hersey number (the product of fluid dynamic viscosity and sliding velocity, divided by the load) (Lu et al., 2006). By standardising fluid viscosity, it can be deduced that friction is directly influenced by the sliding velocity and the load (a high sliding velocity and low load will result in low friction). The Stribeck curve provides a means of calculating three distinct lubrication regimes. That is, boundary lubrication (where sliding velocity is low and load is high, thus resulting in potential contact of surface asperities), mixed lubrication (a combination of boundary and fluid-film regimes) and fluid-film (where sliding velocity is high and load is low, thus encouraging a layer of lubrication between surfaces that prevents contact of asperities) (Lu et al., 2006; Wang et al., 2006). A boundary lubrication regime has the potential to lead to contact of asperities, high levels of friction and potentially wear of joint surfaces (Stewart, 2010; Stewart et al., 1997).

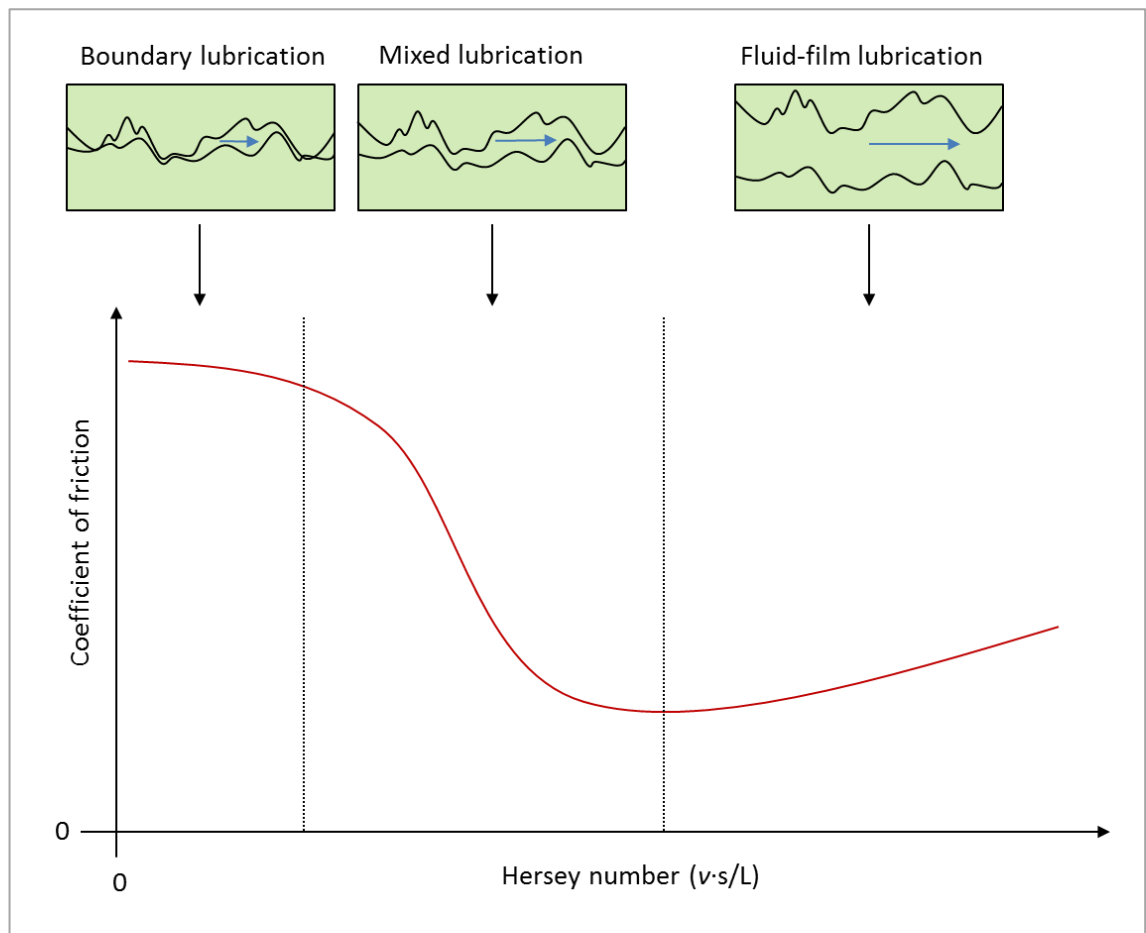


Figure 7. Stribeck curve demonstrating the general relationship between the coefficient of friction, fluid dynamic viscosity (ν), sliding velocity (s) and load (L) between two surfaces. The curve shows the transition of friction from high (boundary lubrication) to low (fluid-film lubrication).

The natural hip joint is surrounded by a layer of load distributing articular cartilage and lubricated with synovial fluid. The cartilage deforms under load, becoming smooth, thereby increasing the distribution of load and reducing contact stress (Stewart, 2010). Cartilage will also aid fluid film lubrication. This is a continuous film of fluid separating the articulating surfaces and must be thicker than the combined roughness of surfaces, in order to avoid surface contact and associated high friction and wear (Stewart, 2010; Stewart et al., 1997). Fluid film thickness, in the natural hip, has been predicted to equal $\sim 1.5 \mu\text{m}$ (Jin et al., 1993; Mow et al., 1993).

The theory of fluid film lubrication has been described by two processes: entrainment film and squeeze film. Fluid entrainment occurs when the motion of the articulating surfaces in a joint, drag fluid into contact. In the hip, relative motion of the femoral head to the acetabular cup will increase the pressure of the synovial fluid to a point where it

may separate the two surfaces. Deformation in the cartilage (white layer in Figure 8) will spread the pressure across a larger area, thereby further increasing the surface separation force (Stewart, 2010) (Figure 8).

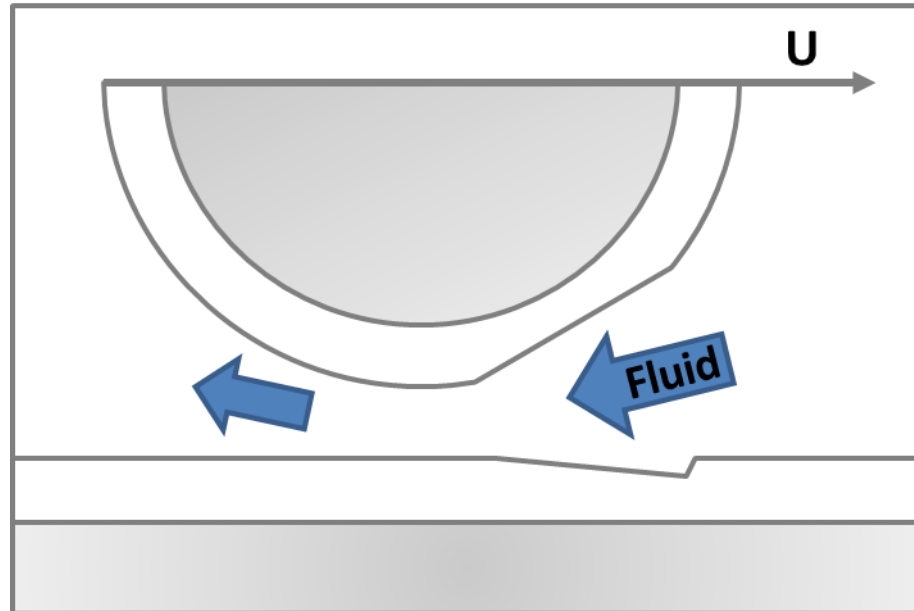


Figure 8. Schematic of fluid entrainment, in which relative motion between surfaces drags fluid into contact ($U = \text{Velocity}$). Adapted from Stewart (2010).

Hamrock and Dowson (1978) produced a formula in which the variables associated with fluid entrainment were detailed (Equation 1). Film thickness was described as proportional to the equivalent radius of the bearings (R), the viscosity of the lubricant (η), the sliding velocity (u), and inversely proportional to the load (w) and the material stiffness (E'). The equivalent radius of the bearing is calculated from the product of the radius of the two surfaces in contact, divided by their difference (eg. $R^1 \cdot R^2 / R^1 - R^2$). Therefore, as the radial clearance is decreased, the equivalent bearing radius (R) increases. Whilst the overall radius is important, the radial clearance holds a crucial role in fluid entrainment. The film can be influenced by the manufacturer through the design of the implant. What cannot be controlled is variation due to patient characteristics, for example, age and BMI. Both age and BMI are likely to increase the load and reduce motion at the joint, hence influencing the lubrication conditions. **It is also important to note that the fluid film is linked to the activities an individual engages in, as high loads at a slow pace are likely to reduce the fluid film (Hamrock and Dowson, 1978).**

$$\text{Film} = 2.789 R \left\{ \frac{\eta u}{E'R} \right\}^{0.65} \left\{ \frac{w}{E'R^2} \right\}^{-0.21} \quad [\text{Equation 1}]$$

Squeeze film involves the movement of two separated surfaces together, which if occurring fast enough with soft surfaces, will trap pools of lubricating fluid between the contact surfaces before leaking out over time. Similar to fluid entrainment, cartilage deformation will assist in this situation, by restricting fluid from leaving the contact area (Stewart, 2010) (Figure 9).

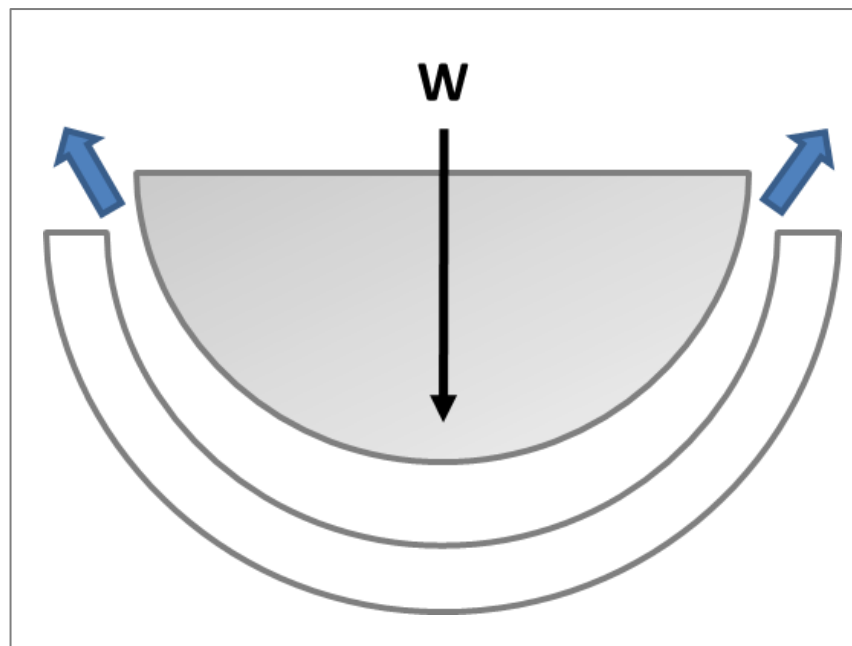


Figure 9. Schematic of squeeze film formation for a cylinder on a soft flat layer ($W =$ Load). Lubricant is trapped between the sudden contact of surfaces and slowly leaks out over time. Adapted from Stewart (2010).

Higginson (1978) proposed a number of variables influencing this process (Equation 2). The film thickness generated is proportional to the equivalent radius of the bearing (R) and the viscosity of the lubricant (η), and inversely proportional to the load (w), the material stiffness (E') and, unlike for fluid entrainment, time (t). Deformation of the surface will trap fluid, preventing surface asperity contact until a point at which the film thickness reduces to a similar magnitude as the surface roughness. Similar to fluid entrainment, prolonged loading with slow motion will influence the lubrication conditions as more fluid will leak out, potentially leading to negative bearing conditions at the joint.

$$\text{Film} = 2.86 R \left\{ \frac{w}{E'R^2} \right\}^{0.167} \left\{ \frac{dtE'}{n} \right\}^{-0.5} \quad [\text{Equation 2}]$$

Jin et al. (1993) applied these two theories of lubrication to the natural hip joint during walking. Within the stance phase, at the point in which motion is variable and loads are high, squeeze film formation can occur during initial contact and will protect the cartilage surfaces from contact. The depleted fluid film layer will then be replenished, through fluid entrainment, during the swing phase. Reduced viscosity and breaking down of this film layer, such as during arthritis, may lead to contact between surfaces at the joint and therefore lead to cartilage degradation, pain and potentially a requirement for joint replacement. The ideal condition in a joint is with a sufficiently large film thickness, compared to the surface roughness, as this will prevent surface interaction and consequently lead to low friction and theoretically no wear (fluid-film lubrication regime) (Stewart, 2010). The roughness of bearing surfaces in an artificial hip are therefore crucial, with hard ceramic materials showing the least roughness (~0.004 $\mu\text{m Ra}$) when compared to metal (~0.02 $\mu\text{m Ra}$) and polyethylene (~1 $\mu\text{m Ra}$). However, polyethylene will be polished/ burnished *in vivo* which may reduce the surface roughness over time (Jin et al., 1997). It is relevant to state that for polyethylene implants, the lubrication conditions are likely to remain within a boundary condition lubrication regime due to the roughness of the polyethylene surface.

In addition to joint replacement lubrication (between components), lubrication is crucial in the natural hip, with implications for cartilage-cartilage wear. Although cartilage-cartilage friction is close to zero, there are mechanisms in which the lubrication can break down, leading to potential wear of cartilage asperities (Mow and Ateshian, 1997; Radin and Paul, 1971). Information regarding these mechanisms is detailed in section 1.2.1..

1.5.2. Wear

Wear will occur at the hip due to the interaction of surface asperities of the two bearing surfaces during motion. In the artificial hip, microscopic polyethylene wear occurs in the form of abrasion, adhesion and fatigue (Stewart, 2010). Abrasion can be observed when a harder surface makes contact with a softer surface, producing wear particles similar in size to the roughness of the harder surface. Adhesion and fatigue can be described as the

momentary sticking together of contacting surfaces, leading to cyclical shear stress and eventually fatigue of the asperity. Wear particles produced through adhesion and fatigue are generally larger than those caused by abrasion (Stewart, 2010). Fatigue wear may also lead to macroscopic debris through delamination. This is the failure of a material, in the form of separation of layers, due to cyclic loading that exceeds the materials fatigue strength. Delamination is not a common issue for hip replacements, as the joint experiences relatively low stress occurring primarily at the pole of the cup (Stewart, 2010). It is predominantly cross-shear forces that cause wear to polyethylene. Polyethylene consists of carbon and hydrogen elements, in which carbon molecules are bonded together both intra- and inter- molecularly to form the materials structure. The physiological motion across three axes of rotation leads to cross-shear forces and may cause the chemical bonds between adjacent polyethylene chains to break (Wang, 2001).

The wear factor enables the comparison of wear between different surfaces (Calonius and Saikko, 2003). Small scale pin on plate testing allows for the control of loading, velocity, motion and lubrication to determine the wear factor at one specific point of contact. An issue with this is that it does not determine the wear factor across the whole surface and does not take age or activity type in to account. The wear factor (Equation 3) was developed from the theory that wear rate is proportional to load and sliding distance, where: k = wear factor; V = wear volume; n = number of cycles; L = applied load; s = sliding distance. Thus, in a controlled test, each variable can be investigated.

$$K = V / (n \int L s) \quad \text{[Equation 3]}$$

Using the wear factor (K) the volume of wear (V) (Equation 4) can be estimated, where: V is equal to the product of K , L (applied load) and s (sliding distance) (Lancaster, 1973). This was later adapted by (Kang et al., 2008a) to include the effects of cross-shear (X_{shear}).

$$V = X_{shear} \cdot K L S \quad \text{[Equation 4]}$$

The wear factor is dependent on a number of variables such as the bearing surface materials, the joint lubrication conditions, the applied stress and the localised cross-shear

(Bennett et al., 2008). Even small amounts of wear can lead to large amounts of sub-micron wear particles being produced, which may enter the periprosthetic tissue surrounding the implant. Polyethylene wear can lead to the biological response, periprosthetic osteolysis, where macrophages are activated and bone loss may occur due to increased bone reabsorption (Ingham and Fisher, 2005). This can complicate revision surgery, with bone loss potentially leading to component loosening and/ or fracture (Bragdon et al., 1996). A direct link has been shown between osteolysis and the volume of wear particles produced by an implant (Smith and Unsworth, 2000). Volumetric wear is inversely proportional to material hardness, leading to the incorporation of hard-on-hard bearing surfaces in order to reduce wear (Smith et al., 2001).

Multi-directional motion (cross-shear) at contacting surfaces is a key factor involved in the wear of UHMWPE in hip replacements (Kang et al., 2008a; Kang et al., 2008b; Turell et al., 2003). Linear motion paths will cause 'strain hardening' and ultimately increase the materials resistance to wear. Conversely, cross-shear motion will cause both tensile and shear forces in multiple directions. This will likely lead to strain hardening in one direction, yet high levels of wear in the perpendicular axis (Turell et al., 2003; Wang et al., 1997a). Saikko and Calonius (2002) reported a linear relationship between the directional change of a velocity vector and the amount of wear in THRs *in vitro*. Turell et al. (2003) complimented this work by showing how the motion path shape (linear vs multidirectional) influences the wear factor (Figure 10). Cross-shear motion at the hip joint is discussed in more depth within section 1.5.3..

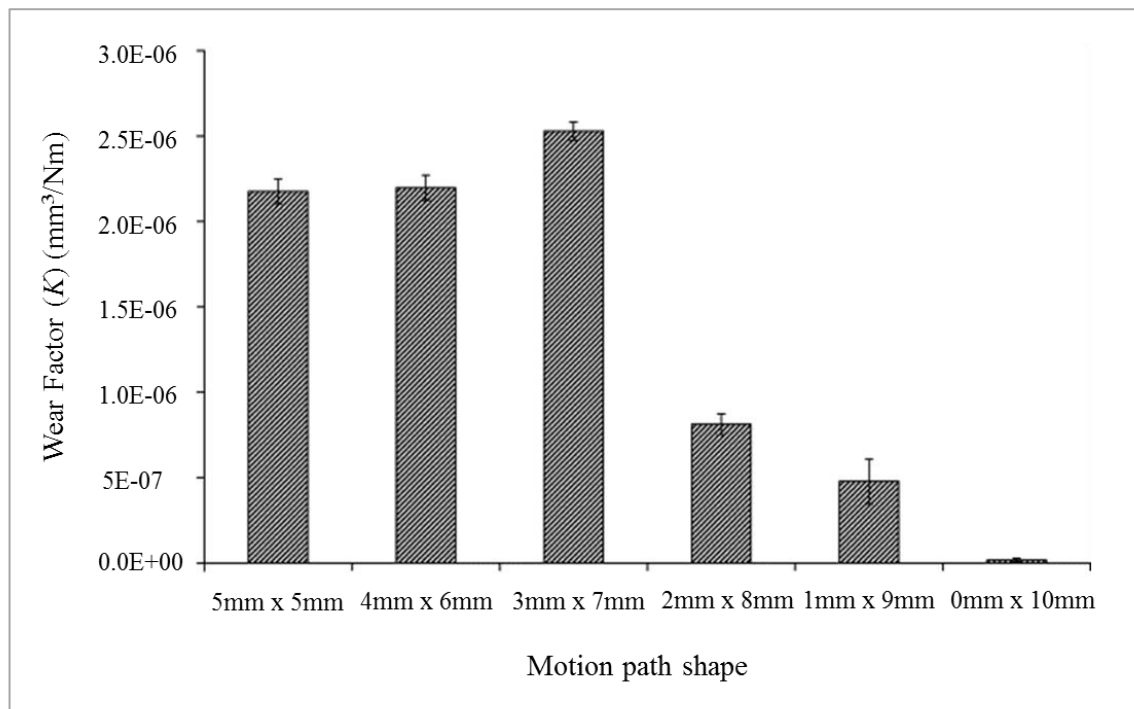


Figure 10. Comparison of wear factors for five different rectangular motion path patterns and linear tracking. Adapted from Turell et al. (2003).

1.5.2.1. *In Vivo* Wear

An UHMWPE acetabular component has been shown to wear against metal at a rate of approximately 0.1 mm/ year (40 mm³/ year) (Griffith et al., 1978; Hall et al., 1996; Livermore et al., 1990; Oonishi et al., 1998; Shaju et al., 2005). With the thickness of cups generally equalling less than 6 mm, this level of wear can be expected to take 60 years before the plastic is worn through (Wang, 2001). For this reason the complete wear through of the acetabular cup is unlikely *in vivo*, although wear debris does have the potential to lead to osteolysis and the potential for loosening/ revision surgery (Wang, 2001). Edge loading of the femoral component on the rim of the cup is a well-documented mechanism for accelerated polyethylene wear *in vivo* (Al-Hajjar et al., 2013; Al-Hajjar et al., 2017; Al-Hajjar et al., 2010; Walter et al., 2004). Movement of the joint centre, due to wear, may reduce the range of motion of the bearing and ultimately lead to impingement and failure of the prosthesis.

1.5.2.2. *In Vitro* Wear

1.5.2.2.1. Joint Simulation

Joint simulators have been used for over three decades and are designed to replicate the loads, motions and environmental conditions that are expected to occur for a joint

replacement *in vivo* (section 1.4.2.). Wear simulator studies indicate that wear rates for common bearing surfaces (ceramic/ metal on polyethylene) yield results between 0.03 mm and 0.4 mm per 10^6 cycles (Bennett et al., 2008; Dowson and Jobbins, 1988; Saikko, 1996; Smith and Unsworth, 2001). This replication of walking suggests that wear is likely to be relatively low and that the size of wear particles and physiological implications are the primary issue. Variation between studies is likely due to a number of factors including, but not limited to: simulator manufacturer, number of axes of motion (influencing cross-shear), type of lubrication and type of bearing surface. Studies must continue to aim to replicate human motion more accurately by understanding the tribological variation between individuals and simulating movements other than walking. Additionally, the introduction of microseparation, stumbling and start-up-stopping in simulators may further improve the realistic representation of motion (Kang et al., 2006). **However, the activities causing severe cross-shear loading, edge loading and microseparation, remains unclear.**

1.5.2.2.2. *Computational Wear Simulation*

Theoretical computational models allow specific factors to be easily isolated in order to investigate the effects and wear mechanisms involved (Kang et al., 2006). Theoretic wear studies will often implement a finite element method in order to predict the contact pressure at the articulating surfaces (Kang et al., 2006). An issue is that this can be time consuming to build and compute (Kang et al., 2006). Another method is an elasticity equation, which allows for the accurate estimation of the contact pressure at the acetabular cup (Bartel et al., 1985; Jin et al., 1999). Although worn areas have shown similarities between experimental and computational results, when validated with a hip simulator study, computational work has previously been shown to underestimate volumetric wear by up to 30% (Kang et al., 2008a).

Kang and colleagues (Kang et al., 2006) developed a contact and wear model for a hip implant. The model allowed for the estimation of contact pressure on the femoral head and UHMWPE cup using finite element modelling and an elasticity equation. Key parameters included in the model were femoral head radius, acetabular cup wall thickness and both the elastic modulus and Poisson's ratio for UHMWPE. The study modelled both ceramic and metal femoral heads articulating on a UHMWPE cup. The wear equations (Equations 3 and 4) were applied to the simulation in order to assess the volume of wear. Both cumulative, linear and volumetric wear showed linear progression with respect to time, whereas a larger wear rate was observed in the early stages (bedding in period).

Following one million cycles, wear rates were relatively consistent, with measured linear and volumetric wear rates at 0.047 mm/year and 28 mm³/year, respectively. These figures are comparative to those seen in the simulator studies previously discussed in this chapter, suggesting reliability in the results.

1.5.3. Motion Path Trajectories

Complex relative motions occur between the femoral head and acetabular cup during locomotion. As motion occurs in different directions, a cross-shear force is applied to the polymer surface at a THR. Multidirectional or 'cross-shear' motion has been described as a key factor in the production of wear debris (Bennett et al., 2002; Bragdon et al., 1996; Ramamurti et al., 1996; Wang et al., 1996; Wang et al., 1997a). During unidirectional linear tracking, a polyethylene cup will experience strain hardening, in which UHMWPE molecules are stretched and orientate preferentially in the direction of sliding, ultimately increasing wear resistance. However, the multi-directional motion expected to occur at the hip during walking will lead to both tensile and shear force in a number of directions (Wang, 2001; Wang et al., 1998; Wang et al., 1997b; Wang et al., 1996; Wang et al., 1997a). Although strain hardening may occur in one direction, the surface will experience high levels of wear in the perpendicular direction (Turell et al., 2003; Wang et al., 1997a). The inclusion of cross-shear motion is crucial to the accurate prediction of polyethylene wear, through simulator and computational study (Kang et al., 2008b; Knight et al., 2005). Wear paths between bearing surfaces can be tested experimentally by fixing a hard pin to the acetabular cup, which will scratch the surface of the femoral head when mounted in a joint simulator (Barbour et al., 1999; Barbour et al., 2000). To truly understand this mechanism, however, realistic motions, loading and lubrication regimes must also be replicated.

A generic theoretical model was proposed by Wang (Wang, 2001; Wang et al., 1996) stating that cross-shear is influenced by multi-directional sliding, frictional work and cross linking intensity. The trajectory of relative motion, at the point of contact between the femoral head of the implant and the acetabular cup, can be described as the 'motion path'. The motion path represents the actual path taken by a single point, or by multiple representative points, on the femoral head as it passes through a movement cycle (Ramamurti et al., 1996). The size and shape of these paths has been shown to influence wear of UHMWPE in THRs. Paths are generally expected to display a quasi-elliptical or rectangular shape during the gait cycle, although variations have been identified between

different gait patterns for subjects (Barbour et al., 1999; Bennett et al., 2000; Ramamurti et al., 1996; Turell et al., 2003; Wang et al., 1997a). The wear rate has been found to vary along a motion path, with higher instantaneous cross-shear occurring at points where the path changes direction (Dressler et al., 2011). Additionally, the number of turns in a path was found to be directly proportional to cumulative wear. Through pin-on-plate testing, Dressler and colleagues identified high wear rates immediately following a 90° change in direction. This wear rate, however, was found to drop to near zero should linear sliding follow the turn. This transition was reported to occur over the distance of <5 mm, after the change in direction (Dressler et al., 2011).

More recently, pin-on-disk testing has indicated that although cross-shear wear is elevated at angles as low as 40°, this does not significantly increase with an increase in the angle. A statistical difference was not identified between wear rates at 40°, 70° and 90° changes in direction (VanLaanen, 2013). It is important to note that the contact area between surfaces will contain an infinite number of loci points, meaning that an identified motion path will overlap with adjacent paths within the same area (Figure 11) (Barbour et al., 1999). Not only is wear related to the motion path shape; it is specifically dependent on the crossing of motion path trajectories (Ramamurti et al., 1996).

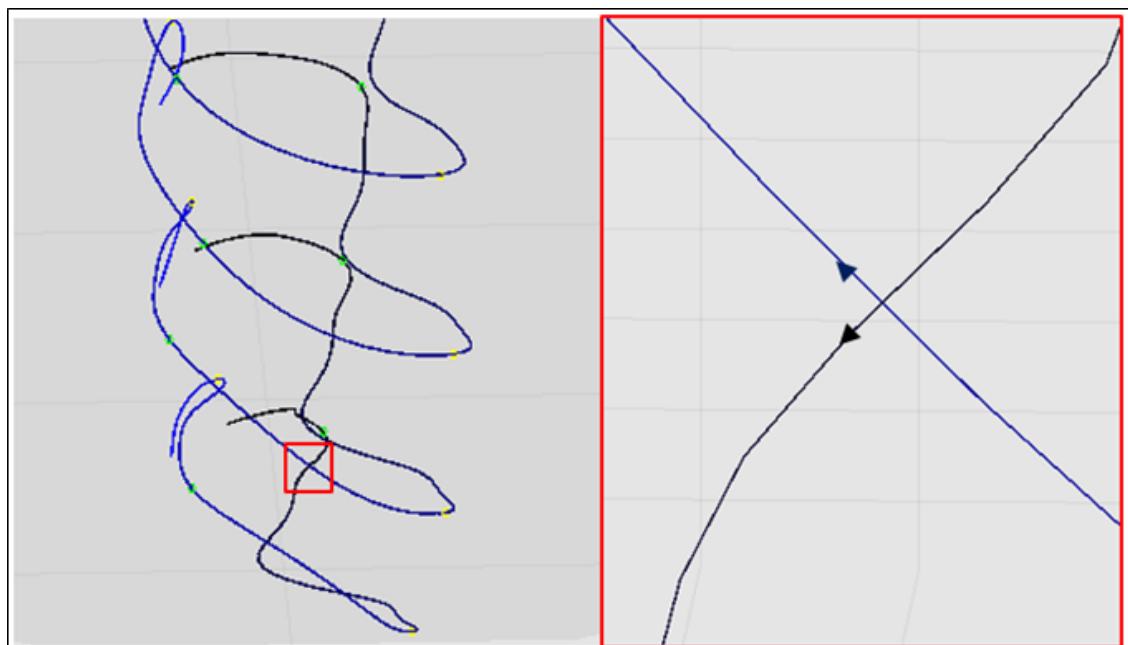


Figure 11. Multiple overlapping hip motion paths are shown for one walking gait cycle from first initial contact (black) to second initial contact (blue) (left). The crossing of motion path vectors are magnified within the red box (right) and demonstrate the point at which the polyethylene liner would experience high cross-shear.

Aspect ratios (ARs) provide a method of quantifying the degree of multidirectional cross-shear motion, through analysing three-dimensional motion paths. The AR is calculated by the division of the width of a motion path, at a specific point on the femoral head, by the height (Figure 12). The ‘width’ of the trajectory is measured as the maximum dimension of a line perpendicular to the line of maximum ‘length’ (Bennett et al., 2002). A wide, open motion path will result in a smaller AR, when compared to a narrow shape, representing the potential for more multidirectional motion and wear. Narrow elliptical shapes have the potential for an AR of anything between 1 and ∞ , with higher ARs indicating more linear motion and therefore the potential for strain hardening and lower wear rates (Bennett et al., 2008; Saikko and Caloni, 2002). Another way to quantify motion path data is the sliding distance. This is the absolute 3D distance transversed by a single point on the femoral head, in relation to the acetabular cup surface, during motion. An increased sliding distance and decreased AR is associated with increased wear (Bennett et al., 2002). Generally, motion paths are calculated through computational methods and can be validated using hip simulators.

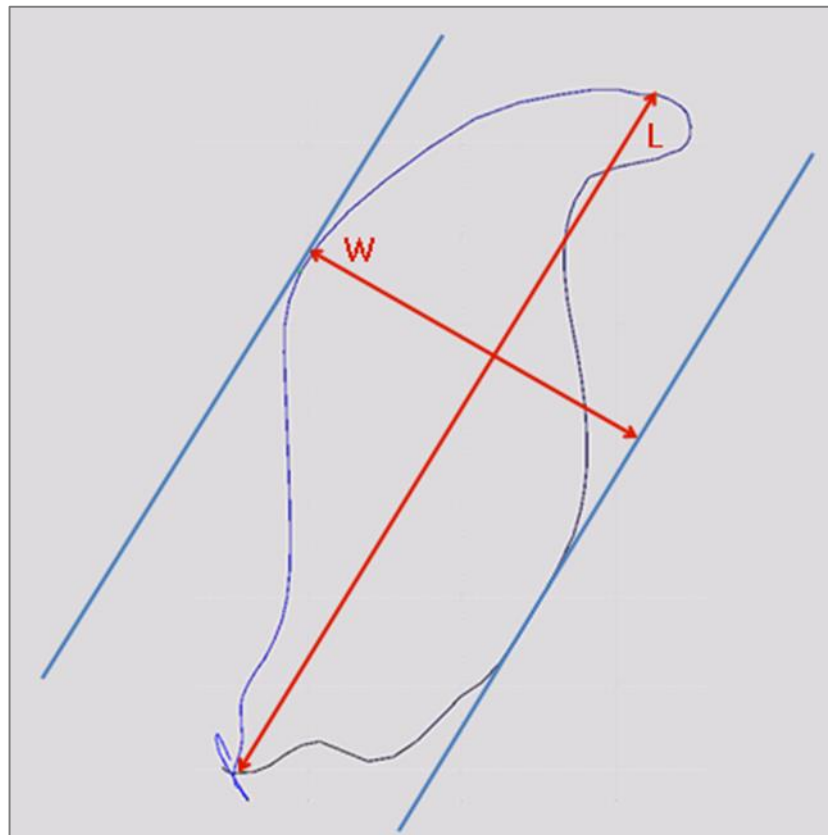


Figure 12. Quantification of a walking motion path, through dividing length/height (L) by the perpendicular width (W), thus resulting the aspect ratio.

1.5.3.1. Hip simulator

Physiological motions have been used within the Leeds Mk II simulator, in order to analyse motion paths at the hip (Barbour et al., 1999). Motion paths were traced on multiple femoral head points, relative to the acetabular cup. Motion paths showed elliptical shapes with 'complex tails'. The tail or 'figure of eight' was seen at the extreme points of flexion and represents the generation of transverse friction forces around heel strike (initial contact). As would be expected, the elliptical wear path showed significantly higher wear than a linear path (58.3% increase in wear rate). It is important to address that *in vivo* data is likely to show higher wear rates than simulator testing due to femoral head scratching, older acetabular cups (which may increase oxidation and degradation) and variation in the magnitude and frequency of exercise (Barbour et al., 1999).

More recently, Turell et al. (2003) incorporated 6 articulating patterns into an AMTI OrthoPOD™ pin-on-plate hip simulator. Analysis of wear tests suggested that motion paths will have a significant impact on UHMWPE wear. Square motion paths (5 mm x 5 mm) with lower ARs showed significantly increased volumetric wear, when compared to linear paths (1 mm x 9 mm, 2 mm x 8 mm, 0 mm x 10 mm) with higher ARs. These findings support work by Barbour (Barbour et al., 1999) and the theory that wear rate is dependent upon the shape of motion paths, which is ultimately dependant on the gait cycle.

Calonius and Saikko (2002) found changes in the shape of wear paths to alter the corresponding wear volume, thereby supporting the theory that multidirectional motion will impact wear levels. Eight contemporary hip simulators were tested with the same ISO input kinematics: BRM, Advanced Mechanical Technology Institute (AMTI), Munich, Leeds Mk I (physiological anatomical simulator), ISO 14242-1 simulator motions, Durham Mk II, Leeds Mk II and ProSim. Results showed variation between different simulators, with both linear and circular motion paths seen on the femoral head. It is also notable that slight differences were seen between motion paths on the femoral head and the acetabular cup; this is because one bearing surface must be computed as stationary, to determine the movement of one component in relation to the other. Differences seen between simulators are due to the way in which motion is applied. The majority of simulators apply motion in the Euler sequence 'abduction/adduction, internal/external rotation, flexion/extension'. However, magnitudes and phase angles of the applied motion may vary. The BRM simulator showed both the longest sliding distance (34.4 mm) and the lowest mean AR (1.0). In comparison, the shortest sliding

distance was seen with the Leeds Mk II (19.7 mm). Not all ARs were resulted in the paper, but it was shown that motion paths varied between simulators, from circular paths (BRM simulator) and figure of eights (Durham Mk II) to more linear paths (Leeds Mk II). Differences seen between hip simulators highlight the variation in how motion is applied by different manufacturers and begs the question whether the smoothed gait information used in simulators can accurately replicate the complex gait cycle seen clinically. The range of motion path trajectories highlights the need to look at variation between femoral head points, individuals and activities. This may be crucial, in order to accurately replicate cross-shear experimentally.

1.5.3.2. Computational Simulation

Early work on motion paths conducted by Ramamurti et al. (1996) calculated 20 points on the right femoral head (32 mm diameter) for one subject. Points were labelled 1-10 in the superior-inferior (or medial-lateral) direction and 11-20 in the posterior-anterior direction, with points crossing over at the pole of the femoral head (Figure 13). The femoral head and neck was assumed to be orientated in the 'correct' anatomical position of 45° inclination and 20° of anteversion. The 3D computational model showed rectangular and quasielliptical shapes, with variation of the direction, width and length of paths depending on the position of the point on the femoral head. This suggests that the directionality of cross-shear force is varied across the UHMWPE acetabular cup. Notably, some points extended outside the circle of the cup during parts of the gait cycle, a phenomenon reported more recently by Saikko and Calonijs (2002). This represents points where contact was lost with the polyethylene surface and suggests that edge loading may have occurred at some stage. The average sliding distance was calculated as 17.0 mm; this represents the distance travelled (arc length) by points on the femoral head in relation to the acetabular cup surface. Ramamurti et al. (1996) suggested that alterations in the size and orientation of the femoral head, as well as the type of activity, would influence the shape and distance of motion paths. Stair climbing, rising from a chair and athletics were stated as activities which would likely influence the wear paths and therefore potential multidirectional shear forces. However, no evidence has been published to support this claim. It is important to state that Ramamurti et al. (1996) did not use Euler angles, but instead used a fixed Cartesian coordinate system, and did not verify the results experimentally. This may bring the reliability of the results into question, although it is generally accepted that the findings were crucial for the development of methods for understanding motion paths and cross-shear at the hip.

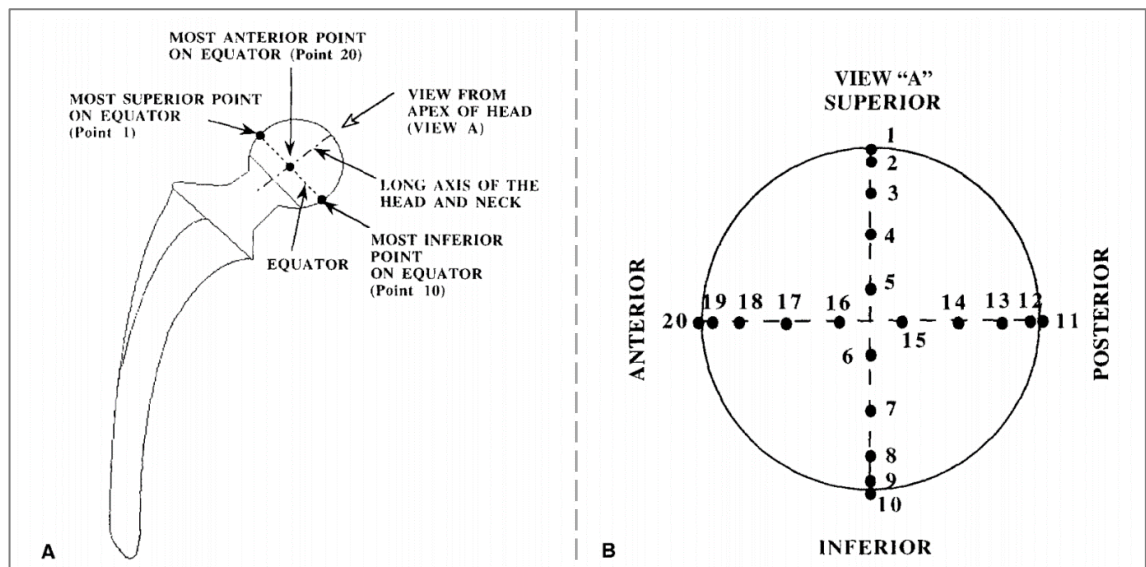


Figure 13. Anteroposterior view of a generic femoral stem, indicating important landmarks on the femoral head (left). View from the apex of the femoral head, showing 10 points running on a semi-circle from superior to inferior and 10 points running from posterior to anterior. The 20 points seen within the adapted image, represent locations where motion paths were calculated by Ramamurti et al. (1996). It is noteworthy that in the current study, although the same point locations were used, ‘inferior-superior’ was referred to as ‘medial-lateral’ and points were numbered differently.

By developing the method put forward by Ramamurti et al. (1996), Bennett et al. (2000) designed a MATLAB simulation programme in order to generate motion path trajectories for 19 THR patients and 9 normal subjects. Gait analysis was performed on all subjects and kinematic information was input to the programme in order to identify 20 points on the surface of the right femoral head. The femoral neck was assumed to be at 20° anteversion for all cases. In keeping with similar studies, Bennett et al. (2000) identified variation in the shape, length and direction of motion paths, including: oblong, quasielliptical, figure of 8 and longitudinal shapes. The average sliding distance was reported as 22.3 mm for normal subjects and 18.1 mm for hip replacement patients. A positive correlation was identified between wear and the inverse of the sliding distance ($R^2 = 0.28$). The maximum distances transversed by a single point were generally seen at the superior, anterior and posterior points of the femoral head. However, this was not quantified in any detail. Sliding distance is well accepted as an important factor for wear and highlights the need to assess activities other than walking, which may show increased sliding at the cup surface.

In a follow up study using the same data, Bennett et al. (2002) determined loci points in 3D, before being plotted in 2D to allow for the mean AR to be calculated. Although 2-D plotting is not as accurate as 3D, differences in the AR are likely to be minimal between the two methods. When comparing normal subjects to THR patients, the patient group exhibited a greater average AR (4.5 compared to 3.5). A positive correlation was identified between wear and the inverse of the AR ($R^2 = 0.35$). This was to be expected given the implications for multidirectional motion and suggests that a small, thin path will cause less wear than a long, wide path. Variation was seen between subjects for the AR and was attributed to natural variation in gait patterns.

ISO walk data (Paul, 1966) has been used for input hip angular data, to compute the relative motion between the femoral head and acetabular cup (Calonius and Saikko, 2002; Calonius and Saikko, 2003; Saikko and Calonius, 2002). Alongside this, motion paths were validated using a sharp pin embedded into the acetabular cup, which when used in a joint simulator, produced grooves on the femoral head. All simulators showed variation in path shape, across the femoral head. Additionally, considerable variation was seen between simulators, highlighting the influence of different manufacturers and methodologies (Figure 14) (Calonius and Saikko, 2003). When the HUT-3 simulator motion paths were compared to ISO walk data (Paul, 1966), the simulator showed smoother, more elliptical paths (due to the smoothed input data). Sliding distance and velocity were both increased for the HUT-3 simulator, compared to walking, indicating potential limitations in the replication (Calonius and Saikko, 2002; Calonius and Saikko, 2003; Saikko and Calonius, 2002). This demonstrates the potential error that can be embedded within the data during the smoothing process.

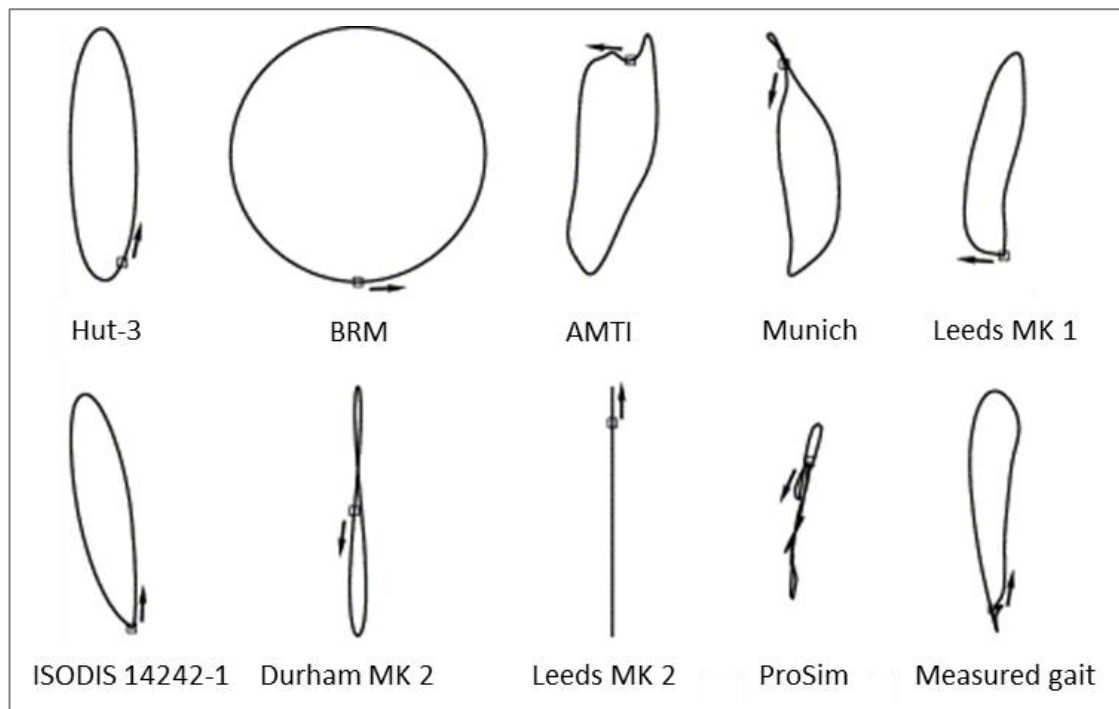


Figure 14. Computed motion paths at the point of resultant loading. Trajectories are presented for different simulators and for ISO walk data from Paul (1966). Square indicates heel strike and arrow indicates direction of sliding. Adapted from Calonius and Saikko (2003).

More recently, Kang et al. (2008b) developed a computational model in which the degree of cross-shear was quantified for a polyethylene pin articulating against a metal plate. The cross-shear ratio was defined as the frictional work (perpendicular to the principle molecular orientation), divided by the total frictional work. Cross-shear can ultimately be defined as linear motion divided by transverse motion. Pin contact point cross-shear was influenced by its position and showed variable magnitudes due to the continuously changing pin rotation and therefore frictional force direction. Pin motion was varied, ranging from a purely linear track with a cross-shear ratio of 0, to a maximum rotation with a cross-shear ratio of 0.254. Cross-shear was shown to increase the wear factor by more than fivefold, when compared to unidirectional wear.

A large scale study by Bennett et al. (2008) investigated the relationship between multidirectional motion at the hip joint in terms of AR, sliding distance and wear rate. The study included 164 hip replacement patients, all of which participated in gait analysis, allowing for the computational quantification of multidirectional motion. Three-dimensional wear paths were identified for subjects, using 20 points on the acetabular cup. Motion was then quantified through the AR of two-dimensional wear paths produced

during the gait cycle. The average predicted wear for subjects was 0.14 mm/year and the average AR equalled 4.02 (range 2.13 to 10.87). Motion paths were varied, from wide, open paths to thin, longitudinal paths. The average sliding distance was reported as 19.2 mm. Although a greater wear rate was expected to be associated with the inverse of the AR, the correlation was reported as weak. There was, however, a positive correlation reported between sliding distance and wear rate. The lack of association between the mean AR and wear underlines the multifaceted nature of wear, with factors such as local lubrication, loading conditions and the presence of third body particles important contributors which are difficult to quantify *in vivo*. The femoral head surface roughness was identified as a key factor which was not controlled during this study and which may influence wear results by affecting the friction coefficient.

Barnett (2009) computed motion paths for a number of points across the femoral head and acetabular cup. Following this, cross-shear was calculated for individuals during normal walking gait. Generally, quasi-elliptical motion paths with complex tails were observed. Some variation could be seen across the femoral head, with complex figure-of-eight shapes also present. Variation was evident both between patients (due to gait technique) and between femoral head points. As seen previously, a number of motion paths fell outside of the hemisphere of the acetabular cup. Cross-shear ratios were reported between 0.20 and 0.35, with wear rates of approximately 30 mm³/ year. It is noteworthy that the study calculated cross-shear across the contact area, as opposed to the entire femoral head. This sets Barnett's findings apart from previous work, such as Ramamurti's work, which did not appreciate the importance of contact area to the accuracy of cross-shear data (Barnett, 2009; Ramamurti et al., 1996). Motion paths were validated using the Leeds ProSim hip wear simulator, which employed flexion/extension and internal/external rotation to replicate walking gait. Sharp stainless-steel pins were attached to nine points on the polyethylene acetabular cup in order to produce scratches, which represent the motion paths on the femoral head. Due to the smooth input cycles used for the simulator, the scratches exhibited smooth shapes. Barnett (2009) stated that when comparing motion paths from the simulator to those seen computationally, similarities were evident and confirmed the validity of the motion path calculation.

The most recent study to assess motion paths was conducted by Budenberg et al. (2012) and compared healthy subjects to a post-THR leg length inequality (LLI) group. Findings were consistent with previous work, with computational results indicated mostly circular and quasi-elliptical shaped motion paths for healthy subjects. The LLI group

demonstrated similar motion path shapes to the healthy group, albeit with a significantly lower mean AR (healthy: 1.89; LLI: 1.76). A key error within this study is that the ARs lower range limit was reported as 0.16. Given that the AR should divide the height by the width, this value should always be ≥ 1 . For this reason, it is possible that human error has influenced these results during the measurement of ARs.

1.5.3.3. Summary of Motion Paths

Research suggests that the average sliding distance for THR patients can be expected to fall between 17.0 mm and 19.2 mm (Bennett et al., 2008; Bennett et al., 2002; Saikko and Calonius, 2002). Motion paths between bearing surfaces at the hip vary between and within subjects, showing oblong, quasielliptical, longitudinal and complex figure-of-eight shapes. The average aspect ratio for walking is expected to fall between 1.7 and 4.5 (Bennett et al., 2008; Bennett et al., 2002; Budenberg et al., 2012). However, it important to appreciate that whilst computational studies provide predictions of the interaction of bearing surfaces, the results are an estimation and ultimately reliant on comparisons with simulator and *in vivo* study. Both Barnett (2009) and Saikko and Calonius (2002) validated computational models through hip simulator studies, suggesting that the trigonometric methodology holds reliability. Many computational models calculated motion paths and mean aspect ratios across the entire femoral head surface area (including positions not in contact and outside of the geometry of the surface). Assessing specific wear paths that will be directly contacted by the resultant hip reaction force, as seen in Calonius and Saikko (2003), may provide more meaningful data. Alongside this, incorporating contact area, as seen in work by Bennett, is likely to be beneficial when drawing conclusions from motion path data (Archard, 1953; Bennett et al., 2008; Bennett et al., 2002).

Calonius and Saikko (Calonius and Saikko, 2003) highlighted the importance of sliding velocity when analysing bearing surfaces in a joint, as increasing velocity will decrease friction and is therefore likely to reduce wear. To take this a step further, calculating sliding acceleration may provide a method for quantifying changes in direction of a path, thus predicting the instantaneous cross-shear. It is important to address the multifactorial nature of wear, not just for motion paths, but also factors such as microseparation and edge loading. For this reason, it is crucial to analyse both global biomechanics (hip angular motion) and local biomechanics (motion paths, hip reaction force and contact area) synonymously.

The literature suggests that motion path trajectories are likely to be closely linked to individual biomechanics and activity type. However, research into the motion paths of a range of activities is lacking. Assessing motion paths for a range of individuals and activities is likely to be beneficial to the understanding of cross-shear wear. More specifically, the calculation of aspect ratios, sliding distances/ velocities and contact area would provide a deeper understanding of how global kinematics influence localised motion at the hip. Coupling this with corresponding hip reaction forces is also crucial, in order to understand the nature of potential force tracks. Ultimately, incorporating this information into joint simulators, in order to replicate accurate physiological motion, may improve the reliability of testing conditions.

1.5.4. Edge Loading

Edge loading can be defined as contact of the femoral head on the edge of the acetabular component of a THR. Edge-loading may occur when the resultant hip reaction force passes near to the edge of the acetabular component (Kwon et al., 2012). More specifically, loading of the acetabular cup within a distance of $\leq 10\%$ of the radius has previously been described as edge loading (eg. within 1.4 mm of a 28 mm diameter acetabular liner) (Kwon et al., 2012). This suggestion was based upon edge-wear scars observed from retrievals (Kwon et al., 2010).

Although the long term success of THR is encouraging, edge loading has been identified as a contributing factor to the failure of prostheses *in vivo* (Hua et al., 2016) through disrupting the fluid-film lubrication between components and increasing wear levels (Liu et al., 2006). Numerical studies have indicated contact of THR components outside of the rim of the cup (Mak et al., 2002; Underwood et al., 2012). Alongside this, retrievals have shown deep wear scars (stripe wear) across the rim of the acetabular cup (Figure 15 and 16) (Kwon et al., 2010; Matthies et al., 2011; Nevelos et al., 2001; Walter et al., 2004). Al-Hajjar and colleagues identified that edge loading can be replicated using hip simulators at appropriate adverse conditions (such as micro-separation and cup orientation) (Al-Hajjar et al., 2013). Micro-separation (during the swing phase of gait) will shift the femoral head laterally, relative to the acetabular cup. At heel strike, the head may contact the rim of the cup whilst sliding back into the centre of rotation, thus producing stripe wear and increased wear rates (Al-Hajjar et al., 2010). The separation of components has been shown through fluoroscopy work, further adding to the reliability surrounding this phenomenon (Lombardi Jr et al., 2000). This work has ultimately lead to an adaptation to the ISO standards for pre-clinical testing of THR components (ISO

14242). The evidence strongly suggests that edge loading is likely to influence the long term success rates of THR.

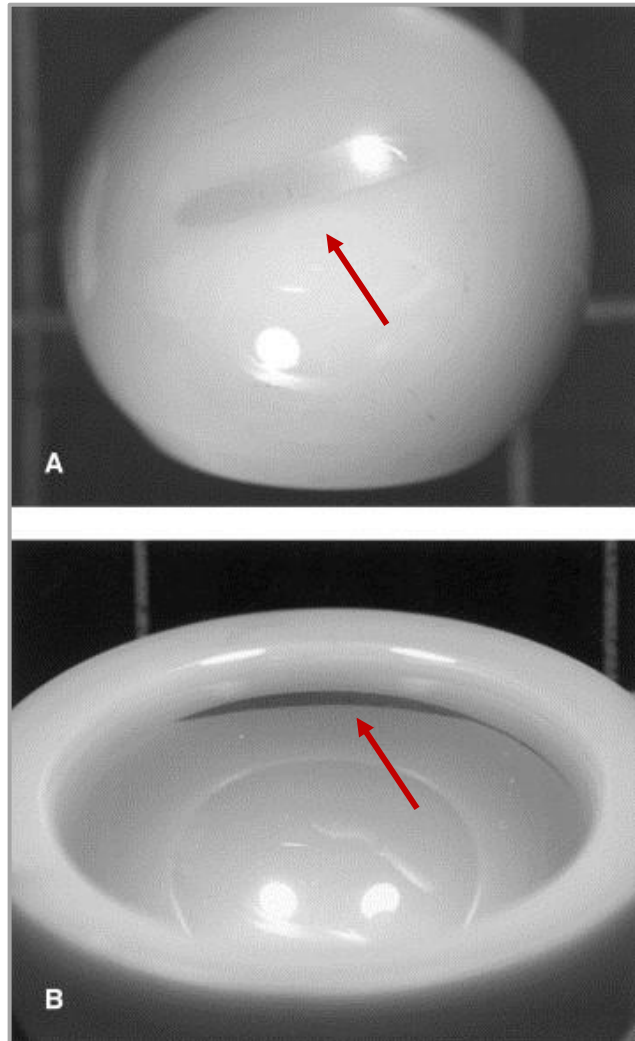


Figure 15. (A) The stripe on this retrieved alumina ceramic head has been coloured with felt pen for analysis. (B) The stripe on this retrieved alumina ceramic liner has been coloured with graphite pencil for photography. Adapted from Walter et al. (2004).

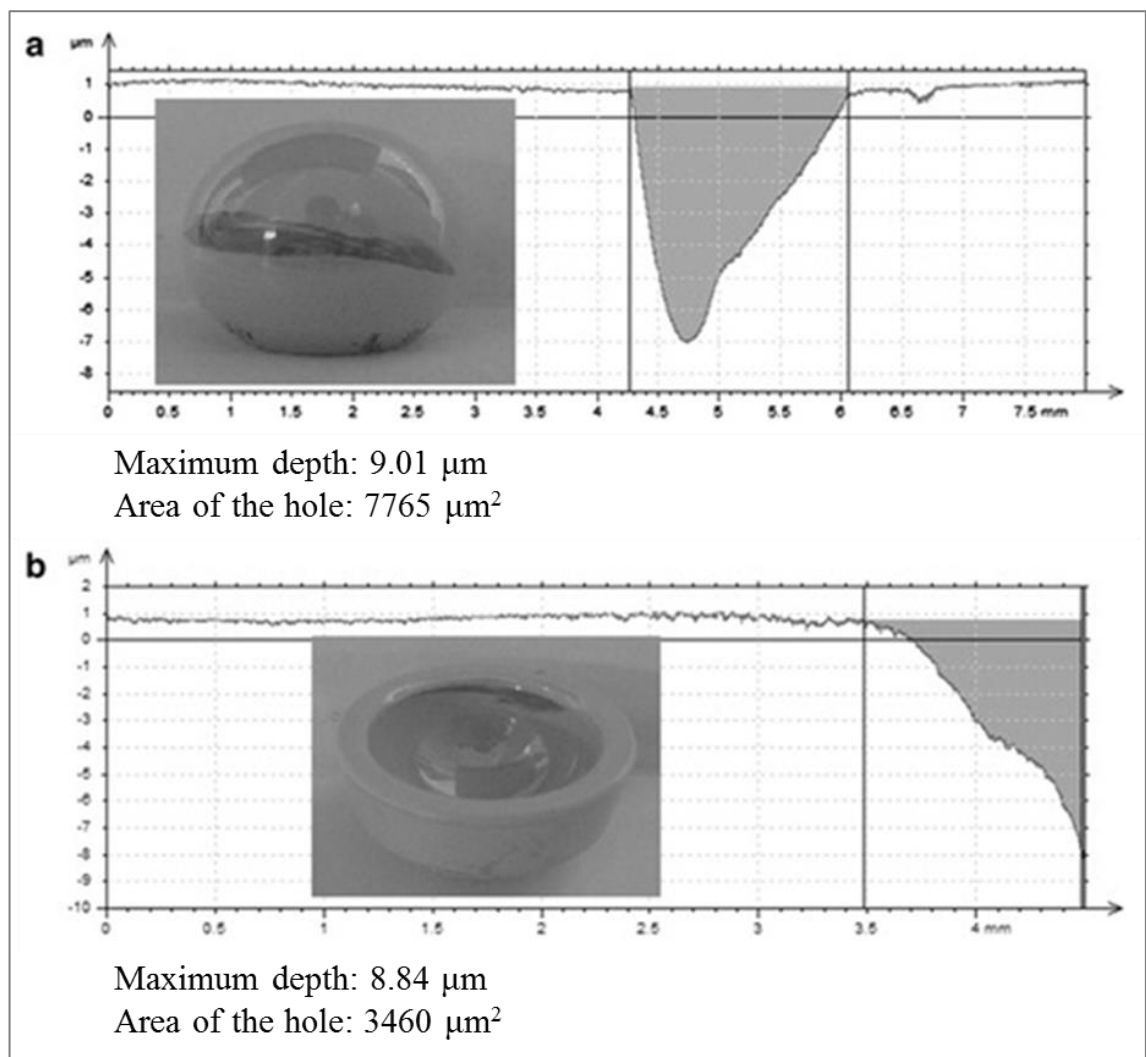


Figure 16. Example of Talysurf traces and photographs of femoral head and acetabular cup components demonstrating stripe wear. Wear depth and area is shown in micrometres (μ). Adapted from Al-Hajjar et al. (2013).

The cause of edge loading at the hip has been related to prosthetic design (radial clearance and cup coverage), malposition of components (cup angle and head offset), impingement and dislocation (Hua et al., 2016; Kwon et al., 2010; Kwon et al., 2012). Individual activity patterns have also been identified as a contributing factor to the level of edge loading (Mellon et al., 2011). Deep flexion activities are believed to exacerbate edge loading (van Arkel et al., 2013), however there is limited research on the level of edge loading associated with specific activities. Through a finite element model, Hua et al. (2016) predicted edge loading to occur during normal walking, ascending and descending stairs during steep inclination angles ($\geq 55^\circ$). As the inclination angle increased, the predicted duration of edge loading for activities increased. This duration was also found to be activity specific, with normal walking showing the longest duration of edge loading.

Activities which did not show edge loading included standing up, sitting down and knee bending. However in contrast to this, Walter et al. (2004) suggested that ceramic head retrievals indicated that the majority of edge loading occurs during high flexion activities, other than walking (Figure 17). Determining the level of edge loading for a range of activities may provide an insight to the reasons for prosthesis failure amongst certain individuals. This must then be validated experimentally, by incorporating the adverse conditions set out in ISO 14242-4 (2018).

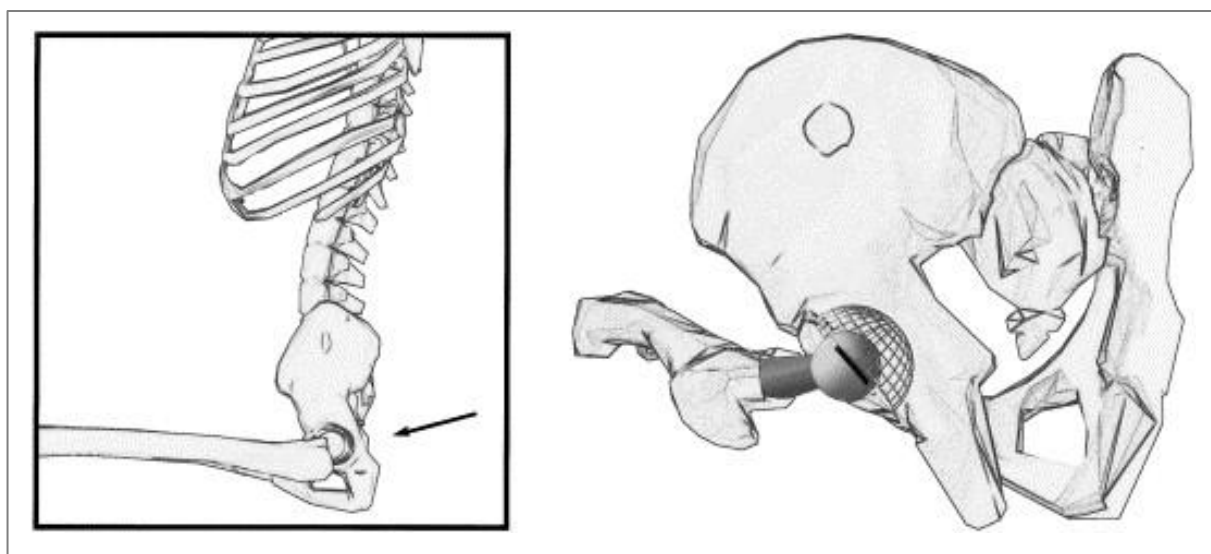


Figure 17. Posterior edge loading. In this adapted illustration, an anteverted stem and an anteverted cup are seen. With the hip flexed to approximately 90°, such as when the patient rises from a chair or climbs a high step, the load is directed approximately posteriorly. Therefore, the posterior edge of the liner produces a line of contact on the superior surface of the head, which is highly retroverted with respect to a line of latitude on the head and remote from the equator. This fits the wear pattern seen in nine patients within the study by Walter et al. (2004).

1.5.5. Summary

Despite concerns in the literature regarding the wear of polyethylene, there are few cases of hip replacements actually wearing out (Livermore et al., 1990). The generation of debris, which may impact long term performance of the prosthesis, appears to be a more relevant issue. Therefore, it seems sensible to address the fundamental reasoning behind the production of excessive wear debris, rather than continuing to test the long term wear of prostheses. Investigation into motion paths of the femoral head on the acetabulum has begun to provide this answer by considering the degree of multidirectional cross-shear

and the likelihood of edge contacts. Analysing aspect ratios and sliding distances for motion paths may be crucial for determining a potential cause for excessive wear. Combining this with edge loading information and across a range of different movements may allow for the identification of key contributing factors which will promote excessive wear of a THR for an individual.

1.6. Hip Replacement and Physical Activity

Previously, joint replacements have typically been used for elderly, inactive individuals. Developments over the past twenty years have seen technological advancements both in terms of implant design and manufacturing. This has led to a number of new groups in the population receiving replacements, including younger, more active patients (Clifford and Mallon, 2005). A considerable functional improvement can be seen after a total hip replacement (THR), with most patients walking pain and assistance free after 6-12 months post-surgery (Brown et al., 1980; Murray et al., 1975; Murray et al., 1972). High levels of intense activity in patients with joint replacements is likely to lead to increased forces crossing the reconstructed joint, increased wear between surfaces and increased stress at the bone-implant fixation surface, when compared to low levels of activity (Healy et al., 2008). The general consensus regarding suitable sports/ activities post-surgery is diverse (Clifford and Mallon, 2005). It is difficult to determine the appropriateness of activity for patients, due to the high level of variability between individuals as well as biomechanical differences between specific activities (Morlock et al., 2001; Schmalzried et al., 1998). However, research relating to THR and activity levels has begun to provide an argument for the appropriateness of common activities, as well as the impact these may have on the replacement itself.

1.6.1. Physical Activity Levels

1.6.1.1. Walking

The average number of gait cycles for a healthy, asymptomatic individual is generally expected to reach between one and two million per year, with variation between individuals and patient groups (Schmalzried et al., 1998). Through the use of pedometers, Schmalzried (2012) documented a 45 fold range in hip replacement patient activity (ranging from 395 to 17,718 steps per day). A patient averaging 17,718 steps per day would expect to complete over 3 million gait cycles per year – this is considerably lower than the 1 million cycles that is commonly used in pre-clinical testing of hip replacements. Patients below the age of fifty are perceived to be at a higher risk of early post-operative failure, partly due to their higher levels of activity (Kuhn et al., 2013). Schmalzried et al. (1998) identified a 30% increase in average steps per day for hip/ knee replacement patients under sixty, compared to those over sixty. Schmalzried (2012) later identified decreases in both gait cycle frequency and walking speed for older hip replacement patients. Mean activity was decreased by 16% from the time of implantation (2.04 million

walking cycles per year), to 10-13 years postoperatively (1.71 million walking cycles per year). Contrastingly, Sechriest II et al. (2007) suggested that THR patient activity for under 50's is likely to be closer to an older population than initially believed. Sechriest and colleagues evaluated activity levels for thirty-four patients at a mean of 6.3 years after THR. An average of 1.2 million cycles per year was identified for this relatively young sample (mean age 42 years). These findings were similar to results for older THR patient age groups, such as the reported value of 1.4 million cycles per year for individuals at an average age of 58 (Goldsmith et al., 2001), 1.3 million cycles at an average age of 71.5 years (Silva et al., 2002) and 1.2 million cycles at an average age of 72 years (Schmalzried et al., 2000).

Schmalzried et al. (1998) reported that men walked 28% more, on average, than women. In general, there is contrasting data regarding age and activity levels for patients and it is clear that some variation will occur between subgroups (NJR, 2018). Clinically, there has been debate as to whether differences are present between genders, with regards to THR survivorship, as females have been found to be more at risk of revision surgery (NJR, 2018; Prosser et al., 2010). A prognostic study by Kostamo et al. (2009) has indicated that this is unlikely, with no statistical differences found between survivorship and revision rates for 3461 patients. This was supported by more recent work, suggesting that differences in survivorship/ revision rates between genders are likely to be due to a combination of other factors, such as implant design (Donahue et al., 2016; Prosser et al., 2010).

Pedometers are likely to underestimate walking activity, as data is recorded indirectly through pelvic oscillations (Schmalzried, 2012; Silva et al., 2002). A microprocessor worn on the ankle yields more accurate results than a pedometer, allowing for the collection of walking speed and pattern data. Through the use of microprocessors, Schmalzried (2012) found average THR patient activity to approach 2 million gait cycles per year. The use of a pedometer in the same study, found significantly lower results, at 0.9 million cycles (under recording by an average of 34% cycles per day). Taking into account potential underestimation and variation between subjects, it is reasonable to expect hip replacement patients to range between 1 and 2 million gait cycles per year. One million gait cycles per year would equate to \approx 5500 steps per day (this is considerably lower than the recommendation of 10,000 steps) (Choi et al., 2007). This raises the question of what 'active' really means for a THR patient group and whether there are patient sub groups who do regularly meet the recommendations on steps per day. It is

important to note that recording gait cycles through the use of pedometers/microprocessors, means that activities other than walking could not be investigated. The studies within this section were unable to comment on the types and intensities of activities for individuals. Although level walking is likely to be the most common activity completed by individuals, it is also important to appreciate that lower levels of more dynamic activities could potentially lead to a higher risk of wear to a THR.

1.6.1.2. Common Daily Activities

Walking makes up a large percentage of an individual's daily activity and may be the chief cause of THR wear, due to the high number of repetitions. With this being said, it is still important to address participation in other daily activities.

Generally, THR surgery is associated with regained function and increased activity levels (when compared to pre-operative). Following interviews, Visuri and Honkanen (1978) showed a number of marked improvements to patients following a THR (n = 294; mean follow up 4.3 years). Walking ability was limited in 95% before the surgery and in just 12% post-operatively. The amount of individuals unable to clean their homes (pre-operative: 67%; Post-operative 16%), complete a shop (46%; 10%), tie their shoes (75%; 29%) and pull on stockings (43%; 3%) were all reduced after the operation. The proportion of patients who were able to take care of themselves increased from 21% preoperative to 62% after the operation. Kuhn et al. (2013) found similar results, supporting the suggestion that activity levels will increase after the operation. THR patients (aged ≤ 50) increased their mean daily steps (30% increase) and engaged in more low (1.9% increase), moderate (1.4% increase) and high (0.4% increase) intensity activity after the operation. It is important to appreciate that with reduced pain, patients may engage in potentially high risk activities (in relation to prosthesis wear) post-operatively.

Morlock et al. (2001) used a portable activity monitoring system to identify the frequency and duration of daily activities for 31 THR patients. Data was recorded throughout the day, for ten hours (mean age 62.5 ± 11.5 years). Two inclination sensors for the thigh and the calf, alongside one goniometer positioned at the knee, allowed information for the activities lying, sitting, standing, walking and stair climbing to be recorded. Sitting was found to be the most frequent activity (44.3% of the time recorded), followed by standing (24.5%), walking (10.2%), lying (5.8%) and stair climbing (0.4%). It is also notable that 14.8% of activity could not be recognised. The median number of steps and stairs used was found to be 6048 and 164, respectively. The number of steps per day resulting from

this study is approximately 20% higher than those reported in previous literature (Morlock: 6048 steps; Schmalzried: 4988 steps) (Schmalzried et al., 1998). This may be due to a more active subject group, or possibly due to an overestimation within the algorithm used for the system. However, based on the study, 1.1 million cycles could be expected per year. This seems realistic, albeit slightly low, when compared to previous findings for post-operative THR patients (Goldsmith et al., 2001; Schmalzried, 2012; Schmalzried et al., 2000; Sechriest II et al., 2007; Silva et al., 2002). Sitting was identified as the most frequent activity by individuals and is therefore an activity which is important to investigate in relation to the hip tribology. Sitting for long periods of time might be expected to have a negative impact on the lubrication at the joint and therefore promote contact at the bearing surfaces (through squeeze film at the joint). Additionally, we are rarely stationary when sitting. Reaching, leaning and crossing legs are just three movements which may lead to potential cross-shear motion and edge loading at the hip joint. When you combine this with 'stand to sit' and 'sit to stand' movement, it is likely to be an important activity to investigate further.

Stair climbing has been identified as a daily task which may be detrimental to the components of a THR due to an increased hip range of motion, compared to level walking (Bergmann et al., 2001; Bergmann et al., 1995; Kotzar et al., 1995). Morlock et al. (2001) reported variation between subjects for stair climbing. Just 20% of individuals did one or more stair climbing cycles for every nine walking cycles, whereas approximately 25% of patients did less than one stair climbing cycle per fifty walking cycles. The difference between the two walking activities was identified as increases in anteroposterior axes of the abductor and hip contact forces during stair climbing. Additionally, the vastus medialis was only activated during stair climbing. In addition to stair climbing, stumbling (Bergmann et al., 2001; Bergmann et al., 1993; Stolk et al., 2002), rising from a chair and any high impact tasks (Stolk et al., 2002) can be classified as a potential risk for THR patients.

1.6.1.3. Sport and Recreation

Visuri and Honkanen (1980) evaluated the effects of THR surgery on recreational exercise behaviours through retrospective interviews (n = 539; mean follow up 4.2 years). In keeping with previous work (Visuri and Honkanen, 1978), a THR showed a positive effect on the activity levels of patients following the operation, compared to pre-operative. A number of activities showed increases in participation after THR, including walking (53% increase), cycling (22%), swimming (17%) and skiing (9%). Additionally,

the patient's abilities to perform everyday activities was found to increase alongside a decreased dependence on other people.

More recently, a large scale longitudinal study across four centres used questionnaires to investigate activity levels of 420 individuals who underwent THR due to advanced hip OA (Huch et al., 2005). Most patients (97%) had performed sporting activities during their life and 36% had maintained sports activities at the time of surgery. Five years on from the operation, this had increased to 52%. Biking, hiking and swimming were identified as important lifetime sports activities among patients undergoing hip replacement. Few patients continued these activities pre-operatively, however most patients returned to and maintained these activities at the 5 year follow up. Biking (>50%), swimming and hiking (>40%) were found to be the most popular activities at the 5 year follow up point. Few individuals continued participation in gymnastics (<20%), jogging, tennis and dancing (<5%). Reported activity levels of THR patients before and after the operation were consistent with findings published by Wylde et al. (2008), supporting the reliability of the study (Morlock: Pre-op: 36%; Post-op: 52%; Wylde: Pre-op: 35%; post-op: 61%) (n = 2085). The slight difference between findings is likely due to the fact that Wylde and colleagues reported data for five types of joint replacements, rather than just THRs.

Wylde et al. (2008) indicated variation across the pre-operative activity engagements of joint replacement patients. Age (sport participation declined with age), gender (participation higher for males) and type of operation were cited as contributing factors. Of the 26% of individuals who stated that the replacement did not allow them to continue sport post-operatively, pain was the most commonly cited reason. The most obvious decline was seen for high-impact sports, with individuals not returning to participate in badminton (51% of patients), tennis (38%) and dancing (32%). The most common pre-operative sports were low impact activities including swimming, walking and golf. Cycling, walking, bowling and swimming have all been reported as common activities in which patients engage in prior to a THR (Chatterji et al., 2004; Huch et al., 2005). There appears to be a shift from participation in high-impact sports (such as jogging and tennis) before surgery, to an increase in low-impact sports (such as exercise walking and aqua aerobics) after the hip replacement surgery (Chatterji et al., 2004).

Although large scale studies have reported THR patient engagement in physical activity, both pre and post-operatively, the potential influence of these activities on the prosthesis is not yet understood. Other than walking, there is a gap in the literature that should be

addressed. Other relevant activities should be analysed biomechanically, in relation to the wear of the prosthesis, in order to truly understand the appropriateness of post-operative physical activity.

1.6.2. Physical Activity and Wear

Whilst there are obvious benefits of exercise for THR patients, average wear rates have been found to be higher for a very physically active group of individuals (2.1 mm), when compared to an inactive group (1.5 mm) (Gschwend et al., 2000). It was predicted that a longer follow up may show higher levels of aseptic loosening for the active group. The active individuals that showed high wear rates and osteolytic changes at the interface, regularly hiked in mountains for prolonged periods of time. The findings suggest that there may be a limit to the positive effect of exercise, for THR patients, likely related to the forces exerted at the hip during certain activities.

Contrastingly, both Dubs et al. (1983) and Widhalm et al. (1990) found revision rates to be significantly higher for an inactive group, when compared to an active group. Contradictions in the literature and a lack of detailed tribological studies into daily activities, have led to inconsistencies in expert opinions about recommendations for activities following THR. However, when considering the ‘baby boomer’ generation and older athletes aiming to return to high level, competitive sport (Gomez and Morcuende, 2005; Meira and Zeni, 2014), an understanding of the influence of physical activity post-THR is clearly important.

Ritter and Meding (1987) suggested that “intelligent participation” in sport such as walking, golf and bowling will avoid harm to the prostheses (Ritter and Meding, 1987). Similarly, Huch et al. (2005) concluded that moderate activity is safe, yet high impact sports (such as soccer and tennis) should be advised against following THR. In light of the lack of evidenced information on athletic activity post joint replacement, McGrory et al. (1995) conducted a survey on twenty-eight orthopaedic surgeons and fifteen fellows/residents at the Mayo Clinic. Responses suggested that participation in low impact activities should be recommended (including bowling, cycling, swimming and golf), whereas high-impact sports should be avoided. In 1999, fifty-four members of the Hip Society completed a survey in order to identify recommendations for forty-three athletic activities (Healy et al., 2008). Activities were classified into “allowed,” “allowed with experience,” or “not recommended”. The same survey was then completed again in 2005. The number of sports which were classified as “allowed” increased, suggesting the

development of a more relaxed view of exercising with a joint replacement by the members in 2005 (Healy et al., 2008) (Table 1). The general consensus was that low-contact, low-impact activities could be recommended post-operatively. High-contact, high-impact activities, however, should be discouraged. A potential flaw in this suggestion is that some low impact activities may still present a high degree of cross-shear force at the joint, owing to the potentially complex motion occurring at the hip. Additionally, edge loading may occur, thus reducing the contact area and increasing surface stress (Al-Hajjar et al., 2013; Al-Hajjar et al., 2017). Even at low loads, this may be detrimental to the prosthesis if taking place regularly over a prolonged period. Again, this highlights the need to assess a range of activities and the influence they may have on the interaction between bearing surfaces at the joint.

Table 1. Results of the Hip Society survey. Activities are compared between 1999 and 2005 meetings, meaning some removed/ added activities may not be included. Adapted from Healy et al. (2008).

Allowed	1999	2005	Allowed with Experience	1999	2005
Stationary cycling	✓	✓	Bowling	✓	
Ballroom dancing	✓	✓	Canoeing	✓	
Golf	✓	✓	Road cycling	✓	
Shuffleboard	✓	✓	Hiking	✓	
Swimming	✓	✓	Horseback riding	✓	✓
Doubles tennis	✓		Cross-country skiing	✓	✓
Normal walking	✓	✓	Rowing		✓
Bowling		✓	Ice skating		✓
Canoeing		✓	Roller skating		✓
Road cycling		✓	Downhill skiing		✓
Square dancing		✓	Stationary skiing		✓
Hiking		✓	Doubles tennis		✓
Speed walking		✓	Weight lifting		✓
			Weight machine		✓
No Consensus	1999	2005	Not Recommended	1999	2005
Square dancing	✓		Baseball	✓	
Fencing	✓		Basketball	✓	✓
Rowing	✓		Football	✓	✓
Ice skating	✓		Gymnastics	✓	
Roller skating	✓		Handball	✓	
Downhill skiing	✓		Hockey	✓	
Stationary skiing	✓		Jogging	✓	✓
Speed walking	✓		Rock climbing	✓	
Weight lifting	✓		Soccer	✓	✓
Weight machine	✓		Squash/racquetball	✓	
Baseball		✓	Singles tennis	✓	
Gymnastics		✓	Volleyball	✓	
Handball		✓			
Hockey		✓			
Rock climbing		✓			
Squash/racquetball		✓			
Singles tennis		✓			
Volleyball		✓			

In a similar attempt to understand activity recommendations post THR, 139 surveys were completed at the 2007 annual meeting for the ‘Association for Hip and Knee Surgeons’ (Swanson et al., 2009). Similar to the data from 2005 reviewed by Healy et al. (2008), higher-impact activities were generally discouraged. More than 95% of the returned surveys suggested that engagement in low-impact activities including walking, stair climbing, cycling, swimming and golf should never be discouraged. Of the activities commonly discouraged, variation could be seen between surgeons. The majority discouraged jogging, sprinting and skiing, although surgeons operating on a higher volume of patients were generally more lenient with which activities are acceptable. It is noteworthy that of the recommendations collated in 1999, 2005 and 2007, there was no strong scientific evidence behind suggestions. The guidelines largely rely on the clinical experience of surgeons.

Activity recommendations from the 2005 Hip Society survey were compared to patient self-reported activity levels following THR (Delasotta et al., 2012). The 61 patients (all aged below 50) largely participated in recommended activities, with just two individuals engaging in those discouraged (squash and jogging). Findings indicated that younger patients appear to be more active than previously thought. The use of self-reported activity data is a limitation, as not only are participants liable to overestimate their total activity levels, it is also possible that patients will avoid admitting to ignoring recommendations from their physician. Furthermore, activities regularly engaged in by patients such as golf, swimming and cycling may still have a negative influence on the prosthesis, given the lack of scientific understanding of the activities. Although weight bearing is low in these activities, it is possible that cross-shear motion and edge loading will occur at the hip and potentially contribute to wear of the acetabular cup. It is therefore crucial to assess activities such as these, to scientifically determine the potential influence they may have on bearing surfaces of the hip implant. This will ensure patients are not being recommended to perform certain activities without a detailed biomechanical assessment of their appropriateness beforehand.

1.6.3. Post-operative Functionality

Gait analysis studies have identified a number of post-operative adaptations for THR patients, when compared to healthy control groups. Adaptations occurring at the hip have included altered extensor and abductor capabilities (Foucher et al., 2007; Perron et al., 2000), asymmetric ground reaction forces (McCrory et al., 2001) and joint loading

(Kyriazis and Rigas, 2002; Li et al., 2014). Despite an excellent post-operative functional outcome for most individuals, THR patients often experience gait alterations for over one year after the operation, with optimal hip performance generally reached between 8-10 years (Foucher et al., 2007; Kyriazis and Rigas, 2002). Investigations into THR patient gait has been conducted using both experimental (measuring prostheses/ gait analysis) and computational approaches. Results from *in vivo* studies are crucial for validating computational hip replacement design using computational modelling, stress calculations and hip joint simulation devices. Additionally, they provide evidence for physiotherapists when addressing the rehabilitation process of patients.

1.6.3.1. Instrumented Implants

Early investigations have established that mathematical predictions often overestimate contact forces, in comparison to data from instrumented implants (Bergmann et al., 1993; Heller et al., 2001; Stansfield et al., 2003). Similar overestimations were seen between direct measurement (Davy et al., 1988; Rydell, 1966) and mathematic predictions (Crowninshield et al., 1978) for walking up stairs and rising from a chair. Hip reaction forces for THR patients, during level walking, were found to range between 2.4 and 4.1 proportional to body weight when measured *in vivo* (Bergmann et al., 2001; Bergmann et al., 1993; Brand et al., 1994; Damm et al., 2013a; Damm et al., 2013b; Davy et al., 1988; Kotzar et al., 1991; Schwachmeyer et al., 2013).

Bergmann et al. (2001) completed the most notable investigation into hip joint loading during common daily activities. Nine activities were included: level walking (slow, normal and fast), walking upstairs, walking downstairs, sit to stand, stand to sit, a two-one-two legged stance and knee bend. Gait analysis was completed for four individuals who were 17 months post-operative from a THR (average age 61 years). Results focused on loading of the femoral implant component. Hip reaction forces and gait patterns showed small intra-subject variability and larger inter-subject variation for patients. A number of key findings were described by Bergmann. The rotational contact force (causing much of the implant torque) was larger when going up stairs than for level walking. On average, peak forces were 9% higher when walking downstairs, compared to walking upstairs (proportional to body weight). A sit to stand demonstrated increased hip loading than a stand to sit, although this was still lower than level walking. During level walking (4 km/h), the hip joint was loaded at an average of 2.4 proportional to body weight. This was slightly reduced when standing on one leg and knee bends showed considerably decreased loading at the hip joint. From the activities assessed, results

indicate that level walking and stair ascent/descent may cause the highest loading to the prosthesis. Bergmann and colleagues provided a good analysis of these common activities. However, a number of regular daily activities were not included within the study. Additionally, the study failed to consider any cross-shear analysis for the activities. Although loading is important, without the corresponding cross-shear motion, the implications are limited.

1.6.3.2. Gait Analysis

A number of common manoeuvres were assessed biomechanically by Nadzadi et al. (2003), with the aim of investigating dislocation risks for individuals with a THR. Joint kinematics and hip joint reaction forces were calculated for seven high dislocation risk manoeuvres. Ten subjects were included in the study (Male: 5 Female: 5; Mean age: 49.7 years; Age range: 44-59 years). The activities completed were: sit to stand from a normal seat (46 cm); sit to stand from a low seat (39 cm); seated with crossed legs; seated while reaching to the floor; standing while reaching to the floor; standing while turning upper body away; lying supine; rolling. Sit to stand from a low seat was ultimately found to be the movement most prone to dislocation of those measured. A number of the manoeuvres, specifically sitting while reaching to the floor and standing while reaching for the floor, showed peak hip contact forces notably higher than the 4-5 times body weight normally associated with walking gait. Both reaching whilst sitting and reaching whilst standing showed the highest magnitudes for posterior (9 kN and 6 kN, respectively) and inferior (2 kN and 1 kN, respectively) hip reaction forces. Reaching whilst standing also showed the highest magnitude of medial hip reaction force at 3 kN. Nadzadi et al. (2003) suggested that hip reaction forces may be increased for activities in which the upper-body centre of gravity is offset to the hip joint centre. For example, the upper-body centre of gravity was approximately 40 cm offset relative to the hip joint centre during the sit to stand, compared to just 15 cm during the double support phase of walking. The implications for this is that higher muscle forces would be required for certain activities (such as standing/ sitting and reaching to the floor) in order to achieve moment equilibrium. This would consequentially lead to higher joint reaction forces. When considering this, Nadzadi and colleagues (2003) claimed that hip reaction forces of up to 10 times body weight would not be unrealistic for some activities.

Talis et al. (2008) further investigated the biomechanics for a number of daily activities, using two embedded force platforms. Unilateral hip replacement patients completed maximal voluntary contractions, quiet standing, standing up from a chair and walking

were all assessed. Patients demonstrated significantly increased loading of the non-operated limb, compared to the operated side. This asymmetry was particularly noticeable when standing up from a chair.

More recently, stair negotiation was assessed for patients (18 months post-operative) who have had either THR or hip resurfacing arthroplasty (Queen et al., 2013). These groups were then compared to a healthy control group. The two patient groups were found to ascend stairs with an increased peak hip flexion angle and decreased hip extension angle, when compared to the control. The patient group also descended stairs with decreased hip flexion moments. The importance of these findings is supported in the literature by the identification of higher levels of micro-motion, mechanical instability and therefore damage of the prosthesis associated with stair negotiation (Kassi et al., 2005; Stolk et al., 2002).

Ewen et al. (2012) reviewed the literature surrounding post-operative gait for hip replacement patients. Seven studies were reviewed in order to complete a meta-analysis for the results. All studies assessed gait patterns for individuals 6 months post-operative and compared results to healthy control groups. This time frame ensured that patients had completed suitable levels of rehabilitation (Perron et al., 2000). Five of the seven studies reported kinetic, kinematic as well as spatiotemporal data. Reductions in walking velocity, stride length and sagittal hip range of motion was observed for THR patients. It was noted that the range of motion may be impacted by the orientation of the stem in the frontal plane. Further to this, a number of adaptations were seen for hip moments. The orientation of the femoral stem and the type of surgical approach were identified as major contributing factors to the gait adaptations observed. The femoral stem orientation may alter the range of motion at the hip (this is also dependent on the acetabular cup angle), whereas the type of surgical approach will influence the type of muscular damage ensued. Although abductor damage has been reported for anterior, lateral and posterior approaches, the anterior approach is generally thought to result in less damage to the abductor muscles than the other two approaches (Jolles and Bogoch, 2003; Masonis and Bourne, 2002; Meneghini et al., 2006; Moretti and Post, 2017). It is likely that the amount and degree of damage to abductor muscles will have an influence on the level of gait abnormality post-operatively and potentially lead to issues such as Trendelenburg gait (Barry et al., 2018; Müller et al., 2011; Pfirrmann et al., 2005).

The abnormalities identified for hip replacement patient groups highlights the potential functional influences that the surgery may have. There is much to be gained from

tribological analysis of a large healthy group, in order to begin to understand the variation occurring between individuals and the potential influence that different movements have on the bearing surface of a THR. However, it is important to appreciate that patient variability is likely to be large and biomechanical abnormalities may be present when comparing to a healthy group. Above all, it is key to appreciate that stratification of patients is key and that one size does not fit all, when making implications from gait data.

1.6.3.3. Computational Simulations

Previously, hip reaction forces have been calculated computationally using the musculoskeletal modelling software AnyBody (Li et al., 2015; Li et al., 2014). Peak hip reaction force was reported as 3.3 proportional to body weight, for an asymptomatic THR patient group (Li et al., 2014). Although this was of a similar magnitude to a healthy control group (3.4 proportional to body weight), the patient group demonstrated a different force pattern across the movement. Unlike the characteristic double peak seen for healthy subjects, the patient group demonstrated a marked decrease at the second peak (corresponding to the propulsive phase of gait). This was attributed to the difference in functionality between the groups, potentially relating to a decrease in hip range of motion (Li et al., 2014). A later study by Li et al. (2015) reported reduced loading conditions for a THR patient group, compared to the earlier study (3 proportional to body weight). However, similar to the first study, a second, smaller hip reaction force peak was observed.

Computational studies indicate that stair climbing is likely to lead to higher levels of loading at the hip (than level walking), thus impacting the stability of both cemented (O'Connor et al., 1996) and cementless (Kassi et al., 2005) implants. Foucher et al. (2008) assessed the gait of fifteen THR subjects (1 year post-operative) during stair climbing. Peak hip external adduction moments, external rotation moments and initial peak reaction forces were all lower (between 14% and 26%) for THR subjects, when compared to a healthy control group. Alongside this, hip extension moments were dramatically increased for the THR group (78% increase). Abnormal external adduction and rotation moments were attributed to the reduced function of the hip abductors for patients. Whereas the increase in extension moments was attributed to increased activity of the hip flexors, in relation to the hip extensors, during the stair climbing. Interestingly, patient adaptations did not occur alongside an increased hip reaction force (THR group: 3.0 proportional to body weight; control group: 3.5 proportional to body weight). Hip reaction forces were similar to previously reported findings of stair climbing (Bergmann et al.,

2001; Kotzar et al., 1991), suggesting that adaptations to joint moments does not necessarily indicate alterations to hip loading. It is important to appreciate that the walking speed for post-operative patients is likely to be slower for up to 2-4 years (Perron et al., 2003). It could be speculated that patients may experience reduced hip reaction forces during this period.

Although walking tasks have been analysed considerably through computational simulations, there is a lack of research on other common activities. Given the engagement of patients in a range of activities and the *in vivo* data available for movements such as sitting and standing, it seems logical to aim to biomechanically analyse a broader range of movements in relation to a THR.

1.6.4. Summary

Whilst level walking is the most common activity completed by most THR patients, it is important to consider lower levels of more dynamic activities, when considering polyethylene wear. Activities of daily living and dynamic sports/activities may influence prosthesis wear, particularly for younger individuals who may have higher physical activity levels. When considering the current study, it seems reasonable to assume that high impact sports are rarely completed by post-operative THR patients. Walking, low weight bearing sports (such as cycling and golf) and high flexion activities (such as sitting, standing and bending over) are likely to be more relevant for analysis. It may be beneficial to complete a preliminary questionnaire based study in order to further identify common activities for THR patients.

It is important to appreciate that biomechanical adaptations are common for post-operative patients and can be present for a number of years. When assessing the hip tribology for healthy individuals, it is therefore crucial to outline the fact that data for post-operative patients is likely to be much more variable. Additionally, gait analysis focusing on patients should occur at an appropriate time for the individual following successful rehabilitation and avoid activities which may provide a risk to dislocation. Within the current study, it is logical to assess a healthy population group, in order to replicate the motions of a younger, more active, asymptomatic THR group that is at a high risk of failure.

2. Aim and Objectives

The primary aim for this study was to investigate the link between global hip biomechanics and localised tribological variables, in relation to theoretical wear of the polyethylene surface of a total hip replacement, and at a tissue engineered hip cartilage substitution. Further to this, the study aims to provide information relating to rehabilitation/biomechanics and biotribology goals for post-operative hip replacement patients. This was met through the biomechanical and tribological analysis of eighteen healthy participants, who completed thirteen common daily activities. Specific objectives focussed on hip joint biomechanics and assessed activities in terms of:

- 1) Angular kinematics.
- 2) Cross-shear motion (relative motion paths between surfaces).
- 3) Joint reaction forces.
- 4) Edge loading (femoral head contact on the acetabular rim).

Kinetic and kinematic data was collected through the use of a 13 camera Qualisys Oqus system (QualisysTM Medical AB, Goteborg, Sweden) synchronised with two AMTI force platforms (AMTI, Advanced Mechanical Technology Inc., Watertown, MA, USA). Hip angles and moments were subsequently calculated within Visual3D (Visual3D standard, v5.01.18, C-Motion, Germantown, MD, USA).

Cross-shear was analysed by calculating the relative sliding motion between the femoral head and the acetabular cup (motion paths). Motion paths were calculated using both a novel Visual3D workspace and a proprietary MATLAB program (MATLAB, 2016, MathWorks, Natick, MA, USA). Motion paths were analysed in detail, thus providing results relating to cross-shear motion, potential lubrication conditions and risk of wear at the hip.

Hip reaction forces were calculated within the musculoskeletal modelling software, AnyBody (AnyBody, version 6.0, AnyBody Technology, Aalborg, Denmark). By combining hip angular data and hip reaction force vectors, edge loading was assessed within a SolidWorks visualisation model (SolidWorks 2017, Dassault Systèmes SolidWorks Corporation, Waltham, MA, USA). Edge loading results provide implications for potential wear at the polyethylene liner in a total hip replacement.

The aim and objectives of this thesis are critically important in relation to pre-clinical testing of hip prostheses, testing of tissue engineered cartilage and understanding the appropriateness of different activities for post-operative hip replacement patients.

3. Overview

3.1. Methods

Four main methodologies were utilised in order to achieve the main aim of investigating the link between global hip biomechanics and localised hip tribology. Movement Analysis method (section 4.2) describes the methodology associated with the collection, processing and analysis of biomechanical gait data. Musculoskeletal Simulation methods (section 5.2) describe the set-up and analysis of multi-body simulations which were run within AnyBody (AnyBody, version 6.0, AnyBody Technology, Aalborg, Denmark). Tribology methods includes the calculation and analysis of motion paths (sections 6.2.1, 6.2.2 and 6.2.3) and the visualisation of potential edge loading of the acetabular rim (section 6.2.4, 6.2.5 and 6.2.6).

Raw data was collected and exported to Visual3D as C3D files. Within Visual3D, raw data was processed in order to result vertical ground reaction forces, hip joint angles and hip joint moments. Further to this, motion paths were calculated from hip angles, for each trial. Hip angles and ground reaction forces were input to the AnyBody TLEM model, where hip reaction forces were calculated. A Python macro was utilised in order to batch process these calculations for all subjects. Joint angles were also exported from Visual3D to MATLAB, where motion path aspect ratios and sliding distances were calculated. Finally, the joint angles and hip reaction forces were input to a SolidWorks visualisation model, where potential edge loading was predicted (Figure 38).

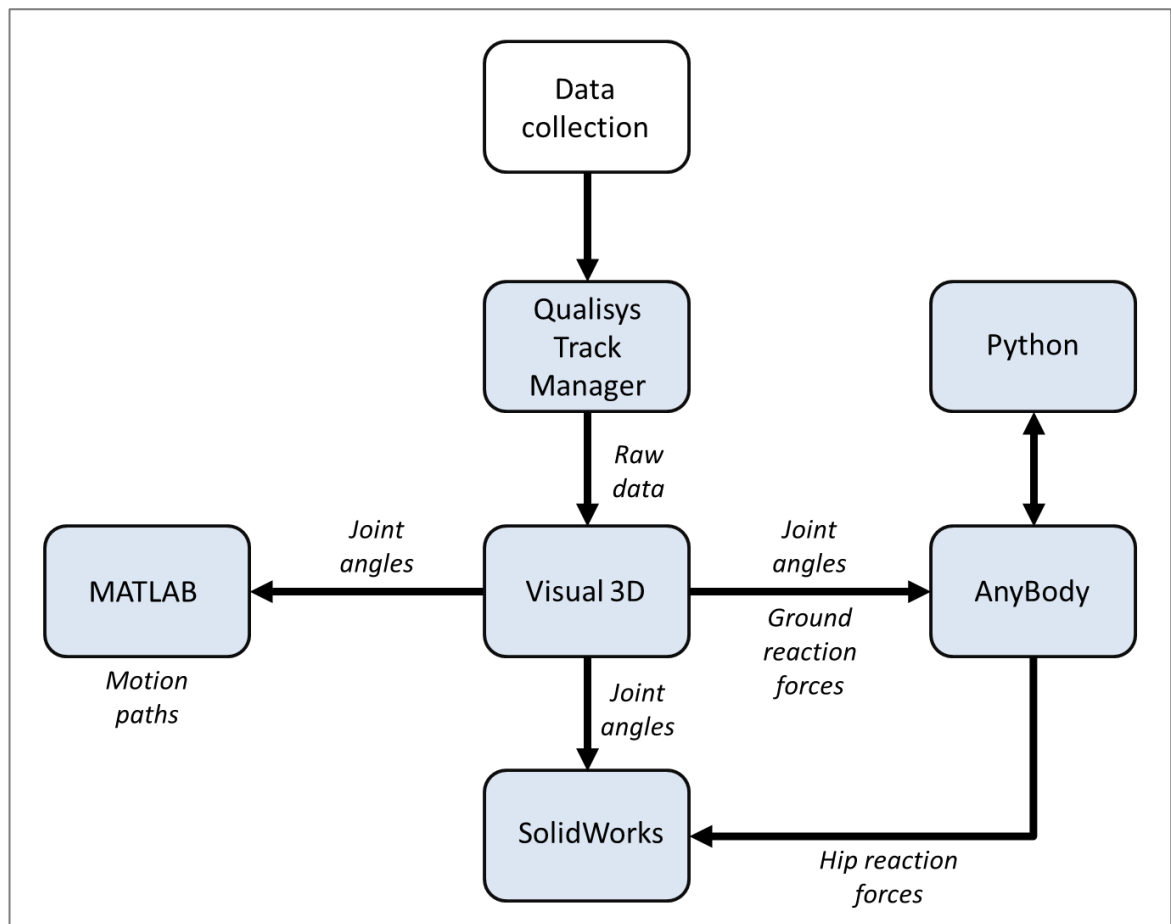


Figure 18. Workflow demonstrating the movement of data between software in order to assess hip tribology.

3.2. Results

Ten healthy male and eight healthy female subjects (Mean \pm Standard Deviation; Age: 44 \pm 19 y; Height: 1.7 \pm 0.1 m; Body mass: 76 \pm 13Kg) completed thirteen common daily activities within a movement analysis laboratory (see full demographics in Table 8). Through the use of retro-reflective markers, an optoelectronic camera system (QualisysTM Medical AB, Goteborg, Sweden) and two force platforms (AMTI, Advanced Mechanical Technology Inc., Watertown, MA, USA), kinetic and kinematic data was collected and synchronised for activities. Each subject completed activities five times, to improve reliability of the data. However, it is noteworthy that for some activities, less than 18 subjects were analysed (Table 9). This was due to various reasons, including an inability of the participant to complete the activity, excessive noise within the data signal and/ or frequent dropping out of a number of marker trajectories.

This chapter results five key biomechanical variables, calculated for each of the thirteen activities (Table 9). Global kinematics are presented in sections 4.3. (Movement Analysis). Ground reaction forces, moments, hip reaction forces and impulses are presented in section 5.3. (Musculoskeletal Simulations chapter). Localised hip motion path trajectories and edge loading is resulted in section 6.3 (Tribology chapter).

Table 2. Demographics for the eighteen healthy subjects who completed thirteen common daily activities within a movement analysis laboratory.

Subject demographics	
N	18
Sex (Male: Female)	10 Male 8 Female
Age Range	20 to 70
Age (Mean \pm SD)	44 \pm 19
Weight Range (kg)	50.2 to 106.1
Weight (kg) (Mean \pm SD)	76.3 \pm 13.1
Height Range (m)	1.5 to 1.8
Height (m) (Mean \pm SD)	1.7 \pm 0.1
BMI (kg/m ²) Range	19 to 35
BMI (kg/m ²) (Mean \pm SD)	26 \pm 4

Table 3. Activities completed and corresponding variables that were calculated. The number of subjects (n) are shown in brackets for each activity and variable. Note that in some cases, subject numbers were reduced due to an inability to process the data reliably. This occurred due to the subject's inability to complete the activity successfully, excessive marker drop-out or excessive noise within the data. The cross (✖) represents activities in which a force platform could not be used.

	Hip angles (n)	Vertical ground reaction forces (n)	Hip moments (n)	Hip reaction forces (n)	Motion path trajectories (n)
Walk	✓ (17)	✓ (17)	✓ (17)	✓ (16)	✓ (17)
Walk turn	✓ (18)	✓ (17)	✓ (18)	✓ (17)	✓ (18)
Incline walk	✓ (18)	✖	✖	✖	✓ (18)
Decline walk	✓ (17)	✖	✖	✖	✓ (17)
Stand to sit	✓ (8)	✓ (8)	✓ (8)	✓ (7)	✓ (8)
Sit to stand	✓ (8)	✓ (8)	✓ (8)	✓ (7)	✓ (8)
Sit cross legged	✓ (14)	✖	✖	✖	✓ (14)
Squat	✓ (11)	✓ (11)	✓ (11)	✓ (9)	✓ (11)
Stand reach	✓ (12)	✓ (12)	✓ (12)	✓ (12)	✓ (12)
Kneel reach	✓ (13)	✓ (12)	✓ (13)	✓ (10)	✓ (13)
Lunge	✓ (17)	✓ (17)	✓ (17)	✓ (13)	✓ (17)
Golf swing	✓ (18)	✓ (18)	✓ (18)	✓ (16)	✓ (18)
Cycling	✓ (10)	✖	✖	✖	✓ (10)

3.3. Discussion

Movement Analysis, Forces and Tribology results are discussed in sections 4.4, 5.4 and 6.4, respectively. Results are then discussed synonymously within the Overall Discussion (Chapter 7). Chapter 7 also discusses implications, limitations and future work for the thesis as a whole.

3.4. Conclusion

An overall conclusion of the thesis is included within Chapter 8. This is followed by References (Chapter 9) and Appendices (Chapter 10).

4. Movement Analysis

4.1. Introduction

Within this chapter, global hip biomechanics are investigated for a range of common activities. The chapter describes the methods involved in the collection and processing of raw kinematic and kinetic data. Global hip joint kinematics are resulted and discussed for each activity. This is then followed by a conclusion, relating to the overall kinematic results. It is noteworthy that although this chapter includes the collection of all raw data, force and tribological results are included within chapters 5 and 6, respectively.

4.2. Methods

This method describes the collection of kinetic and kinematic data for eighteen healthy subjects, completing a range of common daily activities. This was achieved using a 3D optoelectronic camera system synchronised to two embedded force platforms. Following data collection, joint angles, vertical ground reaction forces and hip moments were calculated.

4.2.1. Patient Activity Questionnaire

A review of the literature provided a basis for determining which activities to include within data collection (Morlock et al., 2001; Nadzadi et al., 2003). Furthermore, in the interest of method development, a patient activity questionnaire was sent to the Leeds Biomedical Research Unit (LBRU) at Chapel Allerton Hospital, Leeds. This was circulated by the LBRU Business Manager and was covered by LBRU ethics. The questionnaire was completed by total hip replacement (THR) patients (over the age of 18) and included a wide range of activity related questions (Appendix – section 10.1.). The questionnaire was completed and returned by nine individuals (Mean age: 70 ± 7 ; Gender: 4 male 5 female; BMI: 27 ± 4). All patients had received a THR between 3 and 17 years ago. Of the 9 patients, 5 had a double hip replacement and 3 had also received at least 1 knee replacement. None of the patients had received revision surgery.

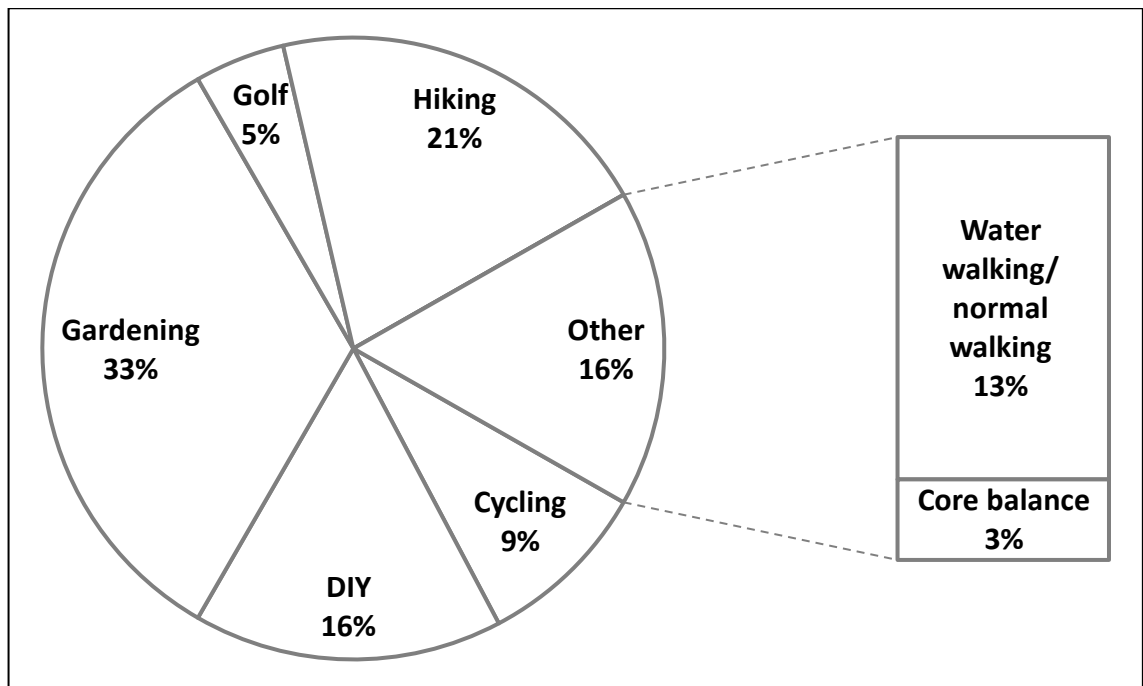


Figure 19. Total time spent per week engaging in activities by total hip replacement patients (n=9). Activities were only included if the collective group engaged for over 2 hours per week.

Figure 18 shows that gardening was the most common activity engaged in by THR patients (33%), followed by hiking (21%) and DIY (16%). It was concluded that alongside walking activities, patients are likely to experience high levels of hip flexion during activities such as gardening and DIY, which involve bending down or kneeling. It was also apparent that cycling, golf and core balance classes (such as yoga and pilates) are common within the THR patient population. When considering the literature alongside the LBRU questionnaire, 13 activities were decided upon to be included within the study. These were a walk, walk turn (at 90° to the left), incline walk, decline walk, stand to sit, sit to stand, sit cross legged, squat, stand reach, kneel reach, lunge, golf swing and cycle. More detail on the activities are presented in (section 4.2.6.).

4.2.2. Ethics for Data Collection

The study protocol was ethically approved according to the guidelines of The University of Leeds Ethics Committee (MEEC 16-021). This process included the completion of a risk assessment form for the movement analysis lab, which highlighted and scored the likelihood and severity of potential risks to the researcher and participant (Appendix – section 10.2.4.). The overall risk was calculated as low. The recruitment strategy was also submitted for ethical approval and involved contacting a range of sports and social groups in Leeds (such as running clubs, bowls clubs and educational groups) via email. A number

of posters were also displayed in and around the University of Leeds campus (Appendix – section 10.2.1.).

When contacted by a potential participant, a Participant Information document was sent to the individual via email (Appendix – section 10.2.2.). Should the individual still be happy to be involved in the study, a Screening Questionnaire (Appendix – section 10.2.3.) was sent to the individual to be completed and returned. The Screening Questionnaire required participants to detail any health issues that they may have, which could cause them to be ineligible for the study. Exclusion criteria included health issues that may present themselves when completing activities of daily living. On arrival to the lab, a consent form was read and signed by the participant (Appendix – 10.2.3.). All participants were made aware that they had the right to withdraw from the study at any time and that a two week cooling-off period was in place following the data collection, in which the data could still be removed from the study.

4.2.3. Lab Set-up

4.2.3.1. Hardware

The movement analysis laboratory is a 10 by 10 meter space, which allowed for the set-up of a thirteen-camera Qualysis Oqus 3D motion capture system (Qualisys™ Medical AB, Goteborg, Sweden), two AMTI (BP400600) force platforms (AMTI, Advanced Mechanical Technology Inc., Watertown, MA, USA) and a computer to synchronise the equipment (Figure 19).

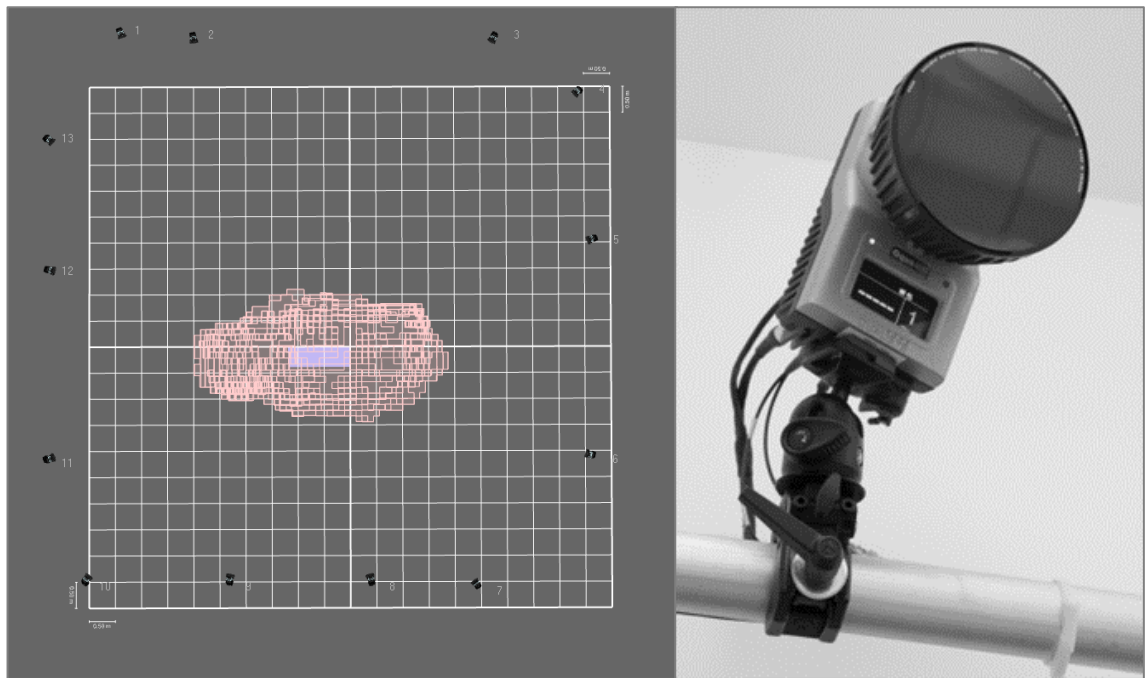


Figure 20. Movement analysis lab space (10 x 10 m) is shown on the left, surrounded by thirteen Qualisys Oqus cameras and containing two AMTI force platforms (blue). The calibrated movement volume surrounds the force platforms. Qualisys Oqus cameras surrounded the movement area and were fixed to a rail running 3 m above the ground (right).

Kinematic data was collected using the optoelectronic motion capture camera system at a sampling frequency of 400 Hz. Cameras were fixed to a 3 meter high rail, in a square around the movement area. This ensured that all markers could be seen in at least three cameras throughout movements, therefore reducing the requirement for interpolation tools to fill gaps in the marker trajectories (Riberto et al., 2013). Ground reaction forces were collected using two, in line, 600 x 400 mm AMTI (BP400600) embedded force platforms. Force platforms were synchronised to the camera system and sampled at 1200 Hz.

4.2.3.2. *Calibration*

The total lab area allowed for a 15 metre walkway. Calibration was completed for the entire 3D movement area prior to data collection. This area was calibrated using an L-shaped reference structure and a T-shaped calibration wand (Figure 20). Four spherical reflective markers were fixed to the L-shaped frame: one at the corner (origin); one on the short arm (200 mm from the origin) and two on the long arm (550 mm and 770 mm from the origin). The frame was fixed to the boundary of the force platform, with the long

arm pointing in the direction of movement (sagittal plane). This allowed for the origin and orientation of body segments to be determined.



Figure 21. L-shaped reference structure and a T-shaped calibration wand required for Qualisys calibration.

The calibration wand was moved through the entire 3D measurement area whilst being rotated and transversed, in three directions, at a uniform speed. Two markers were mounted to the wand, the centres of which were 751.2 mm apart. The Qualisys system was calibrated by analysing the coordinates of each marker, from multiple cameras, thereby resulting in a finite volume which allowed for reliable kinematic information (Franjic and Wozniak, 2014). Calibration was deemed suitable if the standard deviation reconstructed wand length error, analysed through the calibration sequence, was found to be less than ± 0.6 mm. In addition to the kinematic calibration, force platforms were calibrated to zero before each trial took place, thus removing any residual error.

4.2.4. Participant Information

Eighteen subjects participated in the study (10 male and 8 female) (Mean \pm Standard Deviation; Age: 44 ± 19 y; Height: 1.7 ± 0.1 m; Body mass: 76 ± 13 Kg) (Table 2). Participants were recruited from the University of Leeds and local community groups such as running clubs, golf clubs and 'University of the Third Age'. Individuals were largely recruited through poster advertisement and email chains. Inclusion criteria ensured that participants were over the age of eighteen, healthy and free from any injury, illness or pathology which may impact natural gait.

Table 4. Subject demographics for subjects who participated in the movement analysis.

Subject demographics	
N	18
Sex (Male: Female)	10: 8
Age Range (y)	20 to 70
Age (Mean \pm SD)	44 \pm 19
Weight Range (kg)	50.2 to 106.1
Weight (kg) (Mean \pm SD)	76.3 \pm 13.1
Height Range (m)	1.5 to 1.8
Height (m) (Mean \pm SD)	1.7 \pm 0.1
BMI (kg/m ²) Range	19 to 35
BMI (kg/m ²) (Mean \pm SD)	26 \pm 4

4.2.5. Participant Set-up

Participants wore spandex shorts and no top (males) or a tight sports bra (females) in order to avoid unwanted marker movement and allow for accurate positioning of anatomical markers. Any reflective areas on shoes and shorts were covered with black duct tape and any jewellery was removed. Height and weight was collected using a stadiometer and digital scales, respectively. Prior to data collection, thirty-nine 15.9 mm pearl reflective markers were attached to anatomical landmarks on the subject (B & L Engineering, CA, USA). Anatomical landmarks were identified through palpation in accordance with standardised techniques outlined by Jan (2007). Four tracking clusters (four-marker semi-rigid thermoplastic shell) were attached to the thigh and shank in order to define technical co-ordinate systems at the lower limb (Figure 21). The definition and location of markers are outlined in Table 3. Marker positions were selected in order to allow for the definition of body segments in accordance with Visual3D guidelines and previously validated models (Bell et al., 1989; Bell et al., 1990; C-Motion, 2018; Cappozzo et al., 1995). The modelling of body segments is described in more detail within section 4.2.7.3.

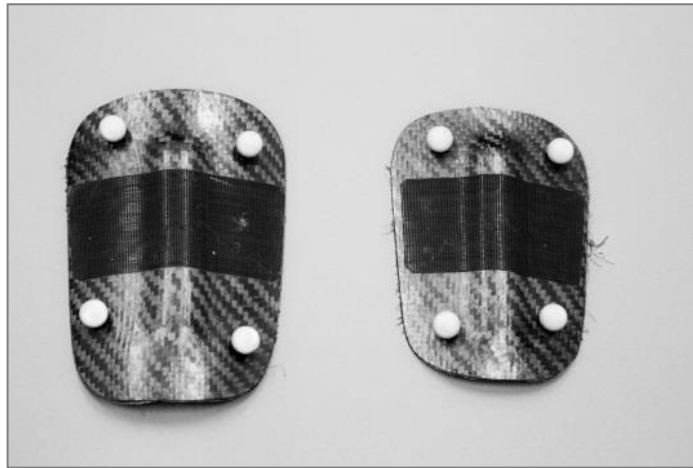


Figure 22. Four-marker semi-rigid thermoplastic shell used as tracking markers during kinematic data collection.

Table 5. Location of external skin markers. Co-ordinate system ‘A’ refers to the anatomical markers and ‘T’ to the tracking markers. Those with both ‘A’ and ‘T’ were used to define both anatomical and technical co-ordinate systems. Markers were mirrored on the left and right side (excluding sternum and vertebra markers).

Marker	Co-ordinate System	Location
SHO	A	Anterior acromio-clavicular joint
MELB	A	Most medial aspect of the medial epicondyle
LELB	A	Most lateral aspect of the lateral epicondyle
WRA	A	Most lateral and proximal styloid process of the ulna
WRB	A	Most lateral and proximal styloid process of the radius
ASIS	A	Anterior superior iliac spine
PSIS	A	Posterior superior iliac spine
GT	A	Most lateral aspect of the femoral head (Greater trochanter)
THI1	T	Lateral aspect of the thigh
THI2	T	Lateral aspect of the thigh
THI3	T	Lateral aspect of the thigh
THI4	T	Lateral aspect of the thigh
MKNE	A	Most medial projection of the medial femoral condyle
LKNE	A	Most lateral projection of the lateral femoral condyle
TIB1	T	Lateral aspect of the shank
TIB2	T	Lateral aspect of the shank
TIB3	T	Lateral aspect of the shank
TIB4	T	Lateral aspect of the shank
MANK	A	Most medial projection of the medial malleolus
LANK	A	Most lateral projection of the lateral malleolus
CAL	A, T	Central aspect of the calcaneus
MCAL	A, T	Medial aspect of the calcaneus
LCAL	A, T	Lateral aspect of the calcaneus
MT1P	A, T	Most medial projection of the base of the first metatarsal head
MT5P	A, T	Most lateral projection of the base of the fifth metatarsal head
MT1D	A, T	Most medial projection of the head of the first metatarsal head
MT5D	A, T	Most lateral projection of the head of the fifth metatarsal head

It is noteworthy that although a full body marker set was used, with a total of 54 markers, the upper body was not modelled. A high number of markers were used to avoid potential marker occlusion and to allow for full body modelling, should it be required in the future.

4.2.6. Data Collection

A static trial was completed prior to the dynamic trials, allowing for the position of anatomical markers to be identified. This standardised static trial required subjects to adopt the anatomical position for three seconds (Figure 22). If markers moved or fell off during a movement, a new static trial was required, in order to ensure the baseline anatomical positions were identified again.

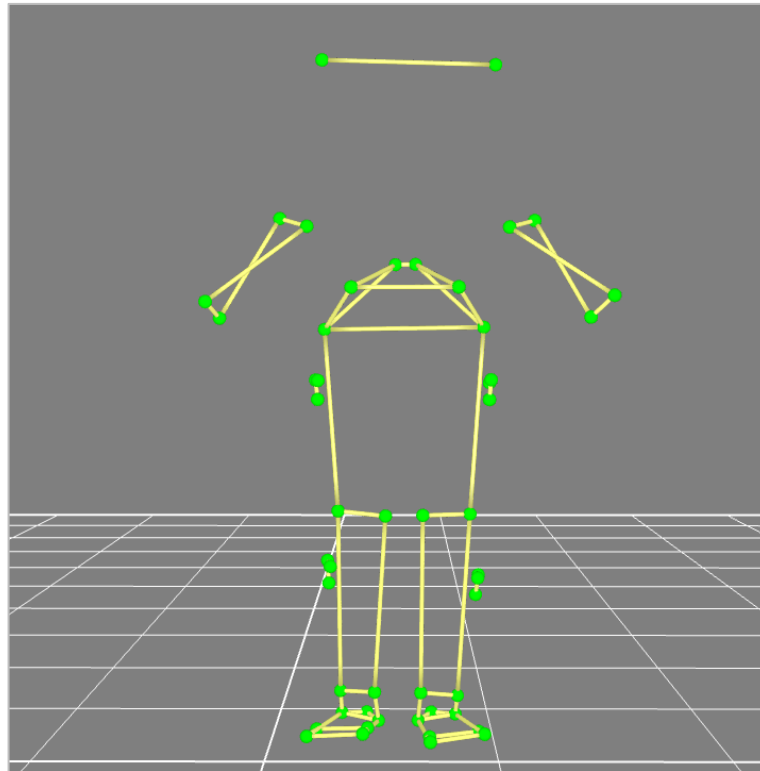


Figure 23. Static trial within Qualisys Track Manager, containing 54 reflective markers.

Each subject completed five trials for a total of thirteen activities: level walk, walk turn, incline walk, decline walk, stand to sit, sit to stand, sit cross legged, squat, stand reach, kneel reach, lunge, golf swing and cycle. Activities were completed within the calibrated movement volume. Tracking marker clusters, plus thirty-eight anatomical markers, allowed for full body kinematic data collection of activities. Each camera emitted an infra-red light, which reflected off the markers, back to the camera. This information was sent to Qualisys Track Manager, therefore allowing the 3D position of the marker within the global coordinate system, to be determined. The AMTI force platforms were synchronised to the camera system and recorded ground reaction force vectors throughout each movement. Piezoelectric sensors built into the force platform generate a voltage

when deformed. Therefore, deformation of the force platform results in a representative amplitude, allowing the ground reaction force to be calculated.

Before each activity, subjects were allowed a number of ‘practice’ attempts. This provided subjects time to acclimatise to the lab setting and complete movement in a ‘day-to-day’ way. In addition to this, it allowed the researcher to adjust the subjects starting position to ensure that both feet cleanly landed on the centre of the force platforms during locomotor activities. This starting position was defined using black duct tape. When completing activities, subjects were asked to look forwards in order to avoid the temptation to adjust stride patterns in an attempt to land on the force platforms.

4.2.6.1. Walking

Each subject completed five successful trials for each walking condition at a comfortable, self-selected pace. This was achieved by allowing participants a number of practice walks prior to data collection, in order to become comfortable and adopt a natural gait. The walkway was 15 m in length, allowing for a number of steps before and after force measurement. For level walking, a successful trial involved each foot landing cleanly on the one force platform each. In order to ensure that participants did not ‘target’ the platform, a start position was determined from practice walks, thus ensuring natural contact with the platform. For the walk turn, the right foot landed on the first force platform and the subject turned 90° to their left to take their second step. During incline and decline walk, subjects walked up a standardised gradient ramp, with Rise: Run of 1:12. Force data was not measured during incline/ decline walks as a force platform was not embedded in the ramp.

4.2.6.2. Sitting and Standing

Subjects completed both a ‘sit to stand’ and a ‘stand to sit’. A 0.47 m stool, with no arms or back support, was used for all subjects (this was closely matched to the ‘normal’ chair height of 0.46 m used by Nadazi et al. in 2003). The lack of support also acted to limit marker occlusion. The chair height was not adjusted for subjects of different heights, as it is unlikely that an individual would have control over this in a day to day situation. The task was standardised by instructing individuals not to avoid use of their arms to push up from the chair. One foot was placed in the centre of each force platform throughout the movement and participants were asked to hold a static position at the beginning and end of the movement. This allowed the researcher to determine where the movement began and ended.

The final seated task involved subjects sitting on the same 0.47 m stool and crossing the right leg over the left leg. Participants were asked to rest their lateral ankle onto the top of their left thigh, hold for one second, before uncrossing the legs back onto the force platforms. It was not possible to collect force data throughout this activity (for the right hip).

4.2.6.3. Squat

With one foot on each force platform, subjects held an upright standing position for one second. After squatting down to $\approx 90^\circ$ knee flexion, individuals returned to the start position.

4.2.6.4. Stand Reach

Subjects stood upright with each foot in the centre of a force platform. The task was to reach as close to the floor as possible, with straight legs and without touching the force platform, before returning to the start position.

4.2.6.5. Kneel Reach

Subjects knelt on the floor with each knee in the centre of a force platform and the torso upright. Subjects then reached as far forwards as possible, before returning to the original position.

4.2.6.6. Lunge

The subjects were required to contact the first force platform with the left foot, before stepping onto the second platform with the right foot and lunging down (ensuring that the left knee did not contact the force platform). Following the lunge, the subject stepped up and out of the lunge and continued to walk along the walkway.

4.2.6.7. Golf Swing

Subjects completed a full golf swing using a driver. A plastic golf tee was placed in front of the subject, at a comfortable distance, as an aim. From the start of the swing, a full back swing was executed, before the club was rotated down towards the tee and followed through to completion. For those who had not swing a club before, a demonstration was given and the hand positioning was explained.

4.2.6.8. Cycle

A racing bike was attached to a turbo trainer and the seat height was adjusted to allow for a slight flexion angle at the knee. Once the subject was comfortable, they were asked to

cycle at a comfortable pace until ten trials of data were collected. Due to the bike frame, marker drop-out was common during this activity, so it was aimed to secure five good trials of data for each individual. One movement cycle was defined as the right foot at the highest point on the pedal, cycled through to the same point. It was not possible to collect force data for this activity, as an embedded force transducer would be required.

4.2.7. Data Processing

The following section outlines the theoretical background of biomechanical movement analysis, before describing the processes required to transform raw signal into organised and meaningful data.

4.2.7.1. Theoretical Background

4.2.7.1.1 *Segment Positions and Orientation*

In order to quantify the 3D kinematics of a body, the relative position and orientation of adjacent segments must be determined. When defining segments within the global co-ordinate system (GCS), an orthogonal right handed Cartesian co-ordinate system was applied to segments (Local co-ordinate system: LCS). Segments (eg. bones) were assumed as rigid, thus knowledge of the length and orientation of the segment (within the LCS) meant that the entire segment could be modelled (Nigg et al., 1999; Robertson et al., 2013). Three non-collinear markers were required on each segment in order to determine the LCS, and therefore position and orientation within a GCS. Thus, three axes were defined in each co-ordinate system: 1) the unit vector in the plane between two markers; 2) the unit vector orthogonal to the plane; 3) the cross-product between the first two axes (Nigg et al., 1999). Although three markers are the minimum requirement to determine three axes, four-marker clusters were attached to segments in this study, ensuring that the segment could still be modelled, should there be any marker drop-out (Figure 21).

4.2.7.1.2 *Soft Tissue Artefact*

Soft tissue artefact (STA) is an effect influenced by the viscoelasticity of the skin, muscular contractions and the shifting of subcutaneous mass that influences the estimation of joint centres. STA will lead to errors relating to marker locations, segment positions and joint kinematics. Barré et al. (2015) summarised STA as the translation and rotation of a marker cluster in relation to bone (STA rigid motion) and errors relating to the cluster scaling, homothety (enlargement in relation to a fixed point), deformation, and

stretch (STA non-rigid motion). Although four-marker clusters may reduce the STA (non-rigid) motion, marker location and STA (rigid-motion) patterns will still influence the STA errors associated with data collection.

Barré et al. (2015) developed a comprehensive average map for the distribution of STA at the lower limb during treadmill gait. From this, four-marker clusters were attached to the lower limb in order to analyse STM rigid-motion. A stereophotogrammetric system tracked eighty lower limb markers. Marker displacement reached 24.9 mm and 15.3 mm at proximal areas of the thigh and shank, respectively. STA rigid-motion was increased at the thigh, compared to the shank, with the root mean squared (RMS) error equalling 8.1° and 1.2°. No marker cluster was shown to correctly compensate for STA rigid-motion. Translational errors were also high for both areas, with the RMS error ranging from 3 mm to 16.2 mm.

A number of studies have completed similar work to Barré et al. (2015), often utilising fluoroscopy as a mode for calculating lower limb skin artefact (Peters et al., 2010). Studies have considered the greater trochanter, thigh cluster, head of the fibula, lateral malleolus and shank cluster for analysis. The translational RMS varied from 3 mm (lateral malleolus during relaxed muscle) to 25 mm (Greater trochanter during cycling) (Peters et al., 2010).

These results highlight the magnitude of STA errors associated with skin markers. It is important to appreciate that STA is multi-faceted. Errors are likely to be built into the data with variation in the pattern and magnitude of STA between both activities and body segments. It seems beneficial to use four-marker clusters where possible in order to compensate for STA non-rigid motion. Although the compensation for STA rigid-motion is not always possible, the accuracy of marker placement is clearly vital for minimising data collection errors.

4.2.7.1.3 Right Hand Rule and Cardan Sequence

Cardan angles (also known as Tait-Bryan angles) are an accepted system for representing joint orientations for an anatomical structure (Nigg et al., 1999). Cardan angles define an ordered sequence of rotations about each of the three axes (X, Y, Z) in the GCS. Unlike Euler angles, a Cardan angle sequence must include all three rotations in order to represent the rotation of a segment. There are six orders in which these rotations can take place and each will result a slightly different position and orientation of a segment (x-y-z, y-z-x, z-x-y, x-z-y, z-y-x, y-x-z) (Schache et al., 2001; Sinclair et al., 2012).

As a default, Visual3D implements a Cardan sequence of flexion/ extension (X), followed by abduction/ adduction (Y) and finally internal/ external rotation (Z). All signals are processed in keeping with the ‘right hand rule’, that is the X axis pointing laterally to the right, the Y axis pointing anteriorly and the Z axis pointing superiorly (Figure 23). Hence, the joint angles will be zero when the axes of the proximal and distal segments are realigned. For this reason, the right hip flexion, adduction and internal rotation are positive, whilst extension, abduction and external rotation are negative. For the left hip, flexion and extension follow the same sign convention as the right but adduction/ abduction and internal/external rotation are reversed.

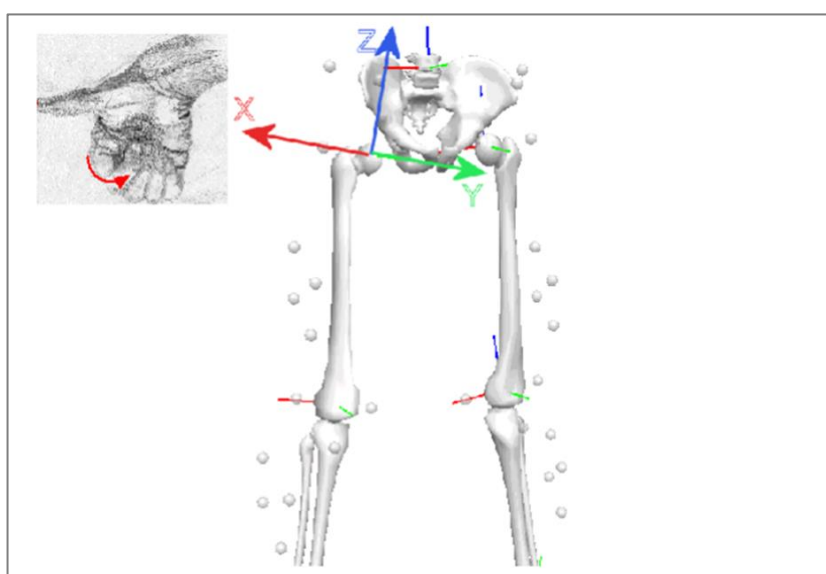


Figure 24. Schemata illustrating the right hand rule used for 3D analysis using a vertical axis (Z), horizontal axis (X) and perpendicular axis (Y) (C-Motion, 2018).

4.2.7.1.4 Noise and Data Filtering

Random errors, known as noise, are unwanted signal components built into data. Raw data (marker kinematics) collected within the movement analysis lab are likely to include some level of noise. This may be introduced by measurement tools and/ or biological artefacts in the form of unwanted electrical signals or vibrations. These errors, which generally occupy high frequencies, must be reduced during data processing (Winter, 2009). Low pass filters are one method for rejecting the low amplitude, high frequency noise embedded into a signal. A specific cut off frequency is selected for the filter, whereby all signals above the determined frequency are negated. This results in a reduction of the noise component in the overall signal, leaving the true data largely uninfluenced. Although the low frequency movement signal and the high frequency noise

generally occupy opposite ends of the frequency spectrum, there is some crossover (Winter, 2009). For this reason, the choice of an appropriate cut-off frequency is crucial in order to compromise between the high and low frequency data. Although the filtering of marker kinematics is often determined in relation to the literature, the optimum cut-off frequency for a specific data set can be calculated using residual analysis (Winter, 2009).

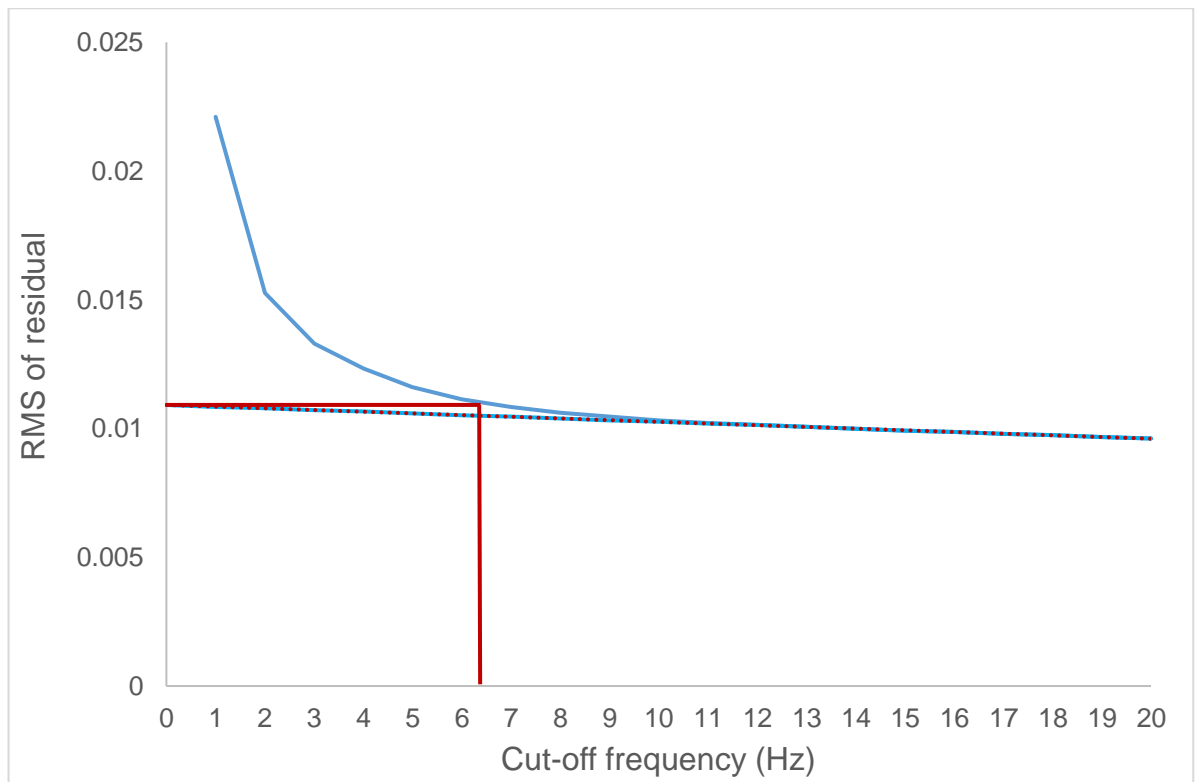


Figure 25. An example of residual analysis for inferior-superior motion of the greater trochanter marker during walking. The root mean square (RMS) of residual is the total error between the raw and filtered signal. The dotted trend-line (intersect) runs from the 20 Hz cut-off frequency to the y-axis. The red line runs horizontally from the x-axis intersect to the RMS curve and then vertically down to the y-axis: this estimates the cut-off frequency.

Residual analysis involves filtering raw data at a number of frequencies, before calculating the residuals between the filtered and raw data at each cut-off value. When the residual value is plotted against the cut-off value, a straight line can be plotted at the point where the residual becomes a linear function of the cut-off frequency. This line can be used as a guide to then determine an appropriate cut-off frequency, assuming that the signal distortion and the amount of noise passing through the filter are equal (Winter, 2009) (Figure 24). Although it is unrealistic to complete this analysis for all of the data in a study, running the test for an example of the data will give a realistic estimation for the approximate cut-off frequency to use. A negative of this method is that although an appropriate cut-off can be determined, the analysis is unlikely to yield an ‘optimum’ frequency, as each marker for each subject will result a different result (Yu et al., 1999). In addition to this, the type of activity will also influence the noise level (Schreven et al., 2015). It seems reasonable to filter the data within a known range of realistic frequencies

(as described within the literature), whilst managing the cut-off frequency in more detail independently to the data itself.

4.2.7.1.5 Marker Drop-out

During motion trials, thirteen cameras were positioned above and around the movement area. In order to identify the 3D position of a marker, in a coordinate system, a marker must be in view of at least two cameras. When a marker is obscured by an object or the subject, it will ‘drop-out’ of the field of view for that period of time. In some instances, this error can be rectified during processing. However, in other cases this may lead to errors for entire body segments and ultimately the resulting data may become unusable. Generally, marker drop-out is rare during walking gait. However, within this study of common daily activities: chairs, bike frames, ramps and high levels of hip flexion were causes of marker occlusion for some subjects.

During data collection, a number of methods were used to reduce marker drop-out. These included the use of four-marker clusters (instead of three), use of a stool for sitting tasks (rather than a chair with a back) and use of tight fitted clothing (to avoid baggy material blocking the view of cameras). With hindsight, it would have been beneficial to include more markers on the pelvis segment to attempt to reduce obscurity. With that being said, during some movements, marker obscurity was inevitable (due to technique and/ or soft tissue).

Within Qualisys Track Manager, it was possible to ‘gap fill’ for some of the marker drop-out seen within the data. A polynomial interpolation was calculated for any gaps in the signal that were ≤ 10 frames. This corrected for small gaps within the signal and allowed for reliable segment orientations to be defined during body modelling.

4.2.7.2. Qualisys Processing

Kinematic data were reduced within Qualisys Track Manager to remove unwanted movement. Motion files were cropped to remove unwanted frames, ensuring that the required movement cycle could be processed. A template was created in which markers were defined by consistent and computationally readable names (this was crucial for later modelling) (Figure 25). For each subject, one movement trial was manually labelled using this marker template. Once completed for a movement trial, an ‘Automatic Identification of Markers’ (AIM) model was generated and applied to the remaining motion files for that subject.

Once a movement file was labelled, the marker trajectories were visually checked within the graphical interface. Should a marker move erratically, with unnatural bouncing/jerking motions, the relevant frames were split in order to identify the error. In some situations, this was due to an error in which a small number of frames were labelled incorrectly for adjacent markers - this was easily corrected for. In other cases, true error was embedded within the signal, meaning that some frames were required to be deleted. Due to manual deletion of frames and ‘drop-out’ of markers due to obscurity, the ‘fill level’ of some markers were below 100%. Although a fill level of 100% was not essential for defining the marker trajectory, large gaps consequentially lead to gaps within the resulting joint angle data. Given the aim of this work, the pelvis and right thigh markers were required to have a fill level of approximately 100% with minimal gaps. A polynomial interpolation was applied to marker trajectories to calculate a line of best fit for gaps below ten frames. This provided a reliable estimation of the markers displacement. At this point, any trials with incomplete, key marker trajectories were discarded.

All data was converted to C3D files and batch exported to Visual3D (Visual3D standard, v5.01.18, C-Motion, Germantown, MD, USA). In the interest of computational efficiency, two identical workspaces were created in Visual3D – each containing nine subjects.

Trajectory	Fill Level	Range	Type	X	Y	Z	Residual
R_SHO	100.0%	575 - 900	Measured	-227.43	445.23	1398.89	0.90
L_SHO	100.0%	575 - 900	Measured	-235.92	752.75	1400.57	0.73
R_MELB	100.0%	575 - 900	Measured	-210.11	357.90	1072.57	0.31
R_LELB	100.0%	575 - 900	Measured	-251.70	312.79	1108.92	0.39
L_MELB	100.0%	575 - 900	Measured	-223.73	833.73	1073.97	0.64
L_LELB	100.0%	575 - 900	Measured	-288.52	871.84	1099.93	0.19
R_WA	100.0%	575 - 900	Measured	-191.50	170.64	913.40	0.85
R_WB	100.0%	575 - 900	Measured	-170.20	123.53	970.74	0.66
L_WA	100.0%	575 - 900	Measured	-281.26	1005.31	909.90	0.50
L_WB	100.0%	575 - 900	Measured	-259.36	1058.62	952.09	0.53
R_ASIS	100.0%	575 - 900	Measured	-69.68	486.10	919.82	0.58
L_ASIS	100.0%	575 - 900	Measured	-57.36	699.14	908.59	0.43
R_P SIS	100.0%	575 - 900	Measured	-345.02	583.21	952.42	0.40
L_P SIS	100.0%	575 - 900	Measured	-339.75	654.64	951.08	0.43
R_GT	100.0%	575 - 900	Measured	-236.97	382.29	837.41	0.54
L_GT	100.0%	575 - 900	Measured	-197.55	817.87	859.10	0.40
R_THI1	100.0%	575 - 900	Measured	-274.17	415.99	539.39	0.84
R_THI2	100.0%	575 - 900	Measured	-248.82	398.52	628.24	0.46
R_THI3	100.0%	575 - 900	Measured	-187.33	402.30	608.79	1.06
R_THI4	100.0%	575 - 900	Measured	-211.17	418.49	514.78	0.65
L_THI1	100.0%	575 - 900	Measured	-146.69	753.35	541.87	0.70
L_THI2	100.0%	575 - 900	Measured	-125.97	769.47	631.96	0.74
L_THI3	100.0%	575 - 900	Measured	-182.23	796.04	637.06	0.87
L_THI4	100.0%	575 - 900	Measured	-207.78	781.69	541.57	1.16
R_MKNE	100.0%	575 - 900	Measured	-229.29	560.30	453.76	0.51
R_LKNE	100.0%	575 - 900	Measured	-206.63	441.20	459.86	0.55
L_MKNE	100.0%	575 - 900	Measured	-227.85	641.71	445.14	0.94
L_LKNE	100.0%	575 - 900	Measured	-194.10	755.31	463.22	0.61
R_TIB1	100.0%	575 - 900	Measured	-284.22	398.99	300.08	0.24
R_TIB2	100.0%	575 - 900	Measured	-280.42	403.35	396.00	1.01
R_TIB3	100.0%	575 - 900	Measured	-226.23	420.78	389.13	1.32
R_TIB4	100.0%	575 - 900	Measured	-238.84	412.16	302.54	0.67
L_TIB1	100.0%	575 - 900	Measured	-235.28	786.62	310.09	1.03
L_TIB2	100.0%	575 - 900	Measured	-228.84	780.17	406.72	1.07
L_TIB3	100.0%	575 - 900	Measured	-286.35	786.55	407.65	1.37
L_TIB4	100.0%	575 - 900	Measured	-283.18	792.08	318.73	0.97
R_MANK	100.0%	575 - 900	Measured	-248.90	525.98	85.01	0.91
R_LANK	100.0%	575 - 900	Measured	-262.45	442.36	74.30	1.45
L_MANK	100.0%	575 - 900	Measured	-248.36	662.80	90.84	0.94
L_LANK	100.0%	575 - 900	Measured	-266.89	740.97	75.22	0.57
R_MCAL	100.0%	575 - 900	Measured	-296.24	523.70	33.48	0.72
R_LCAL	100.0%	575 - 900	Measured	-312.10	444.17	39.08	0.93
L_MCAL	100.0%	575 - 900	Measured	-282.68	665.25	29.21	0.92
L_LCAL	100.0%	575 - 900	Measured	-291.98	750.49	32.50	0.69
R_MT1P	100.0%	575 - 900	Measured	-202.68	514.61	25.01	0.67
R_MT5P	100.0%	575 - 900	Measured	-229.55	416.14	21.56	0.67
R_MT1D	100.0%	575 - 900	Measured	-131.61	509.36	18.73	1.20
R_MT5D	100.0%	575 - 900	Measured	-144.13	396.45	19.66	0.90
L_MT1P	100.0%	575 - 900	Measured	-194.15	671.25	29.60	1.04
L_MT5P	100.0%	575 - 900	Measured	-206.04	772.71	28.58	0.80
L_MT1D	100.0%	575 - 900	Measured	-128.70	674.98	23.18	0.74
L_MT5D	100.0%	575 - 900	Measured	-154.93	785.51	23.82	0.97

Figure 26. Qualisys marker template, showing from left to right: trajectory name, fill level (drop-out), movement range, signal type and marker coordinates (X: medial-lateral; Y: anterior-posterior; Z: inferior-superior).

4.2.7.3. Visual3D Processing

Motion files were imported to Visual3D (Visual3D standard, v5.01.18, C-Motion, Germantown, MD, USA). Files were grouped by activity within the workspace tab, thus allowing specific data groups to be graphed and exported together. Static trials were added as a 'hybrid model from C3D file'. This allowed the static file to be modelled and assigned to the corresponding motion files. A model template was created for one static file and saved as an MDH file. This allowed remaining static files to be automatically modelled (using the MDH file) before being assigned to motion files.

Following the modelling process, pipelines were applied to the data in order to calculate and filter kinetic and kinematic data.

4.2.7.3.1 Segmental Models

Body segments (pelvis, thigh, shank and foot) were defined using anatomical and tracking marker positions, from static files (Cappozzo et al., 1995). This allowed for a 3D model of body segments to be created. Height and weight were input for each subject model, providing crucial information for moment calculations and kinetic normalisation at a later point.

4.2.7.3.1.1 Pelvis Segment: Method Development

Anterior superior iliac spine markers (ASIS) dropped out more frequently than any other marker. This occlusion was due to the high levels of hip flexion involved in a number of the activities and the covering of markers by soft tissue. This was not an issue when just one ASIS marker was covered, as the pelvis segment could be constructed using the remaining ASIS marker and two posterior superior iliac spine (PSIS) markers. However, when both the left and right ASIS markers were obscured, the pelvis segment could not be created, therefore hip data could not be calculated during the given time period. A polynomial gap fill was not possible for this issue, as during a number of trials, markers were obscured for longer than ten frames and were often at the base of the movement (meaning it was difficult to accurately estimate the marker motion).

Virtual Pelvis

In order to combat the issues with ASIS drop-out, an attempt was made to model a 'virtual pelvis' in which virtual ASIS markers (ASIS_v) were used instead of the raw markers. Two methods were explored in order to counteract the issues of marker drop-out.

Method 1

The 'Visual3D Composite Pelvis' was created using the left and right PSIS and the left and right ASIS (RPV_1). The same static file was used as the model and 'motion' file, to allow calculations to be made. All four pelvis markers were transformed from the lab coordinate system to the pelvis coordinate system. The transformed PSIS markers were subtracted from the corresponding ASIS markers (eg. R_P SIS– R_ ASIS). This defined the displacement between the two markers, in three dimensions. Two virtual landmarks could then be created (R_ ASIS_v and L_ ASIS_v) in the same position as the raw ASIS markers, within the pelvis coordinate system. However, when creating a pelvis using the ASIS_v markers, the pelvis still dropped-out during short periods within the motion. The reason for this is that the virtual landmarks were linked to RPV_1, as they must be created within this coordinate system in order to match the motion of the ASIS. This confirmed that in order to create a virtual pelvis, more than four-markers would be required. In hindsight, two extra markers should have been used at the iliac crest. However, there is still no certainty that these would not have also been obscured. In 'Method 2', an attempt was made to create the 'Visual3D Composite Pelvis' using greater trochanter markers, rather than the ASIS.

Method 2

A second attempt was made to create a virtual pelvis, without using ASIS markers. The same steps seen in method 1 were followed, however the 'Visual3D composite pelvis' was created using the greater trochanter in place of the ASIS (RPV_2). This ensured that the virtual landmarks created would not drop-out during the movement. The ASIS_v markers (now created within the new composite pelvis coordinate system) did not drop-out at any point of the movement. These virtual landmarks were compared to the raw IliacCrest markers in order to identify the level of error within this method.

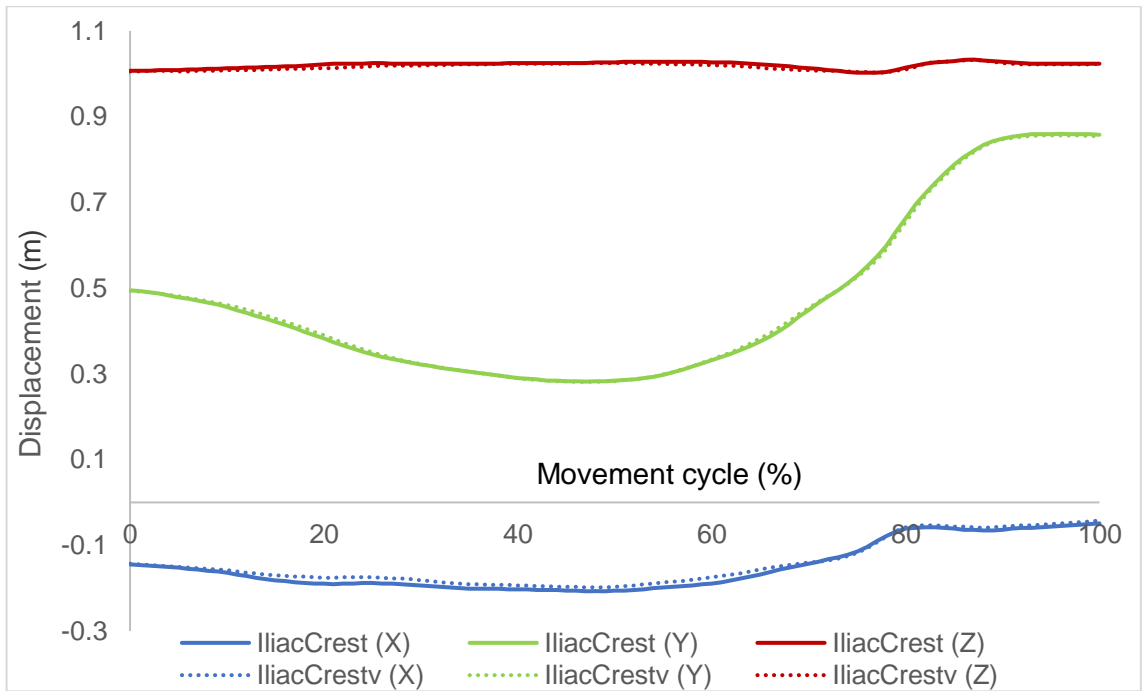


Figure 27. Displacement of the right ASIS (ASIS) and virtual ASIS (ASIS_v) markers during a golf swing. Displacements are in the medial (-) lateral (+) (X), anterior (+) posterior (-) (Y) and proximal (-) distal (+) (Z) directions.

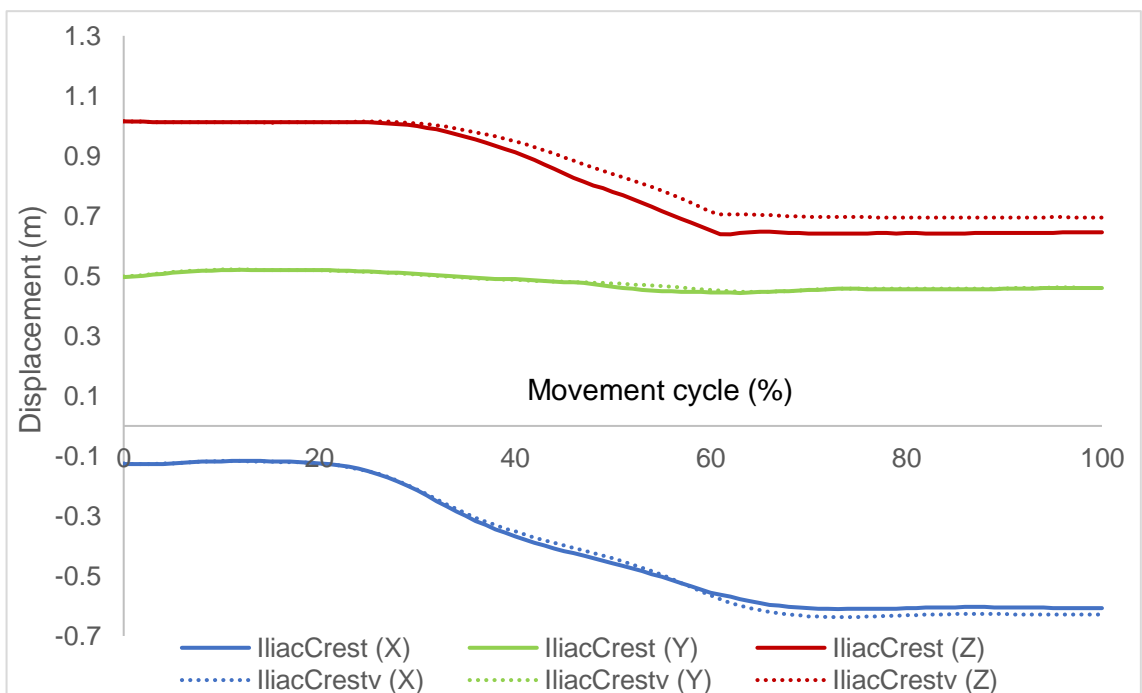


Figure 28. Displacement of the right ASIS (ASIS) and virtual ASIS (ASIS_v) markers during a stand to sit. Displacements are in the medial (-) lateral (+) (X), anterior (+) posterior (-) (Y) and proximal (-) distal (+) (Z) directions.

Figures 26 and 27 show the error between raw ASIS markers and the virtual ASIS markers derived using 'Method 2'. The golf swing showed small average errors between marker displacements along all three axes (mean error (m) \pm SD: X: 0.00 \pm 0.00; Y: 0.00 \pm 0.01; Z: 0.00 \pm 0.00) (Figure 26). Small errors were observed in the X axis (anterior-posterior), with a maximum error of 0.01 m. However, when considering the small errors across all axes, it is reasonable to suggest that there is good agreement between the ASIS and ASIS_v markers during the golf swing.

When considering stand to sit data, the level of error was magnified (Figure 27). (mean error (m): X: 0.00; Y: 0.00; Z: 0.04). A mean error of 0.04 m was observed for displacement in the Z axis (proximal-distal). The maximum error in the Z axis was almost double the mean, at 0.07 m. This discrepancy is large, especially considering that the error was equal to just over a fifth of the total proximal-distal displacement of the ASIS marker (0.37 m). This error was identified at the base of the movement (when seated). It is likely that this error is caused by an inability of the ASIS_v markers to account for pelvic tilt at this point. This is because the virtual markers were created from RPV_2, which incorporated greater trochanter markers rather than the ASIS. This meant that this pelvis segment was flat and was therefore, unable to account for pelvic tilt. For this reason, it would be unrealistic and inaccurate to define a pelvis in this way.

Summary

With just four pelvis markers, the only logical definition of the pelvis was the 'V3D Composite Pelvis', using both PSIS markers and both ASIS markers. Any trials with occlusion of both ASIS markers (for longer than ten frames) were therefore removed. For this reason, subject sizes were reduced for a number of high flexion activities (*Activity: Subject size; Sit cross legged: 14; Squat: 11; Stand reach: 11; Kneel reach: 13; Lunge: 17; Cycling: 10*). This was a last resort, but was the only way to ensure that hip data was accurate and reliable. In future work, at least six pelvis markers should be used when collecting kinematics for high flexion activities. Specific details for modelling of this segment are included in section 3.1.7.3.1.2..

4.2.7.3.1.2 Pelvis Coordinate System

The ‘Visual3D Composite Pelvis’ was defined with the left and right anterior superior iliac spine (ASIS) and posterior superior iliac spine (PSIS) markers. The origin of the pelvis segment coordinate system was defined as the mid-point between the middle of the ASIS and PSIS markers (Figure 28).

Hip joint centres were defined as virtual landmarks and calculated automatically within the model. The in-built calculation was adapted from work by Bell and colleagues (Bell et al., 1989; Bell et al., 1990).

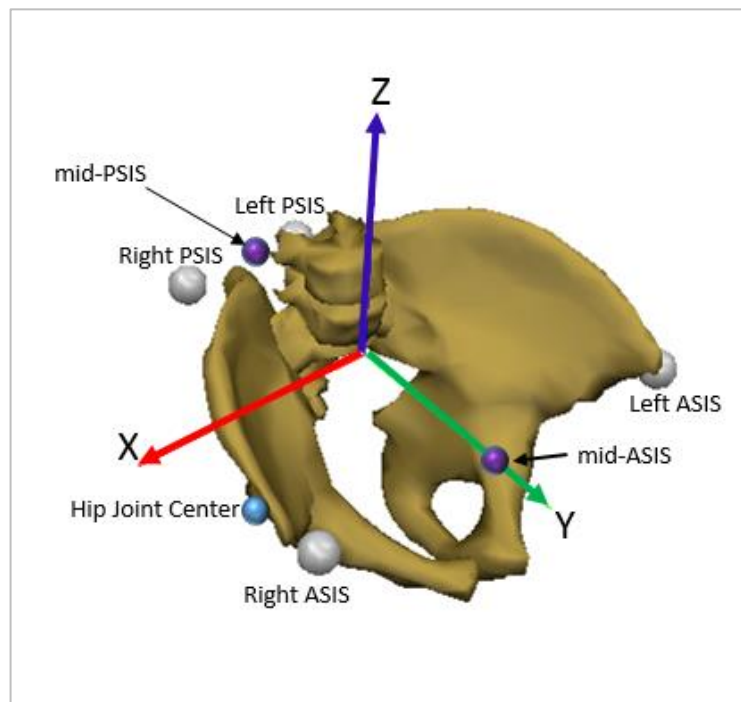


Figure 29. Composite pelvis showing the origin of the pelvis between the mid-ASIS and mid-PSIS. The local coordinate system of the pelvis is shown by X (Medial-Lateral), Y (Anterior-Posterior) and Z (Inferior-Superior) axes (C-Motion, 2018).

4.2.7.3.1.3 Thigh Coordinate System

The thigh segment was defined using the greater trochanter (proximal joint), lateral knee and medial knee (distal joint) anatomical markers. As just one marker was present at the proximal end of the thigh, the thigh radius was manually defined. Thigh radius was defined as a quarter of the distance between the greater trochanter markers on each leg ($0.25 * \text{DISTANCE}(\text{R_GT}, \text{L_GT})$) (C-Motion, 2018). The thigh cluster tracking markers defined the position and orientation of the segment.

4.2.7.3.1.4 Shank Coordinate System

The shank segment proximal joint was defined using the medial and lateral knee markers, whereas the distal segment was defined by the medial and lateral ankle markers. The corresponding shank clusters acted as tracking markers for these segments.

4.2.7.3.1.5 Foot Coordinate System

The proximal joint was defined using the medial and lateral ankle; the distal joint was defined by the 1st and 5th distal metatarsal markers. The 1st and 5th proximal metatarsal and the calcaneus acted as tracking markers for this segment.

4.2.7.3.2 Filtering Data

A Butterworth low-pass filter with a cut-off frequency of 8 Hz was used for the smoothing of kinematic marker trajectories. This was chosen through visually assessing the data as a whole and the effects of a number of realistic filters. However, the decision was also influenced by residual analysis and the literature, which confirmed that human movement signal generally occurs in high amplitudes at low frequencies (Winter, 1984).

4.2.7.3.3 Data Labels

Data labels were manually created within Visual3D and defined key time points within movement cycles. This included the beginning and end of kinematic/ kinetic signals for each activity. Labels allowed movement cycles to be normalised to 100 data points and relevant signals to be exported.

4.2.7.3.4 Kinematics

A pipeline was used to calculate right hip joint angles for all trials. The resulting angle was a transformation between the pelvis and thigh coordinate systems, described by a rotation matrix. The proximal segment (pelvis) was used as a reference segment in this instance. This rotation was represented as a Cardan sequence, which in this case was flexion-extension followed by abduction-adduction and finally internal-external rotation.

4.2.7.3.5 Ground Reaction Force

Ground reaction forces were measured by force platforms, which were embedded flush with the floor of the lab. Analogue signals were converted to force (Newtons) automatically within the software. Force vectors provided meaningful information, whilst also driving joint moment and joint reaction force calculations at a later point in the analysis.

4.2.7.3.6 Joint Moments

Net internal joint moments were calculated within Visual3D, using a Newton-Euler inverse dynamic calculation. The calculation estimated the required turning effect of the internal, anatomical structures across the hip joint, in order to complete a given movement. Two fundamental equations of motion were required for this calculation: 1) Force is equal to mass times acceleration, 2) moment of force is equal to mass times linear acceleration (Selbie et al., 2014). Within Visual3D, the proximal segment is used as the resolution coordinate system. Therefore, the right hip moment was resolved in the segment coordinate system of the pelvis.

Resulting moments were normalised proportional to body weight ($pBWT \cdot m$) to ensure that magnitudes were influenced by individual biomechanics, rather than weight. This acted to reduce differences due to gender and allowed moment data to be compared between individuals (Moisio et al., 2003).

Moments provided an estimation of the net turning force occurring across joint ligaments and muscles, and thus, the torques that might be expected to occur at a hip replacement. Further to this, adduction moments are significantly correlated with localised joint loading (which is another important variable when considering prosthesis loading) (Foucher et al., 1999).

4.2.7.4. Data Organisation and Formatting

Data was exported from Visual3D and into Microsoft Excel spreadsheets. A document was created for each activity and within each document, ground reaction forces, hip angles, and hip moments were organised in separate sheets. Hip reaction forces and motion path data was later added to these spreadsheets. Another spreadsheet was used to organise the mean data for variables. Within each document, data was normalised, descriptive statistics were completed (mean, range and standard deviations) and comparisons were made between age and gender. It was also at this point, where data could be graphed together and any signal errors could be identified (such as noise and marker drop-out).

4.2.7.4.1 Normalisation

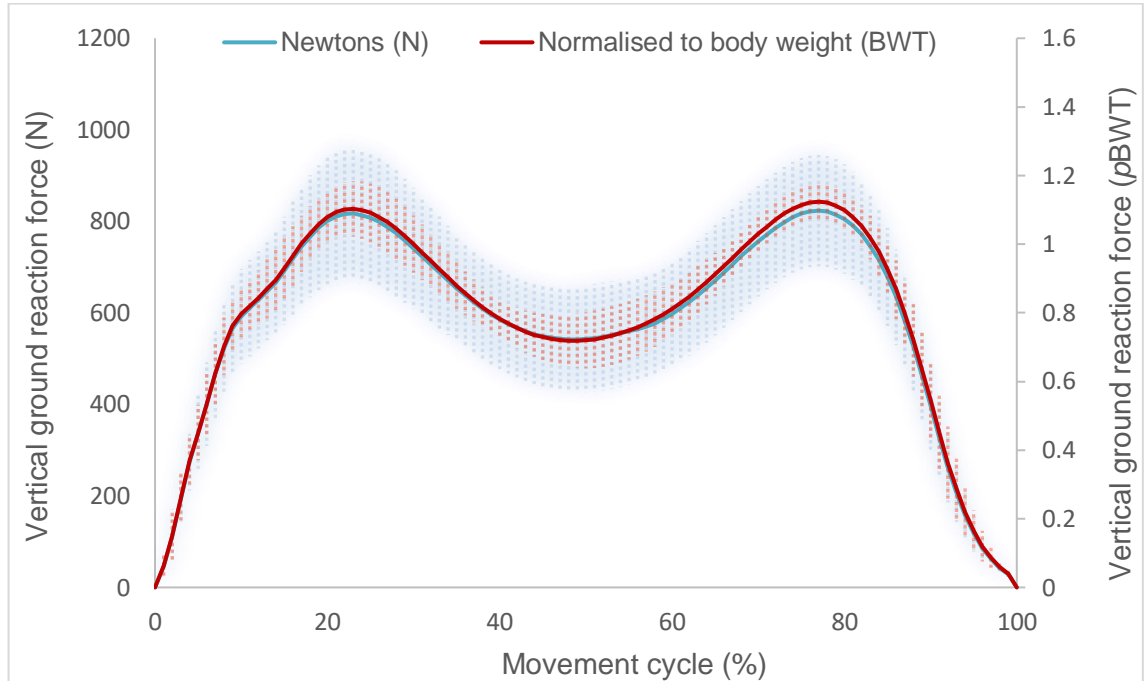


Figure 30. Mean right vertical ground reaction force during one gait cycle for a level walk. The raw data (Newtons) is compared to the normalised data (proportional to body weight or *p*BWT). Standard deviations above and below the mean are shown as shaded error bars.

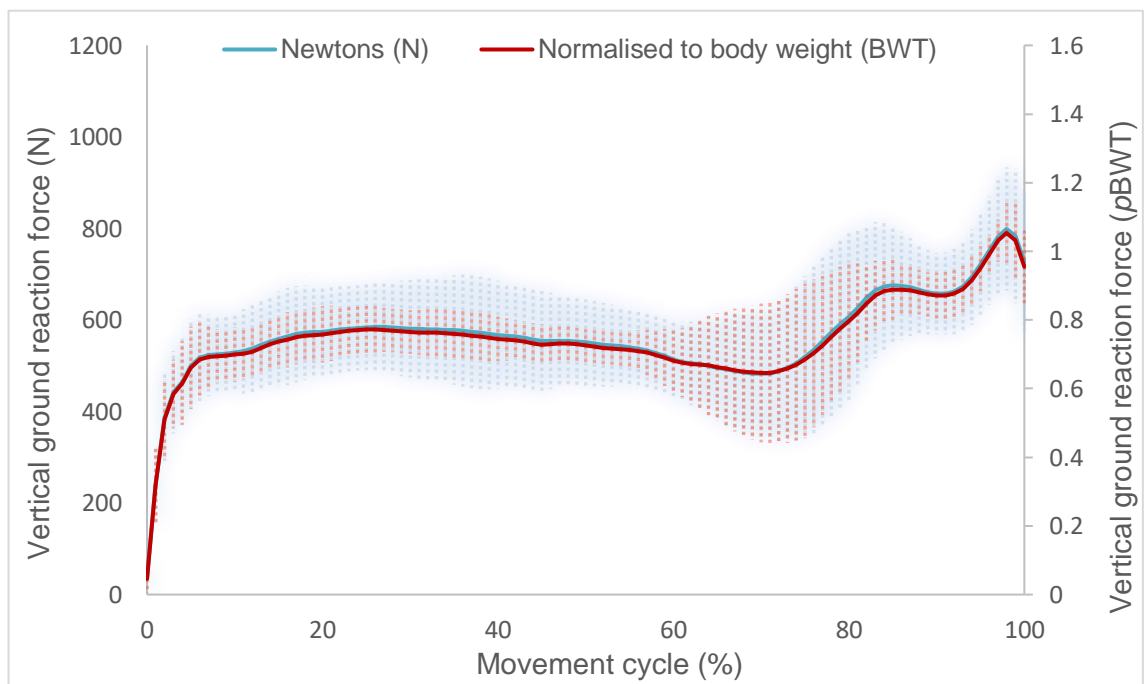


Figure 31. Mean right vertical ground reaction force during one movement cycle for a lunge. The raw data (Newtons) is compared to the normalised data (proportional to body weight or *p*BWT). Standard deviations above and below the mean are shown as shaded error bars.

Figure 29 compared the walking vertical ground reaction force (vGRF) when calculated in Newton's and when normalised proportional to body weight (pBWT) (n=18). Both followed the same force pattern, however when normalised to pBWT, a small increase was observed at the two peaks. However, this increase was negligible, with a difference of <0.1 pBWT. When considering the variation for the two methods, normalising to body weight reduced the standard deviation by up to a factor of two, for a level walk.

When considering Figure 30, again, the pattern of force production was essentially the same between the two methods. At some points throughout the force cycle, the standard deviation was halved when applying the normalisation process. Having said this, the graph demonstrated equally high levels of variation between 60 and 80% of the lunge cycle. It is at this point (when the lunge is at its deepest and an individual must propel the body forwards and upwards) where biomechanical variation might be expected to occur. This observation may suggest that although the normalisation process has occurred, it still included periods of 'true' variation in the movement (perhaps down to technique or functionality), whilst ignoring variation purely due to the mass of the subject.

After assessing the effects of normalisation, the current study normalised kinetic data in relation to mass, in an attempt to dampen the variation due to the weight of the subjects. Vertical ground reaction forces were linearly normalised to subject mass, as has been accepted as common practice within biomechanics over the past twenty years (Wannop et al., 2012). The resulting joint moments (calculated from a combination of kinetics and kinematics) were normalised to mass and height (Moisio et al., 2003; Sum et al., 1998).

The data presented in figures 29 and 30, provide an assurance that although the mean variation will be decreased, important phases of high variation within movements (unrelated to mass) will still be present within the results. With that being said, it should be noted that subject height and mass are included in Table 8, allowing the reader to convert any normalised data back to the raw form if required.

4.2.7.4.2 Data Quality Control

An excel spreadsheet was created for each of the thirteen activities, within which were a number of sheets for the organisation of each variable. Within each variable sheet, descriptive statistics were calculated and subjects were grouped by age and gender for analysis. A master document was created in order to document the mean data curves for activities and variables. It was at this point where the data was visually checked for errors. Any excessive noise or marker drop-out within the data was identified and rectified/

removed. Additionally, it was ensured that the start and end of movement cycles were matched. The data was then used for graphing and tabulation within Microsoft Excel, MATLAB or SolidWorks.

4.2.8. Statistical Analysis

Descriptive statistics (means, peaks, ranges and standard deviations) and T-tests were calculated within Microsoft Excel. Statistical differences were calculated between age groups (under 55 and over 55) and gender groups (male and female) for average motion path aspect ratios (cross-shear). The paired T-test for independent samples (two-tailed and equal variance) compared the mean aspect ratios (across 20 points on the femoral head) of subjects.

When the test was ran, the obtained value (t) was automatically compared to a table of critical values, taking into account the degrees of freedom (n-1), tails of the test (2) and degree of risk (0.05). The 0.05 confidence limit indicated that if significance was found, 95% of the time, the difference between the two conditions was not due to chance. If the obtained value (t) was higher than the critical value (T), the null hypothesis was not accepted. However, if the obtained value was smaller than the critical value, the null hypothesis was accepted. Therefore, $(P(T \leq t) \text{ two-tail})$, represents the probability (P) of t occurring by chance, for a two-tailed test. If P is smaller than or equal to 0.05, the difference between the data sets can be said to be significant (Field, 2013).

4.3. Results

4.3.1. Hip Joint Kinematics

Three-dimensional kinematics allow for the description of motion, independent to force. Joint kinematics were collected using a thirteen camera, Qualisys Oqus system. Retro-reflective markers were attached to palpable anatomical landmarks and segments. Body segments were modelled within Visual3D (Visual3D standard, v5.01.18, C-Motion, Germantown, MD, USA), allowing for angular kinematics to be calculated between adjacent segments (in this case, the right thigh and the pelvis).

Mean right hip angle data are presented for each of the thirteen activities. Each activity is plotted for one movement cycle. For walking tasks this entailed one full stride, beginning at initial contact. More detail is provided for the definition of movements within the methods section (4.2.6.). The corresponding movement times for activities are shown in Figure 39. Figures 40 to 78 show hip angular data (rotation and velocity), in each axis, with standard deviations shown as error bars. Section 4.3.2. describes the range of motion (ROM) for activities and section 4.3.3. to 4.3.7. addresses peak data and variation between subjects.

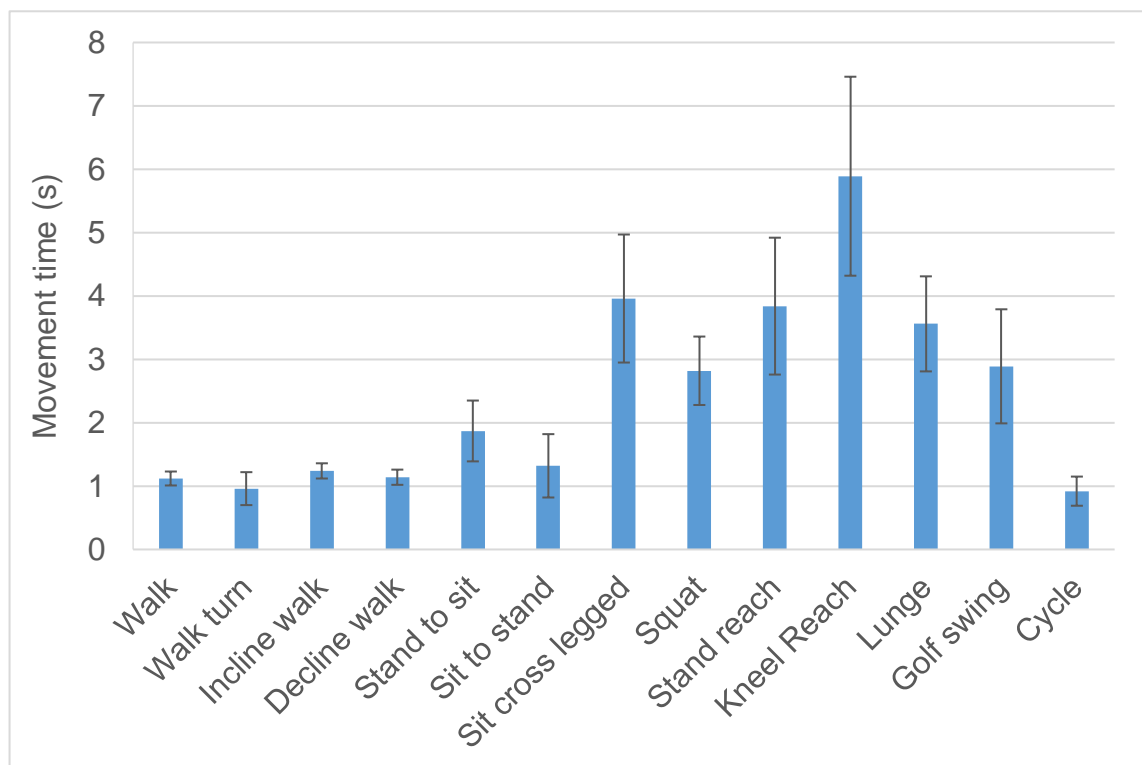


Figure 32. Mean movement time in seconds (s) for thirteen activities. Standard deviations are shown as error bars.

All walking tasks took between 1 and 1.2 seconds for one gait cycle (Figure 39). Although standard deviations were small for these activities, the walk turn showed an increased variation (± 0.3 s) in comparison to the straight forward walking tasks (all ± 0.1 s). Cycling was comparable to the walk turn, both in terms of the movement time (0.9 s) and the standard variation (± 0.2 s) across subjects. On average, stand to sit took 0.6 seconds longer than sit to stand, however variation was similar for the two tasks (both ± 0.5). Sit cross legged, squat, stand reach, lunge and golf swing resulted movement times between 2.8 and 4.0 seconds, with variation between ± 0.5 seconds (squat) and ± 1.1 seconds (stand reach). Kneel reach resulted both the longest average movement time (5.9 seconds) and the highest variation (± 1.6 seconds). Generally, variation increased with an increase in movement time, ranging from 1 ± 0.1 seconds (walk) to 5.9 ± 1.6 seconds (stand reach).

4.3.1.1. Walk

Each walking cycle was measured for one stride, starting at first right foot initial contact and ending at the second right foot initial contact (Figure 40). The first 60% of the cycle represents the right lower limb stance phase, whereas the last 40% of the cycle describes the swing phase.

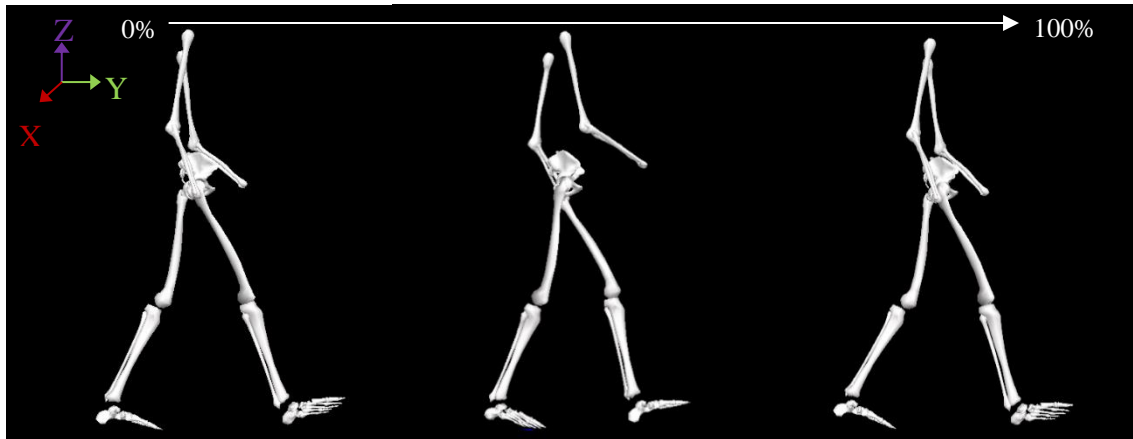


Figure 33. Walking model within Visual3D showing a walking gait cycle from start (left) to finish (right).

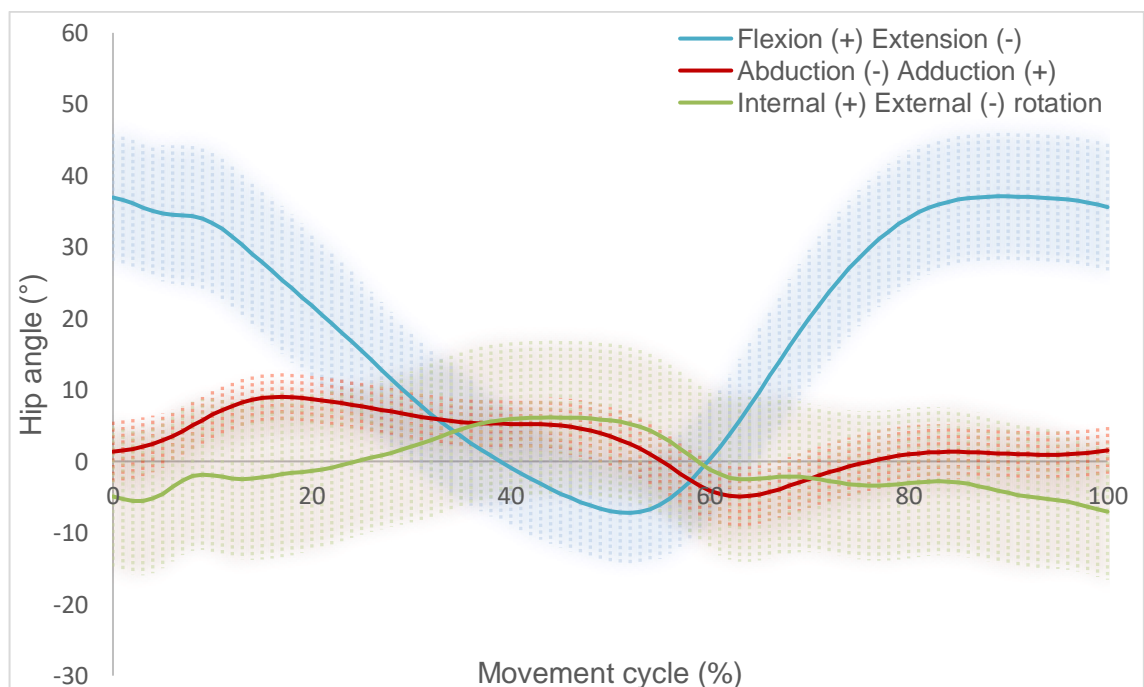


Figure 34. Mean right hip angle during one gait cycle for a level walk. Standard deviation above and below the mean are shown as shaded error bars (n=17).

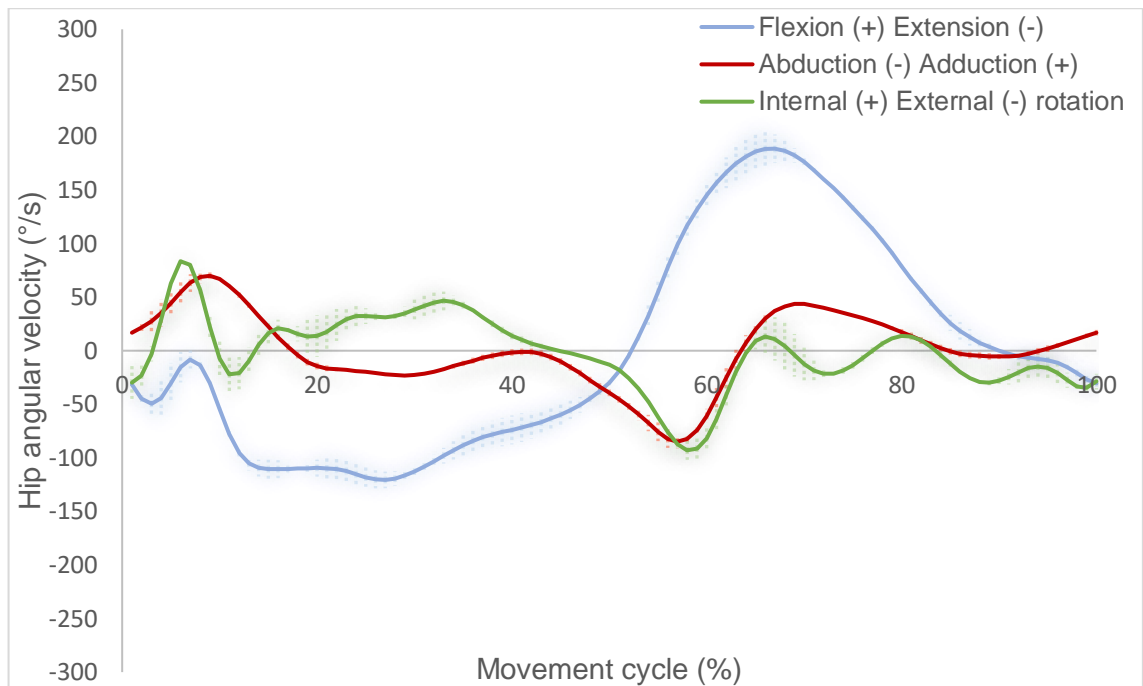


Figure 35. Mean right hip angular velocity during one gait cycle for a level walk. Standard deviation above and below the mean are shown as shaded error bars (n=17).

When walking, the hip extended from initial contact, reaching a maximum extension angle at $\approx 50\%$ of the gait cycle (Figure 41). The hip then flexed from heel-off, through the propulsion phase of gait, before plateauing at $\approx 85\%$ of the gait cycle (mid-swing). During the swing phase (60-100% of the gait cycle) the right leg rotated forward in preparation for initial contact. Angular velocity was higher during hip flexion (50-85% of the cycle) compared to the hip extension period (0-50% of the gait cycle) (Figure 42). Hip flexion angle range of motion (ROM) was 44° . Hip adduction was observed throughout the stance phase (0-60% of the gait cycle), reaching a maximum angle of 9° (Figure 41). The hip abducted at toe-off (peak abduction: 5°) and displayed neutral abduction-adduction angular motion during the swing phase. Internal rotation occurred from initial contact and up to the push-off phase ($\approx 50-60\%$ of the gait cycle), peaking at an internal rotation of 6° . Internal-external rotation of the hip plateaued during the push-off phase and externally rotated from toe-off and throughout the swing phase.

Mean standard deviations (SDs) were similar for hip flexion-extension ($\pm 9^\circ$) and internal-external rotation ($\pm 11^\circ$), whereas a marked decrease was observed for the abduction-adduction angle ($\pm 4^\circ$). The SD between subjects was consistent throughout the gait cycle for hip kinematics. However, flexion-extension variation was slightly decreased (2°

below average) at push-off (50-60% of the gait cycle) and increased when approaching initial contact and throughout the stance phase.

During the stance phase, hip velocity reached an extension velocity of 121 °/s (Figure 42). The peak angular velocity was seen during hip flexion at the initial swing phase (67% of the gait cycle) and reached 189 °/s. Velocity inter-subject variability remained low throughout the movement.

4.3.1.2. Walk Turn

The walk turn gait cycle started at right initial contact. At this point, the body rotated and the second step was 90° to the left. The movement cycle ended with the second initial contact of the right foot (one stride) (Figure 43).

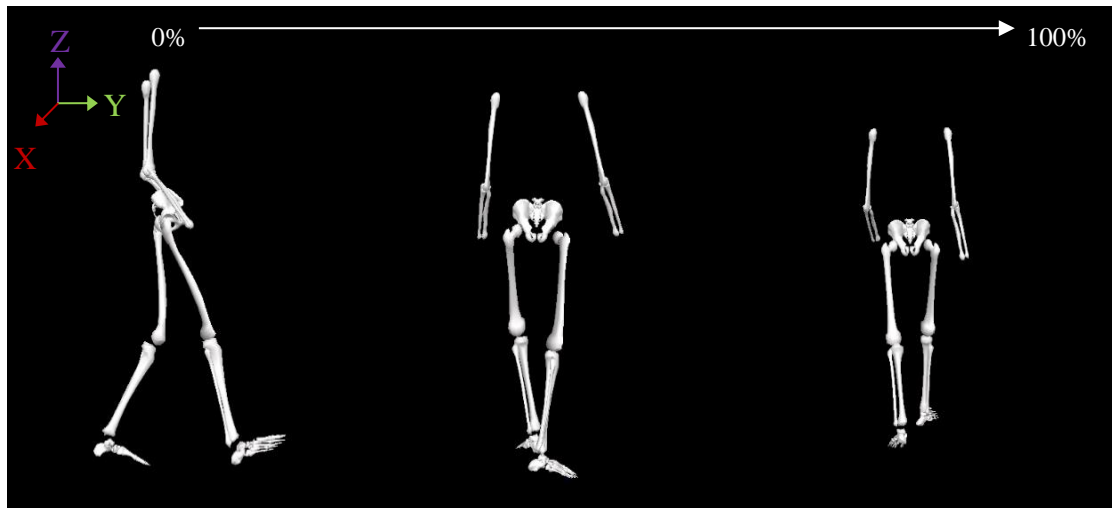


Figure 36. Walking model within Visual3D showing a walk turn gait cycle from start (left) to end (right).

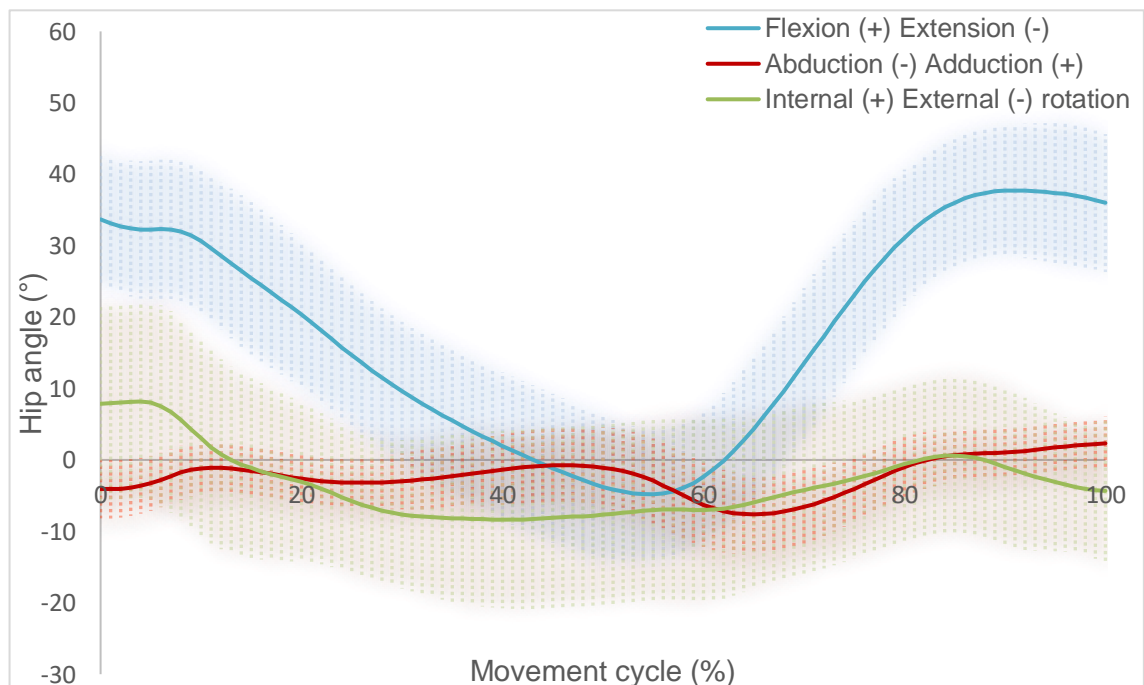


Figure 37. Mean right hip angle during one gait cycle for a walk turn. Standard deviation above and below the mean are shown as shaded error bars (n=18).

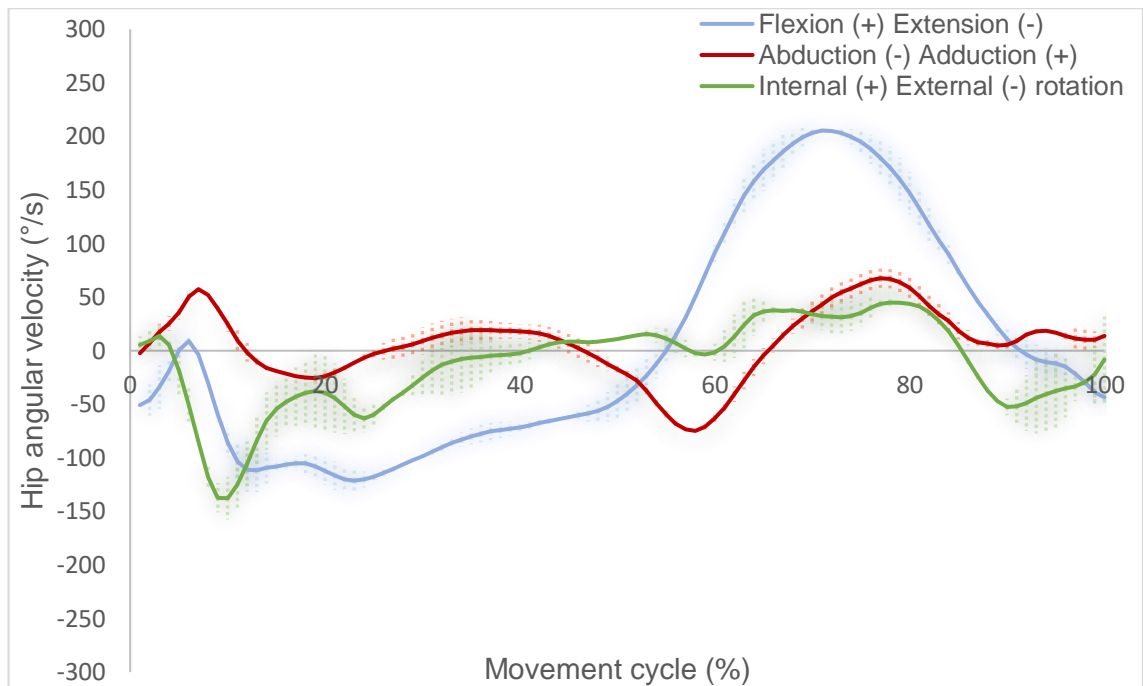


Figure 38. Mean right hip angular velocity during one gait cycle for a walk turn. Standard deviation above and below the mean are shown as shaded error bars (n=18).

As would be expected, the walk turn hip kinematics (Figure 44) showed similarities to the normal walk. Flexion-extension patterns were almost identical to the normal walk (Figure 44), with a 43° range of motion. However, the flexion angle at initial contact was reduced (4° reduction) in comparison to the normal walk. A net abduction angle was observed throughout the gait cycle, which peaked at toe-off (7.5°). The hip was initially internally rotated at initial contact (8°), before a period of external rotation approaching push-off. At this point, the angle plateaued at an externally rotated angle of 8°. During the swing phase (≈60-100% of the gait cycle), the hip internally rotated to a neutral position, before preparing for initial contact. The main observations for the walk turn, in comparison to the normal walk, were the externally rotated hip and reduced flexion angle at initial contact alongside a net abduction angle throughout the stance phase.

Average SDs for flexion-extension, abduction-adduction and internal-external rotation were $\pm 10^\circ$, $\pm 4^\circ$ and $\pm 12^\circ$ respectively. Generally, the variation was consistent throughout the gait cycle for kinematics. With that being said, the abduction-adduction SD was noticeably larger during the push of phase of gait and the internal-external rotation showed higher variance at initial contact (0-10%) (Both 2° above the corresponding average SD).

Walk turn showed similar angular velocity trends to the normal walk (Figure 45). An initial peak extension velocity was seen during the stance phase (121 °/s), followed by a peak flexion velocity at the initial swing phase (205 °/s). It is noticeable that the walk turn showed an initial external rotation peak (138 °/s) in comparison to the internal rotation peak seen for the normal walk.

4.3.1.3. Incline Walk

The incline walk movement cycle started with right foot initial contact. Individuals walked up the straight 1:12 ratio ramp with the movement cycle ending at second initial contact of the right foot (Figure 46).

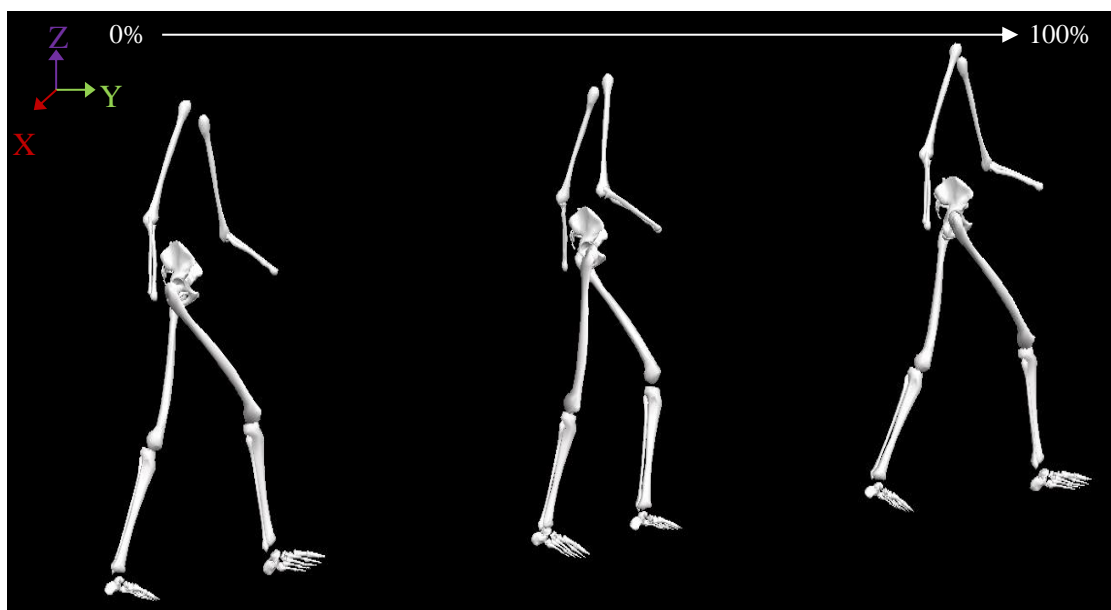


Figure 39. Walking model within Visual3D showing an incline walk gait cycle from start (left) to end (right).

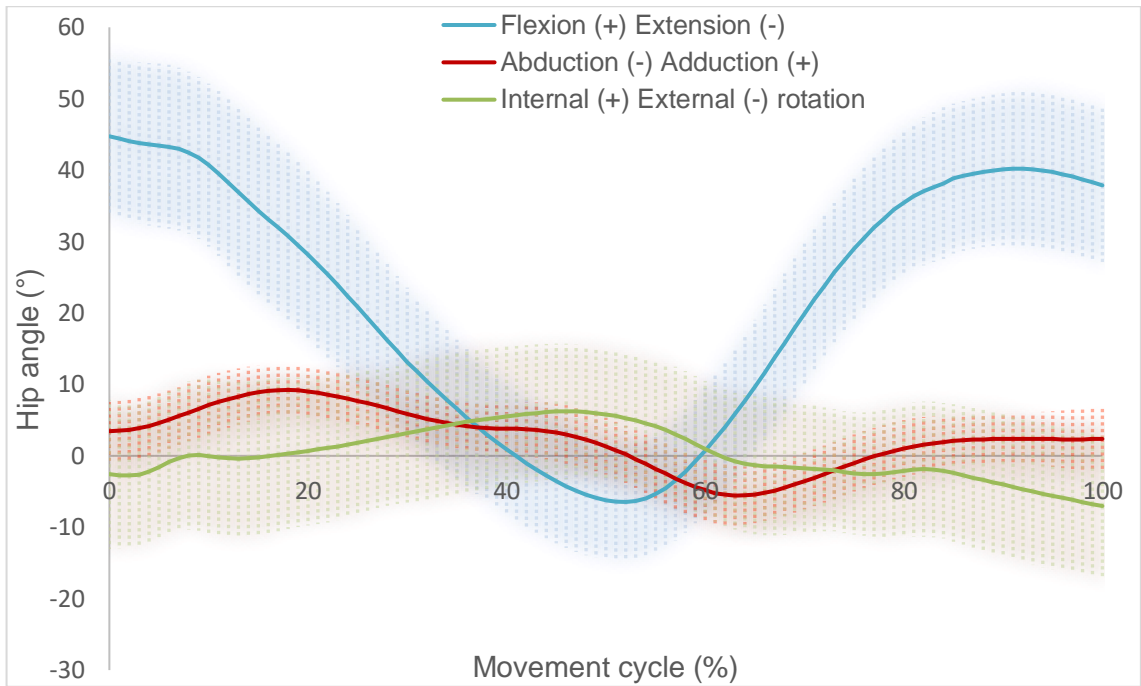


Figure 40. Mean right hip angle during one gait cycle for an incline walk (1:12 ramp). Standard deviation above and below the mean are shown as shaded error bars (n=18).

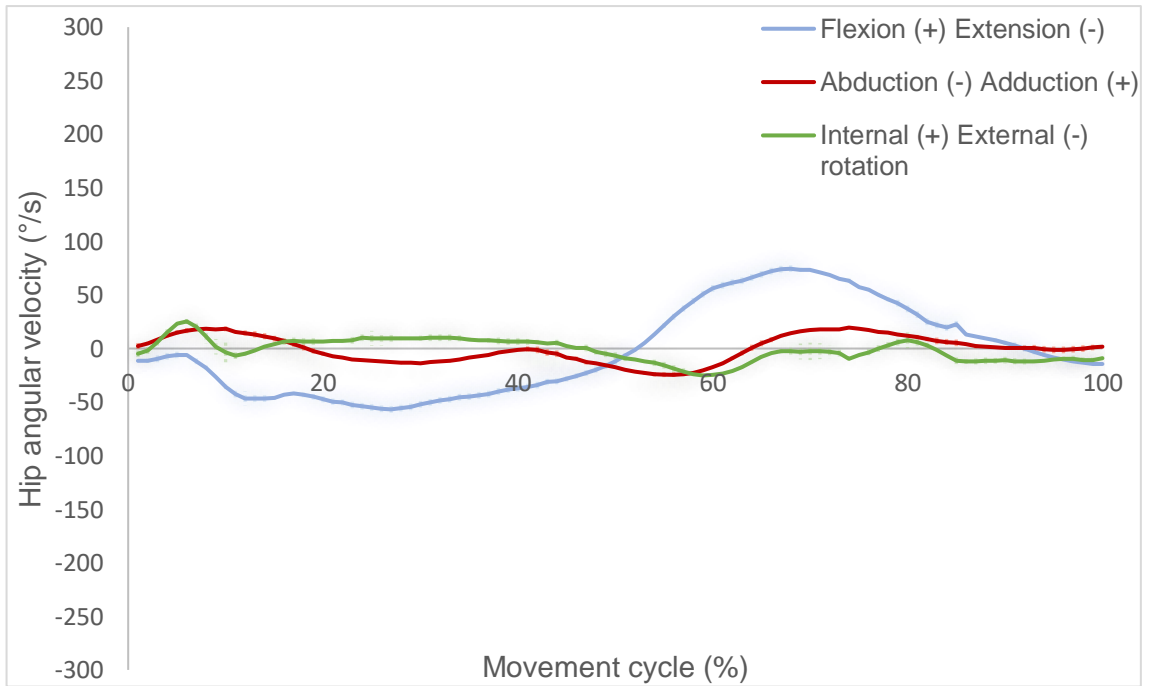


Figure 41. Mean right hip angular velocity during one gait cycle for an incline walk (1:12 ramp). Standard deviation above and below the mean are shown as shaded error bars (n=18).

Incline walk (Figure 47) displayed similar kinematic patterns to the level walk. Notable contrasts to the level walk include the increased mean hip flexion at initial contact (44° compared to 37°) and overall increased flexion-extension range of motion (50° compared to 45°). Mean incline walk SDs for flexion-extension, abduction-adduction and internal-external rotation were $\pm 10^\circ$, $\pm 4^\circ$ and $\pm 10^\circ$ respectively. Variation was consistent throughout the gait cycle for this movement. Hip angular velocity patterns for the incline walk (Figure 48) were comparable to the level walk. Peak velocities were noticeably decreased during the incline walk, with an initial extension peak of $57^\circ/\text{s}$ and a swing phase flexion peak of $74^\circ/\text{s}$.

4.3.1.4. Decline Walk

The decline walk movement cycle ran from first initial contact to second initial contact of the right foot. The movement took place in a straight line, down a 1:12 ratio ramp (49).

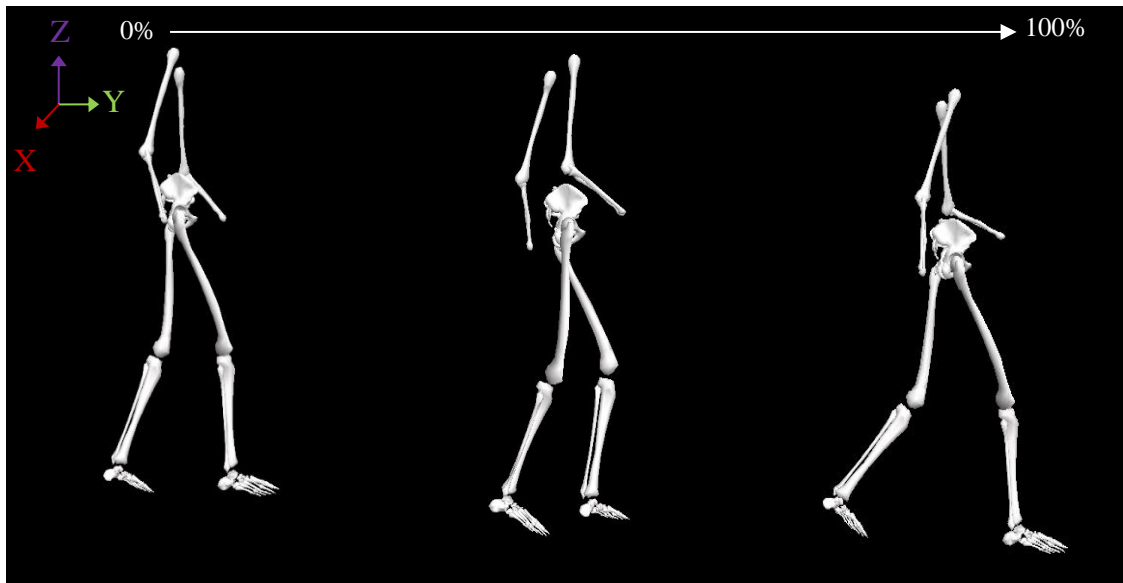


Figure 42. Walking model within Visual3D showing a decline walk gait cycle from start (left) to end (right).

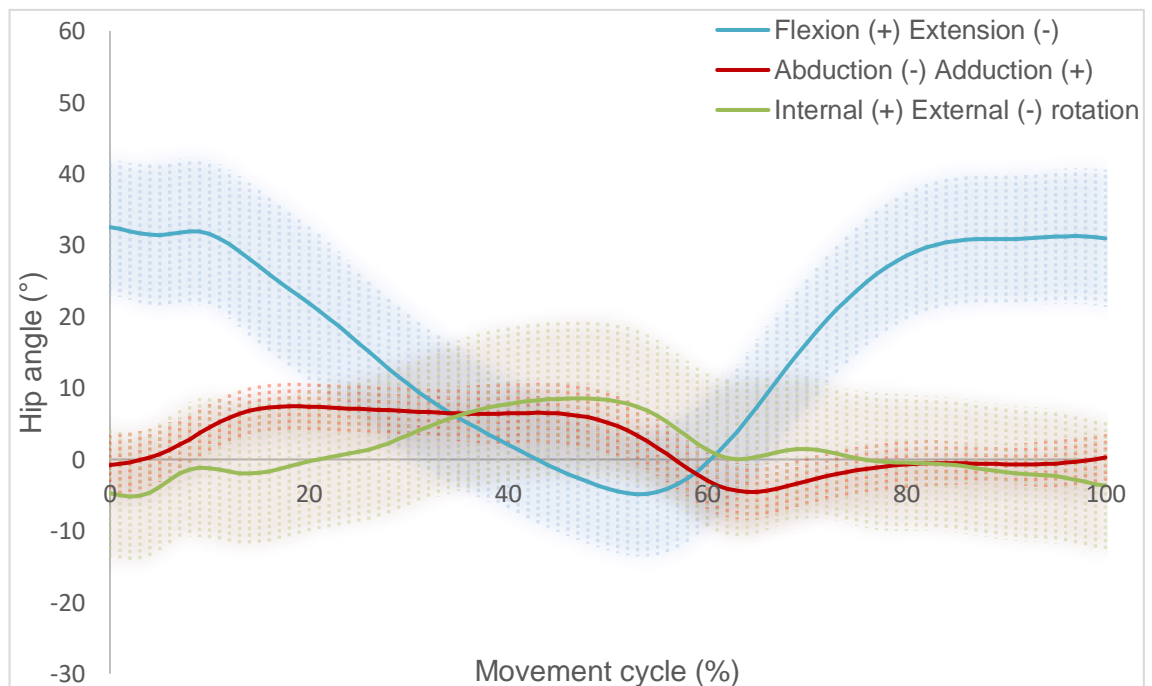


Figure 43. Mean right hip angle during one gait cycle for a decline walk (1:12 ramp). Standard deviation above and below the mean are shown as shaded error bars (n=18).

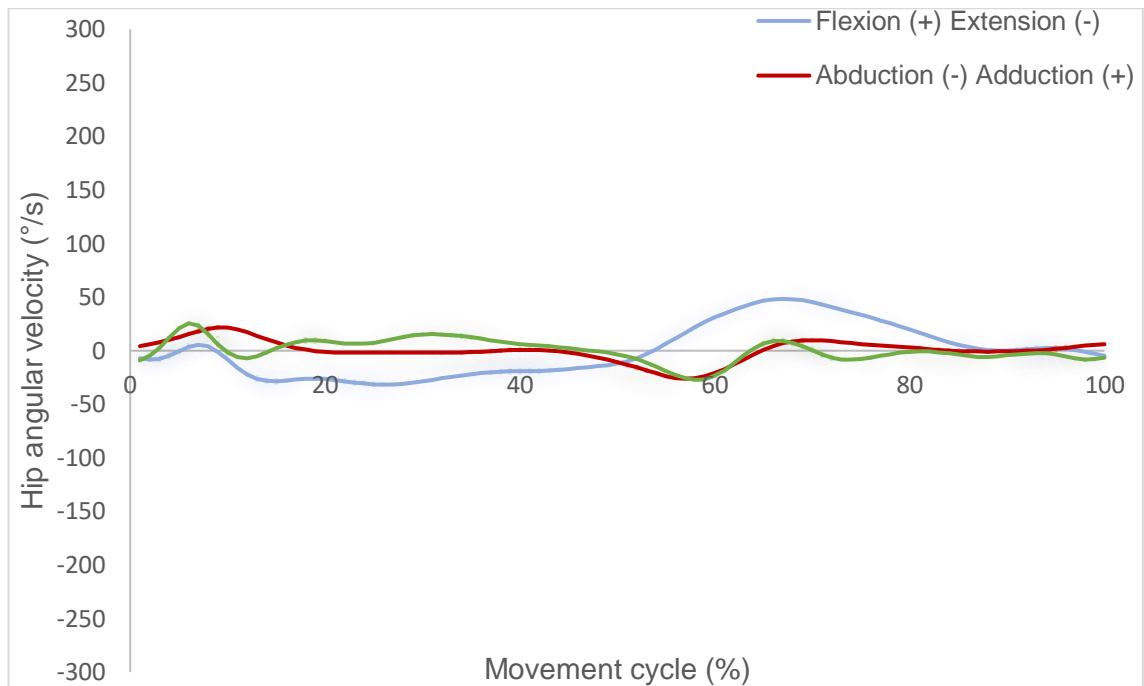


Figure 44. Mean right hip angular velocity during one gait cycle for a decline walk (1:12 ramp). Standard deviation above and below the mean are shown as shaded error bars (n=18).

As would be expected, the decline walk (Figure 50) shared similar hip kinematics to the level and inline walk. However, the decline walk displayed a decreased initial contact hip flexion than both the level and incline walk (level walk: 50° ; incline walk: 45° ; decline walk: 32°). Hip flexion peaked at 32° and the range of motion equalled 37° . The mean decline walk SDs were comparable to that of the incline walk (flexion-extension: $\pm 10^{\circ}$; abduction-adduction: $\pm 4^{\circ}$; internal-external rotation: $\pm 10^{\circ}$). The decline walk velocity (Figure 51) was similar to the level and incline walk, although peak velocities were decreased in comparison. The initial extension velocity was $32^{\circ}/s$ and the swing phase, flexion velocity was $48^{\circ}/s$.

4.3.1.5. Stand to Sit

The stand to sit cycle started with the participant in an upright, standing position. Participants then sat down onto a 47 cm stool (Figure 52).

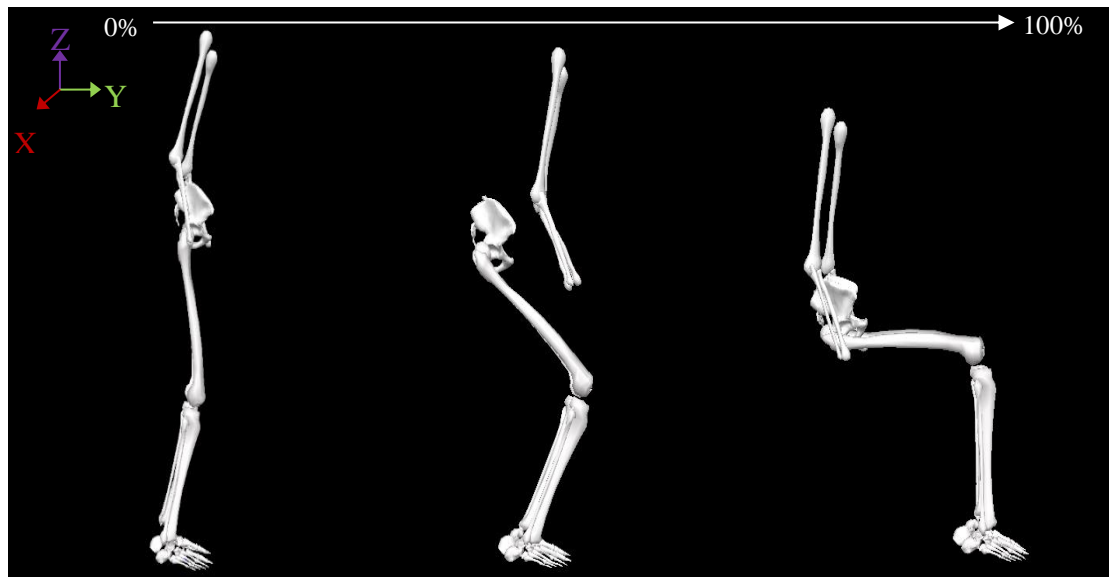


Figure 45. Walking model within Visual3D showing a stand to sit cycle from start (left) to end (right).

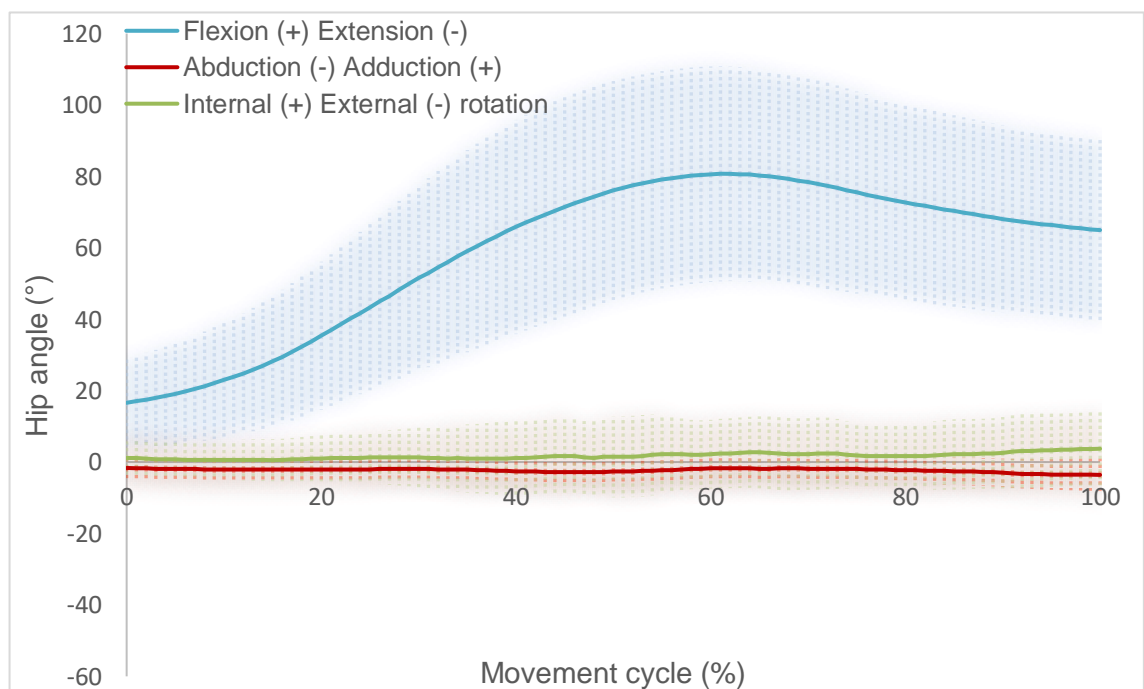


Figure 46. Mean right hip angle during one movement cycle for a stand to sit (chair height: 47 cm). Standard deviation above and below the mean are shown as shaded error bars (n=8).



Figure 47. Mean right hip angular velocity during one movement cycle for a stand to sit (chair height: 47 cm). Standard deviation above and below the mean are shown as shaded error bars (n=8).

The mean standing flexion angle equalled 16° (at 0% of the gait cycle) (Figure 53). This initial flexion angle ranged from 2° to 28° for subjects. The hip flexed as individuals sat down, reaching a mean peak of 81° (ROM: 64°). The hip then extended to 66° , as the pelvis tilted posteriorly in order to balance on the chair. The SD was noticeably larger when stood statically ($\pm 12^{\circ}$), compared to when sitting down ($\pm 26^{\circ}$) and the overall average ($\pm 26^{\circ}$). Hip abduction-adduction was neutral throughout the movement, with a SD of $\pm 3^{\circ}$. The hip was internally rotated when sitting (peaking at 4°), however the SD of $\pm 9^{\circ}$ suggests that internal-external rotation is likely to vary between participants in this task. When sitting down from a standing position, the hip flexion velocity increased and peaked at $132^{\circ}/s$ (Figure 54). The velocity then decreased to $0^{\circ}/s$ as the individual sat down on the seat, with a slight increase in external velocity when seated (peaking at $54^{\circ}/s$).

4.3.1.6. Sit to Stand

From a seated position on a 47 cm stool, individuals stood up into an upright position (without using their hands to push up from the stool) (Figure 55).

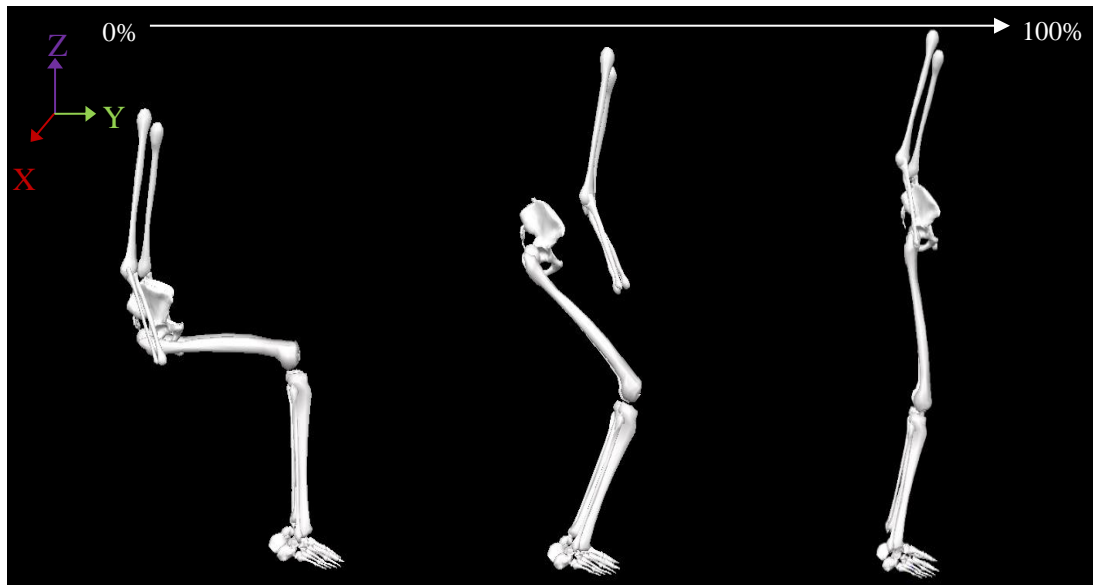


Figure 48. Walking model within Visual3D showing a sit to stand cycle from start (left) to end (right).

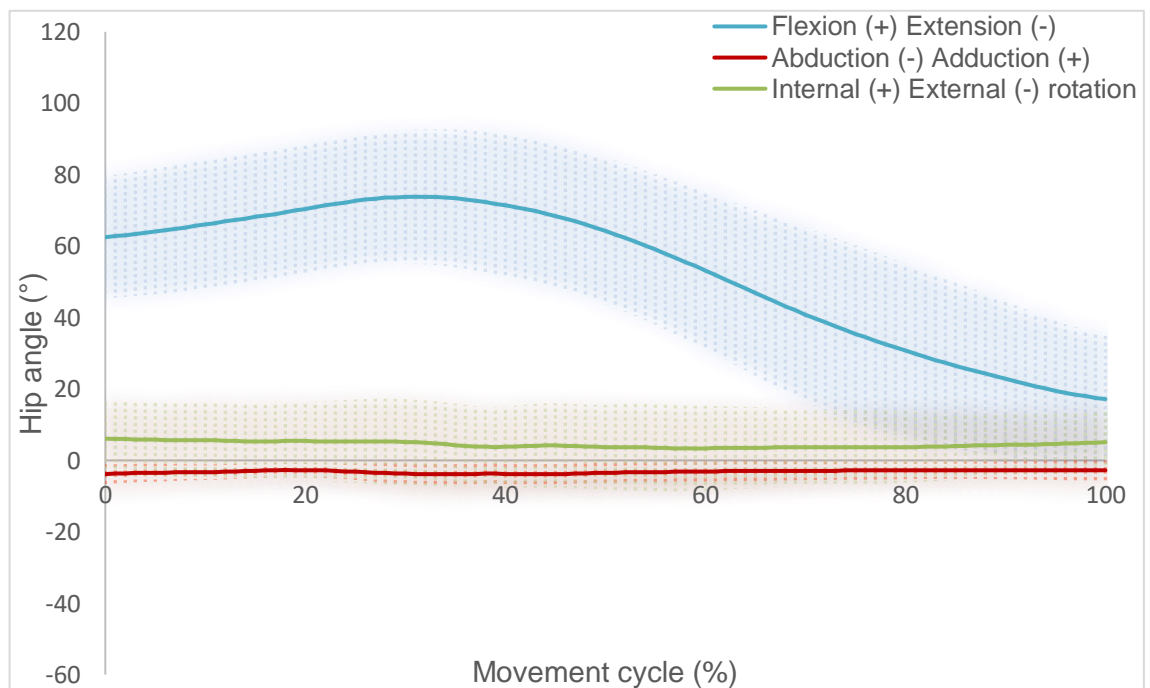


Figure 49. Mean right hip angle during one movement cycle for a sit to stand (chair height: 47 cm). Standard deviation above and below the mean are shown as shaded error bars (n=8).

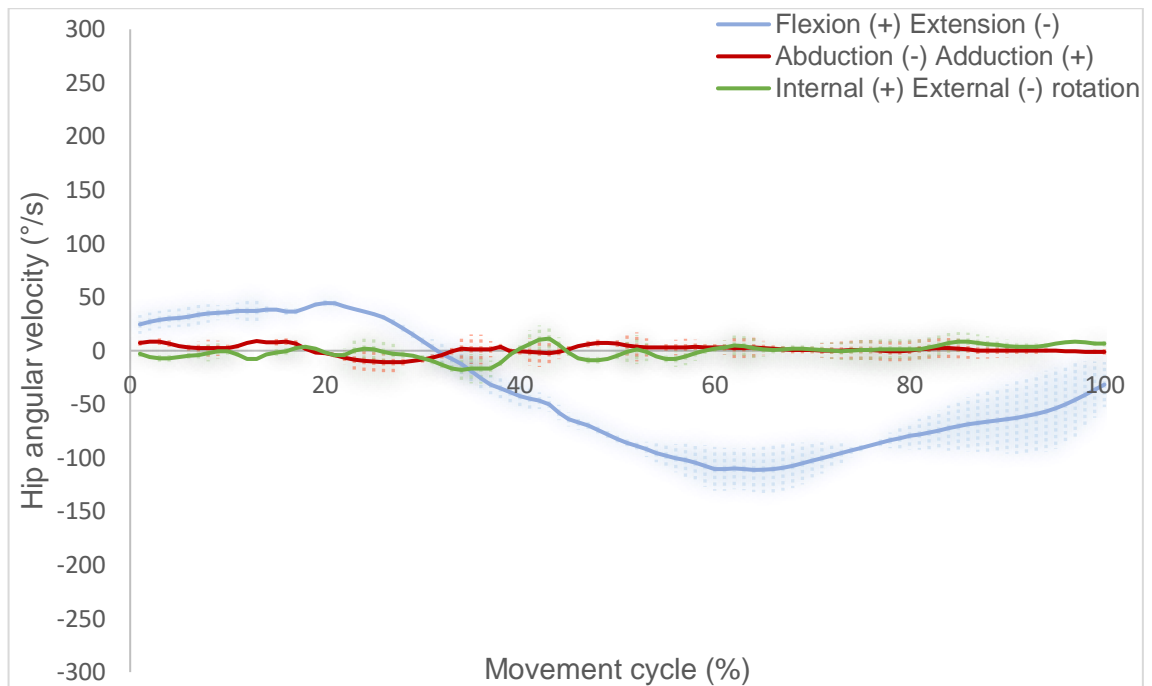


Figure 50. Mean right hip angular velocity during one movement cycle for a sit to stand (chair height: 47 cm). Standard deviation above and below the mean are shown as shaded error bars (n=8).

From a seated position (63°), the hip initially flexed by 11° , before extending through to a standing position (17°) (Figure 56). The average SD was lower than that for the stand to sit ($\pm 21^\circ$ compared to $\pm 26^\circ$) and showed more consistency throughout the movement. Similar to the stand to sit, SD was increased during the dynamic phase of the movement, however this observation was less obvious. The abduction-adduction angle showed a similar pattern to the stand to sit, with a small SD ($\pm 3^\circ$) and linear pattern of motion. The hip internally rotated to a peak of 6° , with a SD of $\pm 11^\circ$. During stand to sit, the hip extended and angular velocity increased to a peak of $111^\circ/\text{s}$ (Figure 57). Once stood up, the velocity reduced as the body reached a neutral posture.

4.3.1.7. Sit Cross Legged

From a seated position on a 47 cm stool, participants crossed their right leg over their left, before returning to the original seated position. Participants were instructed to cross their legs so that the outside of their right ankle was in contact with the top of their left knee. In addition to this, it was requested that the arms were not used to help lift the right leg over the left (Figure 58).

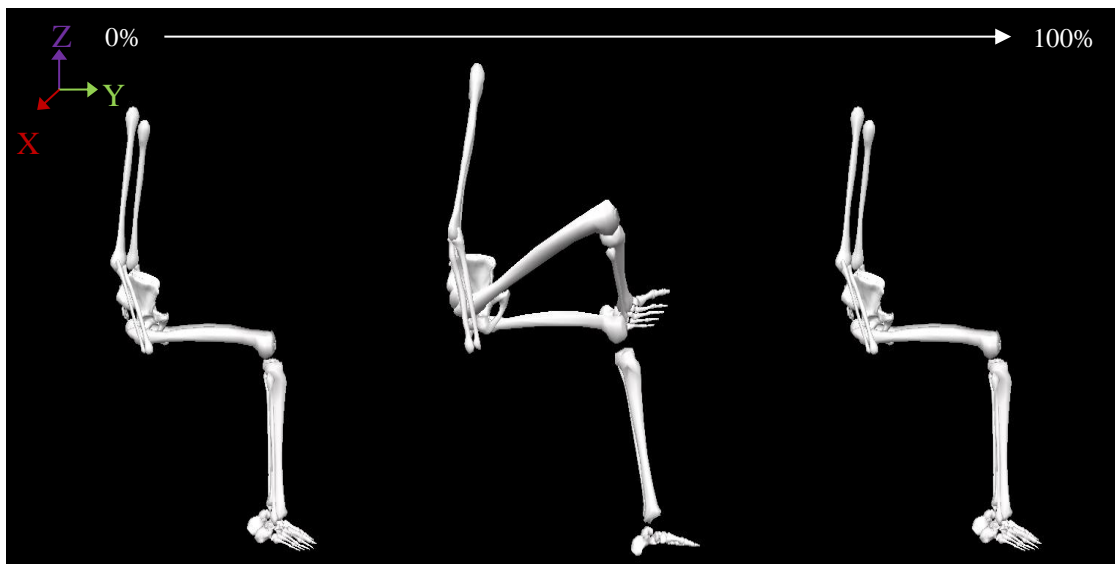


Figure 51. Walking model within Visual3D showing a sit cross legged cycle from start (left) to end (right).

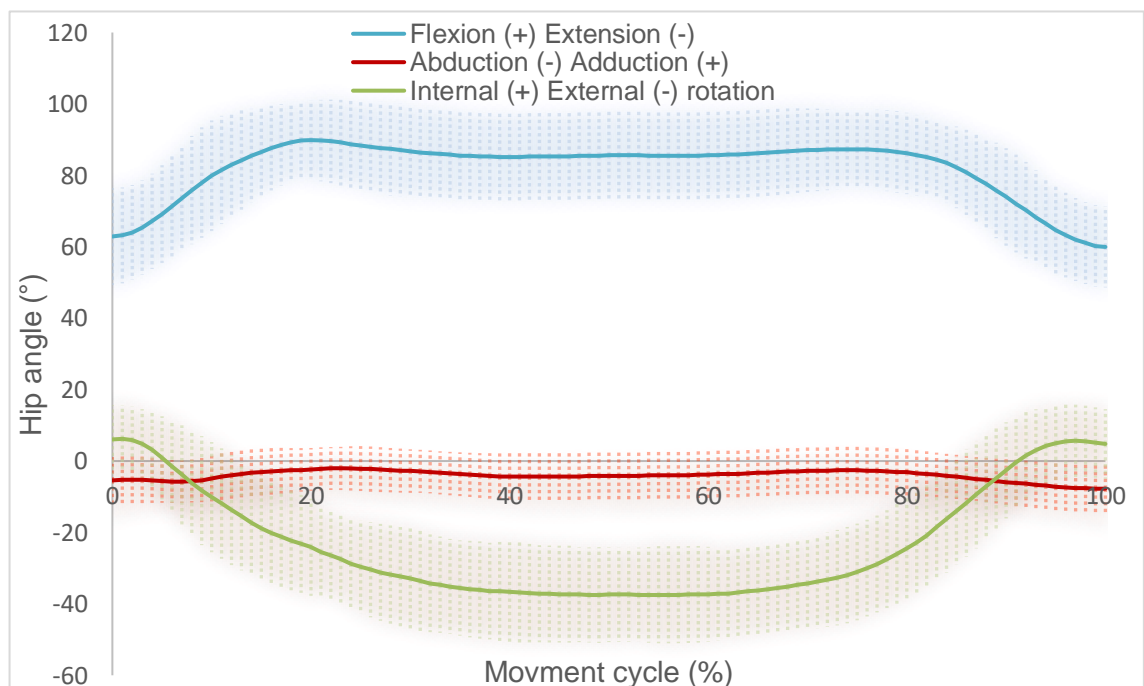


Figure 52. Mean right hip angle during one movement cycle for sitting and crossing legs (right crossed over left) (chair height: 47 cm). Standard deviation above and below the mean are shown as shaded error bars (n=14).

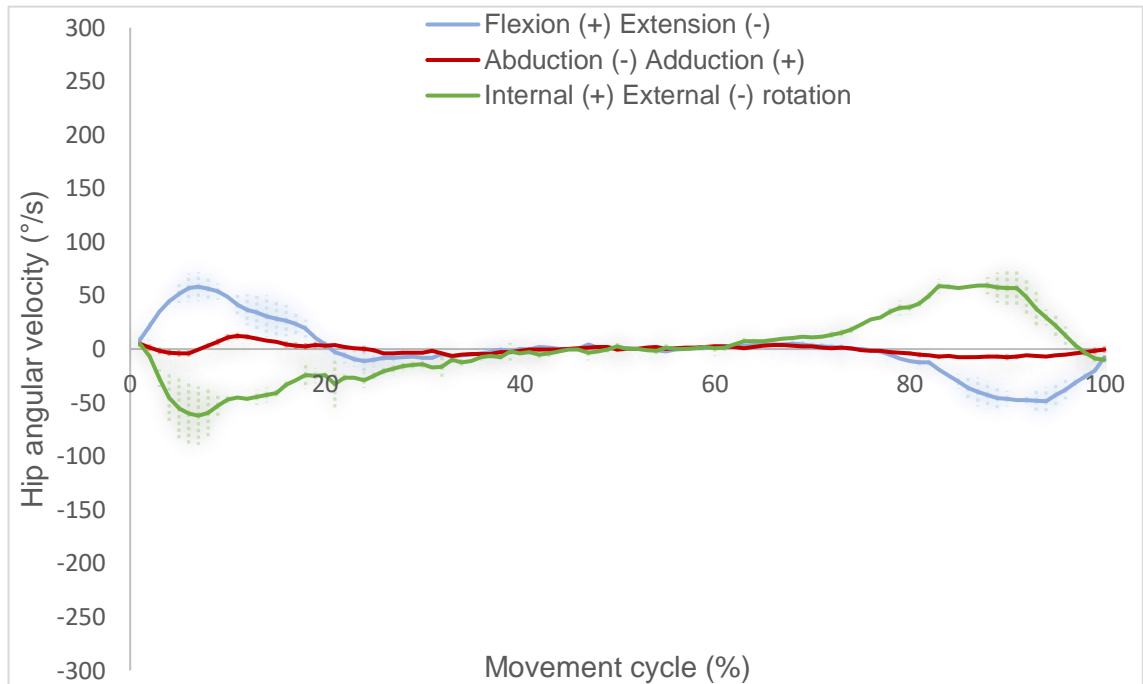


Figure 53. Mean right hip angular velocity during one movement cycle for sitting and crossing legs (right crossed over left) (chair height: 47 cm). Standard deviation above and below the mean are shown as shaded error bars (n=14).

Initially, when seated, the hip was flexed to 63° (Figure 59). As the right leg was raised and crossed over the left knee, the hip flexed and reached a peak of 90°, before extending back to the original seated position. The hip was abducted throughout the movement, with little fluctuation in the angular position. When seated, the hip was internally rotated (6°). External rotation at the hip allowed the right shank to lift up and on to the left knee (peaking at 38°) before returning to the original, seated position.

The SDs showed consistency throughout the movement, averaging at 12° (flexion-extension), 6° (abduction-adduction) and 13° (internal-external rotation). When crossing the right leg over the left, peak flexion (56 °/s) and external rotation (62 °/s) velocities were observed (Figure 60). Extension (49 °/s) and internal rotation (57 °/s) velocities were then shown as the right leg was un-crossed.

4.3.1.8. Squat

From an upright standing position, participants were requested to squat down to as close to 90° at the knee as possible, whilst keeping their back straight. The movement cycle ended once the body had returned to the starting position (Figure 61).

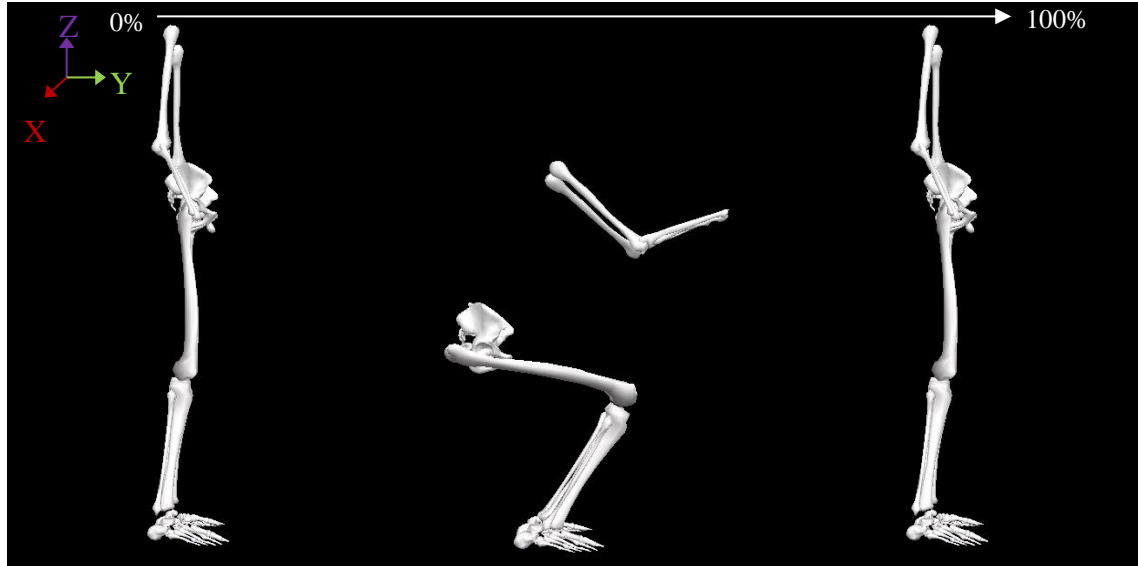


Figure 54. Walking model within Visual3D showing a squat cycle from start (left) to end (right).

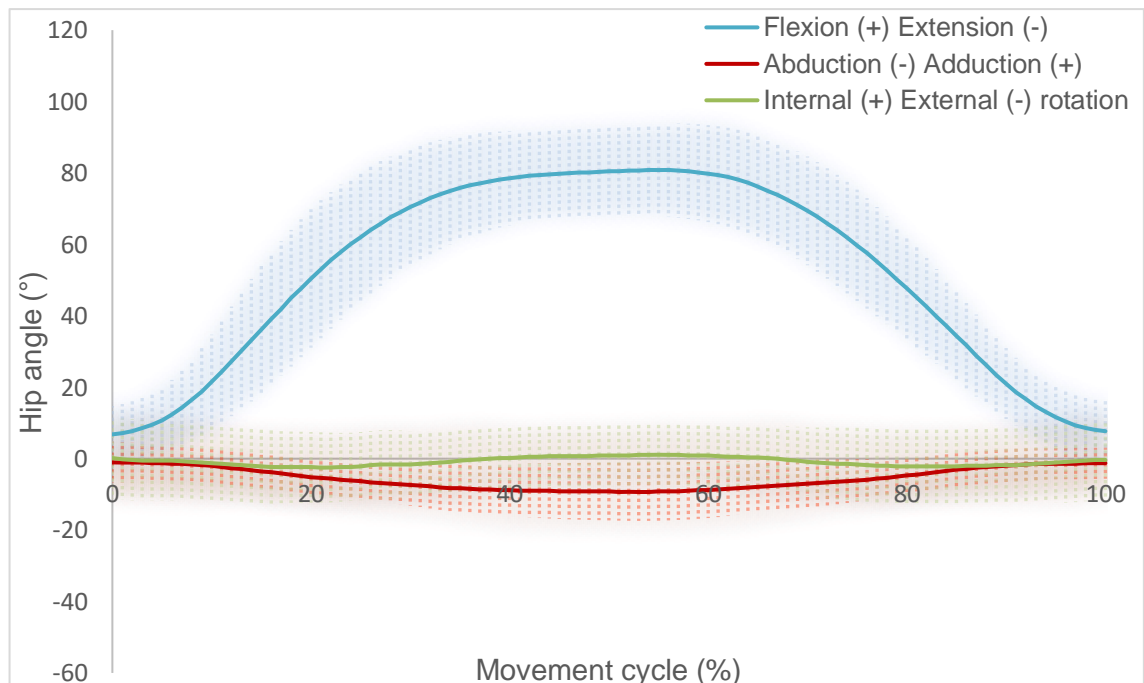


Figure 55. Mean right hip angle during one movement cycle for a squat. Standard deviation above and below the mean are shown as shaded error bars (n=13).

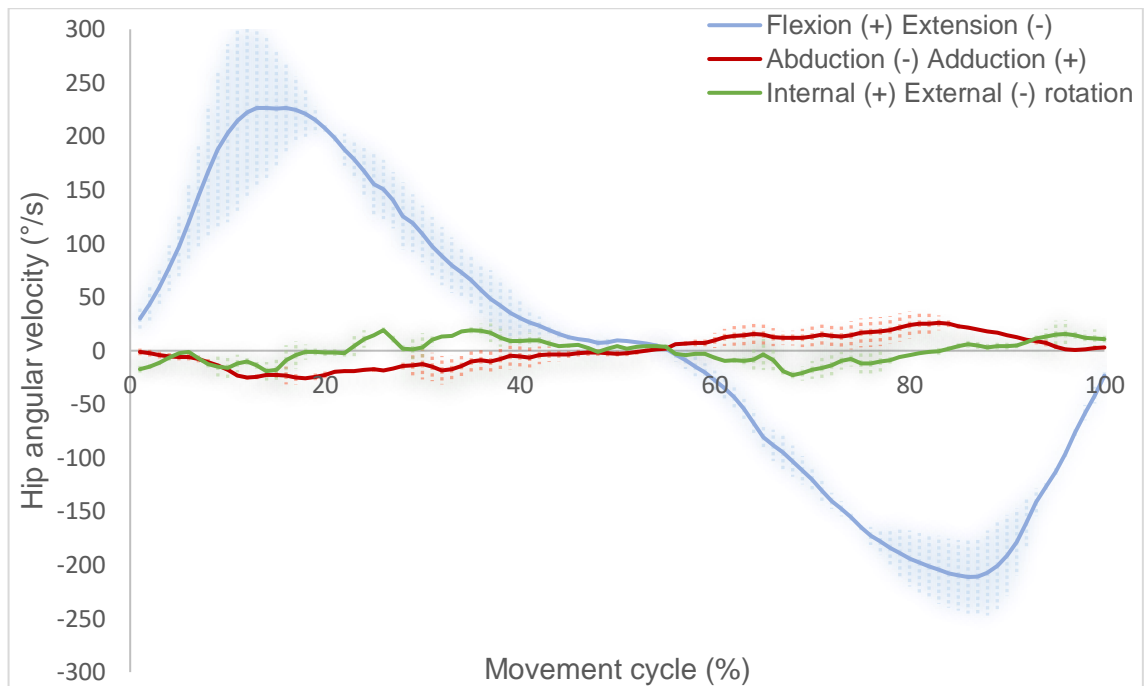


Figure 56. Mean right hip angular velocity during one movement cycle for a squat. Standard deviation above and below the mean are shown as shaded error bars (n=13).

From a standing position (7° flexion), the hip flexed into a squat, peaking at a flexion angle of 80° (Figure 62). The hip then followed a symmetrical pattern, to extend back to a standing position (ROM: 74°). The SD indicated less variation at the beginning and end of the movement, with the maximum variation occurring when flexed down into the squat position (max SD: $\pm 19^{\circ}$). Hip flexion SD averaged out at 14° across the entire task. From an initial neutral position the hip adducted when squatting down, peaking at 9° , before abducting back to 0° . The SD in this axis was $\pm 6^{\circ}$, with increased variation when in the squat position (the standard deviation was twice as large at 50% of the activity compared to at 100%). The hip was slightly internally rotated when in the squat position, with a consistent average SD of $\pm 10^{\circ}$ throughout the activity.

During the downwards phase of the squat, the flexion angular velocity peaked at $226^{\circ}/s$ (Figure 63). This reduced to $0^{\circ}/s$ at the deepest position of the squat, before displaying a peak extension angular velocity of $211^{\circ}/s$, when propelling up and out of the squat position.

4.3.1.9. Stand Reach

From a standing position, participants flexed at the hip and reached down (without touching the floor). Once at full hip flexion, individuals returned back to the starting position (Figure 64).

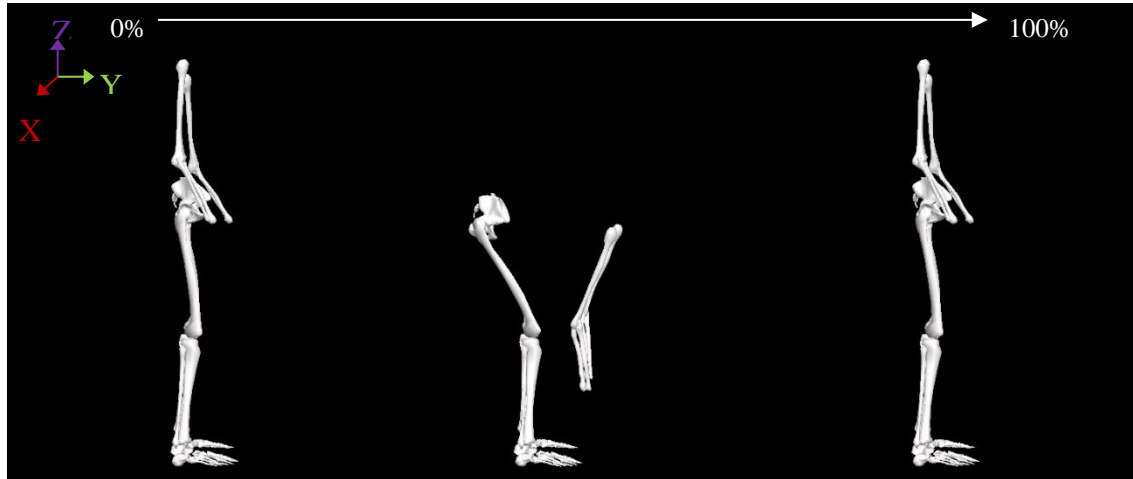


Figure 57. Walking model within Visual3D showing a stand reach cycle from start (left) to end (right).

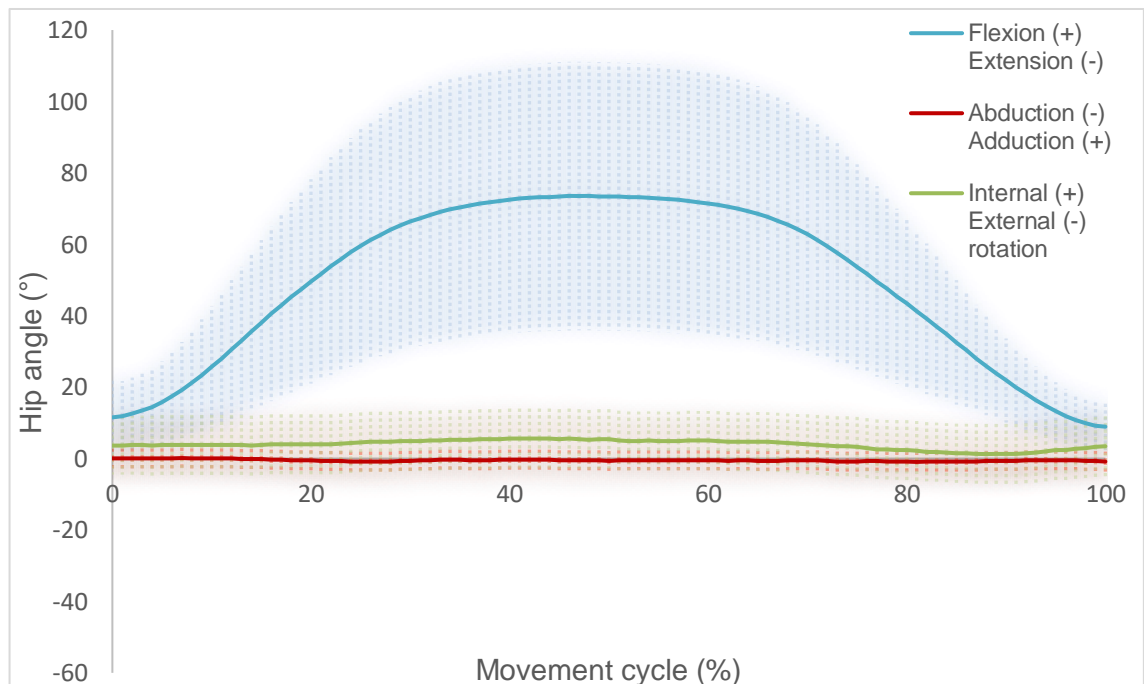


Figure 58. Mean right hip angle during one movement cycle for standing and reaching down to the floor. Standard deviation above and below the mean are shown as shaded error bars (n=12).

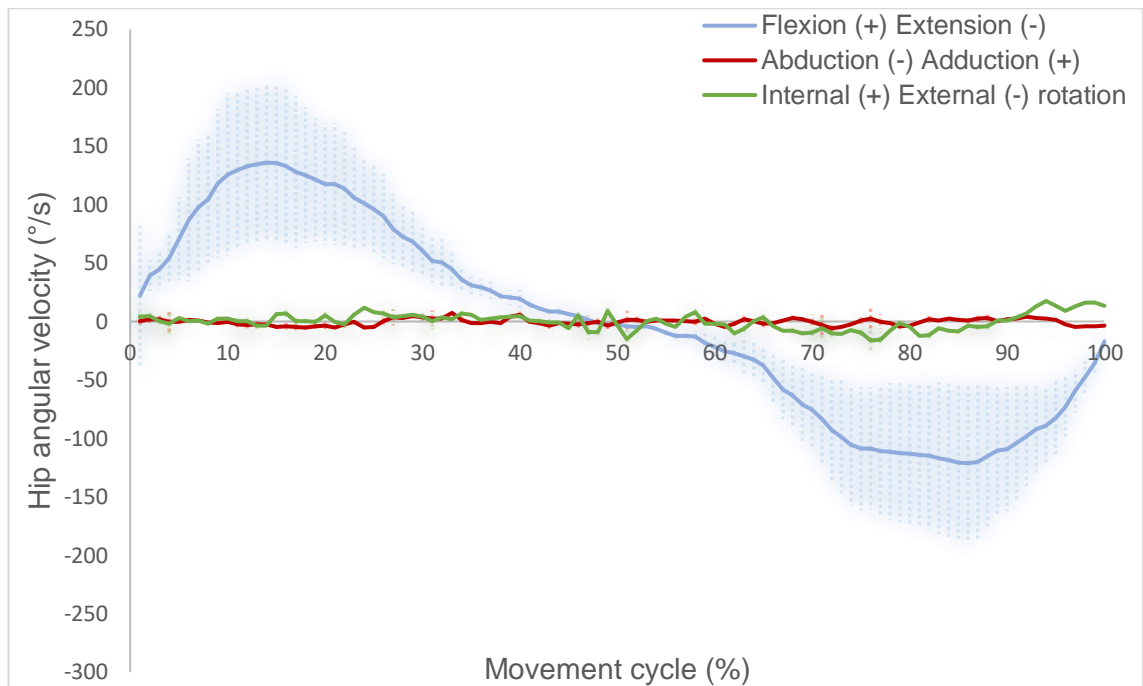


Figure 59. Mean right hip angular velocity during one movement cycle for standing and reaching down to the floor. Standard deviation above and below the mean are shown as shaded error bars (n=12).

From a standing position (12°), the hip flexed and the pelvis tilted anteriorly allowing the arms to reach down to the floor (Figure 65). The hip peaked at a flexion angle of 74° and began to extend back to the initial standing position (ROM: 65°). When standing, flexion-extension variation was low (minimum SD: 6°). In contrast, at full reach (50% of the movement) the SD indicated a high level of variability between individuals ($\pm 38^\circ$). The average SD across the movement was equal to $\pm 27^\circ$. The abduction-adduction angle remained neutral at $\approx 0^\circ$, with consistent variability throughout the movement (mean SD: $\pm 3^\circ$). The hip was internally rotated throughout, peaking at 6° and showed consistent variation throughout the movement (mean SD: $\pm 8^\circ$).

When reaching down to the floor from a standing position, the hip flexion velocity peaked at $136^\circ/\text{s}$ (Figure 66). Angular velocity returned to zero when the bodies position was held still at full reach. Individuals then extended the hip back to the standing position, peaking at an extension velocity of $121^\circ/\text{s}$.

4.3.1.10. Kneel Reach

The movement cycle began in a knelt position, with the torso upright. Participants flexed at the hip to reach as far forward as possible, before returning to the start position (Figure 67).

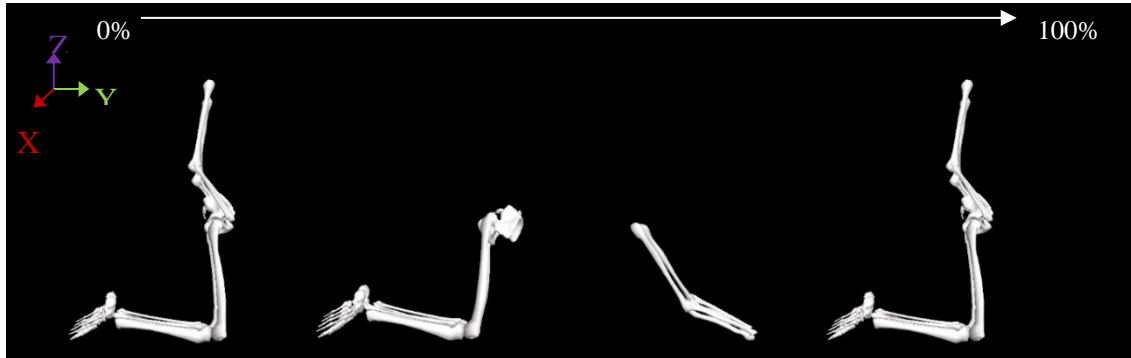


Figure 60. Walking model within Visual3D showing a kneeling reach cycle from start (left) to end (right).

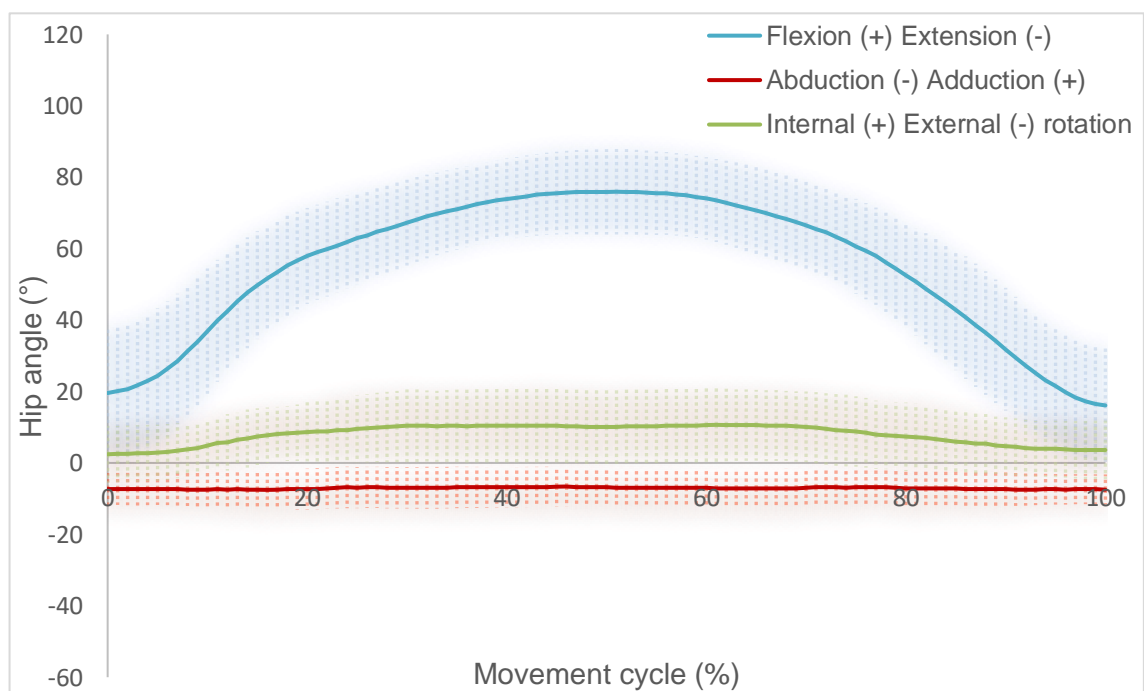


Figure 61. Mean right hip angle during one movement cycle for kneeling and reaching forwards. Standard deviation above and below the mean are shown as shaded error bars (n=13).

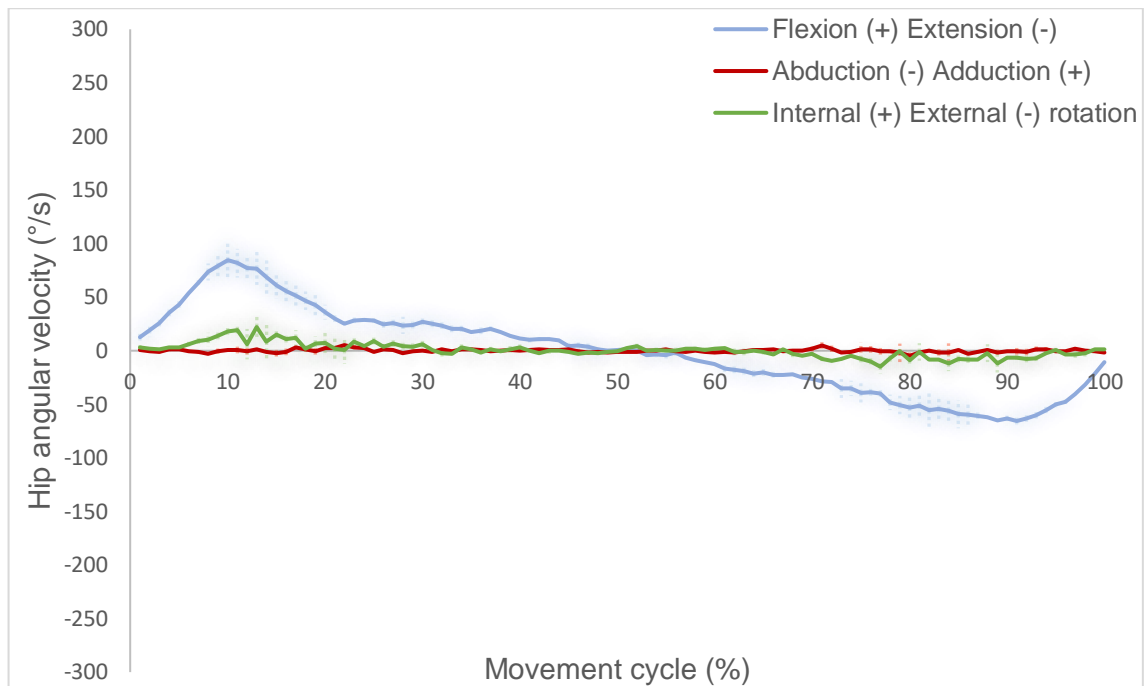


Figure 62. Mean right hip angular velocity during one movement cycle for kneeling and reaching forwards. Standard deviation above and below the mean are shown as shaded error bars (n=13).

Kneel reach kinematics display a hip flexion angle of 21° at the beginning of the movement, when knelt with an up-right torso (Figure 68). As individuals reached forwards towards the ground, the hip flexed to a peak of 76° (ROM: 60°). Kneel reach flexion-extension profile exhibited more variation during the static position, compared to when reaching forwards. The SD averaged to ±14°, which was noticeably lower than the stand reach task. The hip was abducted throughout the movement with negligible angular changes and a consistent variation throughout the activity (mean SD: ±5°). The hip internally rotated when reaching forwards and externally rotated when returning to the original, kneeling position (peak internal rotation: 10°). Variation for the internal-external rotation was increased during the dynamic reaching phase of the movement (mean SD: ±9°).

From an upright, kneeling position individuals reached forwards and experienced a peak hip flexion angular velocity of 82 %/s (Figure 69). The hip then extended back to the original kneeling position and experienced a peak extension velocity of 66 %/s.

4.3.1.11. Lunge

The movement cycle began at left foot initial contact. Participants stepped onto their right foot and lunged down lowering the knee close to, but not touching, the floor. The second half of the movement saw participants propel up and out of the lunge, with the movement cycle ending at the next left initial contact (Figure 70).

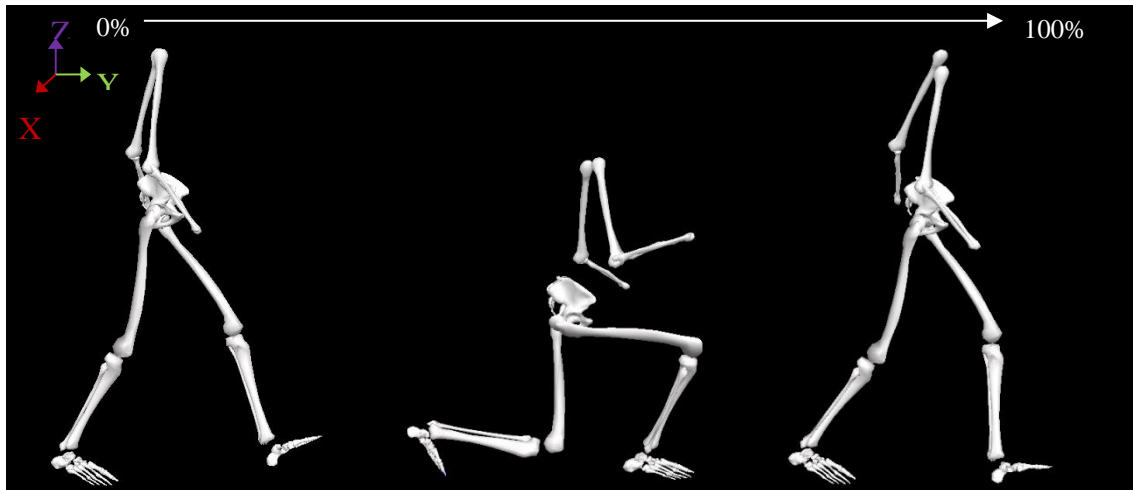


Figure 63. Walking model within Visual3D showing a lunge cycle from start (left) to end (right).

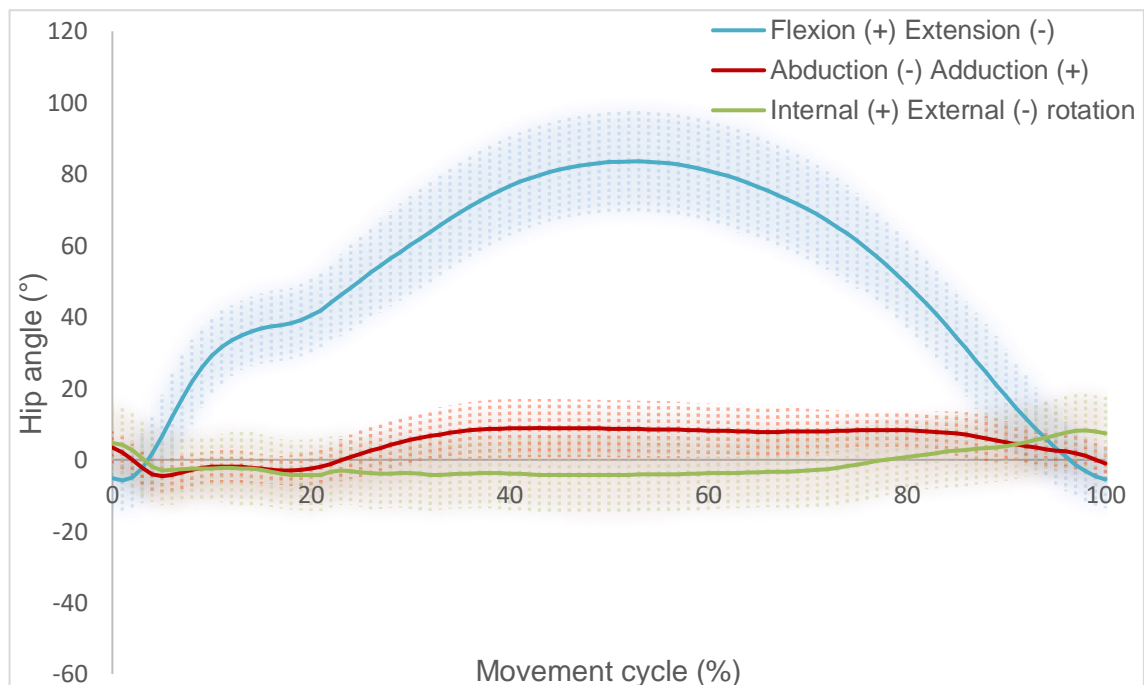


Figure 64. Mean right hip angle during one movement cycle for a right footed lunge. Standard deviation above and below the mean are shown as shaded error bars (n=17).

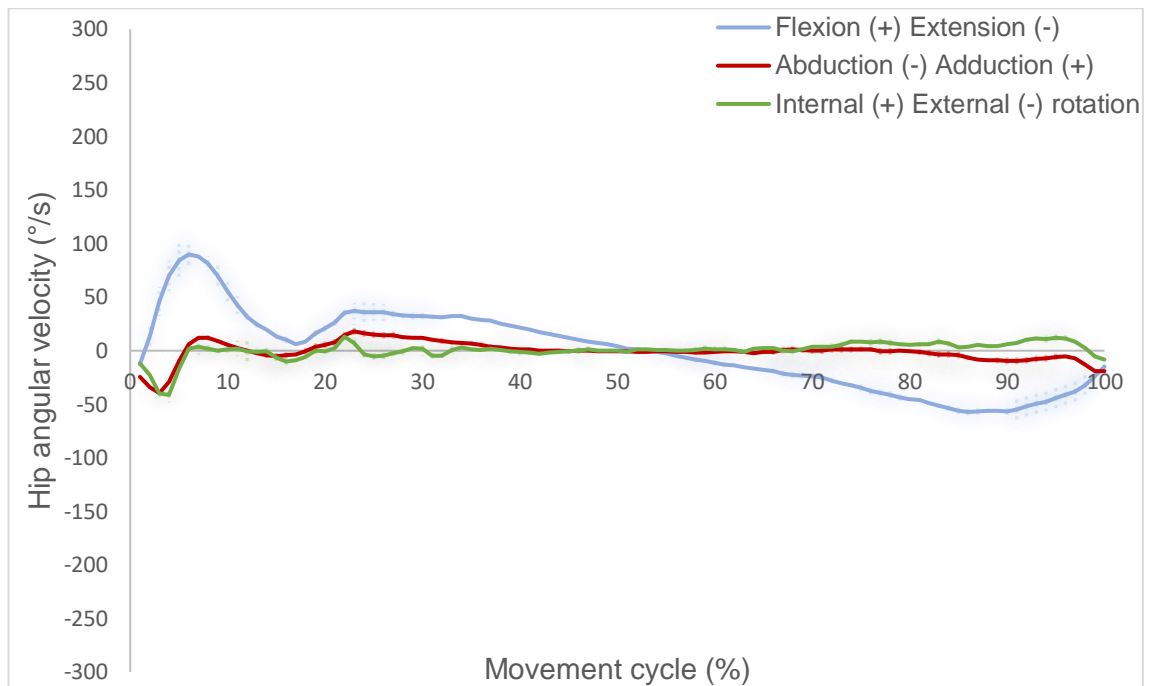


Figure 65. Mean right hip angular velocity during one movement cycle for a right footed lunge. Standard deviation above and below the mean are shown as shaded error bars (n=17).

From an initially extended position, the right leg swung forwards and flexed at the hip. Angular velocity during this phase was comparative with a normal walk (4-11% of the cycle) (Figure 71). The angular velocity then decreased from initial contact ($\approx 15\%$ of the cycle), as the torso moved over the lower limb (anterior pelvic tilt) during the downward, decelerating phase of the lunge. The hip continued to flex, up to a peak of 84° , at which point the right foot was flat and the lunge was at its deepest position. The hip then extended through the ascending, propulsion phase up until toe-off. The flexion-extension SD was increased when the hip was at its most flexed (30-70% of the cycle) (peak SD: $\pm 15^\circ$; mean SD: $\pm 13^\circ$).

The hip abducted during the swing phase of the lunge. From initial contact and throughout the contact phase of the lunge, the hip adducted and plateaued at 9° . Variation was up to 3° larger during the start and end of the lunge cycle, compared to the middle (mean SD: $\pm 6^\circ$). A net external rotation occurred throughout the lunge, with a short 25% period of internal rotation throughout the propulsion phase (mean SD: $\pm 10^\circ$).

Hip flexion angular velocity peaked at $88^\circ/\text{s}$ during the swing phase, approaching initial contact (7% of the movement) (Figure 72). A second flexion peak of $36^\circ/\text{s}$ was observed once the right foot was planted and the body moved down into the lunge. Angular velocity

reached 0 °/s at the lowest point of the lunge, before an increased extension velocity occurred during the propulsive phase of the movement (peaking at 57 °/s).

4.3.1.12. Golf Swing

The movement started with the golf club head lowered to a plastic tee. Participants twisted at the hip and swung the club backwards over their right shoulder, before swinging down and through a plastic tee. The final part of the movement cycle saw the club follow through up and over the left shoulder (Figure 73).

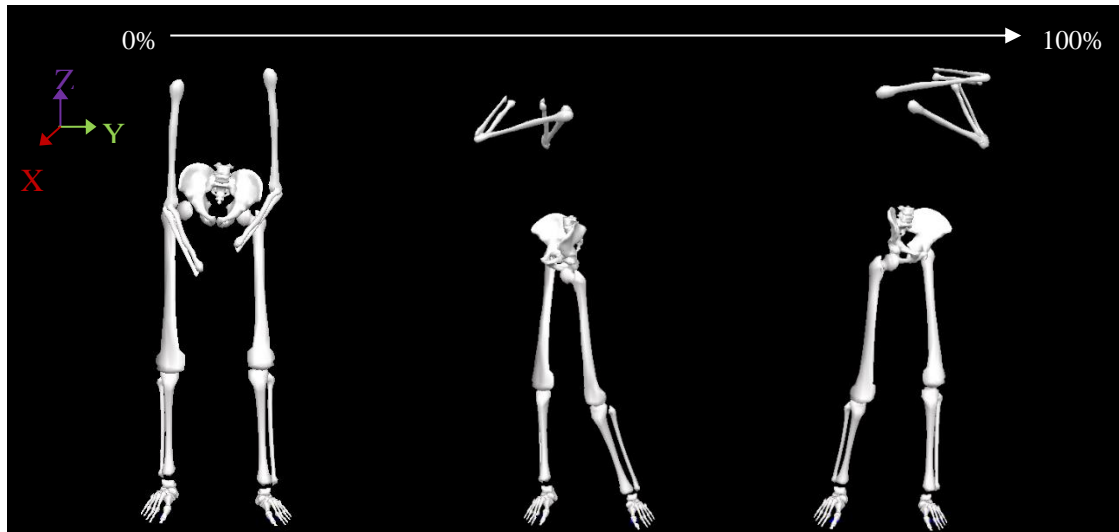


Figure 66. Walking model within Visual3D showing a golf cycle from start (Left) to end (Right).

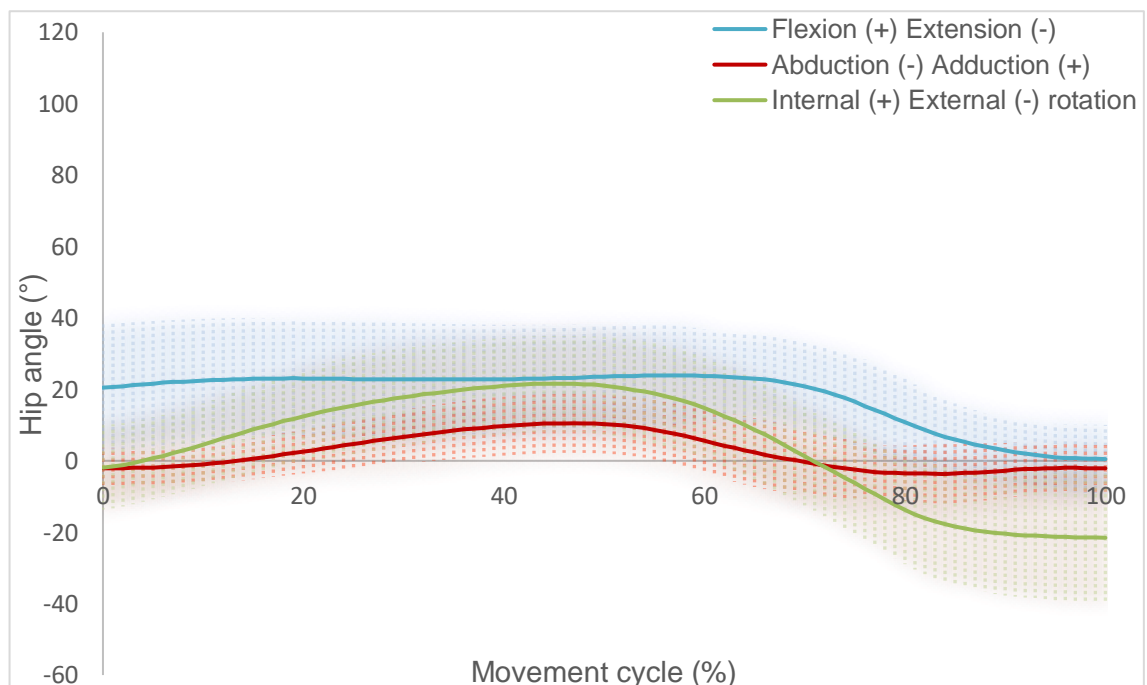


Figure 67. Mean right hip angle during one movement cycle for a golf swing. Standard deviation above and below the mean are shown as shaded error bars (n=18).

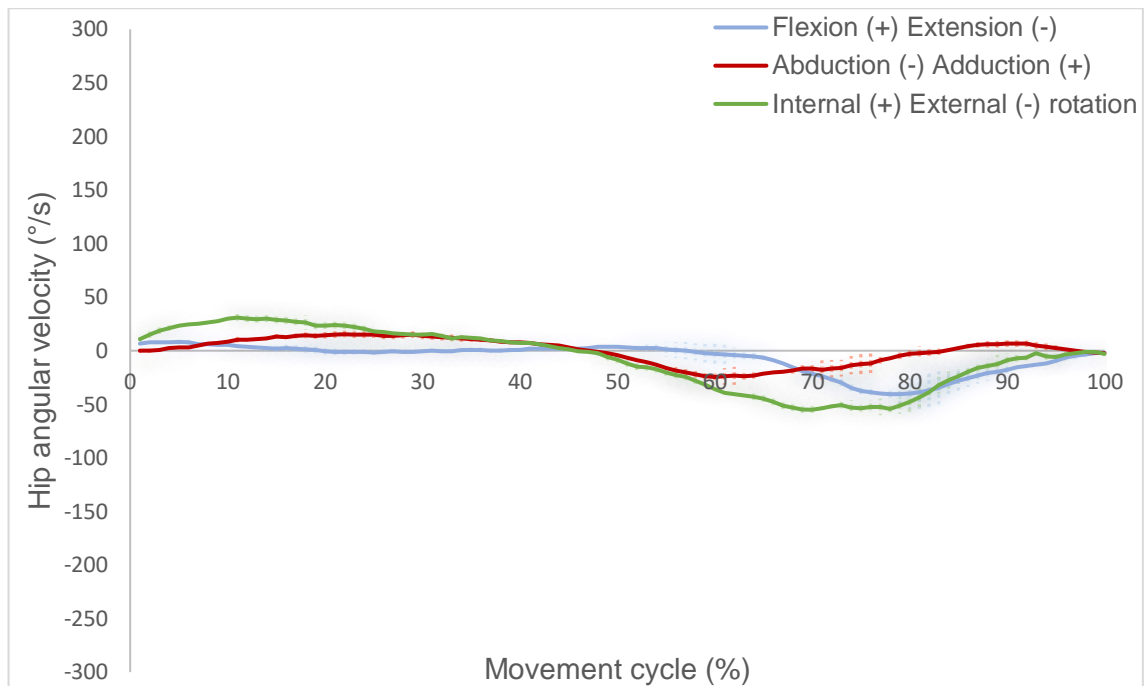


Figure 68. Mean right hip angular velocity during one movement cycle for a golf swing. Standard deviation above and below the mean are shown as shaded error bars (n=18).

The hip was flexed between 21° and 24° degrees throughout the backswing (≈0-50% of the swing) and the downswing (≈50-70% of the swing) (Figure 74). During the follow through (≈70-100% of the swing), the hip extended up until the end of the swing (0°). From an initial neutral position, the hip adducted and internally rotated, reaching peaks of 11° and 22° at the top of the swing, respectively. During the downswing, the hip abducted and externally rotated. During the follow through, the hip abduction-adduction angle plateaued at 0°, whilst continuing to externally rotate, reaching a peak angle of 21° at the top of the follow through.

Variability was high across the kinematics, averaging at ±14° (flexion-extension), ±8° (abduction-adduction) and ±14° (internal-external rotation). Flexion-extension SD indicated high variability during the back swing (±16°), which reduced throughout the downswing (±14°) and was lowest during the follow through (±11°). Abduction-adduction SD was highest at impact (≈70% of the swing), peaking at ±9.6°. In contrast to flexion-extension, the hip rotation variability was lowest during the back swing (±13°) and increased through the downswing (±14°) and the follow through (±17°).

During the back swing, peak adduction (15 °/s) and internal rotation (31 °/s) angular velocities were observed (Figure 75). During the follow through of the golf swing, angular

velocities peaked at 41, 25 and 55 °/s for hip extension, abduction and external rotation, respectively.

4.3.1.13. Cycle

The movement cycle for cycling started with the pedal at the highest possible point and ended once the pedal had rotated 360° (Figure 76).

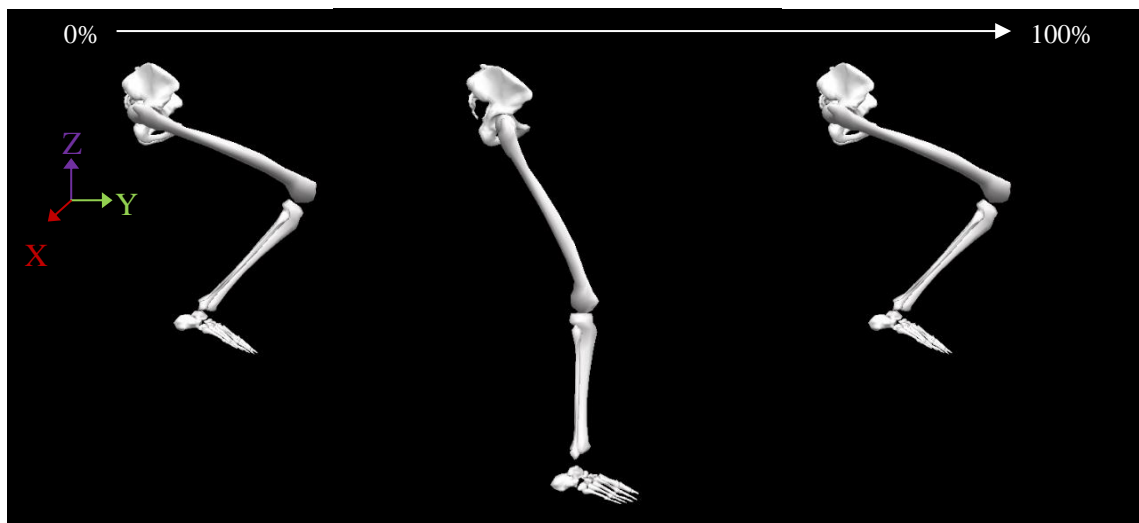


Figure 69. Walking model within Visual3D showing a cycle from start (Left) to end (Right).

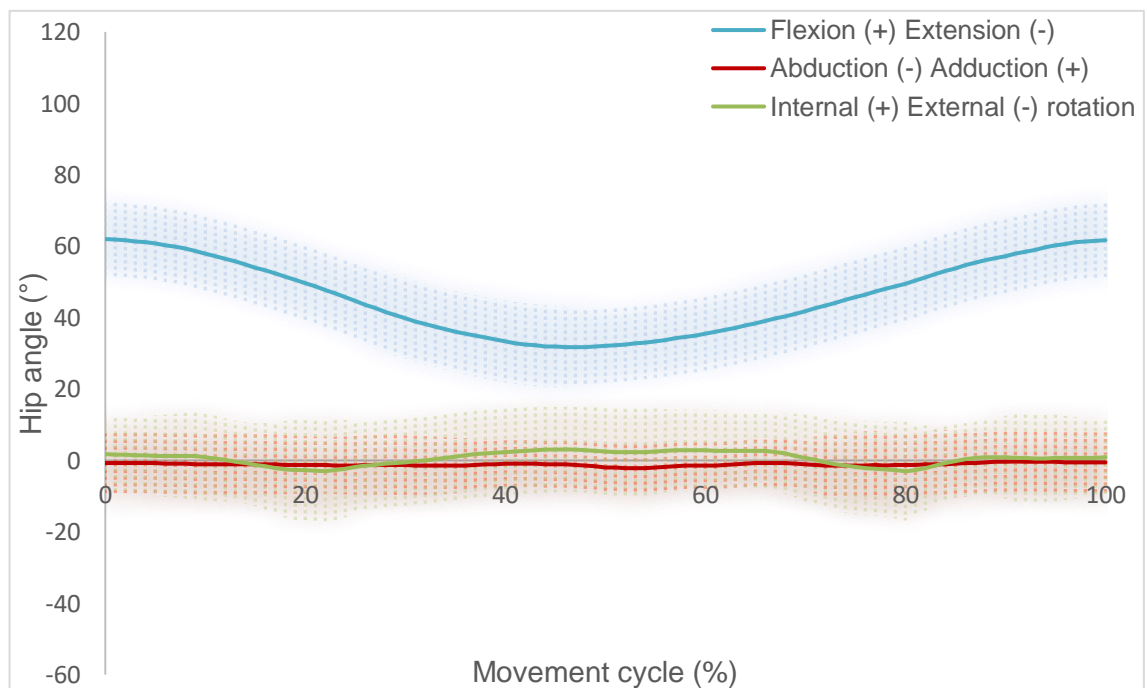


Figure 70. Mean right hip angle during one movement cycle for cycling. Standard deviation above and below the mean are shown as shaded error bars (n=10).

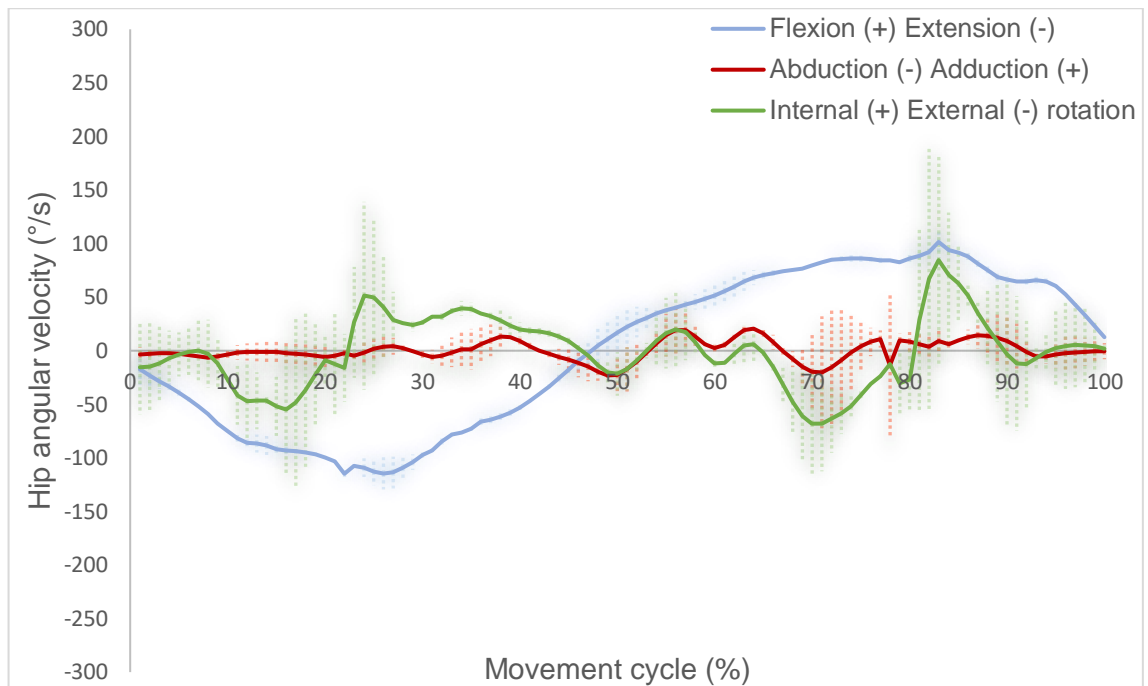


Figure 71. Mean right hip angular velocity during one movement cycle for cycling. Standard deviation above and below the mean are shown as shaded error bars (n=10).

The cycle began with the hip flexed to 62°, at which point the bicycle pedal was at the highest point (Figure 77). The hip extended as the pedal rotated around to the lowest point, with the hip flexion angle reducing to a minimum of 32° (ROM: 30°). The hip then flexed once again, in a cyclical pattern, back to the origin position. Hip abduction-adduction demonstrated a linear pattern, ranging between 2° abduction and 1° of adduction. Internal-external rotation showed a range of 6°, peaking with an internal rotation at the point where the pedal was lowest (3°). Variation remained consistent throughout the movement cycle for all hip kinematics, averaging at $\pm 11^\circ$ (flexion-extension), $\pm 8^\circ$ (abduction-adduction) and $\pm 12^\circ$ (internal-external rotation).

A peak extension angular velocity occurred as the pedal was rotated from high to low (Figure 78). Hip velocities were ≈ 0 °/s at the lowest point of the cycle. Hip flexion velocity then increased to a peak of 94 °/s as the pedal rotated back to the starting position.

4.3.2. Range of Motion

The range of motion (ROM) was calculated by subtracting the minimum angle, from the maximum angle in each axis of rotation. This may have implications for the localised motion paths (particularly the sliding distances) and joint reaction force loading position for activities.

Table 6. Mean range of motion for hip angular rotation about three axes (X: flexion-extension; Y: abduction-adduction; Z: internal-external rotation). Data are presented for thirteen activities. Peak values for each axis are highlighted in bold.

	Range of motion (°)		
	Flexion-extension	Abduction-adduction	Internal-external rotation
Walk	44	14	13
Walk turn	43	10	17
Incline walk	51	15	13
Decline walk	37	12	14
Stand to sit	64	2	3
Sit to stand	57	1	3
Sit cross legged	30	6	44
Squat	74	8	4
Stand reach	65	1	4
Kneel reach	60	1	8
Lunge	89	13	13
Golf	23	14	43
Cycle	30	2	6

Flexion-extension ROM varied considerably between activities (Table 10). The lunge showed the largest ROM for hip flexion-extension (89°), followed by the squat (74°) and the stand reach (65°). Activities demonstrating the lowest ROM in this axis were the golf swing (23°), cycling and sitting cross legged (both 30°).

Abduction-adduction ROM was negligible for five of the activities (stand to sit, sit to stand, stand reach, kneel reach and cycling). However, it is possible that this data is

skewed due to the averaging process (abduction and adduction motions may be cancelled out when considering the average net values across subjects). Other activities demonstrated ROM's between 6° and 15°, with the incline walk (15°), golf swing and walk (both 14°) showing the largest ROM.

Internal-external rotation of the hip was variable across the thirteen activities. Six activities showed a mean ROM below 10°. Five activities demonstrated a mean ROM between 13° and 17°. Sitting cross legged (44°) and the golf swing (43°) showed considerably higher internal-external ranges, compared to the other activities.

4.3.3. Peak Hip Angles

Table 7. Peak hip angles (degrees) in each axis (flexion-extension, abduction-adduction and internal-external rotation). The highest peak angles, across activities, are highlighted in bold.

	Hip angle (°)					
	Flexion	Extension	Abduction	Adduction	Internal rotation	External rotation
Walk	37	7	5	9	6	7
Walk turn	38	5	8	2	8	8
Incline walk	45	6	6	9	6	7
Decline walk	33	5	5	7	9	5
Stand to sit	81	-17	4	-2	4	-1
Sit to stand	74	-17	4	-3	6	-3
Sit cross legged	90	-60	8	-2	6	37
Squat	81	-7	9	-1	1	2
Stand reach	74	-9	1	0	6	-1
Kneel reach	76	-16	8	-7	11	-2
Lunge	84	6	5	9	8	4
Golf swing	24	0	4	11	22	22
Cycle	62	-32	2	0	3	3

Sit cross legged showed the highest peak flexion angle (90°) (Table 11). Lunge (84°), stand to sit (81°) and squat (81°) all showed similarly high flexion peaks. Hip extension was only seen in locomotion activities, with the walk showing the highest peak (7°). Squat showed the highest abduction peak (9°), whereas the golf swing showed the highest

adduction peak (11°). The golf swing showed the highest internal rotation peak (22°) and second highest external rotation peak (22°). The highest external rotation peak was seen during sit cross legged (37°).

4.3.4. Kinematic Variation

The mean standard deviation (SD) does not consider fluctuations in the variability throughout a movement cycle, however it does describe the general level of inter-subject variation within the kinematics (Table 12). Nine of the thirteen activities showed an average flexion-extension SD between $\pm 10^\circ$ and $\pm 15^\circ$. The stand to sit ($\pm 26^\circ$), sit to stand ($\pm 21^\circ$) and stand reach ($\pm 27^\circ$) stood out, with regards to their high average SD for hip flexion-extension. When considering the maximum SD across the entire movement cycle, these same three activities displayed the highest peak flexion-extension variations (stand to sit: $\pm 31^\circ$; sit to stand: $\pm 25^\circ$; stand reach: $\pm 28^\circ$). A number of activities showed little change in this respect, however the squat, kneel reach and golf swing all showed noticeable increases of $\pm 5^\circ$, $\pm 5^\circ$ and $\pm 4^\circ$, respectively.

Mean abduction-adduction angle SDs were highest for the golf swing and cycling (both $\pm 8^\circ$), whilst other activities ranged between $\pm 3^\circ$ and $\pm 6^\circ$. When considering peak SDs, all activities showed an increase in variation by ± 1 - 2° from the mean (the golf swing and cycling demonstrated the largest peak variation at $\pm 10^\circ$). The golf swing (mean: $\pm 14^\circ$; peak: $\pm 18^\circ$) and cycle (mean: $\pm 12^\circ$; peak: $\pm 15^\circ$) also resulted the highest internal-external rotation SDs.

Table 8. Average and peak standard deviation for activities. Inter-subject variation is shown in three axes of motion (flexion-extension (F-E), abduction-adduction (Ab-Ad) and internal-external rotation (I-E)). Peak values within each column are highlighted in bold.

	Average standard deviation (°)			Peak standard deviation (°)		
	F-E	Ab-Ad	I-E	F-E	Ab-Ad	I-E
Walk	±9	±4	±11	±10	±5	±12
Walk turn	±10	±4	±12	±11	±6	±14
Stand to sit	±26	±3	±9	±31	±5	±11
Sit to stand	±21	±3	±11	±25	±4	±12
Stand reach	±27	±3	±8	±38	±4	±9
Squat	±14	±6	±10	±19	±8	±11
Sit cross legged	±12	±6	±13	±15	±7	±15
Incline walk	±10	±4	±10	±12	±4	±11
Decline walk	±10	±4	±10	±11	±5	±11
Lunge	±13	±6	±10	±15	±8	±11
Kneel reach	±14	±5	±9	±19	±6	±11
Golf	±14	±8	±14	±18	±10	±18
Cycle	±11	±8	±12	±11	±10	±15

4.3.5. Peak Hip Velocities

Hip angular velocity describes the change in hip angle, over a given time (degrees per second). This may have implications for the joint lubrication as well as the potential wear between surfaces at the hip.

Table 9. Peak hip angular velocity (degrees per second) in each axis (flexion-extension, abduction-adduction and internal-external rotation). Maximum peak velocities, across activities, are highlighted in bold.

	Angular velocity (°/s)					
	Flexion	Extension	Abduction	Adduction	Internal rotation	External rotation
Walk	189	-121	70	-85	83	-93
Walk turn	206	-121	68	-75	45	-138
Incline walk	74	-57	20	-24	25	-25
Decline walk	48	-32	22	-26	26	-27
Stand to sit	133	-54	12	-11	20	-26
Sit to stand	44	-111	9	-11	11	-18
Sit cross legged	58	-49	12	-8	59	-62
Squat	227	-211	26	-26	19	-23
Stand reach	136	-121	7	-6	18	-16
Kneel reach	85	-66	5	-5	22	-15
Lunge	90	-57	18	-40	13	-41
Golf swing	8	-41	15	-25	31	-55
Cycle	101	-115	21	-23	85	-68

Table 13 describes angular velocities for activities. Flexion-extension (F-E) angular velocity peaks were highest during the squat (flexion: 227°/s; extension: 211°/s; range: 438°/s). In contrast, the lowest F-E values were seen for the golf swing (flexion: 8°/s; extension: 41°/s; range: 49°/s). The walk showed the highest abduction-adduction (Ab-Ad) angular velocity (abduction: 70°/s; adduction: 85°/s; range: 125°/s), whereas kneel reach had the lowest Ab-Ad velocity (abduction: 5°/s; adduction: 5°/s; range: 10°/s). Internal-external rotation (I-E) velocity range was highest for the walk turn (internal: 45°/s; external: 138°/s; range: 183°/s) and lowest for the sit to stand (internal: 11°/s;

external: 18°/s; range: 29°/s). It is notable that the incline and decline walk showed lower angular velocity values, compared to the level walk and walk turn.

4.3.6. Variation and Age

Stand to sit, sit to stand, stand reach and cycle all showed differences of over 1, when motion path ARs were compared between age groups (under 55 and over 55). Given that global hip kinematics are closely linked to local motion paths, the same activities were used to compare hip angular data between the two age groups.

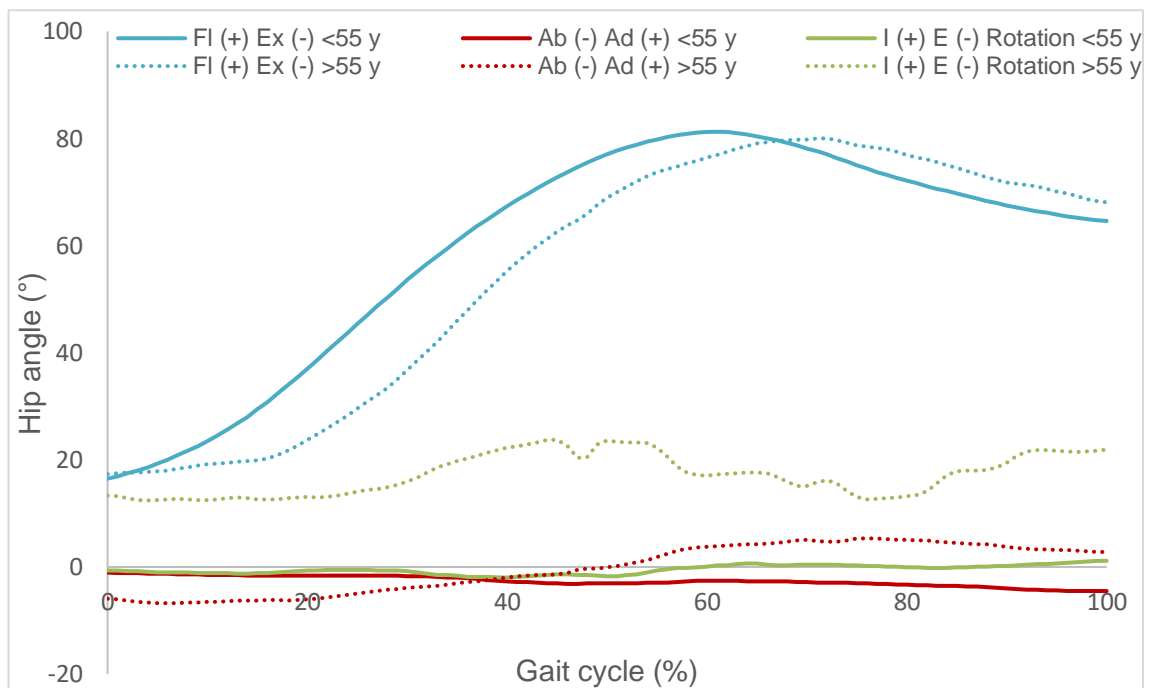


Figure 72. Mean right hip angle during one gait cycle for a stand to sit. Flexion-extension (blue), abduction-adduction (red) and internal-external rotation (green) is presented. Mean data is shown for groups under (solid line) (n=7) and over (dotted line) (n=1) 55 years of age.

Stand to sit kinematics showed similar patterns of motion between age groups, with variation between peak angles and range of motion (ROM). Although hip flexion peaked at different times (possibly due to small differences in movement initiation time between groups), the peak flexion angles were comparable (<55: 81°; >55: 80°). The older group displayed more exaggerated abduction-adduction, compared to the younger group, with an increased ROM (+9°). The older group exhibited an internally rotated hip throughout the movement, whereas the younger group remained neutral. Internal-external rotation ROM was increased by 8° for the older group.

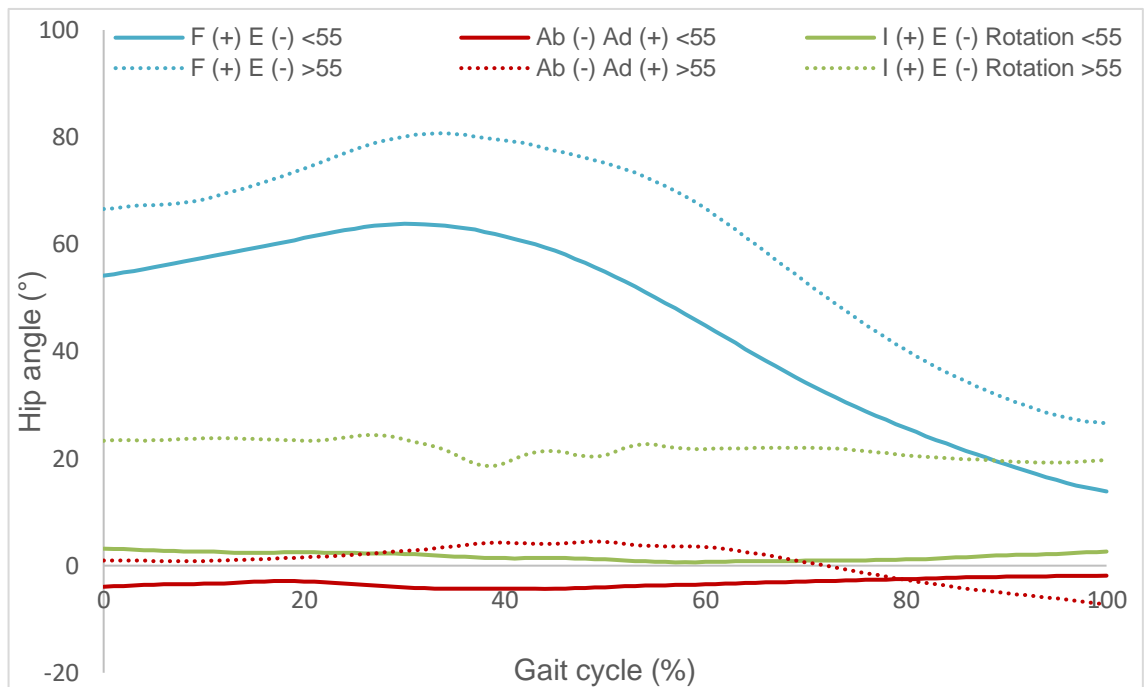


Figure 73. Mean right hip angle during one gait cycle for a sit to stand. Flexion-extension (blue), abduction-adduction (red) and internal-external rotation (green) is presented. Mean data is shown for groups under (solid line) (n=7) and over (dotted line) (n=1) 55 years of age.

Sit to stand peak flexion angles showed differences between under (64°) and over (81°) 55 year olds (Figure 159). The younger group extended the hip with a faster angular velocity and displayed a lower flexion angle when standing (-13°). Similar to the stand to sit, the older group displayed a higher ROM for abduction-adduction ($+9^{\circ}$) and internal-external rotation ($+3^{\circ}$). The older group also displayed an internally rotated hip angle throughout the movement, in contrast to the neutral angle seen for the younger group.

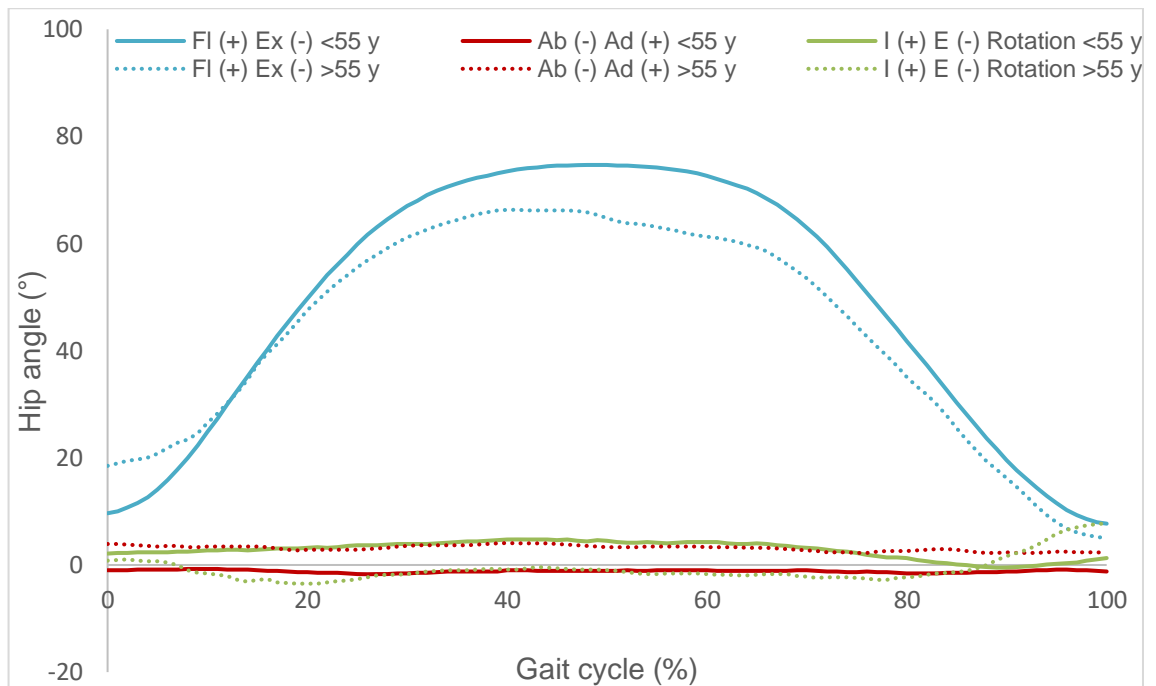


Figure 74. Mean right hip angle during one gait cycle for a stand reach. Flexion-extension (blue), abduction-adduction (red) and internal-external rotation (green) is presented. Mean data is shown for groups under (solid line) (n=9) and over (dotted line) (n=1) 55 years of age.

Stand reach hip flexion-extension was similar for the two age groups (Figure 160). An increased peak flexion angle was observed for those under 55 (+9°). Abduction-adduction and internal-external rotation showed similar patterns for both groups. The older group showed a net adduction angle alongside external rotation at the hip. The younger group, however, showed a neutral abduction-adduction angle with an internally rotated hip.

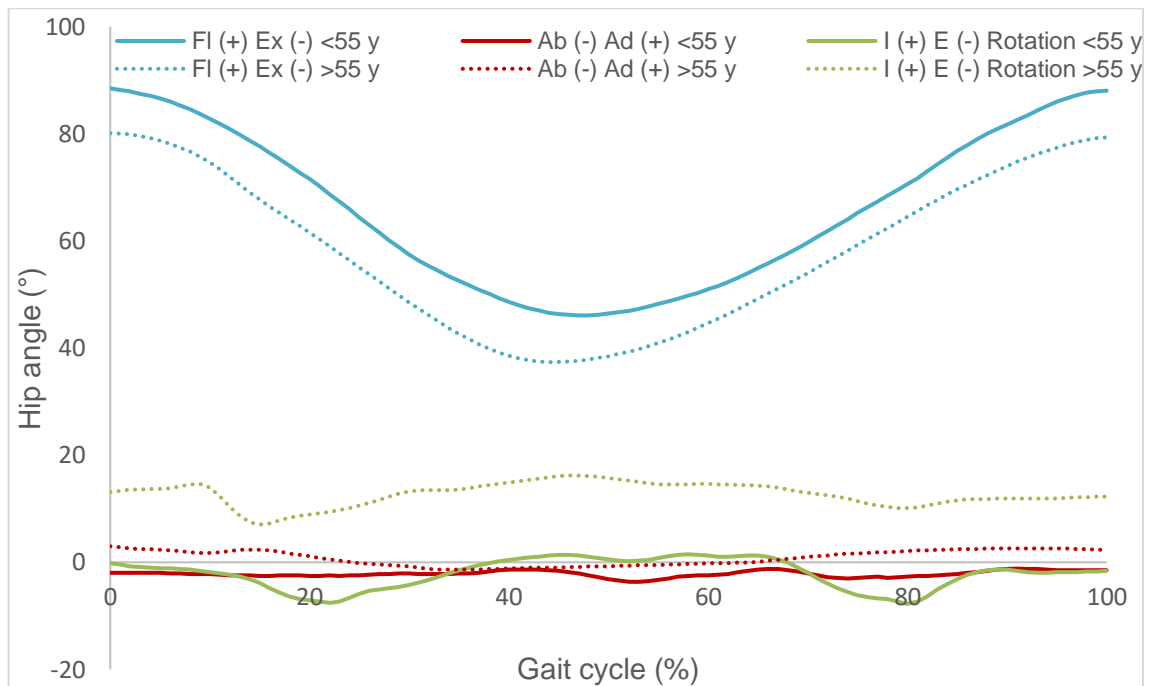


Figure 75. Mean right hip angle during one gait cycle for a cycle. Flexion-extension (blue), abduction-adduction (red) and internal-external rotation (green) is presented. Mean data is shown for groups under (solid line) (n=8) and over (dotted line) (n=2) 55 years of age.

Cycle flexion-extension profiles were similar for both groups, with similar a ROM (<55: 42°; >55: 43°) (Figure 161). The older group displayed an adducted hip for the majority of the movement, in contrast to the abducted hip displayed for the younger group. However, abduction-adduction ROM was similar for the two groups (<55: 3°; >55: 4°). The older group displayed hip internal rotation throughout the movement, whereas the younger group generally showed external rotation. The ROM for this rotation was similar for both groups (both 9°).

4.3.7. Variation and Gender

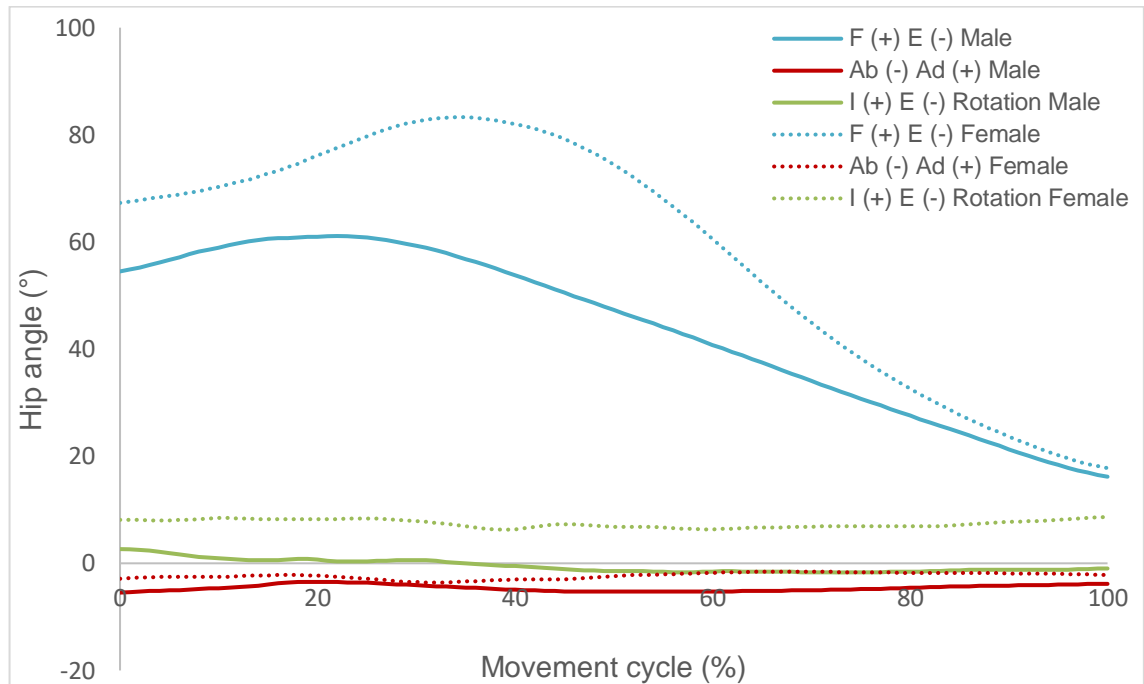


Figure 76. Mean right hip angle during one gait cycle for a sit to stand. Flexion-extension (blue), abduction-adduction (red) and internal-external rotation (green) is presented. Mean data is shown for male (solid line) (n=3) and female (dotted line) (n=5) groups.

Females showed higher hip flexion levels throughout the sit to stand movement with a peak increase of 22° (Figure 163). Consequentially, females had a higher flexion-extension range of motion (ROM) (66°) compared to males (45°). Both groups showed a net abduction hip angle, with minimal fluctuations, throughout the movement. Females displayed an externally rotated hip throughout, in contrast to the neutral hip rotation seen for the male group.

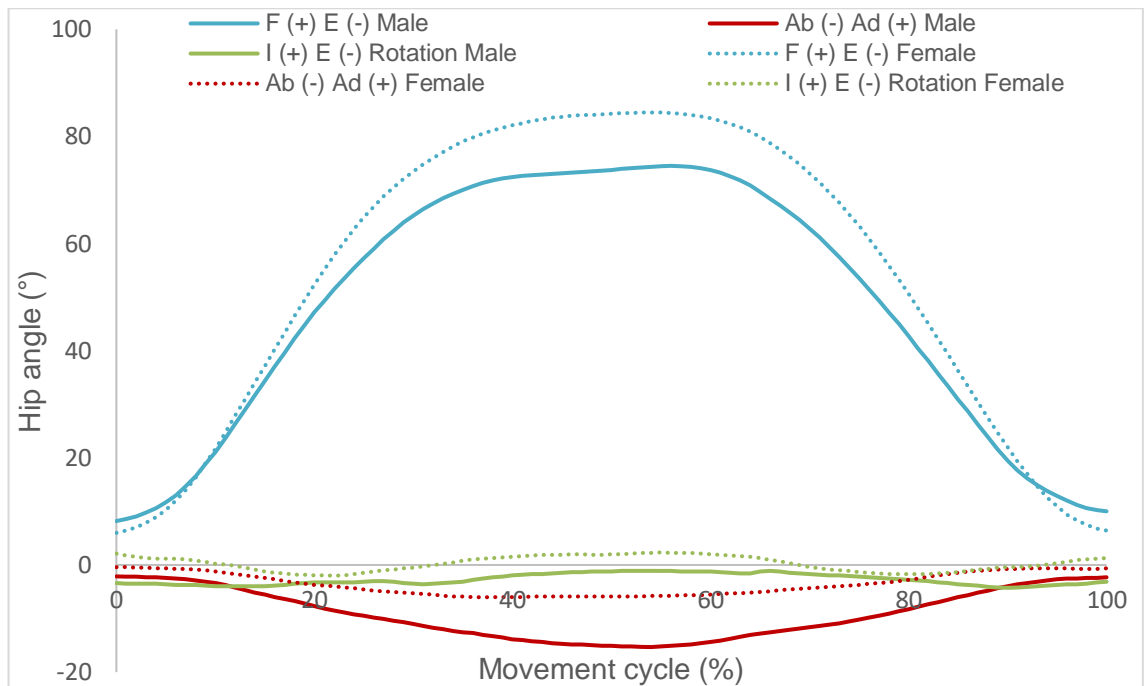


Figure 77. Mean right hip angle during one gait cycle for a squat. Flexion-extension (blue), abduction-adduction (red) and internal-external rotation (green) is presented. Mean data is shown for male (solid line) (n=4) and female (dotted line) (n=7) groups.

During the squat, females showed a higher peak hip flexion angle, compared to males (+10°) (Figure 164). This led to a 12° higher flexion-extension ROM for females. Both groups displayed hip abduction throughout the squat, however this was exaggerated in the male group with a higher abduction peak (+9°). Internal-external rotation was comparable for the two groups.

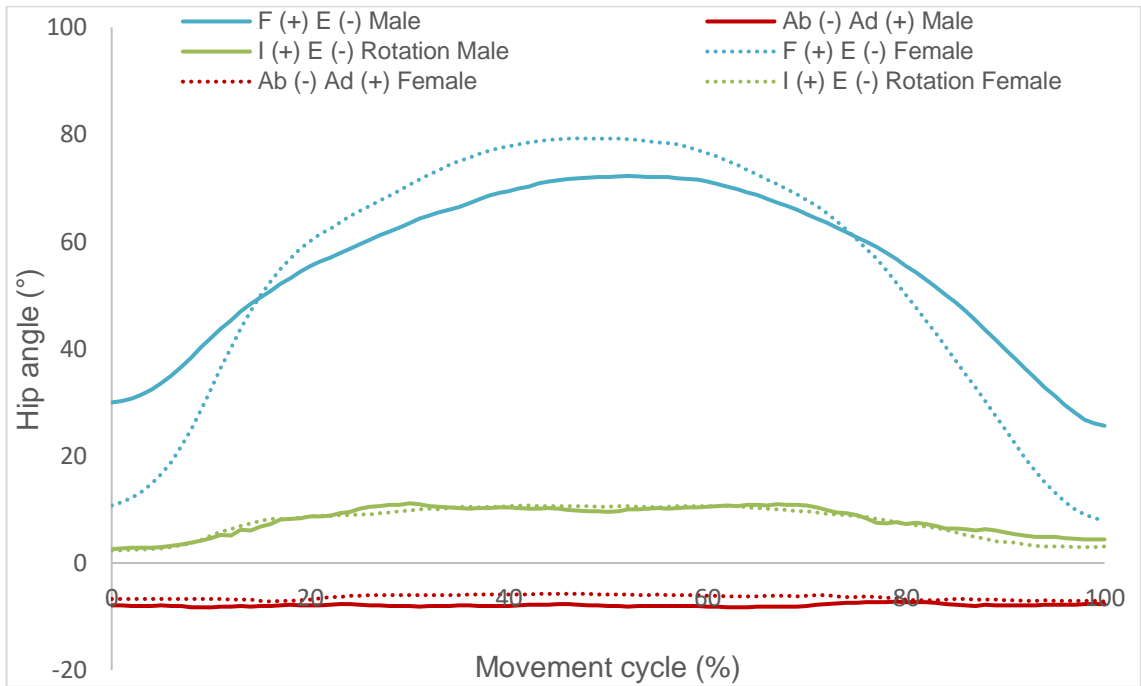


Figure 78. Mean right hip angle during one gait cycle for a kneel reach. Flexion-extension (blue), abduction-adduction (red) and internal-external rotation (green) is presented. Mean data is shown for male (solid line) (n=6) and female (n=7) (dotted line) groups.

On average, females adopted a more upright posture than males when knelt, as shown by the lower flexion angle at the start and end of the movement (Figure 165). Females also demonstrated a higher peak flexion angle (+7°) and flexion-extension ROM (+25°) than males. Both hip abduction and internal rotation were similar for the two groups.

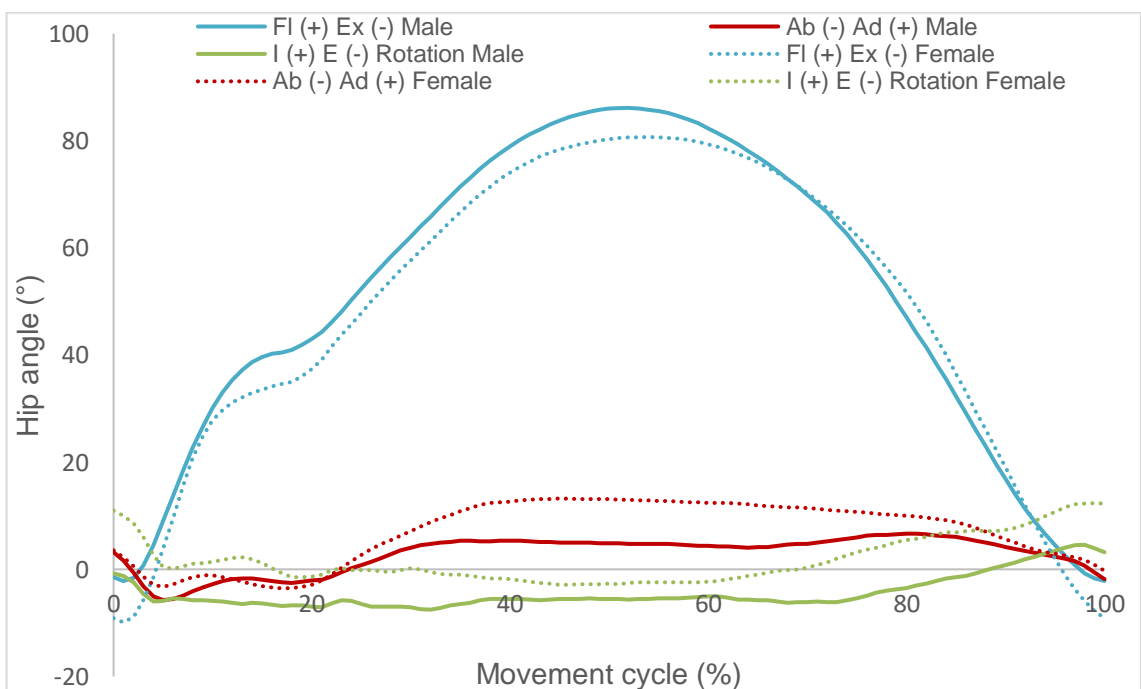


Figure 79. Mean right hip angle during one gait cycle for a lunge. Flexion-extension (blue), abduction-adduction (red) and internal-external rotation (green) is presented. Mean data is shown for male (solid line) (n=9) and female (dotted line) (n=8) groups.

Hip flexion-extension was similar for both gender groups and demonstrated comparable peaks (Male: 86°; Female: 81°) and ROM (Male: 88.5°; Female: 91°) during the lunge (Figure 166). Females showed an increased hip adduction peak compared to males (+7°), but followed a similar pattern of angular motion. Internal-external rotation at the hip also showed a similar pattern for groups, however males were more externally rotated throughout the movement (male peak abduction was 7° compared to 3° for females).

4.3.8. Summary

Activities with the largest range of motion were lunge (flexion-extension), incline walk (abduction-adduction) and sit cross legged (internal-external rotation). It was notable that a number of activities (including stand to sit, sit cross legged, squat and lunge) showed high flexion peaks. The range of motion will influence motion paths occurring between relative surfaces at the hip, thus potentially influencing hip wear.

Mean and peak standard deviations were highest for the stand reach (flexion-extension), golf swing/ cycling (abduction-adduction) and golf swing (internal-external rotation). Peak variation was increased for all activities, compared to the mean (increasing between $\pm 1^\circ$ and $\pm 13^\circ$). A large standard deviation may suggest that kinematic outliers are present within the subject sample, and may therefore exhibit a different level of cross-shear at the hip, compared to the mean.

In general, angular velocity was highest when the hip flexed and extended during activities. The highest peak velocity was shown at hip flexion during the squat, equalling $227^\circ/\text{s}$ (SD: $\pm 43^\circ/\text{s}$). Lower velocities were found for abduction-adduction and internal-external rotation. Adduction velocity was highest for the walk, peaking at $85^\circ/\text{s}$ (SD: $\pm 6^\circ/\text{s}$) and external rotation was highest for the walk turn, peaking at $138^\circ/\text{s}$ (SD: $\pm 20^\circ/\text{s}$). Hip angular velocity may have implications for lubrication of the joint, which may in turn be relevant to wear, when considering both a total hip replacement and tissue engineered cartilage.

4.4. Discussion

Within this section, global hip kinematics are discussed for thirteen common activities (section 4.4.1. to 4.4.11.). Kinematic variation (section 4.4.12.) and movement time (section 4.4.13.) are then discussed, before an overall discussion (section 4.4.14.) and summary (section 4.4.15.) of the kinematic data.

Hip kinematics were analysed for eighteen subjects, who completed thirteen common activities in a movement analysis lab. Hip angular motions and angular velocities were analysed for each activity, in each axis of rotation (flexion-extension (F-E), abduction-adduction (Ab-Ad), internal-external rotation (I-E)). The peak angle, range of motion (ROM) and standard deviation (SD) was reported for each activity, in each of the three axes. Ultimately, hip angles will influence the relative motion paths between hip surfaces (cross-shear) and the sliding velocity between surfaces (consequentially influencing lubrication).

4.4.1. Walk

Hip angle data resulted typical patterns for level walking (section 4.3.1.1. and 4.3.2.). Mean walking ROM (F-E: 44°; Ab-Ad: 14°; I-E: 13°) was comparable to a large scale biomechanical study by Kadaba et al. (1990), in which 40 healthy subjects (aged 18 to 40) were evaluated three times a day on three separate test days (F-E: 43°; Ab-Ad: 12°; I-E: 13°). Similarities between the current data set and Kadaba's results, lend credibility to both the walking kinematic results and the overall methodology used for data collection.

Hip angular velocity was high for the walk, compared to other activities, showing the third highest flexion velocity (189°/s) (occurring during the swing phase) and joint second highest extension velocity (121°/s) (occurring at mid-stance) (Section 4.3.5.). The walk also demonstrated the highest Ab-Ad velocities (abduction: 70°/s; adduction: 85°/s) and second highest I-E rotation velocities (internal: 83°/s; external: 93°/s). Global joint velocities influence localised motion path sliding velocities. Increased hip angular velocity may suggest increased peak sliding velocities at the joint and therefore a more desirable lubrication regime between joint surfaces (Katta et al., 2008a; Stewart, 2010; Stewart et al., 1997). That being said, if two surfaces come into direct contact (potentially due to squeeze film effects), a higher sliding acceleration may contribute to higher wear rates (Bragdon et al., 1996; Wang, 2001). Hip velocities, for the walk, were high during the swing phase (indicating that fluid may be drawn into the joint) and low at initial contact (indicating the potential for boundary lubrication conditions) (section 4.3.1.1.) (Katta et al., 2008a; Stewart, 2010; Stewart et al., 1997). This indicates that a variable lubrication regime is likely to occur throughout one stride. Similar velocity patterns were also seen for other walking tasks (walk turn, incline walk and decline walk).

Previously, hip F-E velocity has been assessed for a normative population group (Granata et al., 2000). Flexion (192°/s) and extension (119°/s) peak velocities were reported – both of which closely resembled mean values within the current study (both within $\pm 3^\circ/\text{s}$). Although angular data is comparable to the literature for a self-selected comfortable walk, it is important to appreciate that different walking speeds are likely to result variable joint velocity values.

It is important to note at this point, that the current study reports results for a healthy population group. Although this data shows similarities to a younger, more functional THR group, it must be acknowledged that a patient group is likely to show reductions in sagittal ROM (Ewen et al., 2012; Lunn et al., 2019). This was shown in a meta-analysis,

in which THR patients demonstrated a sagittal plane hip ROM of 23° to 41°, compared to a range of 31° to 51° for a healthy control group (Ewen et al., 2012). Differences in F-E may be further increased when comparing older THR patients to a control (Foucher, 2016; Lunn et al., 2019). The 44° sagittal plane ROM reported in the current study shows more similarities to a younger, high functioning patient, than an older, symptomatic patient (section 4.3.2.).

The walking data shows considerable angular motion and variable velocities in each of the three planes, throughout the movement cycle (with peak velocities shown in the sagittal plane). This suggests a variable lubrication regime, with possible fluid entrainment (during the swing phase) and possible fluid film depletion during the deceleration, stance phase. When considering pre-clinical testing of devices, this is an important factor to consider in order to replicate *in vivo* environmental joint conditions.

4.4.2. Walk Turn

Although cutting manoeuvres (running and turning at 90°) have been investigated, a walk turn is yet to be analysed biomechanically (Fox, 2018). Similar to the walk, walk turn exhibited an externally rotated hip, albeit with less flexion at initial contact (section 4.3.1.2.). Additionally, a net abduction angle was observed throughout the walk turn, whereas the straight walk showed a combination of both abduction and adduction (walk ROM: F-E: 44°; Ab-Ad: 14°; I-E: 13°; walk turn ROM: F-E: 43°; Ab-Ad: 10°; I-E: 17°) (section 4.3.2.). It is likely that kinematic differences between the two walks are a result of internal rotation of the pelvis segment (anti-clockwise), in preparation for the propulsive phase of the turn. For this reason, it is likely that the relative motion and loading between surfaces at the hip will vary between the two walking tasks.

Walk turn F-E hip velocity was the second highest of all activities, behind the squat (flexion: 189°/s; extension: 121°/s) (section 4.3.1.2. and 4.3.5.). Results were similar to the straight walk, although peak flexion velocity was higher for the walk turn (+17°/s), possibly due to increased anterior tilting of the trunk. Walk turn peak abduction velocity was similar to the level walk (-2°/s), whereas the adduction peak was lower (-10°/s). It is notable that the walk turn demonstrated the highest external rotation peak of all activities (138°/s). This occurred as a result of the change in direction at initial contact, where the hip externally rotated at a high angular velocity. It is possible that the high external rotation, coupled with flexion and abduction, may lead to cross-shear at the hip. With this being said, the high sliding velocity throughout the movement is likely to mean that a

desirable lubrication regime is present between surfaces, thus the surfaces may not actually come into contact.

4.4.3. Incline and Decline Walk

Although incline and decline walk showed similar kinematic patterns to the level walk, F-E ROM was increased for incline walk and decreased for decline walk, relative to the level walk (walk: 44 °; incline walk: 51°; decline walk: 37°). Similarly, Ab-Ad ROM was increased for the incline walk and decreased for the decline walk, when compared to the level walk (walk: 14°; incline walk: 15°; decline walk: 12°). The I-E rotation was similar for all three walking tasks (walk: 13°; incline walk: 13°; decline walk: 14°) (section 4.3.1.3.). Kinematic differences are likely to exist due to the requirement of the body to adapt to changes in the centre of mass during incline/ decline walking (Dewolf et al., 2018).

Similar to the current study (walk: 37°; incline walk: 44°; decline walk: 32°), previous work has reported increased hip flexion at initial contact for incline walking, when compared to level and decline walking, as a higher foot position is required for clearance when walking uphill (Gholizadeh et al., 2018). Furthermore, a decreased hip extension was reported during incline and decline walking, compared to level walking (Gholizadeh et al., 2018). Again, this was also seen in the present study, with peak hip extension angles of 7°, 6° and 5° for the level walk, incline walk and decline walk, respectively. The reduced hip extension angle, during incline walking, is thought to assist the opposite limb positioning on the higher surface when walking at an incline (Gholizadeh et al., 2018). The decreased extension angle during decline walking, may be an outcome of the typically seen reduction in step length when walking downhill (Gholizadeh et al., 2018). Kinematic differences between walking tasks may influence relative motion paths and sliding distances at the hip, thus potentially leading to a difference in cross-shear when walking at different angles.

The incline walk showed a considerably reduced hip velocity, in each axis, when compared to the normal walk (section 4.3.5.). Velocity ranges were reduced by 179°/s (F-E), 111°/s (Ab-Ad) and 126°/s (I-E). These reductions were most likely due to a reduced walking speed for the incline walk. A similar reduction in angular velocity (compared to level walking) was seen for the decline walk, albeit with a larger decrease in F-E peak velocity than seen for the incline walk (decrease of 230°/s (F-E), 107°/s (Ab-Ad) and 123°/s (I-E)) (section 4.3.5.). Reduced hip angular velocities occurring during incline/

decline walking (compared to level walking) are likely to reduce the localised sliding velocities between bearing surfaces. Consequentially, this may lead to a reduction in the fluid film thickness at the joint. With this being said, velocity and load must be considered together in order to assess this. A reduced fluid film may lead to a reduction in contact area and thus an increase in contact stress at the joint.

4.4.4. Stand to Sit and Sit to Stand

Stand to sit (StSi) and sit to stand (SiSt) showed standing hip flexion angles of 16° and 17°, respectively (section 4.3.1.5 and 4.3.1.6.). Both tasks resulted similar mean standing angles, suggesting that data collection was reliable between trials. Given that 18 subjects were used, ranging in age from 20 to 70, variability was seen in hip flexion angles at static standing. This initial angle varied due to the posture of the individual and ranged from 0° to 23°. Mean seated flexion angles were 81° (StSi) and 63° (SiSt). Again, this seated position varied between individuals and was influenced by both posture and height (given that chair height was kept at 0.47 m, leg length may have influenced the flexion angle).

The StSi and SiSt showed similar kinematic results (albeit mirrored). Sitting down, however, showed a higher mean hip F-E ROM (SiSt: 57°; StSi: 64°). Ab-Ad ROM was similar (StSi: 2°; SiSt: 1°) and I-E ROM was the same for both tasks (4°) (Figure 169). It is worth noting that F-E angle standard deviations (SDs) were high during dynamic periods of sitting ($\pm 26^\circ$) and standing ($\pm 21^\circ$). This indicates differences in the technique and/ or posture between individuals, which may have led to variation between motion path sliding distances and aspect ratios at the hip. A high F-E ROM, for example, is likely to increase the anterior-posterior sliding between surfaces, thus increase the sliding distance and potentially increase the aspect ratio (particularly for a point located on the anterior-posterior arc of the femoral head).

Roebroek et al. (1994) found SiSt F-E ROM to reach approximately 100°. This was considerably larger than the 57° reported in the current study. Roebroek and colleagues also reported a larger initial flexion angle during SiSt (20°), compared to the current study (11°). These differences were likely due to a younger mean average age within the literature (27 ± 4 years) compared to the current study (44 ± 19 years). Another possible reason for the reduced hip ROM, is that Roebroek adapted the seat height based on knee length; this was not done in the current study. It is noteworthy that F-E angular velocities reported by Roebroek and colleagues (velocity range: 153 °/s) were similar to those in the current study (velocity range: 155 °/s) (Roebroek et al., 1994).

Nadzadi et al. (2003) analysed a SiSt from a 0.46 m height chair. Similar to the current study, it was established that subjects initially flexed at the hip, past the seated position, before ascending into a standing position. Hip angular ROMs (F-E: 115°; Ab-Ad: 8°; I-E: 8°) were considerably higher than the current study (F-E: 57°; Ab-Ad: 1°; I-E: 3°). The main contributing factor to this ROM discrepancy is differences in both the seated and standing posture of the two subject groups. Additionally, the group in the current study required less initial flexion at the hip (11°) in order to move up and out of the stool, compared to the subjects in Nadzadi's study (30°). This initial flexion is a technique, in which an upward momentum can be achieved during standing.

Both StSi and SiSt showed considerably reduced angular velocities, when compared to walking tasks. The F-E velocity ranges were higher for StSi (187°/s) than SiSt (155°/s). This was likely due to an increased F-E ROM over time for StSi, compared to the SiSt. The Ab-Ad and I-E velocities were similar for both activities.

During dynamic periods of sitting and standing, it is likely that the joint experiences fluid film lubrication, in an environment where the high velocity encourages fluid entrainment. However, it is possible that during periods of low velocity (when raising up or lowering down to the seat slowly), a mixed or boundary lubrication regime is present, in which lubrication starving may lead to contact or the surface asperities.

4.4.5. Sit Cross Legged

The sit cross legged task saw subjects lift and cross the right ankle over the top of the left thigh. This resulted in a seated flexion angle of 63° (equal to the SiSt seated angle) (section 4.3.1.7.). The F-E ROM was the second lowest of all activities (30°). Abduction was minimal, with a ROM of 6°. I-E rotation, however, showed the highest ROM when compared to other activities (44°) (section 4.3.2.). This was to be expected, given the rotation required at the right hip in order to cross the right ankle onto the left thigh.

Nadzadi et al. (2003) analysed the right leg crossing over the left, however in contrast to the current study, the femur rested on top of the contralateral leg, rather than the ankle. Nadzadi found the movement to start at 80° flexion, before producing a further flexion of 20-30°. The Ab-Ad ROM was approximately 15°, whereas I-E ROM was 30°. When comparing to Nadzadi's study, the current work showed a reduced mean initial flexion angle (-17°), however the flexion ROM did fall within the reported range (20-30°). The current study also found a smaller Ab-Ad and larger I-E ROM, which was likely due to differences in the definition of the movement.

Hip angular velocities were low when sitting cross legged (section 4.3.1.7.). Velocity peaks were observed at the start and end of the movement (F-E range: 107°/s; Ab-Ad range: 20°/s; I-E range: 121°/s). It is likely that lubrication starving (boundary lubrication regime) will occur during the low velocity period of this movement, when the leg is crossed in a static position (Katta et al., 2008a; Stewart, 2010; Stewart et al., 1997). Loading the joint during this boundary lubrication regime may lead to damage at the polyethylene surface of the cup or at the asperities of tissue engineered cartilage substitution – particularly should this occur alongside cross-shear motion.

4.4.6. Squat

The current study analysed a typical squat, in which the back was straight and the knees flexed to approximately 90° (section 4.3.1.8.). The F-E, Ab-Ad and I-E ROMs were 74°, 8° and 4°, respectively (section 4.3.2.). It is noteworthy that although F-E ROM was 74°, there is scope for this to increase with a deeper squat.

Within the literature, a similar squat showed a maximum hip flexion of 90° (16° higher than the current study) (Flanagan et al., 2003). The increased flexion was likely because participants held a bar in front of them for balance, thus leaning forwards and increasing hip flexion. This may also have encouraged a deeper squat, due to the aided balance. Contrastingly, Hemmerich and colleagues reported squat ROM to be 95 ±27° of flexion (Hemmerich et al., 2006). In this case, the ROM reported in the current study (74°) falls within the reported standard deviation.

Within an ‘activities of daily living’ literature review, a deep squat was found to result values of over 130° flexion, 10-30° abduction and 5-36° external rotation (Mulholland and Wyss, 2001). As the current study did not implement a full squat, the flexion ROM was lower than this review (possibly also influenced by the standing posture of participants) (Mulholland and Wyss, 2001). Ab-Ad ROM values within the current study fell slightly below the range stated in the review (-2°), as did the I-E ROM (-1°). Again, this highlights the possibility for more dynamic hip angular motion, during a deeper squat.

Within the current study, the squat showed the highest F-E velocity of all activities (Flexion: 227 °/s; Extension: 211°/s) (section 4.3.1.8.). Both Ab-Ad and I-E velocities were relatively low throughout the movement. With this being said, resultant hip angular velocity was close to 0°/s when at the bottom of the squat. Considering hip loading during this period, it is possible that a THR (and the natural hip) would be vulnerable to wear, given that the fluid film is likely to be depleted due to squeeze film at the joint (Katta et

al., 2008a; Stewart, 2010; Stewart et al., 1997). Should cross-shear occur alongside a loaded hip, during a boundary lubrication regime, it is possible that surface wear will occur.

4.4.7. Stand Reach

The stand reach showed a high hip F-E ROM (65°), alongside small Ab-Ad (1°) and I-E (4°) ranges (section 4.3.1.9. and 4.3.2.). Nadzadi et al. (2003) reported angular motion for a 'stoop' (reaching to the left foot with the right hand, from a standing position). ROM was reported for flexion (60-70°), adduction (20-25°) and external rotation (10-20°). The current study was agreeable with the F-E results reported by Nadzadi. Ab-Ad and I-E motion was higher in the literature, as unlike the current study, the 'stoop' involved twisting at the waist in order to touch the left foot with the right hand.

Similar to the squat, stand reach saw high F-E velocities during the dynamic period of the movement (Flexion: 136°/s; Extension: 121°/s) (section 4.3.2.). F-E velocities were approximately 0°/s when fully flexed. Both Ab-Ad and I-E velocities were low throughout the activity. When fully flexed at the hip and in a static position, fluid is likely to have been squeezed out from the joint space and contact of surface asperities is possible. However, wear is also dependent on the motion at this point. Should cross-shear occur synonymously, this may be potentially damaging to hip surfaces.

4.4.8. Kneel Reach

Kneel reach demonstrated the joint highest F-E ROM (89°), alongside Ab-Ad and I-E ROMs of 13° (section 4.3.1.1.0. and 4.3.2.). Hemmerich and colleagues analysed a kneeling task in which individuals moved from a standing position, down into a kneeling position and then back up to standing. It is difficult to compare ROM results due to the different definitions of the movement. Maximum flexion, abduction and external rotation angles were 74°, 21° and 16°, respectively (compared to 76°, 7° and 10° in the current study). Increased abduction and external rotation angles within the literature, may have been affected by the movement down into the kneeling position, from standing.

Kneel reach resulted low hip angular velocities throughout the movement, with small peak flexion (85°/s) and extension (66°/s) velocities during the dynamic periods of the activity (section 4.3.1.10.). This may suggest lubrication starving for long periods of the movement cycle (Katta et al., 2008a; Stewart, 2010; Stewart et al., 1997). A depleted fluid film at the hip will reduce the contact area and potentially increase contact stress between

surfaces. This may lead to surface wear, however, this is also dependent on the degree of cross-shear and magnitude of hip loading.

4.4.9. Lunge

Within the present study, the lunge resulted the joint highest F-E ROM (89°) of all activities, 25° higher than the second highest (StSi). Both Ab-Ad and I-E ROMs equalled 13° (section 4.3.1.11. and 4.3.2.). A number of studies have assessed lunging hip flexion, however analysis in the other two planes is lacking. It is difficult to compare F-E ROM to the literature, as the definition of the lunge movement cycle varies between studies. With this being said, the peak flexion angle seen in the current work (84°) is comparable to previously reported flexion angles of 91° (Kuntze et al., 2010), 87° (Farrokhi et al., 2008) and 88° (Flanagan et al., 2004). Comparisons to the literature support the reliability of the findings, whilst suggesting that peak flexion angles could increase further than those shown in the current study.

The lunge showed a peak angular velocity between 0 and 10% of the cycle (heel-off) (90°/s) (section 4.3.1.11.). Kinematics at this point showed similarities to heel-off during walking. Net angular velocity was 0°/s at the bottom of the lunge (55%), which may indicate a reduction in the joints fluid film lubrication at this point (Stewart et al., 1997). Should the fluid film be sufficiently reduced and accompanied by cross-shear motion and loading, it is possible that a polyethylene cup/ engineered cartilage substitution may become damaged through surface wear.

4.4.10. Golf Swing

Individuals were required to complete a full golf swing (backswing – downswing – follow through), using a driver. The right hip (trail hip) was analysed. The F-E ROM (23°) was relatively low in comparison to other activities (section 4.3.1.12.). Ab-Ad ROM was 13° and I-E was 43° (I-E was the second highest of all activities) (4.3.1.12. and 4.3.2.). Although research into golf, hip angular kinematics is lacking within the literature, a number of studies have assessed spine and shoulder biomechanics. One study reported the trail hip, peak external rotation velocity at 145 °/s (Gulgin et al., 2009). This was almost three times larger than the mean value seen in the current study and is likely to be due differences in ability levels between subject groups.

Within the current study, golf swing hip velocities were relatively low throughout (4.3.1.12.). A noticeable peak in extension (41°/s), abduction (25°/s) and external rotation angular velocity (55°/s) was observed at the bottom of the down swing (impact with the

ball). Given that maximal club head velocity is required at this point (to impart maximum force to the ball), the peak in hip angular velocities seems logical. The low hip angular velocities may lead to lubrication starving at the joint and possible contact of surface asperities, whereas the higher velocities are likely to encourage a fluid film regime between surfaces. This highlights the importance of understanding the kinematic variation between individuals, particularly given that the speed of a golf swing will vary considerably between people of different abilities.

4.4.11. Cycle

Mean cycling ROMs were low in comparison to other activities, at 30° (F-E), 2° (Ab-Ad) and 6° (I-E) (4.3.1.13. and 4.3.2.). Although hip angular kinematic data is lacking within the literature, Bini et al. (2019) reported a mean hip flexion ROM of 40°. This increased ROM, compared to the current study, is likely due to the seat height chosen by participants and the type of bike used (a manual racing bike was used in the current study, whereas an electrically assisted bike was used in the literature).

Cycling resulted relatively high F-E velocities (Flexion: 101°/s; Extension: 115°/s), whereas Ab-Ad velocity remained low throughout (section 4.3.1.13.). It is notable that the cycle showed the highest internal (85°/s) and third highest external (68°/s) hip velocity of all activities. This corresponds to internal and external sliding velocities of 20.8 mm·s² and 16.6 mm·s². Variation in velocities, throughout the cycle, may influence the corresponding sliding velocities and accelerations at the joint. Thus, this may have implications for the lubrication regime (fluid film thickness) and cross-shear throughout the movement.

4.4.12. Kinematic Variation

Mean and peak standard deviations (SDs) describe variation between subjects, for each activity. Stand to sit (mean: $\pm 26^\circ$; peak: $\pm 31^\circ$), sit to stand (mean: $\pm 21^\circ$; peak: $\pm 25^\circ$) and stand reach (mean: $\pm 27^\circ$; peak: $\pm 28^\circ$) showed the highest mean and peak F-E variation (4.3.4.). Given that these activities also displayed high F-E ROMs, the high variation is likely to be related to standing posture and/ or hip flexibility. This variation is likely to be mirrored within motion path sliding distance results.

The golf swing (mean: $\pm 8^\circ$; peak: $\pm 10^\circ$) and cycle (mean: $\pm 8^\circ$; peak: $\pm 10^\circ$) showed the highest Ab-Ad SDs (4.3.4.). These high variations may be due to the adoption of different techniques between subjects. It is likely that subjects had varying experience in the two activities, thus resulting in a wide variation of techniques. This theory is backed up by the fact that the golf swing (mean: $\pm 14^\circ$; peak: $\pm 18^\circ$) and cycle (mean: $\pm 12^\circ$; peak: $\pm 15^\circ$) also resulted the two highest I-E variation values.

Ultimately, variation in global kinematics is related to variation in local motion paths between joint surfaces. For this reason, differences in individual technique and/or functionality is likely to have an effect on hip tribology and potentially wear.

4.4.13. Movement Times

The cycle time for a given activity, alongside ROM (in each plane), will influence the sliding distance of motion paths between surfaces at the hip. Consequentially, this may affect wear rates at the joint (Bennett et al., 2002). Kneel reach showed the longest movement cycle (≈ 2 seconds longer than the next closest activity) (section 4.3.1.). It is important to note, however, that the SD was also largest for kneel reach (± 1.6 seconds). Sit cross legged, squat, stand reach, lunge and golf swing could be grouped together, with similar cycle times (2.8 to 4 seconds). The remaining seven activities all showed movement cycles under 1.9 seconds (section 4.3.1.). Variation in movement times, between individuals, will have implications for both hip kinematics and loading. For example, sitting down more slowly may lead to an individual experiencing high hip contact forces for longer and lower global/ local sliding velocities. Both will have implications for lubrication regimes at the joint and ultimately, wear of a polyethylene liner/ tissue engineered cartilage substitution (Katta et al., 2008a; Stewart, 2010; Stewart et al., 1997).

4.4.14. Overall Discussion

Lunge (F-E), incline walk (Ab-Ad) and sit cross legged (I-E) resulted the highest ROMs. The lunge stood out as having the highest resultant hip ROM (Figure 169). Both ROM and activity cycle time will contribute to the sliding distance of relative motion paths at the hip. From the data, it might be predicted that the lunge would result the highest average sliding distance, given the high ROM (particularly in flexion) and movement time of 3.6 seconds (4th longest movement cycle). In addition to this, the sliding velocity is of interest, as this is related to the lubrication regime occurring at the joint. Angular velocity is directly related to both sliding velocity and joint fluid film thickness. This relationship is demonstrated in Figure 170, where fluid film thickness (μm) shows a positive relationship with angular velocity ($^{\circ}/\text{sec}$). This may have ramifications for the wear experienced during certain activities. Clearly, this is also dependent on the cross-shear loading at the hip.

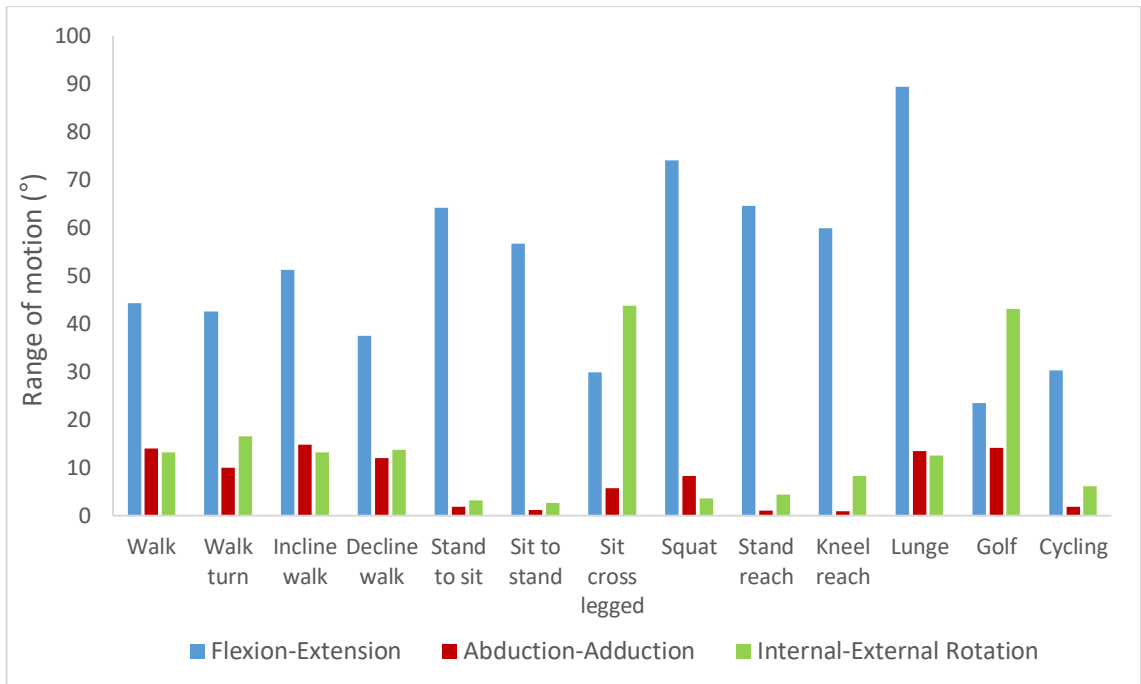


Figure 80. Average hip angular range of motion, in three axes, for thirteen common activities (n=18).

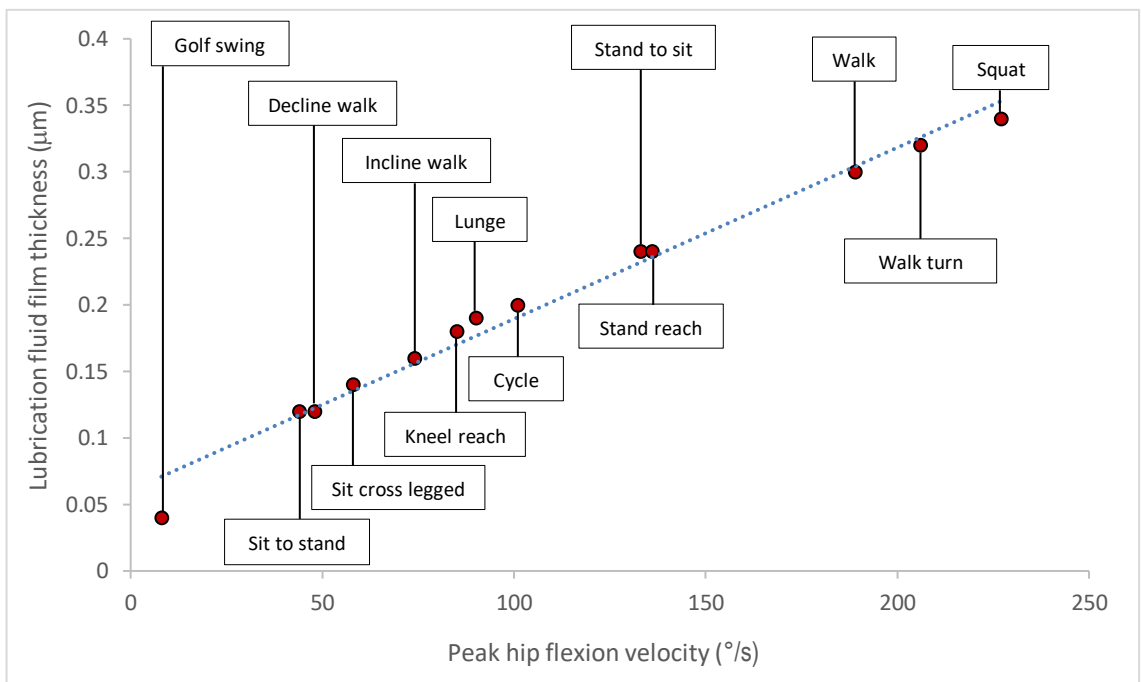


Figure 81. The relationship between hip flexion velocity and fluid film thickness at a total hip replacement (metal-on-polyethylene). The load was standardised at 1000 N for all activities, therefore the linear trend-line indicates a positive relationship between sliding distance and wear. The fluid entrainment calculations were taken from Hamrock and Dowson (1978).

When considering the influence of hip angular velocity alone (independent to force), an increase in velocity is directly related to an increase in the fluid film thickness. Thus, it might be postulated that activities with low angular velocities throughout (such as golf swing, sit to stand and decline walk) are at risk of depleted fluid films and the potential for surface contact and wear. Higher velocities are likely to draw fluid into the joint, through entrainment, and increase the contact area, thus reducing contact stress (Figure 170).

Walking tasks, sit cross-legged, lunge and golf swing showed hip angular motion in all three axes (Figure 169). It might be predicted that these activities would produce more elliptical motion paths and lower mean aspect ratios. Contrastingly, the stand to sit, sit to stand, squat, stand reach and kneel reach all resulted high F-E ROMs, alongside minimal Ab-Ad and I-E rotation (Figure 169). It can be postulated that these would produce higher mean aspect ratios and more linear motion paths. Variation in motion path trajectories is likely to correspond to the kinematic variation seen globally. Thus, it might be predicted that stand to sit, sit to stand and stand reach will show the highest variation in motion path aspect ratios, compared to other activities, due to the high kinematic variation associated with these movements.

Hip angles influence the position of the femoral head in the acetabular cup, and therefore the position at which the cup is loaded. High flexion activities (SiSt, StSi, sit cross legged, squat, stand reach, kneel reach and lunge) may cause the cup to be loaded closer to the posterior rim (and potentially cause excessive wear through edge loading). It is important to appreciate, however, that surgical positioning (cup inclination and anteversion angle) will also influence the position of loading. Lewinnek et al. (1978) suggested that the gold standard for cup orientation should be an inclination angle of $40^{\circ} \pm 10^{\circ}$ and an anteversion angle of $15^{\circ} \pm 10^{\circ}$. Steep cup inclination angles (eg. 65°) have been associated with edge loading and increased wear rates (when tested with microseparation) (Al-Hajjar et al., 2013). This possibility should also be considered, when identifying mechanisms for wear within common activities.

4.4.15. Summary

Global hip kinematics influence both localised motion paths, lubrication and the position of resultant loading on the acetabular cup. Hip angular data is therefore a fundamental variable in determining surface wear to a polyethylene liner (at a THR) or natural/tissue engineered cartilage (at the natural hip). In order to fully understand the contact mechanics at the hip, detailed motion paths and joint loading must also be explored. Analysing localised motion paths provides crucial information relating to cross-shear occurring at the joint, which when coupled with loading, may lead to excessive surface wear.

4.5. Conclusion

Kinematic variation was seen at the hip both between and within activities. It is possible that this global variation is an indicator of the localised motion that may exist between bearing surfaces at the hip. Global kinematics provide a top-level picture of the kinematic ranges and variations associated with activities; it is crucial, however, to consider these data alongside corresponding hip forces in order to fully understand the movements. Once this has been considered, it is possible to investigate the localised biomechanics and tribology between bearing surfaces and begin to understand the potential influence that activities may have on soft tissue and/or joint replacement at the hip.

5. Musculoskeletal Simulations

5.1. Introduction

This chapter consists of the calculation, resulting and discussion of force data, for a range of common activities. Musculoskeletal simulation methods are discussed within section 5.2.. These methods provided a framework for the calculation of joint reaction forces at the hip. Section 5.3. results the localised hip reaction force data for activities. Note that ground reaction force and moment data is included within Appendix 10.6.. The results are followed by a discussion (section 5.4.) and conclusion (section 5.5) of the findings.

5.2. Methods

Motion capture and ground reaction force data was imported into the multi-body dynamics modelling system, AnyBody and acted as drivers for the model (AnyBody, version 6.0, AnyBody Technology, Aalborg, Denmark). The Twente Lower Extremity Model (TLEM), taken from the open access, AnyBody Repository, was used for analysis (Figure 31). The previously validated musculoskeletal lower-extremity model was adapted and used to perform inverse dynamic calculations, in order to estimate hip reaction forces (Carbone et al., 2015; Forster, 2004; Manders et al., 2008). The 6 degree of freedom model incorporates 159 muscles and 11 rigid bodies representing the talus, foot, shank, patella and thigh for both legs, plus the pelvis. Trunk segments were also included within the model in order to provide attachment sites for the psoas major muscles, and were constrained to the pelvis. Muscles, joint centres and inertial parameters for the model are based on an anthropometric data set from the University of Twente (Horsman, 2007).



Figure 82. Anterior (left) and posterior (right) view of the Twente Lower Extremity Model (TLEM).

5.2.1. Model Calculations

The lower-extremity model forms the template for segment geometries. Motion capture and ground reaction force (GRF) data provide boundary conditions for kinematic optimisation and inverse dynamics of the model.

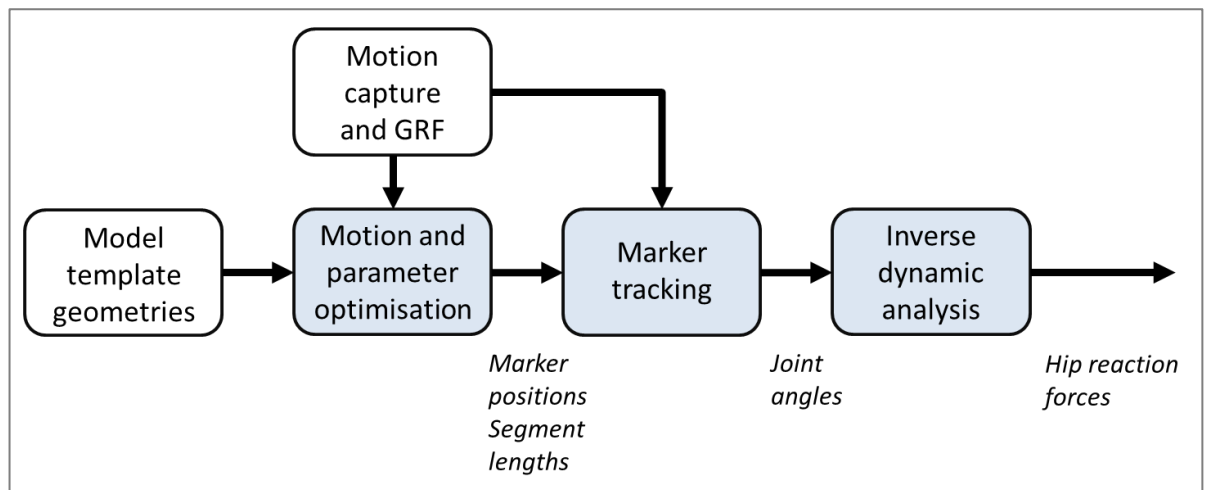


Figure 83. Flow chart of the processes involved in the musculoskeletal lower body model. White sequences represent input parameters and boundary conditions, whereas blue sequences represent processes executed within the AnyBody software. Outputs are shown in italics.

5.2.1.1. Motion and Parameter Optimisation

The ‘motion and parameter optimisation sequence’ optimised segment orientations and lengths, based on the boundary conditions imported from C3D motion files (Figure 32). Three markers, from the four-marker clusters at lower limb segments, were used for motion and parameter optimisation. The three markers provided a total of nine constraints (3D rotation by each marker). Given that a segment only has 6 degrees of freedom (three translational and three rotational), the markers were used to determine other unknown factors within the model (such as segment lengths). An in-built algorithm optimised the position of segment nodes and the position of experimental markers, in order to minimise the difference between the two locations (this accounts for the unknown distance between a marker and a bony landmark below the skin). Accurate determination of initial positions reduced the computing requirement to solve the optimisation and inverse dynamics problem. Once this step was complete, anthropometrical parameters and marker locations were updated and kinematics could be run (Figure 32) (AnyBody, 2019).

5.2.1.2. Marker Tracking and Inverse Dynamics

The ‘inverse dynamic analysis sequence’ loaded the optimised model parameters that were calculated previously. The sequence ran ‘marker tracking’ and if required, movements were calibrated by adjusting tendon lengths to match new bone lengths. Muscles were then ‘switched on’ and inverse dynamics were completed in order to determine the forces acting within the system (Figure 33). If the system was ‘statically

determinate’ (meaning no more than three points were in contact with the ground), just one unique set of reaction forces were required to balance the system. However, for a ‘statically indeterminate’ system (with four or more points in contact with the ground), there was an infinite number of combinations in which the body could be balanced (AnyBody, 2019). This is because the human body will contract and relax muscles until a comfortable equilibrium is achieved (the load may be redistributed a number of times when static). For this reason, the AnyBody model acts to replicate this process in order to solve the ‘load sharing problem’ and reach an optimised distribution of load (AnyBody, 2019). Once this step was completed, hip reaction force vectors could be exported from the software.

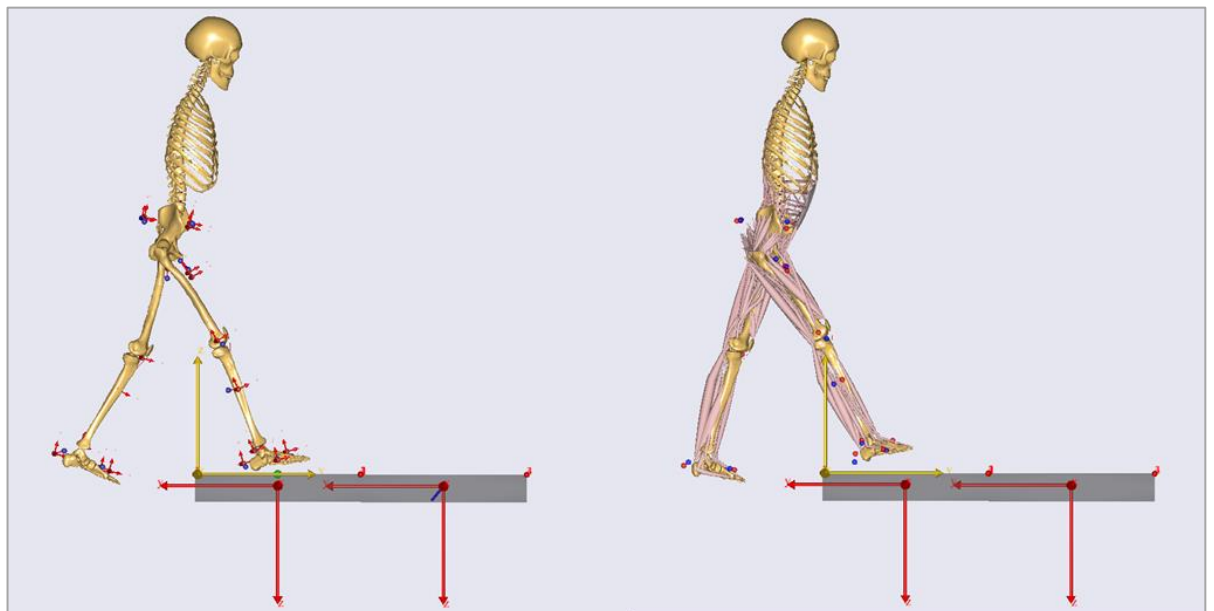


Figure 84. Kinematic analysis model (left) and inverse dynamic analysis model (right) from AnyBody. Experimental markers (blue) and AnyBody segment nodes (red) are shown alongside two AMTI force platforms.

5.2.2. Model Adaptations

The lower-extremity model was adapted to allow the script to run using the lab set-up and motion capture data from the current study. Firstly, the marker protocol was adapted in order to match the marker names defined within Qualisys Track Manager (Figure 25). It was ensured that any changes within the AnyScript code remained consistent throughout the entirety of the model. In order to locate parts of the code requiring adaptation, the model was run repetitively and errors were followed to the appropriate section of the

model tree. In addition to marker name changes, force platforms were adapted in order to match those used within the lab (these were type 4, AMTI platforms). A final change was made to the ‘trial specific data’ in order to incorporate height/ weight metrics and locate the appropriate C3D motion file. Changes to the ‘trial specific data’ were required before each of the ≈ 500 simulations that were run. For this reason, an ‘if statement’ was written into the script, meaning that the model could locate C3D files from an ‘input’ folder within the desktop and define the appropriate metrics automatically.

5.2.3. Python Macro Script

An AnyBody specific toolkit (AnyPyTools) was downloaded in order to allow the AnyBody graphical user interface (GUI) to be controlled through Python (Python, 2.7.14, Python Software Foundation, Wilmington, DE, USA). The toolkit allowed for faster, reproducible simulations through automated batch processing (Lund et al., 2019). A macro was written within Python, which: 1) opened the GUI; 2) ran the motion and parameter optimisation; 3) ran the inverse dynamics and 4) exported hip reaction force data (Appendix – 10.4.). This macro allowed for a large number of simulations to be automated, thus reducing time and computational cost. Should a simulation fail, the GUI was opened and the problem was fixed manually.

5.2.4. Joint Reaction Forces: Resultant Force and Impulse

Hip reaction forces (HRFs) were exported from AnyBody. Resultant HRFs were calculated from the MedioLateral (X), ProximoDistal (Y) and AnteroPosterior (Z) vectors (Equation 5). The orientation of the resultant HRF was then calculated using simple trigonometry.

$$\textit{Resultant HRF} = \sqrt{X^2 + Y^2 + Z^2} \quad \text{[Equation 5]}$$

Impulse was estimated using the trapezium rule, to multiply hip reaction force (HRF) by time (Equation 6).

$$\textit{Total impulse} \approx \frac{1}{2} \textit{frame rate} [HRF_0 + 2(HRF_1 + HRF_2 + \dots + HRF_{n-1}) + HRF_n] \quad \text{[Equation 6]}$$

Resultant HRFs and impulses were calculated for all activities with a recorded ground reaction force.

5.3. Results

5.3.1. Mean Ground Reaction Force

Ground reaction force describes the equal and opposite force applied by the ground, to an object or body. This was collected using two AMTI force platforms, embedded flush with the ground. When the force platform was loaded by an individual, a 3D force vector was resulted, allowing for the analysis of the kinetics associated with a given movement or activity. This force vector is a crucial input variable in order to complete inverse dynamics calculations to result hip moment and reaction forces.

Within the Appendix (section 10.6.), vertical ground reaction forces (vGRF) are presented. The vGRF resulted the largest magnitude of force, when considering all three vectors, during all activities. For this reason it was the most appropriate mode for analysing the kinetics of motion. It is noteworthy that incline/decline walk is not included, as a force platform was not embedded within the ramp. Additionally, sit cross legged and cycling could not be included, as the right foot was not in contact with a force platform during the movements.

5.3.2. Hip Moments

A moment of force can be described as the cross product of the moment arm distance (perpendicular distance between the axis of rotation and the application of force) and the magnitude of force (Robertson et al., 2013). Moments were normalised to body weight (Nm/kg) and calculations were resolved in the distal segment coordinate system (pelvis). The hip moment describes the net internal moment, produced by the muscles and ligaments at the hip, in order to balance the net external moment produced through the ground reaction force. When considering a total hip replacement, hip moments provide information about the potential torque acting at the prosthesis. Hip joint moments are reported in three axes (X: flexion-extension; Y: abduction-adduction; Z: internal-external rotation), alongside standard deviations, within the Appendix (section 10.6.).

5.3.3. Mean Hip Reaction Force

Hip reaction forces (HRFs) describe the reaction of force vectors acting from the femoral head on to the acetabular cup. This equal and opposite force, therefore describes direct loading of the cup.

Forces were calculated within Anybody (AnyBody, version 6.0, AnyBody Technology, Aalborg, Denmark) using ground reaction force inputs, alongside segment positions and orientations within the global coordinate system. For a statically determinate system, there is just one correct solution to balance the body at any given point. Joint reaction forces were calculated for eight of the activities using this method, in AnyBody. For a system which is not statically determined (three activities), AnyBody was required to contract and relax muscles within the model until a reasonable equilibrium was attained. More detail relating to this method is included in (section 3.2.).

Hip joint reaction forces were normalised to proportion of body weight (p BWT) and presented in Figures 137 to 145 (anterior-posterior, medial-lateral, proximal-distal vectors). Corresponding standard deviations (SD) are shown alongside the joint forces.

5.3.3.1. Walk

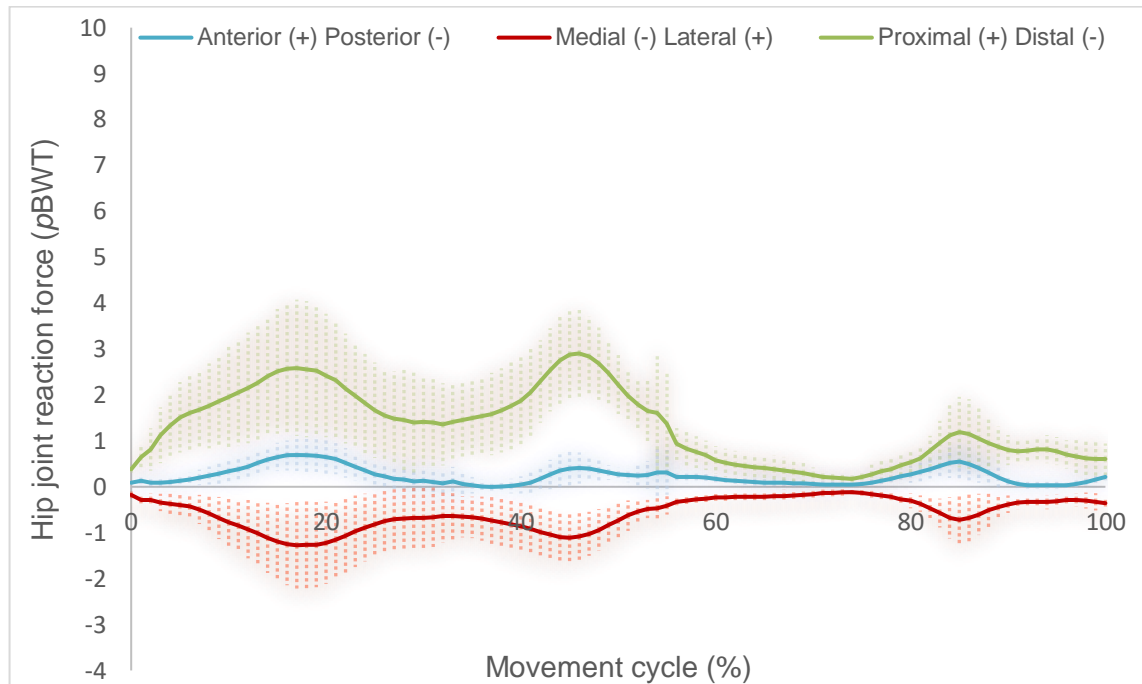


Figure 85. Mean right hip reaction force during one gait cycle for a level walk. Standard deviation above and below the mean are shown as shaded error bars (n=16).

Anterior, medial and proximal HRF vectors displayed two peaks during the stance phase (corresponding to the vertical ground reaction force peaks) and a smaller peak during the swing phase (Figure 137). At initial contact, anterior, medial and proximal forces peaked to 0.7, 1.3 and 2.6 *pBWT*, respectively. Forces decreased into a ‘valley’ during mid-stance, before peaking again during the propulsion phase of gait (anterior: 0.4 *pBWT*; medial: 1.1 *pBWT*; proximal: 2.9 *pBWT*). HRFs were reduced to approximately zero following toe off, before exhibiting a third, smaller peak during the swing phase (anterior: 0.5 *pBWT*; medial: 0.7 *pBWT*; proximal: 1.1 *pBWT*).

Mean standard deviations (SDs) were ± 0.2 , ± 0.4 and ± 0.7 *pBWT* for anterior-posterior (A-P), medial-lateral (M-L) and proximal-distal (P-D) force, respectively. For each of the force vectors, variation was highest at the first peak, during the loading phase of gait (peak SD: A-P: 0.5 *pBWT*; M-L: 1.0 *pBWT*; P-D: 1.5 *pBWT*). An unusual SD was observed at $\approx 55\%$ of the gait cycle for A-P and P-D forces. It is likely that this irregular spike was due to embedded noise within the data.

5.3.3.2. Walk Turn

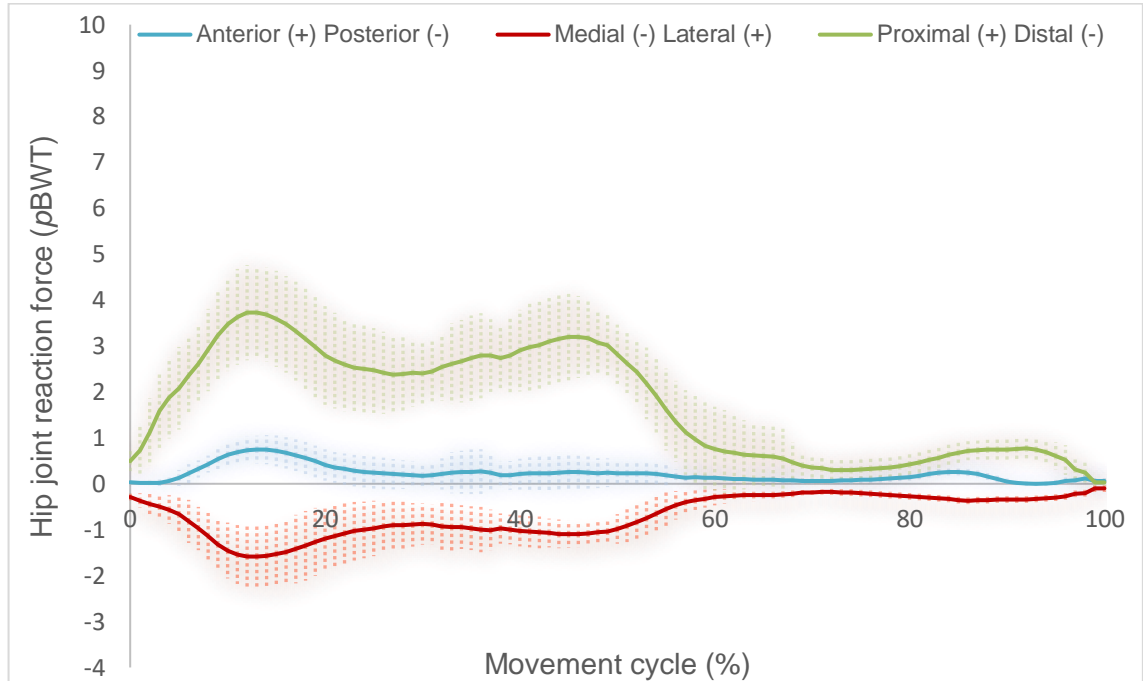


Figure 86. Mean right hip reaction force during one gait cycle for a walk turn. Standard deviation above and below the mean are shown as shaded error bars (n=17).

Walk turn HRFs showed similarities to the straight walk (Figure 138). All force vectors displayed an initial peak during loading (anterior: 0.7 pBWT; medial: 1.6 pBWT; proximal: 3.7 pBWT). A reduced second peak was observed for medial and proximal loading of the hip (medial: 1.1 pBWT; proximal: 3.2 pBWT), whereas anterior force plateaued at 0.2 pBWT. Small peaks were seen during the swing phase for anterior (0.2 pBWT) and proximal forces (0.8 pBWT).

Mean SDs for A-P, M-L and P-D forces were ± 0.2 , ± 0.3 and ± 0.7 pBWT, respectively. Variation was highest during the stance phase and peaked at weight acceptance (A-P: 0.3 pBWT; M-L: ± 0.8 pBWT; P-D: ± 1.1 pBWT).

5.3.3.3. *Stand to Sit*

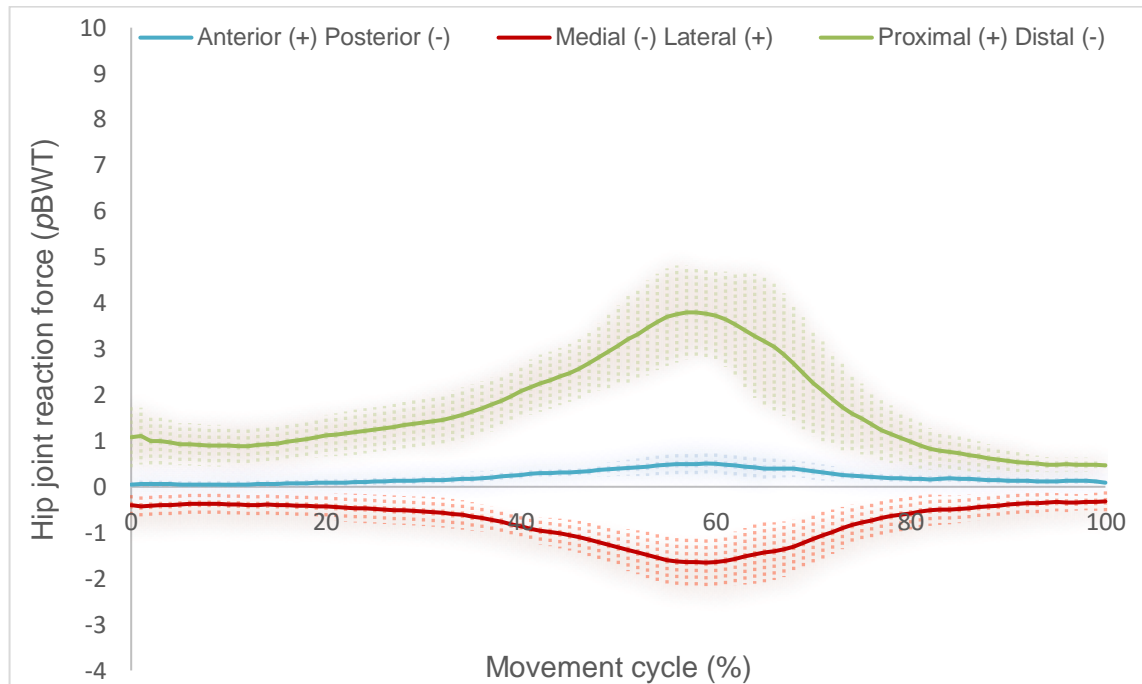


Figure 87. Mean right hip reaction force during one movement cycle for a stand to sit (chair height: 47 cm). Standard deviation above and below the mean are shown as shaded error bars (n=7).

When stood in a neutral position, the hip was subjected to a medial (0.4 pBWT) and proximal (1.0 pBWT) reaction force (Figure 139). When moving down from a standing position into a seated position, HRFs were increased and peaked when in contact with the seat (anterior: 0.5 pBWT; medial: 1.7 pBWT; proximal: 3.8 pBWT). Following peak loading, anterior and medial forces decreased to a magnitude comparable to standing. The proximal force reduced to a magnitude equal to half of the standing reaction force (0.5 pBWT).

Mean SDs were ± 0.1 , ± 0.4 and ± 0.6 pBWT for A-P, M-L and P-D forces, respectively. Peak variation was synonymous with peak loading for all force vectors (A-P: ± 0.2 pBWT; M-L: ± 0.6 pBWT; P-D: ± 1.4 pBWT).

5.3.3.4. *Sit to Stand*

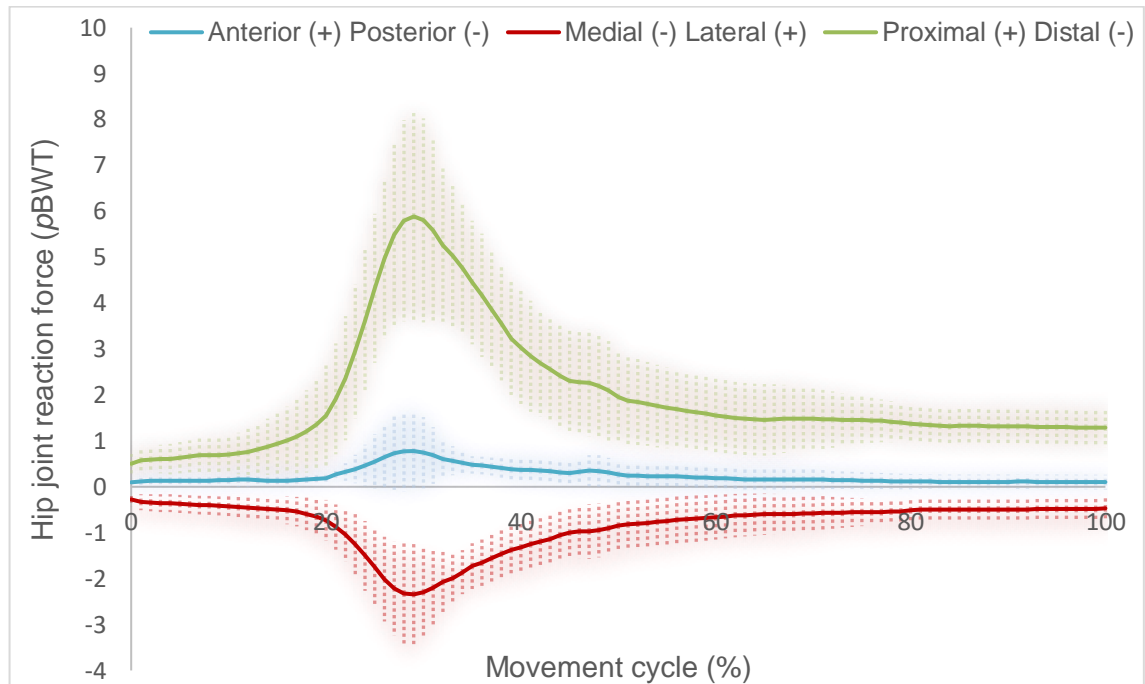


Figure 88. Mean right hip reaction force during one movement cycle for a sit to stand (chair height: 47 cm). Standard deviation above and below the mean are shown as shaded error bars (n=7).

From a seated position (anterior: 0.1 pBWT; medial: 0.3 pBWT; proximal: 0.5 pBWT), forces increased when standing up, peaking at ‘seat-off’ (anterior: 0.8 pBWT; medial: 2.3 pBWT; proximal: 5.8 pBWT) (Figure 140). Reaction forces reduced once individuals left the seat. The A-P and M-L forces decreased in magnitude and reached similar values as when seated. Proximal forces were approximately twice as large when standing, compared to when seated (1.3 pBWT).

Average SDs were similar to the stand to sit, except that variation was increased for P-D forces (A-P: ± 0.2 pBWT; M-L: ± 0.4 pBWT; P-D: ± 0.8 pBWT). Variation peaked at the same point as peak magnitudes (seat-off). Peak SDs were ± 0.9 , ± 1.1 and ± 2.3 pBWT for anterior, medial and proximal forces, respectively.

5.3.3.5. *Squat*

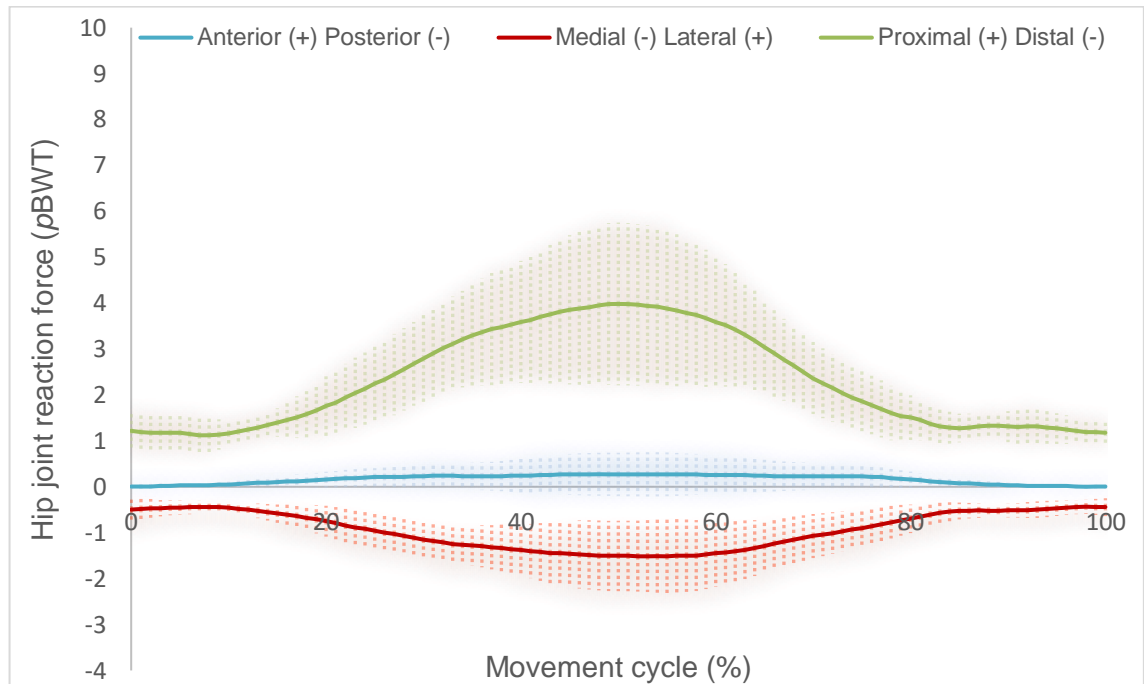


Figure 89. Mean right hip reaction force during one movement cycle for a squat. Standard deviation above and below the mean are shown as shaded error bars (n=11).

As individuals moved down into the squat, anterior, medial and proximal HRFs increased and peaked at the lowest point of the squat (anterior: ± 0.3 pBWT; medial: ± 1.5 pBWT; proximal: ± 4.0 pBWT) (Figure 141). The second half of the squat mirrored the first half, displaying a reduction in anterior, medial and proximal loading of the hip.

Average SDs were ± 0.2 , ± 0.4 and ± 0.8 pBWT for A-P, M-L and P-D forces, respectively. Variation peaked when the squat was at the lowest point (A-P: ± 0.5 pBWT; M-L: ± 0.8 pBWT; P-D: ± 1.8 pBWT).

5.3.3.6. *Stand Reach*

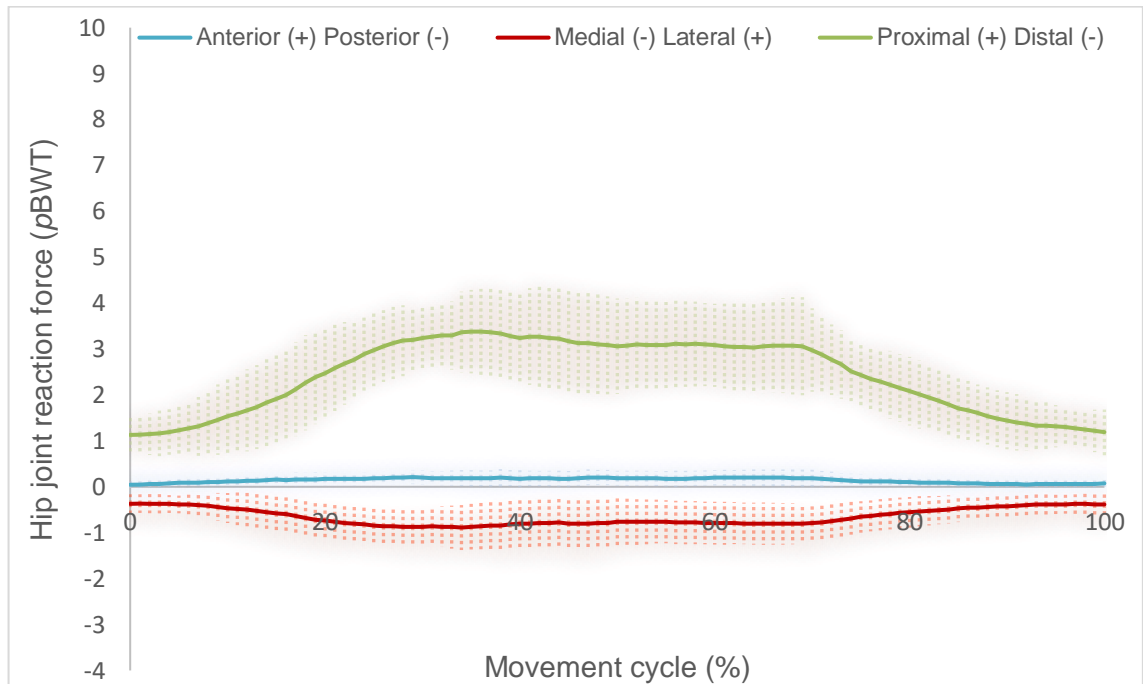


Figure 90. Mean right hip reaction force during one movement cycle for standing and reaching down to the floor. Standard deviation above and below the mean are shown as shaded error bars (n=12).

From a standing position, anterior, medial and proximal loading of the hip increased (Figure 142). Forces peaked at the point where the hip was fully flexed (anterior: 0.2 pBWT; medial: 0.8; pBWT; proximal: 3.4 pBWT).

Mean variation across the movement (SD) was ± 0.1 , ± 0.4 and ± 0.8 pBWT for A-P, M-L and P-D forces, respectively. Variation showed little fluctuation throughout the movement, however it was slightly decreased at the beginning and end of the cycle.

5.3.3.7. *Kneel Reach*

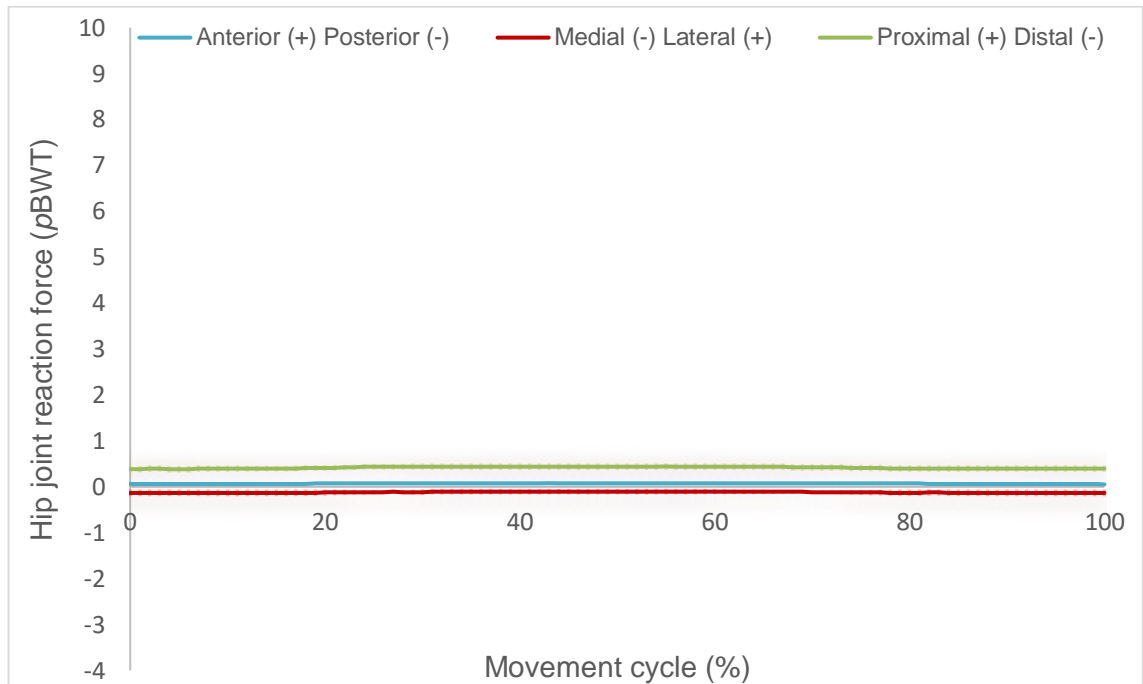


Figure 91. Mean right hip reaction force during one movement cycle for kneeling and reaching forwards. Standard deviation above and below the mean are shown as shaded error bars (n=10).

When kneeling and reaching forwards, hip reaction forces remained low and consistent throughout (Figure 143). Forces peaked at 0.1 pBWT (anterior), 0.1 pBWT (medial) and 0.4 pBWT (proximal). Mean variation was ± 0.1 (A-P), ± 0.4 (M-L) and ± 0.8 (P-D) pBWT.

5.3.3.8. *Lunge*

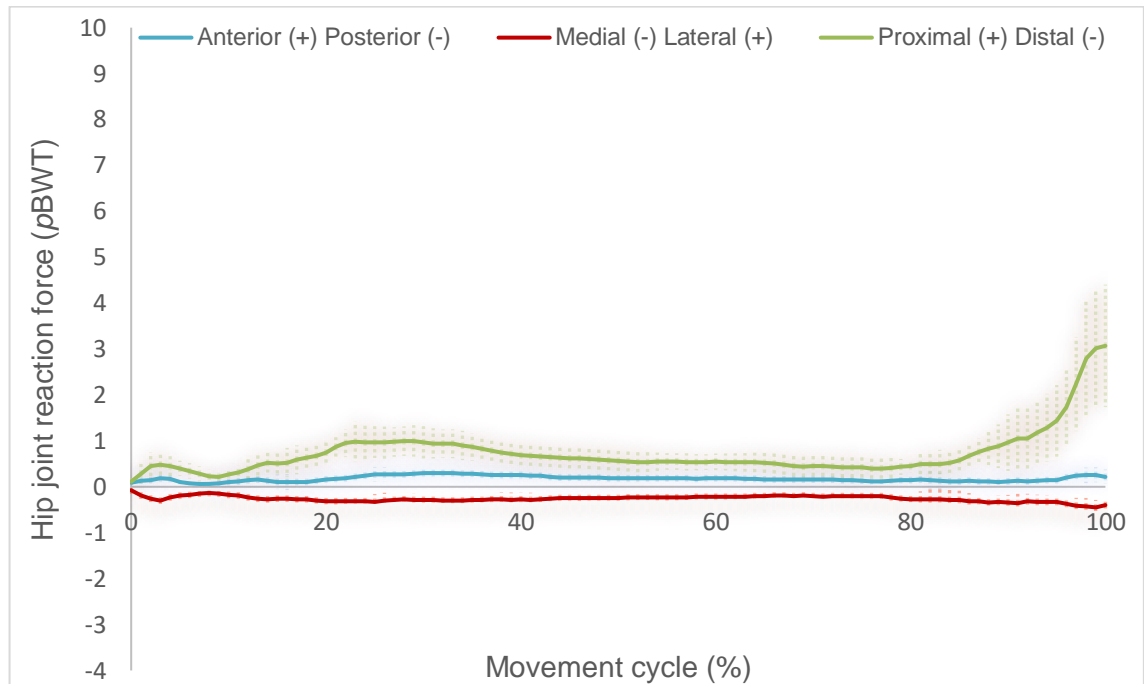


Figure 92. Mean right hip reaction force during one movement cycle for a right footed lunge. Standard deviation above and below the mean are shown as shaded error bars (n=13).

Anterior and medial forces showed little fluctuation with regards to magnitude and remained at averages of 0.2 and 0.3 pBWT respectively (Figure 144). Proximal reaction forces showed a first peak at initial contact (1.0 pBWT), followed by a larger peak during the propulsion phase of the movement (3.1 pBWT).

Average SDs were ± 0.1 , ± 0.1 and ± 0.3 pBWT for A-P, M-L and P-D force, respectively. The level of variation was consistent throughout the lunge for A-P and M-L forces. The P-D forces, however, showed a marked increase in variation during the propulsive phase of gait, peaking at ± 1.3 pBWT.

5.3.3.9. *Golf Swing*

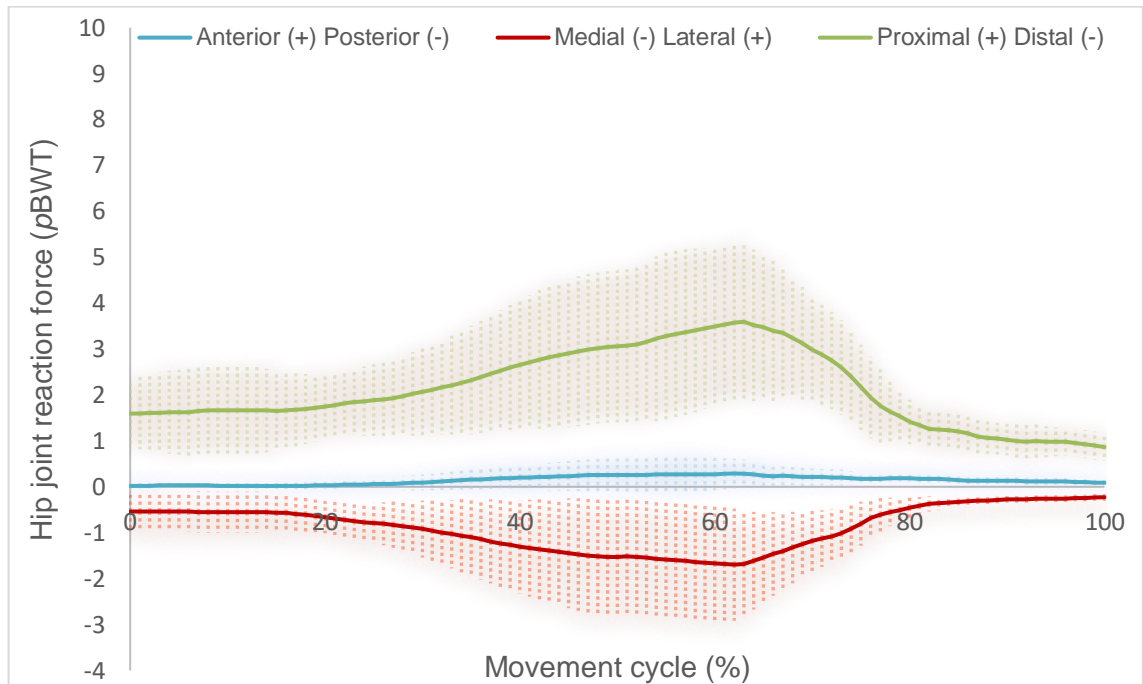


Figure 93. Mean right hip reaction force during one movement cycle for a golf swing. Standard deviation above and below the mean are shown as shaded error bars (n=16).

Anterior, medial and proximal forces increased throughout the backswing and downswing, peaking at the bottom of the downswing (anterior: 0.3 pBWT; medial: 0.8; pBWT; proximal: 3.4 pBWT) (Figure 145). Forces then decreased throughout the follow through.

Mean SDs were ± 0.2 (A-P), ± 0.6 (M-L) and ± 1.0 (P-D) pBWT. Variation increased for each of the force vectors at the bottom of the downswing, peaking at ± 0.4 (A-P), ± 1.3 (M-L) and ± 1.8 (P-D) pBWT.

5.3.4. Resultant Hip Reaction Forces

Resultant hip reaction forces describe the resultant force, calculated from medial-lateral, anterior-posterior and proximal-distal force vectors. This was calculated by squaring each vector, summing them and then square rooting. This was completed at each percentage of the movement cycle. The magnitude and position of these forces will influence loading and potential wear of a polyethylene acetabular cup.

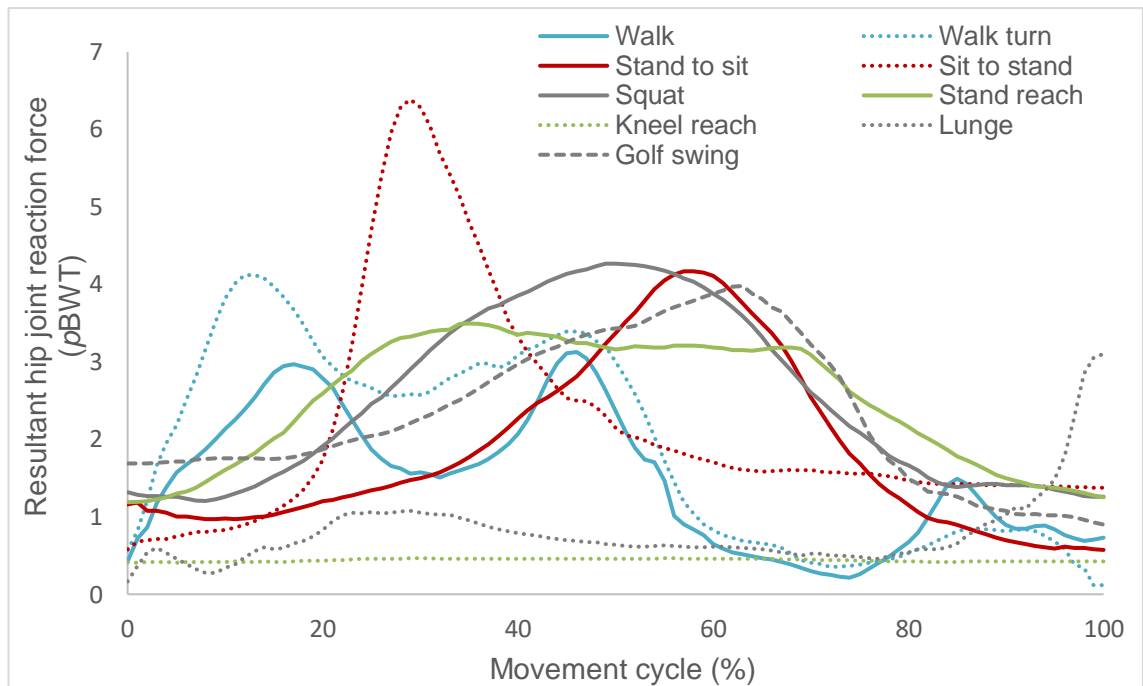


Figure 94. Mean resultant hip reaction forces during one movement cycle for activities, proportional to body weight (*p*BWT).

Figure 146 demonstrates the variation in resultant HRFs for different activities. Peak forces occurred at different times in the movement cycle, for different activities. Sit to stand showed a considerably larger peak reaction force (6.4 *p*BWT) when compared to other activities. Walking activities showed the typical double peak during the stance phase, with a smaller peak during the swing phase. The kneel reach stood out as the activity in which loading was consistently of a low magnitude.

Table 10. Peak hip reaction forces normalised to proportion of body weight (*p*BWT). Resultant vectors are calculated from the anterior-posterior, medial-lateral and proximal-distal force. Resultant hip reaction force magnitudes (**bold**), standard deviations (**SD**) and angles (*italics*) are shown. Angles reported are the relative rotational values between a vertical vector and the resultant vector. Rotations are about the medial (*X*), anterior (*Y*) and superior (*Z*) axes.

	Peak resultant force \pmSD (Vector angle: <i>X, Y, Z</i>) (<i>p</i>BWT)
Walk	3.1 \pm1.1 (110°, 82°, 22°)
Walk turn	4.1 \pm1.1 (113°, 80°, 25°)
Stand to sit	4.2 \pm1.1 (113°, 83°, 24°)
Sit to stand	6.4 \pm2.6 (112°, 83°, 23°)
Squat	3.5 \pm1.9 (111°, 86°, 21°)
Stand reach	4.3 \pm1.0 (104°, 87°, 15°)
Kneel reach	0.5 \pm0.1 (104°, 80°, 17°)
Lunge	3.1 \pm1.3 (97°, 86°, 8°)
Golf swing	4.0 \pm1.9 (115°, 86°, 25°)

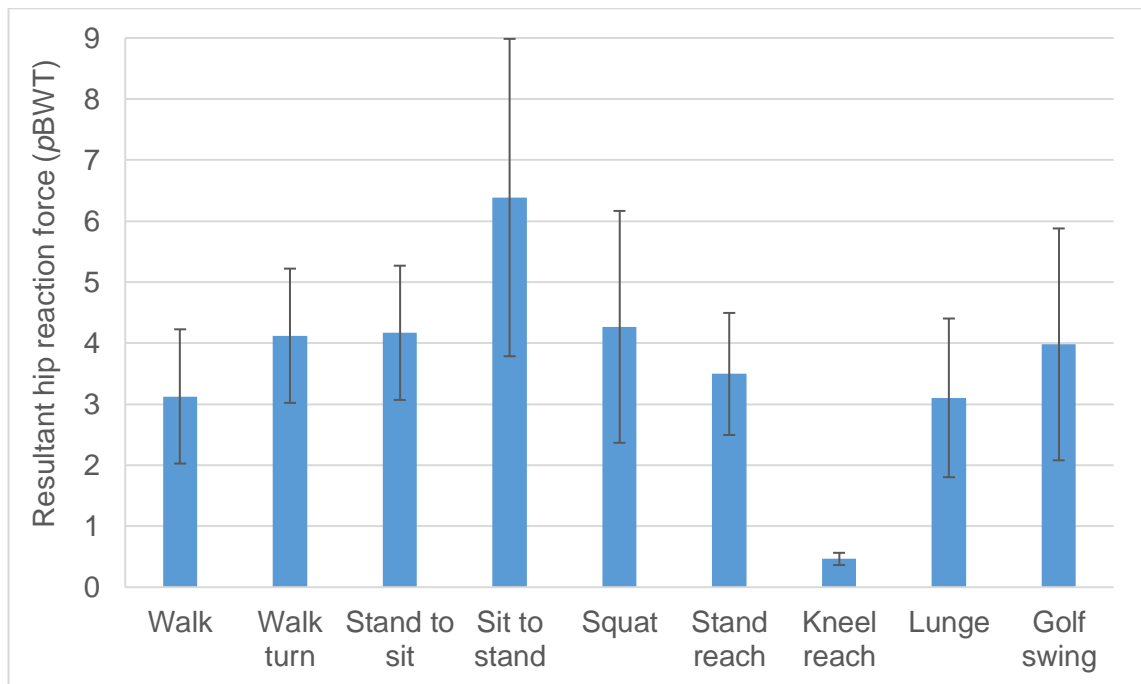


Figure 95. Peak resultant hip reaction force (proportional to body weight, *pBWT*) with standard deviation shown as error bars.

HRF vector orientations were calculated using the left-hand rule with X (medial to lateral), Y (posterior to anterior) and Z (proximal to distal) axes. Sit to stand resulted the highest magnitude resultant vector (6.4 *pBWT*), followed by the squat (4.3 *pBWT*) and stand to sit (4.2 *pBWT*) (Table 15 and Figure 146). Kneel reach stood out with the lowest magnitude of loading, at just 0.5 *pBWT*. Vector positions ranged between: 97° and 115° from X; 80° and 87° from Y; 8° and 25° from Z. Thus, the resultant force vector for each activity was applied from a medial and anterior position on the femoral head. HRF orientations and corresponding contact points on the acetabular cup are presented in section 4.5.10., where mean hip reaction forces are modelled within a CAD software.

The resultant HRF SD was highest for sit to stand (± 2.6 *pBWT*), squat (± 1.9 *pBWT*) and golf swing (± 1.9 *pBWT*). Anterior-posterior (A-P) standard deviations (SDs) were similar across all subjects (between ± 0 and ± 0.2 *pBWT*). Medio-lateral (M-L) SD was largest for the sit to stand task (± 0.9 *pBWT*) and proximal-distal (P-D) SD was highest for the golf swing (± 0.6 *pBWT*). Peak reaction force SDs indicate points within activities that may have a high level of variation between subjects. The golf swing showed the highest peak SD for both A-P (± 1.3 *pBWT*) and M-L (± 1.0 *pBWT*) force. The sit to stand task resulted the largest peak SD for proximal-distal loading (± 2.3 *pBWT*) (Table 16).

Table 11. Average and peak standard deviation for hip reaction forces. Inter-subject variation is shown for loading in three planes (Anterior-Posterior (A-P), Medial-Lateral (M-L) and Proximal-Distal (P-D)). The highest variation, by activity, is highlighted within each column (bold).

Standard deviation (ρ BWT)	Average standard deviation			Peak standard deviation		
	A-P	M-L	P-D	A-P	M-L	P-D
Walk	± 0.2	± 0.5	± 0.4	± 1.0	± 0.7	± 1.5
Walk turn	± 0.2	± 0.5	± 0.3	± 0.8	± 0.7	± 1.1
Stand to sit	± 0.1	± 0.2	± 0.4	± 0.7	± 0.6	± 1.4
Sit to stand	± 0.2	± 0.9	± 0.4	± 1.1	± 0.8	± 2.3
Squat	± 0.2	± 0.5	± 0.4	± 0.8	± 0.8	± 1.8
Stand reach	± 0.1	± 0.2	± 0.4	± 0.6	± 0.8	± 1.2
Kneel reach	± 0.0	± 0.0	± 0.1	± 0.1	± 0.1	± 0.1
Lunge	± 0.1	± 0.2	± 0.1	± 0.2	± 0.3	± 1.3
Golf Swing	± 0.2	± 0.4	± 0.6	± 1.3	± 1.0	± 1.8

5.3.5. Hip Reaction Impulse

Impulse was calculated for activities by integrating hip contact force – time graphs. Frame time was calculated for each activity and used within the calculations (section 5.2.4.). Impulse is resulted as proportion of body weight seconds ($pBWT \cdot s$) and describes the force applied to the hip, over a given period of time. Ultimately, this provides information relating to the total force occurring throughout the movement time (Table 17).

Table 12. Total hip impulse reaction force (proportion of body weight seconds: $pBWT \cdot s$) occurring at anterior, medial and proximal positions on the femoral head. Maximum impulse values are highlighted in bold.

Impulse ($pBWT \cdot s$)	Anterior	Medial	Proximal	Resultant
Walk	0.3	0.6	1.5	1.6
Walk turn	0.2	0.7	1.7	1.8
Stand to sit	0.3	0.9	2.1	2.3
Sit to stand	0.3	0.9	2.3	2.5
Squat	0.2	1.2	3.1	3.3
Stand reach	0.3	1.2	4.5	4.7
Kneel reach	0.2	0.4	1.5	1.6
Lunge	1.0	1.5	4.4	4.7
Golf swing	0.4	2.6	6.2	6.7

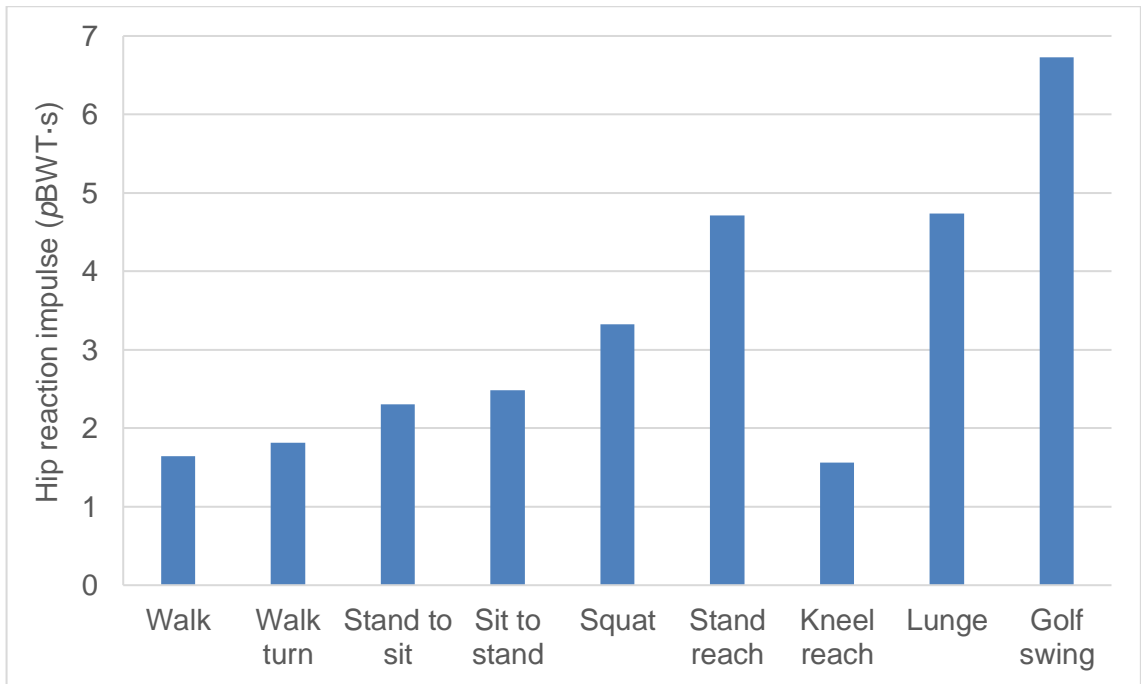


Figure 96. Resultant hip reaction impulse (proportion of body weight seconds, $pBWT \cdot s$).

Impulse was highest for the golf swing ($6.7 pBWT \cdot s$), lunge and stand reach (both $4.7 pBWT \cdot s$) (Figure 148). This was likely due to a combination of long movement times and/ or consistent joint loading (due to having both feet in contact with the floor throughout). Lower impulses occurred for activities with multiple contact points with the ground (sit to stand, stand to sit and kneel reach) and those with a swing phase for the right leg (walk and walk turn).

5.3.6. Variation and Age

Mean peak hip reaction forces (HRFs) were calculated for individuals under and over 55, for 13 activities. Differences between the two age groups were then calculated. For activities that showed a difference of over 1 proportion of body weight (*p*BWT) between groups, HRF was compared across the whole movement cycle. It is noteworthy that stand to sit and sit to stand HRFs were not included in this section, as two age groups could not be identified given the sample size.

Table 13. Mean peak resultant hip reaction forces for under and over 55 year olds, normalised to proportion of body weight (*p*BWT). Differences between age groups is shown, with discrepancies over one *p*BWT in bold.

Peak hip reaction force (<i>p</i>BWT)	Under 55	Over 55	Difference
Walk	3.4	2.9	0.5
Walk turn	4.1	5.0	0.9
Stand to sit	-	-	-
Sit to stand	-	-	-
Squat	4.5	3.6	0.9
Stand reach	3.8	3.0	0.8
Kneel reach	0.4	0.5	0.1
Lunge	3.1	3.3	0.2
Golf swing	3.3	4.4	1.1

Mean peak HRFs were larger for the older group, compared to the younger group, in four of the seven activities. The younger group showed higher loading in three activities (Table 20).

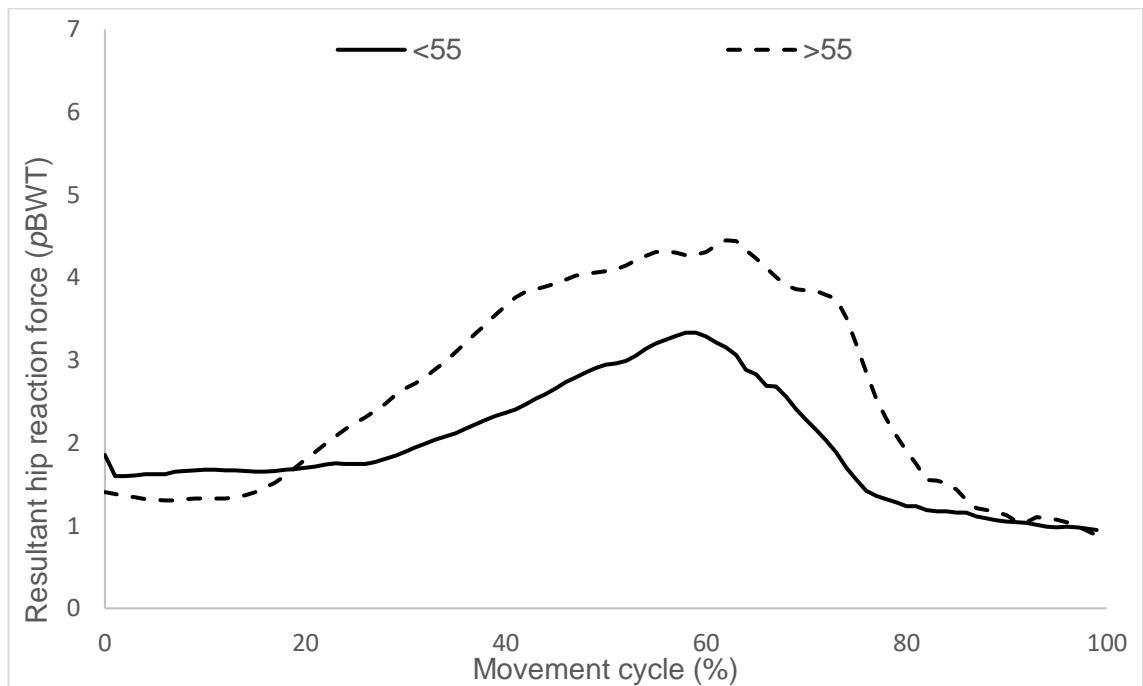


Figure 97. Mean resultant hip reaction force for a golf swing. Under 55 year olds (<55 y: solid line) (n=10) and over 55 year olds (>55 y: dashed line) (n=6) are compared.

HRFs were similar at the beginning and end of the golf swing for the two age groups (Figure 162). The older group loaded the hip at a higher rate and magnitude during the backswing, compared to the younger group (20-50%). HRF peaked during the downswing (50-70%), with higher hip loading for the older group (4.4 pBWT) compared to the younger group (3.3 pBWT). Forces then returned to similar levels during the follow through (70-100%).

5.3.7. Variation and Gender

Peak hip reaction forces (HRFs) were taken from mean force curves for activities (section 5.3.3.). For this section, subjects were grouped by gender and peak HRFs were determined from mean curves. Peak data showing a difference of over 1 proportion of body weight (*p*BWT) were then plotted across the whole movement cycle for the given activity.

Table 14. Mean peak resultant hip reaction forces for males and females, normalised to proportion of body weight (*p*BWT). Differences between genders is shown, with discrepancies over one *p*BWT in bold.

Peak hip reaction force (<i>p</i> BWT)	Male	Female	Difference
Walk	3.2	4.0	0.8
Walk turn	3.8	4.7	0.9
Incline walk	-	-	-
Decline walk	-	-	-
Stand to sit	4.6	4.1	0.5
Sit to stand	6.3	6.4	0.1
Squat	3.5	4.7	1.2
Stand reach	3.2	3.8	0.6
Kneel reach	0.5	0.5	0
Lunge	2.8	3.3	0.5
Golf swing	3.3	4.9	1.6

The golf swing (1.6 *p*BWT) and squat (1.2 *p*BWT) were the only activities to show a difference of over 1 *p*BWT between genders. Both of these activities saw females produce a higher peak HRF. Seven of the eleven activities saw females produce a higher peak HRF than males. One activity resulted males with a larger peak force than females (stand to sit) and one activity resulted no difference (kneel reach) (Table 22).

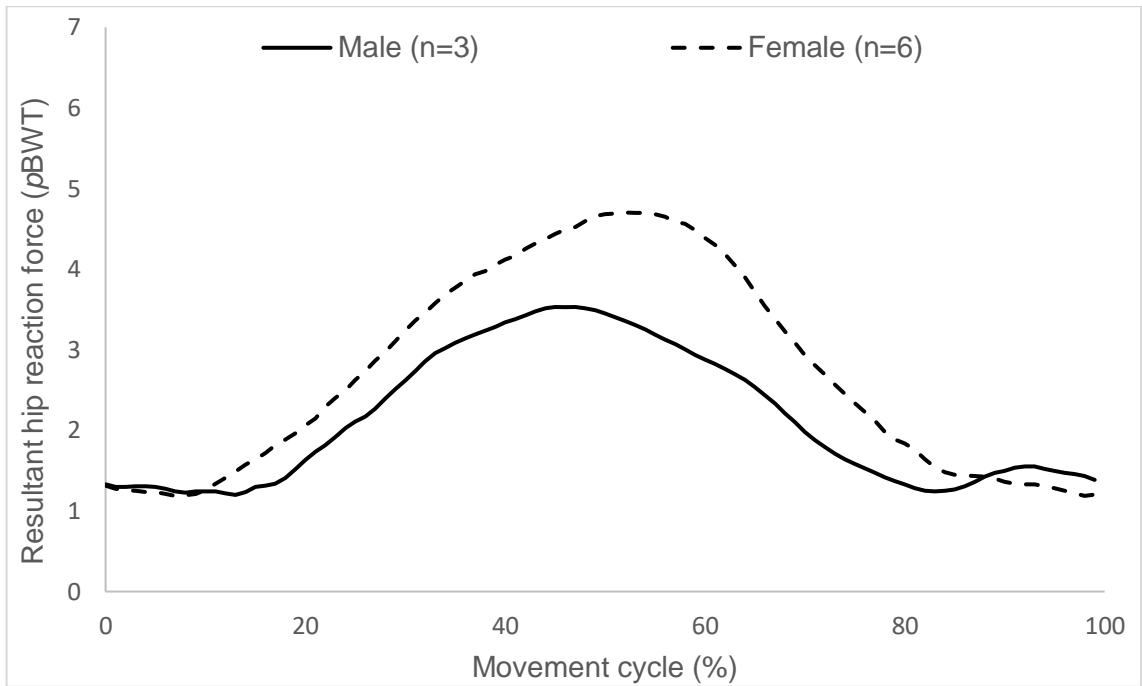


Figure 98. Mean resultant hip reaction force for a squat. Male (solid line) (n=3) and female (dashed line) (n=6) groups are compared.

Resultant HRFs were similar for males and females when standing (start and end of the squat) (Figure 167). Females peaked later in the squat cycle and at a higher hip force magnitude than the male group (+1.2 pBWT).

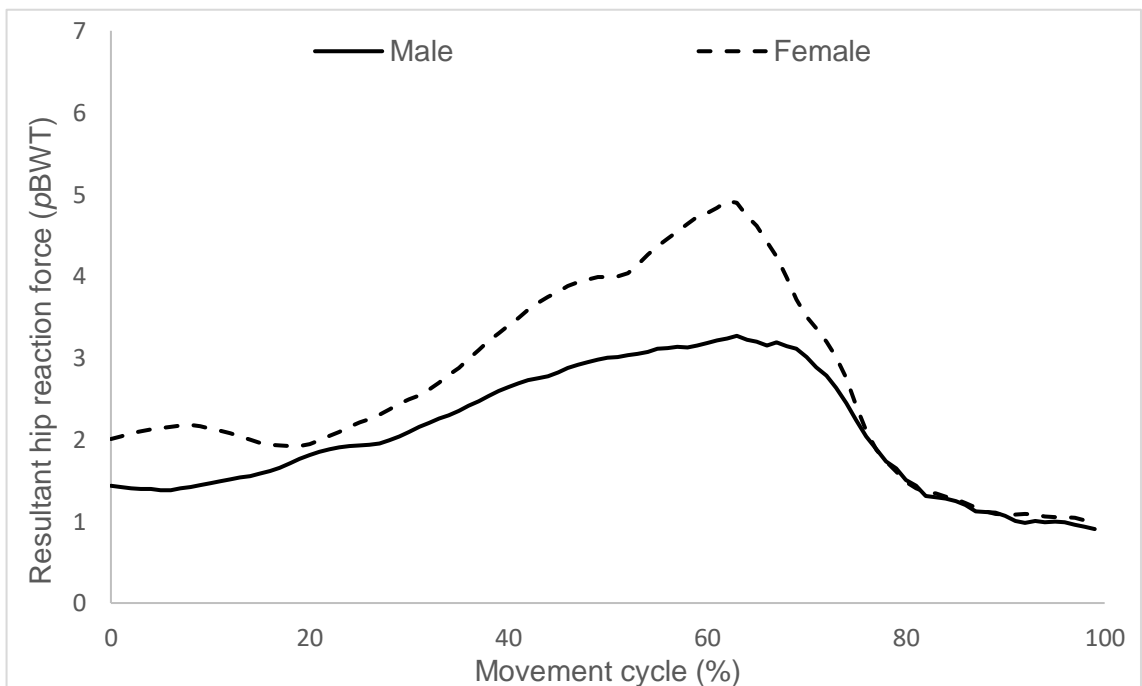


Figure 99. Mean resultant hip reaction force for a golf swing. Male (solid line) (n=9) and female (dashed line) (n=7) groups are compared.

Females demonstrated a higher resultant hip force throughout the backswing (0-50%) and downswing (50-70%) (Figure 168). Hip forces peaked during the downswing and were 1.6 *p*BWT higher for females, compared to males. Forces during the follow through were similar for both groups.

5.3.8. Summary

Resultant hip reaction forces ranged from 0.5 (kneel reach) to 5.9 (sit to stand) proportion of body weight (*p*BWT). The angle for the resultant vector varied between activities but was always applied to the cup from a medial and anterior position on the femoral head. More detail on the force vector position and contact area on the cup, is shown in Chapter 6. Standard deviations suggest a high level of hip reaction force variation for the golf swing and the sit to stand task. Resultant impulse was highest for the golf swing (6.7 *p*BWT·s), followed by the lunge and stand reach (both 4.7 *p*BWT·s).

5.4. Discussion

Within this section, hip kinetics are discussed for nine common activities (section 5.4.1. to 5.4.10.). This is preceded by an overall discussion and summary of the findings (section 5.4.11 and 5.4.12).

Ground reaction forces (GRFs) were measured for eighteen subjects, using two AMTI force platforms (AMTI, Advanced Mechanical Technology Inc., Watertown, MA, USA). It is noteworthy that force data could not be measured for incline/ decline walk, sit cross legged and cycle. Joint moments were calculated from the GRF and provide an estimation of the tensile forces occurring at structures crossing the hip (flexion-extension (F-E), abduction-adduction (Ab-Ad) and internal-external rotation (I-E) moments).

GRFs provided boundary conditions for musculoskeletal simulations, in which hip reaction forces (HRFs) and impulses (the product of HRF and time) were estimated (Anybody Modelling System 6.0, Anybody Technology, Aalborg, Denmark). For each activity, anterior-posterior (A-P), medial-lateral (M-L), proximal-distal (P-D) and resultant HRFs were calculated, alongside standard deviations (SDs).

HRFs, impulses and moments provide important information relating to the forces crossing the hip joint. This is relevant to the loading and potential wear of the polyethylene cup in a THR and tissue engineered cartilage substitution at the hip. HRFs and impulses are discussed within this section. GRFs and hip moments are presented and discussed within the Appendix (section 10.6.).

5.4.1. Walk

During walking, resultant HRFs showed a typical two peaked pattern, with an initial smaller peak (2.9 *pBWT*) and second larger peak (3.1 *pBWT*) (section 5.3.3.1.). These two peaks were observed in each axis of loading, with the resultant HRF loading occurring at an anterior, lateral and distal position on the femoral head (Table 8). The first peak represents weight acceptance, following initial contact, whereas the second peak represents the propulsive phase of the movement, following heel-off. The peak resultant HRF (for the walk) was the joint lowest, when compared to other activities (3.1 *pBWT*) (section 5.3.3.10.). However, given the standard deviation (SD) of ± 1.1 *pBWT* for the walk, the HRF range crossed-over with all other activities. This demonstrates that there is overlap between activities, for hip loading, depending on the individual. It seems reasonable to consider ‘extreme’ conditions, when investigating failure mechanisms for THR. It may therefore be beneficial to concentrate not only on mean peaks, but also the extremes of the SD range.

Hip impulse during walking showed the joint lowest magnitude, alongside kneel reach (1.6 *pBWT*·s) (section 5.3.4.). This low value was partly due to fluctuations in HRF during the walking cycle, as loading was not consistent throughout. Fluctuations may be beneficial when considering joint lubrication, as fluid entrainment will occur when force is reduced (during the swing phase) (Jin et al., 1993; Stewart, 2010; Stewart et al., 1997). A second reason for the low impulse value is that the walking cycle was one of the shorter movement cycles, at 1.1 seconds.

Average walk HRF SDs are reported in Table 16 (A-P: ± 0.2 *pBWT*; M-L: ± 0.5 *pBWT*; P-D: ± 0.4 *pBWT*). Variation was low during the swing phase ($< \pm 0.1$ *pBWT*) and peaked during weight acceptance (this peak reached ± 1.5 *pBWT* during P-D loading). The high variation at weight acceptance may be due to walking speed, thus a more dynamic movement is likely to result higher forces. Current ISO testing standards for THRs recommend a maximal load of approximately 4 *pBWT* (ISO 14242, 2019) (Paul, 1966). This falls above the average, yet within the SD range, of the current study (3.1 ± 1.1 *pBWT*).

Within the literature, HRFs have been calculated both computationally and through instrumented implants. *In vivo* peak HRFs, measured using instrumented implants, have been reported between 2.4 and 4.1 *pBWT* (Bergmann et al., 2001; Bergmann et al., 1993; Brand et al., 1994; Damm et al., 2013a; Damm et al., 2013b; Davy et al., 1988; Kotzar et al., 1991; Schwachmeyer et al., 2013). Findings from the current study fall within this

range (3.1 *p*BWT). The variation seen within the literature is likely to have occurred due to patient group sizes with varying levels of postoperative functionality (Bergmann et al., 2001). Reported values within the literature support the reliability of the computational method used in the present study. It is noteworthy that Bergmann identified values as high as 4.8 *p*BWT, for one patient, when walking (the patient had gait abnormalities and walked at 5 km/h) (Bergmann et al., 1993). This is 0.7 *p*BWT higher than the top of the SD range reported in the current study, further highlighting the variability in hip loading during walking. It was suggested that muscular dysfunction can lead to higher HRFs, as the undamaged muscles (with potentially smaller moment arms) may be required to assist movement (Bergmann et al., 1993). Again, this demonstrates the importance of understanding the extreme ranges for force data, particularly when considering pre-clinical durability testing of devices.

Two recent computational studies (AnyBody Technology) compared HRFs between healthy and asymptomatic THR patient groups (Li et al., 2015; Li et al., 2014). Peak HRFs were reported both in 2014 (Healthy: 3.0 *p*BWT; THR: 3.4 *p*BWT) and 2015 (Healthy: 3.3 *p*BWT; THR: 3.8 *p*BWT). Both studies reported a significantly decreased second peak for a patient group, which was attributed to a potential gap in functionality, expressed through a decreased range of hip motion and reduced hip loading (Li et al., 2014). This was not seen in the healthy group. More recently, De Pieri et al. (2019) reported peak HRFs of 2449 N for asymptomatic patients (AnyBody Technology). Although subject masses were not given, this value would approximately equate to 3.1 *p*BWT (for an average mass of 80 kg). Although this is lower than previously reported values, the large subject size within the study (132 patients between 57 and 85) suggests that it is an accurate representation of hip forces. Similar to previous work, De Pieri et al. (2019) also observed a reduced second HRF peak for THR patients.

The 3.1 *p*BWT peak in the current study falls within the reported range for healthy subjects (Li et al., 2015; Li et al., 2014), whilst showing similar magnitudes to asymptomatic patient data (De Pieri et al., 2019; Li et al., 2015; Li et al., 2014). Although HRFs within the current study are agreeable with reported values for well-functioning THR patients, it is important to appreciate that the typically reduced second peak is not seen within data from healthy subjects and may not occur for a younger, asymptomatic patient group (De Pieri et al., 2019).

5.4.2. Walk Turn

Walk turn resultant HRF showed a similar, two peaked force trace to the walk. However, unlike the walk, the first peak was larger (4.1 *pBWT*) than the second (3.4 *pBWT*) (5.3.3.2.). The larger first peak corresponded to a change in kinematics at this point, compared to the straight walk, in order to turn 90° to the left. Essentially, it appears that a larger mean force was required at the hip in order to turn the body and propel forwards at an angle. Visually, the walk turn profile shows a reduced ‘trough’ between peaks. It is likely that the angular velocity of the movement itself, influenced peak forces and the ‘trough’ depth.

Similar to the straight walk, anterior, lateral and proximal resultant loading from the femoral head showed two peaked profiles. Variation for walk turn HRFs were similar to the straight walk, although the peak P-D SD was lower, at ± 1.1 *pBWT* (5.3.3.10.). Again, comparable to the walk, SD was low during the swing phase and highest at the weight acceptance phase.

Impulse was 0.2 *pBWT*·s higher for walk turn, compared to the walk (section 5.3.4.). The 1.8 *pBWT*·s walk turn impulse, however, was still lower than the majority of other activities due to fluctuations in HRFs (particularly due to the swing phase) and a short movement time (1 second).

5.4.3. Stand to Sit and Sit to Stand

When standing upright, the stand to sit (StSi) showed a resultant HRF of 1.1 *pBWT*, whereas the sit to stand (SiSt) showed a larger value of 1.3 *pBWT*. When seated, StSi (0.5 *pBWT*) and SiSt (0.6 *pBWT*) showed similar forces (section 5.3.3.3. and 5.3.3.4.). The small discrepancy seen between activities in these static positions, was likely due to intra-subject variation between trials. The resultant peak HRF was higher for SiSt (6.4 *pBWT*) than StSi (4.2 *pBWT*) (section 5.3.3.10.). The SiSt demonstrated the highest peak resultant HRF of all activities, likely due to the propulsive nature of standing up. Resultant forces were dominated by P-D forces and increased further by a peak lateral reaction force. As you might expect, both proximal (+2.1 *pBWT*) and lateral (+0.7 *pBWT*) forces were higher for the SiSt, than StSi. In addition to this, SiSt showed a higher loading rate for P-D forces at the hip, as the movement was more explosive than sitting and completed over a shorter time, on average (0.6 seconds shorter) (sections 5.3.3.3. and 5.3.3.4.).

Peak resultant HRF SD, however, was approximately twice as high for the SiSt (± 2.6 *pBWT* or $\pm 41\%$ of the peak), compared to the StSi (± 1.1 *pBWT* or $\pm 21\%$ of the peak)

(section 5.3.10.). The high variation for SiSt is likely due to differences in the manipulation of the centre of mass, between subjects. Shifting the centre of mass forwards (by rotating the torso anteriorly) allows for an increase in momentum and thus a lower requirement for muscle co-contraction at the hip. Conversely, standing with the torso perpendicular to the femur (from the sagittal view), is likely to increase hip loading due to an increased requirement for muscular contraction at the joint. It is worth noting at this point, that SiSt had the highest P-D peak SD of all activities. The high SD suggests that there will be cross-over between those at the lower range of SiSt HRF and those at the higher range of StSi HRF. However, SiSt appeared to have the potential for the highest HRF of all activities, with those at the top of the SD potentially experiencing hip loading as high as 9 *pBWT*.

When comparing impulse, both StSi (2.3 *pBWT*·s) and SiSt (2.5 *pBWT*·s) values were similar (section 5.3.4.). This similarity occurred due to a balance between lower forces occurring over a longer period of time when sitting, compared to higher forces over a shorter period of time when standing. Impulses for both StSi and SiSt were mid-range, when compared to other activities (Table 17).

Previously, peak HRFs for a symptomatic THR patient group have been reported at 1.6 *pBWT* and 1.9 *pBWT* for a StSi and SiSt, respectively (*in vivo* measurement) (Bergmann et al., 2001). The highest peak HRF for a single patient was reported as 2.0 *pBWT* and 2.2 *pBWT* for StSi and SiSt, respectively. These values are considerably lower than the subject averages in the current study (StSi: 4.2 *pBWT*; SiSt: 6.4 *pBWT*). This is likely because Bergmann's group assessed post-operative, low functioning patients, as opposed to the asymptomatic, healthy cohort in the current study. It is notable that movement times were shorter in the current study, both for StSi (1.9 seconds shorter) and SiSt (1.2 seconds shorter). A faster movement time may indicate a more dynamic movement, with a higher requirement of hip force to complete the movement within the shorter duration of time. The longer time to sit down, for the patient group, may have resulted in a slower downward velocity and thus a reduced requirement for decelerating, eccentric muscular contractions (forces) at the hip (Vaughan-Graham et al., 2019). Another possible explanation for the decreased values within the literature is that when standing up, Bergmann's patient group may have utilised their centre of mass to increase upward momentum, in order to reduce the requirement of hip muscles (possibly due to loss of function at the hip). The data suggests that inter-subject variability is likely to be high for

sitting and standing (Bergmann et al., 2001) and that the extremes of the HRF range may vary considerably between asymptomatic and symptomatic subjects.

5.4.4. Squat

The squat showed the fifth highest peak HRF (3.5 ± 1.9 pBWT) and fourth highest impulse (3.3 pBWT·s) when compared to other activities (section 5.3.3.5.). The HRF was a combination of a larger proximal load (4.0 pBWT) and smaller lateral load (1.5 pBWT), acting from the femoral head. Impulse was more than twice as high as the walk and was one of the higher impulse values (behind golf swing, lunge and stand reach). Impulse was influenced by a large HRF, occurring over the majority of the movement cycle (>2.0 pBWT for over 50% of the cycle). This indicates that the joint was loaded for a prolonged period of the movement cycle.

Squat HRF data is limited within the literature. Haberly and Pavol (2013), however, submitted a thesis in 2003 in which various squat depths were analysed in relation to HRFs. Higher squat HRF was found to be linked to squat depth and increased trunk flexion. Peak trial data ranged from 1.0 pBWT to 9.0 pBWT within Haberly and Pavol's study. The corresponding trend line saw HRF values of 2.0 pBWT at 45° knee flexion and 6.0 pBWT at 90° knee flexion. The mean peak within the current study (3.5 ± 1.9 pBWT) seems reasonable, given that the value falls between a shallow and deep squat reported by Haberly and Pavol (2013). Similar to other high flexion activities, such as sitting and standing, variation appears to be large for squat HRF values. This may be due to variation in hip flexion angular motion and ultimately squat depth, between individuals.

5.4.5. Stand Reach

Stand reach resulted in a peak HRF of 4.3 ± 1.0 pBWT (section 5.3.3.6.). In keeping with many of the other activities, this was a combination of proximal and lateral loading at the femoral head. The peak occurred at the bottom of the reach, when the hip was at maximal flexion and a larger hip force was required to balance the body position. Stand reach impulse was 4.7 pBWT·s (the joint second highest of all activities) (section 5.3.4.). This high impulse was due to a high HRF occurring throughout the majority of the movement cycle (>2 pBWT for 60% of the movement cycle) and a long movement time (3.8 seconds – third highest of all activities) (section 4.1.).

5.4.6. Kneel Reach

Kneel reach had the smallest resultant peak HRF of all activities (0.5 *pBWT*) (section 5.3.3.7. and 5.3.3.10). This was due to having four limbs in contact with the ground, thus spreading the load between joints. The SD for the peak kneeling force was also the lowest of all activities (± 0.1 *pBWT*), suggesting that even the extremes of the range are unlikely to show high hip forces. Further to this, kneel reach showed the joint lowest impulse (1.6 *pBWT*·s) (in spite of having the longest movement time of all activities, at 5.9 seconds) (sections 5.3.4.). When considering these values, it seems unlikely that this activity will result in excessive loading between bearing surfaces a THR.

5.4.7. Lunge

The lunge showed a low initial HRF, during the swing phase (< 0.5 *pBWT*) (section 5.3.3.8.). This increased to approximately 1.0 *pBWT* at initial contact and when lowering down into the lunge. Peak loading occurred during the propulsion phase of the movement, as individuals ascended up and out of the lunge. This peak was the same value as seen for walking (3.1 *pBWT*), albeit with a slightly higher corresponding SD (SD: Lunge: ± 1.3 *pBWT*; Walk: ± 1.1 *pBWT*) (sections 5.3.3.10.). Lunge HRF impulse was the joint second highest of all activities (4.7 *pBWT*·s) (section 5.3.4.). Although peak loading was not particularly high for the lunge, the movement cycle was relatively long (3.6 s), thus increasing the impulse across the movement time.

Although lunge kinematics is reported within the literature, HRF data has not been published. The peak of 3.1 *pBWT* seems reasonable when considering that the walking propulsive peak was the same value. The highest magnitude within the SD range (4.4 *pBWT*) was low when considering values for other, less dynamic activities. It is important to appreciate that although variation was not particularly high for the lunge, different lunge techniques may result varying HRF values. Lunging during a sport such as badminton, for example, is likely to lead to higher hip loading rates (Kuntze et al., 2010).

5.4.8. Golf Swing

The golf swing showed a peak HRF of 4.0 ± 1.9 *pBWT* (section 5.3.3.9.). This was comparable to the walk turn (4.1 *pBWT*), stand to sit (4.2 *pBWT*) and stand reach (4.3 *pBWT*) (section 4.3.3.10). Proximal and lateral hip loading, during the golf swing, peaked at the bottom of the downswing (at impact with the ball). This seems reasonable given that the aim of the swing is to produce maximum force, and thus impart maximum velocity, at ball impact.

Golf swing SD, occurring at peak HRF (± 1.9 pBWT), was comparable to other activities. However, when considering force vectors independently, peak HRF variation was highest for the golf swing in both anterior-posterior (± 1.3 pBWT) and medial-lateral (± 1.0 pBWT) directions. In addition to this, the golf swing showed the highest average proximal-distal standard deviation throughout the movement. This variation is likely to have occurred due to the adoption of different techniques between individuals. The potential variation in technique may influence the magnitude of resultant vectors acting between the femoral head and cup. Interestingly, the golf swing HRF impulse was the highest of all activities (2 pBWT·s higher than the next closest value). The high impulse for the golf swing (6.7 pBWT·s) occurred not only due to the consistently high proximal HRF, but also due to the consistently high lateral HRF. This may have implications for the hip joint lubrication regime throughout the activity (as force is inversely related to fluid film thickness) (section 5.3.4.).

As HRFs are yet to be investigated for a golf swing, it is not possible to draw comparisons from the literature. However, given that ground reaction forces were up to four times larger in the literature (for regular golfers) compared to the current study (largely made up of first time golfers), it is likely that an increase in HRFs would also be seen within a golfing population (Hume et al., 2005).

5.4.9. Variation and Age

Peak HRFs showed a difference of over 1 pBWT (between age groups) for just one of the activities (golf swing) (section 5.3.5.). The golf swing showed a 1.1 pBWT increased peak HRF for individuals over 55, compared to those under 55 (section 5.3.5.). It is possible that the increased peak HRF during the golf swing, was due to an increased golfing ability within the older group. It is noteworthy that the walk turn (0.9 pBWT), squat (0.9 pBWT) and stand reach (0.8 pBWT) saw marked differences between age groups. The walk turn saw an increased HRF for the older group – this may have been due to less control at heel strike in virtue of reduced hip muscular functionality. The squat and stand reach saw higher HRFs for the younger group (possibly due to increased hip flexion in these individuals). These suggestions are difficult to back up, however, due to the small subject sizes and lack of statistical analysis.

5.4.10. Variation and Gender

Just two activities showed a difference of over 1 pBWT between genders (squat and golf swing) (section 5.3.6.). Both saw an increase in the peak HRF for females, compared to

males. The increased HRF for females during the squat (+1.2 *p*BWT), was likely due to the corresponding increase in hip flexion at that point, compared to males (+10°). Further analysis into the relationship between peak hip flexion angles and HRFs (with regards to gender) may provide a basis for understanding why HRF were increased for females in some activities and not in others.

5.4.11. Overall Discussion

Peak resultant hip reaction force (HRFs) ranged from 0.5 (kneel reach) to 6.4 (sit to stand) *pBWT* and were all orientated from an anterior, lateral and proximal position on the femoral head. Sit to stand is likely to provide the highest risk of excessive hip loading, particularly when considering that the peak HRF reached 9 *pBWT* at the top of the standard deviation (SD). It is worth noting that a number of other activities showed peak HRFs of over 4 *pBWT* (walk turn, stand to sit, stand reach and golf swing) and have the potential to excessively load the acetabular cup in a THR. Additionally, local stress levels may influence pathological changes to healthy bone and cartilage, meaning that the HRF results are also relevant to a healthy population and individuals with tissue engineered cartilage substitution (Yoshida et al., 2006).

Hip impulse values ranged from 1.6 (walk and kneel reach) to 6.7 (golf swing) *pBWT·s*. Golf swing (6.7 *pBWT·s*), stand reach and lunge (both 4.7 *pBWT·s*) had the highest impulse values, suggesting that the hip was loaded for a prolonged period of time during these movement cycles. This may have implications for joint lubrication, as prolonged loading may lead to boundary lubrication conditions due to squeeze film effects (Stewart, 2010; Stewart et al., 1997). Consequentially, this may lead to contact of surface asperities and wear.

When considered independently, load is proportional to both wear and fluid film thickness (Figures 175 and 176). However, it is important to appreciate that hip loading does not necessarily result in wear. The localised sliding conditions and degree of cross shear (influenced by motion path trajectories between hip surfaces) are key variables, as these will influence the speed and distance over which a force is applied. Additionally, the position of loading on the cup will determine the possibility of edge loading and potential for excessive wear. The position of acetabular cup loading is affected by hip angular kinematics, cup orientation angles, force vector orientations and contact area. These must be considered synonymously when determining implications for HRFs and wear of the acetabular cup.

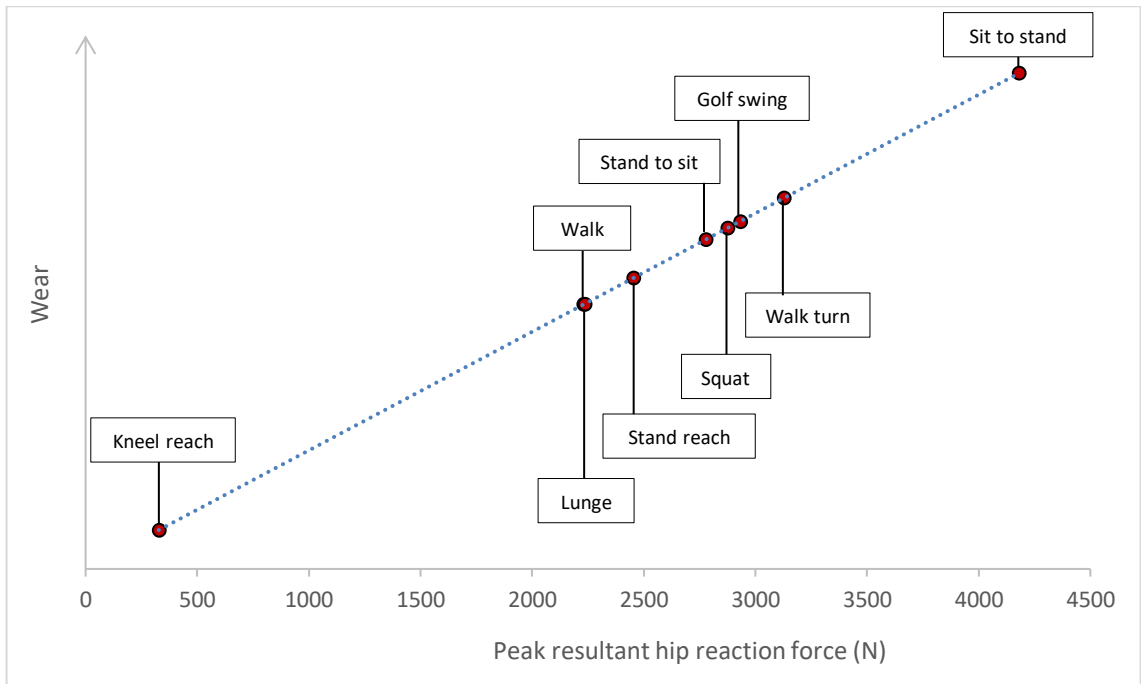


Figure 100. Theoretical representation of the relationship between hip loading and relative wear. The linear trend-line indicates a positive relationship between the two variables, when considered independently.

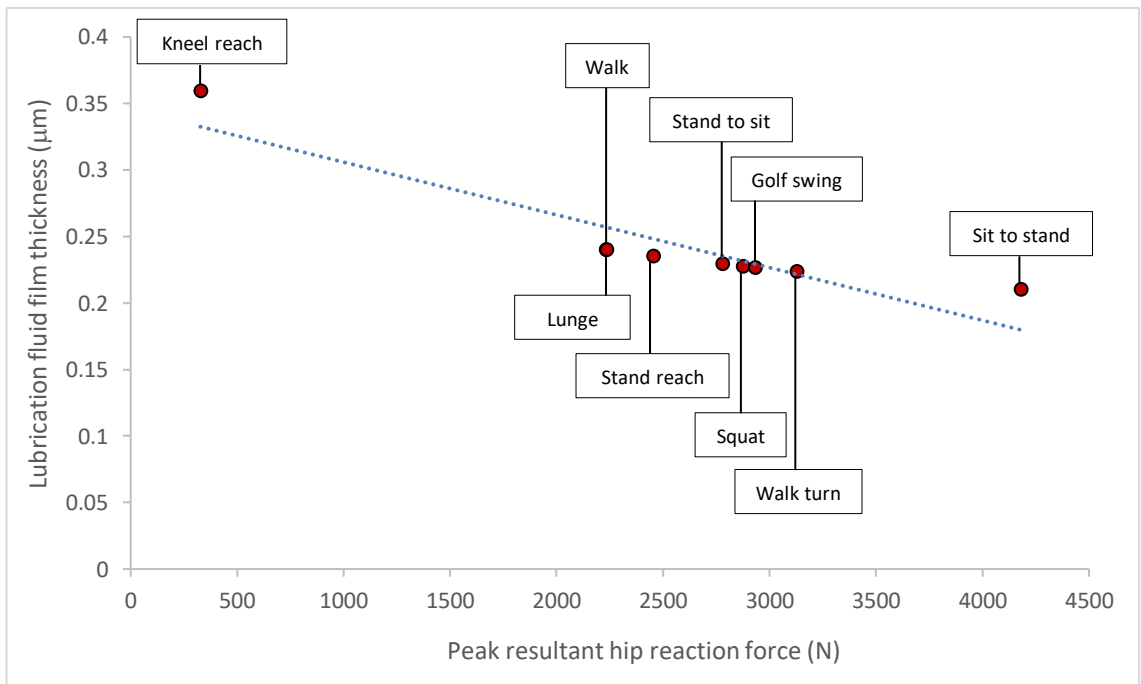


Figure 101. The relationship between hip reaction force and fluid film thickness at a total hip replacement (metal-on-polyethylene). The sliding velocity was standardised to 3 radians per second for all activities, therefore the linear trend-line indicates an inverse relationship between hip reaction force and wear. The fluid entrainment calculations were taken from Hamrock and Dowson (1978).

5.5. Conclusion

As would be expected, ground reaction forces and hip moments showed variation between and within activities. Consequentially, hip reaction forces ranged from 0.5 (kneel reach) to 6.4 (sit to stand) pBWT. Localised hip loading is a key variable, when considering surface wear at the hip. The specific timing of hip loading is important, as this must be assessed alongside the corresponding sliding conditions, cross-shear motion and cup loading position. In order to understand hip tribology and the potential risk to wear for a given activity, one must have an understanding of the combined loading, motion and lubrication conditions. Further to this, it is crucial to assess the potential for edge loading, when considering a total hip replacement.

6. Tribology

6.1. Introduction

Within this section, the fundamental biomechanics from sections 4 (kinematics) and 5 (kinetics) are processed in order to investigate hip tribology. Tribology methods (section 6.2) are followed by tribology results, which include hip motion path and edge loading data (section 6.3). Results are then discussed (section 6.4) and an overall conclusion is drawn from the chapter (section 6.5). The findings relate to the localised motion and loading at the hip joint during common activities, thus providing information on the potential risk of wear to a polyethylene THR cup, as well as to soft tissue engineered cartilage that may line the joint.

6.2. Methods

Hip motion is a complex combination of flexion-extension, abduction-adduction and internal-external rotation. This results in potentially complex motion paths of the femoral head, articulating relative to the acetabular cup. Relative sliding was calculated between bearing surfaces, in order to assess cross-shear motion and potential wear at: 1) the surface of a polyethylene acetabular cup liner, within a total hip replacement and 2) the surface of tissue engineered cartilage substitution within the natural hip. Both a proprietary MATLAB program (MATLAB, 2016, MathWorks, Natick, MA, USA) and a Visual3D workspace (Visual3D standard, v5.01.18, C-Motion, Germantown, MD, USA) were used to calculate motion paths. MATLAB was predominantly used to quantify mean motion paths (into aspect ratios and sliding distances) and graph mean results. The Visual3D workspace provided a tool to visually assess the entirety of the data in batch and to assess the variation between subjects.

6.2.1. Motion Path Calculations

Computational simulation of motion paths has previously utilised computer-aided engineering software (Bennett et al., 2002; Budenberg et al., 2012; Ramamurti et al., 1996; Saikko and Calonijs, 2002). Previous calculation methods have incorporated a number of transformation matrices into a script. Transformation matrices multiply a starting position on the femoral head by the corresponding hip angular data, resulting in a new position of the point within a Cartesian coordinate system. The path of a point can therefore be tracked throughout a movement cycle. The underlying maths for this calculation was validated by Budenberg et al. (2012). Budenberg and colleagues mounted

a femoral head within a hip simulator and fixed a felt pen into position, thus allowing motion paths to be drawn and compared to the mathematic calculations.

Equation 7 shows a transformation matrix for the motion path of one point. The defined point (within the femoral head coordinate system) is labelled as X_I , Y_I and Z_I , relative to the centre of the femoral head (0, 0, 0). Hip angular data is input as radians and labelled x (flexion/extension), y (abduction/adduction) and z (internal/external rotation). The trigonometrical matrix identifies the point on the femoral head, at the given instant in time. Outputs X_N , Y_N and Z_N represent the new location of a femoral head point once the rotations have been applied. Completing calculations for a number of points on the femoral head, alongside hip angular data, results the motion path for points during the given movement cycle.

$$\begin{pmatrix} X_N \\ Y_N \\ Z_N \end{pmatrix} = \begin{bmatrix} \cos y \cos z & \sin x \sin y - \cos x \cos y \sin z & \sin x \cos y \sin z + \cos x \sin y \\ \sin z & \cos x \cos z & -\sin x \cos z \\ -\sin y \cos z & \cos x \sin y \sin z + \sin x \cos y & \cos x \cos y - \sin x \sin y \sin z \end{bmatrix} \cdot \begin{pmatrix} X_1 \\ Y_1 \\ Z_1 \end{pmatrix}$$

[Equation 7]

Within MATLAB, motion paths were plotted across the femoral head. The femoral head was represented by a 28 mm diameter hemisphere (180° coverage angle). A 28 mm diameter was chosen to allow the results to be compared to previous motion path studies and because 28 mm is a commonly implanted THR size (NJR, 2018). In keeping with previous research, twenty equally spaced points were defined on the femoral head (Table 4 and Figure 34). Ten points ran from posterior to anterior (1-10) and ten ran from medial to lateral (11-20). The cup hemisphere was fixed at a default orientation of 20° anteversion and 45° inclination.

Table 15. Twenty equally spaced points were defined on the femoral head surface (28 mm diameter). The position of each point, relative to the femoral head centre (0.0 mm, 0.0 mm, 0.0 mm) are shown.

	Medial (-) Lateral (+) (mm)	Anterior (+) Posterior (-) (mm)	Inferior (-) Superior (+) (mm)
Point 1	0.0	-14.0	0.0
Point 2	0.0	-13.2	4.8
Point 3	0.0	-10.7	9.0
Point 4	0.0	-7.0	12.1
Point 5	0.0	-2.4	13.8
Point 6	0.0	2.4	13.8
Point 7	0.0	7.0	12.1
Point 8	0.0	10.7	9.0
Point 9	0.0	13.2	4.8
Point 10	0.0	14.0	0.0
Point 11	-14.0	0.0	0.0
Point 12	-13.2	0.0	4.8
Point 13	-10.7	0.0	9.0
Point 14	-7.0	0.0	12.1
Point 15	-2.4	0.0	13.8
Point 16	2.4	0.0	13.8
Point 17	7.0	0.0	12.1
Point 18	10.7	0.0	9.0
Point 19	13.2	0.0	4.8
Point 20	14.0	0.0	0.0

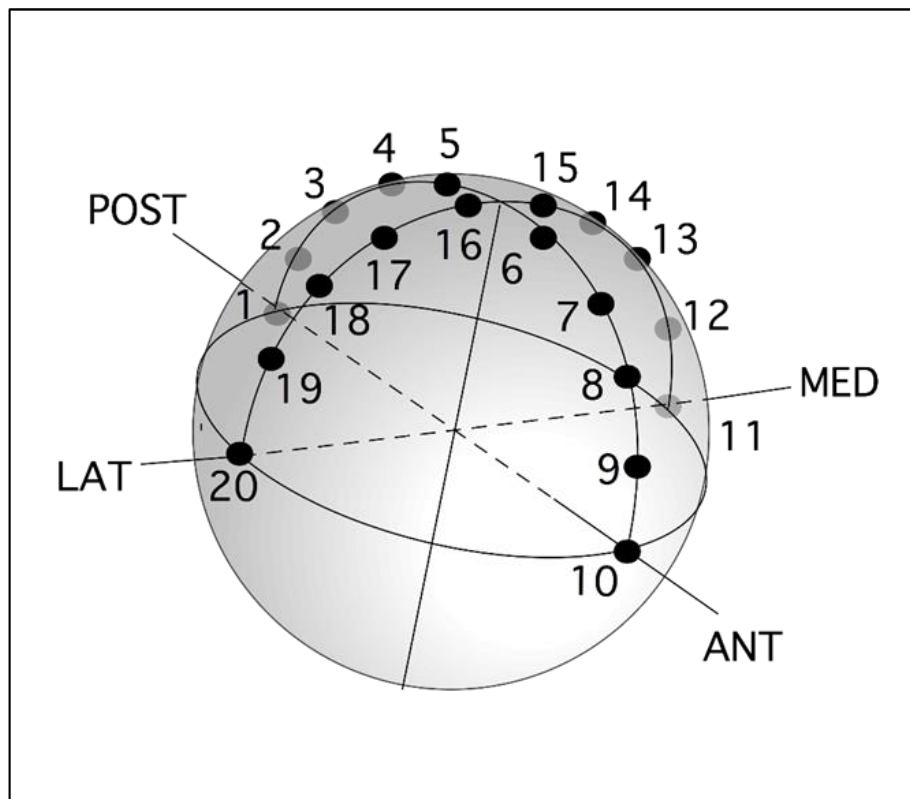


Figure 102. Visual representation of the twenty equally defined points, on the surface of the femoral head, as shown in Table 4. Ten points run from posterior (1) to anterior (10) and ten points from medial (11) to lateral (20).

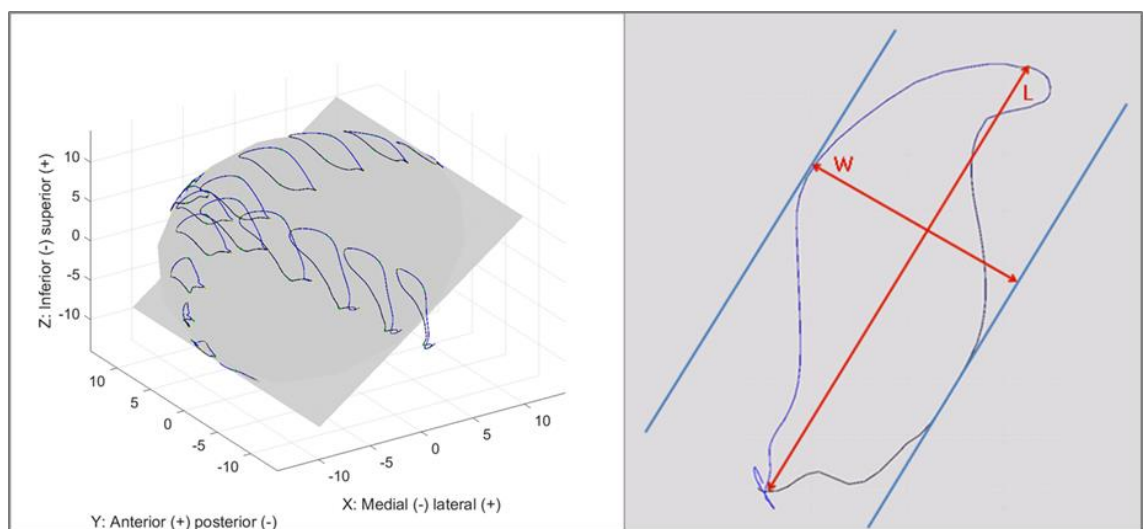


Figure 103. Motion paths plotted at twenty equally spaced locations on a 28 mm femoral head, within MATLAB (left). Visual representation of the calculation of a motion path aspect ratio, whereby the length (L) is divided by the perpendicular width (W) (right).

Within the MATLAB program, mean motion paths were calculated for each of the thirteen activities. Motion paths were quantified into aspect ratios (length of path/perpendicular width of path) (Figure 35). Additionally, the sliding distance (total

distance transverse) of each path was calculated. A limitation to this method is the time and computational requirements to analyse large sets of data – particularly given that the raw data must be formatted in a specific way to be read by the script. Although the software provides accurate results with good visualisation (through 3D graphing), it is unrealistic to run vast amounts of data trials, for multiple subjects, using this method. For this reason, inter-subject analysis may be an extremely time consuming process. Identifying a method for collating and batch exporting this information would facilitate the process of assessing trends and variation occurring within a large data set. Visual3D is largely regarded as the gold standard for the processing of gait data and is designed to cater for large data sets. Incorporating the motion path calculations into Visual3D would improve the process and analysis of motion path analysis for large subject sizes.

6.2.2. Visual3D Method

A Visual3D method was developed and enabled motion path data to be calculated quickly, for large data sets. Raw gait data was imported directly from Qualisys (QualisysTM Medical AB, Goteborg, Sweden). A ‘motion path pipeline’ was applied to the data and automatically batch calculated motion path data for exportation.

6.2.2.1. Motion Path Pipeline

The basic analytical capabilities of Visual3D (V3D) were utilised to allow a ‘virtual joint’ to be constructed and the calculation of motion paths to be integrated into the program. Similar to previous methods, twenty points were defined on a 28 mm femoral head (Table 4 and Figure 34). This was achieved by creating a hemisphere of equally spaced landmarks, relative to the thigh segment, around the hip joint centre (Figure 36). Angular motion of the thigh segment influenced the three dimensional displacement of each landmark. The motion of the twenty landmarks were then calculated relative to the pelvis coordinate system, using the ‘TARGET_PATH’ pipeline This ensured that pelvic tilt was included within the motion paths (C-Motion, 2018). Resulting data was subtracted from the position of the hip centre, therefore scaling the motion within the space of a 28 mm diameter hemisphere. A V3D motion path model (MDH file) was thus created, meaning that this method could be applied to any number of motion trials. This method provided an alternative way to assess motion paths, on a large scale.

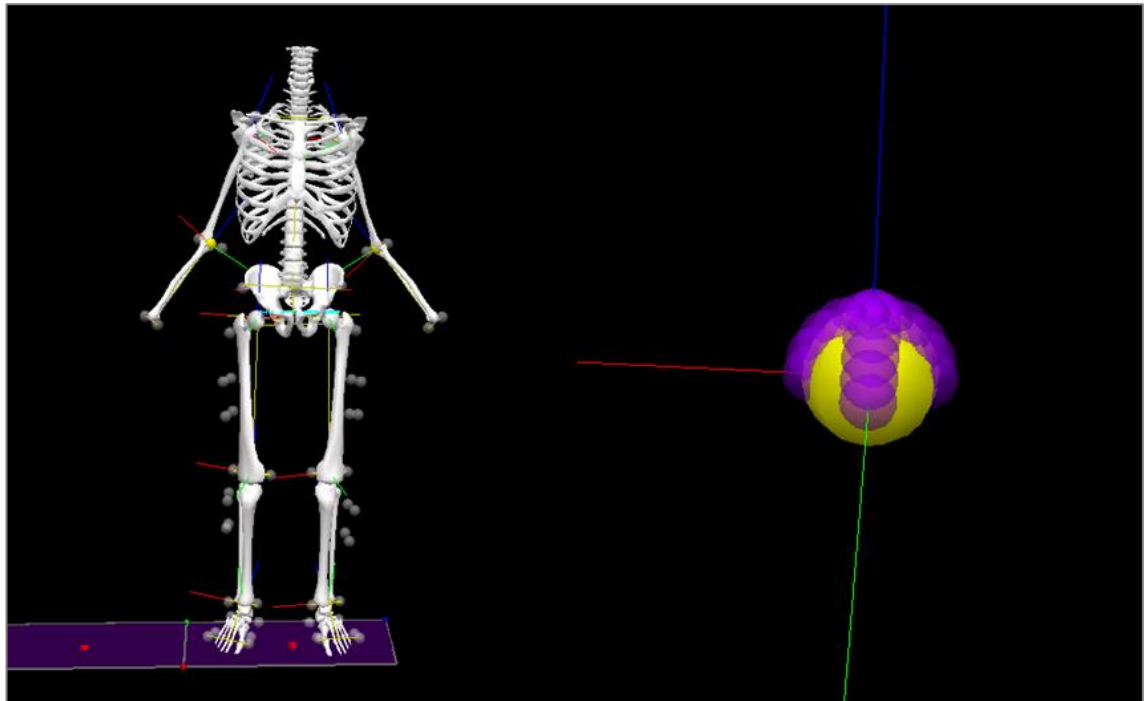


Figure 104. A full body model with 54 markers (grey) is shown (left), alongside the hip centre (yellow) (right) surrounded by twenty equally spaced landmarks (blue). As the thigh segment rotates, landmarks are displaced, thus resulting relative motion paths occurring between bearing surfaces at the hip.

6.2.2.2. Comparison to MATLAB Method

In order to use Visual3D and MATLAB motion path methods synonymously, the two methods were compared to one another for the same input data. A number of variables were matched in order to compare the programs, including: the position of points on the femoral head, the diameter of the femoral head and the coordinate system in which motion paths were calculated. Motions for level walking and a stand to sit were tested (chair height: 47 cm) (n = 1) (Age: 44 y; Gender: F; Height: 1.72 m; Weight: 73.1 kg).

Table 16. Average error and standard deviation between the sliding distances predicted from the Visual3D method and the MATLAB method, for calculating motion paths. Average error and standard deviations, for level walking and sitting down, across twenty points on the femoral head (M-L: Medial-lateral; A-P: Anterior-posterior; I-S: Inferior-Superior).

	Average error (mm)			Standard deviation (\pm mm)		
	M-L	A-P	P-D	M-L	A-P	P-D
Level walking	0.0	0.0	0.0	0.0	0.0	0.0
Sitting down	0.1	0.0	0.0	0.0	0.0	0.0

Comparison of the motion path distances (predicted for the twenty femoral head points) for the two methods is shown in Table 5. The V3D model showed no significant errors when compared to transformation matrices used in the MATLAB program (and utilised in previous studies). The small average error seen for the medial-lateral motion when sitting down (0.1 mm), is likely due to rounding errors between the software, as Visual3D retains greater significant figures with internal calculations compared to when the motion data is exported for external computational analysis. This is a distinct benefit of using the Visual3D method as it is less likely to cause errors associated with data transfer. Table 5 suggests that the two programs could be used interchangeably for a range of activities.

Following the comparison of methods (Table 5), a decision was made to use MATLAB and Visual3D interchangeably for the calculation of relative motion paths between bearing surfaces at the hip. MATLAB was used predominantly for the assessment of mean data (including aspect ratio and sliding distance calculations) and 3D graphing of motion paths. Visual3D was used to calculate paths for all kinematic trials and to visually assess the variation between subjects. Motion paths were differentiated within Microsoft Excel in order to result sliding velocities and accelerations. Fluid film thickness was then calculated for activities, corresponding to peak hip loading.

6.2.3. Motion Path Differentiation and Lubrication Calculations

Sliding velocities (SVs) were calculated by differentiating motion paths. Sliding accelerations (SAs) were then calculated by differentiating the corresponding SVs. The SV provided information relating to joint lubrication, with higher velocities indicating a thicker fluid film and thus, more desirable lubrication regime (Katta et al., 2008a; Stewart, 2010; Stewart et al., 1997). The SA was used to identify points at which the motion path changed direction, as this represents a point within the cycle where instantaneous cross-

shear is high. In fact, wear rates are considerably increased for up to 5 mm, following a 90° change in direction (Dressler et al., 2011). As SA is directly related to the angular change in direction of a motion path, acceleration was used in order to compare cross-shear between activities (lower SA indicates a smaller angular change; higher SA indicates a larger angular change).

Hamrock and Dowson (1978) defined a formula in which fluid entrainment at the hip joint can be estimated. This was applied to each of the activities within the study, which had an associated hip reaction force. The formula (Equation 10) results fluid film thickness using a number of associated variables at the joint. The film thickness is proportional to the equivalent radius of the bearings (R), the viscosity of the lubricant (n), the sliding velocity (u), and inversely proportional to the load (W) and the material stiffness (E'). The equivalent radius of the bearings (R) is calculated from the product of the acetabular cup (R_{cup}) and femoral head (R_{head}) radii, divided by the difference between radii (Equation 8). Thus, a decrease in the radial clearance will lead to an increase in the equivalent radius. The material stiffness, or 'equivalent elastic modulus' (E'), is calculated using the elastic modulus for each of the components (E_1 and E_2) and the respective Poisson's ratio for each component (V_1 and V_2) (Equation 9). It is also noteworthy that sliding velocity (u) was calculated using the product of hip angular velocity and the radius of the femoral head.

$$\text{Equivalent Radius} = \frac{R_{cup} \cdot R_{head}}{R_{cup} - R_{head}} \quad [\text{Equation 8}]$$

$$\text{Equivalent Elastic Modulus} = \left(\left\{ \frac{1-V_1^2}{E_1} \right\} + \left\{ \frac{1-V_2^2}{E_2} \right\} \right)^{-1} \quad [\text{Equation 9}]$$

$$\text{Film Thickness} = 2.789 R \left\{ \frac{nu}{E'R} \right\}^{0.65} \left\{ \frac{W}{E'R^2} \right\}^{-0.21} \quad [\text{Equation 10}]$$

Input values for the calculation of the fluid film thickness were based upon a 28 mm diameter, metal femoral head and a polyethylene acetabular cup (Table 6). Peak hip reaction forces were used within the equation, alongside the associated instantaneous hip angular velocity.

Table 17. Input variables, symbols, values and units for the calculation of fluid film thickness between components of a total hip replacement.

Variable	Symbol	Value	Unit
Viscosity	n	0.005	Pa.s
Angular Velocity	w	Corresponding to peak load	Radians·s
Velocity	u	$w \cdot R_{head}$	m·s
Poisson's Ratio Femoral	V_1	0.3	
Poisson's Ratio Acetabular	V_2	0.4	
Elastic Modulus Femoral	E_1	200	GPa
Elastic Modulus Acetabular	E_2	1	GPa
Equivalent Elastic Modulus	E'	2.37	GPa
Radius of Femoral	R_{head}	0.014	m
Radius of Acetabular	R_{cup}	0.01413	m
Equivalent Radius	R	1.582	m
Applied Load	W	Peak load	N

6.2.4. Edge Loading Analysis

Edge loading can be described as contact of the femoral head component of a total hip replacement (THR) on the acetabular rim. This can be assessed instantaneously when combining the hip reaction force vector orientation, hip angular position and THR component orientations. Within this methods section, Hertz contact area calculations (section 6.2.4.) are provided. Additionally, methods for a SolidWorks model are described, in which force vector positions on the acetabular cup were visualised (SolidWorks 2017, Dassault Systèmes SolidWorks Corporation, Waltham, MA, USA) (6.2.6.).

6.2.5. Hertz Contact Area Analysis

Hertz contact area analysis requires a number of input variables, which ultimately allow for the estimation of contact area between two conforming spheres (femoral head and acetabular cup) (Johnson and Johnson, 1987). The calculation takes into account the Poisson's ratio, elastic modulus and radius of each of the bearing surfaces. In addition to this, the applied load to the acetabular cup is included within the equations (resultant of anterior-posterior, medial-lateral and inferior-superior hip reaction forces). Input variables are shown in Table 7 and the Hertz calculations are shown in Equations 11 to 13.

Table 18. Variables required for Hertz contact area analysis of a metal-on-polyethylene hip replacement (Equation 11 to 13). Symbols, values and units are shown for each variable.

Variable	Symbol	Value	Unit
Applied Load	W	Peak Load	N
Poisson's Ratio Femoral	ν_1	0.3	
Poisson's Ratio Acetabular	ν_2	0.4	
Elastic Modulus Femoral	E_1	220	GPa
Elastic Modulus Acetabular	E_2	1	GPa
Equivalent Elastic Modulus	E^*	1.18	GPa
Radius of Femoral	R_{head}	0.014	m
Radius of Acetabular	R_{cup}	0.014125	m
Equivalent Radius	R	1.582	m

The applied load is the only variable that changes for the calculation of contact area (Table 7). The load was taken from section 5.3.3.10., where mean hip resultant reaction forces are resulted. Poisson's ratio and elastic modulus values correspond to ultra-high molecular weight polyethylene (acetabular cup) and stainless steel (femoral head). The equivalent elastic modulus is a function of the Poisson's Ratio and Elastic Modulus for the two components (Equation 11). The equivalent radius was calculated using the femoral head and acetabular cup radii (Equation 12). Contact area could then be calculated by incorporating the applied load, equivalent elastic modulus and equivalent radius sphere (Equation 13).

$$E^* = \frac{1}{\left(\frac{1-(\nu_1^2)}{E_1}\right) + \left(\frac{1-(\nu_2^2)}{E_2}\right)} \quad \text{[Equation 11]}$$

$$R = \frac{(R_{cup} \times R_{head})}{(R_{cup} - R_{head})} \quad \text{[Equation 12]}$$

$$\text{Contact Radius} = \left(\frac{3 \times W \times R}{4 \times E^*}\right)^{0.33} \quad \text{[Equation 13]}$$

6.2.6. SolidWorks Visualisation Model

A basic ball and socket model was assembled within SolidWorks, in order to visualise the hip reaction force vector in relation to hip angular positioning.

6.2.6.1. Ball and Socket Modelling

A 28 mm diameter sphere (femoral head) and cylinder (thigh axis) was modelled and fixed together. A 28.5 mm acetabular cup component was modelled and fixed within the global coordinate system. The femoral head was positioned within the acetabular cup and allowed to rotate freely, enabling the orientation to be defined by data collected within the movement analysis lab.

6.2.6.2. Axes and Rotations

The cup was rotated to a fixed, default position of 45° inclination and 20° anteversion, in order to match to the default orientation used in the motion path modelling. A number of sketches were made on the femoral head, in order to allow for rotation in 3D. The head was rotated to a flexion-extension position using a sketched line (Head_FE), in relation to the inferior-superior axis (Head_IS), in the frontal plane. A second line (Head_AA) abducted and adducted the head, in relation to Head_IS in the sagittal plane. Given that the inferior-superior axis of the head was shifted during flexion, the preceding abduction-adduction rotations were based upon the new flexed/ extended position of the head. A final sketch line (Head_IE) determined the internal-external rotation of the head with reference to the transverse plane and a lateral sketched line, projected from the hip centre.

6.2.6.3. Hip Reaction Force Vector

A 3D sketch, projected from the hip centre, determined the orientation of the hip reaction force vector (Vector_Axis). A thin cylinder was created as a part, added to the assembly and mated with the hip centre and Vector_Axis (coincident relationship). The length of this part was 15.1 mm, thus allowing a circle to be visualised on the cup (given that the radius of the femoral head was 14 mm and the liner was 1 mm thick). Therefore, changing the orientation of the Vector_Axis altered the position of the circle seen on the cup.

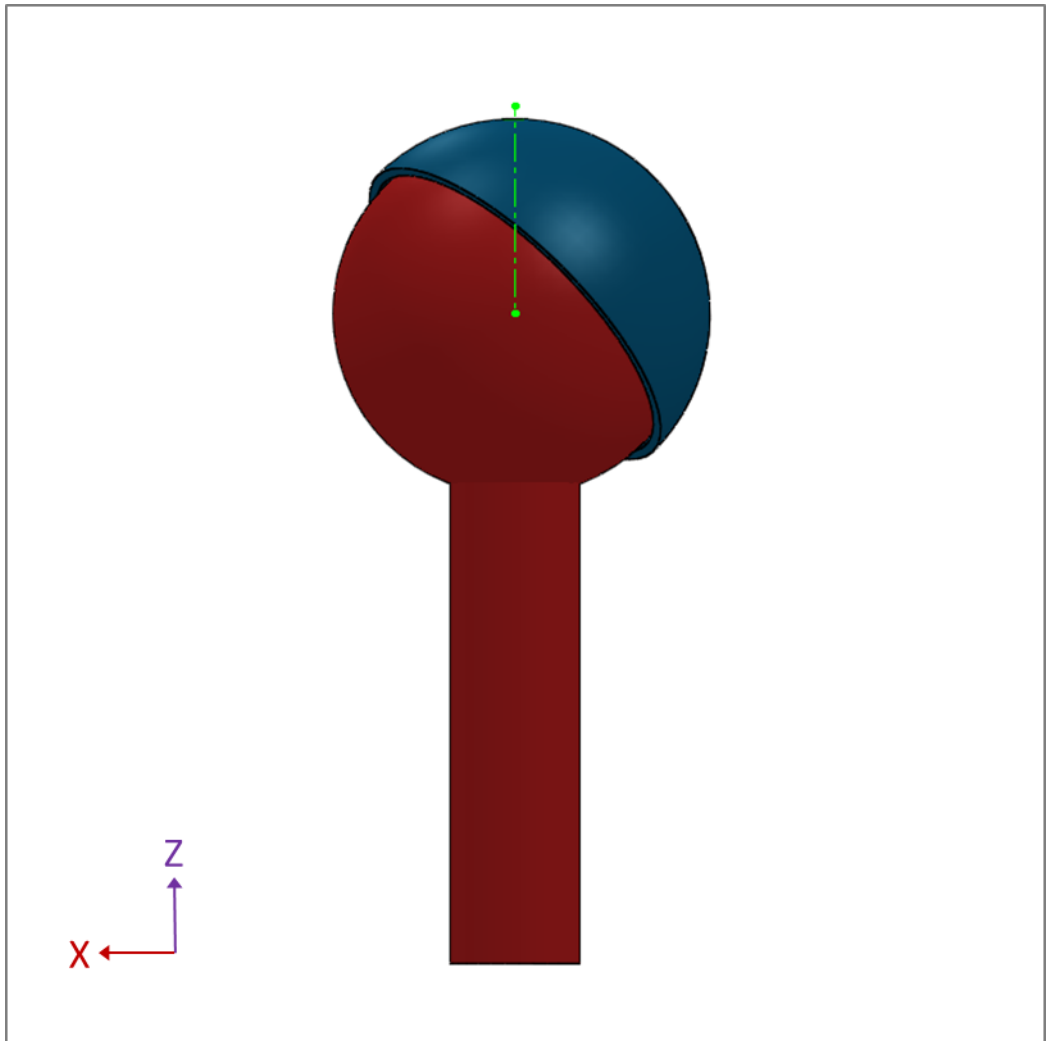


Figure 105. Anterior view of the cup (blue) and femoral component (red) assembly within SolidWorks. Force vector orientation is represented as a green, dotted line. Axis directions are shown as X (lateral) and Z (superior). The cup is fixed to a position of 45° inclination and 20° anteversion.

6.3. Results

6.3.1. Motion Paths

Motion path trajectories describe the relative motion between bearing surfaces at the hip. Within section 3.3.1., the hip was modelled as a 28 mm diameter hemisphere with a 180° coverage angle. The acetabular cup was orientated at 20° anteversion and 45° inclination (Lewinnek et al., 1978; Scheerlinck, 2014). Twenty equally spaced points were defined on the femoral head, with ten running along the medial-lateral arc (1-10) and ten running along the posterior-anterior arc (11-20) (Table 14). The shape and length of motion path trajectories define the degree of cross-shear occurring between surfaces, at a given point (frictional work perpendicular to principle molecular orientation divided by the total frictional work). Cross-shear is directly related to polyethylene wear, thus providing a measure of the potential wear of the cup liner (Kang et al., 2008b).

Figures 79 to 91 result the three dimensional displacement of points on the femoral head, against a fixed cup. Motion paths were quantified into aspect ratios, by dividing the paths height by the perpendicular width (section 6.3.2.). The lowest possible aspect ratio of 1 describes a motion path with equal height and width, thus a high degree of cross-shear. The higher the aspect ratio, the more linear the path and therefore, the lower the degree of cross shear. Figure 95 results mean sliding distances for activities. Sliding distance is the total distance transversed by a singular motion path (section 6.3.3). This metric is directly related to wear and acts as another measure of potential wear to the polyethylene acetabular cup (Bennett et al., 2002; Wang, 2001).

Motion path sliding velocities (section 6.3.4) provide information relating to the relative sliding between surfaces and therefore the lubrication regime that might be expected at a given time (Stewart, 2010; Stewart et al., 1997). Sliding accelerations (section 6.3.4.) describe the change in direction of motion paths. This measurement acts to define the complex shapes of paths, in more detail. Although the aspect ratio is an accepted form of quantifying cross-shear, changes in direction of a path (even those that do not influence the overall aspect ratio) may be a cause of excessive instantaneous cross-shear wear.

Table 19. Coordinate positions of twenty equally spaced points on the femoral head (mm). Positions are in 3D, relative to the coordinate system of a 28 mm diameter femoral head (0.0 mm defines the hip centre). Points 1 to 11 run along the anterior-posterior arc, whereas points 11 to 20 run along the medial-lateral arc.

	Medial (-) Lateral (+)	Anterior (+) Posterior (-)	Inferior (-) Superior (+)
Point 1	0.0	-14.0	0.0
Point 2	0.0	-13.2	4.8
Point 3	0.0	-10.7	9.0
Point 4	0.0	-7.0	12.1
Point 5	0.0	-2.4	13.8
Point 6	0.0	2.4	13.8
Point 7	0.0	7.0	12.1
Point 8	0.0	10.7	9.0
Point 9	0.0	13.2	4.8
Point 10	0.0	14.0	0.0
Point 11	-14.0	0.0	0.0
Point 12	-13.2	0.0	4.8
Point 13	-10.7	0.0	9.0
Point 14	-7.0	0.0	12.1
Point 15	-2.4	0.0	13.8
Point 16	2.4	0.0	13.8
Point 17	7.0	0.0	12.1
Point 18	10.7	0.0	9.0
Point 19	13.2	0.0	4.8
Point 20	14.0	0.0	0.0

6.3.1.1. Walk

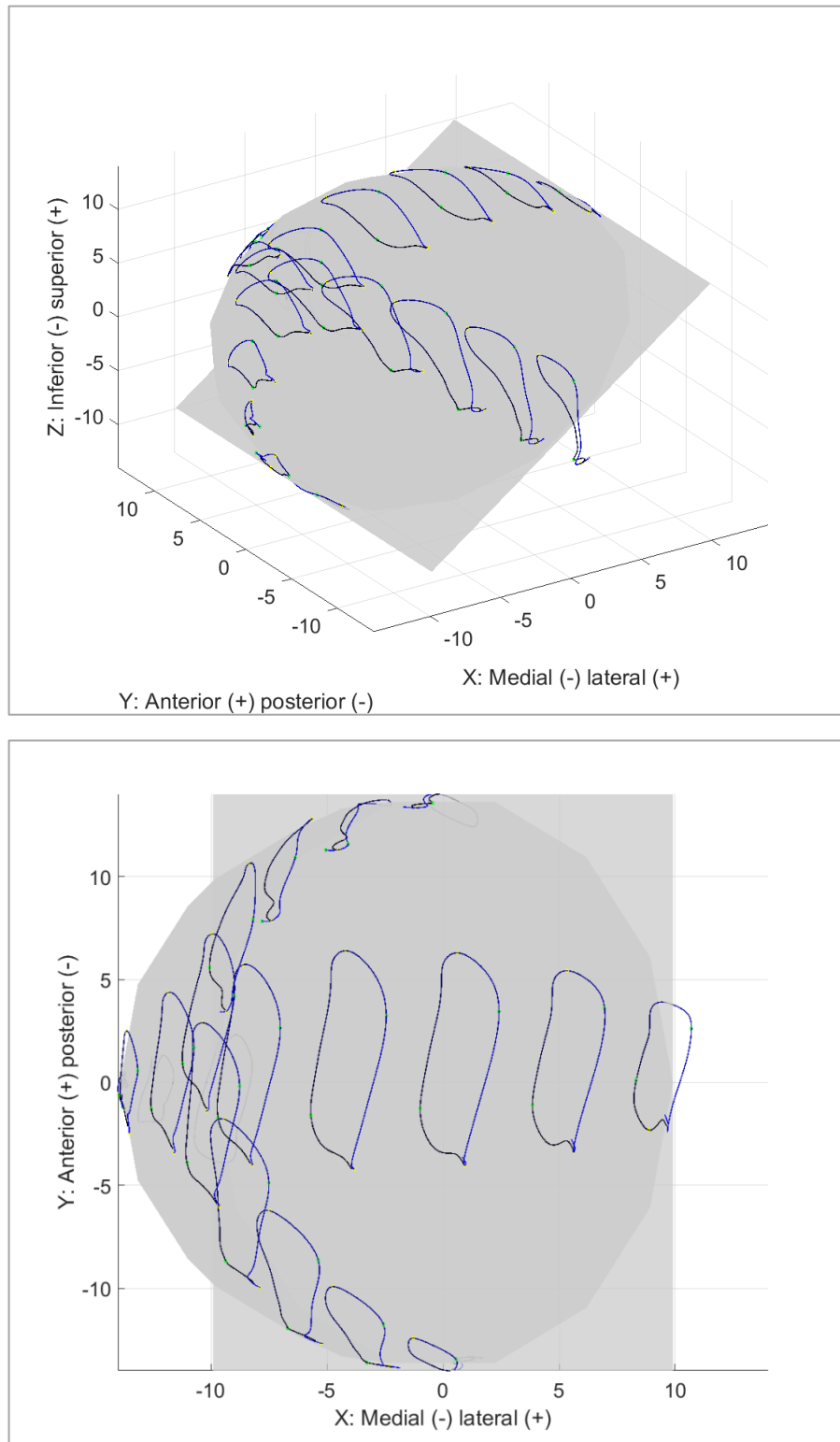


Figure 106. Motion path trajectories throughout a walk cycle, defined at 20 positions on the femoral head. Paths run clockwise from initial contact (black) to second initial contact (blue) (n=17).

6.3.1.2. Walk Turn

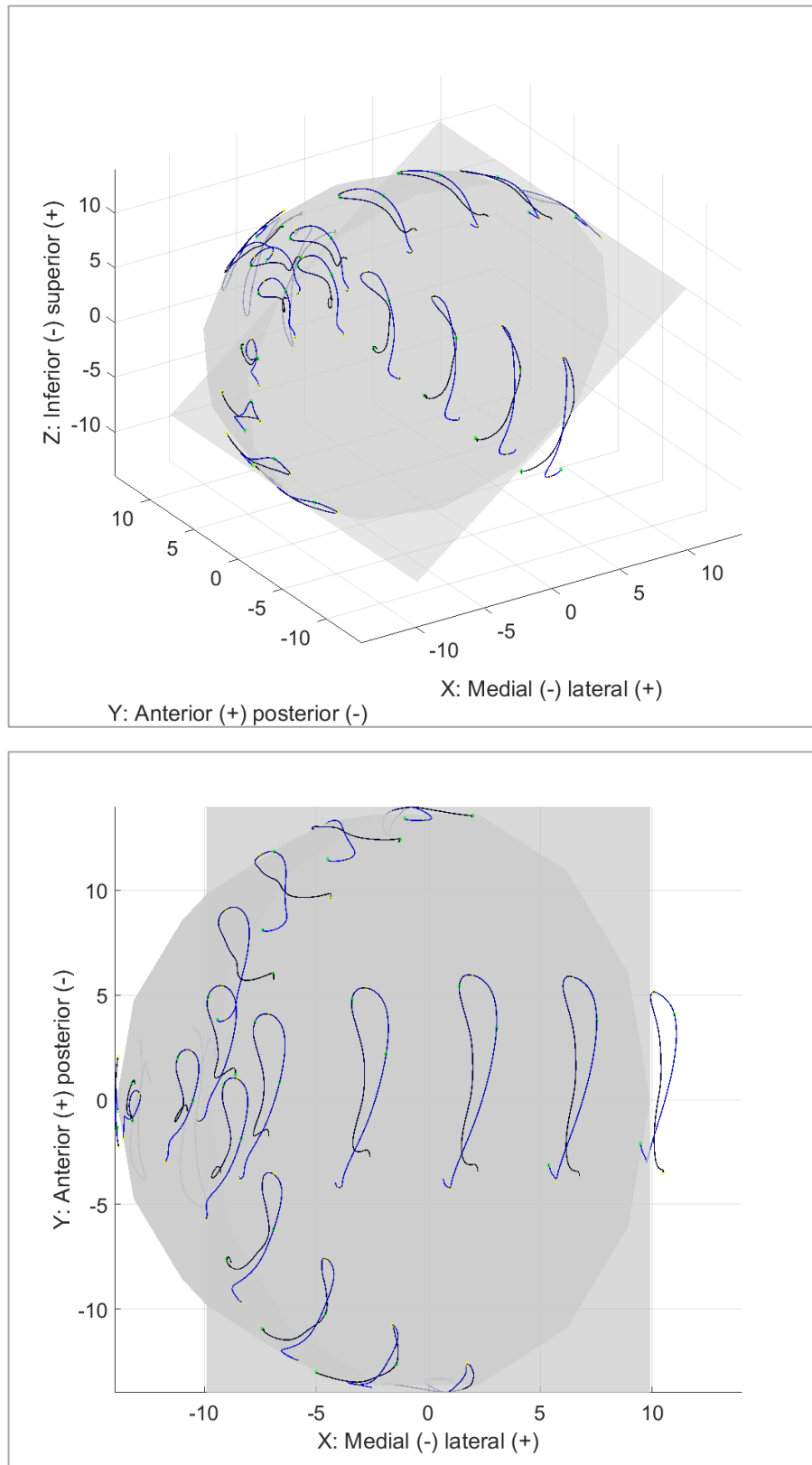


Figure 107. Motion path trajectories throughout a walk turn cycle, defined at 20 positions on the femoral head. Paths run clockwise from initial contact (black) to second initial contact (blue) (n=18).

6.3.1.3. *Incline Walk*

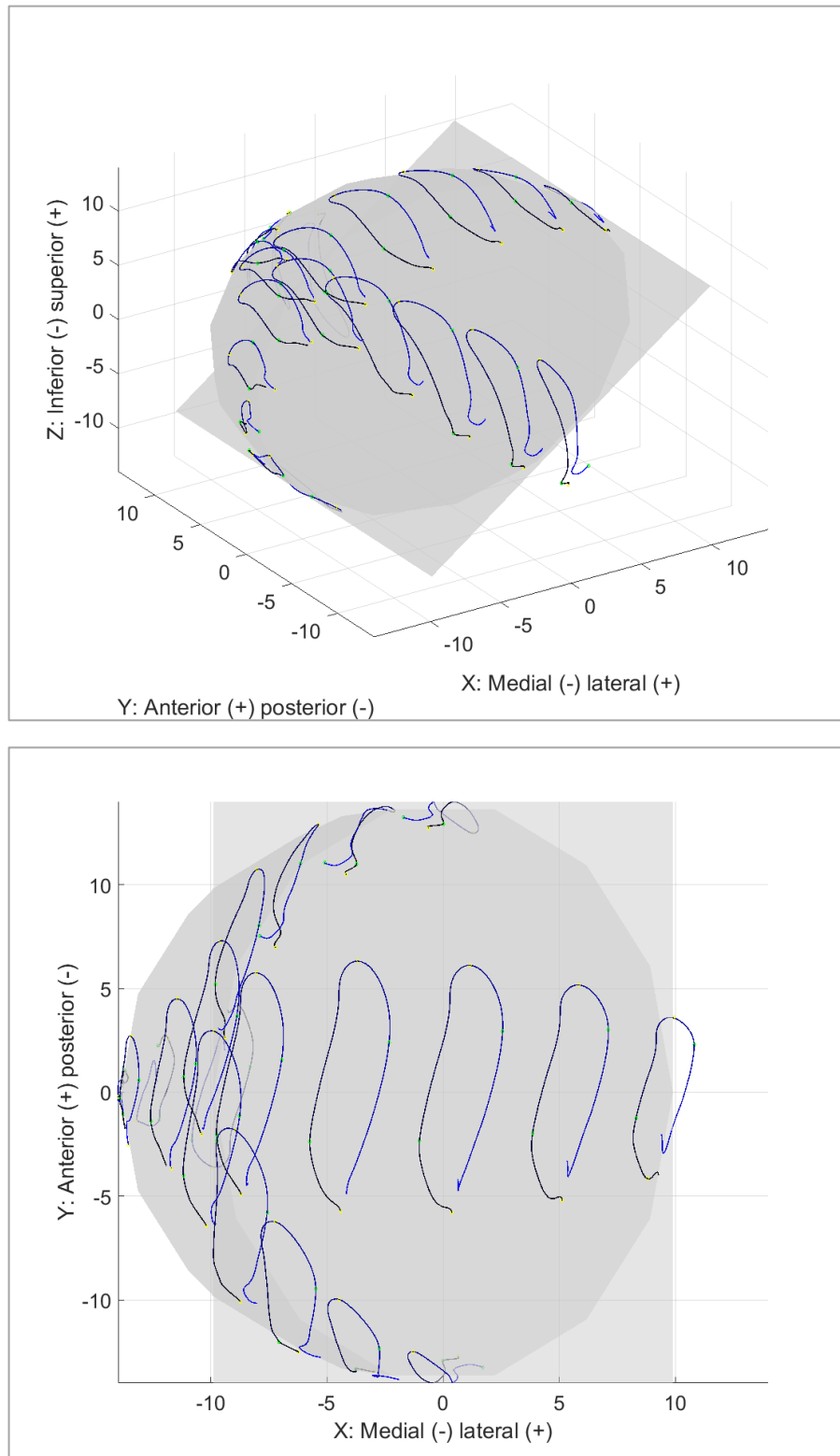


Figure 108. Motion path trajectories throughout an incline walk cycle, defined at 20 positions on the femoral head. Paths run from initial contact (black) to second initial contact (blue) (n=18).

6.3.1.4. *Decline Walk*

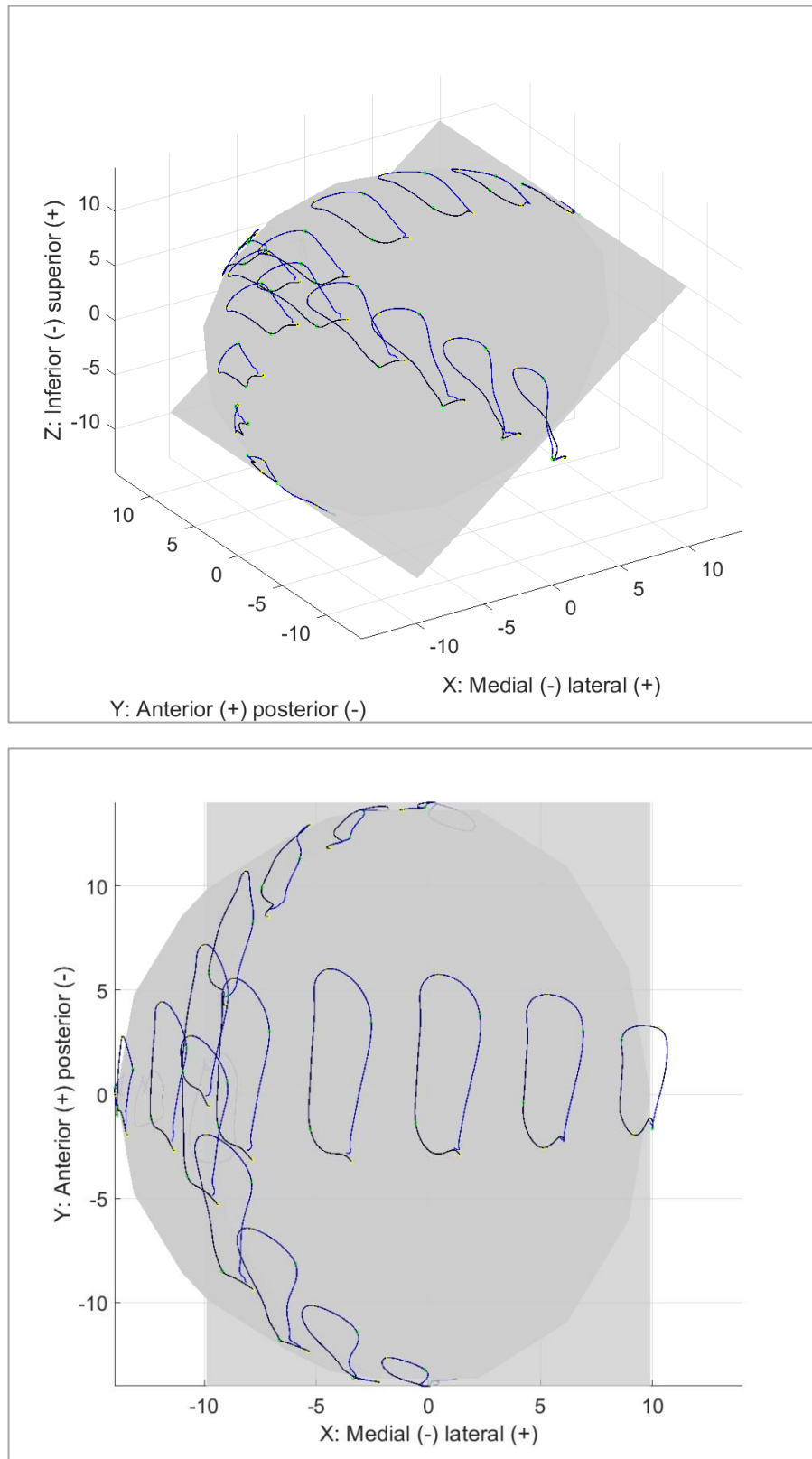


Figure 109. Motion path trajectories throughout a decline walk cycle, defined at 20 positions on the femoral head. Paths run from initial contact (black) to second initial contact (blue) (n=17).

6.3.1.5. *Stand to Sit*

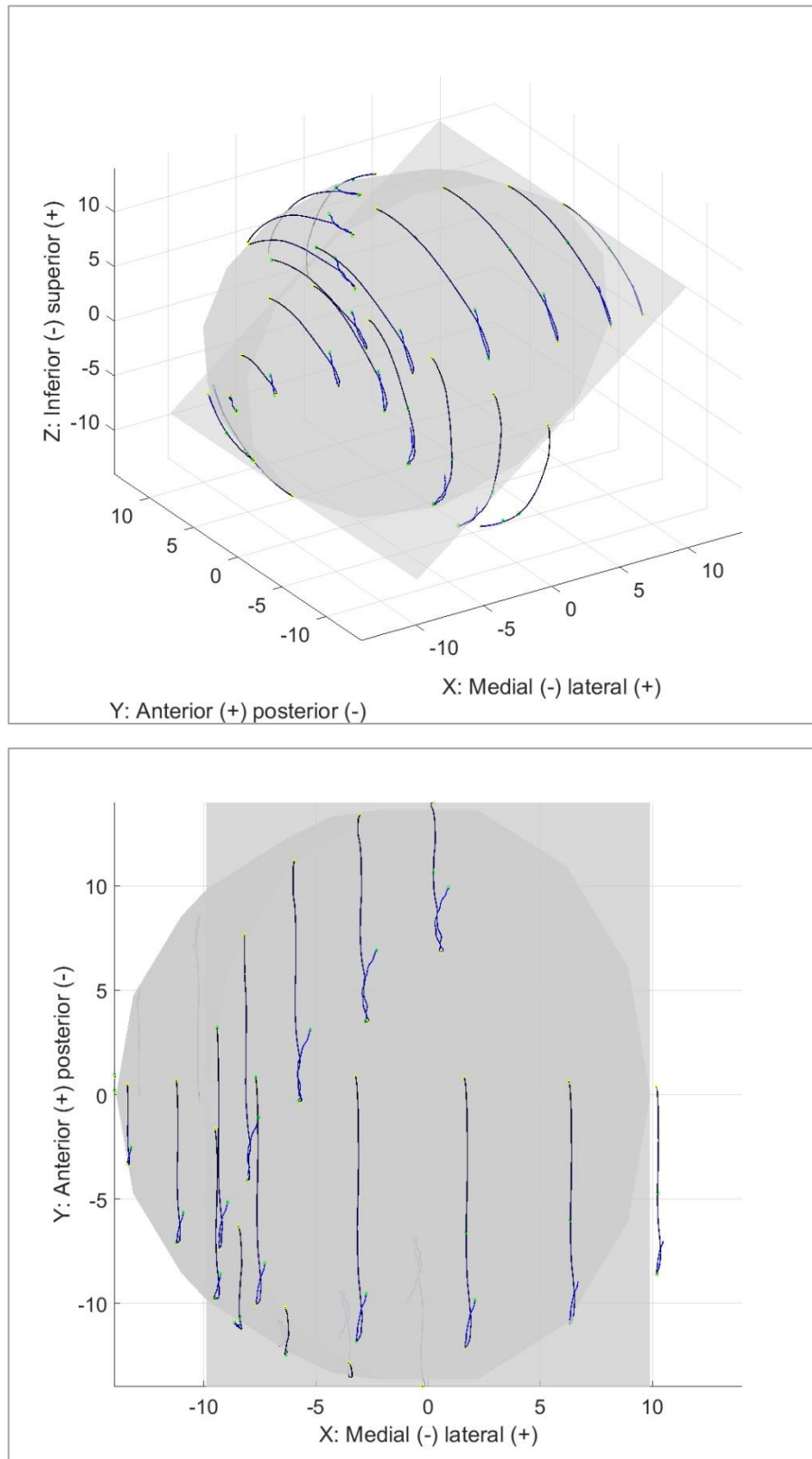


Figure 110. Motion path trajectories throughout a stand to sit cycle, defined at 20 positions on the femoral head. Paths run from initial contact (black) to second initial contact (blue) (n=8).

6.3.1.6. *Sit to Stand*

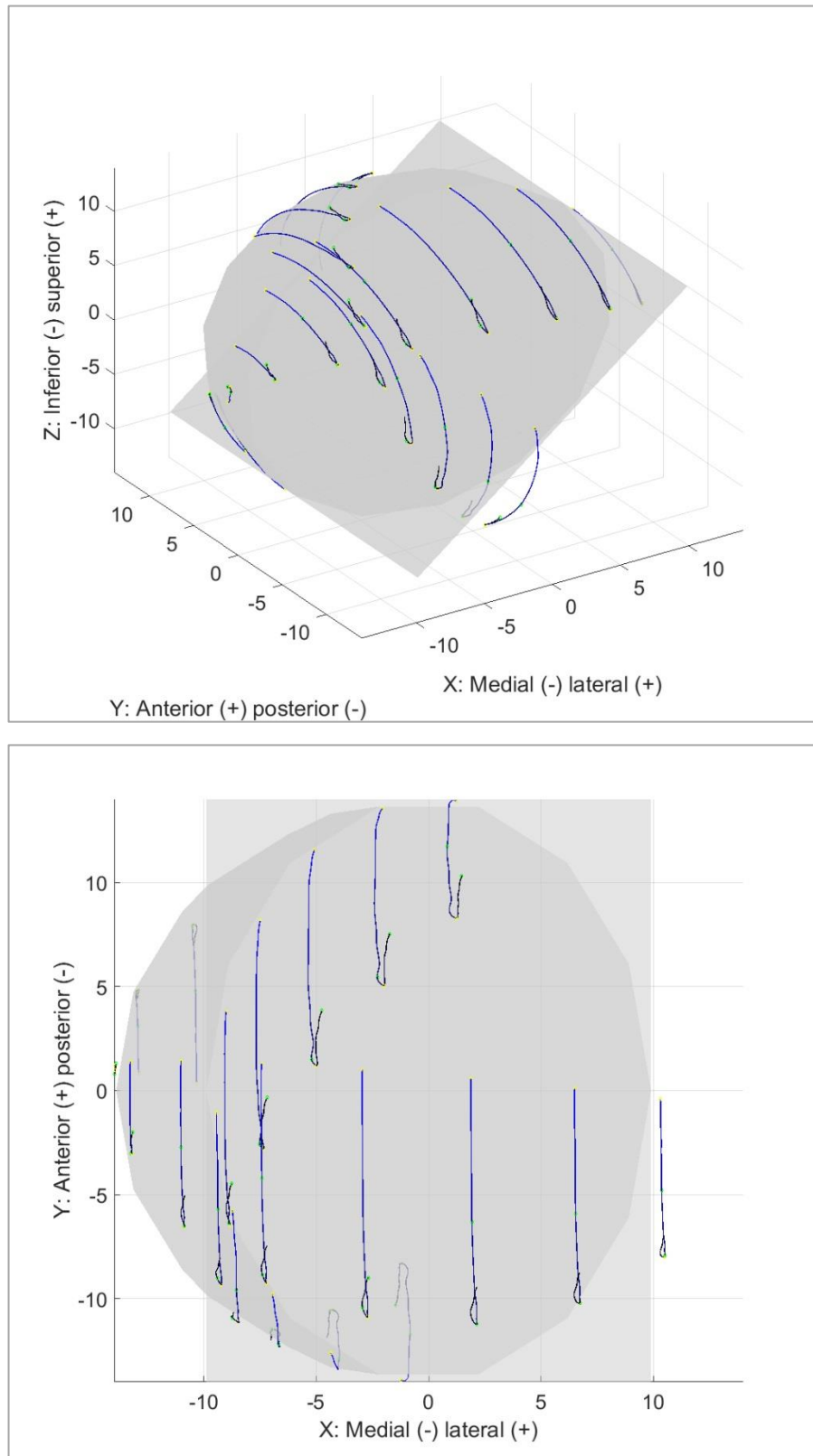


Figure 111. Motion path trajectories throughout a sit to stand cycle, defined at 20 positions on the femoral head. Paths run from initial contact (black) to second initial contact (blue) (n=8).

6.3.1.7. *Sit Cross Legged*

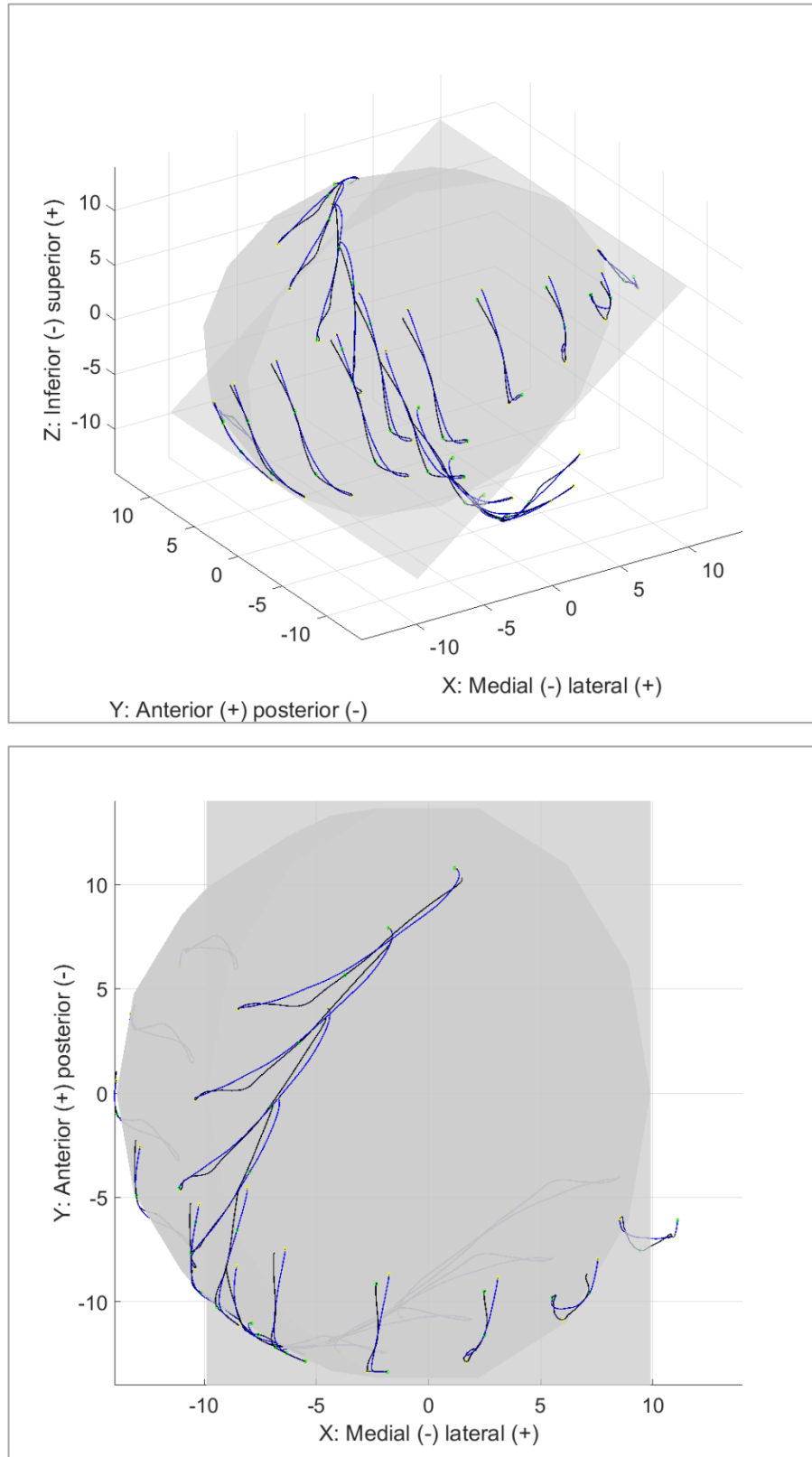


Figure 112. Motion path trajectories throughout a sit cross legged cycle, defined at 20 positions on the femoral head. Paths run from initial contact (black) to second initial contact (blue) (n=14).

6.3.1.8. *Squat*

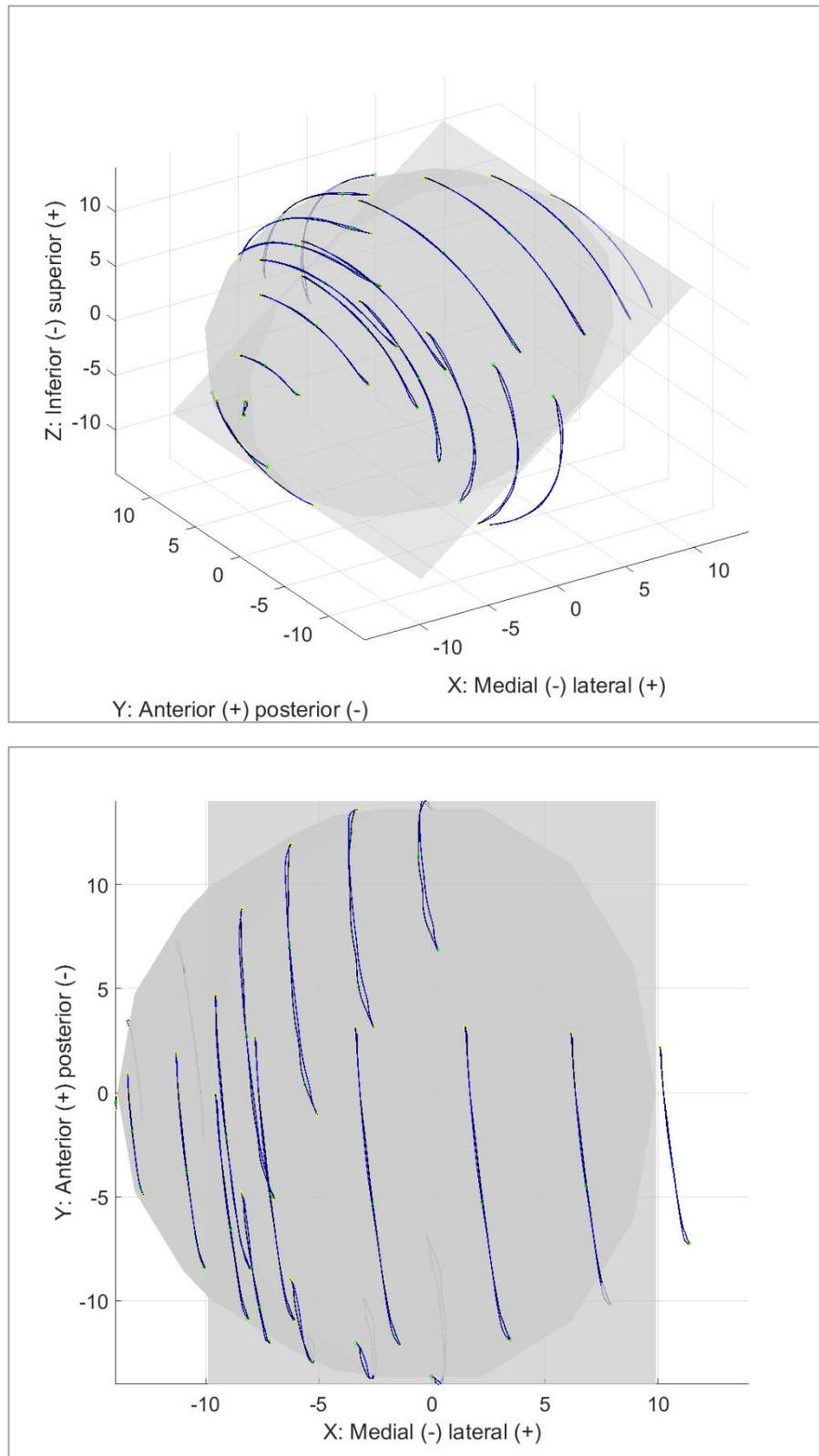


Figure 113. Motion path trajectories throughout a squat cycle, defined at 20 positions on the femoral head. Paths run from initial contact (black) to second initial contact (blue) (n=11).

6.3.1.9. *Stand Reach*

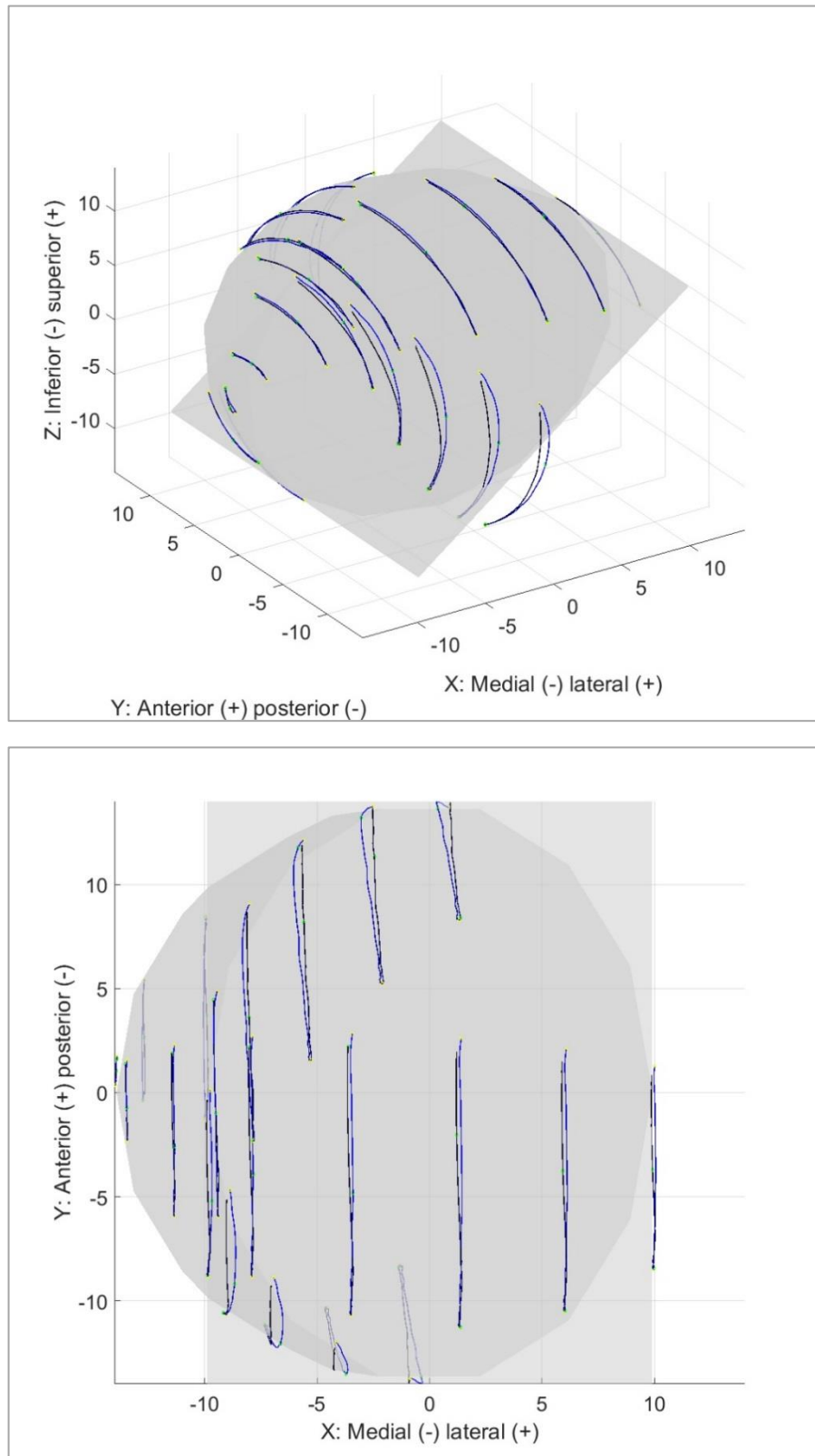


Figure 114. Motion path trajectories throughout a stand reach cycle, defined at 20 positions on the femoral head. Paths run from initial contact (black) to second initial contact (blue) (n=12).

6.3.1.10. Kneel Reach

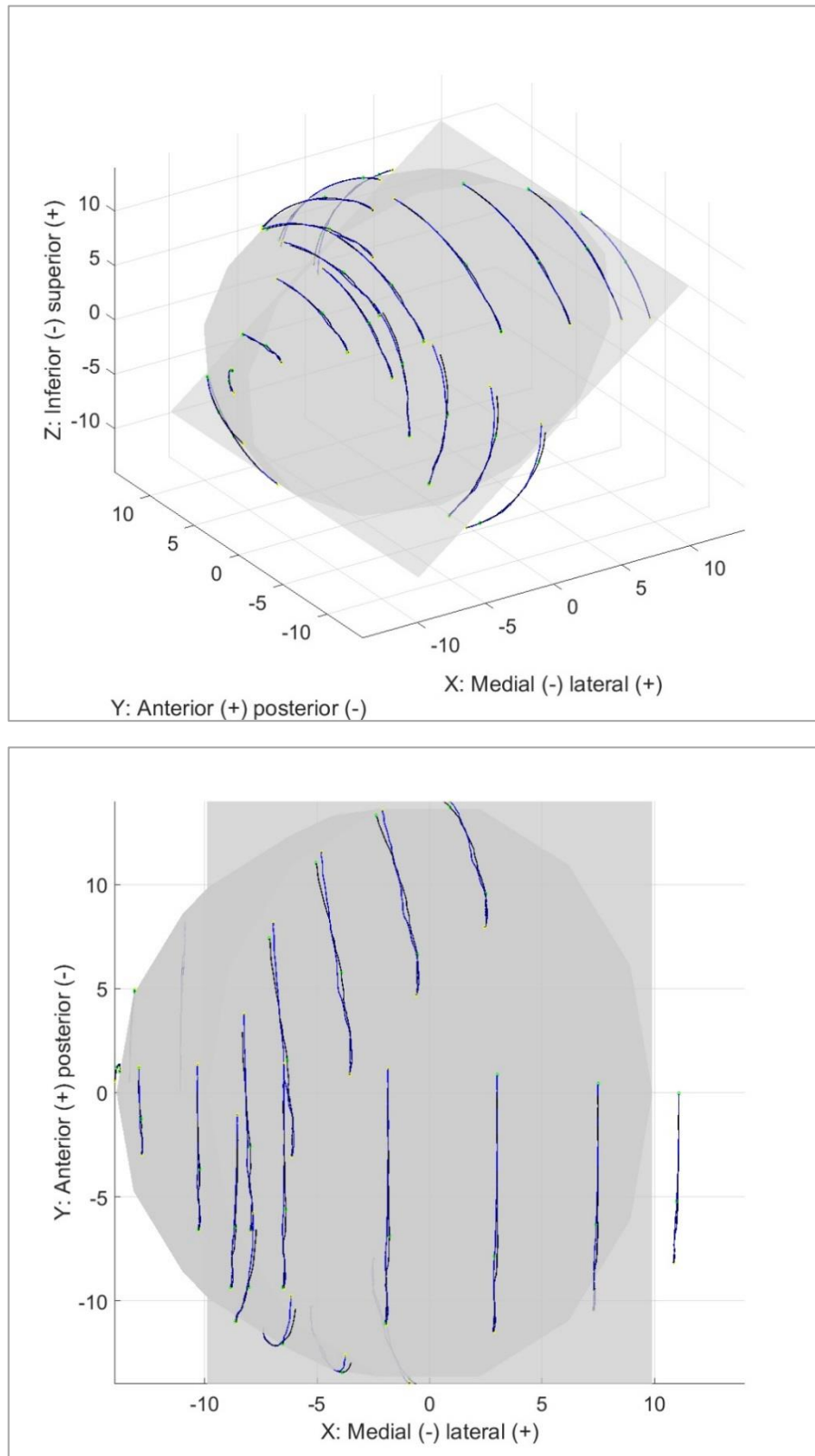


Figure 115. Motion path trajectories throughout a kneeling reach cycle, defined at 20 positions on the femoral head. Paths run from initial contact (black) to second initial contact (blue) (n=13).

6.3.1.11. Lunge

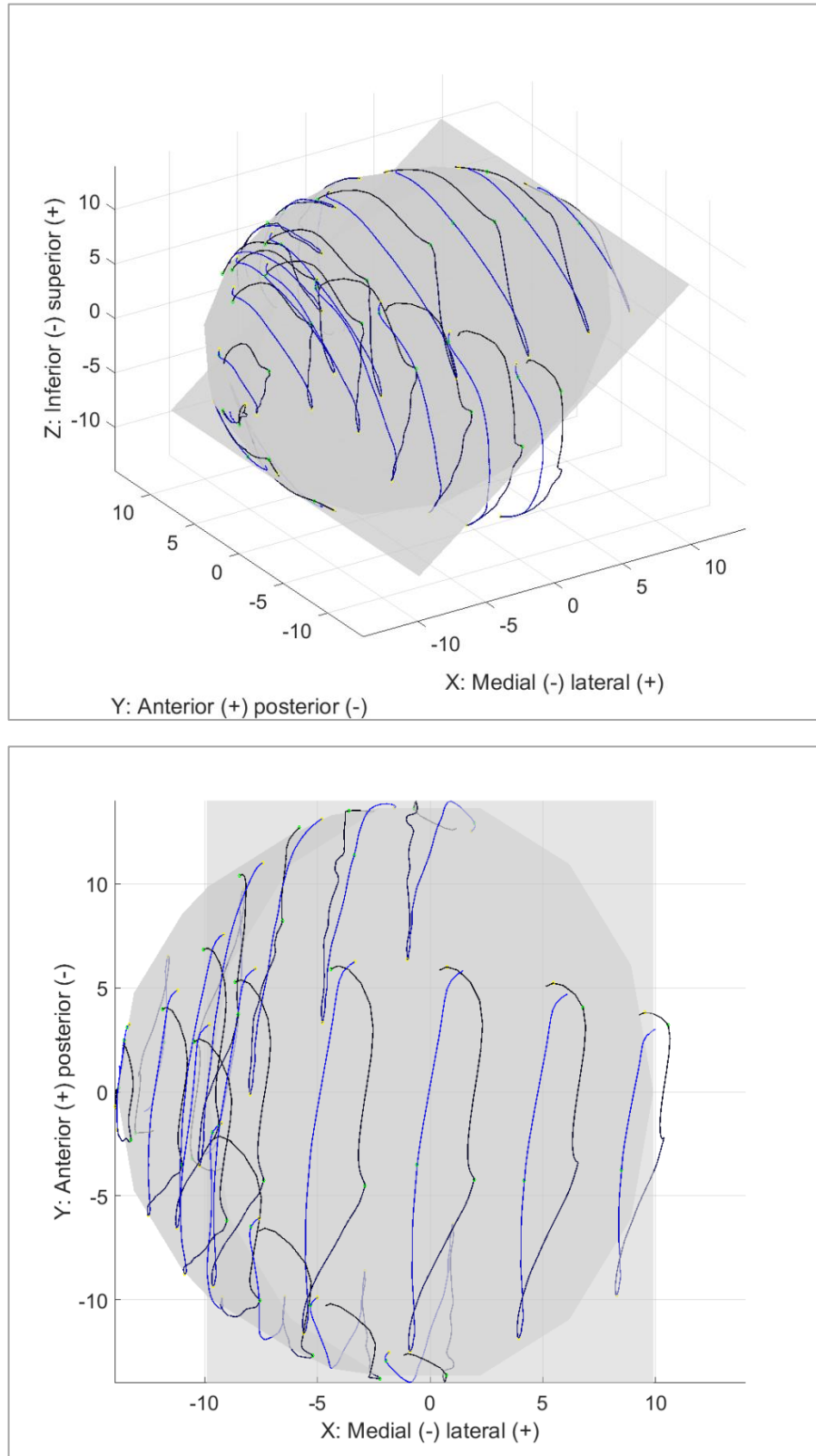


Figure 116. Motion path trajectories throughout a lunge cycle, defined at 20 positions on the femoral head. Paths run from initial contact (black) to second initial contact (blue) (n=17).

6.3.1.12. Golf Swing

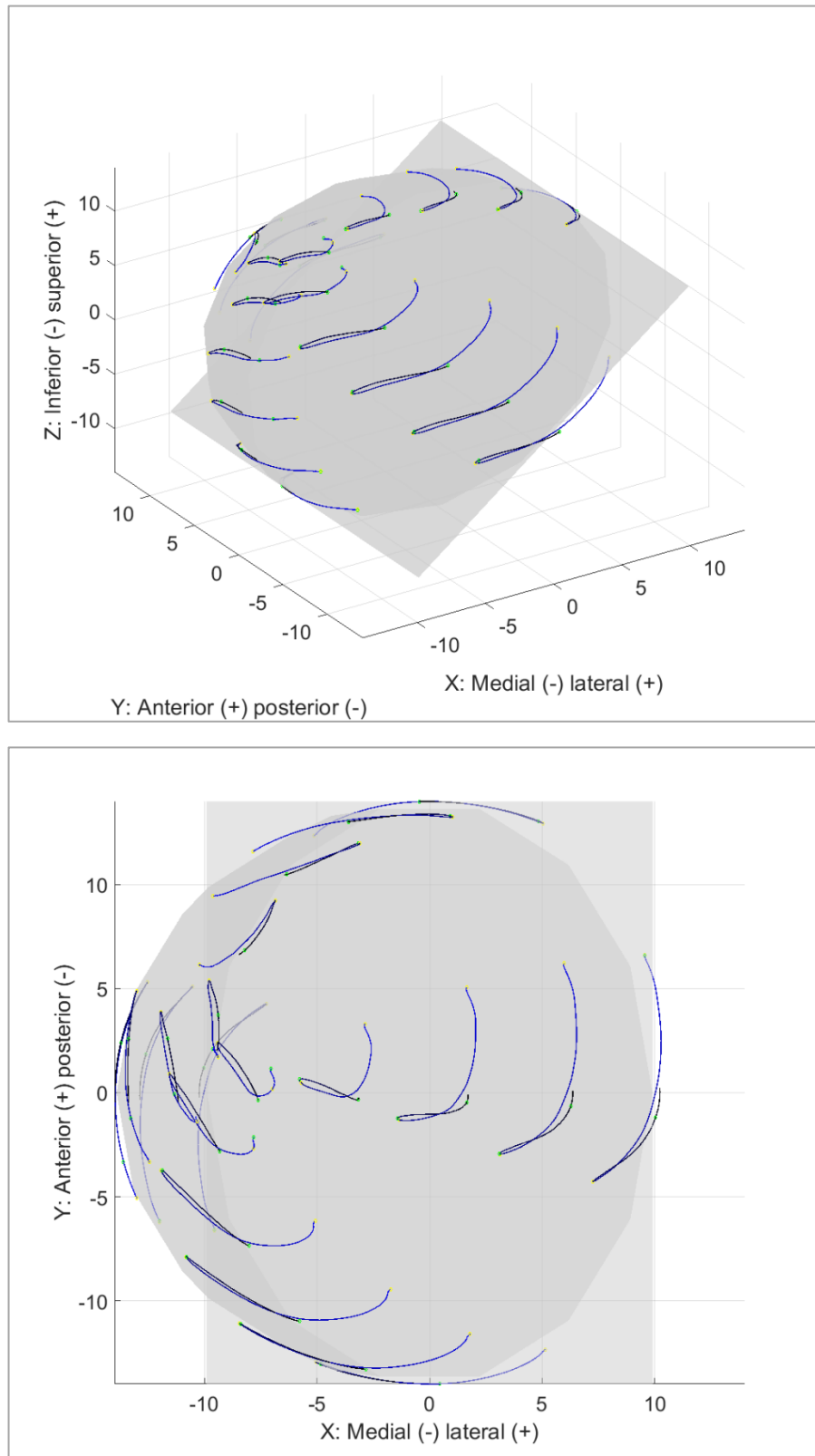


Figure 117. Motion path trajectories throughout a golf swing cycle, defined at 20 positions on the femoral head. Paths run from initial contact (black) to second initial contact (blue) (n=18).

6.3.1.13. Cycle

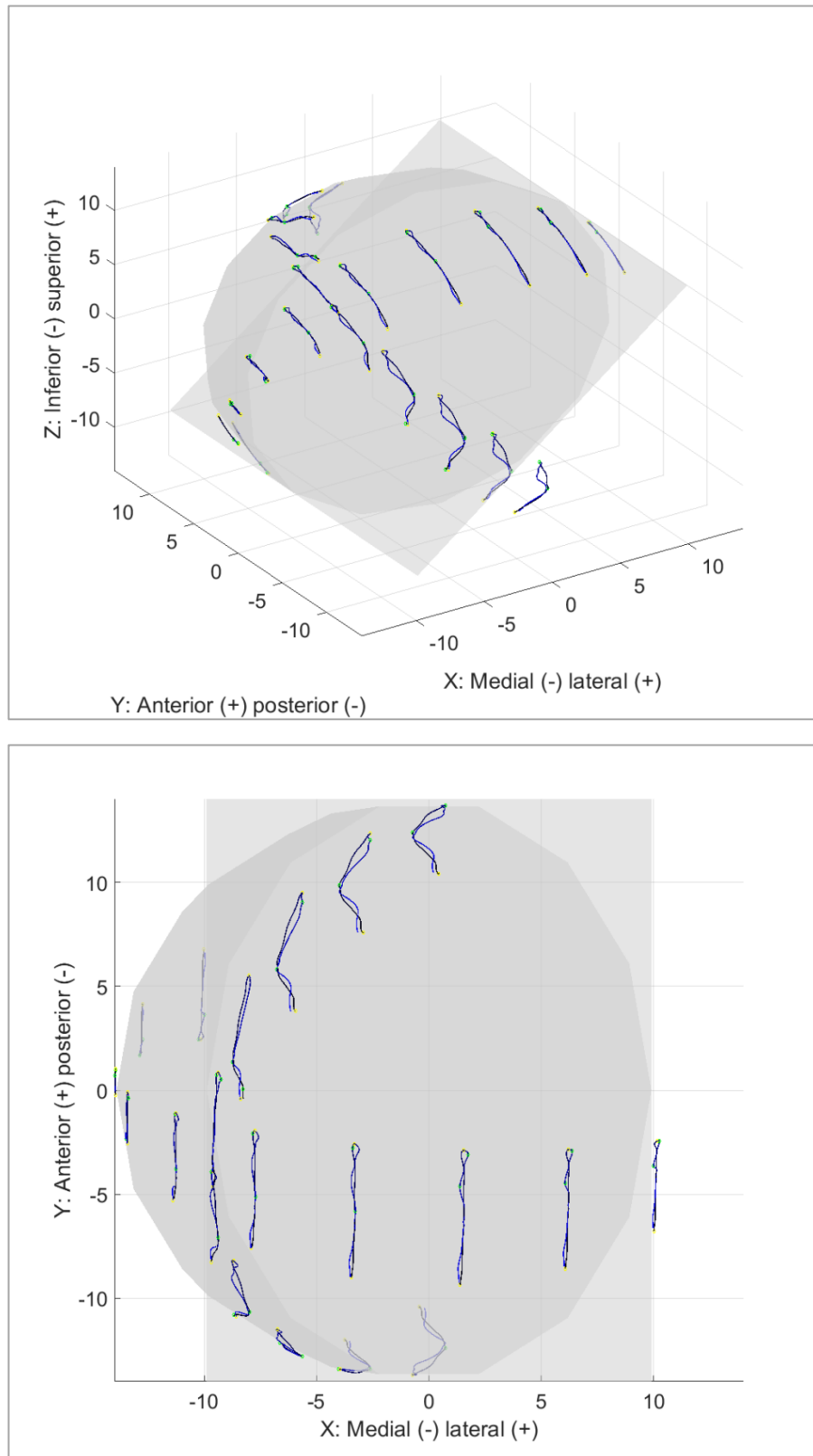


Figure 118. Motion path trajectories throughout a cycle, defined at 20 positions on the femoral head. Paths run from initial contact (black) to second initial contact (blue) (n=10).

Motion paths for the walking cycle (Figure 79) resulted teardrop, quasi-ellipse and figure-8 shapes. Variation was observed between femoral head points, in terms of path width and height. A ‘complex tail’ was seen at initial contact for some points.

Walk turn (Figure 80) showed teardrop motion paths, however unlike the normal walk, paths did not meet up at initial contact. This was due to the difference in hip kinematics at the two initial contacts within the movement. Additionally, in general, paths appeared to be more linear than for the level walk. With this being said, a number of complex trajectories were still present.

Visually, motion paths for the incline and decline walk (Figures 81 and 82) were almost identical to those seen for level walking, with teardrop, quasi-ellipse and figure-8 shapes.

Both stand to sit and sit to stand (Figures 83 and 84) tasks displayed linear motion paths across femoral head points. For both activities, paths crossed back over themselves when in contact with the chair, at the beginning/ end of the movement. Path lengths varied across femoral head points, with the shortest motion path located medially, at point 13.

When sitting cross legged (Figure 85), motion paths were linear with a cross-over of the path occurring as the right leg crossed over the left knee. More complex, elliptical shaped were observed at points 19 and 20, on the lateral side of the femoral head.

Both the squat, stand reach and kneel reach (Figures 86, 87 and 88) showed linear motion paths of varying lengths, with the shortest path observed at point 13 for all movements.

The lunge (Figure 89) showed stretched teardrop shapes across the femoral head, with a crossing over of paths occurring at the lowest point of the lunge cycle. Points 13 and 14 (medially positioned) showed different patterns to the rest of the femoral head, with a ‘complex scribble’ and quasi-ellipse, respectively.

The golf swing (Figure 90) showed both linear and ‘C’ shaped paths across the femoral head points. Similar to other activities, paths were of varying length and crossed back across themselves during the movement.

In general, the cycling activity (Figure 91) showed linear paths. Motion paths exhibited ‘figure-8’ patterns in which the path crossed over itself up to three times.

6.3.2. Motion Path Aspect Ratios

The aspect ratio (path length/ perpendicular width) (AR) was calculated for each of the twenty motion paths. The mean AR (across twenty motion paths) was resulted for each activity, with standard deviations (SDs) to show inter-subject variability. This provides an overview of the potential cross-shear occurring between the femoral head and the cup. Minimum ARs are also presented within this section. These values highlight that although the mean AR may be high (with low cross-shear), the variation between individual motion path trajectories means that there may still be instantaneous points of excessive cross-shear, with low AR motion paths.

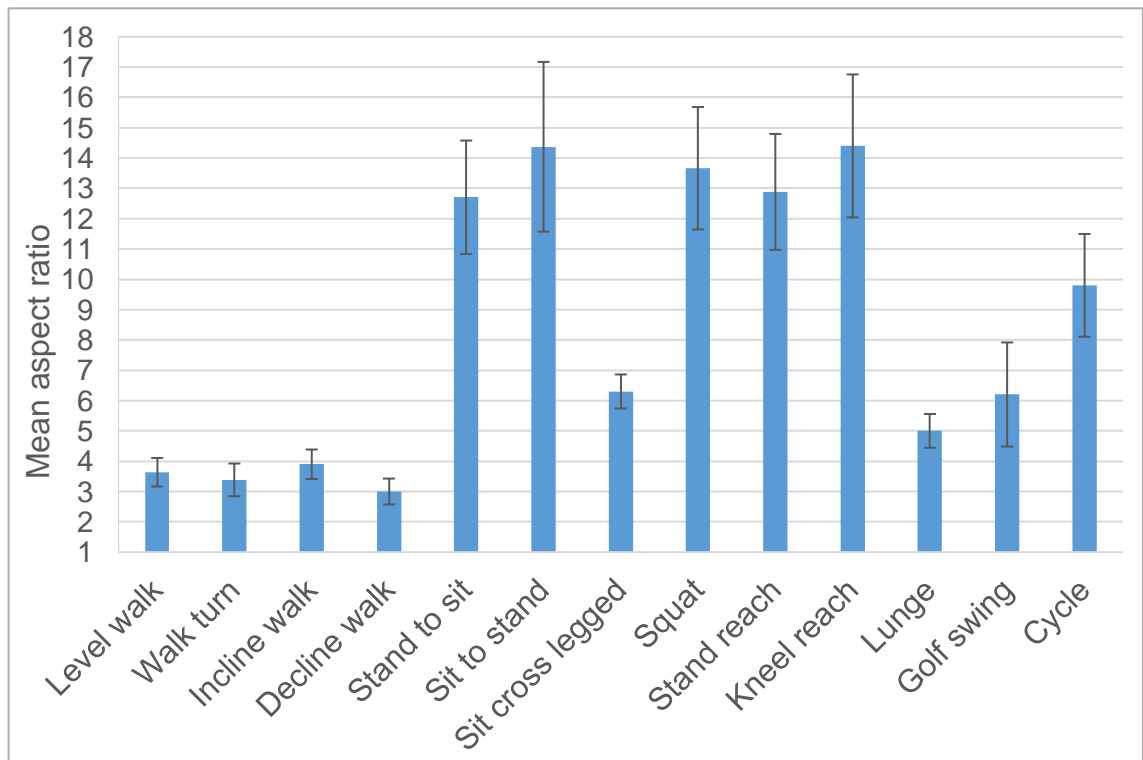


Figure 119. Mean aspect ratios (length/width) for twenty motion path trajectories across the femoral head. Variation between subjects is shown by standard deviations (error bars).

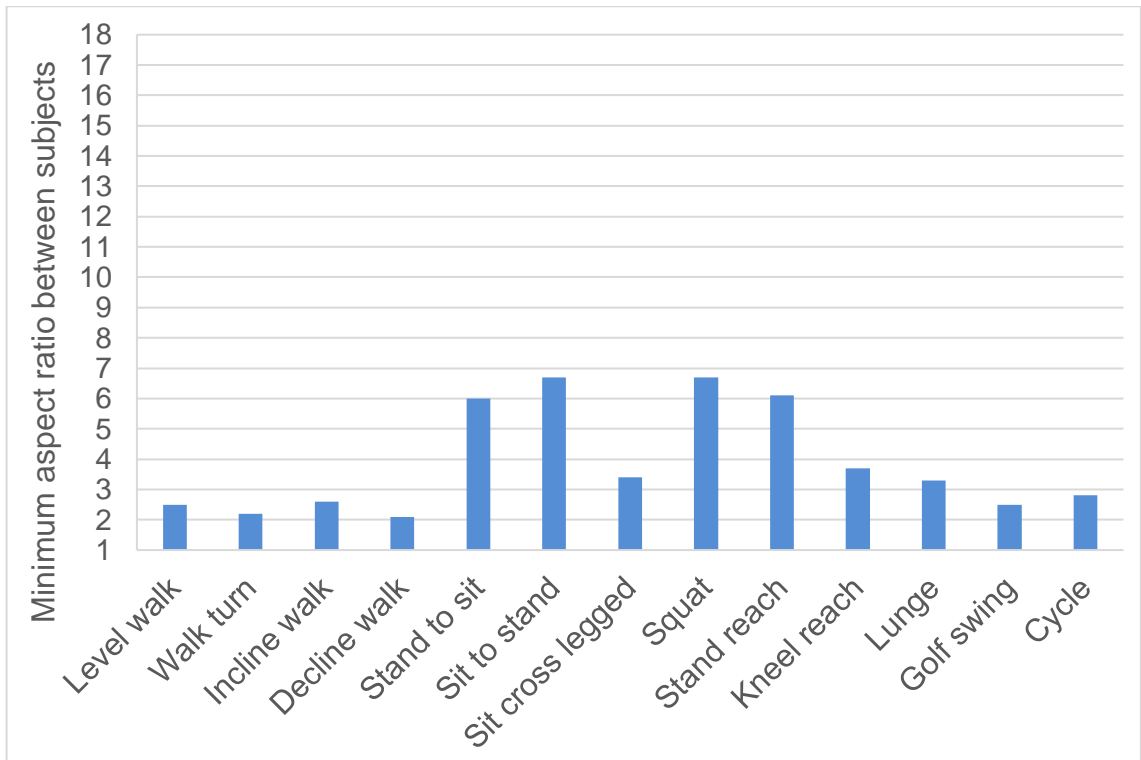


Figure 120. Minimum, mean aspect ratio (height/width) between subjects.

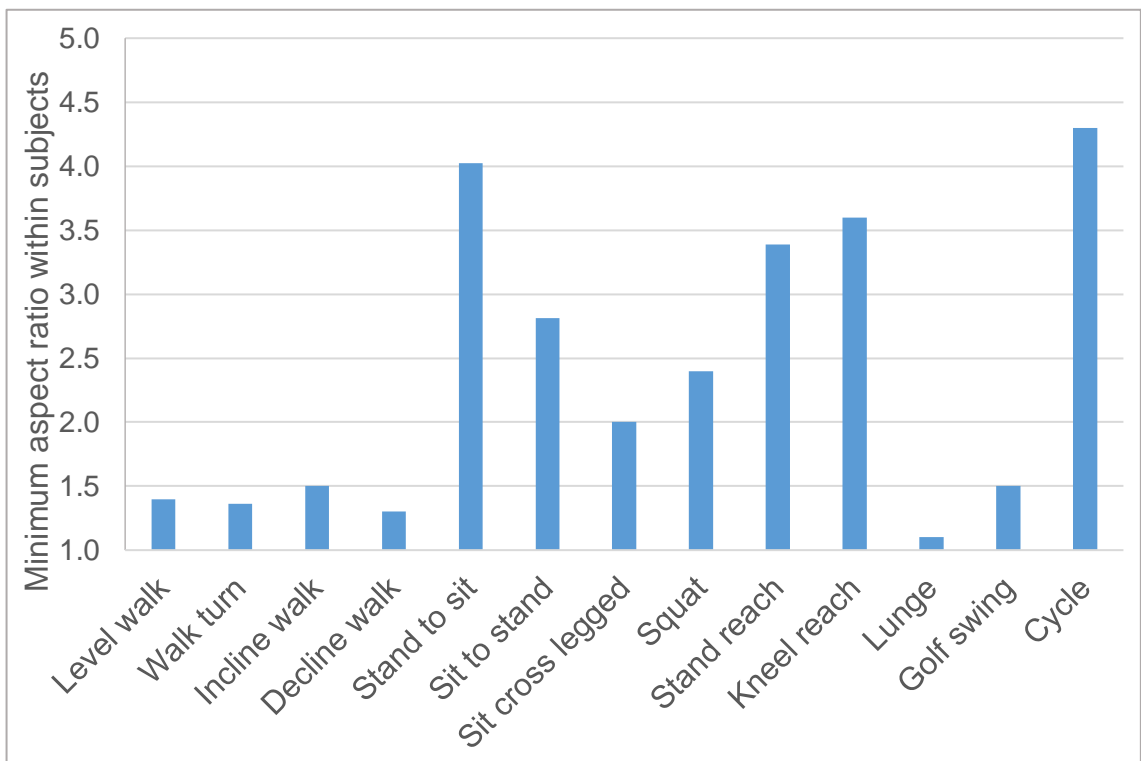


Figure 121. Minimum aspect ratios (height/width) within subjects, when considering twenty motion path trajectories across the femoral head.

Mean ARs provide a way to quantify the shape of motion paths and therefore potential for wear across a polyethylene acetabular cup. Decline walk resulted the lowest mean aspect ratio (AR), when comparing between activities (3.0 ± 0.4) (Figure 92). In contrast, sit to stand (14.4 ± 2.7) and kneel reach (14.4 ± 2.3) showed the highest mean ARs. When considering the data, it is possible to consider activities within three groups. The four walking tasks demonstrated the lowest mean ARs (all between 3 and 3.9). A second group including sit cross legged, lunge, golf swing and cycle resulted mean ARs between 5 and 9.8. The stand to sit (StSi), sit to stand (SiSt), squat, stand reach and kneel reach could be considered as the final group, with the highest mean ARs, ranging from 12.7 to 14.4.

Mean AR variation ranged from ± 0.4 (decline walk) to ± 2.8 (SiSt) (Figure 92). This variation was particularly prominent in activities with higher mean ARs (SD equalled ± 2.8 for SiSt). However, standard deviations may still miss the extremes of the data set. Figure 93 highlights the minimum mean ARs, between subjects, thus providing cross-shear information which may have been lost during the averaging process. It stands out that a number of the high aspect ratio activities (StSi, SiSt, squat, stand reach and kneel reach), had anomalous individuals who showed marked decreases in comparison to the mean. Marked discrepancies between minimum data and the mean were seen for all activities (walk: 1.1; walk turn; 1.2; incline walk: 1.3; decline walk; 0.9; StSi: 6.7; SiSt: 7.7; Sit cross legged: 2.9; Squat: 2.9; Stand reach: 7; Kneel reach: 10.7; Lunge: 1.7; Golf swing: 3.7; Cycle: 7). In general, this discrepancy was larger for activities with a high mean AR. It was partially noticeable for kneel reach, where one subject demonstrated an AR 10.7 lower than the mean.

Variation in motion paths, between femoral head points, was seen for all activities. Figure 94 shows that 6 of the 13 activities (four walking tasks, lunge and golf swing) included a point between the head and cup with an $AR \leq 1.5$. The lowest of these, was seen for the lunge, equalling 1.1. A further three activities (SiSt, sit cross legged and squat) displayed a minimum AR between 2 and 3. The remaining four activities (StSi, stand reach, kneel reach and cycle) resulted minimum ARs between 3 and 4.5.

6.3.3. Sliding Distances

Mean sliding distances describe the average displacement of the twenty femoral head points on the acetabular cup. This is presented for each of the thirteen activities, with subject variation shown as error bars.

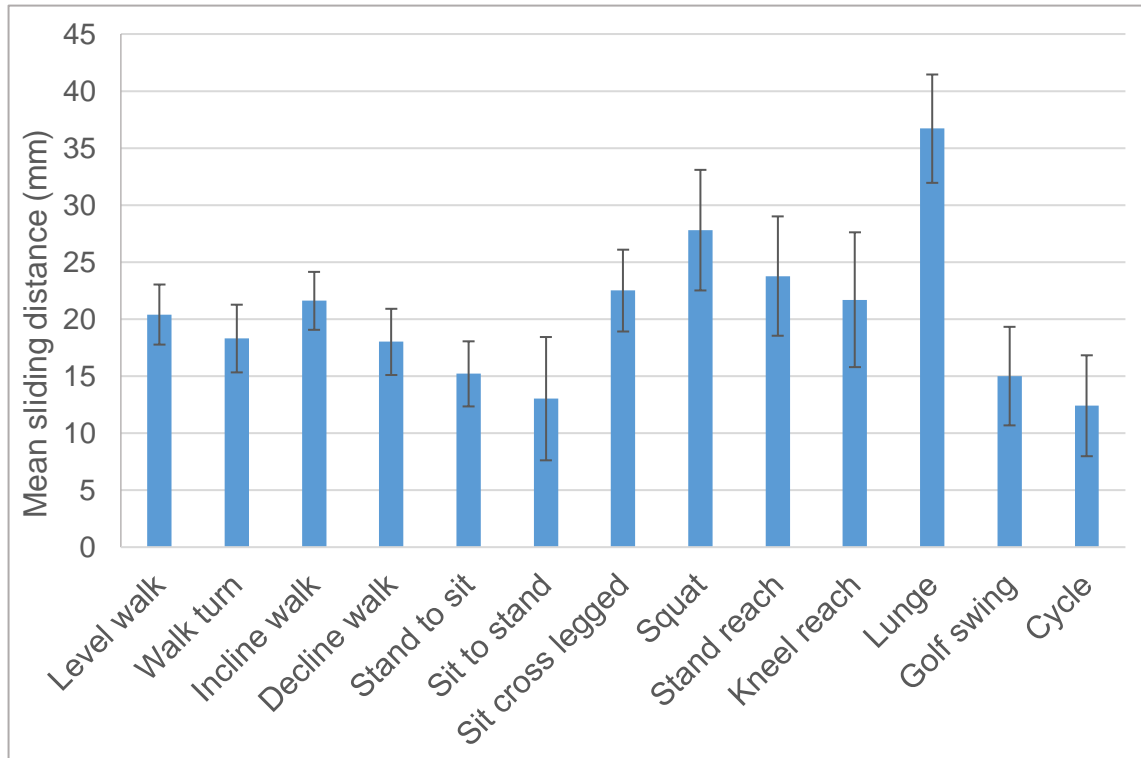


Figure 122. Mean sliding distances for twenty motion path trajectories across the femoral head. Variation between subjects is shown by standard deviations (error bars).

Mean sliding distances ranged from 12 mm (cycle) to 37 mm (lunge) (Figure 95). Standard deviations ranged from ± 3 mm to ± 6 mm, thus highlighting the variation in sliding distances across subjects.

6.3.4. Sliding Velocity and Acceleration

Differentiating motion path trajectories results the sliding velocity between bearing surfaces. Sliding velocity has implications for the lubrication regime and potentially, the wear occurring between surfaces at the hip (whether that be cartilage-cartilage in the healthy hip or metal-polyethylene in a THR) (Stewart, 2010; Stewart et al., 1997). Additionally, sliding velocity provides a mode for identifying changes in direction of a motion path trajectory. A change in the resultant velocity curve (from low \leftrightarrow high) suggests a change in direction of the motion path trajectory.

The 2nd differential of motion path trajectories results the sliding acceleration. Similarly to velocity, an increase in sliding acceleration will have an influence on both cartilage-cartilage and metal-polyethylene interactions. A peak in relative acceleration between surfaces, indicates a change in sliding velocity and motion path displacement. Thus, acceleration peaks represent a change in the direction of a motion path, with the peak magnitude directly influenced by the angle of the directional change. Identifying peak instantaneous acceleration, between surfaces for different activities, may provide an understanding of how hip tribology is influenced by different movements.

Within this section, sliding displacement, velocity (SV) and acceleration (SA) is shown at one point on the femoral head (Point 7: X, Y, Z; 0 mm, 7 mm, 12 mm) for each activity. Point 7 was chosen for analysis as it is located anteriorly on the femoral head (an approximate position in which the hip reaction force acts from - section 5.3.3.10.). Within the Appendix (section 10.4.) a further three femoral head points are presented for each activity (anterior-posterior, medial-lateral, inferior-superior; mm; 0, 14, 0; -14, 0, 0; 7, 0, 12)

6.3.4.1. *Graph Interpretation*

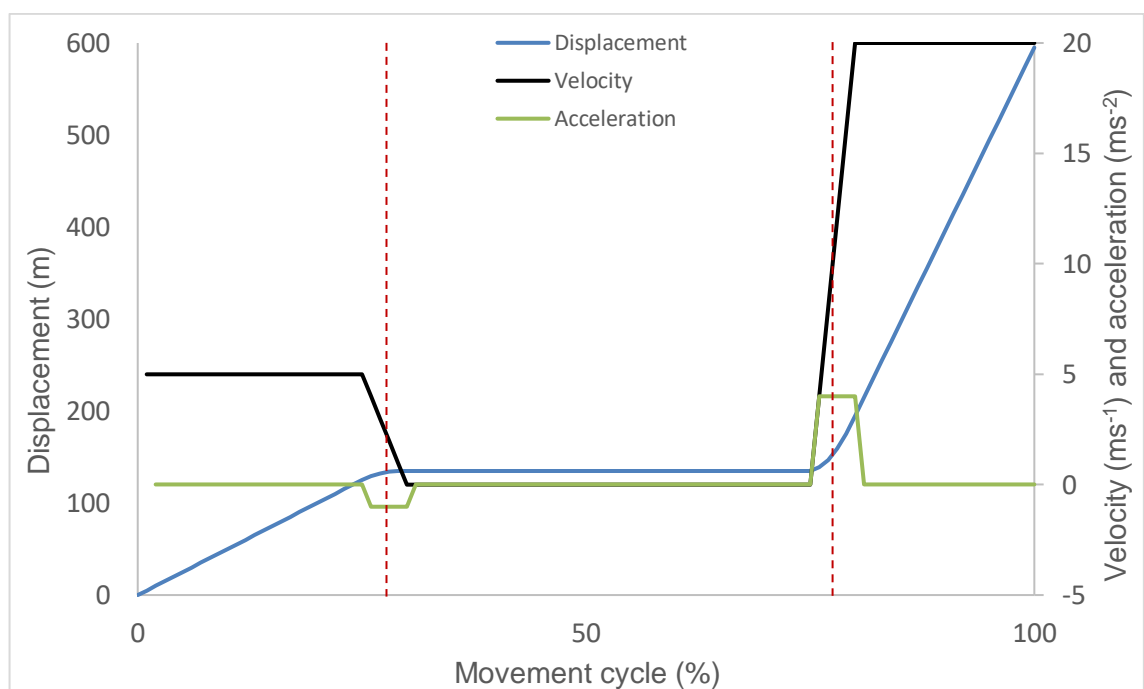


Figure 123. Example of a displacement and velocity curve. Red dashed line shows the point at which the displacement curve changes direction.

Figure 96 is an example of how displacement, velocity and acceleration interact. The red dashed line represents the point at which displacement direction is changed.

Corresponding to this point, the velocity magnitude is altered. The more acute the displacement change angle, the bigger the velocity change magnitude. Equally, the more acute the displacement change angle, the larger the instantaneous acceleration peak. When considering hip motion paths, a change in velocity and therefore, a peak in acceleration, suggests a change in direction of the motion path. A negative acceleration peak indicates a right turn, whereas a positive acceleration peak indicates a left turn.

6.3.4.2. *Walk*

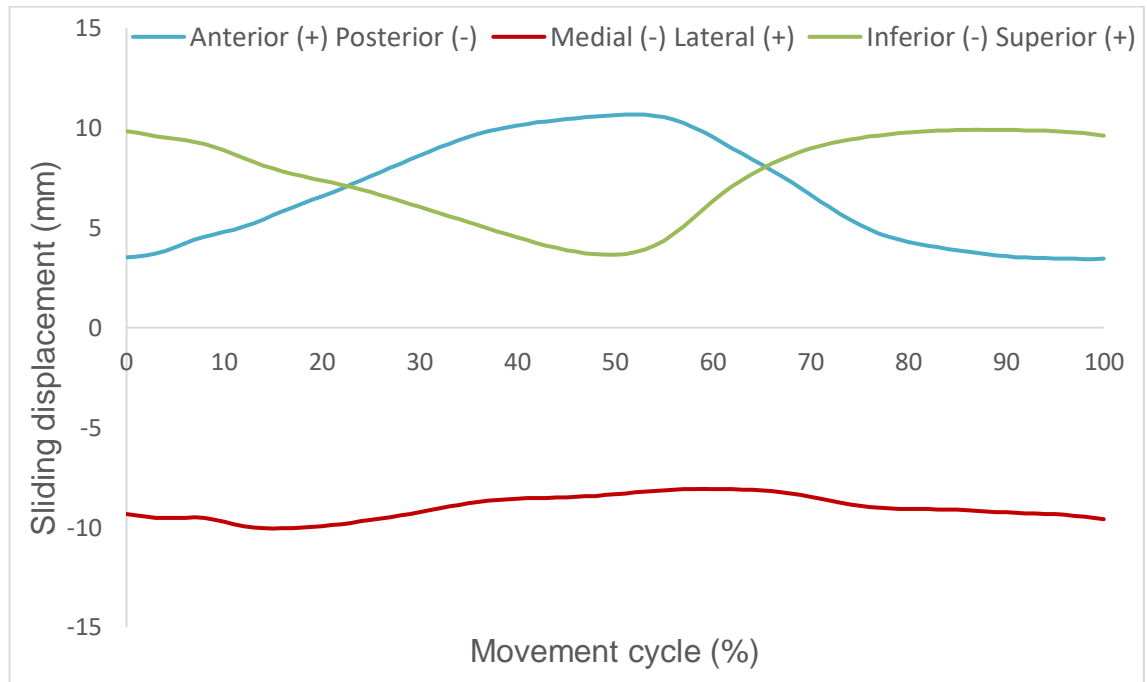


Figure 124. Point 7 (X, Y, Z : 0 mm, 7 mm, 12 mm) for an average walking cycle, showing sliding displacement in anterior-posterior (blue), medial-lateral (red), proximal-distal (green) axes ($n=17$).

When walking, Point 7 on the femoral head was a tear-drop shape, with one obvious change in direction that occurred at approximately 50% of the gait cycle (section 6.3.1.1.). Figure 97 shows that the motion path location was on the anterior-posterior arc, hence the small change in medial-lateral displacement. The path ran anteriorly and inferiorly, as the hip extended ($\approx 0-50\%$). When the hip flexed during the swing phase, the path ran posteriorly and superiorly, back to the start position. The displacement rate of change was lower during the first half of the gait cycle, compared to the second, indicating a higher peak sliding velocity occurring from 50-100% of the movement.

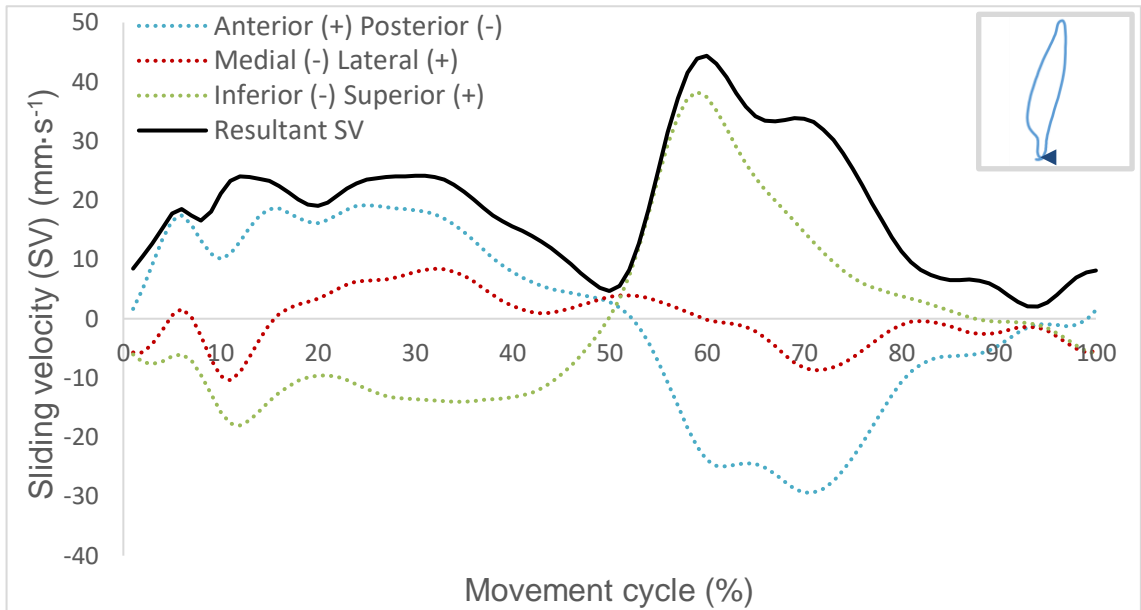


Figure 125. Point 7 (X, Y, Z : 0 mm, 7 mm, 12 mm) for an average walking cycle, showing sliding velocity in anterior-posterior (blue), medial-lateral (red), proximal-distal (green) axes (dotted lines). Resultant sliding velocity is shown in black. The corresponding motion path trajectory is shown in the top right corner, with an arrow showing the direction of motion at movement initiation.

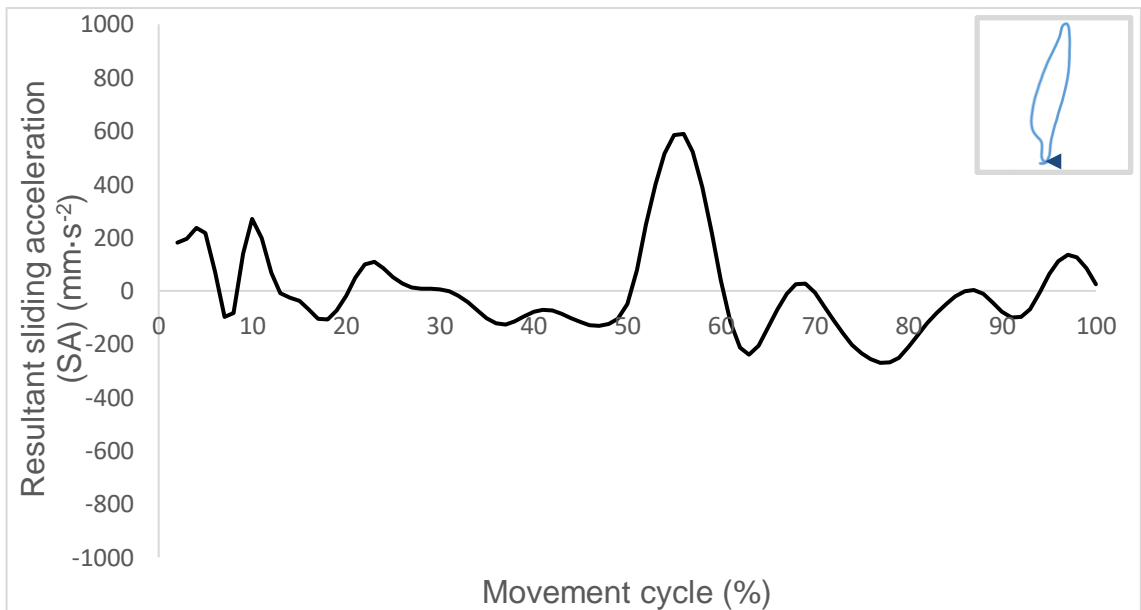


Figure 126. Point 7 (X, Y, Z : 0 mm, 7 mm, 12 mm) for an average walking cycle, showing resultant sliding acceleration. The corresponding motion path trajectory is shown in the top right corner, with an arrow showing the direction of motion at movement initiation.

Figure 98 shows resultant SV occurring between bearing surfaces when walking. Changes in SV indicate changes in the orientation of the motion path. A trough occurred at 50%

of the cycle ($4.6 \text{ mm}\cdot\text{s}^{-1}$). A large velocity change was observed between 50-60% of the gait cycle, culminating in a peak at 60% of the cycle ($44 \text{ mm}\cdot\text{s}^{-1}$) (toe-off). The change in velocity (and corresponding SA peak) highlights an acute change in the motion path direction (Figure 99).

6.3.4.3. *Walk Turn*

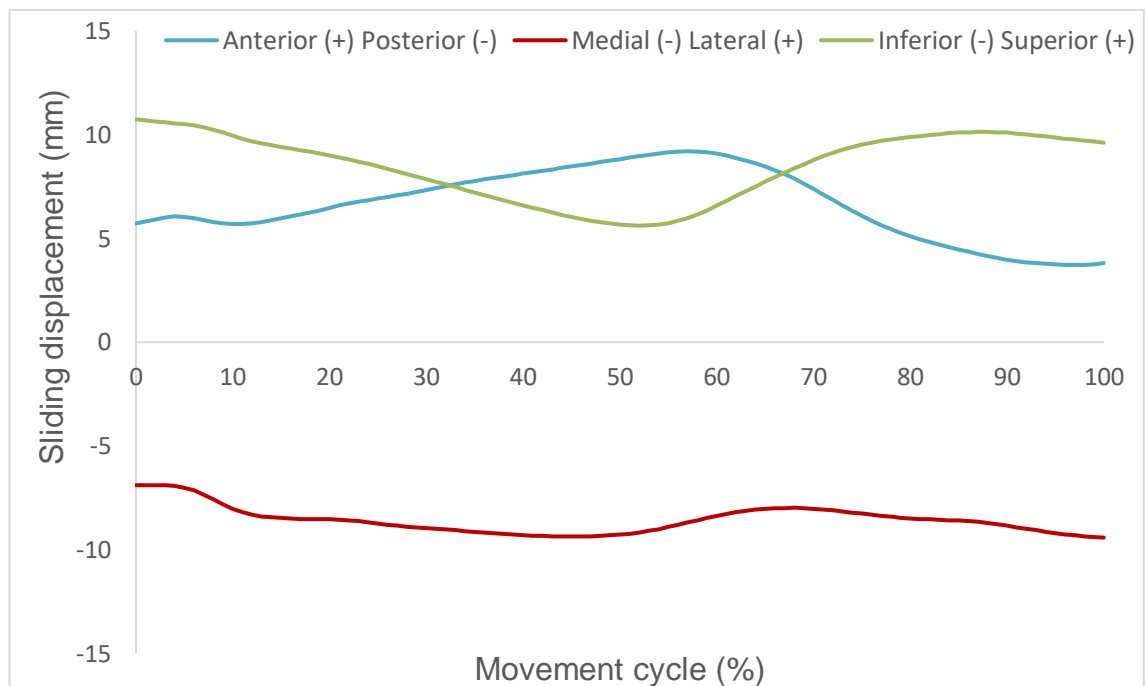


Figure 127. Point 7 (X, Y, Z : 0 mm, 7 mm, 12 mm) for an average walk turn cycle, showing sliding displacement in anterior-posterior (blue), medial-lateral (red), proximal-distal (green) axes ($n=18$).

During the walk turn, femoral head Point 7 resulted a tear-drop shape, with the start and end of the path crossing over (section 6.3.1.2.). As with the normal walk, the path ran anteriorly and inferiorly before changing direction and demonstrating posterior/ superior displacement to return to the starting position (Figure 80). Two acute changes in direction were seen for this motion path: one at $\approx 10\%$ of the cycle and one at $\approx 70\%$ of the cycle (Figure 100).

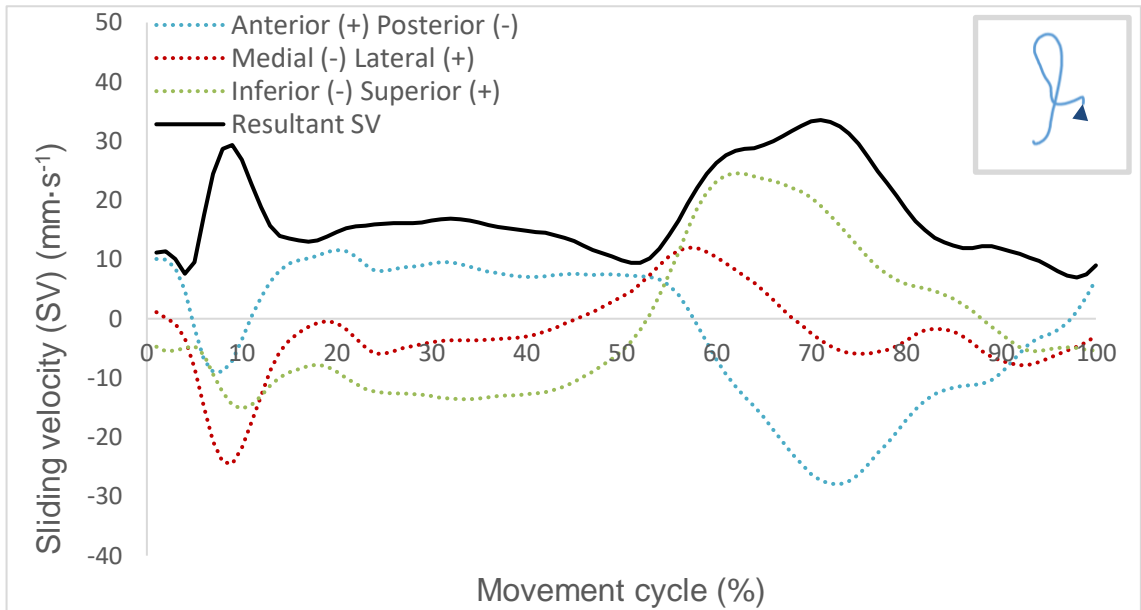


Figure 128. Point 7 (X, Y, Z : 0 mm, 7 mm, 12 mm) for an average walk turn cycle, showing sliding velocity in anterior-posterior (blue), medial-lateral (red), proximal-distal (green) axes (dotted lines). Resultant sliding velocity is shown in black. The corresponding motion path trajectory is shown in the top right corner, with an arrow showing the direction of motion at movement initiation.

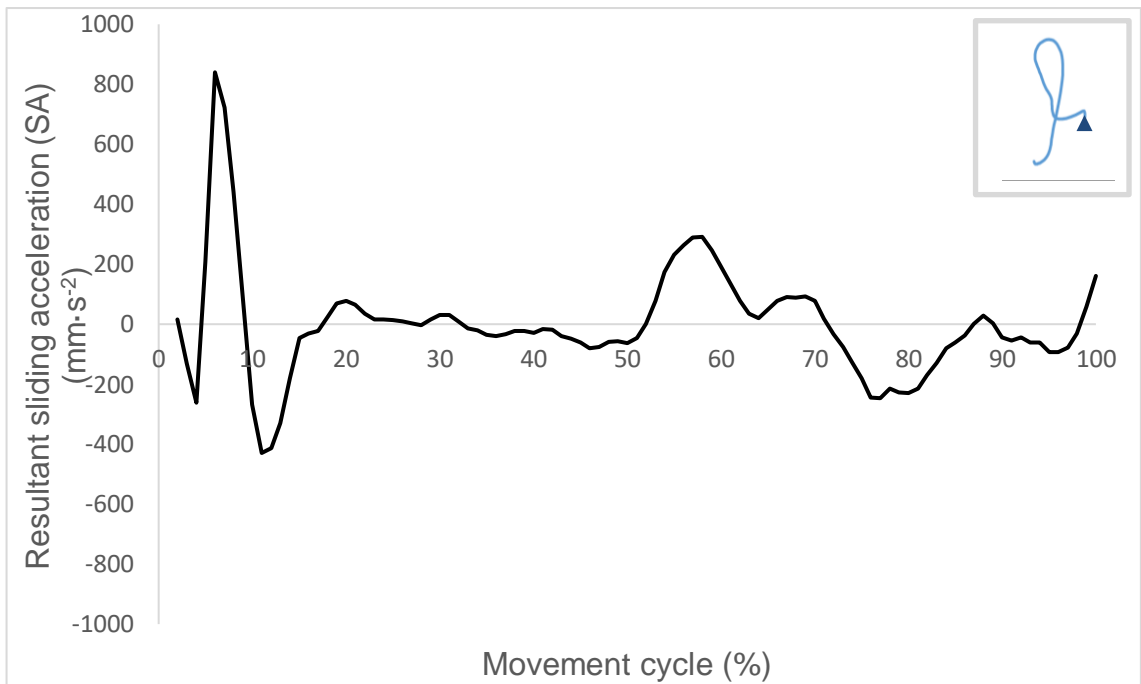


Figure 129. Point 7 (X, Y, Z : 0 mm, 7 mm, 12 mm) for an average walk turn cycle, showing resultant sliding acceleration. The corresponding motion path trajectory is shown in the top right corner, with an arrow showing the direction of motion at movement initiation.

Two peaks were observed within the resultant walk turn SV curve: one at $\approx 10\%$ (840 ms^{-2}) and one at $\approx 70\%$ (250 ms^{-2}) of the gait cycle (Figure 101). Changes in velocity, and corresponding changes in motion path direction, were highlighted as peaks in the SA curve. Figure 102 indicates that the first motion path change in direction, occurred over a shorter space of time and with higher SA (more acute angle), compared to the second.

6.3.4.4. *Incline Walk*

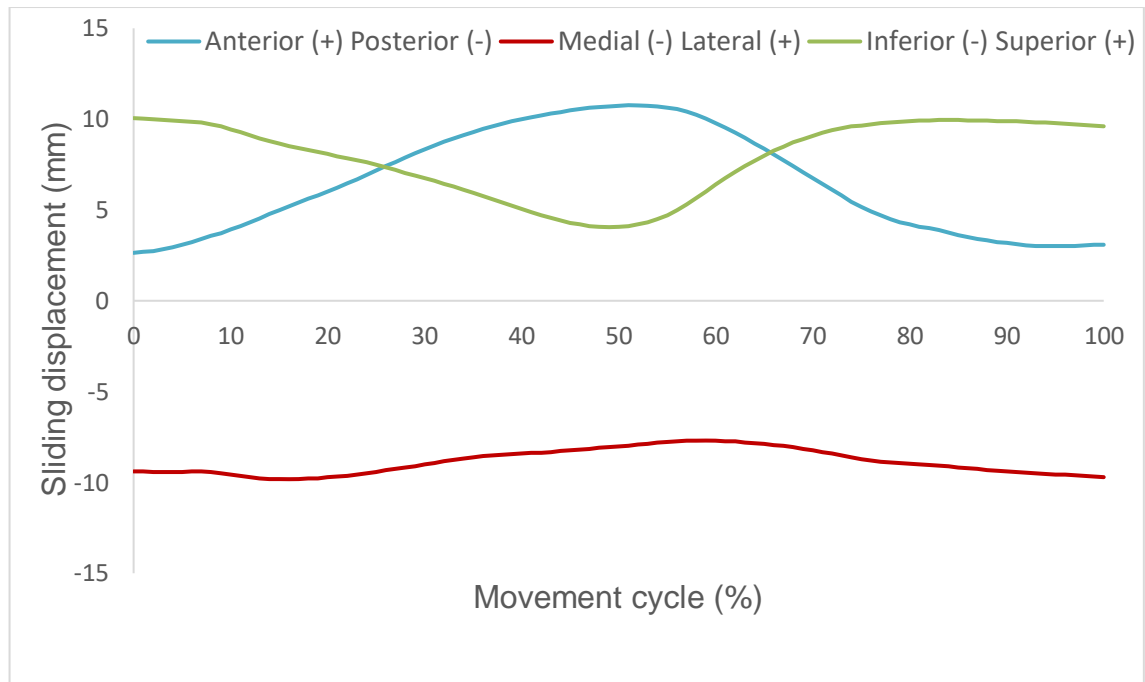


Figure 130. Point 7 (X, Y, Z: 0 mm, 7 mm, 12 mm) for an average incline walk cycle, showing sliding displacement in anterior-posterior (blue), medial-lateral (red), proximal-distal (green) axes (n=18).

Similar to the level walk, incline walk showed a tear-drop shaped motion path at femoral head Point 7. The path changed direction at $\approx 50\%$ of the gait cycle, indicating a change in sliding velocity at this point (section 6.3.1.3.). Figure 103 shows that the motion path location was on the anterior-posterior arc, as small changes in medial-lateral displacement can be observed. The motion path trajectory ran from a posteriorly and superiorly, before exhibiting anterior and inferior motion to return to the original Point 7 position. The displacement curve suggests that the velocity peak was higher during the second half of the motion, compared to the first half, as the rate of change in displacement is higher.

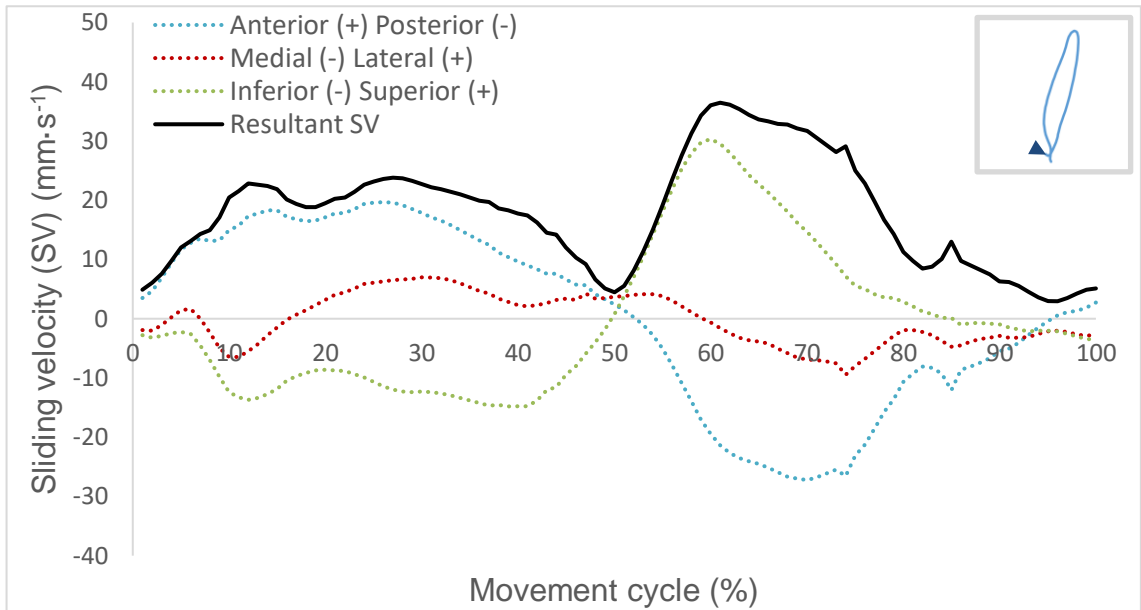


Figure 131. Point 7 (X, Y, Z: 0 mm, 7 mm, 12 mm) for an average incline walk cycle, showing sliding velocity in anterior-posterior (blue), medial-lateral (red), proximal-distal (green) axes (dotted lines). Resultant sliding velocity is shown in black. The corresponding motion path trajectory is shown in the top right corner, with an arrow showing the direction of motion at movement initiation.

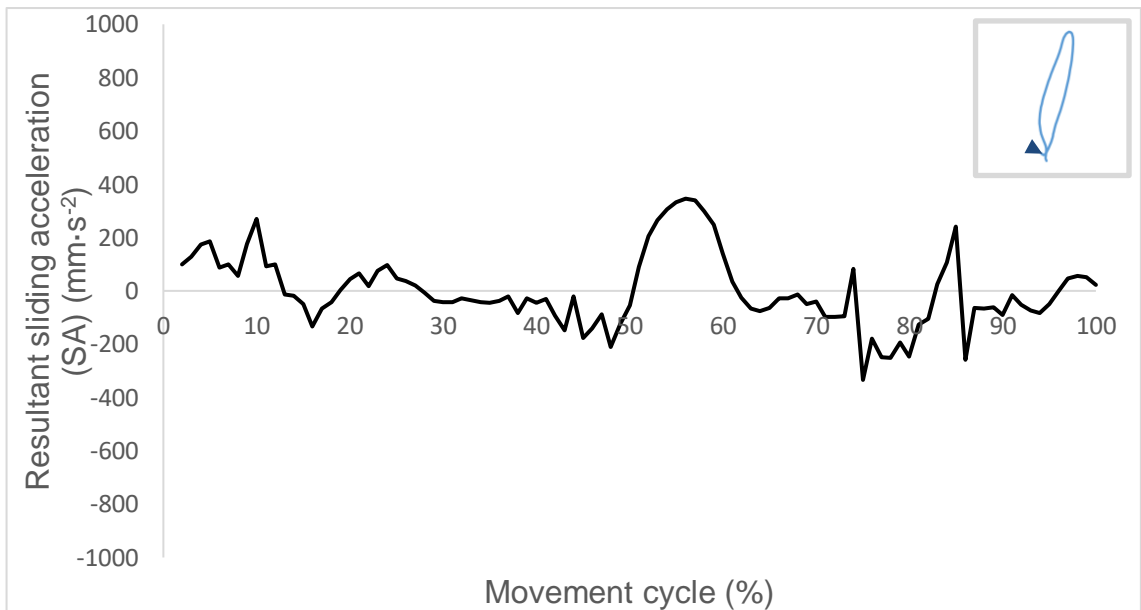


Figure 132. Point 7 (X, Y, Z: 0 mm, 7 mm, 12 mm) for an average incline walk cycle, showing resultant sliding acceleration. The corresponding motion path trajectory is shown in the top right corner, with an arrow showing the direction of motion at movement initiation.

Figure 104 shows the resultant SV occurring between bearing surfaces when walking up a 1:12 ratio ramp. Changes in SV indicate a resultant change in direction of the motion

path. The SV varied throughout the movement, with both peaks and troughs. The most obvious occurred between 50 and 60% of the movement. The SA shows both positive and negative acceleration peaks, with the largest occurring at $\approx 55\%$ of the movement cycle (Figure 105). This peak corresponds to the change in SV.

6.3.4.5. *Decline Walk*

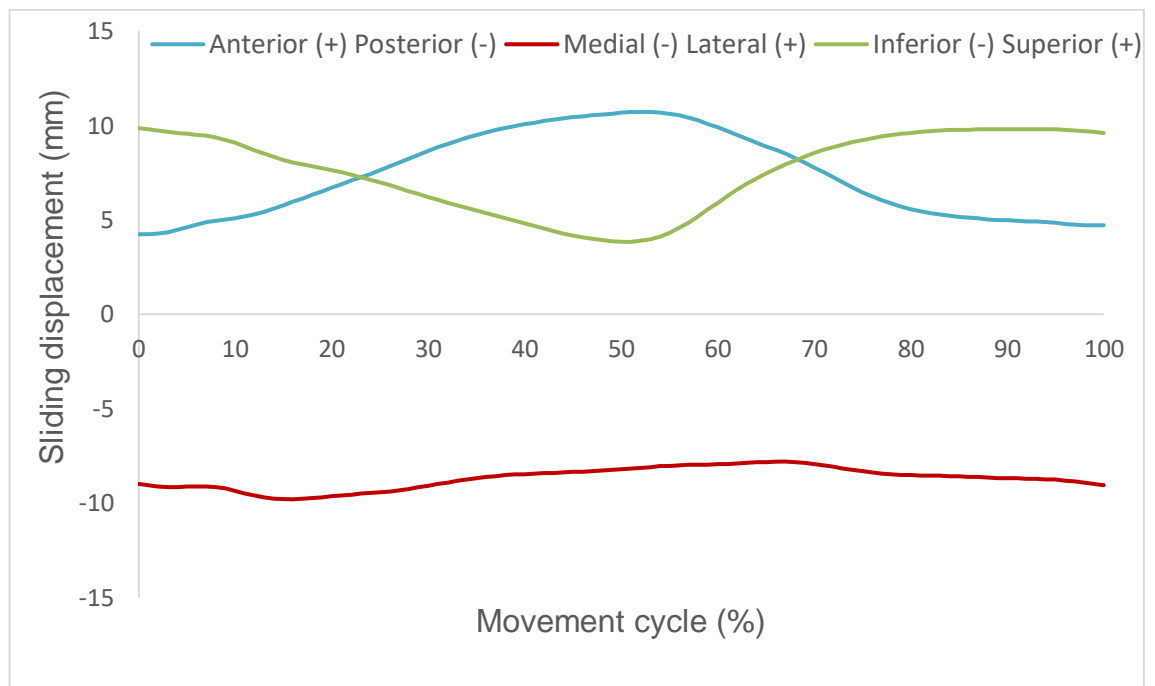


Figure 133. Point 7 (X, Y, Z : 0 mm, 7 mm, 12 mm) for an average decline walk cycle, showing sliding displacement in anterior-posterior (blue), medial-lateral (red), proximal-distal (green) axes ($n=18$).

Decline walk Point 7 showed a similar path to the incline walk (Figure 106). Two obvious changes in displacement occurred (both for anterior-posterior and medial-lateral), with a higher rate of change occurring in the second half of the movement cycle.

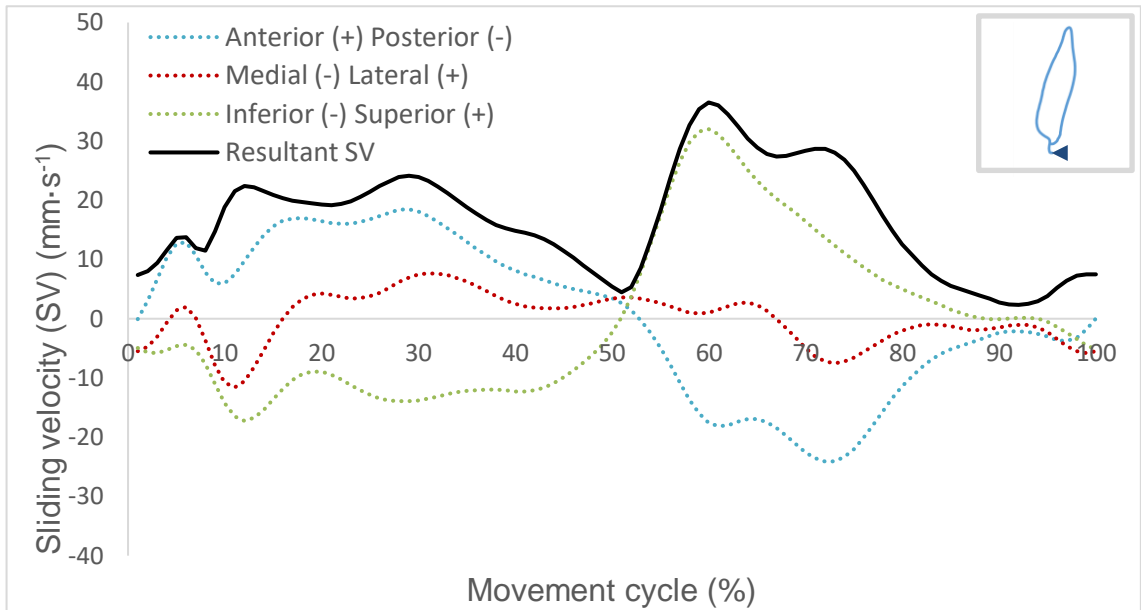


Figure 134. Point 7 (X, Y, Z : 0 mm, 7 mm, 12 mm) for an average decline walk cycle, showing sliding velocity in anterior-posterior (blue), medial-lateral (red), proximal-distal (green) axes (dotted lines). Resultant sliding velocity is shown in black. The corresponding motion path trajectory is shown in the top right corner, with an arrow showing the direction of motion at movement initiation.

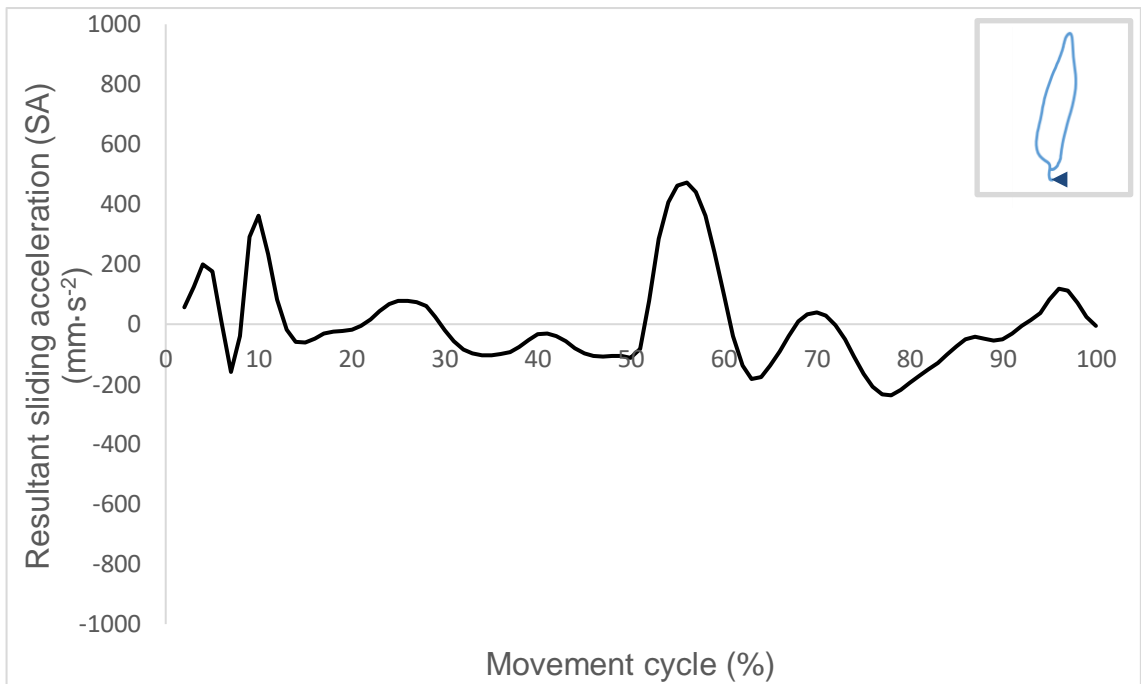


Figure 135. Point 7 (X, Y, Z : 0 mm, 7 mm, 12 mm) for an average decline walk cycle, showing resultant sliding acceleration. The corresponding motion path trajectory is shown in the top right corner, with an arrow showing the direction of motion at movement initiation.

In keeping with the other straight forward walking tasks, decline walk displayed two SV peaks, with the second being of a higher magnitude (Figure 107). The acceleration data showed a number of peaks and troughs, with the instantaneous peak acceleration occurring at $\approx 55\%$. Unlike other straight walking task, decline walk showed a larger SA peak at 10% of the cycle (360ms^{-2}) (Figure 108).

6.3.4.6. *Stand to Sit*

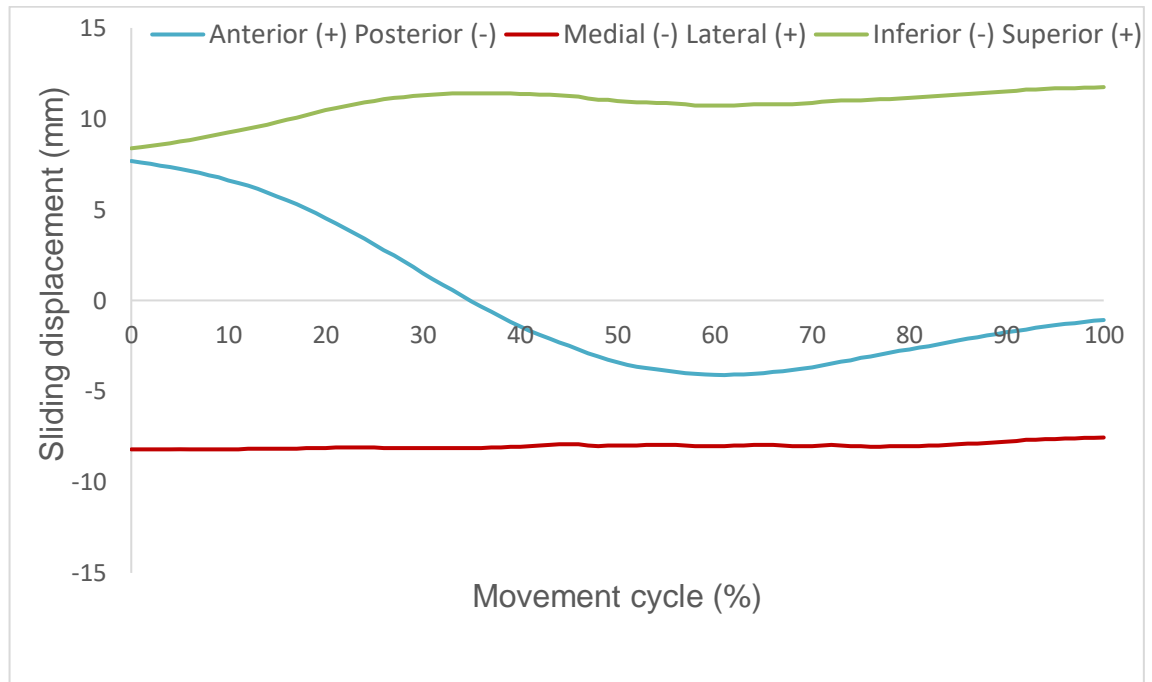


Figure 136. Point 7 (X, Y, Z: 0 mm, 7 mm, 12 mm) for an average stand to sit cycle, showing sliding displacement in anterior-posterior (blue), medial-lateral (red), proximal-distal (green) axes (n=18).

During the stand to sit, femoral head Point 7 showed a linear path running from anterior to posterior. Once sat down in the chair, the anterior-posterior motion path plateaued, followed by a small anterior motion (Figure 109). This caused the 3D path to reverse back over itself (sections 6.3.1.5 and 6.3.1.6.). The path shifted superiorly during the movement and showed little change in the medial-lateral motion (Figure 109).

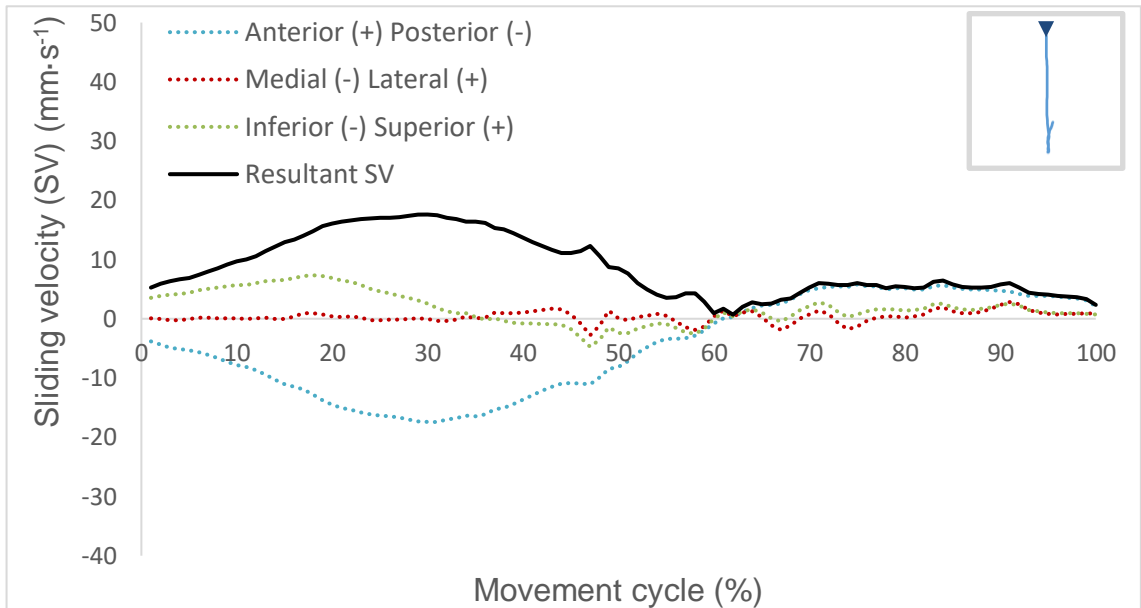


Figure 137. Point 7 (X, Y, Z: 0 mm, 7 mm, 12 mm) for an average stand to sit cycle, showing sliding velocity in anterior-posterior (blue), medial-lateral (red), proximal-distal (green) axes (dotted lines). Resultant sliding velocity is shown in black. The corresponding motion path trajectory is shown in the top right corner, with an arrow showing the direction of motion at movement initiation.

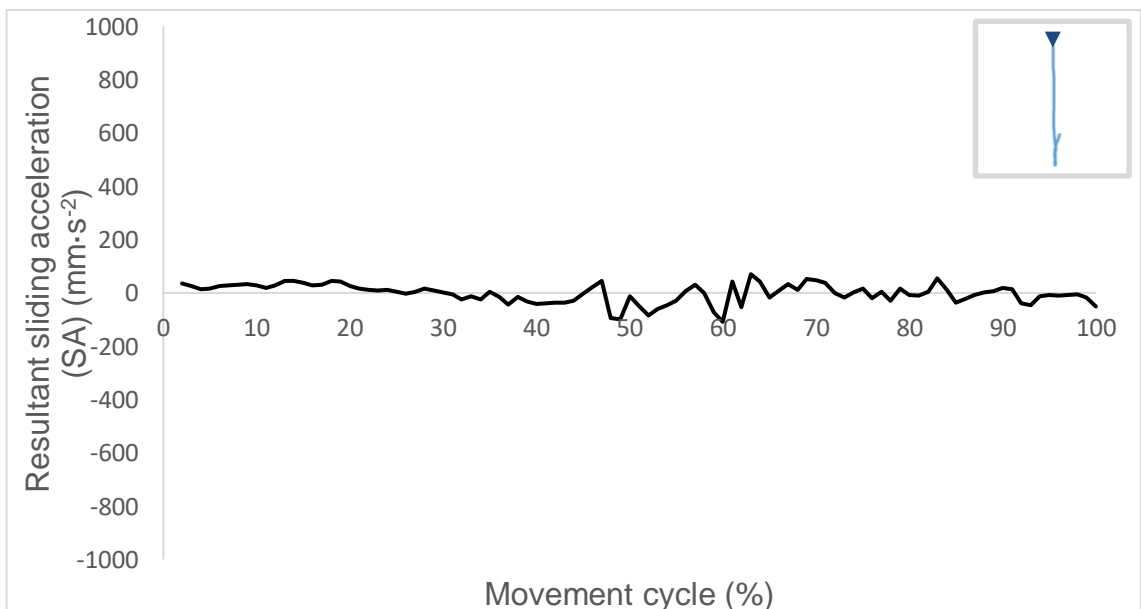


Figure 138. Point 7 (X, Y, Z: 0 mm, 7 mm, 12 mm) for an average stand to sit cycle, showing resultant sliding acceleration. The corresponding motion path trajectory is shown in the top right corner, with an arrow showing the direction of motion at movement initiation.

When standing and seated, SV was low due to being in a static position. The SV increased and peaked during the dynamic movement of sitting down. In spite of this, SA was low throughout, as the rate of change of both displacement and velocity were low (Figure 110 and 111).

6.3.4.7. *Sit to Stand*

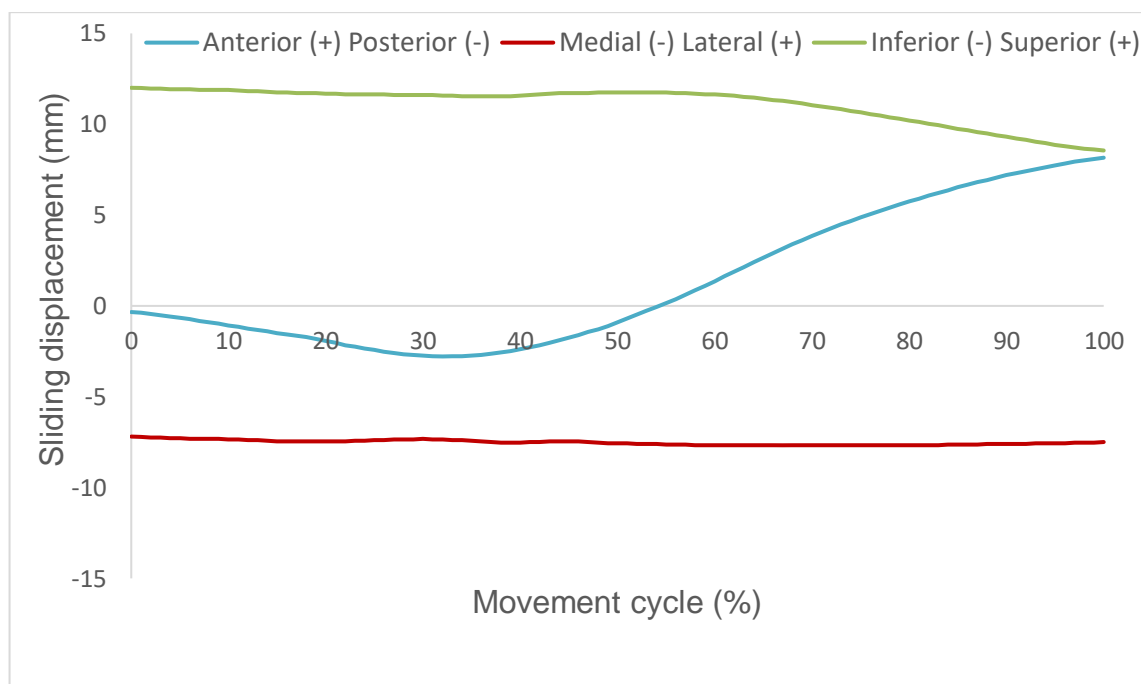


Figure 139. Point 7 (X, Y, Z : 0 mm, 7 mm, 12 mm) for an average sit to stand cycle, showing sliding displacement in anterior-posterior (blue), medial-lateral (red), proximal-distal (green) axes (n=18).

During sit to stand, femoral head Point 7 showed the opposite path to the stand to sit. The linear path initially ran posteriorly before showing a larger displacement in the anterior direction (Figure 112). The path shifted inferiorly during the movement and showed little change in the medial-lateral motion.

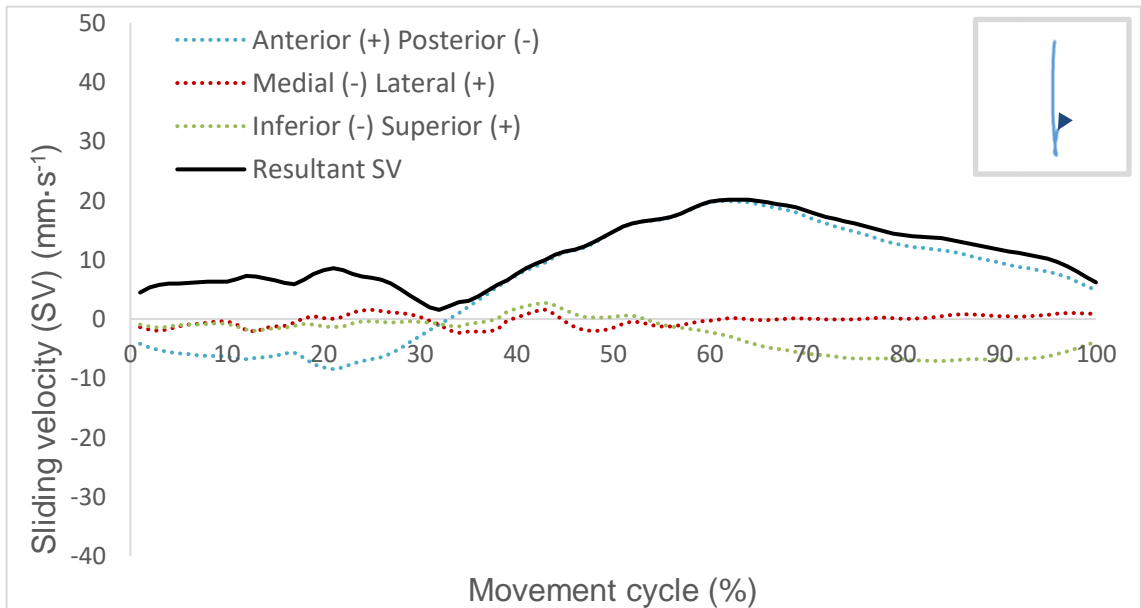


Figure 140. Point 7 (X, Y, Z: 0 mm, 7 mm, 12 mm) for an average sit to stand cycle, showing sliding velocity in anterior-posterior (blue), medial-lateral (red), proximal-distal (green) axes (dotted lines). Resultant sliding velocity is shown in black. The corresponding motion path trajectory is shown in the top right corner, with an arrow showing the direction of motion at movement initiation.

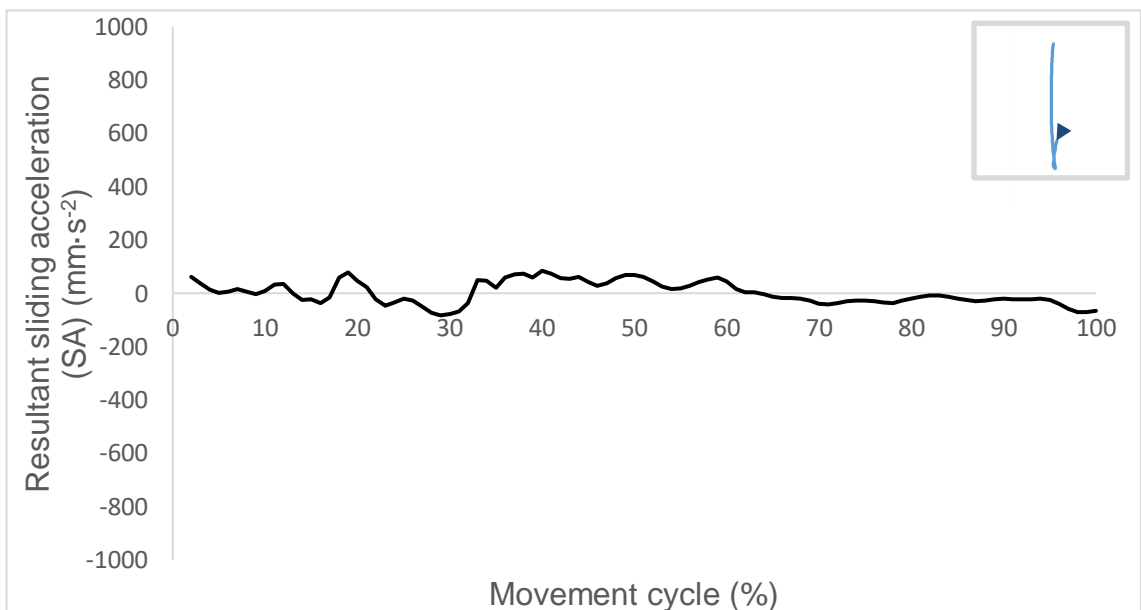


Figure 141. Point 7 (X, Y, Z: 0 mm, 7 mm, 12 mm) for an average sit to stand cycle, showing resultant sliding acceleration. The corresponding motion path trajectory is shown in the top right corner, with an arrow showing the direction of motion at movement initiation.

The SV was low during the static standing and seated position at the stand and end of the movement (Figure 113). During the dynamic standing up, SV peaked. Similarly to the stand to sit, SA was low throughout, as the rate of change of both displacement and velocity was low (Figure 114).

6.3.4.8. *Sit Cross Legged*

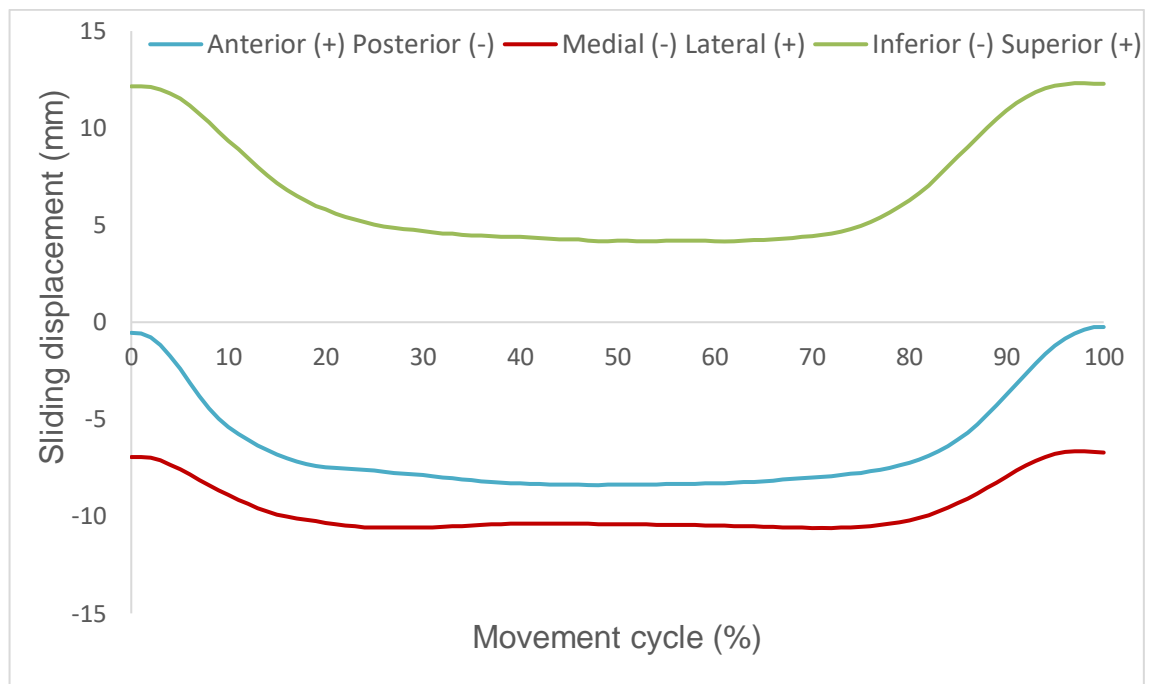


Figure 142. Point 7 (X, Y, Z: 0 mm, 7 mm, 12 mm) for an average sit cross legged cycle, showing sliding displacement in anterior-posterior (blue), medial-lateral (red), proximal-distal (green) axes (n=14).

Figure 115 shows the motion path at Point 7 on the femoral head for sitting and crossing the right leg over the left knee. From an anterior, lateral and superior position, the motion path displaced posteriorly, medially and inferiorly as the right leg was crossed. The path plateaued when the body was static, before returning to the original position when the leg was uncrossed.

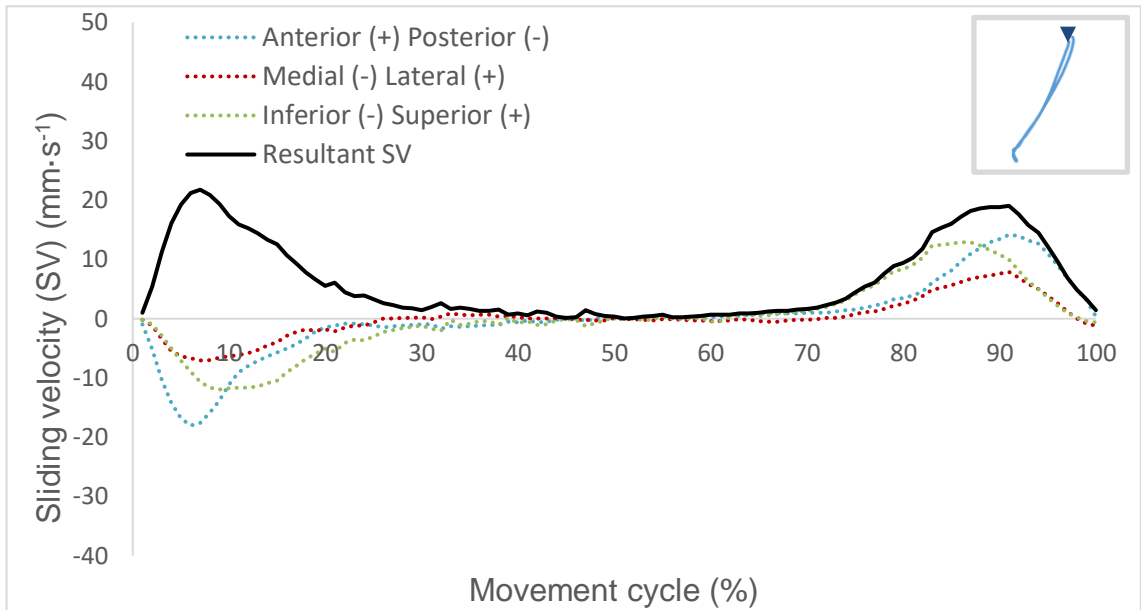


Figure 143. Point 7 (X, Y, Z: 0 mm, 7 mm, 12 mm) for an average sit cross legged cycle, showing sliding velocity in anterior-posterior (blue), medial-lateral (red), proximal-distal (green) axes (dotted lines). Resultant sliding velocity is shown in black. The corresponding motion path trajectory is shown in the top right corner, with an arrow showing the direction of motion at movement initiation.

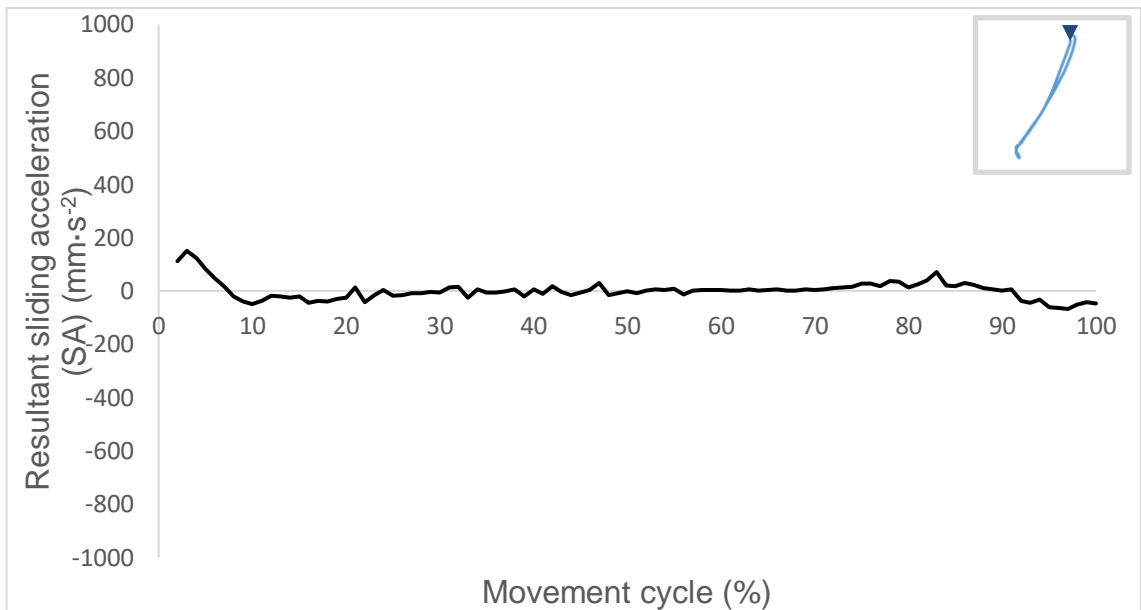


Figure 144. Point 7 (X, Y, Z: 0 mm, 7 mm, 12 mm) for an average sit cross legged cycle, showing resultant sliding acceleration. The corresponding motion path trajectory is shown in the top right corner, with an arrow showing the direction of motion at movement initiation.

The SV peaked when the right leg was crossed and uncrossed (Figure 116). The corresponding SA was low throughout, with a small peak ($200 \text{ mm}\cdot\text{s}^{-2}$) when the right leg was crossed (Figure 117).

6.3.4.9. *Squat*

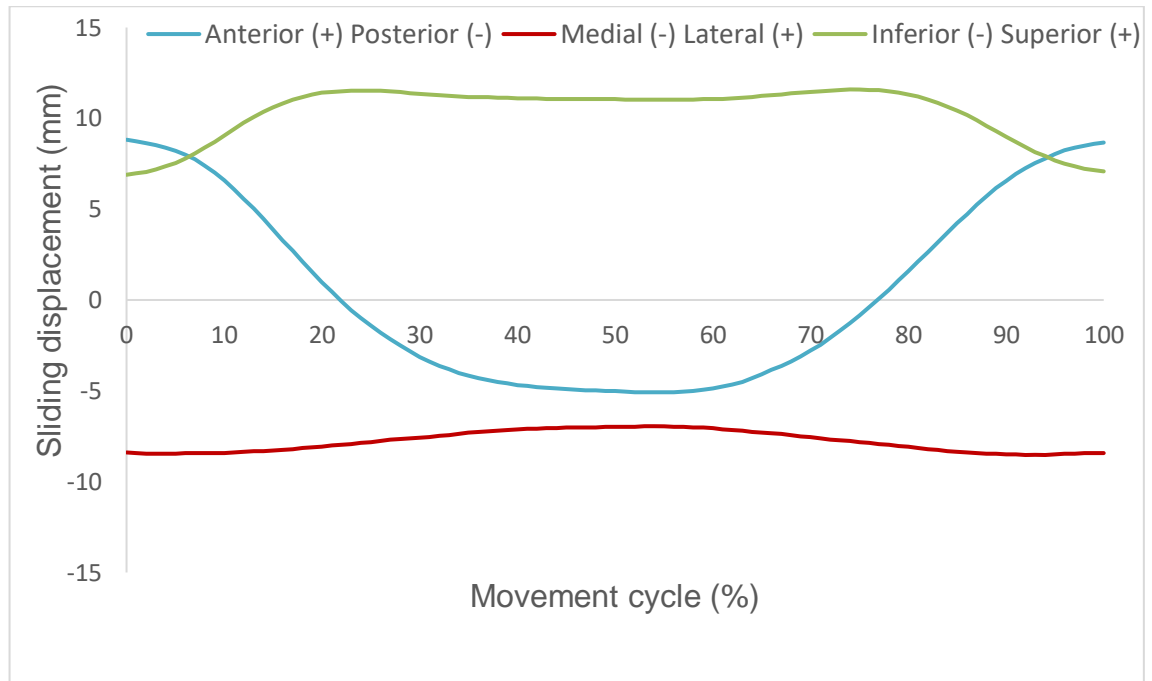


Figure 145. Point 7 (X, Y, Z : 0 mm, 7 mm, 12 mm) for an average squat cycle, showing sliding displacement in anterior-posterior (blue), medial-lateral (red), proximal-distal (green) axes ($n=11$).

Point 7 for the squat displayed a linear path. Initially, when squatting down, the path ran posteriorly and superiorly. After plateauing during the static squat position, the path displaced anteriorly and inferiorly back to a standing position (Figure 118).

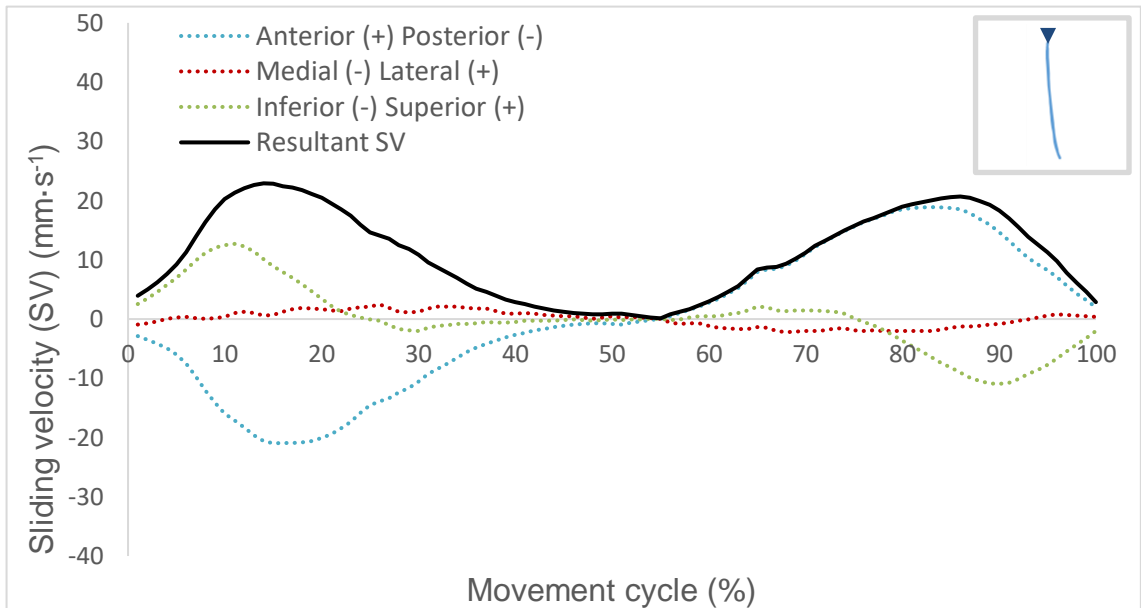


Figure 146. Point 7 (X, Y, Z: 0 mm, 7 mm, 12 mm) for an average squat cycle, showing sliding velocity in anterior-posterior (blue), medial-lateral (red), proximal-distal (green) axes (dotted lines). Resultant sliding velocity is shown in black. The corresponding motion path trajectory is shown in the top right corner, with an arrow showing the direction of motion at movement initiation.

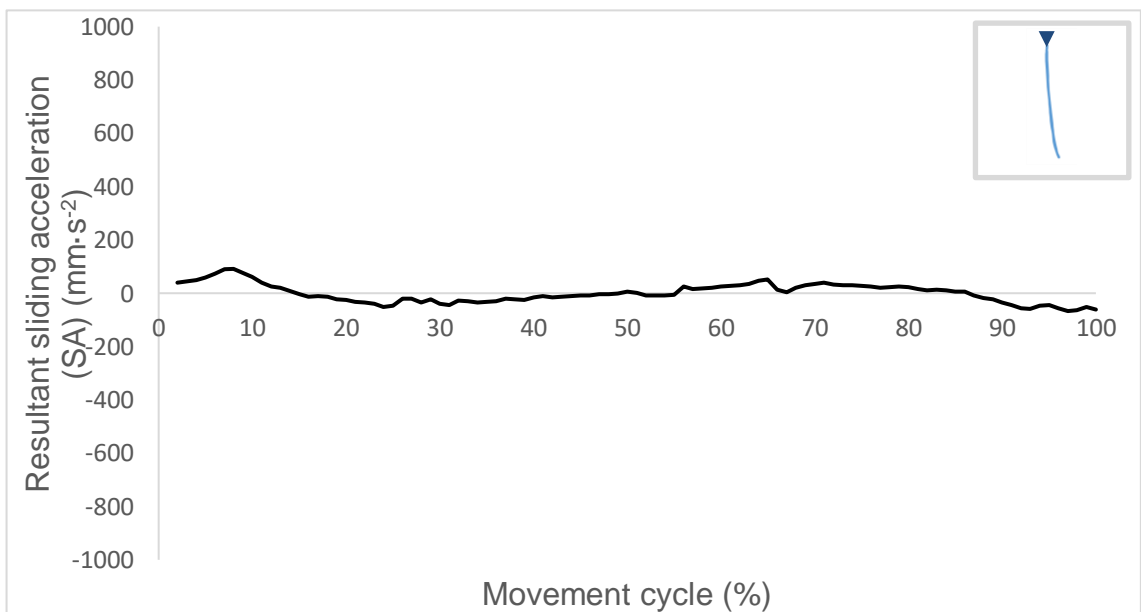


Figure 147. Point 7 (X, Y, Z: 0 mm, 7 mm, 12 mm) for an average squat cycle, showing resultant sliding acceleration. The corresponding motion path trajectory is shown in the top right corner, with an arrow showing the direction of motion at movement initiation.

Two SV peaks were observed: one when squatting down and one when returning up to the standing position (Figure 119). However, the rate of change in displacement and velocity was low, meaning that the SA was low throughout the movement (Figure 120).

6.3.4.10. Stand Reach

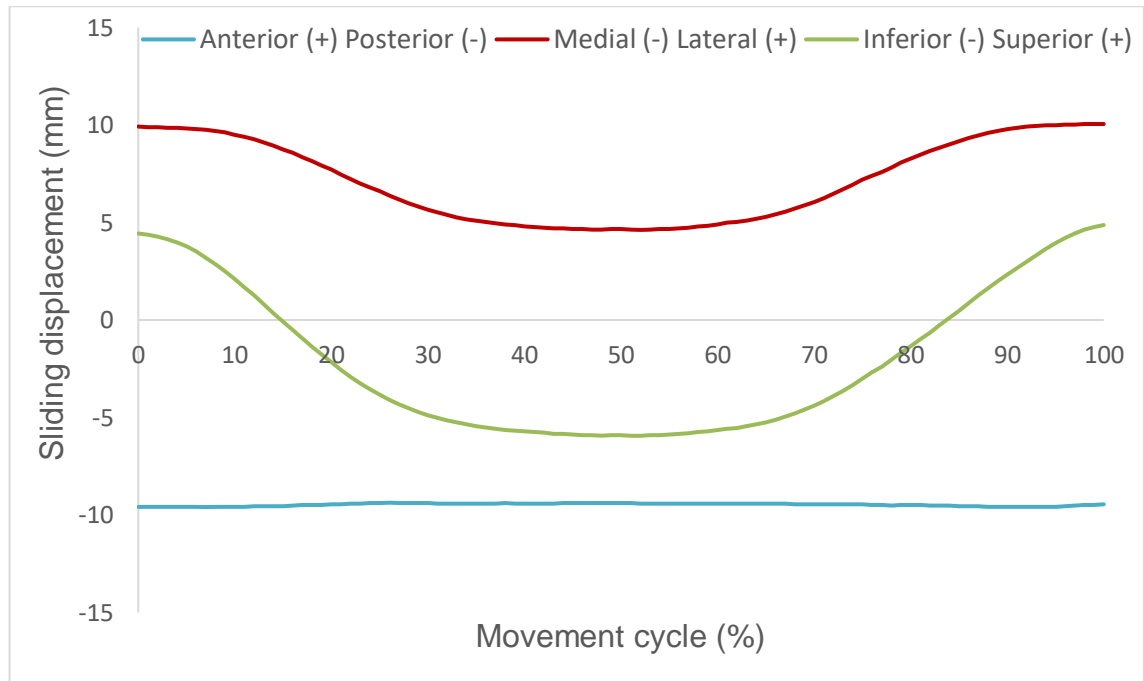


Figure 148. Point 7 (X, Y, Z: 0 mm, 7 mm, 12 mm) for an average stand reach cycle, showing sliding displacement in anterior-posterior (blue), medial-lateral (red), proximal-distal (green) axes (n=11).

Point 7 showed a linear path for the stand reach, initially running posteriorly and inferiorly, before changing direction to run anteriorly and superiorly. The path was mirrored, with a plateau occurring in the middle, when in a static position at full reach (Figure 121).

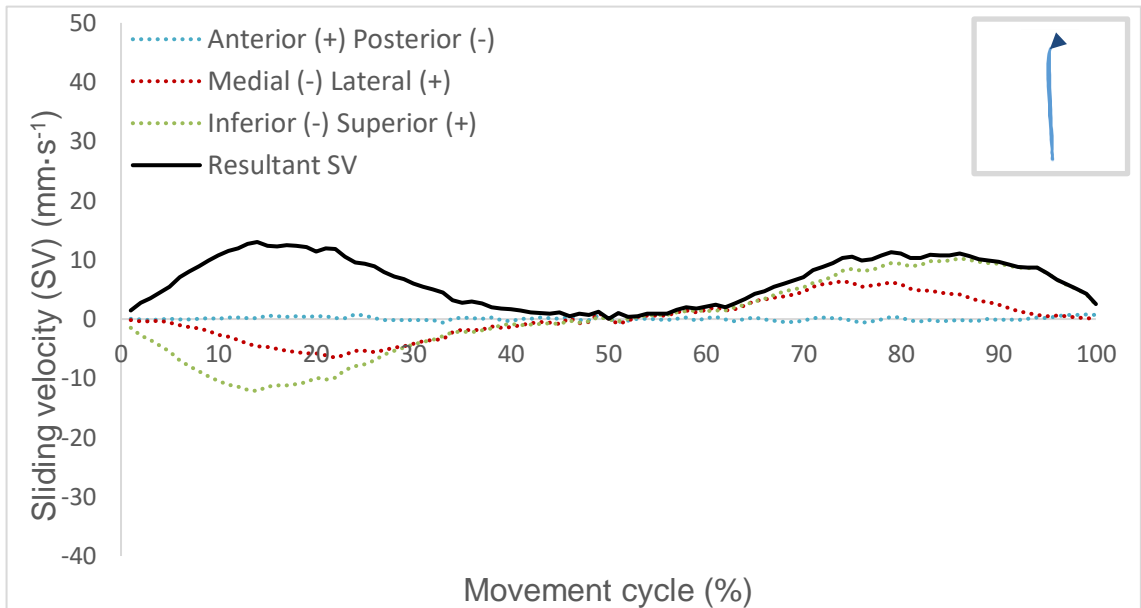


Figure 149. Point 7 (X, Y, Z: 0 mm, 7 mm, 12 mm) for an average stand reach cycle, showing sliding velocity in anterior-posterior (blue), medial-lateral (red), proximal-distal (green) axes (dotted lines). Resultant sliding velocity is shown in black. The corresponding motion path trajectory is shown in the top right corner, with an arrow showing the direction of motion at movement initiation.

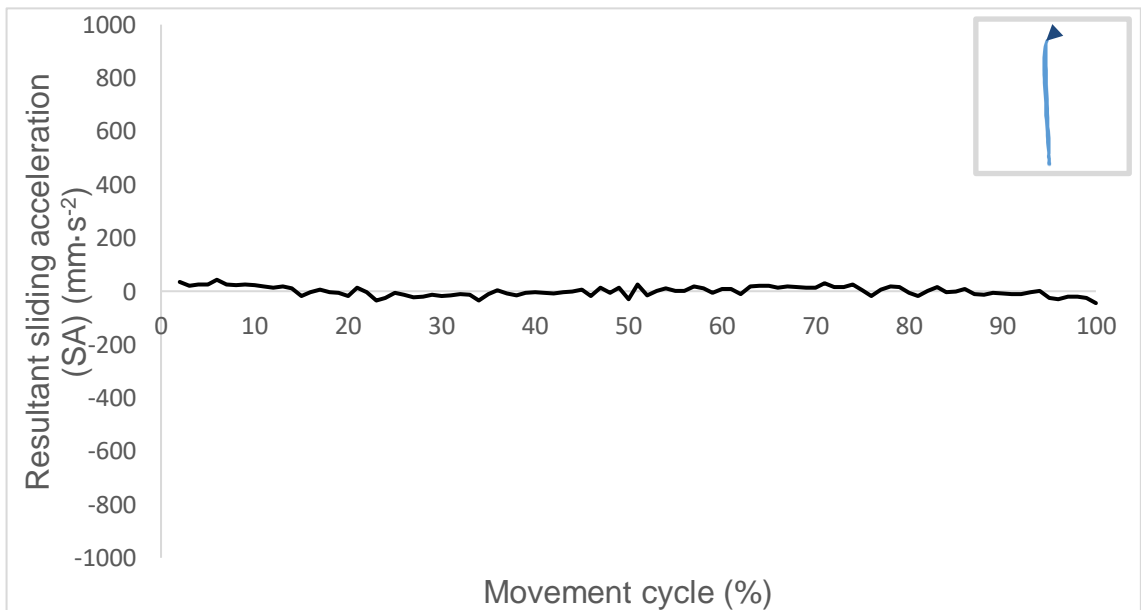


Figure 150. Point 7 (X, Y, Z: 0 mm, 7 mm, 12 mm) for an average stand reach cycle, showing resultant sliding acceleration. The corresponding motion path trajectory is shown in the top right corner, with an arrow showing the direction of motion at movement initiation.

Two SV were observed, occurring during the dynamic motion of flexing and extending at the hip (Figure 122). The rate of change in displacement and velocity was low, resulting in a small SA throughout the movement (Figure 123).

6.3.4.11. *Kneel Reach*

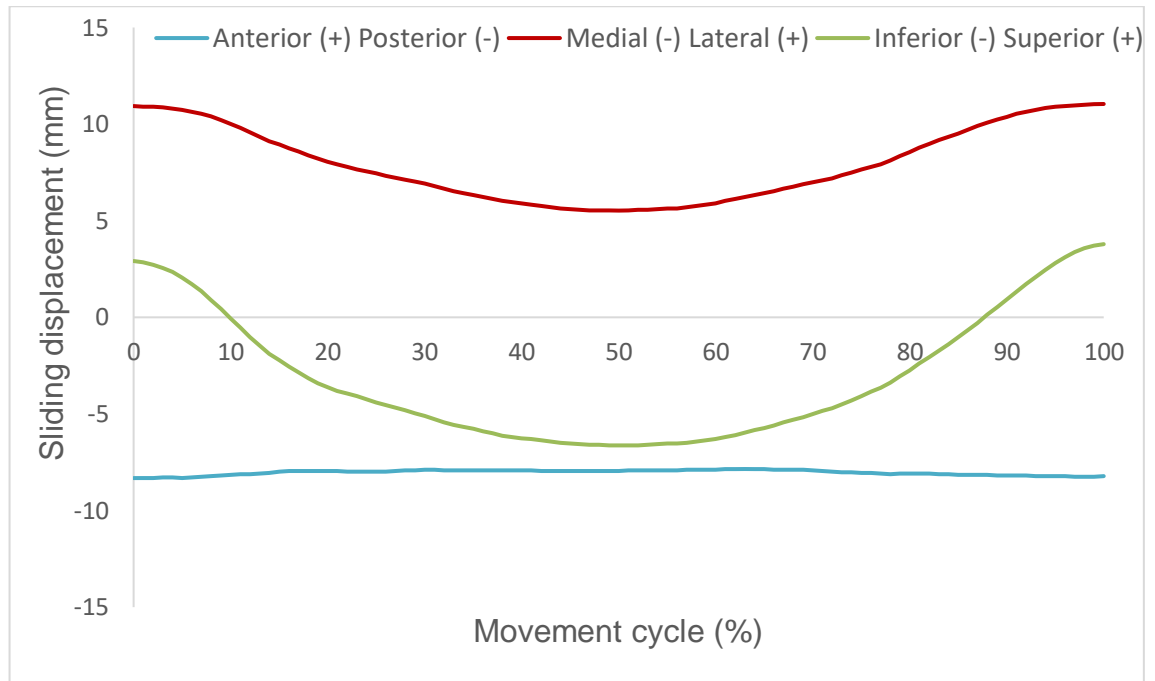


Figure 151. Point 7 (X, Y, Z : 0 mm, 7 mm, 12 mm) for an average kneel reach cycle, showing sliding displacement in anterior-posterior (blue), medial-lateral (red), proximal-distal (green) axes ($n=13$).

When kneeling forwards, much like the standing reach, Point 7 showed a linear path with a 180° change in direction at 50% of the cycle (Figure 124).

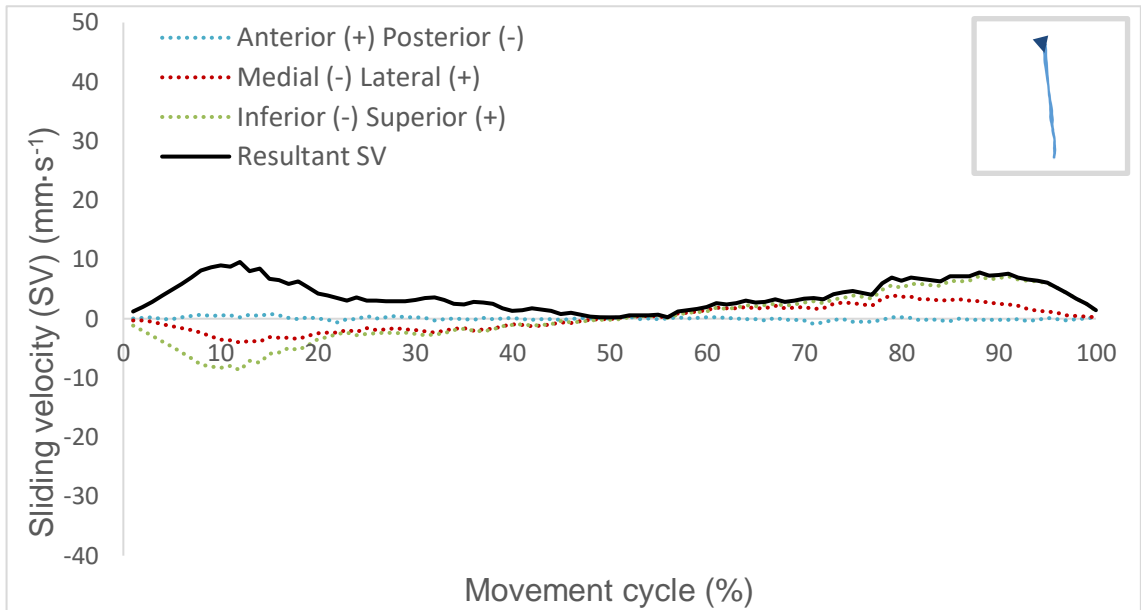


Figure 152. Point 7 (X, Y, Z : 0 mm, 7 mm, 12 mm) for an average kneel reach cycle, showing sliding velocity in anterior-posterior (blue), medial-lateral (red), proximal-distal (green) axes (dotted lines). Resultant sliding velocity is shown in black. The corresponding motion path trajectory is shown in the top right corner, with an arrow showing the direction of motion at movement initiation.

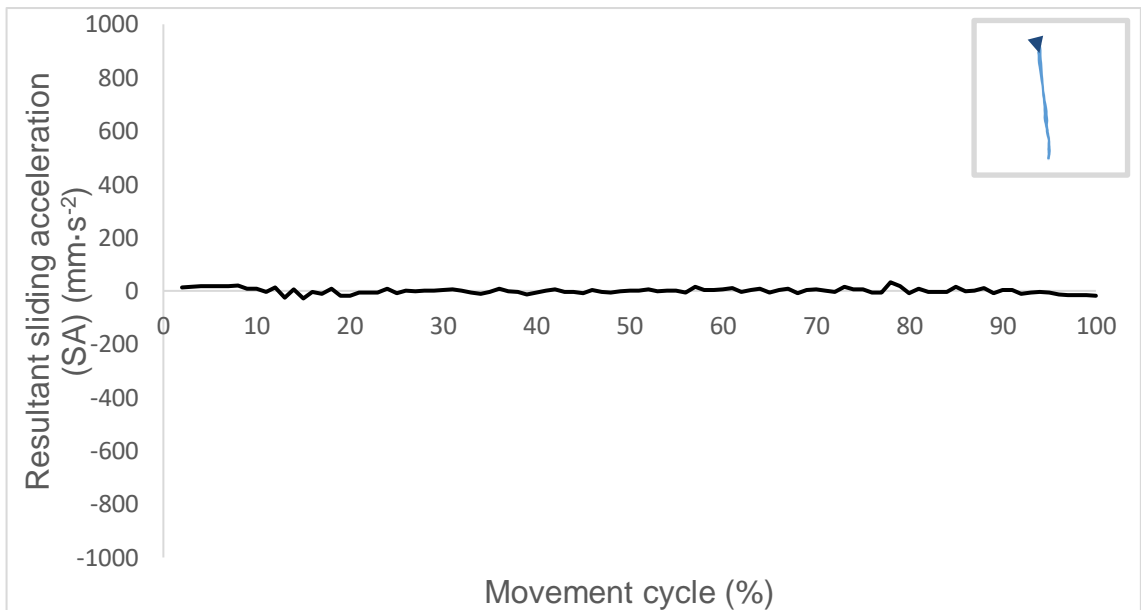


Figure 153. Point 7 (X, Y, Z : 0 mm, 7 mm, 12 mm) for an average kneel reach cycle, showing resultant sliding acceleration. The corresponding motion path trajectory is shown in the top right corner, with an arrow showing the direction of motion at movement initiation.

Two small SV peaks were seen during the dynamic movement of the kneel reach, however the changes in motion were subtle, thus the SA was low throughout (Figures 125 and 126).

6.3.4.12. *Lunge*

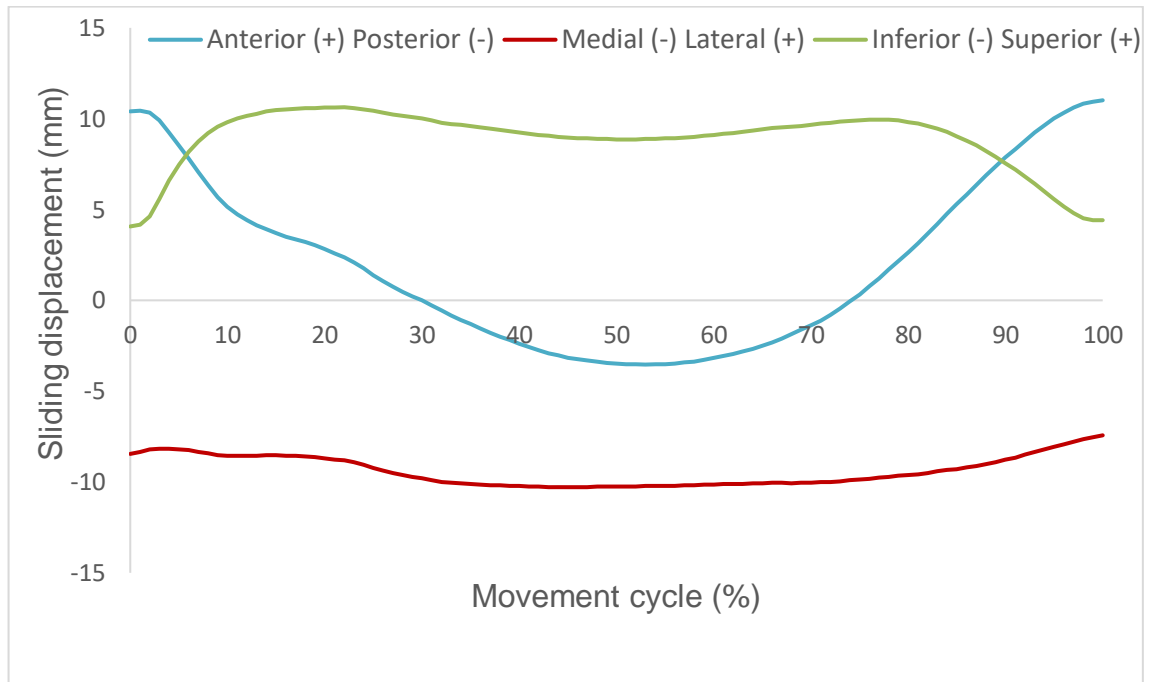


Figure 154. Point 7 (X, Y, Z: 0 mm, 7 mm, 12 mm) for an average lunge cycle, showing sliding displacement in anterior-posterior (blue), medial-lateral (red), proximal-distal (green) axes (n=17).

During the lunge, Point 7 displayed a stretched tear drop shape (section 6.3.1.11.). When lunging down, the path displaced posteriorly and superiorly on the acetabular cup (Figure 127). After a short plateau at the deepest position of the lunge, the path displaced anteriorly and inferiorly, when stepping up and out of the lunge. The path ended at approximately the same location as the start position. A steep posterior displacement was observed between 0 and 10% of the cycle. Following this, the rate of change in the anterior-posterior axis became more gradual.

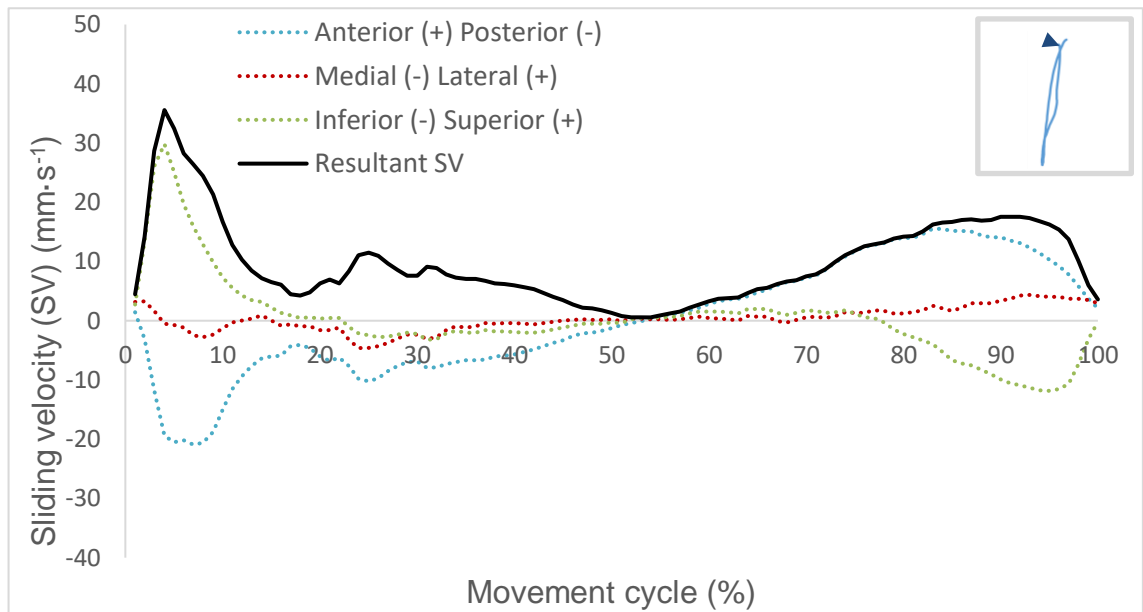


Figure 155. Point 7 (X, Y, Z : 0 mm, 7 mm, 12 mm) for an average lunge cycle, showing sliding velocity in anterior-posterior (blue), medial-lateral (red), proximal-distal (green) axes (dotted lines). Resultant sliding velocity is shown in black. The corresponding motion path trajectory is shown in the top right corner, with an arrow showing the direction of motion at movement initiation.

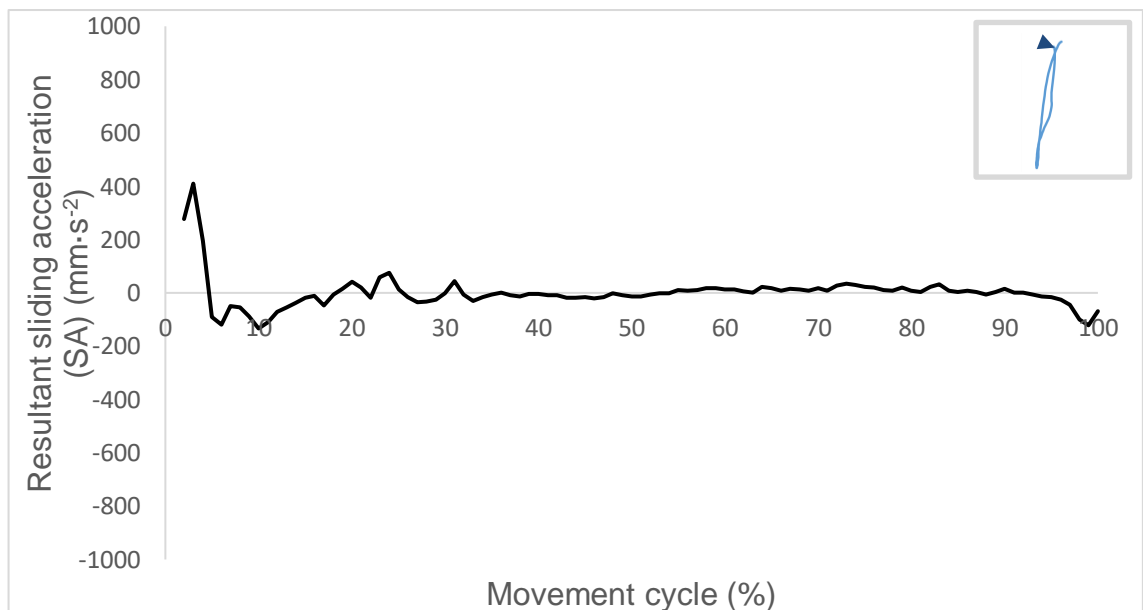


Figure 156. Point 7 (X, Y, Z : 0 mm, 7 mm, 12 mm) for an average lunge cycle, showing resultant sliding acceleration. The corresponding motion path trajectory is shown in the top right corner, with an arrow showing the direction of motion at movement initiation.

Two SV peaks were observed during the lunge (Figure 128). A larger and steeper peak was seen within the first 10% of the movement ($35 \text{ mm}\cdot\text{s}^{-1}$) and a smaller, shallower peak

was seen during the last 10% of the movement ($17 \text{ mm}\cdot\text{s}^{-1}$). The SA showed a large peak within the first 10% of the cycle ($410 \text{ mm}\cdot\text{s}^{-2}$), followed by low accelerations throughout the remainder of the movement cycle (Figure 129).

6.3.4.13. *Golf Swing*

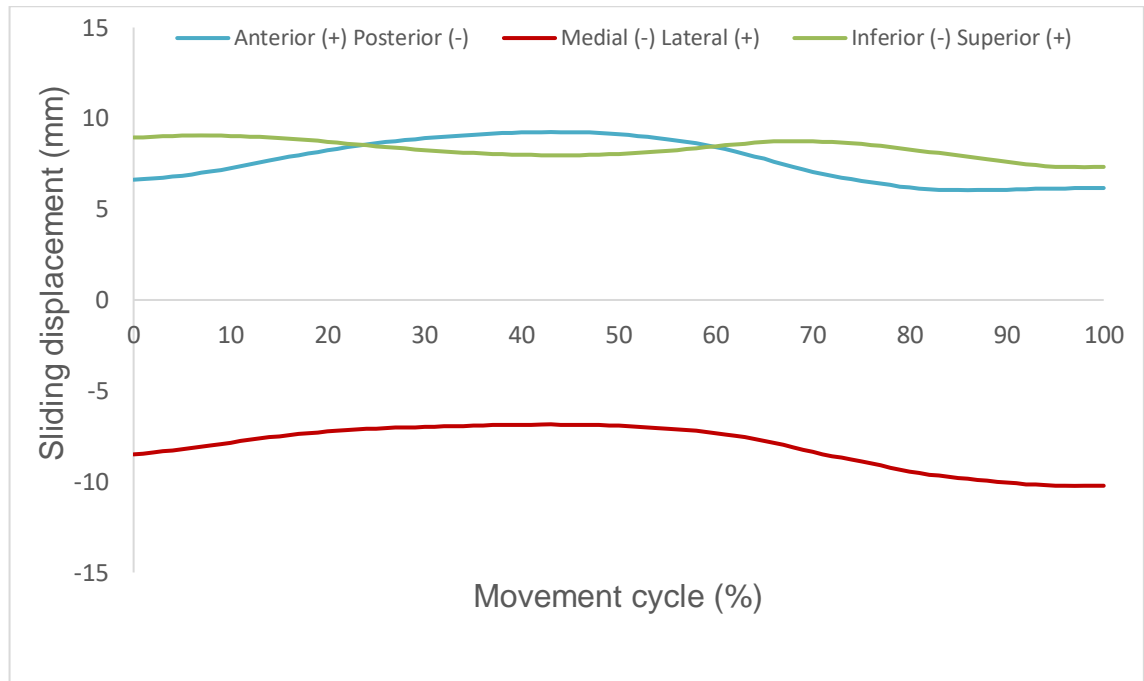


Figure 157. Point 7 (X, Y, Z : 0 mm, 7 mm, 12 mm) for an average golf swing, showing sliding displacement in anterior-posterior (blue), medial-lateral (red), proximal-distal (green) axes ($n=18$).

During the golf swing, Point 7 showed a curved linear motion path. Small, gradual displacements were seen in each of the three axes (Figure 130).

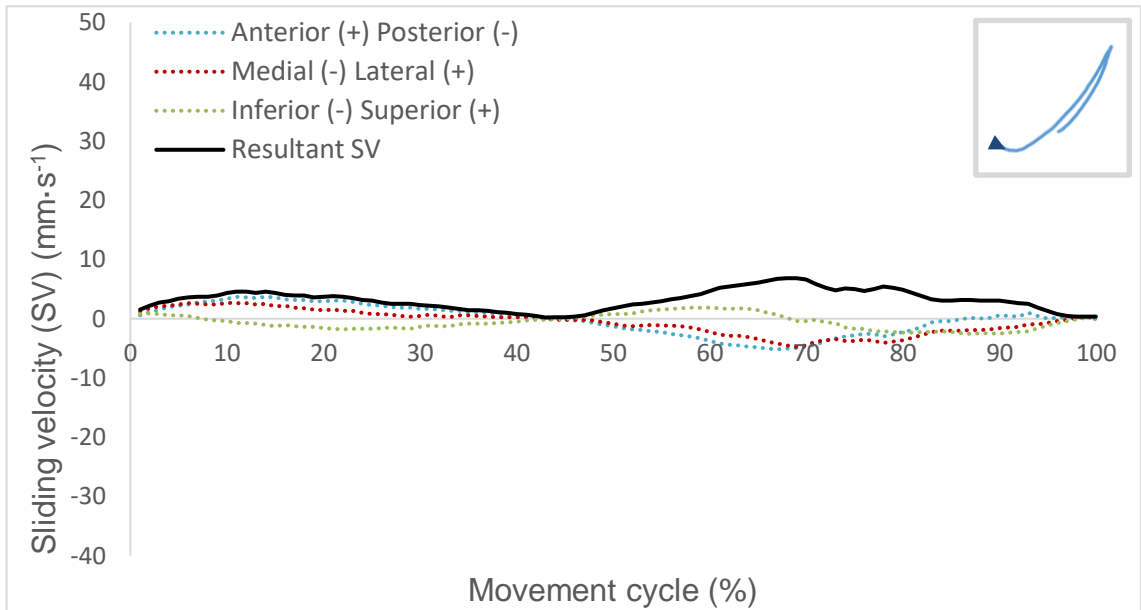


Figure 158. Point 7 (X, Y, Z : 0 mm, 7 mm, 12 mm) for an average golf swing cycle, showing sliding velocity in anterior-posterior (blue), medial-lateral (red), proximal-distal (green) axes (dotted lines). Resultant sliding velocity is shown in black. The corresponding motion path trajectory is shown in the top right corner, with an arrow showing the direction of motion at movement initiation.

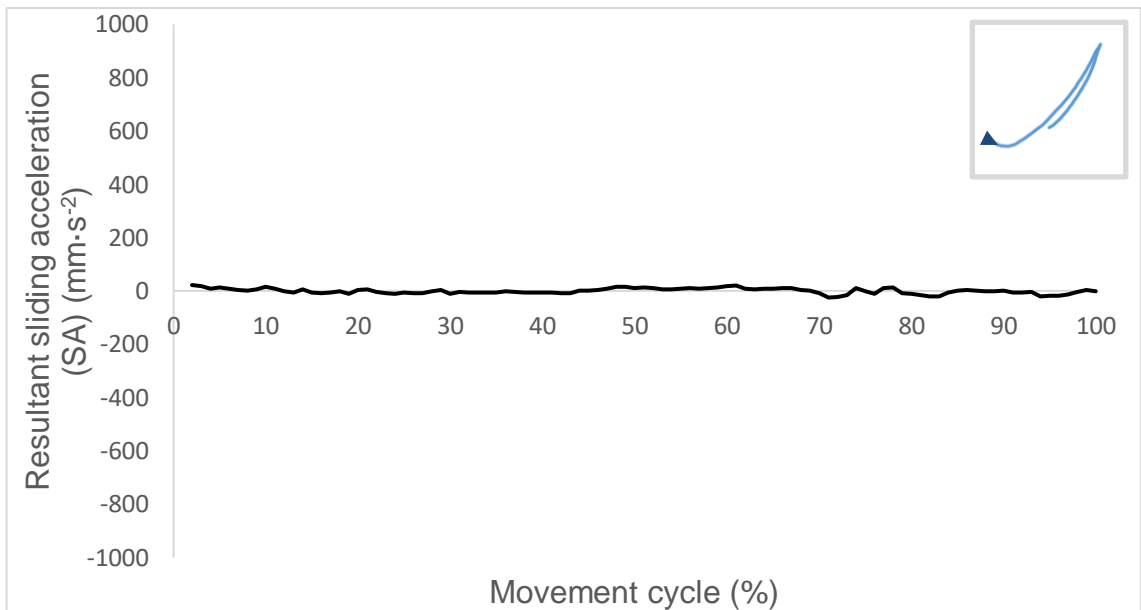


Figure 159. Point 7 (X, Y, Z : 0 mm, 7 mm, 12 mm) for an average golf cycle, showing resultant sliding acceleration. The corresponding motion path trajectory is shown in the top right corner, with an arrow showing the direction of motion at movement initiation.

Two small SV peaks were observed during the golf swing. These small velocity peaks were shallow, thus leading to a slow SA throughout the movement cycle (Figure 131 and 132).

6.3.4.14. Cycle

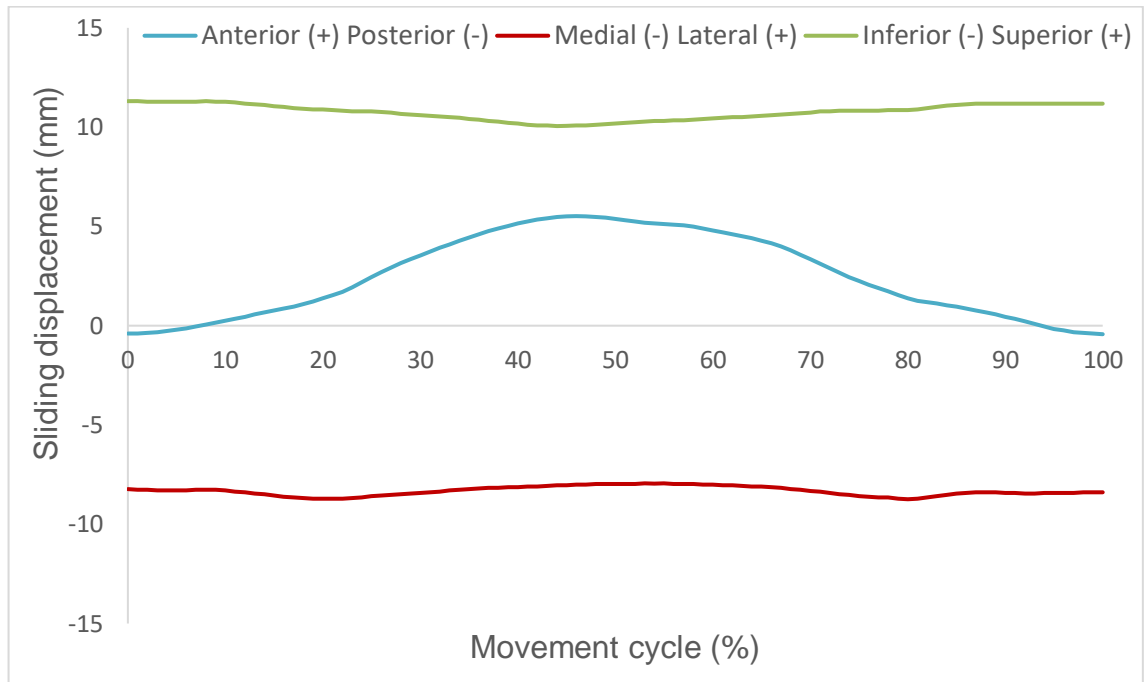


Figure 160. Point 7 (X, Y, Z : 0 mm, 7 mm, 12 mm) for an average cycle, showing sliding displacement in anterior-posterior (blue), medial-lateral (red), proximal-distal (green) axes ($n=10$).

The motion path at point 7, during the cycle, showed a linear pattern with a thin figure-8 (Figure 133). As the foot pedalled down to the ground, the motion path displaced anteriorly. From the pedals lowest position and up to the initial position, the path changed direction and displaced posteriorly on the femoral head. Small changes were seen in medial-lateral and proximal-distal motions.

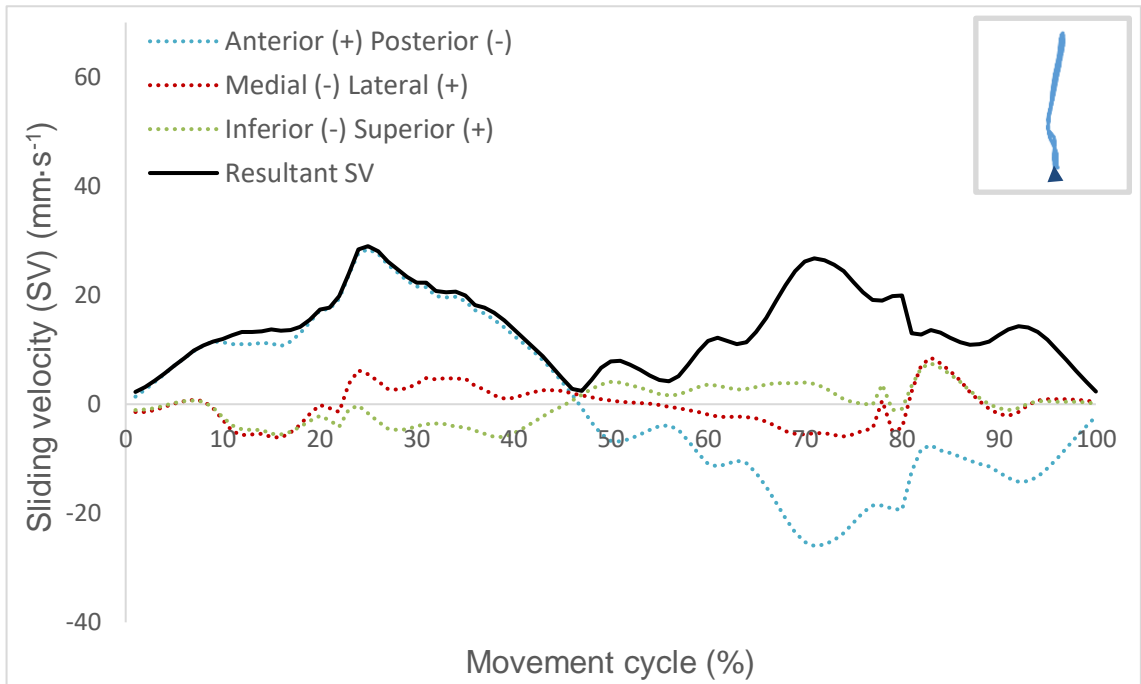


Figure 161. Point 7 (X, Y, Z : 0 mm, 7 mm, 12 mm) for an average cycle, showing resultant sliding acceleration. The corresponding motion path trajectory is shown in the top right corner, with an arrow showing the direction of motion at movement initiation.

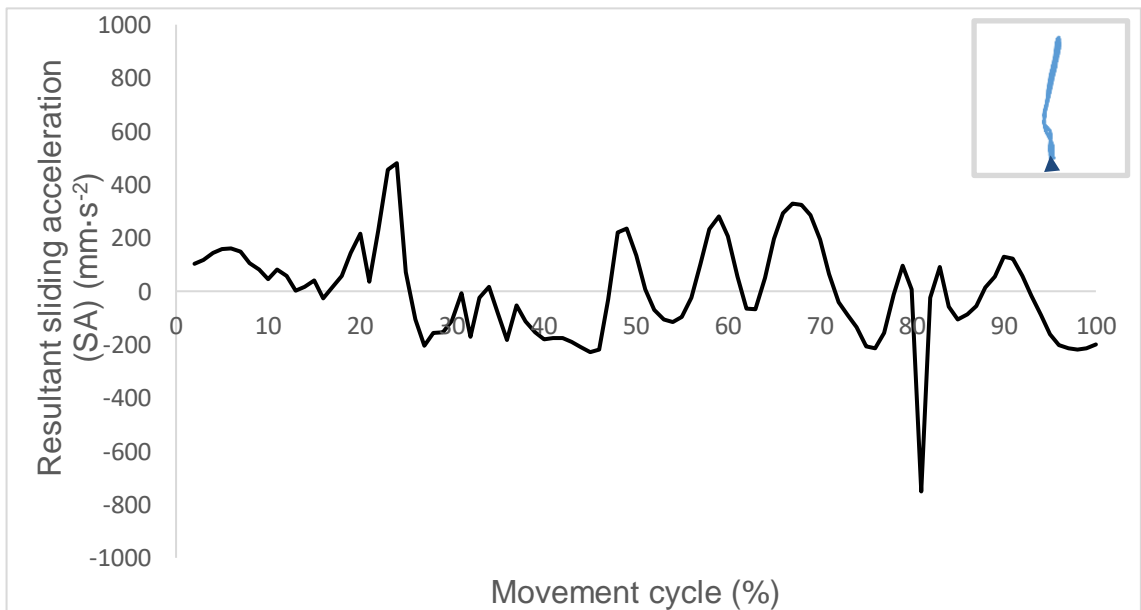


Figure 162. Point 7 (X, Y, Z : 0 mm, 7 mm, 12 mm) for an average cycle, showing sliding velocity in anterior-posterior (blue), medial-lateral (red), proximal-distal (green) axes (dotted lines). Resultant sliding velocity is shown in black. The corresponding motion path trajectory is shown in the top right corner, with an arrow showing the direction of motion at movement initiation.

Two SV peaks were seen during the cycle, with one in the first half and one in the second half. Both peaked at approximately $30 \text{ mm}\cdot\text{s}^{-1}$ (Figure 134). The resulting SA curve

showed a positive peak during the first half of the cycle ($480 \text{ mm}\cdot\text{s}^{-2}$) and a negative peak during the second half ($751 \text{ mm}\cdot\text{s}^{-2}$) (Figure 135).

6.3.4.15. Peak Sliding Accelerations

Peak sliding accelerations (SAs) are shown for each activity (Figure 136). A peak SA indicates a change sliding velocity (SV) and thus a change in sliding displacement (SD). A high SA therefore suggests a point in which the motion path changes direction and may put the surface at risk of cross-shear wear. The higher the peak SA, the steeper the angular change in the motion path.

A second benefit of SA analysis is that, when considering the synovial joint, prolonged periods of slow SV and SA coupled with loading may cause lubrication starvation. Thus, low SA may indicate activities in which the fluid is drained from the joint, friction is increased and potential wear ensued.

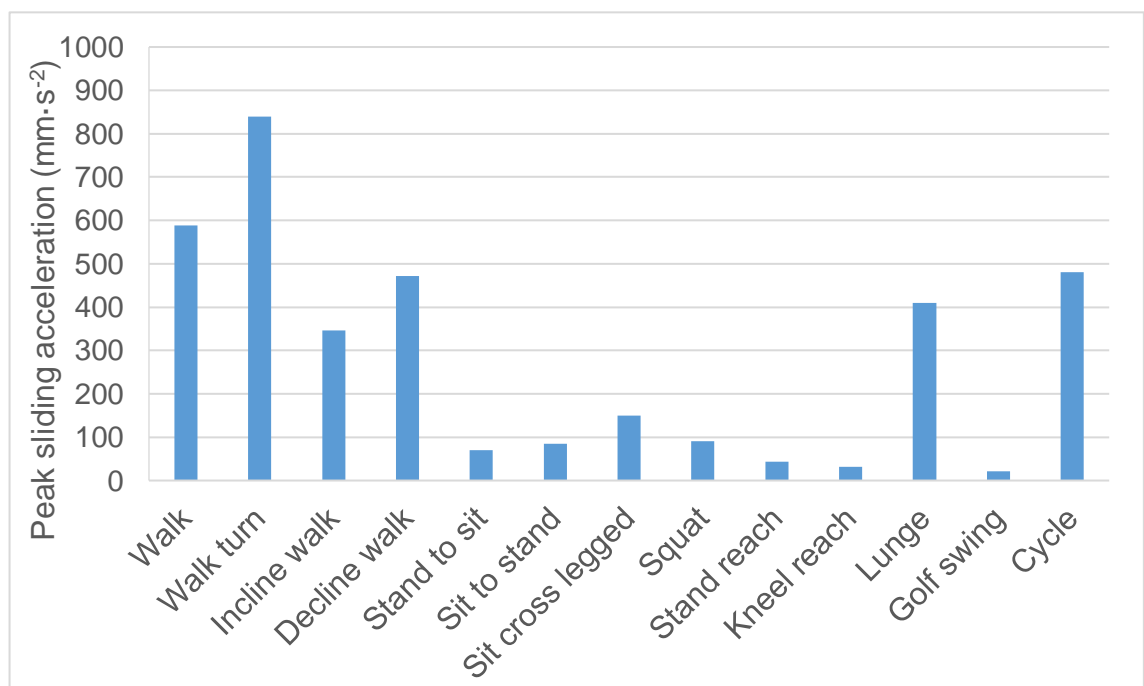


Figure 163. Peak sliding accelerations, between bearing surfaces at the hip, for a range of activities.

Walk turn showed the highest peak acceleration ($840 \text{ mm}\cdot\text{s}^{-2}$) and was closely followed by the walk ($589 \text{ mm}\cdot\text{s}^{-2}$). Cycle, decline walk, lunge and incline walk showed the next highest peak accelerations and were all above $300 \text{ mm}\cdot\text{s}^{-2}$. Sit cross legged showed a peak SA of $151 \text{ mm}\cdot\text{s}^{-2}$. Stand to sit, sit to stand and squat all showed peak SA below $100 \text{ mm}\cdot\text{s}^{-2}$, whereas stand reach, kneel reach and golf swing were all below $50 \text{ mm}\cdot\text{s}^{-2}$. The golf swing showed the lowest peak hip SA at just $22 \text{ mm}\cdot\text{s}^{-2}$.

6.3.5. Variation and Age

Aspect ratios (ARs) were calculated by dividing the motion path height, by the perpendicular width. A lower AR indicates a more rounded or elliptical motion path, with potentially excessive cross-shear motion between surfaces. A higher AR indicates a more linear motion path trajectory with minimal cross-shear (section 6.3.1.).

Table 20. Mean aspect ratio of motion path trajectories, for groups under and over 55 years of age. The difference between groups is reported, with discrepancies more than 1 highlighted in bold. Significance is reported from an equal variance, two-tailed T-test, with a confidence limit of 0.05.

Aspect Ratio	Under 55 years	Over 55 years	Difference	Significance ($P < 0.05$)
Walk	3.1	3.5	0.4	×
Walk turn	3.0	3.1	0.1	×
Incline walk	3.3	3.3	0.0	×
Decline walk	2.6	2.8	0.2	×
Stand to sit	8.8	7.3	1.5	×
Sit to stand	10.5	9.0	1.5	×
Sit cross legged	4.2	4.2	0.0	×
Squat	9.6	9.1	0.5	×
Stand reach	9.7	7.6	2.1	×
Kneel reach	8.4	8.4	0.0	×
Lunge	4.1	3.8	0.3	×
Golf swing	4.8	4.0	0.8	×
Cycle	5.1	7.0	1.9	×

Stand to sit, sit to stand, stand reach and cycle all showed a difference of more than 1, when mean motion path ARs were compared between age groups (Table 19). Incline walk, sit cross legged and kneel reach showed no difference between ARs for the two groups. The remaining five activities showed small differences, ranging from 0.1 (walk turn) to 0.8 (golf swing). It is noteworthy that none of the activities showed a significant difference when tested with an equal variance, two-tailed T-Test. This may be due to sample size, but more likely, suggests that a true difference does not exist between ARs for the two age groups.

6.3.6. Variation and Gender

Aspect ratios (ARs) (motion path height divided by perpendicular width) were compared between genders. Higher ARs indicate more linear sliding and thus lower cross-shear, whereas ARs closer to 1 indicate more elliptical sliding with higher cross-shear (section 6.3.1.).

Table 21 Mean motion path aspect ratios, for male and female groups. The difference between groups is reported, with discrepancies more than 1 highlighted in bold. Significance is reported from an equal variance, two-tailed T-test, with a confidence limit of 0.05.

Aspect Ratio	Male	Female	Difference	Significance ($P<0.05$)
Walk	3.3	3.1	0.2	×
Walk turn	3.0	3.1	0.1	×
Incline walk	3.1	3.5	0.3	×
Decline walk	2.5	2.7	0.2	×
Stand to sit	9.1	8.3	0.9	×
Sit to stand	9.3	11.0	1.7	×
Sit cross legged	4.3	4.1	0.2	×
Squat	10.1	9.1	1.0	×
Stand reach	9.3	9.3	0.0	×
Kneel reach	6.6	9.9	3.3	✓
Lunge	4.3	3.7	0.6	✓
Golf swing	4.5	4.6	0.1	×
Cycle	5.4	5.5	0.1	×

Mean ARs were higher for males than females in five of the thirteen activities (Table 21). Females resulted a higher AR in seven activities, whereas there was no mean difference for one activity. Three activities showed a mean difference of over 1 (sit to stand, squat and kneel reach). Just two activities demonstrated a statistical difference to a confidence limit of 0.05 (kneel reach and lunge). Activities showing a mean difference of ≥ 1 and/or a statistical difference between genders, were compared for hip kinematics in section 4.8.2..

6.3.7. Edge Loading

Both the magnitude and position of hip force vectors will influence the wear of a polyethylene acetabular cup (Bergmann et al., 2001; Li et al., 2014). The resultant hip reaction force (HRF) was calculated, using the three force vectors acting on the hip (anterior-posterior, medial-lateral and inferior-superior). This was normalised to proportion of body weight (*p*BWT). Peak resultant HRFs were identified for each activity and the corresponding orientation was calculated. The corresponding hip angle (pelvis relative to the thigh) and time within the movement cycle (%) was also noted alongside each peak force. A final calculation included in this section is the contact area for peak resultant HRFs between the femoral head and the acetabular cup. This was calculated using the Hertz contact equation – more detail is shown for these calculations within section 6.2.5..

Within this section, peak HRF magnitudes, orientations, contact areas and corresponding times within the movement cycle are tabulated for activities (Table 18). For each activity, force vectors and hip angular positions were modelled within SolidWorks (SolidWorks 2017, Dassault Systèmes SolidWorks Corporation, Waltham, MA, USA) to aid visualisation of potential edge loading at the joint (Figures 149 to 157).

Table 22. Peak resultant hip reaction force (proportional to body weight) and vector orientation (relative to X: medial-lateral; Y: anterior-posterior; Z: proximal-distal axes) are shown for activities. Corresponding hip angle and time within the movement cycle are also shown.

	Peak resultant reaction force (Vector angle: X,Y,Z)	Hip angle (X, Y, Z)	Contact area diameter (cup coverage %)	Movement cycle (%)
Walk	3.1 (110°, 82°, 22°)	(-5°, 5°, 6°)	12.75 mm (41%)	46
Walk turn	4.1 (113°, 80°, 25°)	(28°, -1°, 0°)	14.24 mm (52%)	13
Stand to sit	4.2 (113°, 83°, 24°)	(80°, -2°, 2°)	13.70 mm (48%)	58
Sit to stand	6.4 (112°, 83°, 23°)	(74°, -4°, 5°)	15.68 mm (63%)	29
Squat	3.5 (111°, 86°, 21°)	(80°, -9°, 1°)	13.85 mm (49%)	49
Stand reach	4.3 (104°, 87°, 15°)	(70°, 0°, 5°)	13.15 mm (44%)	35
Kneel reach	0.5 (104°, 80°, 17°)	(68°, -7°, 10°)	6.76 mm (12%)	31
Lunge	3.1 (97°, 86°, 8°)	(-5°, 7°, 7°)	12.74 mm (41%)	100
Golf swing	4.0 (115°, 86°, 25°)	(23°, 4°, 11°)	13.94 mm (50%)	63

Sit to stand showed the highest peak HRF at the hip (6.4 *p*BWT). The stand reach (4.3 *p*BWT), stand to sit (4.2 *p*BWT), walk turn (4.1 *p*BWT) and golf swing (4.0 *p*BWT) made up the next four highest magnitudes and were all similar in force application. The squat was slightly lower in magnitude, at 3.5 *p*BWT. The walk and lunge both showed 3.1 *p*BWT, whereas kneel reach resulted the lowest force value at just 0.5 *p*BWT (Table 18). Contact area diameter increased with the magnitude of loading (Table 18). The sit to stand

showed the largest contact area (15.68 mm), whereas kneel reach resulted the lowest (6.76 mm).

Hip peak loading occurred when ground reaction forces were high – if not maximal (section 4.6. and 8.7.). The walk peak loading occurred at 46% of the cycle, which corresponds to approximately the heel off (in anticipation for the propulsive phase of gait). It is noteworthy that a similar magnitude was resulted at heel strike during walking. The walk turn peak HRF occurred following heel strike (13%), when lower limb loading rate was high. Stand to sit HRF was highest following initial contact with the seat. In contrast, the sit to stand hip loading was highest just before leaving the seat (58%). The squat peak HRF occurred at approximately 50% of the movement cycle, when the centre of mass was at its lowest and the hip was fully flexed. Stand reach and kneel reach hip forces peaked at 35% and 31%, respectively, at points approaching full hip flexion. The lunge reached peak forces at 100% of the cycle, when the right heel had lifted off the floor and the body was propelled upwards out of the lunge position (this corresponded to max ground reaction force). The golf swing peak HRF occurred during the downswing, at 63% of the movement cycle (when ground reaction force was also maximal).

For the walk, the peak force vector acted on the anterior and lateral portion of the acetabular cup (Figure 149). As the walk turn peak force occurred at approximately heel strike (in contrast to post heel off for the walk), the vector contacted the acetabular cup laterally and approximately in line with the medial-lateral axis (close to the pole of the cup) (Figure 150). The stand to sit peak force acted posteriorly and slightly medially on the acetabular cup (Figure 151). A similar position was resulted for the stand to sit (Figure 152). In addition to this, other high flexion activities, including the squat (Figure 153), stand reach (Figure 154) and kneel reach (Figure 155) showed contact of the resultant HRF occurring posteriorly and slightly offset medially from the cups anterior-posterior axis. The lunge showed a peak force acting anteriorly and approximately 7 mm away from the medial lip of the cup (Figure 156). The golf swing resulted a peak force acting close to the pole of the cup, albeit at the lateral side of the anterior-posterior axis (Figure 157).

6.3.7.1. *Walk*

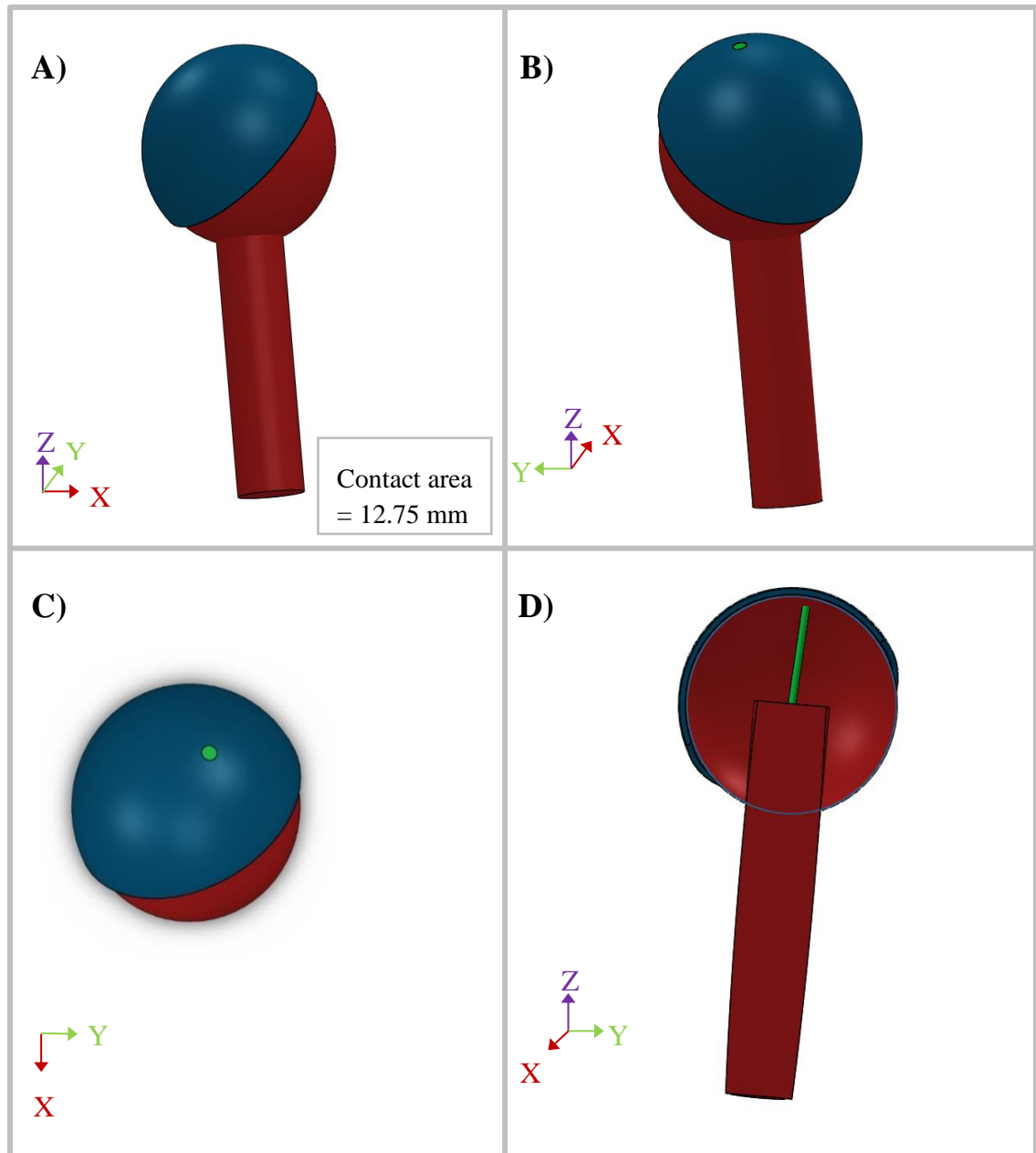


Figure 164. Femoral head (red) and cup (blue) rotated to the angular position of peak hip reaction force for a walk. Contact loci of the force vector is shown as a green circle and the orientation of the vector is represented by a green cylinder. Axis directions are shown as X (lateral), Y (anterior) and Z (superior). Posterior (A), medial (B), superior (C) and lateral cross-section (D) views are displayed.

6.3.7.2. *Walk Turn*

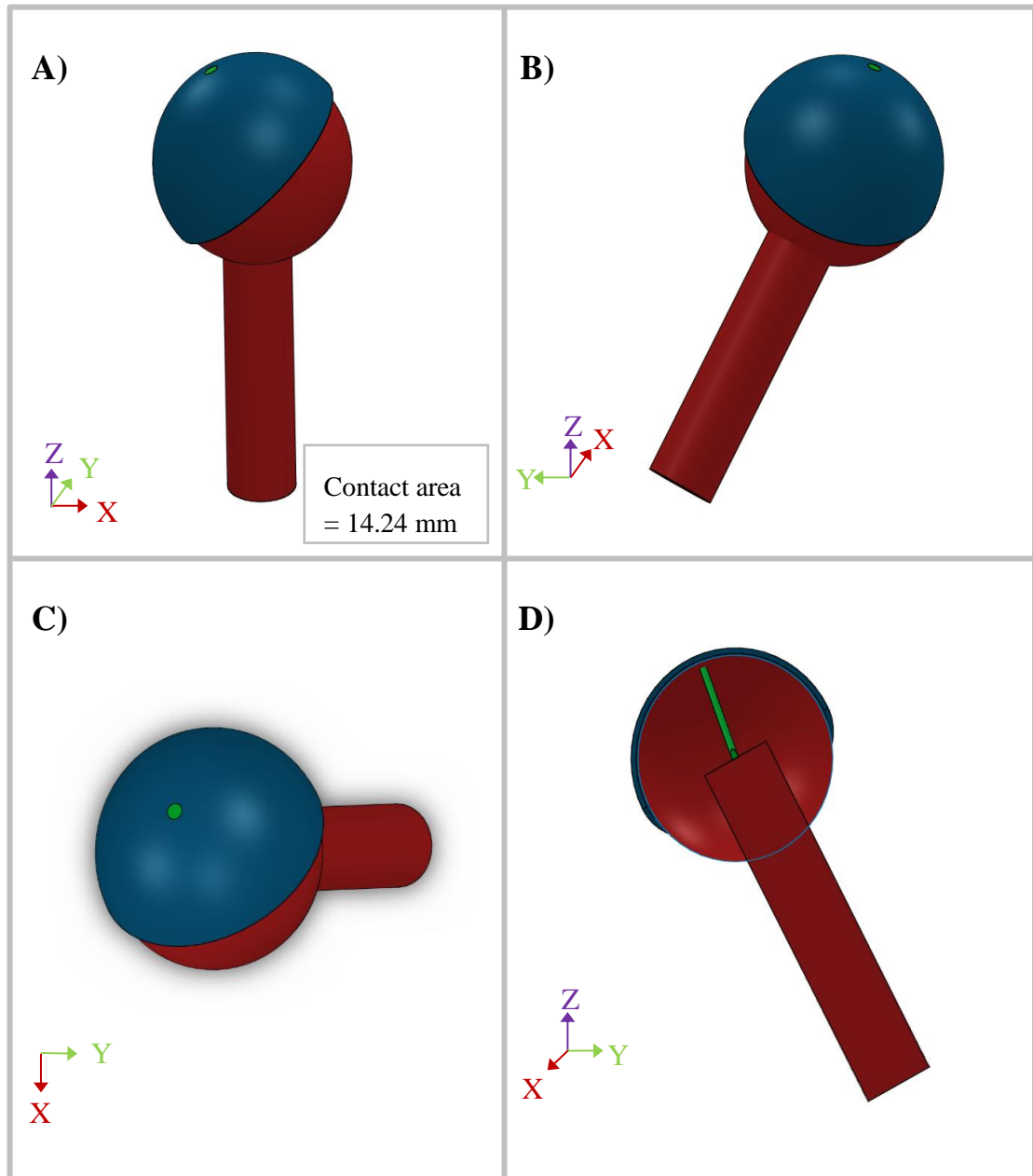


Figure 165. Femoral head (red) and cup (blue) rotated to the angular position of peak hip reaction force for a walk turn. Contact loci of the force vector is shown as a green circle and the orientation of the vector is represented by a green cylinder. Axis directions are shown as X (lateral), Y (anterior) and Z (superior). Posterior (A), medial (B), superior (C) and lateral cross-section (D) views are displayed.

6.3.7.3. *Stand to Sit*

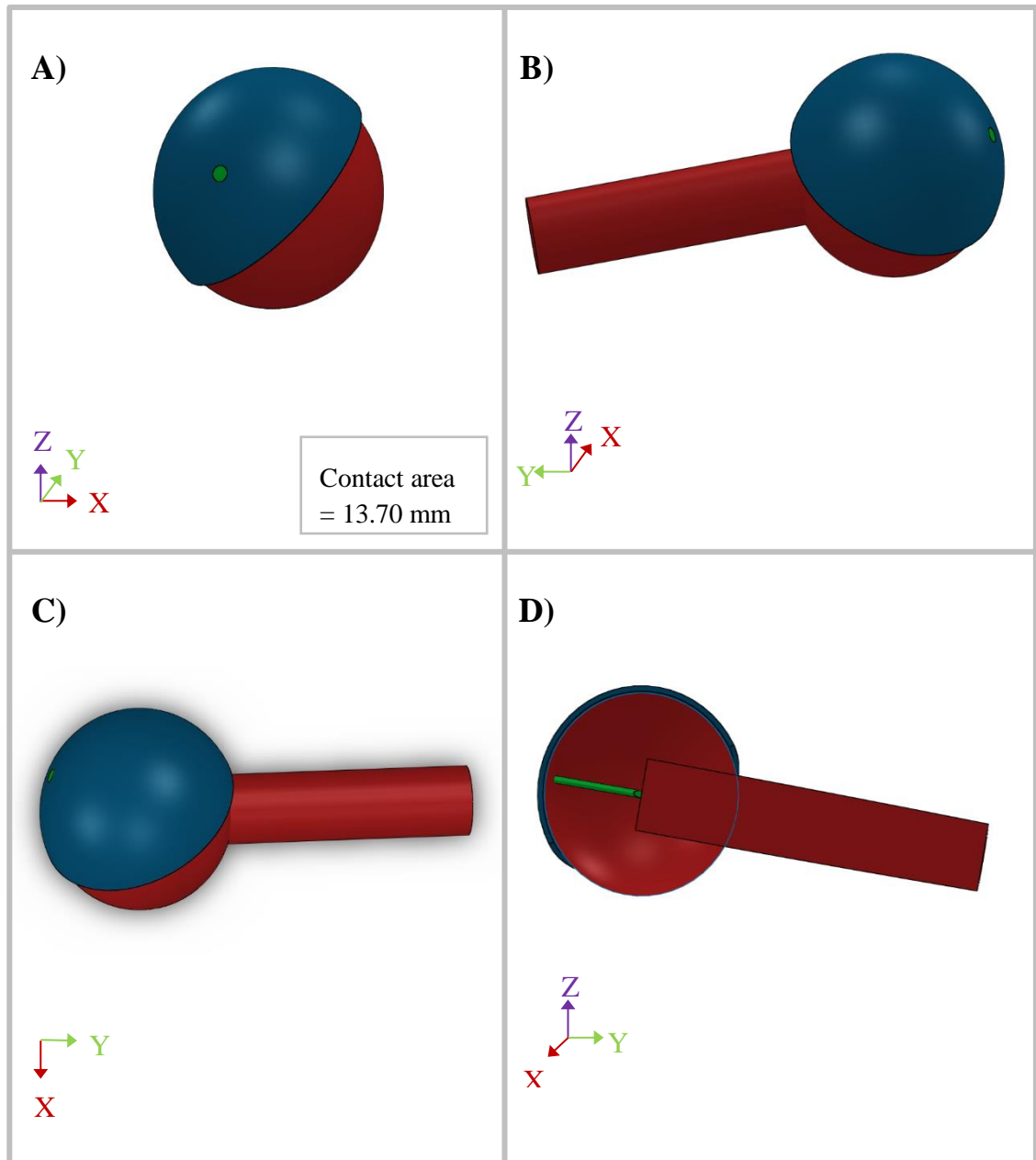


Figure 166. Femoral head (red) and cup (blue) rotated to the angular position of peak hip reaction force for a stand to sit. Contact loci of the force vector is shown as a green circle and the orientation of the vector is represented by a green cylinder. Axis directions are shown as X (lateral), Y (anterior) and Z (superior). Posterior (A), medial (B), superior (C) and lateral cross-section (D) views are displayed.

6.3.7.4. *Sit to Stand*

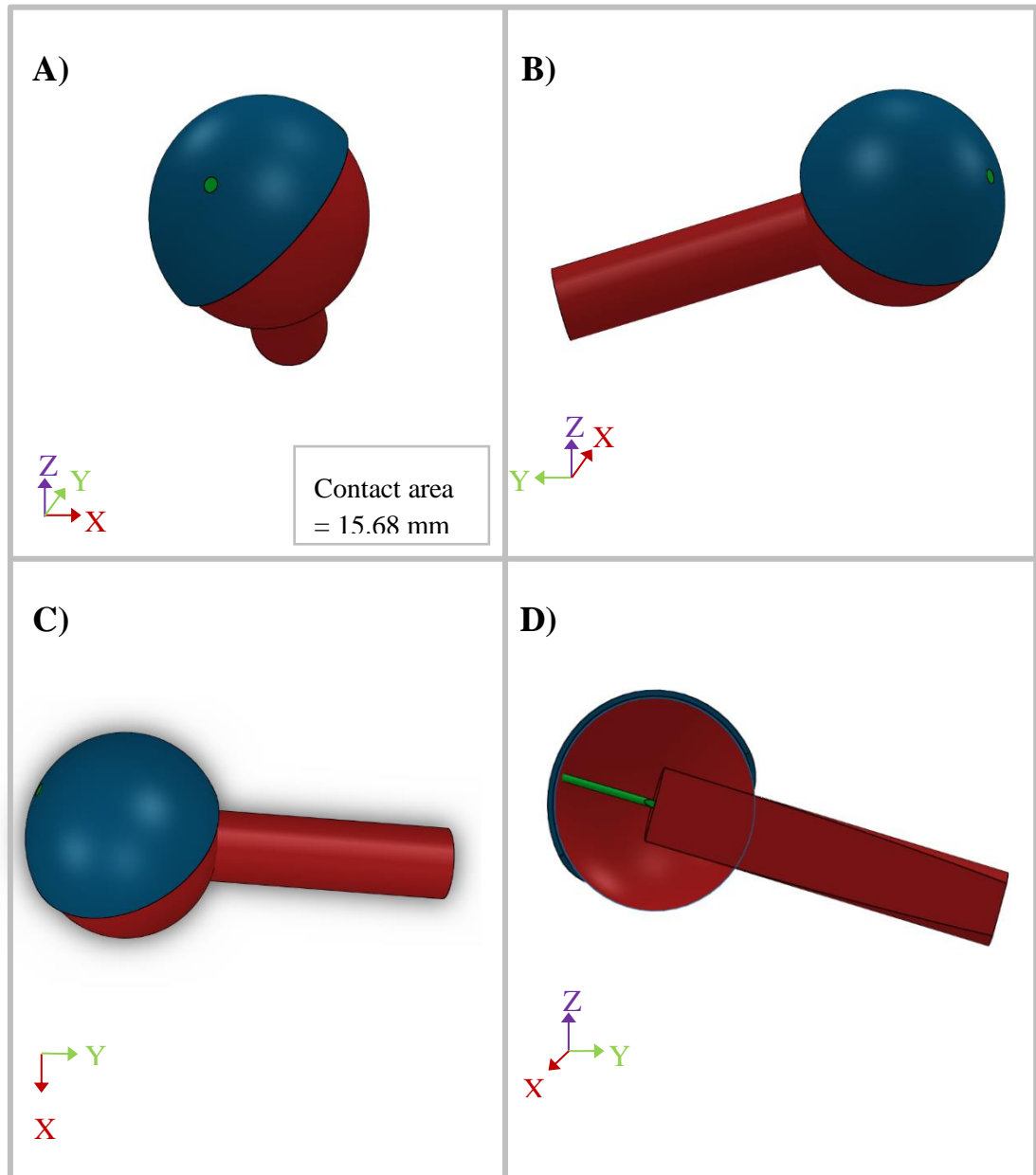


Figure 167. Femoral head (red) and cup (blue) rotated to the angular position of peak hip reaction force for a sit to stand. Contact loci of the force vector is shown as a green circle and the orientation of the vector is represented by a green cylinder. Axis directions are shown as X (lateral), Y (anterior) and Z (superior). Posterior (A), medial (B), superior (C) and lateral cross-section (D) views are displayed.

6.3.7.5. *Squat*

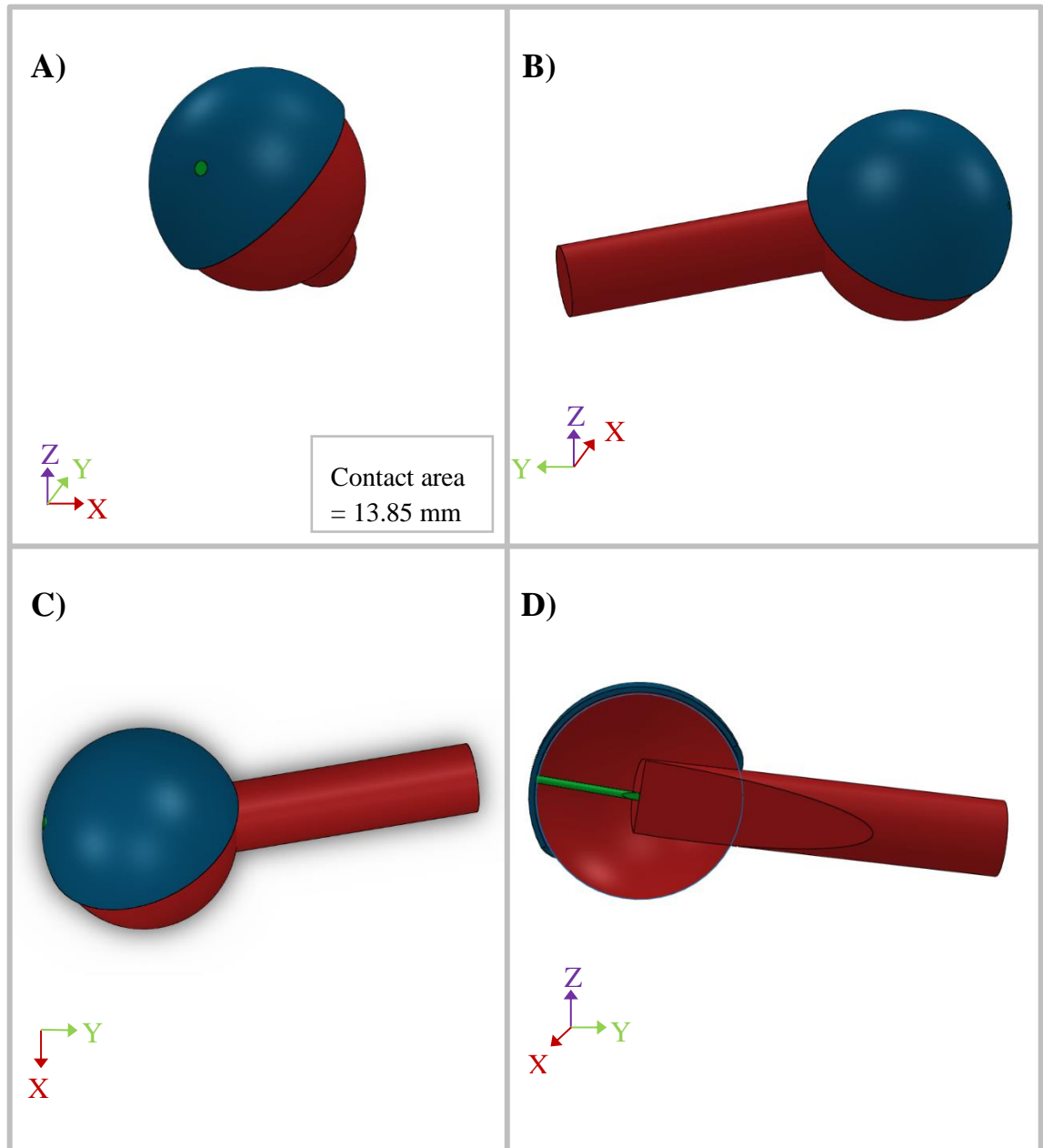


Figure 168. Femoral head (red) and cup (blue) rotated to the angular position of peak hip reaction force for a squat. Contact loci of the force vector is shown as a green circle and the orientation of the vector is represented by a green cylinder. Axis directions are shown as X (lateral), Y (anterior) and Z (superior). Posterior (A), medial (B), superior (C) and lateral cross-section (D) views are displayed.

6.3.7.6. *Stand Reach*

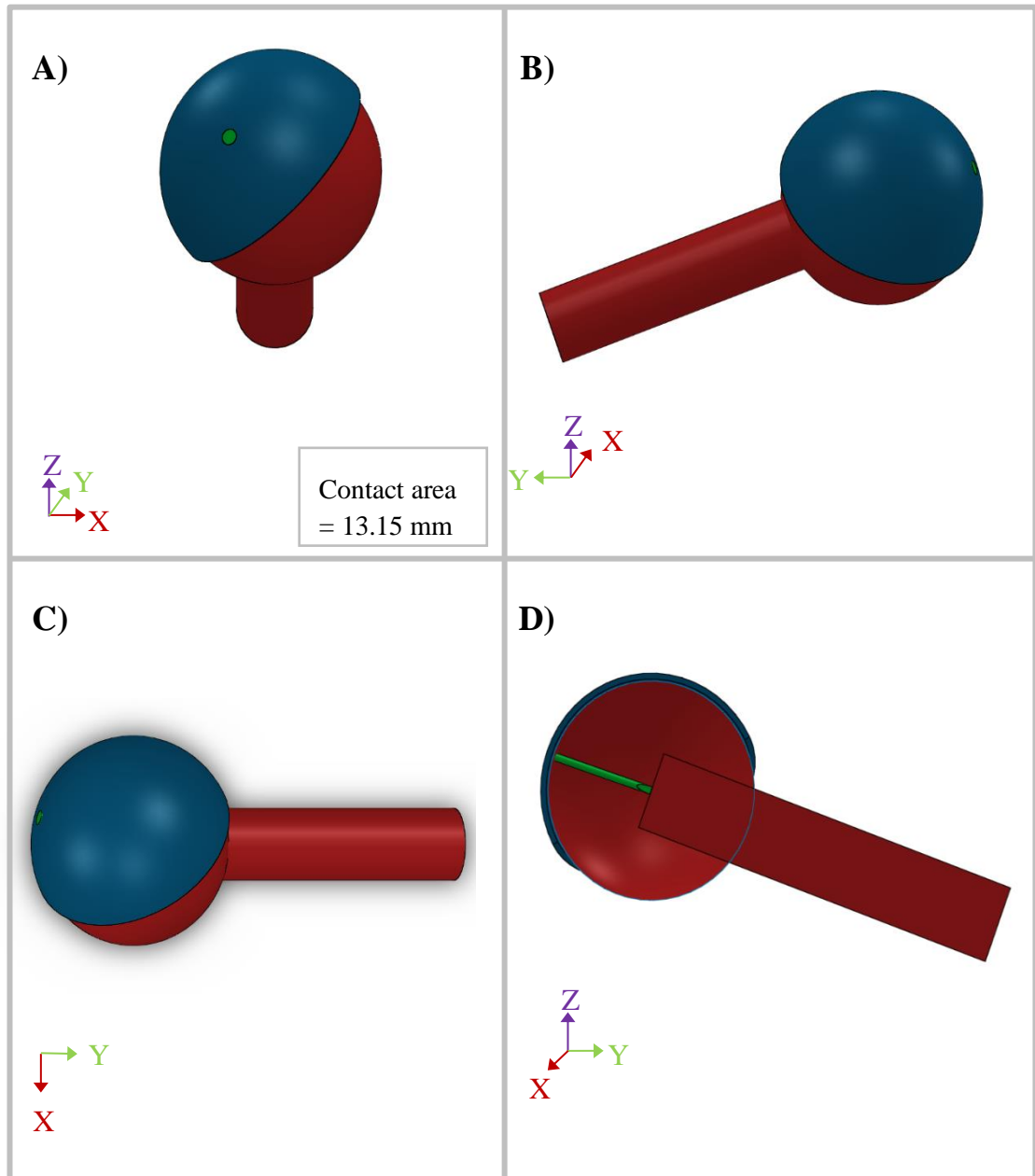


Figure 169. Femoral head (red) and cup (blue) rotated to the angular position of peak hip reaction force for a stand reach. Contact loci of the force vector is shown as a green circle and the orientation of the vector is represented by a green cylinder. Axis directions are shown as X (lateral), Y (anterior) and Z (superior). Posterior (A), medial (B), superior (C) and lateral cross-section (D) views are displayed.

6.3.7.7. *Kneel Reach*

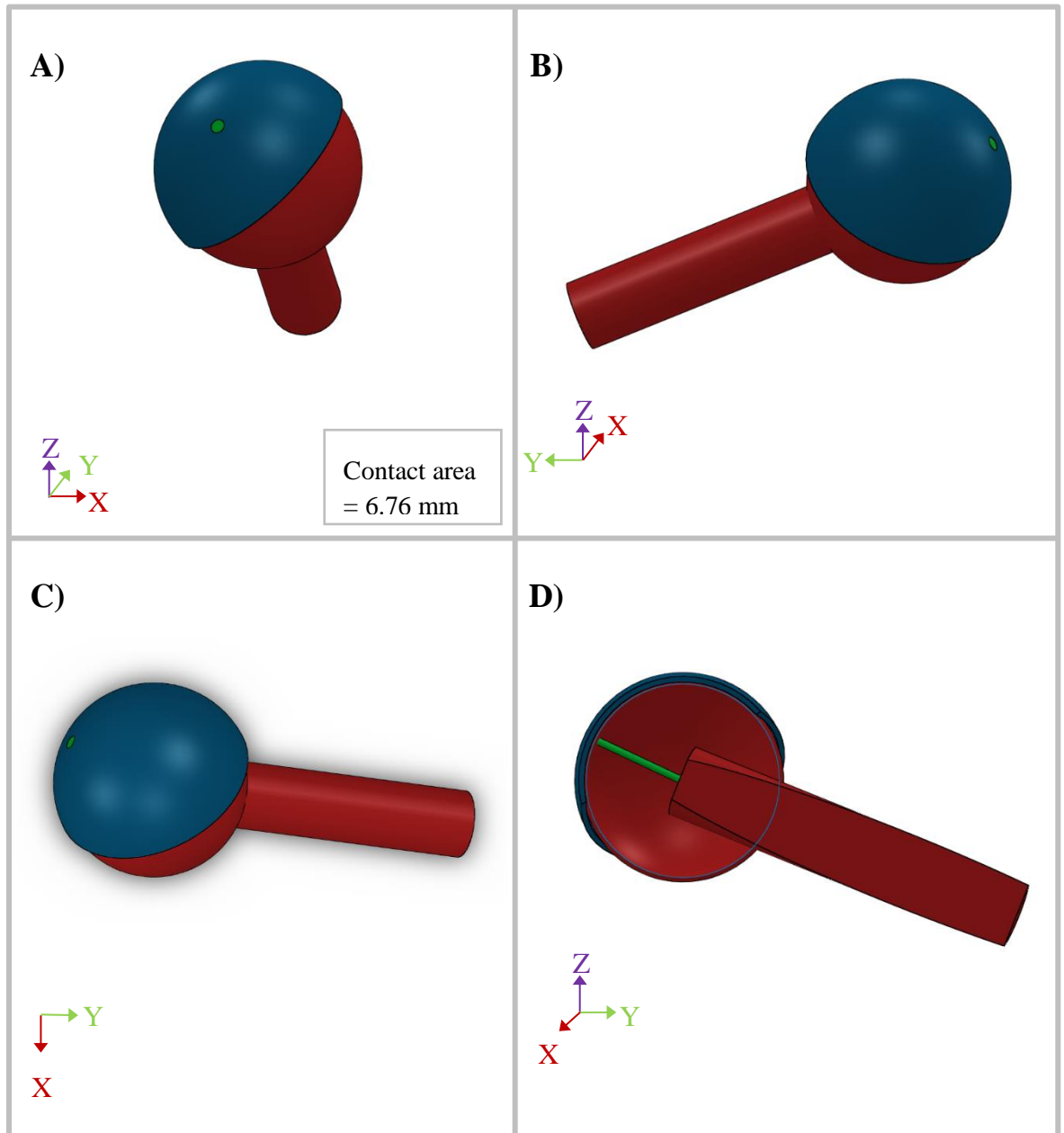


Figure 170. Femoral head (red) and cup (blue) rotated to the angular position of peak hip reaction force for a kneel reach. Contact loci of the force vector is shown as a green circle and the orientation of the vector is represented by a green cylinder. Axis directions are shown as X (lateral), Y (anterior) and Z (superior). Posterior (A), medial (B), superior (C) and lateral cross-section (D) views are displayed.

6.3.7.8. *Lunge*

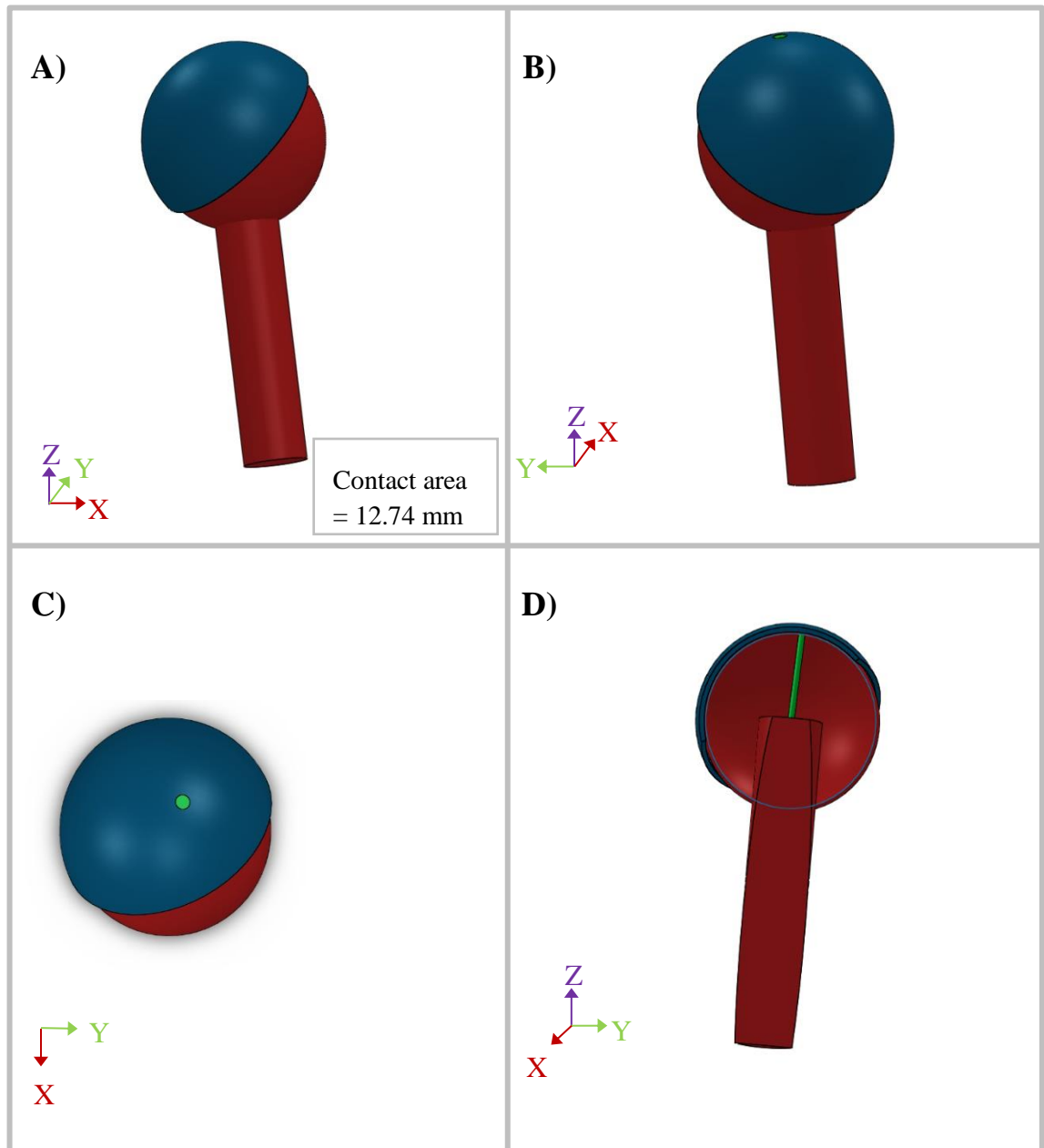


Figure 171. Femoral head (red) and cup (blue) rotated to the angular position of peak hip reaction force for a lunge. Contact loci of the force vector is shown as a green circle and the orientation of the vector is represented by a green cylinder. Axis directions are shown as X (lateral), Y (anterior) and Z (superior). Posterior (A), medial (B), superior (C) and lateral cross-section (D) views are displayed.

6.3.7.9. *Golf Swing*

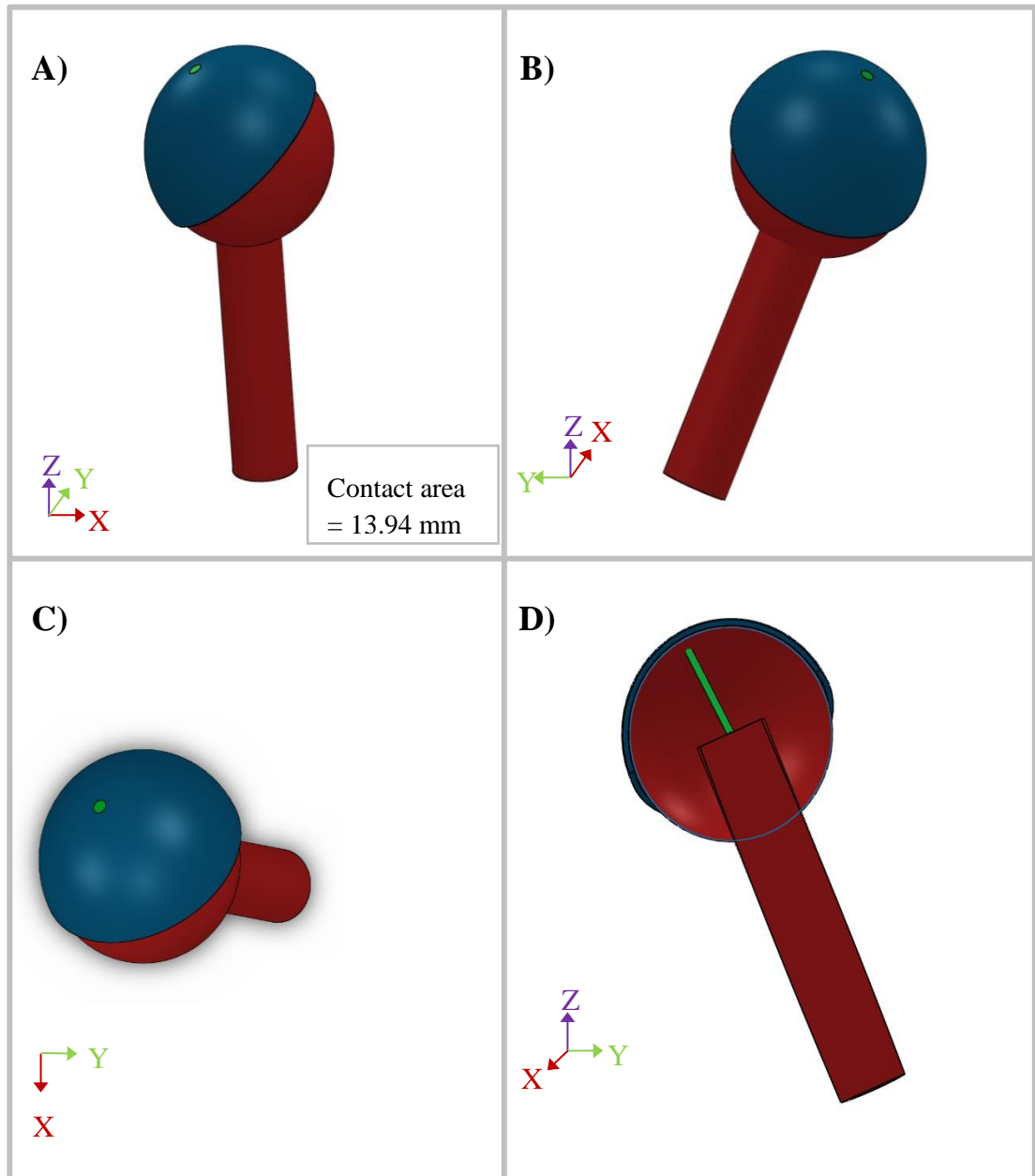


Figure 172. Femoral head (red) and cup (blue) rotated to the angular position of peak hip reaction force for a golf swing. Contact loci of the force vector is shown as a green circle and the orientation of the vector is represented by a green cylinder. Axis directions are shown as X (lateral), Y (anterior) and Z (superior). Posterior (A), medial (B), superior (C) and lateral cross-section (D) views are displayed.

6.3.7.10. *Summary*

Sit to stand showed the highest peak hip reaction force (6.4 *p*BWT) and thus the largest contact area (15.68 mm diameter). Contrastingly, the kneel reach showed both the lowest peak reaction force (0.5 *p*BWT) and the smallest contact area (6.76 mm diameter). Activities displayed peak hip loading at different times within the movement cycle, but there appeared to be a trend of activities showing peaks at the point of maximal (or high) ground reaction forces. Additionally, hip reaction force peaks often occurred when hip flexion was high (or maximal). The lunge and walk were the exception to the rule in this case, with peak loading occurring when the hip was extended. However, in the case of walking, a similarly high hip reaction force was seen at heel strike (when the hip was flexed).

The resultant, peak hip reaction force acted medially and anteriorly from the femoral head for all activities. However, due to the acetabular cup orientation and hip angular position, loading position on the cup varied. High flexion activities saw posterior loading of the cup, with an increase in hip flexion moving the force contact closer to the posterior rim. The two activities with peak forces acting with the hip extended (walk and lunge) were the only instances in which the cup was loaded on the anterior side of the hemisphere. Similarly, most activities saw force contact close to the anterior-posterior axis, with the walk, walk turn and lunge resulting a more lateral cup loading position in comparison to the other activities. Having said this, given that flexion-extension showed the highest range of motion, this variable appeared to have the biggest influence on the potentiality of edge loading from peak force vectors (on the posterior edge).

It is likely that a combination of loading magnitude, contact area and loading position (relative to the cup edge) will influence wear of a polyethylene acetabular component. Furthermore, combining this information with the localised sliding conditions between bearing surfaces would provide a fuller understanding of the tribological conditions and vulnerability of the joint to wear.

6.4. Discussion

Within this chapter, the tribological results from section 6.3. are discussed in detail. Section 6.4.1. discusses the method development activities associated with the processing of hip motion paths. Motion path data is then discussed for each activity (section 6.4.2.). The third and final section of this chapter discusses the potential for edge loading of the femoral head on the acetabular cup (section 6.4.3).

6.4.1. Method Development – Novel Cross-shear Calculation

This section discusses the novel cross-shear calculation methodology that was used within the study (section 6.2.2.). A virtual hip joint was modelled within Visual3D (V3D), in order to calculate relative motion paths between hip surfaces. By using V3D, motion paths could be calculated quickly and in batch for a large number of motion files (C3D files). The method was validated against previously utilised methods, in which transformation matrices are written into a MATLAB script (Budenberg et al., 2012). The residual error was less than 0.01 mm between programs, suggesting that the two methods can be used synonymously (section 6.2.2.). This negligible error is likely due to rounding errors between programs, as V3D retains greater significant figures with internal calculations (compared to excel input data for the MATLAB method). This is a distinct benefit of using the V3D model as it is less likely to cause errors associated with data transfer.

Simulation of motion paths has previously relied on computer aided engineering software, in which a number of transformation matrices are written into a script (Bennett et al., 2002; Budenberg et al., 2012; Ramamurti et al., 1996; Saikko and Calonius, 2002). This can be a time consuming process with regards to formatting of input data (hip angles) and running the program repetitively. V3D is largely regarded as the gold standard for processing of gait data – the methodology within this thesis allows the researcher to directly extract motion path data from a C3D motion file within V3D. This novel method is user-friendly (no programming experience is required) and removes the need to transfer data between software. Due to the inbuilt capabilities of V3D, large sets of motion data can be collated and batch processed together. This significantly reduces processing time of large data sets (when compared to previous methods) and is a beneficial tool when analysing variation within and between data. Further to this, with the ability to process large sets of data together within one V3D ‘workspace’, the researcher can graph motion paths alongside corresponding motion file videos and hip angular data. This is a distinct benefit when interpreting data and determining trends.

A novel ‘virtual joint’ motion path model was developed within Visual3D gait analysis software. The model facilitates the production of joint surface motion path calculations and thus provides a more holistic view of the influence of body movement/ activity on implant tribology. The Visual3D method shows a number of distinct benefits when compared to traditional motion path calculation methods. This includes: a reduction in processing time (and ability to batch process), the option to visually navigate motion files alongside corresponding motion paths and the avoidance of error associated with file transfer. With this being said, benefits of the MATLAB method include the ability to graph in 3D and to run trigonometrical calculations to calculate aspect ratios of motion paths (path height divided by width). As the two methods have been validated against one another, in some instances it may be appropriate to utilise both.

6.4.2. Motion Paths – Detailed Hip Contact Mechanics

Within this section, motion path data is discussed for thirteen common activities (section 6.4.2.1. to 6.4.2.12.). This is followed by an overall discussion (section 6.4.2.13.) and summary (section 6.4.2.14.) of the findings.

Localised motion paths, occurring between bearing surfaces at the hip, determine the degree of cross-shear between the femoral head and acetabular cup. Linear motion paths are associated with low cross-shear and thus, low wear rates. More complex motion paths, with perpendicular crossing of trajectories, lead to high cross-shear and potential surface wear (Barbour et al., 1999; Budenberg et al., 2012; Turell et al., 2003). When coupled with force, a high degree of cross-shear may lead to wear of the polyethylene liner. When considering soft tissue, high levels of cross-shear may lead to the wear of tissue engineered cartilage substitution at the hip.

Motion path trajectories were calculated at 20 points on a 28 mm diameter femoral head (section 6.3.1.). Points 1-10 ran in an arc from posterior to anterior, whereas points 11-20 ran medial to lateral. Average aspect ratios (path length/width) were calculated across the 20 points, for each activity (section 6.3.2.). Motion path sliding distances, velocities and accelerations were also reported for each activity (section 6.3.3 and 6.3.4.). Sliding velocities and acceleration were reported at Point 7, which is located distally and anteriorly on the femoral head (Point 7: *Medial, Anterior, Distal*; 0 mm, 7 mm, 12 mm) (Figure 171). This point was chosen for analysis as it is located at the femoral position in which the peak hip reaction force (HRF) vector acts during activities (approximately) (Table 15). A further three femoral head points are reported within the Appendix, should the reader wish to take a deeper look into the sliding at different femoral head positions (section 10.4).

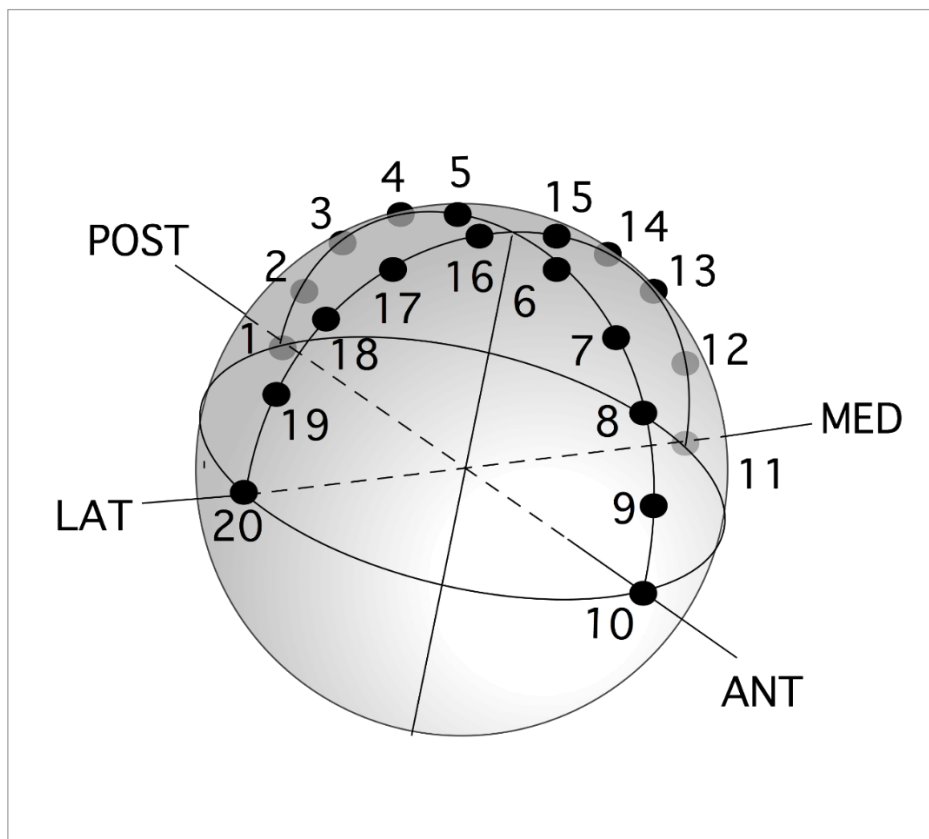


Figure 173. Twenty landmarks equally spaced in a hemisphere, around the hip joint centre. Anterior, posterior, medial and lateral directions are labelled.

Aspect ratios (ARs) provide a quantification for the degree of cross-shear occurring between surfaces. An AR of 1 indicates multi-directional motion and high cross-shear, whereas increasing ARs (>1) indicate decreasing cross-shear with more linear motion path trajectories (Bennett et al., 2008; Bennett et al., 2002; Saikko and Calonijs, 2002; Turell et al., 2003; Wang, 2001; Wang et al., 1997b; Wang et al., 1996; Wang et al., 1997a). Sliding distances have implications for wear, with a higher sliding distance showing a direct relationship with polyethylene wear (Bennett et al., 2008; Bennett et al., 2002; Saikko and Calonijs, 2002). Sliding velocities (SVs) and sliding accelerations (SAs) provide information relating to both wear and lubrication, at the joint (Katta et al., 2008a; Radin and Paul, 1971; Stewart, 2010; Stewart et al., 1997). When considered independently to load, an increase in sliding velocity corresponds to a reduction in the joints fluid film thickness, and thus an increased potential for surface wear within a boundary lubrication regime (Hamrock and Dowson, 1978). High peak SA indicates a change in the direction of a motion path and therefore, potential for instantaneous cross-shear wear (Dressler et al., 2011). It is noteworthy that walking motion paths are the only

results to have been reported within the literature, meaning that it is not possible to compare a number of the novel, motion paths that were calculated within this study.

6.4.2.1. *Walk*

Walking motion path trajectories exhibited teardrop, quasi-ellipse and figure-8 shapes (mean AR: 3.6 ± 0.5) (section 6.3.1.1. and 6.3.2.). In keeping with previous literature, these varied across the femoral head, with some showing a 'complex tail' at initial contact (Barnett, 2009; Bennett et al., 2008; Bennett et al., 2002; Bennett et al., 2000; Ramamurti et al., 1996; Saikko and Calonijs, 2002). Variation between different femoral head points was demonstrated by the range of ARs observed across the twenty points (1.4 to 10.6) ($n=18$) (section 6.3.2.). Similar variation, across femoral head points, was seen for all activities. With that being said, not all femoral head points are in contact with the cup throughout the gait cycle, meaning that the true average AR may change throughout the movement.

The mean AR for walking trials (3.6 ± 0.5) was comparative to reported values for healthy subjects within the literature (3.5) (Bennett et al., 2002). Previous work has suggested that this value may increase by 1 AR, for a THR patient group (Bennett et al., 2002). This increase may occur due to reduced functionality and alterations to hip kinematics, for some THR patients. Within the current study, one individual exhibited a mean walking AR as low as 2.5. This highlights that certain individuals may be more susceptible to excessive cross-shear than others. When considering early failure of an implant, walking technique may be a key factor, given that the degree of cross-shear is influenced by hip kinematics. Mean and minimum AR values for walking were amongst the lowest of all activities, supporting the suggestion that level walking is a key influencer of THR wear.

The average sliding distance for walking (20.4 ± 2.6 mm) (section 6.3.3.) was similar to values reported within the literature for healthy subjects (22.3 mm) (Bennett et al., 2002). However, unsurprisingly, distances did not fall within the range reported for low functioning THR patients (17 mm to 19.2 mm) (Bennett et al., 2008; Bennett et al., 2000; Saikko and Calonijs, 2002). The reduced sliding distance for THR patients, during walking, is likely due to an overall reduction in sagittal plane hip ROM (Lunn et al., 2019). This may be due to age and/or post-operative musculoskeletal damage. A younger, more functional patient group might be expected to show similar ARs to the current study.

Localised sliding velocities and accelerations are yet to be reported within the literature. Walking SV (at Point 7) peaked at heel strike ($24 \text{ mm} \cdot \text{s}^{-1}$), showed a trough at mid-stance

($5 \text{ mm}\cdot\text{s}^{-1}$), before peaking again during the swing phase ($44 \text{ mm}\cdot\text{s}^{-1}$) (section 6.3.4.). A low SV was also observed following the swing phase ($2 \text{ mm}\cdot\text{s}^{-1}$). A reduced SV, alongside high cyclic loading, has been found to limit the degree of fluid entrainment and potentially lead to a break down in fluid films. Subsequently, this may lead to elevated levels of friction and increased surface damage (Katta et al., 2008a; Stewart, 2010; Stewart et al., 1997). Periods of low SV (at 50% and 95% of the gait cycle) represent times at which hip wear may occur (whether that be for a THR or tissue engineered cartilage substitution). The corresponding SA showed two peaks, with the larger occurring at 55% of the gait cycle. SA peaks represented points at which the motion path trajectory changed direction (caused by simultaneous hip extension, abduction and/or external rotation). The magnitude of peaks are related to the angle of the motion path change in direction. Peak SA for walking ($589 \text{ mm}\cdot\text{s}^{-2}$) was the second highest of all activities, behind walk turn, and indicates an acute, clockwise turn of the motion path (a negative peak would indicate a counter-clockwise direction) (6.3.4). Given that changes in the direction of motion paths are linked to wear (Dressler et al., 2011; Wang, 2001), the peak SA appears to be a reasonable method for identifying points of high instantaneous cross-shear within a movement cycle.

6.4.2.2. Walk Turn

Walk turn motion paths displayed teardrop trajectories (section 6.3.1.2. and 6.3.2.). Unlike the straight walk, the beginning and end of paths did not meet at initial contact (as the motion was not cyclical). Visually, paths appeared more linear when compared to walking. However, there appeared to be more crossing over of trajectories. Walk turn mean AR was slightly lower than the walk, at 3.4 ± 0.5 (section 6.3.2.). The minimum AR, both across femoral head points (Walk: 1.4; Walk turn: 1.4) and across subjects (Walk: 2.5; Walk turn: 2.2) was similar for both walking tasks (section 6.3.2.). It is interesting to note that in this case, although kinematics and motion path trajectories were different between the walk and walk turn, the mean AR value was very similar. This highlights the fact that ARs do not tell the full story of motion paths (or cross-shear) and that a deeper analysis may be needed.

The mean sliding distance, for walk turn, was shorter than for the straight walk (Walk: $20.4 \pm 2.6 \text{ mm}$; Walk turn: $18.3 \pm 3.0 \text{ mm}$) (section 6.3.3.). This may be due to the lower mean (and higher variation) for the walk turn movement time (0.96 ± 0.26), compared to the walk (1.12 ± 0.11). For this reason, individuals at the lower SD range completed the walk turn 0.31 seconds faster than the lower SD range for the walk. Both walk turn and

walk SV showed a peak (at initial contact), a trough (at mid-stance) and a second peak (at the propulsion phase) (section 6.3.4.). The initial SV peak was higher and lasted for a shorter period of time, for the walk turn (Walk: $24 \text{ mm}\cdot\text{s}^{-1}$ for 25% of the movement; Walk turn: $27 \text{ mm}\cdot\text{s}^{-1}$ for <10% of the movement). The second SV peak, however, was higher for the walk (Walk: $43 \text{ mm}\cdot\text{s}^{-1}$; Walk turn: $34 \text{ mm}\cdot\text{s}^{-1}$).

The initial SV peak led to a higher SA for the walk turn, compared to the walk ($623 \text{ mm}\cdot\text{s}^{-2}$ increase) (6.3.4.). SA during the propulsive phase, however, was $299 \text{ mm}\cdot\text{s}^{-2}$ higher for the straight walk. This suggests that both the walk and walk turn saw changes in the direction of motion paths at heel strike and during the propulsive phase of gait (at heel off). This change in direction was more acute at initial contact for the walk turn, whereas it was more acute at the propulsion phase for the level walk. The initial contact SA peak for the walk turn ($840 \text{ mm}\cdot\text{s}^{-2}$), was the highest value reported for any activity (the next closest was $589 \text{ mm}\cdot\text{s}^{-2}$ for the walk). This suggests that the walk turn may be at a high risk of cross-shear at this point. With this being said, the high SV corresponding to this point, suggests that the fluid film is unlikely to be drained during this period of the movement (Katta et al., 2008a; Stewart, 2010; Stewart et al., 1997). Therefore it is possible that component surfaces will not come in to contact.

6.4.2.3. Incline and Decline Walk

Incline and decline walk motion paths were comparable to the level walk, showing teardrop, quasi-ellipse and figure-8 shapes (section 6.3.1.3. and 6.3.1.4.). Incline walk demonstrated narrower ellipses than the decline walk. This was quantified through the larger AR for the incline walk (3.9 ± 0.5) than the decline walk (3.0 ± 0.4) (section 6.3.2.). This may be due to the higher F-E ROM for the incline walk (Incline: 51° ; Decline: 37°), alongside similar abduction-adduction and I-E rotation ranges. In fact, the decline walk showed the lowest mean (3.0) and minimum (2.1) AR of all activities. With this being said, the difference between walk, incline walk and decline walk ARs was minimal.

Mean sliding distance was higher for the incline walk ($21.6 \pm 2.5 \text{ mm}$) than the decline walk ($18 \pm 2.9 \text{ mm}$) (section 4.4.15.). The primary cause of this was the higher F-E ROM for the incline walk, compared to decline ($+14^\circ$). Similar to level walking, incline and decline walk showed SV peaks at initial contact and heel off, with a trough at mid-stance (6.3.4.). Although SV magnitudes were similar between the three walking tasks, the SA peak was lower for incline ($346 \text{ mm}\cdot\text{s}^{-2}$) and decline ($472 \text{ mm}\cdot\text{s}^{-2}$) walking. This may

suggest less cross-shear motion occurring at initial contact, for incline and decline walking, compared to level walking.

6.4.2.4. Stand Sit and Sit Stand

Both stand to sit (StSi) and sit to stand (SiSt) displayed linear motion path trajectories. This was shown by high ARs (StSi: 12.7 ± 1.9 ; SiSt: 14.4 ± 2.8) (sections 6.3.1.5., 6.3.1.6. and 6.3.2.). Individuals within the SD showed linear, unidirectional motion paths for sitting and standing, suggesting that cross-shear motion is limited. However, the variation across femoral head positions was high, with minimum ARs of 4.0 (StSi) and 2.8 (SiSt) (occurring medially on the femoral head). It is difficult to interpret this information, however it does highlight that the degree of cross-shear motion may vary considerably across the head and cup. Based on mean data, it is likely that these lower AR paths were still linear in nature and just demonstrated shorter sliding distances (sections 6.3.1.5. and 6.3.1.6.).

Sliding distances for StSi and SiSt were 15 mm and 13 mm, respectively (section 6.3.4.). When considering a stand-sit-stand, the sliding distance is more comparable to other activities (28 mm). For both sitting and standing, SVs peaked during the dynamic phase of the movement, at $18 \text{ mm}\cdot\text{s}^{-1}$ and $20 \text{ mm}\cdot\text{s}^{-1}$, respectively (section 6.3.4.). Corresponding SAs were low for both, peaking at $70 \text{ mm}\cdot\text{s}^{-2}$ (StSi) and $84 \text{ mm}\cdot\text{s}^{-1}$ (SiSt) (6.3.4.). When considering SV, the fluid film layer may drain when seated/ standing in a static position. Lubrication will be drawn back into the joint during the dynamic period of the task, due to the increase in SV (Katta et al., 2008a; Stewart, 2010; Stewart et al., 1997). The low SA confirms the lack of directional changes in motion paths and suggests that the degree of cross-shear will be low throughout the movement. For this reason, it can be postulated that strain hardening will occur at a polyethylene cup surface during these activities.

6.4.2.5. Sit Cross Legged

Linear motion paths were observed during the sit cross legged task (section 6.3.1.7.). Relative motion showed a ‘cross-over’ of trajectories, due to differences in kinematics between crossing and un-crossing the leg. The mean AR (6.3 ± 0.6) was higher than walking tasks, but lower than the higher flexion tasks (such as sitting, standing, squatting and reaching) (section 6.3.2.). One individual demonstrated an AR as low as 3.4, suggesting that this activity could be completed with varying techniques. Similar to other activities, motion paths varied across femoral head points, with a minimum AR reported

at 2.0. When plotted, the path was still linear, albeit with a shorter sliding distance than other femoral head points. This is unlikely to be detrimental to wear, given that strain hardening is likely to occur between hip surfaces.

Mean sliding distance (22.5 ± 3.6 mm) was similar to values seen for walking (section 6.3.3.). The corresponding SV peaked as the leg was lifted up ($22 \text{ mm}\cdot\text{s}^{-1}$) and dropped down ($19 \text{ mm}\cdot\text{s}^{-1}$) (section 6.3.4.). As the leg was externally rotated and rested on the left knee, SV decreased to $0 \text{ mm}\cdot\text{s}^{-1}$. Although force was not recorded, SiSt hip reaction forces suggest that $0.6 p\text{BWT}$ of loading might be expected when seated (this may increase further as the hip reached a higher peak flexion value when crossing). Given this assumption, it is possible that the hip could be loaded with $>0.6 p\text{BWT}$, whilst SV is $0 \text{ mm}\cdot\text{s}^{-1}$. Hypothetically, this may be detrimental to hip wear, given that the fluid film is likely to be depleted at this point. The corresponding SA showed a small initial peak ($123 \text{ mm}\cdot\text{s}^{-2}$), followed by small accelerations close to $0 \text{ mm}\cdot\text{s}^{-2}$ (section 6.3.4.). This demonstrates the unidirectional nature of motion paths observed throughout the movement.

6.4.2.6. *Squat*

The squat exhibited linear motion paths, with a noticeably short sliding distance occurring at Point 13 (medial point on the femoral head) (section 6.3.1.8.). The squat showed a similar AR to other high flexion activities, at 13.7 ± 2.0 (section 6.3.2.). The lowest, mean AR seen for an individual subject was 6.7. This suggests that paths remain linear for all subjects, albeit with a potentially shorter average sliding distance in some cases (section 6.3.3.). The minimum AR seen across femoral head points occurred at the medially positioned, Point 13 (2.4) (section 6.3.2.). This was due to a considerably reduced sliding distance, and is therefore unlikely to influence the surfaces cross-shear as the path remained linear.

The squat showed the second longest mean sliding distance (27.8 ± 5.3 mm) (section 6.3.3.). The corresponding SV showed two small peaks during descent ($22.9 \text{ mm}\cdot\text{s}^{-1}$) and ascent ($20.8 \text{ mm}\cdot\text{s}^{-1}$) (section 6.3.4.). A trough occurred at the bottom of the squat ($0.1 \text{ mm}\cdot\text{s}^{-1}$). Lubrication is likely to be drawn into the hip joint during the dynamic phase of the squat, when SV peaks. In contrast, lubrication is likely to drain out of the joint at the bottom of the squat, potentially leaving the cup vulnerable to wear (Katta et al., 2008a; Stewart, 2010; Stewart et al., 1997). However, as motion paths are linear with high ARs, the degree of cross-shear is low at this point. The low SA throughout the squat highlights

the unidirectional nature of motion paths. Hypothetically, multi-directional motion at the base of the squat (possibly due to a loss of balance) could lead to the potential for cross-shear loading and contact of hip surfaces. However, when considering the data within the current study, polyethylene fibers are likely to experience strain hardening throughout the movement.

6.4.2.7. *Stand and Kneel Reach*

Stand reach and kneel reach showed similar localised hip motion to other high flexion activities, with long linear motion paths (sections 6.3.1.9. and 6.3.1.10.). Mean ARs (Stand reach: 12.9 ± 1.9 ; Kneel reach: 14.4 ± 2.4) and sliding distances (Stand reach: 23.8 ± 5.2 ; Kneel reach: 21.7 ± 5.9) were similar to other high flexion activities (section 6.3.2 and 6.3.3.).

Both reaching tasks showed two sliding velocity peaks. Peak velocities were low for stand reach (Peak 1: $12.4 \text{ mm} \cdot \text{s}^{-1}$; Peak 2: $11.0 \text{ mm} \cdot \text{s}^{-1}$) and even lower for the kneel reach (Peak 1: $8.1 \text{ mm} \cdot \text{s}^{-1}$; Peak 2: $7.2 \text{ mm} \cdot \text{s}^{-1}$) (section 6.3.4.). Given the lack of multi-directional motion between bearing surfaces, SAs remained at $\approx 0 \text{ mm} \cdot \text{s}^{-1}$ throughout both reaching activities (6.3.4.). Although lubrication may be limited and friction increased between hip surfaces during reaching tasks, the degree of cross-shear will be low. For this reason, it is unlikely that the joint is at risk of excessive cross-shear wear.

6.4.2.8. *Lunge*

The lunge showed stretched tear-drop motion path trajectories, with a cross-over occurring at the lowest point of the lunge (when global hip kinematics changed from flexion to extension) (section 6.3.1.11.). Paths varied across the femoral head during the lunge, with a 'complex scribble' and quasi-ellipse occurring at Points 13 and 14 (both medial), respectively. The mean AR was the lowest of all activities, bar the walking tasks (5.0 ± 0.6) (section 6.3.2.). The minimum AR was at Point 14 (laterally positioned) (1.1). This was the lowest mean AR seen between bearing surfaces, for all activities. However, when visually assessing motion paths, the decreased AR was due to a reduction in sliding velocity, rather than increased multi-directionality (section 6.3.1.11.). It is noteworthy that Point 7 (the approximate position of femoral head hip loading), showed a similarly reduced AR of 2.9 (section 6.3.2.).

The lowest mean AR seen for an individual completing the lunge was 3.3 (section 6.3.2.). Although this was not a considerable decrease from the mean, it indicates that lunge technique may influence the degree of cross-shear at the hip. This, however, is likely to

be predominantly due to a reduction in sliding distance, rather than an increase in multidirectional motion.

The lunge showed the longest sliding distance of all activities, equalling 36.7 ± 4.8 mm (8.9 mm longer than the next closest activity) (section 6.3.3.). The long sliding distance, coupled with multidirectional motion paths, may suggest that the lunge is at risk of potentially excessive wear. The SV demonstrated a sharp peak at initial contact ($35.6 \text{ mm}\cdot\text{s}^{-1}$). Sliding slowed down to $0.6 \text{ mm}\cdot\text{s}^{-1}$ at the bottom of the lunge, before peaking again during the propulsive phase ($17.6 \text{ mm}\cdot\text{s}^{-1}$) (6.3.4.). The initial peak SV occurred as the right leg was swung forwards, in preparation for the lunge (at this point, the fluid film will increase). The fluid film thickness is then likely to be reduced at the bottom of the lunge, as sliding velocity slows and the joint adopts a boundary lubrication regime (Stewart, 2010; Stewart et al., 1997).

The corresponding SA showed an initial peak at heel-off of the step before the lunge ($409.8 \text{ mm}\cdot\text{s}^{-2}$) (section 6.3.4.). This indicates a change in direction of the motion path at this point (this occurred as the hip flexed, abducted and external rotated simultaneously). Instantaneous cross-shear is likely to occur at this point in the movement. Acceleration was low for the rest of the lunge cycle, as the only change in direction of the motion path (at 50% of the cycle) was $\approx 180^\circ$, and thus unidirectional.

6.4.2.9. *Golf Swing*

The golf swing showed a mixture of linear and 'C' shaped motion paths. Mean ARs were 6.2 ± 1.7 (sections 6.3.1.12. and 6.3.2.). The minimum AR seen at the femoral head (1.5) occurred on the lateral portion of the head, at Point 17. It is notable that Point 7 (anteriorly positioned) saw a similarly reduced AR, thus potentially increased cross-shear (2.8). Point 7 matched up to the approximate position of the peak hip reaction force, for this activity, and may therefore be a position that is susceptible to excessive wear. The lowest mean AR value seen across subjects, for the golf swing, was 2.5 (section 6.3.2.). This is less than half of the average, suggesting that cross-shear is likely to vary between subjects. It is important to appreciate, however, that a linear path can still result a low AR should the sliding distance be reduced. Given that the golf swing is a technical skill, the AR range is likely to vary when considering more skilled golfers, who complete the movement more dynamically.

Golf swing sliding distance was the third shortest, when compared to other activities (15.0 ± 4.3 mm) (6.3.3.). Sliding velocity was low throughout the swing and SA was the lowest

of all activities (Peak SA: $21.9 \text{ mm} \cdot \text{s}^{-2}$) (section 6.3.4.). The slow, localised sliding speeds may suggest that the fluid film will be reduced during this activity and surface asperities may come into contact through a boundary lubrication regime (Katta et al., 2008a; Stewart, 2010; Stewart et al., 1997). However, this velocity is likely to increase with a more experienced and skilful golfer. The low SA indicates that the motion path is linear with low cross-shear. If a golfer exhibited low localised sliding velocities, alongside high hip reaction forces, the cup may be at risk to wear. With that said, the current data set suggests cross-shear motion will be low throughout.

6.4.2.10. Cycle

Cycle motion paths were linear, however figure-8 shapes were observed at a number of femoral head points. The mean AR was almost three times higher than level walking, at 9.8 ± 1.7 (sections 6.3.1.13 and 6.3.2.). The AR dropped to 4.3 for a point on the lateral side of the femoral head (Point 3).

Sliding distance was $12.4 \pm 4.4 \text{ mm}$ for the cycle (section 6.3.3.). This was the shortest of all activities. The corresponding SV peaked twice (Peak 1: $30.0 \text{ mm} \cdot \text{s}^{-1}$; Peak 2: $26.8 \text{ mm} \cdot \text{s}^{-1}$), with a trough at the bottom of the cycle when the hip was least flexed ($2.5 \text{ mm} \cdot \text{s}^{-1}$) (section 6.3.4.). Interestingly, SA showed positive ($480.4 \text{ mm} \cdot \text{s}^{-1}$) and negative ($-751.0 \text{ mm} \cdot \text{s}^{-1}$) peaks, in line with the SV peaks. These peaks occurred at points in the cycle where the hip flexed/extended, alongside internal/external rotation (and the motion path changed direction). However, although two clear changes in direction occurred for the motion path, these overlaid one another, ultimately leading to a relatively linear trajectory (section 6.3.1.13. and 6.3.2.).

6.4.2.11. Variation and Age

None of the activities showed a significant difference in the mean AR, between groups under and over 55 years of age (Section 6.3.5.). For this reason, it is likely that any differences seen between age groups are due to chance. Stand to sit, sit to stand, stand reach and cycle showed a difference between age groups of over 1 AR. It is likely that the variation within each of the age groups (for these activities) are high and potentially overlap, thus leading to a non-significant difference between them. Nonetheless, these four activities were further compared for hip kinematics. Kinematic differences were observed between age groups, particularly for the sit to stand and stand to sit. Given the lack of significance between motion path ARs, it is probable that although kinematic differences were observed, the pattern and combination of hip angular motion was similar

for both age groups. Ultimately, it seems unlikely that age alone will influence the degree of cross-shear at the hip.

Although cross-shear did not significantly differ between age groups, the data suggests that differences will be seen for hip loading. Further testing, with larger group sizes, is required to determine whether differences in hip loading is significant between age groups. The differences observed in HRF appear to be dependent on the activity. Due to the limited subject group sizes within this study, it is difficult to draw a conclusion for the relationship between age and hip loading.

It is likely that certain activities will show biomechanical differences between age groups, however there was no clear trend relating to cross-shear or hip loading and age. Although small biomechanical differences may occur between age groups, the observed differences between different activities was more obvious. For this reason and given that activity levels have been found to reduce with age (Crombie et al., 2004; Leslie et al., 2001; Yusuf et al., 1996) the difference in the amount and type of activity (between age groups) is a more likely explanation for early revision rates.

6.4.2.12. Variation and Gender

Two activities (kneel reach and lunge) showed significantly different motion path ARs between gender ($P < 0.05$). Three activities (sit to stand, squat and kneel reach) showed a difference in mean ARs of over 1 (section 6.3.6.). Of the four activities that showed a difference between genders, males demonstrated a lower AR for sit to stand and kneel reach, whereas females showed a lower mean AR for the squat and lunge.

Within the literature, differences have been reported for activity levels between males and females (Leslie et al., 2001). This may be a more reasonable theory as to why revision rates vary between genders (given that biomechanical differences showed little consistency). Males demonstrated higher participation rates within moderate and vigorous activity, compared to females. Females, however, showed higher levels of participation in walking, than males (Leslie et al., 2001). Given that walking showed high cross-shear and the potential for excessive hip loading (potentially through anterior edge loading), the higher levels of walking for females may be a possible contributor to the higher early revision rates for a THR. Additionally, it is likely that the increased revision rates for males under 70 years of age, is due to a combination of factors, including implant design and surgical positioning (Donahue et al., 2016; Prosser et al., 2010).

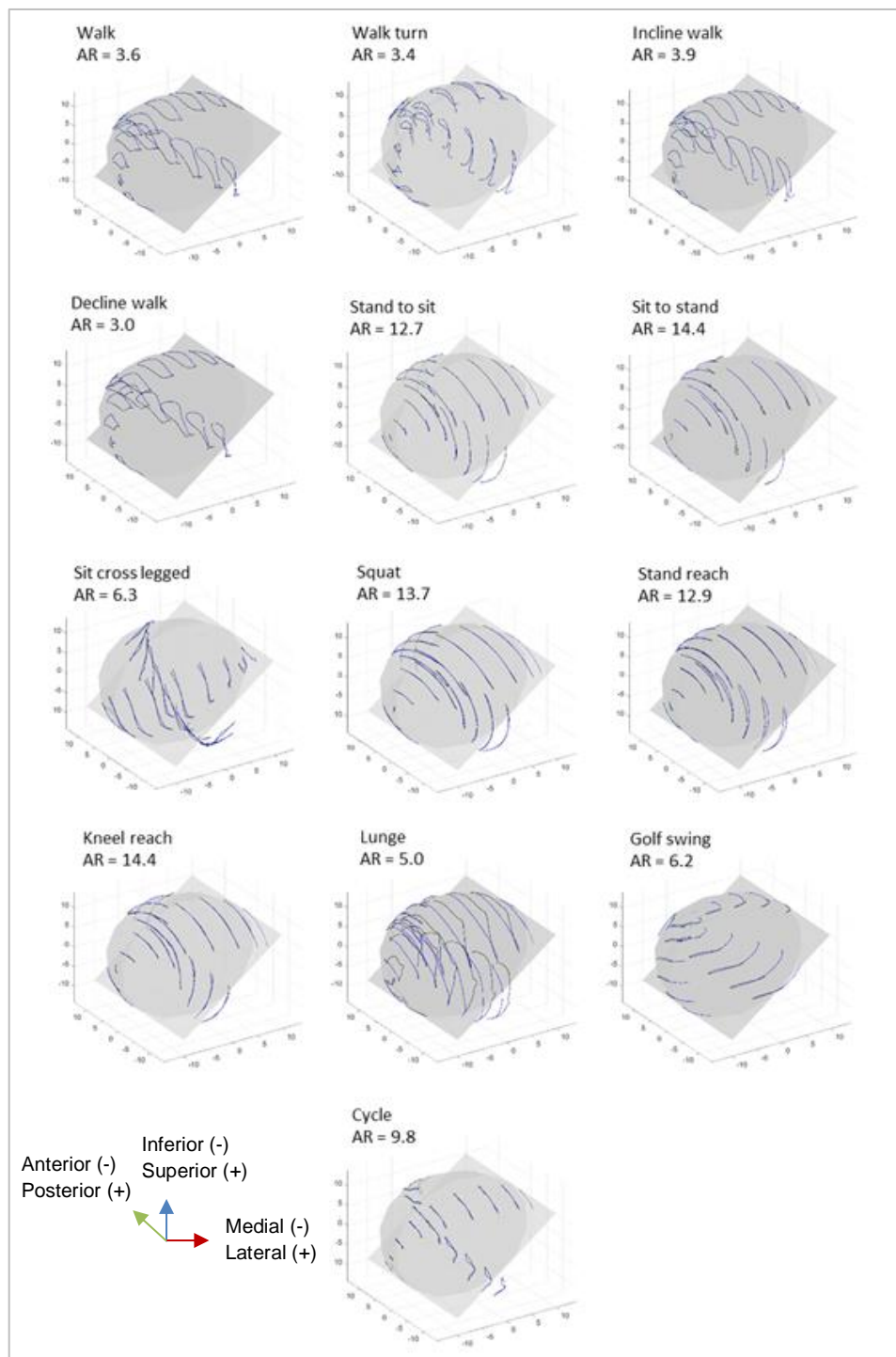


Figure 174. Mean motion path for thirteen common activities. Mean aspect ratio (AR) (motion path height divided by perpendicular width) is shown above each individual graph.

6.4.2.13. Overall Discussion

Motion paths, and the degree of cross-shear, is influenced by the complex global hip kinematics during movement. Depending on the position on the femoral head, combinations of flexion-extension, abduction-adduction and internal-external rotation will determine the shape of motion paths. It is reasonable to assume that motion is required in at least two planes at the same time, in order to result a circular or elliptical motion path (with a low aspect ratio (AR)). Similarly, a high range of motion (ROM) in one plane, coupled by minimal motion in other axes, is likely to produce a more linear path (with a high AR). Hip angular motion, however, will influence motion paths differently depending on the position on the femoral head. During pure rotation the head will rotate about the fixed superior point with negligible relative motion, however medially, the head surface will translate relative to the cup with the motion path being a displacement arc equal in length to the angle of rotation multiplied by the head radius.

It is worth highlighting that a reduction in the AR, does not necessarily result in an increase in cross-shear. This is because the AR may decrease in line with a decreased sliding distance, whilst the motion path shape remains linear. However, it is generally accepted that both sliding distance and motion path aspect ratios are directly related to wear (Figures 173 and 174).

Although biomechanical differences were observed between age and gender, the majority of observed differences between groups were not significant. Further to this, no clear pattern could be determined when comparing groups for ARs and HRFs. It is likely that the differences in revision rates, put forward by the national joint registry, are multi-factorial and more complex than just hip biomechanics. Demographics (BMI and occupation), activity levels (type and duration of activity engagement) and surgical factors (type of prosthesis and average prosthesis positioning) are just three factors which may influence early revision of a total hip replacement. A large scale study would be required to try to identify the key factors influencing early failure rates for certain population groups.

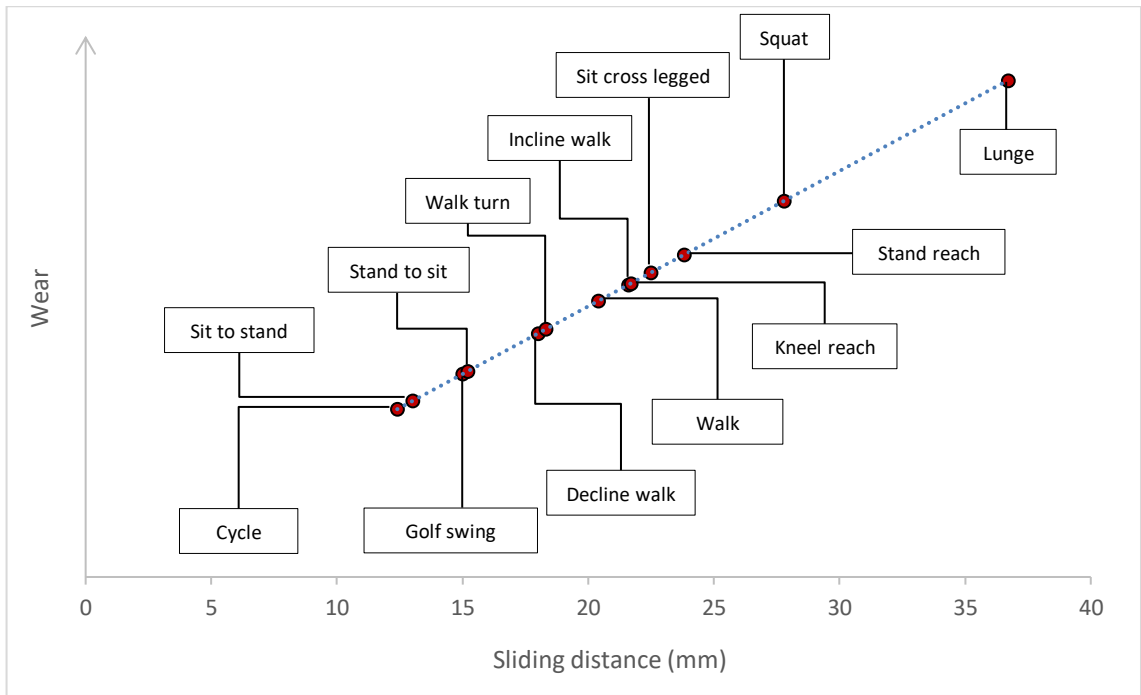


Figure 175. Theoretical representation of the relationship between total sliding distance and relative wear. The linear trend-line indicates a positive relationship between the two variables, as reported in work by Saikko (2014).

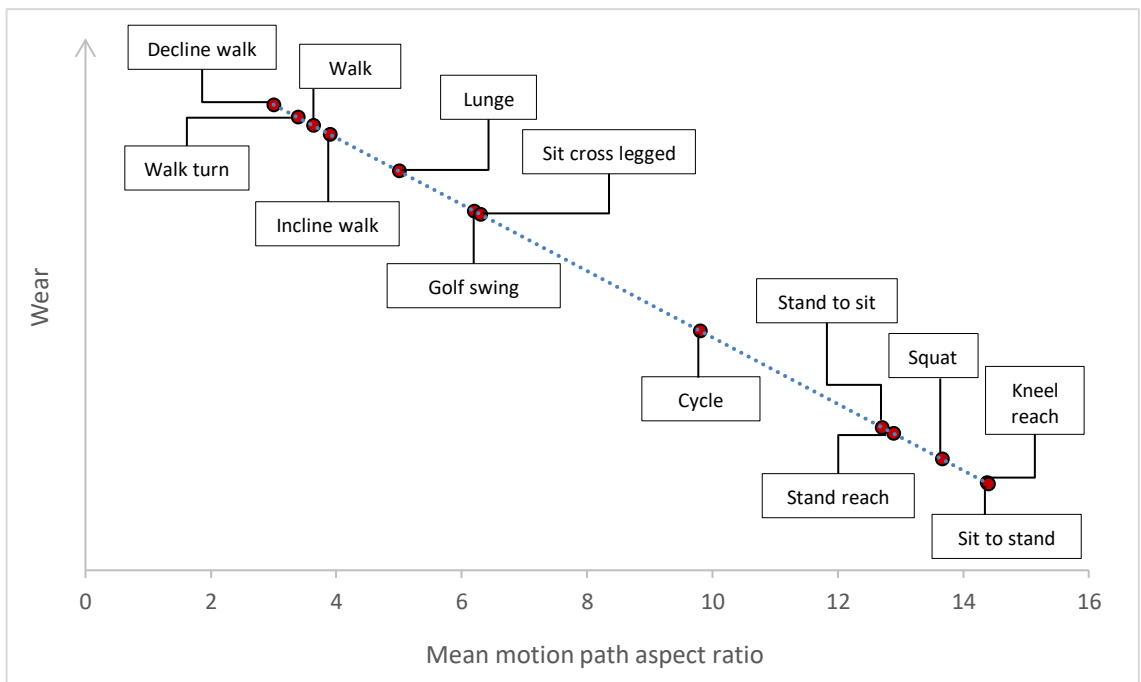


Figure 176. Theoretical representation of the relationship between aspect ratio (motion path height divided by perpendicular width) and relative wear. The linear trend-line indicates an inverse relationship between the two variables, as shown in work by Turell et al. (2003).

Although an inverse relationship can be observed between ARs and relative wear, it is possible that sliding acceleration provides a better measure of instantaneous cross-shear. Sliding acceleration (SA) peaks correspond to changes in the motion path direction, allowing cross-shear to be compared across time periods within a movement cycle. Further to this, sliding velocity (SV) provides a method for understanding the lubrication regime occurring at the joint (Katta et al., 2008a; Stewart, 2010; Stewart et al., 1997). A low sliding velocity indicates fluid film breakdown between bearing surfaces and a potential increase in friction and wear. Contrastingly, a high sliding velocity indicates fluid entrainment at the joint (Katta et al., 2008a; Stewart, 2010; Stewart et al., 1997). Wear is therefore a product of cross-shear (indicated by sliding acceleration), sliding velocity and force.

Motion path variation was seen both between subjects and across femoral head points, for all activities (Figure 172). A motion path AR is inversely related to wear, thus low ARs indicate high levels of relative wear (Figure 174). However, although the minimum AR for an activity may indicate high cross-shear, if the position is not exposed to direct loading, wear is unlikely to occur. For this reason, femoral head Point 7 (distally and anteriorly positioned) may be more relevant than other positions, as it is located at the approximate position of the peak hip reaction force on the femoral head (Table 4, Table 8 and Figure 34).

The four walking tasks (level, turn, incline and decline) showed the lowest mean ARs (all below 4) due to multi-directional hip kinematics. Walking tasks showed a range of SVs throughout the movement cycle (at Point 7), indicating cycles of fluid entrainment and draining. This may have implications for wear, depending on the corresponding force values. Peak SAs for walking tasks (at Point 7), indicated high cross-shear at initial contact and heel-off. Given that hip reaction forces are also high at these points, this may be crucial to cup wear.

Sit cross-legged, lunge, golf swing and cycle showed ARs between 5 and 10. Sit-cross legged and golf swing showed small SVs and SAs at Point 7, indicating potentially limited lubrication alongside low cross-shear. This suggests that excessive THR wear is unlikely, due to the likelihood of strain hardening at the polyethylene surface. The lunge showed high SV and SA at heel-off, indicating that the joint is likely to experience fluid entrainment alongside high cross-shear. Similarly, cycling showed periods of high SV (at 25% and 75% of the cycle), alongside high cross-shear (indicated by SA peaks). Should these periods of high cross-shear correspond to high magnitudes of hip loading, it is

possible that hip surface wear could occur (possibly through squeeze film effects at the joint) (Stewart, 2010; Stewart et al., 1997).

The majority of high flexion activities (sit to stand, stand to sit, squat, kneel reach and stand reach) showed high ARs (>12) alongside low SVs and SAs. Although lubrication is likely to be limited during these activities, the cross-shear motion will be low. Thus, wear due to cross-shear force is unlikely. With this being said, other wear mechanisms (such as edge loading) may still occur at point of high flexion.

6.4.2.14. *Summary*

Activities varied with regards to motion path shape, sliding distance, sliding velocity and sliding acceleration. It seems unlikely that a movement will display high levels of cross-shear, at a point where the sliding velocity is low. It can be speculated that walking tasks are at the highest risk to wear, given the variable sliding velocity and high sliding accelerations occurring at a distal/ anterior position on the femoral head. The lunge, golf swing and cycle may also have the potential for excessive wear, given the peak sliding accelerations identified at the femoral head/ acetabular cup interface. It is likely that linear, high flexion activities will lead to strain hardening of the acetabular liner, rather than cross-shear wear.

In order to fully assess an activities potential for wear, hip reaction force must be taken into account. Plotting sliding velocity (lubrication) and acceleration (cross-shear) against hip reaction forces, may allow for the identification of points within the movement cycle where excessive polyethylene wear could occur. Implications can also be drawn with regards to the wear of tissue engineered cartilage substitution at the hip. Further to this, the potential for edge loading must be considered, given that it is a key factor that will influence surface wear.

6.4.3. Edge Loading

Within this section, hip reaction force orientation (section 6.4.3.1.), contact area (section 6.4.3.2.) and cup loading position (section 6.4.3.3.) is discussed for nine activities. This is followed by a discussion surrounding edge loading (section 6.4.3.4.) and a summary of the data (section 6.4.3.5.).

Edge loading has been described as when the contact area extends over the rim of the acetabular cup component (Hua et al., 2016). The position of peak hip reaction force (HRF), from the femoral head onto the acetabular cup, was visualised for each activity within SolidWorks (Figure 177) (SolidWorks 2017, Dassault Systèmes SolidWorks Corporation, Waltham, MA, USA).

In order to assess the contact position on the cup, a number of variables were considered synonymously. These included cup positioning, global hip kinematics, force vector orientation and contact area. Variables were input to a SolidWorks design, to replicate cup loading for the peak HRF. Default cup positioning was set to 45° inclination and 20° anteversion. It is important to note that the femoral stem (femoral offset) was not modelled during analysis. Although the potential for edge loading was not quantified, the model provided a visualisation of the position that the acetabular cup was loaded (eg. anterior, posterior, medial and lateral). Coupling this with contact area results, provided reasonable evidence as to whether or not edge loading may occur.

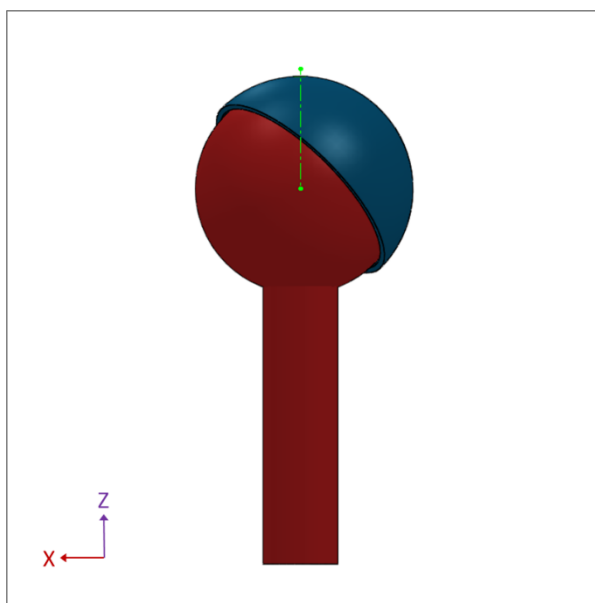


Figure 177. Anterior view of the cup (blue) and femoral component (red) assembly within SolidWorks. Force vector orientation is represented as a green, dotted line. Axis directions are shown as X (lateral) and Z (superior). The cup is fixed to a position of 45° inclination and 20° anteversion.

6.4.3.1. Force Vector Orientation

The orientation of peak resultant HRF vectors, relative to the femoral head coordinate system, varied between activities. All vectors acted from an anterior and lateral position on the femoral head (at peak loading). Vector orientations ranged from 97° to 115° (relative to the medial-lateral axis), 80° to 87° (relative to the anterior-posterior axis) and 8° to 25° (relative to the proximal-distal axis) (section 5.3.3.10 and 6.3.7.). This variation was a function of the variation in hip kinematics, between activities. Although small differences were seen between vector orientations (at the femoral head), global hip kinematics had a larger influence on the ultimate position of cup loading.

6.4.3.2. Force Vector Contact Area

Given that contacting surface geometries and boundary conditions were consistent for all activities, contact areas were directly influenced by the magnitude of hip loading. Peak contact area diameters ranged from 6.76 mm (kneel reach) to 15.68 mm (sit to stand) (section 6.3.7.). Given that the acetabular cup diameter was ≈ 28 mm, 8 of the 9 activities contacted over 40% of the cup at peak loading.

6.4.3.3. Cup Loading Position

Peak HRF during walking (occurring at heel off), contacted anterior and lateral portions of the acetabular cup roof (section 6.3.7.1.). Given that the contact area was estimated to cover 40% of the cup, it is possible that anterior edge loading will occur at this point in the gait cycle (Esposito et al., 2012). Contrastingly, peak hip loading for the walk turn (occurring at heel strike) contacted the roof of the cup, laterally from the pole (section 6.3.7.2.). The increased hip flexion at heel strike, compared to heel off, shifted the contact point posteriorly, closer to the pole of the cup. Although 52% of the cup was loaded at this point, edge loading seems unlikely, given that the force vector contacted the cup centrally, close to the pole. Previous literature has suggested that edge loading can occur at both of the two HRF peaks during walking (between 45 and 55% of the cycle) (Hua et al., 2016). However, this was only found to be the case when the acetabular cup inclination angle was above 65° (Hua et al., 2016). This might explain why edge loading was not obvious within the current study, where the cup inclination angle equalled 45°. Previous *in vivo* studies have suggested that microseparation may occur at heel-strike, thus leading to edge loading (Al-Hajjar et al., 2010; Kwon et al., 2012; Mak et al., 2002). This separation (caused by a mismatch in component positioning) was not included within the current study.

Stand to sit (StSi) and sit to stand (SiSt) showed peak HRFs at similarly high hip flexion angles (80° and 74°, respectively). These high flexion angles saw the point of contact shift posteriorly on the cup. For the data presented, this peak force would almost certainly contact the edge of the cup, given the cup contact areas of 48% (StSi) and 63% (SiSt) (sections 6.3.7.3. and 6.3.7.4.). Hua et al. (2016) did not report edge loading for sitting and standing (based on a finite element model). Contrastingly, previous *in vivo* and retrieval studies have argued that edge loading is likely to occur both when sitting down and standing up (Esposito et al., 2012; Kwon et al., 2012; Walter et al., 2004).

Posterior cup loading was also observed at peak HRFs during the Squat (80° of hip flexion), stand reach (70° of hip flexion) and kneel reach (68° of hip flexion) (sections 6.3.7.5., 6.3.7.6. and 6.3.7.7.). It is likely that posterior edge loading would occur at this point for the squat and stand reach, given the cup contact areas of 49% and 44%, respectively. Kneel reach, however, resulted a contact area of 12% suggesting that edge loading is unlikely.

Peak HRF for the lunge (occurring during the propulsion phase), showed a similarly anterior contact point as reported for the walk, albeit at a more lateral cup position (section 6.3.7.8.). Interestingly, the cup contact area was the same for the lunge and the walk (41%). Both activities may therefore be at risk of anterior edge loading of the cup.

The golf swing exhibited a peak HRF at the bottom of the down-swing. The HRF contacted the acetabular cup roof, medially from the pole (section 6.3.7.9.). Given that this contact point is close to the pole of the acetabular cup, edge loading is unlikely, as the corresponding contact area was just 40% of the cup. Given that this occurred at a point of peak hip flexion for the golf swing, it is unlikely that posterior edge loading would occur during this activity.

Within the literature, peak pressure has been located at the lateral roof of the acetabulum, at mid-stance during walking (for the natural hip). Whereas during standing and sitting, cup loading shifted to the posterior edge of the cup (Walter et al., 2004; Yoshida et al., 2006). Similar loading positions were found in the current study, supporting the reliability of the SolidWorks visualisation model. Posterior loading during high flexion activities, occurred due to the contraction of hip abductors, pulling the femoral head towards the periphery of the joint and edge of the cup. Yoshida and colleagues (2006) highlighted the influence of torso positioning during sitting and standing. Forces were found to be higher when the coronal plane of the torso was positioned perpendicular to the long axis of the

femur, as this limited the use of body weight to generate momentum, thus increasing the muscular requirement. This may be the reason for the high HRF variability seen between subjects when sitting and standing and is likely to influence the position of cup loading (Table 15). For high flexion activities, with potential edge loading, it is important to appreciate that the theoretical contact area may fall outside of the cup liner. For this reason, the ‘actual’ contact area for these activities is likely to be reduced, thus increasing the pressure at the head-cup interface (Al-Hajjar et al., 2013; Al-Hajjar et al., 2017; Hua et al., 2016; Walter et al., 2004). This theory is supported by previous work that has shown higher pressures during high flexion activities (with posterior cup loading), compared to those in which the cup is loaded centrally (Yoshida et al., 2006).

Retrieval analysis has highlighted ‘stripe wear’ whereby both the head and the cup experience wear due to edge loading (Hua et al., 2016; Walter et al., 2004). Although microseparation at initial contact (during walking) is a possible explanation for anterior edge loading, the majority of wear stripes are thought to occur during high flexion activities, through posterior edge loading (Walter et al., 2004). High levels of superior head loading and posterior cup loading were seen during high flexion activities within the current study (stand to sit, sit to stand, squat, stand reach). These activities have the potential to cause retroverted stripes on the femoral head, as seen in retrievals by Walter and colleagues (2004). For polyethylene cup edge loading, it has been suggested that 78% of cases can be expected to occur posteriorly (Shon et al., 2005). This reiterates the rationale that high flexion activities are a possible cause of excessive cup wear.

The implications for edge loading are two-fold. Firstly, a loss of entrainment of synovial fluid is to be expected, resulting in the breakdown of lubricating film at the joint. Secondly, an increased local contact pressure, and therefore reduction in film thickness at the rim, can be observed (Underwood et al., 2012). Ultimately, high HRFs observed close to the edge of the liner (as seen for stand to sit, sit to stand, squat and stand reach) may lead to the failure of the fluid entrainment mechanism and possibly excessive localised wear (Underwood et al., 2012).

6.4.3.4. *Overall Discussion*

A number of the high flexion activities assessed have the potential for posterior edge loading (stand to sit, sit to stand, squat and stand reach). Increases in hip flexion shift the contact area to the posterior edge of the cup, thus reducing the ‘actual’ cup contact and increasing pressure (Al-Hajjar et al., 2013; Al-Hajjar et al., 2017; Hua et al., 2016; Walter et al., 2004). High HRFs coupled with low contact areas, at the cup edge, may reduce the fluid film layer and potentially lead to excessive localised wear. For this reason, these activities demonstrated the highest risk to wear when at peak flexion. Kneel reach showed high peak hip flexion values. However, the corresponding HRF was low, thus leading to a small contact area and reduced likelihood of edge loading (and reduced fluid film).

Walk, walk turn and lunge all demonstrated peaks following heel-off, during the propulsion phase (this was the 2nd and smaller peak for the walk turn). At this point, anterior edge loading is possible, given that the hip is extended and cup contact is shifted anteriorly. Initial contact during walking tasks also demonstrates a risk of edge loading, given that microseparation may occur following the swing phase (Al-Hajjar et al., 2013; Al-Hajjar et al., 2010; Lombardi Jr et al., 2000; Mak et al., 2002; Walter et al., 2004). In summary, initial contact (walk, walk turn) and propulsion (walk, walk turn and lunge) peaks may lead to excessive wear at the head-cup interface, albeit for different reasons.

The golf swing showed peak cup loading at a central position. Given that this was at a point of maximum flexion, posterior edge loading is unlikely. With this being said, the golf swing saw extension of the hip alongside a HRF of 1.0 *p*BWT, during the follow through. Although anterior edge loading is unlikely for the current data set, it is conceivable that more experienced golfers (than the current cohort) who maximise hip loading and extension during this period of the swing, could be at risk.

The position of cup loading provides important information relating to the potential wear of the polyethylene acetabular cup. Still, it is essential to assess localised cross-shear motion and sliding velocities alongside cup loading conditions, in order to gain a fuller picture of the potential wear mechanisms for a given activity. Furthermore, it is important to appreciate that prosthetic design and component malposition will also influence edge loading, alongside the biomechanics of an activity (Hua et al., 2016).

6.4.3.5. *Summary*

Edge loading is a key variable that will influence wear at the polyethylene liner of a total hip replacement. High contact forces combined with low contact areas, at the edge of the acetabular cup, may lead to a reduction in the fluid film, increased friction and thus increased wear. Activities demonstrating high hip flexion, may therefore be at risk of this phenomenon. It is important to note that edge loading is visualised within this thesis and therefore represents a predicted visualisation model. A validated edge loading model, incorporating pelvic tilt, would be required in order to fully understand this phenomenon for individual activities.

6.5. Conclusion

Hip motion path data indicates that certain activities may be at a higher risk of cross-shear motion than others. This appears to be driven by the combination of global kinematics at the hip. Activities with a high ROM in one plane, and minimal motion in the other two, generally showed more linear motion paths with high aspect ratios. Activities with multi-directional global hip kinematics, however, generally showed more multidirectional motion paths with lower aspect ratios. Sliding distances, velocities and accelerations may provide a useful tool for ‘ranking’ activities in terms of their potential risk of inducing cross-shear wear at the hip joint. By combining this with hip reaction forces and the potential for edge loading, a theoretical picture can be built for activities and individuals in relation to wear at the hip. This may provide useful information relating to the durability of THRs/tissue engineered hip cartilage, as well as for post-operative patients during rehabilitation (eg. providing information on the potential risks of certain activities).

7. Overall Discussion

This overall discussion chapter considers the study results synonymously, before drawing conclusions from the work. This ‘Synthesis of Results’ discusses the findings relating to:

- Kinematics (section 4.3)
- Kinetics (section 5.3)
- Motion Paths (6.3)
- Edge Loading (section 6.3)

This is proceeded by overall discussion of:

- Implications (section 7.2)
- Limitations (section 7.3)
- Future Work (section 7.4)

Almost one million total hip replacements (THR) have been implanted in the UK since 2003, with the primary cause cited as osteoarthritis induced cartilage degradation (NJR, 2018). The operation has been commended for decreasing pain and increasing function, with positive long term clinical results (Evans et al., 2019). However, success post-op has been found to decrease for younger, more active patients (<55 years of age) when compared to those who are older and less active (>55 years of age) (Fumes et al., 2001; NJR, 2018). With THR patients becoming younger and more physically active, patient activity is a likely cause of this variation between age groups (Kurtz et al., 2009; NJR, 2018). This has raised concerns surrounding the influence of different activities on hip motion and loading, and thus, the potential for hip surface wear. By assessing this for healthy subjects, the findings can be translated to active, high risk patient groups who have a THR or tissue engineered hip cartilage substitution.

THR wear is directly related to sliding distance (length of relative motion paths between hip surfaces) (Cooper et al., 1993), cross-shear (relative motion path directionality) (Barbour et al., 1999), load (Barbour et al., 1997) and edge loading (contact of the femoral head on the acetabular rim) (Al-Hajjar et al., 2013; Al-Hajjar et al., 2017; Esposito et al., 2012; Hart et al., 2013; Hua et al., 2016; Walter et al., 2004). Although this link is relatively straight forward when considering variables independently, the relationship becomes more complex when considering variables synonymously. In addition to this, one must consider the linear relationship between patient activity levels and wear (Schmalzried et al., 2000). Ultimately, the amount (Schmalzried et al., 2000) and types (Bowsher and Shelton, 2001) of physical activity following a THR, are the driver for potentially excessive wear rates.

Cartilage wear has been linked to load/ contact area and the variation in sliding velocity (Katta et al., 2008a; Lipshitz et al., 1980; Lipshitz and Glimcher, 1975; Lipshitz and Glimcher, 1976). High loads and low sliding velocities influence the lubrication conditions at the hip, thus allowing for potential wear between cartilage-cartilage asperities (Radin and Paul, 1971; Stewart, 2010; Stewart et al., 1997). Again, this mechanism is related to the amount and type of physical activity post-surgery.

This thesis examined the influence of 13 common activities on hip tribology, through assessing both global and local biomechanical variables. The aforementioned variables were considered, in order to understand the potential risk of wear at the hip. Further to this, variation between age and gender was analysed.

7.1. Synthesis of Results

Within this section, all results are considered synonymously and the key findings are discussed. An overall summary is then presented, relating to the thesis results.

This section aims to assess the combined localised motion and loading, occurring between the femoral head and acetabular cup, for each of the 13 activities. This synthesis will focus on motion paths occurring at femoral head Point 7 (*Medial, Anterior, Distal*; 0 mm, 7 mm, 12 mm) as this was positioned distally and anteriorly, at the approximate location of peak hip loading (Tables 14 and 18). Motion path aspect ratios (ARs) and sliding distances are considered, alongside the peak hip reaction force (HRF) and corresponding sliding velocity (SV) and acceleration (SA). The potential for edge loading is also considered for each activity. Bringing these key variables together, provides a basis for conclusions to be drawn on the primary aim of investigating the link between global hip biomechanics and localised tribological variables, in relation to wear, at the hip.

Motion paths showed variation both between subjects and across femoral head points, for all 13 activities. Mean motion path ARs quantify the average cross-shear occurring across the femoral head surface. However, given that not all femoral head points were in contact with the acetabular cup throughout movement, it is likely that this average was skewed. Point 7 was positioned distally and anteriorly on the femoral head. This was located close to the centre of the resultant HRF for activities, thus deeming it a reasonable point for analysis. Due to variation across femoral head points, a high mean AR did not necessarily guarantee a high AR at Point 7. Assessing the SV across a motion path, provided information relating to the lubrication regime at a given time. A low SV indicated a period within the movement cycle, where the fluid film was reduced between bearing surfaces and friction was increased (Katta et al., 2008a; Stewart, 2010; Stewart et al., 1997). Additionally, by assessing peak SAs along a motion path, changes in direction of the trajectory were identified. This highlighted specific periods within the gait cycle, where cross-shear was high (Dressler et al., 2011). Table 23 shows motion path (AR, sliding distance, SV and SA) and HRF data for each of the 13 activities and the Leeds Prosim hip wear simulator (ISO-14242 input data). Figures 178 to 183 demonstrate the relationship between HRF, SV and SA for the walk turn, sit to stand, lunge, golf swing, walk and Leeds ProSim input data. It is noteworthy that similar graphs are presented for other activities within the Appendix (section 10.5.).

Table 23. Motion path aspect ratio (AR), sliding distance, sliding velocity, sliding acceleration and hip contact force (proportional to body weight: p BWT) for 13 activities and the Leeds Prosim hip wear simulator. Aspect ratios are shown both for the average across the femoral head and for Point 7 (Located anteriorly and at the approximate position of femoral head loading: Medial: 0 mm; Anterior: 7 mm; Distal: 12 mm)

	Mean motion path AR	Point 7 motion path AR	Mean sliding distance (mm)	Peak sliding velocity at Point 7 ($\text{mm}\cdot\text{s}^{-2}$)	Peak sliding acceleration at Point 7 ($\text{mm}\cdot\text{s}^{-2}$)	Peak resultant hip contact force (pBWT)
Walk	3.6	4.1	20.4	44.4	588.8	3.1
Walk turn	3.4	2.1	18.3	33.5	840.0	4.1
Incline walk	3.9	4.8	21.6	36.5	346.0	-
Decline walk	3.0	3.7	18.0	36.5	472.3	-
Stand to sit	12.7	8.7	15.2	17.6	70.1	4.2
Sit to stand	14.4	13.1	13.0	20.1	84.2	6.4
Sit cross legged	6.3	10.0	22.5	21.8	150.2	-
Squat	13.7	14.5	27.8	22.9	91.3	4.3
Stand reach	12.9	12.8	23.8	13.0	43.0	3.5
Kneel reach	14.4	13.3	21.7	9.6	32.2	0.5
Lunge	5.0	4.0	36.7	35.6	409.8	3.1
Golf swing	6.2	2.8	15.0	6.8	21.9	4.0
Cycle	9.8	10.8	12.4	28.0	480.5	-
Leeds Prosim	12.2	3.0	19.4	30.1	196.8	3.9

Walking tasks showed the lowest mean ARs, in comparison to other activities (all below 4.1). Although the AR at femoral head Point 7 remained low (all below 5), increases (compared to the mean) were seen for the walk (+0.5), incline walk (+0.9) and decline walk (+0.7). Interestingly, walk turn saw a decrease in the AR at Point 7 (-1.3), indicating an increase in cross-shear at this position (Table 23). All walking tasks demonstrated two SA peaks. These changes in direction of the motion path, occurred at initial contact and toe-off. Corresponding HRFs peaked alongside the first SA peak (and change in direction) of the motion path, at initial contact. However, at the second peak SA (toe-off), HRF was low. Corresponding SVs were high at initial contact and toe-off, as global hip angular velocity was high at these points. This suggests that although the acetabular cup may experience high cross-shear force, the lubrication regime will ensure that bearing surfaces do not come in to contact (Katta et al., 2008a; Stewart, 2010; Stewart et al., 1997). With this being said, it is possible that microseparation (occurring during and following the swing phase) will lead to hip surfaces coming into contact (Al-Hajjar et al., 2013; Al-Hajjar et al., 2017; Al-Hajjar et al., 2010; Mak et al., 2002; Walter et al., 2004). The cup may therefore be at risk of excessive wear at initial contact (particularly for the walk turn, given the high SA and HRF) (Table 23 and Figure 178). Further to this, anterior edge loading may occur for walking tasks at heel-off (during the propulsion phase of gait), as the hip is extended and the contact area is shifted anteriorly. This would reduce contact area and increase stress (Al-Hajjar et al., 2013; Al-Hajjar et al., 2017; Mak et al., 2002).

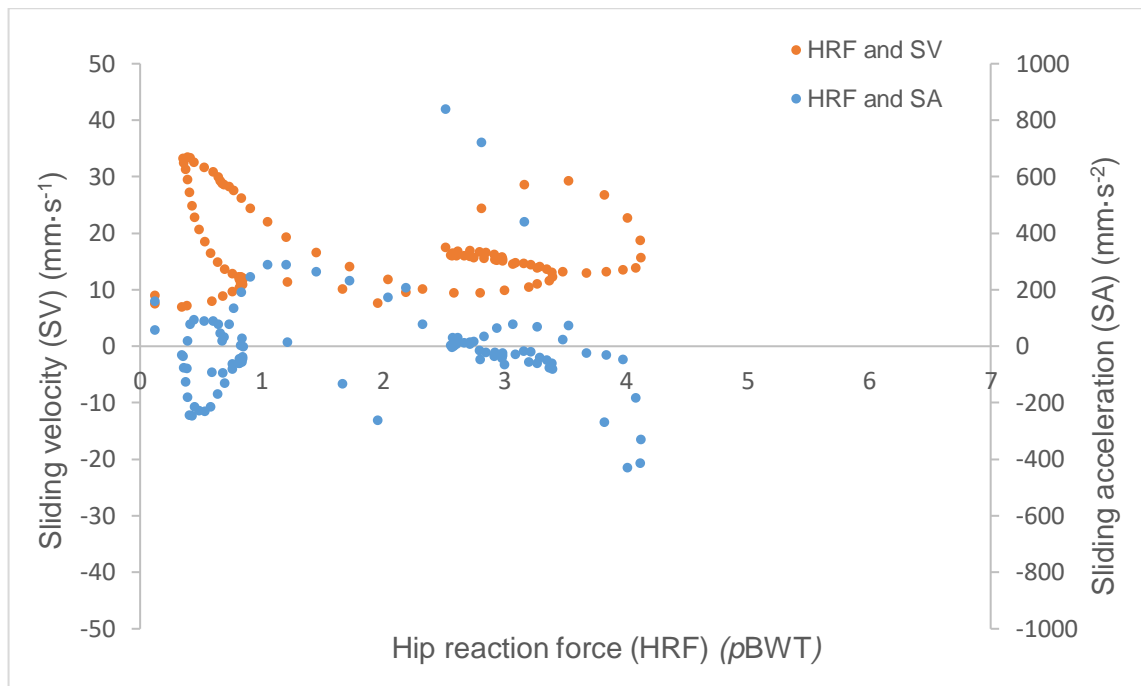


Figure 178. Hip reaction force (proportional to body weight or $pBWT$) is shown alongside the corresponding sliding velocity and sliding acceleration for a walk turn motion path. The motion path is located at femoral head ‘Point 7’ (*Medial, Anterior, Distal*; 0 mm, 7 mm, 12 mm).

Figure 178 shows periods within the walk turn where both high SA and HRF may occur. It also shows the variable SV occurring throughout the movement (in relation to HRF). The peak HRF (4.1 $pBWT$) corresponded to a SA of (413 $mm \cdot s^{-2}$). Additionally, peak SA (840 $mm \cdot s^{-2}$) occurred alongside a force of 2.5 $pBWT$ (interestingly, SV is low at this point: 13 $mm \cdot s^{-2}$). Similar to other walking tasks, these two points within the gait cycle (both occurring at approximately initial contact) may be at risk of excessive wear. However, the tribological conditions were potentially worse for the walk turn than the straight walk, given the increased SA.

Stand to sit (StSi), sit to stand (SiSt), sit cross-legged, squat, stand reach and kneel reach all showed high average ARs. High ARs were also observed at Point 7, alongside low peak SAs (Table 23). This indicated linear motion paths with low cross-shear. For this reason, cross-shear wear at a polyethylene cup or cartilage substitution is unlikely. The high sliding distances associated with these activities is therefore unlikely to increase polyethylene/cartilage substitution wear, as strain hardening will occur (Wang, 2001). With this being said, SVs were low throughout these movements, indicating that the fluid film layer is likely to be reduced at the joint and friction will be increased between bearing surfaces (Katta et al., 2008a; Stewart, 2010; Stewart et al., 1997). Furthermore, all of these

high flexion activities were susceptible to posterior edge loading (except for the kneel reach). It can therefore be suggested that polyethylene wear may be exacerbated in these activities, should the femoral head make contact with the edge of the acetabular cup.

Avoiding unnecessarily high hip flexion is therefore crucial for THR patients, whether that be through avoiding low seats, avoiding deep squats or avoiding bending at the hip. Peak HRFs were generally large for the high flexion activities, due to the requirement for hip flexors to balance the body. The SiSt had the highest peak HRF (6.4 *pBWT*). This was higher than previously reported values within the literature, highlighting the potentially high variability in kinematics for this movement. The peak HRF occurred alongside peak flexion, suggesting that should edge loading occur, head-cup contact force is likely to be high. A number of methods could be implemented to reduce this peak force, such as avoiding low chairs, using the arms when rising, rocking forwards to gain momentum (thus reducing the requirement for hip flexors) and standing up more slowly (thus reducing the HRF whilst maintaining the required impulse).

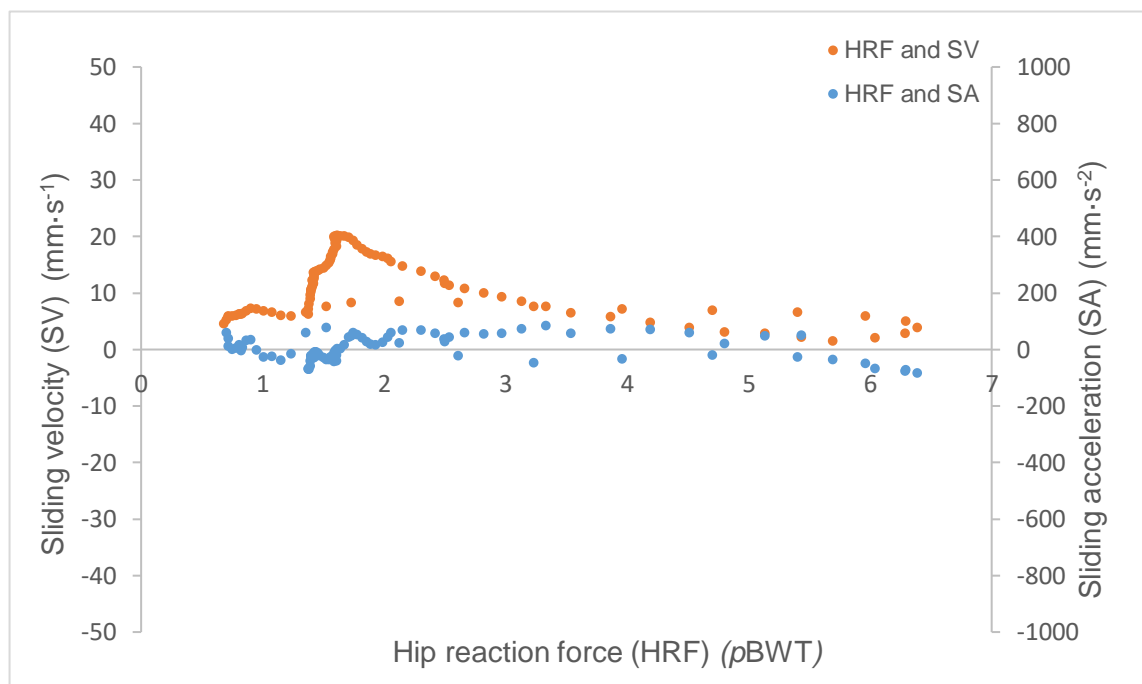


Figure 179. Hip reaction force (proportional to body weight or *pBWT*) is shown alongside the corresponding sliding velocity and sliding acceleration for a sit to stand motion path. The motion path is located at femoral head ‘Point 7’ (*Medial, Anterior, Distal*; 0 mm, 7 mm, 12 mm).

Figure 179 shows high peak HRFs, alongside the consistently low SAs for the sit to stand. The SV is generally low, with a peak occurring at approximately 2 *p*BWT (this was during the dynamic motion of standing up, when hip angular velocity is high). Similar trends were seen for other high flexion activities, albeit with lower peak HRF values (Appendix – section 10.5.). Figure 179 supports the suggestion that, in spite of the high HRFs, cross-shear remains low throughout the sit to stand.

The lunge showed a higher average AR than the walk (+1.4). The AR at Point 7, however, was similar for the two activities (Walk: 4.1; Lunge: 4.0) (Table 23). The lunge resulted a high peak SA, occurring at heel-off, during the step before lunging down. Hip loading, however, was low at this point. The SA remained low when moving down and up into the lunge, due to the linearity of the movement. The peak HRF (3.1 *p*BWT) occurred during the propulsive phase of the movement, where cross-shear was low, suggesting that severe cross-shear surface wear is unlikely at this point. Similar to the walk, SV was high during the majority of the lunge, indicating that a fluid film lubrication regime is likely. However, as the cup loading position was similar for the walk and the lunge, the lunge may be susceptible to anterior edge loading following heel-off (when propelling up and out of the lunge). This may lead to a reduction in contact area and an increase in cup stress (Al-Hajjar et al., 2013; Al-Hajjar et al., 2017; Al-Hajjar et al., 2010; Hua et al., 2016; Walter et al., 2004).

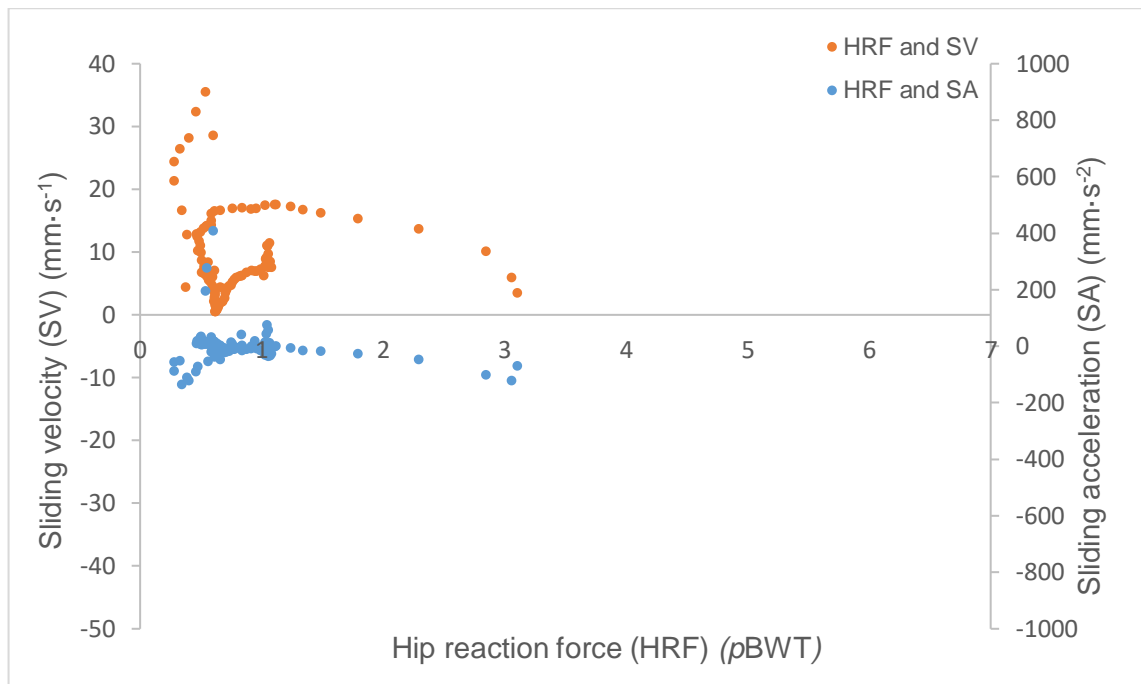


Figure 180. Hip reaction force (proportional to body weight or *pBWT*) is shown alongside the corresponding sliding velocity and sliding acceleration for a lunge motion path. The motion path is located at femoral head ‘Point 7’ (*Medial, Anterior, Distal*; 0 mm, 7 mm, 12 mm).

Figure 180 shows low SA throughout the majority of the lunge, whilst SV ranges from 1 to 36 $\text{mm}\cdot\text{s}^{-1}$. Peak SA ($410\text{ mm}\cdot\text{s}^{-2}$) occurred alongside a HRF of 0.6 *pBWT*, at heel-off of the step before the lunge. Although this may be a potential position where cup wear could occur, the lunge itself is unlikely to demonstrate a risk to cross-shear wear.

The golf swing showed a high average AR (6.2) with a marked reduction at point 7 (2.8) (Table 23). With this being said, SA during the golf swing was the lowest of all activities. This suggests that although the Point 7 AR was low, this was due to a reduced sliding distance, rather than an increase in multi-directional motion. During the golf swing, peak HRF occurred at the bottom of the downswing. The corresponding SA and SV was low at this point. It is therefore unlikely that cross-shear wear will occur (even though the fluid film may be depleted). Due to the lack of hip flexion and extension, posterior edge loading was unlikely for the golf swing within this study. However, this may not necessarily be the case for a more experienced group of golfers, where flexion-extension range of motion at the hip may be increased. It is also important to appreciate that hip loading is likely to increase for a more experienced group of golfers (Hume et al., 2005).

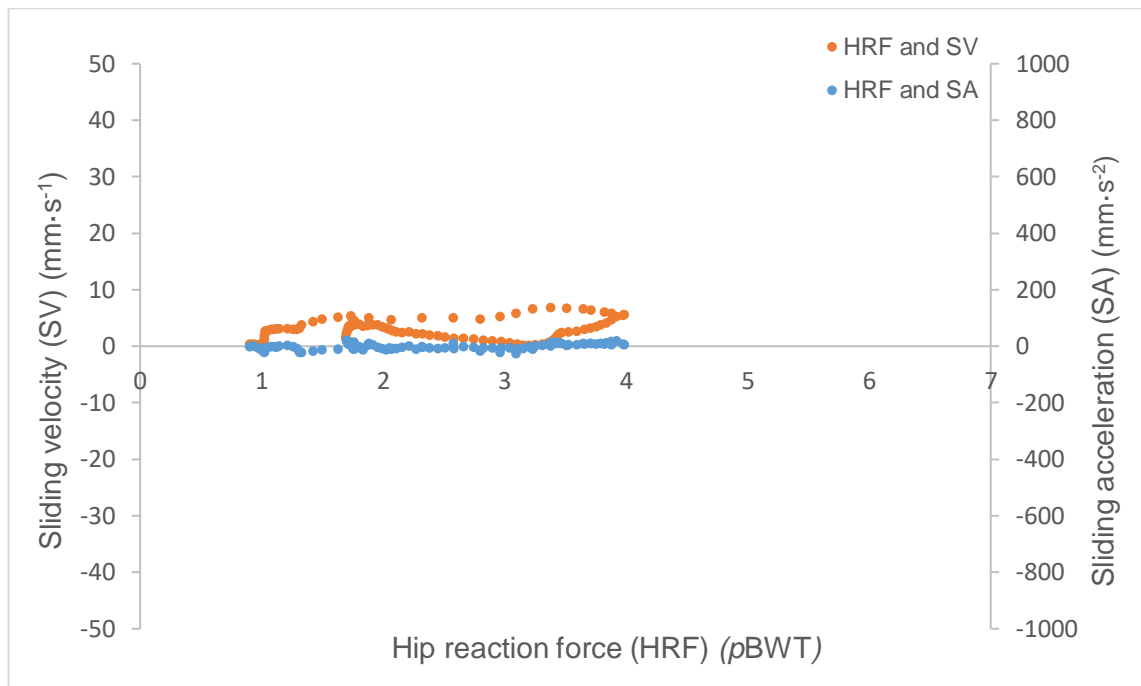


Figure 181. Hip reaction force (proportional to body weight or $pBWT$) is shown alongside the corresponding sliding velocity and sliding acceleration for a golf swing motion path. The motion path is located at femoral head ‘point 7’ (*Medial, Anterior, Distal*; 0 mm, 7 mm, 12 mm).

Figure 181 shows low SV and SA throughout the golf swing. This suggests that cross-shear wear will not occur at the cup during this activity.

Cycling showed high average (9.8) and Point 7 (10.8) ARs. Two SV peaks were observed: one at $\approx 25\%$ and one at $\approx 75\%$ of the cycle. The corresponding SA showed two peaks: one at $\approx 25\%$ and one at $\approx 80\%$ of the cycle (Table 23). Although force was not recorded for the cycle, these two points may represent periods where high cross-shear will occur at the femoral head-cup interface. An implemented force transducer would be required at the bicycle pedal in order to gain a more detailed insight into this activity.

Input kinematics for the Leeds Prosim hip wear simulator (ISO) resulted an average AR of 12.2 (Table 23). Although this appears to be an inaccurate representation when compared to the walking average (3.6), the Point 7 ARs were similar (Walk: 4.1; ISO: 3.0). ISO motion paths appear to be accurate at key points on the femoral head (where the head and cup make contact), whilst more linear paths occurred at points which are unlikely to come into contact. Both the sliding distance (within 1 mm) and peak HRF (within 1 $pBWT$) are similar for the ISO and walking data sets. The ISO SV, however, was underestimated. A 32% reduction was shown at the peak, compared to measured walking data. Additionally, the peak SA may be a cause for concern, given that it is 67%

lower than the value reported for walking within the current study. The implication for this discrepancy is that the ISO input data is considerably underestimates the cross-shear occurring at a key point between the femoral head and acetabular cup, in comparison to the current study. Further to this, not only does the ISO data underestimate walking cross-shear, it does not consider motion path trajectories for other activities. This is unrealistic, as variation between individuals and activities is considerable (within the current study). A combination of motion path trajectories, in which polyethylene fibres experience variable multi-directional motion, is likely to be more realistic when replicating wear of a THR.

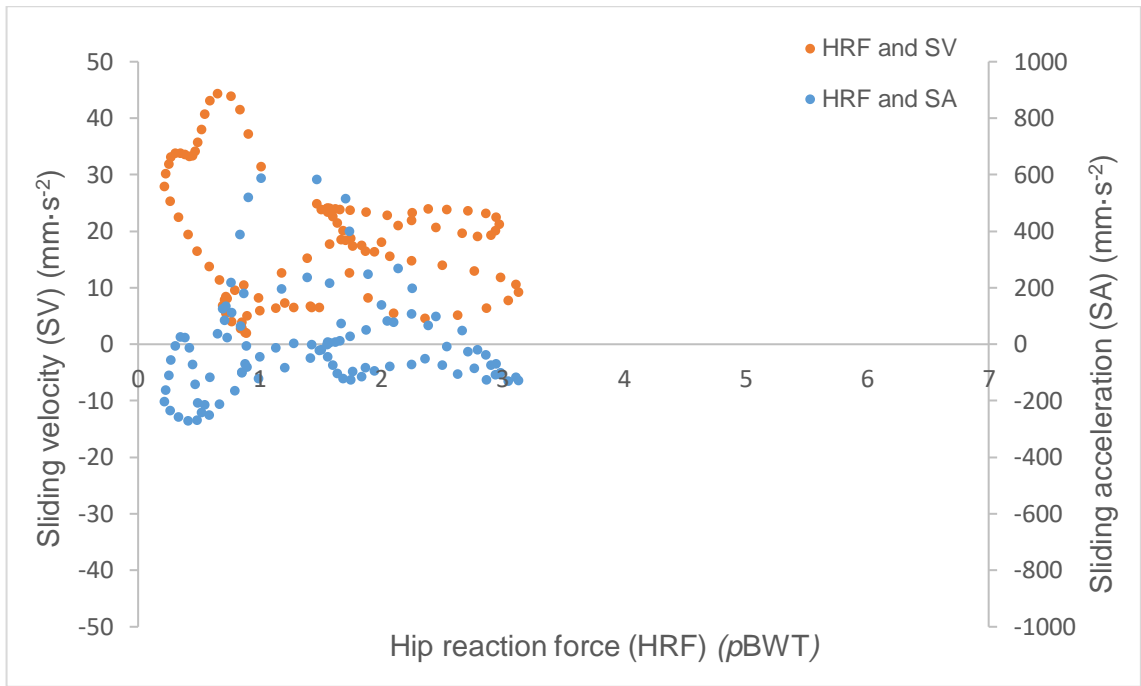


Figure 182. Hip reaction force (proportional to body weight or *pBWT*) is shown alongside the corresponding sliding velocity and sliding acceleration for a walk motion path. The motion path is located at femoral head ‘Point 7’ (*Medial, Anterior, Distal*; 0 mm, 7 mm, 12 mm).

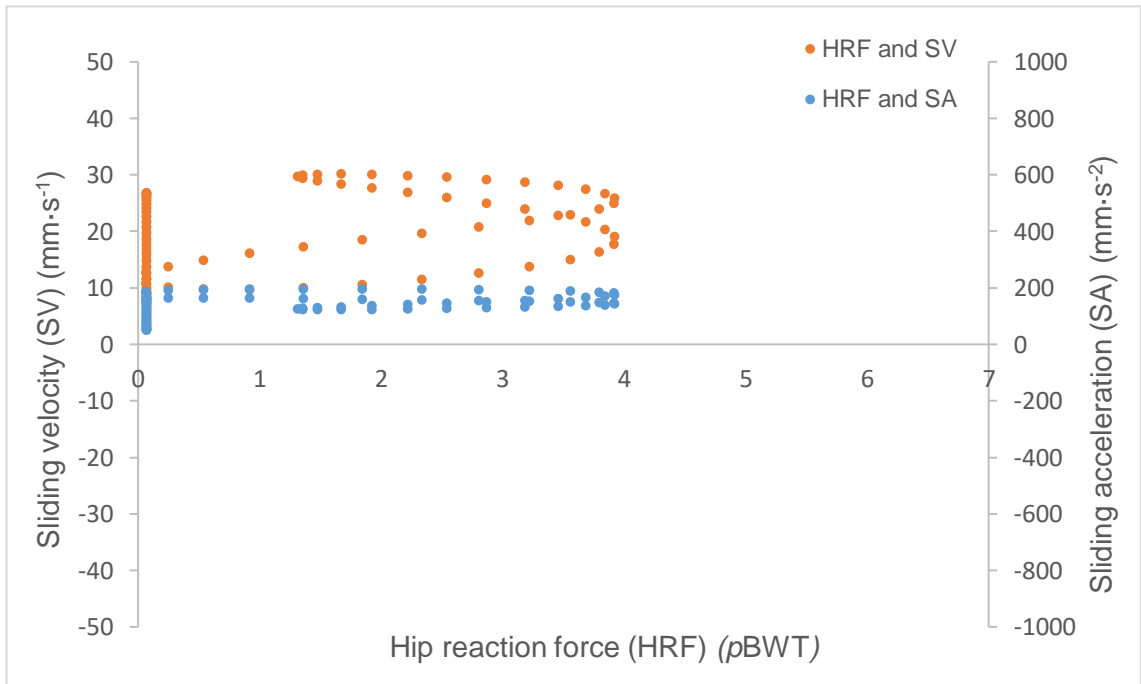


Figure 183. Hip reaction force (proportional to body weight or *pBWT*) is shown alongside the corresponding sliding velocity and sliding acceleration for a Leeds Prosim motion path input. The motion path is located at femoral head ‘Point 7’ (*Medial, Anterior, Distal*; 0 mm, 7 mm, 12 mm).

Figures 182 and 183 show HRF plotted against motion path SV and SA for the walk and the Leeds Prosim input cycle (ISO). The SVs are similar for both graphs, with averages

of approximately $20 \text{ mm}\cdot\text{s}^{-1}$. The walk did, however, show a SV range that was twice as large as the ISO. This suggests that the lubrication conditions will be different for the two motions. The cluster of both SV and SA at 0 pBWT, for the ISO, occurred because the simulator incorporates zero force throughout the swing phase. This was not the case in reality. The key difference between the graphs is the peak SA ($590 \text{ mm}\cdot\text{s}^{-2}$), occurring at 1.5 pBWT for the walk (at initial contact). This period of potentially excessive wear is not present on the ISO graph. Thus, it is possible that the Leeds ProSim simulator underestimates cross-shear wear at this point.

It is important to accurately replicate sliding distances, cross-shear, loading and edge loading within simulators, in order to estimate implant wear. Further to this, it is crucial to replicate the amount of use of the implant and the type of activities that a patient might engage in. Current simulator walking cycles run approximately one million cycles per year (heel strike to heel strike), which equates to ≈ 5500 steps per day. When considering the recommendation of 10,000 steps per day, it is possible that this replication is an underestimation for a more active THR patient group (Choi et al., 2007). Furthermore, the cycles do not incorporate activities other than walking. For this reason, a polyethylene cup is unlikely to experience the variable cross-shear which is likely to occur *in vivo*. It is possible that by testing more adverse conditions for a range of activities, a better understanding of early THR failure can be achieved. It is important to appreciate that this is reliant on collaborations between biomechanists, material scientists and test engineers. It is therefore likely that improving pre-clinical testing will be a complex, multi-disciplinary process.

Summary

Variation was shown for localised hip loading and cross-shear motion, between both activities and individuals. This body of work supports the suggestion that walking will lead to multidirectional motion and potential wear at a total hip replacement. Tribological analysis suggests that high cross-shear and hip reaction forces will occur for walking tasks, at initial contact (walk, walk turn, incline walk and decline walk). Potential wear at this point may be exacerbated should microseparation occur throughout the swing phase and at initial contact. Further to this, it is reasonable to suggest that anterior edge loading may occur at heel-off.

High flexion activities demonstrated a high risk of posterior edge loading. This may be particularly detrimental to activities showing high hip reaction forces (such as a sit to stand). More dynamic activities, such as a lunge and cycle, may also provide a risk to polyethylene wear. The propulsive phase of the lunge demonstrated a potential risk to anterior edge loading (alongside a high hip reaction force). Cycling showed two instantaneous points of high cross-shear - assessing the corresponding hip reaction force would allow for the implications of this to be explored further. The golf swing and kneel reach were two activities which did not indicate a risk to cross-shear wear. It is possible, however, that a different population group to that in the current study (such as more experience golfers) would show different results.

The Leeds Prosim simulator input (ISO) considerably underestimated walking sliding acceleration, and therefore cross-shear, at initial contact. Further to this, input kinetics and kinematics did not account for the cross-shear variation shown within this study. Results suggest that simulator cycles should attempt to incorporate a wider range and variation of input cycles, in order to more realistically wear test polyethylene liners.

7.2. Implications

The localised hip motion path and loading data within this study have three main implications, relating to: 1) pre-clinical testing of hip prostheses, 2) testing of tissue engineered cartilage substitution and 3) understanding the risk associated with different activities following a total hip replacement (THR). In addition to these three implications, the project provides a methodology, describing a tool in which hip replacement cross-shear loading can be estimated.

7.2.1. Pre-clinical Testing

Pre-clinical testing of THR is achieved by mounting the device within a hip simulator (such as the Leeds Prosim hip wear simulator). Kinematic motion and cyclical loads are applied to the device, with the aim of replicating the patterns seen when walking *in vivo*. Although kinematic patterns are simplified for the simulator to run smoothly, it is crucial that input data is representative, in order to ensure realistic wear paths. The motion path and loading data reported within the current study, provides a large data set that is relevant to pre-clinical testing of hip prostheses (n=18). When comparing measured walking data to the Leeds Prosim hip simulator input (ISO-14242) (Paul, 1966), similarities were seen between motion path aspect ratios and hip loading. With this being said, it is crucial to appreciate that although the motion path aspect ratio may be the same for two kinematic inputs, sliding conditions and instantaneous cross-shear occurring throughout the movement cycle may be different. At a closer look, a discrepancy was observed for peak hip sliding acceleration, between measured walking and ISO data. This suggests that hip simulators may be underestimating cross-shear occurring at the acetabular cup. Using information from the current study, one could potentially work towards improving the reliability of the kinematic input data used for simulators. Further to this, the variation reported within the current study provides data that could be used to replicate extreme conditions, for an asymptomatic patient at the edge of the standard deviation.

Pre-clinical testing currently only tests THRs using walking input data. This is counter-intuitive, given that the physical activity levels of THR patients are built up from a number of activities of daily living (Morlock et al., 2001). In order to effectively incorporate other activities into the testing of a THR, it is crucial to understand the biomechanics, localised tribology and inter-subject variability associated with different activities. The current study is the first to assess in detail, the motion paths occurring between bearing surfaces, for a range of activities. It is well established that walking has the potential to cause wear at the acetabular cup liner. This is due to the crossing of

adjacent motion paths throughout the gait cycle (Barbour et al., 1999; Barnett, 2009; Bennett et al., 2008; Bennett et al., 2002; Bennett et al., 2000; Budenberg et al., 2012; Saikko and Caloniuss, 2002; Saikko et al., 2003; Turell et al., 2003). Given the variation seen between motion paths for different movements, completing two or more activities sequentially is likely to exacerbate the crossing of paths at the cup. In order to improve testing accuracy, a number of activities should be simulated in cycles, based on the percentage at which they are completed by THR patients (Morlock et al., 2001). By including realistic variation in the motion path trajectories and hip loading, for a given wear test, the polyethylene is likely to be exposed to more realistic localised wear paths. This may provide more accurate estimations of the longevity of THR for a more active population.

7.2.2. Cartilage Testing

Small defects in articular cartilage can be repaired through the use of replacement tissue, with similar mechanical properties to the native tissue (Katta et al., 2008a). Cartilage plugs have shown increased wear when exposed to increases in normal loads, contact area and relative speed between opposing surfaces (Katta et al., 2008b; Lipshitz et al., 1980; Lipshitz and Glimcher, 1975; Lipshitz and Glimcher, 1976). Further to this, low relative sliding between surfaces has the potential to deplete fluid films and lead to contact and wear of cartilage asperities (Katta et al., 2008a; Stewart, 2010; Stewart et al., 1997). The relative sliding conditions and hip loading reported in this study provide reliable data that can be implemented into the testing of tissue engineered cartilage substitution. The wide range of activities included within this study provide data to realistically rotate and load cartilage substitution in order to replicate the actual conditions that might be expected to occur *in vivo*. The variation reported between subjects also provides important information which describes the ranges in magnitude for a given variable. This may be particularly useful when aiming to replicate extreme conditions.

7.2.3. Activity Risk

The population receiving THRs is becoming younger and more active (Clifford and Mallon, 2005). Due to variation between both individuals and activities, it has been difficult to determine the appropriateness of post-operative activity engagement (Morlock et al., 2001; Schmalzried et al., 1998). When considering a younger, more active patient group, it is reasonable to suggest that certain individuals will meet the recommended daily step count of 10,000 (Choi et al., 2007). For an individual commonly reaching this target,

it is reasonable to suggest that the current pre-clinical testing cycles for hip replacements (2 million steps per year, or ≈ 5500 steps per day) is unrealistic. Furthermore, the commonly used 2 million steps per year within hip simulators, does not account for other common daily activities. This begs the question of what ‘active’ means and whether the activity levels of an ‘active’ total hip replacement patient is truly understood.

The current study reinforces the suggestion that excessive acetabular cup wear may occur during walking. Results emphasise the importance of realistically replicating motion and loading, during pre-clinical testing of devices. Findings also highlight the importance of educating post-operative patients on the potential surface damage that can occur at the prosthesis (particularly during the ‘bedding in’ period) (Sychterz et al., 1999). Given the inter-subject variation between hip motion paths for walking, it must be appreciated that excessive wear may occur as a function of an individual’s biomechanics and that certain patients may be at a higher risk to wear than others.

Results indicated high levels of cross-shear, hip loading and potential edge loading for a number of activities. The dynamic nature of walking and turning 90° resulted in higher levels of cross-shear at initial contact, when compared to walking. This provides an insight into the potential risk associated with dynamic, turning movements. High flexion activities showed high inter-subject variation for both hip motion paths and loading. These data suggest that individual technique (possibly due to flexibility) is a key variable when considering the risk of wear during high flexion activities (such as sitting and standing). The data within this study is beneficial to physiotherapists who are interested in helping patients to protect the prosthesis long-term. Additionally, it provides evidence for advice given on the engagement in sporting activities such as golf, cycling and flexibility training.

7.2.4. Hip Wear Analysis Tool

This project has described a methodology in which hip angular data can be transformed into detailed motion path information. This can be achieved through an automated MATLAB script and/or by batch processed within Visual3D. Further to this, a Python macro script was written in order to allow hip reaction forces to be automatically estimated from C3D movement files (Appendix - section 10.3.) (Lund et al., 2019). Ultimately, the methodology describes a way in which a patient’s gait data can be analysed efficiently, from a tribological perspective. This may be beneficial for analysing sub-groups within a patient population and comparing to control data.

The current data set provides in depth biomechanics of healthy individuals ranging from 20 years old to 70 years old. This information could be used as a control group for future work on hip biomechanics. Further to this, the workspaces (Visual3D), spreadsheets (Microsoft Excel) and scripts (Anybody, Matlab and Python) may also provide the basis for future research into wear at the hip. These programs also have the potential to be developed and applied to other joints, such as the knee.

7.3. Limitations

A number of limitations are associated with the study, relating to both data collection and analysis. Unavoidable errors (noise) are likely to have been embedded in raw data. Applying complex calculations, with various assumptions, to the raw data is likely to have magnified this error. For this reason, it is important to appreciate that the findings within this study are estimations and unlikely to perfectly describe the *in vivo* biomechanics of individuals.

7.3.1. Data Collection

A significant limitation associated with gait analysis is that data calculations are based upon certain assumptions; joint kinetics and kinematics are not measured directly. The motion of surface markers is measured, allowing for segments to be modelled. Human error (associated with marker positioning) and soft tissue artefact will influence the trajectory of markers and thus the definition of segments and joint centres. This potential error is embedded into hip angle, moment and contact force calculations. Varying segment parameters (of up to $\pm 40\%$ of the baseline) have been found to significantly affect hip kinetic estimates by up to 1% of body weight (Pearsall and Costigan, 1999). Further to this, incorrect identification of joint centre locations by ± 30 mm, has been found to affect hip angle and moment results by at least 25% (Stagni et al., 2000). Due to these potential errors, it could be argued that gait analysis does not accurately represent the actual everyday activity pattern of an individual, rather, it describes the potential biomechanics of an individual at a given time (Simon, 2004). The confidence in biomechanical data, could be improved by repeating the same test protocol over a number of days. Although this may reduce error associated with environmental bias, human error and repeatability, inherent errors are still likely to be present due to soft tissue artefact.

7.3.2. Data Analysis

Inter-observer variability results have suggested that the interpretation of gait data will vary between individuals and institutions (Skaggs et al., 2000). The variation reported by Skaggs et al. (2000) was similar to that of established classification systems of various orthopaedic conditions. Accounting for this variability is therefore unnecessary within this study. With this being said, a number of hypothetically avoidable limitations are associated with the computational analysis within this project.

7.3.2.1. AnyBody Modelling

The calculation of inverse dynamics, within musculoskeletal modelling software such as AnyBody, is a well-accepted method for the analysis of human movement. It is important to appreciate that like most computational simulation methods, a number of assumptions are required to solve mathematical problems. This may lead to errors with the resulting output data.

AnyBody models rely on the accuracy of the input kinematics and ground reaction forces. Inaccuracies will lead to a mismatch between the subject and the model, therefore causing error within the optimisation and inverse dynamic calculations (Wehner et al., 2009). Further to this, joint force measurements are influenced by the muscle geometry and activation patterns within the model (Wehner et al., 2009). The lack of realistic muscle wrapping within the model (TLEM model), has previously been found to overestimate hip reaction forces by $\approx 10\%$ (Bergmann et al., 1993; Heller et al., 2001; Stansfield et al., 2003). It is therefore likely, that the joint reaction forces contain some error due to simplified geometries within the model. The best solution to these issues is to incorporate subject geometries (from MRI scans) to scale the model (Li et al., 2014). Rebuilding subject specific models is likely to reduce the aforementioned errors. Unfortunately, the current project did not have the funding or time that would be required to implement this. It must be appreciated that the resulting hip reaction force data was calculated from a default model, based upon an anthropometric data set from the University of Twente (Horsman, 2007). For this reason, some dynamic inconsistency is likely to exist within the model and may lead to residual hip reaction forces. The previously validated model was, however, scaled to height and mass, in order to reduce errors associated with segment lengths, segment orientations and joint centre locations.

7.3.2.2. Edge Loading Visualisation Model

A SolidWorks model was created for the visualisation of peak hip reaction force, at the corresponding hip angular position. When coupled with contact area, the model provides a visualisation of whether edge loading could occur. It is important to appreciate that this is an extremely simplified visualisation, created with the aim of aiding the readers understanding of the combination of variables and tribological implications. It may be beneficial for future work to test edge loading for activities in more detail, however this would require a complex finite element model in which detailed boundary conditions, seeding and geometries would be required.

7.3.2.3. *Data Interpretation*

The current study analysed a number of key biomechanical factors independently across the movement cycle of 13 activities. Peak hip reaction forces were coupled with global hip kinematics, key motion path data and hip contact area in order to gain a fuller picture of the tribological behaviour of the hip joint. Although this information provides evidence for the potential wear mechanisms for different activities, the findings must be tested experimentally (hip simulator or cartilage-cartilage wear testing) in order to fully understand the implications for the results. It is important to appreciate that wear is unlikely to occur through any single mechanism, due to the complexity of tribological and biomechanical variables for different individuals and implants (VanLaanen, 2013). A number of tribological conditions will effect wear rates, including: contact force, contact area, sliding distance, surface roughness, lubrication, cross-shear motion, contact angle, and material properties. Additionally, experimental protocol, manufacturing processes and surgical factors play a crucial role in both polyethylene and cartilage wear. In order to accurately understand hip tribology and wear, the results within this study must be considered alongside each of these key variables.

7.4. Future Work

This body of work has provided an understanding of the link between global hip biomechanics and localised tribological variables, in relation to wear at the polyethylene surface of a THR and tissue substitution at the natural hip. The project also outlines the potential risk of certain activities, following a THR. However, the concluding results present a number of additional research questions in which further investigation would be beneficial.

7.4.1. Pre-clinical Testing

Discrepancies between ISO testing standards and measured walking data, from a tribological perspective, suggest that there may be scope to further explore and develop THR testing methodologies. In addition to this, the detailed data set reported within the current study may be beneficial for the testing of tissue engineered cartilage substitution. Surface motions and loadings may be beneficial when designing realistic methodologies for mechanical testing of soft tissue.

7.4.2. Control Comparison

There is a requirement for better stratified studies, in which the effects of variables such as age and BMI can be characterised for THR patients. The healthy, control data within the current study, may be useful for future studies analysing hip tribology for a patient group. In a broader sense, the detailed biomechanical data reported in the current study will act as a comparison for any future work considering hip motion and loading. This is particularly novel, when considering the range of activities reported.

7.4.3. Knee Cross-shear

The methodology has the potential to be adapted for other human joints. It may be beneficial to adapt cross-shear calculations in order to be applied to a total knee replacement. This would require relative motion paths to be calculated at both contacting surfaces of the medial and lateral condyles. The same AnyBody musculoskeletal model (with input knee angles and ground reaction force) could be used to calculate knee reaction forces.

8. Conclusion

Within this thesis, global biomechanics and local tribology were examined at the hip for thirteen common activities of daily living. This was achieved through experimental work within a movement analysis lab, musculoskeletal simulations and cross-shear analysis.

Relative hip motion paths (and cross-shear) varied between individuals and across activities. Hip angular motion was directly related to localised cross-shear, with multi-directional activities demonstrating a higher risk of cross-shear, compared to more linear activities. In addition to this, low angular velocities and high peak flexion angles were associated with a decreased fluid film at the hip and the potential for surface contact and edge loading. High levels of variation were identified between individuals and across activities for hip reaction forces. This is another crucial variable which is likely to influence lubrication, edge loading and potential wear.

Discrepancies were identified between walking motion path data and hip simulator ISO input data. This highlights a potential limitation within current testing standards and should be considered within future hip wear testing.

This study has resulted a large set of biomechanical and tribological data, for a range of common activities. The variation shown between individuals should be considered when developing protocols for pre-clinical durability testing of both hip replacements and tissue engineered cartilage. Further to this, the variation between activities indicates that current testing standards should consider incorporating a range of activities, rather than just walking. The biomechanical data also provides evidence-based information that can be used to determine the appropriateness of post-operative activity/rehabilitation following a total hip replacement.

9. References

- Abdel, M. et al. 2016a. What is the lifetime risk of revision for patients undergoing total hip arthroplasty? a 40-year observational study of patients treated with the Charnley cemented total hip arthroplasty. *The bone & joint journal*. **98**(11), pp.1436-1440.
- Abdel, M.P. et al. 2016b. What safe zone? The vast majority of dislocated THAs are within the Lewinnek safe zone for acetabular component position. *Clinical Orthopaedics and Related Research*®. **474**(2), pp.386-391.
- Adams, J. and Hamblen, D. 2001. Outline of Orthopaedics. Thirteenth ed. London: Churchill Livingstone.
- Al-Hajjar, M. et al. 2013. Wear of 36-mm BIOLOX® delta ceramic-on-ceramic bearing in total hip replacements under edge loading conditions. *Proceedings of the Institution of Mechanical Engineers, Part H: Journal of Engineering in Medicine*. **227**(5), pp.535-542.
- Al-Hajjar, M. et al. 2017. Wear of composite ceramics in mixed-material combinations in total hip replacement under adverse edge loading conditions. *Journal of Biomedical Materials Research Part B: Applied Biomaterials*. **105**(6), pp.1361-1368.
- Al-Hajjar, M. et al. 2013. Effect of femoral head size on the wear of metal on metal bearings in total hip replacements under adverse edge-loading conditions. *Journal of Biomedical Materials Research Part B: Applied Biomaterials*. **101**(2), pp.213-222.
- Al-Hajjar, M. et al. 2010. Effect of cup inclination angle during microseparation and rim loading on the wear of BIOLOX® delta ceramic-on-ceramic total hip replacement. *Journal of Biomedical Materials Research Part B: Applied Biomaterials*. **95**(2), pp.263-268.
- AnyBody. 2019. *Any Tutorials*. [Online]. Available from: <https://anyscript.org/tutorials/index.html>.
- Archard, J. 1953. Contact and rubbing of flat surfaces. *Journal of applied physics*. **24**(8), pp.981-988.
- Banaszkiewicz, P.A. 2014. *Dislocations after total hip-replacement arthroplasties*. In *Classic Papers in Orthopaedics*. London: Springer.
- Barbour, P. et al. 1997. The influence of stress conditions on the wear of UHMWPE for total joint replacements. *Journal of materials science: Materials in medicine*. **8**(10), pp.603-611.
- Barbour, P. et al. 1999. A hip joint simulator study using simplified loading and motion cycles generating physiological wear paths and rates. *Proceedings of the Institution of Mechanical Engineers, Part H: Journal of Engineering in Medicine*. **213**(6), pp.455-467.
- Barbour, P. et al. 2000. A hip joint simulator study using new and physiologically scratched femoral heads with ultra-high molecular weight polyethylene acetabular cups. *Proceedings of the Institution of Mechanical Engineers, Part H: Journal of Engineering in Medicine*. **214**(6), pp.569-576.
- Barnett, J. 2009. *Motions in Space: The Motions of Femoral Heads over Acetabular Cups*. MSc thesis, University of Leeds.

- Barré, A. et al. 2015. Soft tissue artifact distribution on lower limbs during treadmill gait: influence of skin markers' location on cluster design. *Journal of biomechanics*. **48**(10), pp.1965-1971.
- Barry, J.J. et al. 2018. Recovery and outcomes of direct anterior approach total hip arthroplasty. *Annals of Joint*. **3**(6).
- Bartel, D. et al. 1985. The effect of conformity and plastic thickness on contact stresses in metal-backed plastic implants. *Journal of Biomechanical Engineering*. **107**(3), pp.193-199.
- Beaupre, L.A. et al. 2013. A randomized trial of ceramic-on-ceramic bearing versus ceramic-on-crossfire-polyethylene bearing in total hip arthroplasty: five-year outcomes. *The Journal of arthroplasty*. **28**(3), pp.485-489.
- Bell, A.L. et al. 1989. Prediction of hip joint centre location from external landmarks. *Human Movement Science*. **8**(1), pp.3-16.
- Bell, A.L. et al. 1990. A comparison of the accuracy of several hip center location prediction methods. *Journal of biomechanics*. **23**(6), pp.617-621.
- Bennett, D. et al. 2008. The influence of wear paths produced by hip replacement patients during normal walking on wear rates. *Journal of Orthopaedic Research*. **26**(9), pp.1210-1217.
- Bennett, D. et al. 2002. The influence of shape and sliding distance of femoral head movement loci on the wear of acetabular cups in total hip arthroplasty. *Proceedings of the Institution of Mechanical Engineers, Part H: Journal of Engineering in Medicine*. **216**(6), pp.393-402.
- Bennett, D.B. et al. 2000. Movement loci of selected points on the femoral head for individual total hip arthroplasty patients using three-dimensional computer simulation. *The Journal of arthroplasty*. **15**(7), pp.909-915.
- Bergmann, G. et al. 2001. Hip contact forces and gait patterns from routine activities. *Journal of biomechanics*. **34**(7), pp.859-871.
- Bergmann, G. et al. 1993. Hip joint loading during walking and running, measured in two patients. *Journal of biomechanics*. **26**(8), pp.969-990.
- Bergmann, G. et al. 1995. Is staircase walking a risk for the fixation of hip implants? *Journal of biomechanics*. **28**(5), pp.535-553.
- Bini, R. et al. 2019. Biomechanical and physiological responses to electrically assisted cycling during simulated mail delivery. *Applied Ergonomics*. **75**, pp.243-249.
- Bosker, B. et al. 2007. Poor accuracy of freehand cup positioning during total hip arthroplasty. *Archives of orthopaedic and trauma surgery*. **127**(5), pp.375-379.
- Bowsher, J. and Shelton, J. 2001. A hip simulator study of the influence of patient activity level on the wear of crosslinked polyethylene under smooth and roughened femoral conditions. *Wear*. **250**(1-12), pp.167-179.
- Bozic, K.J. et al. 2010. Risk of complication and revision total hip arthroplasty among Medicare patients with different bearing surfaces. *Clinical Orthopaedics and Related Research*. **468**(9), pp.2357-2362.
- Bragdon, C. et al. 1996. The importance of multidirectional motion on the wear of polyethylene. *Proceedings of the Institution of Mechanical Engineers, Part H: Journal of Engineering in Medicine*. **210**(3), pp.157-165.

- Brand, R.A. et al. 1994. Comparison of hip force calculations and measurements in the same patient. *The Journal of arthroplasty*. **9**(1), pp.45-51.
- Bremer, A. et al. 2011. Soft-tissue changes in hip abductor muscles and tendons after total hip replacement: comparison between the direct anterior and the transgluteal approaches. *The Journal of bone and joint surgery. British volume*. **93**(7), pp.886-889.
- Brown, M. et al. 1980. Walking efficiency before and after total hip replacement. *Physical therapy*. **60**(10), pp.1259-1263.
- Buckwalter, J.A. et al. 2000. *Orthopaedic basic science : biology and biomechanics of the musculoskeletal system*. Rosemont, IL: American Academy of Orthopaedic Surgeons.
- Budenberg, S. et al. 2012. Contact surface motion paths associated with leg length inequality following unilateral total hip replacement. *Proceedings of the Institution of Mechanical Engineers, Part H: Journal of Engineering in Medicine*. **226**(12), pp.968-974.
- C-Motion. 2018. *Visual3D Tutorials*. [Online]. [Accessed 13 September]. Available from: www.c-motion.com.
- Calonius, O. and Saikko, V. 2002. Slide track analysis of eight contemporary hip simulator designs. *Journal of Biomechanics*. **35**(11), pp.1439-1450.
- Calonius, O. and Saikko, V. 2003. Force track analysis of contemporary hip simulators. *Journal of biomechanics*. **36**(11), pp.1719-1726.
- Cappozzo, A. et al. 1995. Position and orientation in space of bones during movement: anatomical frame definition and determination. *Clinical biomechanics*. **10**(4), pp.171-178.
- Carbone, V. et al. 2015. TLEM 2.0—A comprehensive musculoskeletal geometry dataset for subject-specific modeling of lower extremity. *Journal of biomechanics*. **48**(5), pp.734-741.
- Chahal, J. et al. 2013. Managing the patient with failed cartilage restoration. *Sports medicine and arthroscopy review*. **21**(2), pp.62-68.
- Chao, E. et al. 1983. Normative data of knee joint motion and ground reaction forces in adult level walking. *Journal of biomechanics*. **16**(3), pp.219-233.
- Charnley, J. 1970. 2 Total Hip Replacement by Low-Friction Arthroplasty. *Clinical Orthopaedics and Related Research*®. **72**, pp.7-21.
- Charnley, J. et al. 1969. The optimum size of prosthetic heads in relation to the wear of plastic sockets in total replacement of the hip. *Medical and biological engineering*. **7**(1), pp.31-39.
- Chatterji, U. et al. 2004. Effect of total hip arthroplasty on recreational and sporting activity. *ANZ journal of surgery*. **74**(6), pp.446-449.
- Choi, B.C. et al. 2007. Daily step goal of 10,000 steps: a literature review. *Clinical & Investigative Medicine*. **30**(3), pp.146-151.
- Clifford, P.E. and Mallon, W.J. 2005. Sports after total joint replacement. *Clinics in sports medicine*. **24**(1), pp.175-186.
- Cooper, J. et al. 1993. Macroscopic and microscopic wear mechanisms in ultra-high molecular weight polyethylene. *Wear*. **162**, pp.378-384.

- Crombie, I.K. et al. 2004. Why older people do not participate in leisure time physical activity: a survey of activity levels, beliefs and deterrents. *Age and ageing*. **33**(3), pp.287-292.
- Crowninshield, R. et al. 1978. A biomechanical investigation of the human hip. *Journal of biomechanics*. **11**(1), pp.79-85.
- D'antonio, J.A. et al. 2012. Ceramic bearings for total hip arthroplasty have high survivorship at 10 years. *Clinical Orthopaedics and Related Research*®. **470**(2), pp.373-381.
- Damm, P. et al. 2013a. Friction in total hip joint prosthesis measured in vivo during walking. *PLoS One*. **8**(11), pe78373.
- Damm, P. et al. 2013b. In vivo hip joint loads during three methods of walking with forearm crutches. *Clinical Biomechanics*. **28**(5), pp.530-535.
- Davy, D. et al. 1988. Telemetric force measurements across the hip after total arthroplasty. *The Journal of bone and joint surgery. American volume*. **70**(1), pp.45-50.
- De Pieri, E. et al. 2019. Patient Characteristics Affect Hip Contact Forces during Gait. *Osteoarthritis and Cartilage*.
- Delasotta, L.A. et al. 2012. What are young patients doing after hip reconstruction? *The Journal of arthroplasty*. **27**(8), pp.1518-1525. e2.
- Dewolf, A.H. et al. 2018. Kinematic patterns while walking on a slope at different speeds. *Journal of Applied Physiology*.
- Donahue, G.S. et al. 2016. Are females at greater risk for revision surgery after hip resurfacing arthroplasty with the articular surface replacement prosthesis? *Clinical Orthopaedics and Related Research*®. **474**(10), pp.2257-2265.
- Dorlot, J.-M. 1992. Long-term effects of alumina components in total hip prostheses. *Clinical orthopaedics and related research*. (282), pp.47-52.
- Dowson, D. and Jobbins, B. 1988. Design and development of a versatile hip joint simulator and a preliminary assessment of wear and creep in Charnley total replacement hip joints. *Engineering in medicine*. **17**(3), pp.111-117.
- Dressler, M.R. et al. 2011. Predicting wear of UHMWPE: Decreasing wear rate following a change in direction. *Wear*. **271**(11-12), pp.2879-2883.
- Dubs, L. et al. 1983. Sport after total hip arthroplasty. *Archives of orthopädic and traumatic Surgery*. **101**(3), pp.161-169.
- Dumbleton, J.H. et al. 2006. The basis for a second-generation highly cross-linked UHMWPE. *Clinical orthopaedics and related research*. **453**, pp.265-271.
- Esposito, C. et al. 2012. Wear in alumina-on-alumina ceramic total hip replacements: a retrieval analysis of edge loading. *The Journal of bone and joint surgery. British volume*. **94**(7), pp.901-907.
- Evans, J.T. et al. 2019. How long does a hip replacement last? A systematic review and meta-analysis of case series and national registry reports with more than 15 years of follow-up. *The Lancet*. **393**(10172), pp.647-654.
- Ewen, A.M. et al. 2012. Post-operative gait analysis in total hip replacement patients—a review of current literature and meta-analysis. *Gait & posture*. **36**(1), pp.1-6.

- Farrokhi, S. et al. 2008. Trunk position influences the kinematics, kinetics, and muscle activity of the lead lower extremity during the forward lunge exercise. *Journal of orthopaedic & sports physical therapy*. **38**(7), pp.403-409.
- Field, A. 2013. *Discovering statistics using IBM SPSS statistics*. sage.
- Firkins, P. et al. 2001. Quantitative analysis of wear and wear debris from metal-on-metal hip prostheses tested in a physiological hip joint simulator. *Bio-Medical Materials and Engineering*. **11**(2), pp.143-157.
- Flanagan, S. et al. 2003. Squatting exercises in older adults: kinematic and kinetic comparisons. *Medicine and science in sports and exercise*. **35**(4), p635.
- Flanagan, S.P. et al. 2004. Biomechanical attributes of lunging activities for older adults. *Journal of strength and conditioning research/National Strength & Conditioning Association*. **18**(3), p599.
- Forster, E. 2004. *Predicting muscle forces in the human lower limb during locomotion*. thesis, Universität Ulm.
- Foucher, K. et al. 1999. Gait adaptations in postoperative total hip replacement patients are associated with reduced hip contact forces. In: *23rd Annual Meeting of American Society of Biomechanics, Pittsburgh, Pennsylvania*, pp.134-135.
- Foucher, K.C. 2016. Identifying clinically meaningful benchmarks for gait improvement after total hip arthroplasty. *Journal of Orthopaedic Research*. **34**(1), pp.88-96.
- Foucher, K.C. et al. 2007. Preoperative gait adaptations persist one year after surgery in clinically well-functioning total hip replacement patients. *Journal of biomechanics*. **40**(15), pp.3432-3437.
- Foucher, K.C. et al. 2008. Do gait adaptations during stair climbing result in changes in implant forces in subjects with total hip replacements compared to normal subjects? *Clinical Biomechanics*. **23**(6), pp.754-761.
- Fox, A.S. 2018. Change-of-Direction Biomechanics: Is What's Best for Anterior Cruciate Ligament Injury Prevention Also Best for Performance? *Sports Medicine*. pp.1-9.
- Franjic, Z. and Wozniak, P.W. 2014. QualiWand: Towards Optimising Feedback for Motion Capture System Calibration. In: *Graphics Interface 2014 Poster Session Proceedings*, pp.5-6.
- Fumes, O. et al. 2001. Hip disease and the prognosis of total hip replacements: A review of 53 698 primary total hip replacements reported to the Norwegian arthroplasty register 1987-99. *Journal of bone and joint surgery. British volume*. **83**(4), pp.579-586.
- Galante, J.O. and Rostoker, W. 1972. Wear in total hip prostheses: an experimental evaluation of candidate materials. *Acta Orthopaedica Scandinavica*. **43**(sup145), pp.1-46.
- Galvin, A. et al. 2006. Wear of crosslinked polyethylene under different tribological conditions. *Journal of Materials Science: Materials in Medicine*. **17**(3), pp.235-243.
- Geduldig, D. et al. 1976. Experimental investigations of dense alumina ceramic for hip and knee joint replacements. *Engineering in Medicine*. Springer, pp.434-445.
- Gholizadeh, H. et al. 2018. Transtibial amputee gait during slope walking with the unity suspension system. *Gait & posture*. **65**, pp.205-212.

- Goldsmith, A. et al. 2000. A comparative joint simulator study of the wear of metal-on-metal and alternative material combinations in hip replacements. *Proceedings of the Institution of Mechanical Engineers, Part H: Journal of Engineering in Medicine*. **214**(1), pp.39-47.
- Goldsmith, A. et al. 2001. The effect of activity levels of total hip arthroplasty patients on socket penetration. *The Journal of arthroplasty*. **16**(5), pp.620-627.
- Gomez, P.F. and Morcuende, J.A. 2005. Early attempts at hip arthroplasty: 1700s to 1950s. *The Iowa orthopaedic journal*. **25**, p25.
- Granata, K.P. et al. 2000. Joint angular velocity in spastic gait and the influence of muscle-tendon lengthening. *The Journal of bone and joint surgery. American volume*. **82**(2), p174.
- Griffith, M. et al. 1978. Socket wear in Charnley low friction arthroplasty of the hip. *Clinical orthopaedics and related research*. (137), pp.37-47.
- Gschwend, N. et al. 2000. Alpine and cross-country skiing after total hip replacement: 2 cohorts of 50 patients each, one active, the other inactive in skiing, followed for 5-10 years. *Acta Orthopaedica Scandinavica*. **71**(3), pp.243-249.
- Gulgin, H. et al. 2009. Hip rotational velocities during the full golf swing. *Journal of Sports Science and Medicine*. **8**(2), pp.296-9.
- Haberly, G. and Pavol, M. 2013. *Hip loading during the squat exercise*. Masters of science thesis, George Fox University.
- Hall, R. et al. 1996. Wear in retrieved Charnley acetabular sockets. *Proceedings of the Institution of Mechanical Engineers, Part H: Journal of Engineering in Medicine*. **210**(3), pp.197-207.
- Hamill, J. et al. 1984. Ground reaction force symmetry during walking and running. *Research Quarterly for Exercise and Sport*. **55**(3), pp.289-293.
- Hamill, J. and Knutzen, K.M. 2006. *Biomechanical basis of human movement*. Lippincott Williams & Wilkins.
- Hamrock, B.J. and Dowson, D. 1978. Elastohydrodynamic lubrication of elliptical contacts for materials of low elastic modulus I—fully flooded conjunction. *Journal of Lubrication Technology*. **100**(2), pp.236-245.
- Hannouche, D. et al. 2016. Ceramic-on-ceramic THA implants in patients younger than 20 years. *Clinical Orthopaedics and Related Research®*. **474**(2), pp.520-527.
- Harris, W.H. 1995. The problem is osteolysis. *Clinical orthopaedics and related research*. (311), pp.46-53.
- Hart, A. et al. 2013. Which factors determine the wear rate of large-diameter metal-on-metal hip replacements?: Multivariate analysis of two hundred and seventy-six components. *JBJS*. **95**(8), pp.678-685.
- Healy, W.L. et al. 2008. Athletic activity after total joint arthroplasty. *JBJS*. **90**(10), pp.2245-2252.
- Heller, M. et al. 2001. Musculo-skeletal loading conditions at the hip during walking and stair climbing. *Journal of biomechanics*. **34**(7), pp.883-893.
- Hemmerich, A. et al. 2006. Hip, knee, and ankle kinematics of high range of motion activities of daily living. *Journal of orthopaedic research*. **24**(4), pp.770-781.

- Herzog, W. et al. 1989. Asymmetries in ground reaction force patterns in normal human gait. *Med Sci Sports Exerc.* **21**(1), pp.110-114.
- Higginson, G. 1978. Squeeze films between compliant solids. *Wear.* **46**(2), pp.387-395.
- Horsman, M.K. 2007. The Twente lower extremity model. Consistent dynamic simulation of the human locomotor apparatus.
- Hua, X. et al. 2016. The contact mechanics and occurrence of edge loading in modular metal-on-polyethylene total hip replacement during daily activities. *Medical engineering & physics.* **38**(6), pp.518-525.
- Huch, K. et al. 2005. Sports activities 5 years after total knee or hip arthroplasty: the Ulm Osteoarthritis Study. *Annals of the rheumatic diseases.* **64**(12), pp.1715-1720.
- Hume, P.A. et al. 2005. The role of biomechanics in maximising distance and accuracy of golf shots. *Sports medicine.* **35**(5), pp.429-449.
- Ingham, E. and Fisher, J. 2005. The role of macrophages in osteolysis of total joint replacement. *Biomaterials.* **26**(11), pp.1271-1286.
- ISO. 2014. *ISO 14242-1. Implants for surgery — Wear of total hip-joint prostheses — Part 1: Loading and displacement parameters for wear-testing machines and corresponding environmental conditions for test.* [Online]. [Accessed 10-06-2019]. Available from: <https://www.iso.org/obp/ui/#iso:std:iso:14242:-1:ed-3:v1:en:fig:1>.
- Jacobs, N. et al. 1972. Analysis of the vertical component of force in normal and pathological gait. *Journal of Biomechanics.* **5**(1), pp.11-34.
- Jan, S.V.S. 2007. Color atlas of skeletal landmark definitions. *Churchill Livingstone, Elsevier, Philadelphia.*
- Jin, Z. et al. 1993. Fluid film lubrication in natural hip joints. *Tribology Series.* Elsevier, pp.545-555.
- Jin, Z. et al. 1997. Analysis of fluid film lubrication in artificial hip joint replacements with surfaces of high elastic modulus. *Proceedings of the Institution of Mechanical Engineers, Part H: Journal of Engineering in Medicine.* **211**(3), pp.247-256.
- Jin, Z. et al. 1999. An axisymmetric contact model of ultra high molecular weight polyethylene cups against metallic femoral heads for artificial hip joint replacements. *Proceedings of the Institution of Mechanical Engineers, Part H: Journal of Engineering in Medicine.* **213**(4), pp.317-327.
- Johnson, K.L. and Johnson, K.L. 1987. *Contact mechanics.* Cambridge university press.
- Jolles, B. and Zangger, P. 2002. Factors predisposing to dislocation after primary total hip arthroplasty: a multivariate analysis. *The Journal of arthroplasty.* **17**(3), pp.282-288.
- Jolles, B.M. and Bogoch, E.R. 2003. Posterior versus lateral surgical approach for total hip arthroplasty in adults with osteoarthritis. *Cochrane Database of Systematic Reviews.* (4).
- Kadaba, M.P. et al. 1990. Measurement of lower extremity kinematics during level walking. *Journal of orthopaedic research.* **8**(3), pp.383-392.
- Kang, L. et al. 2008a. Wear simulation of ultra-high molecular weight polyethylene hip implants by incorporating the effects of cross-shear and contact pressure.

- Proceedings of the Institution of Mechanical Engineers, Part H: Journal of Engineering in Medicine.* **222**(7), pp.1049-1064.
- Kang, L. et al. 2006. A simple fully integrated contact-coupled wear prediction for ultra-high molecular weight polyethylene hip implants. *Proceedings of the Institution of Mechanical Engineers, Part H: Journal of Engineering in Medicine.* **220**(1), pp.33-46.
- Kang, L. et al. 2008b. Quantification of the effect of cross-shear on the wear of conventional and highly cross-linked UHMWPE. *Journal of biomechanics.* **41**(2), pp.340-346.
- Kassi, J.-P. et al. 2005. Stair climbing is more critical than walking in pre-clinical assessment of primary stability in cementless THA in vitro. *Journal of biomechanics.* **38**(5), pp.1143-1154.
- Katta, J. et al. 2008a. Biotribology of articular cartilage—a review of the recent advances. *Medical engineering & physics.* **30**(10), pp.1349-1363.
- Katta, J. et al. 2008b. Friction and wear of native and GAG deficient articular cartilage. In: *World Biomaterials Congress*, p.1191.
- Keller, T.S. et al. 1996. Relationship between vertical ground reaction force and speed during walking, slow jogging, and running. *Clinical biomechanics.* **11**(5), pp.253-259.
- Khanna, V. et al. 2014. Cartilage restoration of the hip using fresh osteochondral allograft: resurfacing the potholes. *The bone & joint journal.* **96**(11_Supple_A), pp.11-16.
- Kim, Y.-H. et al. 2016. Long-term results of third-generation ceramic-on-ceramic bearing cementless total hip arthroplasty in young patients. *The Journal of arthroplasty.* **31**(11), pp.2520-2524.
- Knight, L. et al. 2005. Influence of cross-shear on the wear of polyethylene: A finite element study. *Transactions of the Orthopaedic Research Society.* p0987.
- Kostamo, T. et al. 2009. No difference in gender-specific hip replacement outcomes. *Clinical orthopaedics and related research.* **467**(1), pp.135-140.
- Kotzar, G. et al. 1995. Torsional loads in the early postoperative period following total hip replacement. *Journal of Orthopaedic Research.* **13**(6), pp.945-955.
- Kotzar, G. et al. 1991. Telemeterized in vivo hip joint force data: a report on two patients after total hip surgery. *Journal of Orthopaedic Research.* **9**(5), pp.621-633.
- Kubo, T. et al. 2015. Hip arthroscopic osteochondral autologous transplantation for treating osteochondritis dissecans of the femoral head. *Arthroscopy techniques.* **4**(6), pp.e675-e680.
- Kuhn, M. et al. 2013. Total hip arthroplasty in patients 50 years or less: do we improve activity profiles? *The Journal of arthroplasty.* **28**(5), pp.872-876.
- Kuntze, G. et al. 2010. A biomechanical analysis of common lunge tasks in badminton. *Journal of sports sciences.* **28**(2), pp.183-191.
- Kurtz, S.M. 2009. *UHMWPE Biomaterials Handbook*. Oxford: Elsevier, Academic Press.
- Kurtz, S.M. et al. 2009. Future young patient demand for primary and revision joint replacement: national projections from 2010 to 2030. *Clinical Orthopaedics and Related Research®.* **467**(10), pp.2606-2612.

- Kwon, Y.-M. et al. 2010. Analysis of wear of retrieved metal-on-metal hip resurfacing implants revised due to pseudotumours. *The Journal of bone and joint surgery. British volume.* **92**(3), pp.356-361.
- Kwon, Y.-M. et al. 2012. In vivo evaluation of edge-loading in metal-on-metal hip resurfacing patients with pseudotumours. *Bone & joint research.* **1**(4), pp.42-49.
- Kyriazis, V. and Rigas, C. 2002. Temporal gait analysis of hip osteoarthritic patients operated with cementless hip replacement. *Clinical Biomechanics.* **17**(4), pp.318-321.
- Lamontagne, M. et al. 2012. Lower-limb joint mechanics after total hip arthroplasty during sitting and standing tasks. *Journal of Orthopaedic Research.* **30**(10), pp.1611-1617.
- Lancaster, J. 1973. Dry bearings: a survey of materials and factors affecting their performance. *Tribology.* **6**(6), pp.219-251.
- Learmonth, I.D. et al. 2007. The operation of the century: total hip replacement. *The Lancet.* **370**(9597), pp.1508-1519.
- Lees, A. and Hurley, C. 1995. 29 Forces in a badminton lunge movement. *Science and racket sports.* p186.
- Leslie, E. et al. 2001. Age-related differences in physical activity levels of young adults. *Medicine and science in sports and exercise.* **33**(2), pp.255-258.
- Lewinnek, G.E. et al. 1978. Dislocations after total hip-replacement arthroplasties. *The Journal of bone and joint surgery. American volume.* **60**(2), pp.217-220.
- Lewis, C.L. and Sahrman, S.A. 2015. Effect of posture on hip angles and moments during gait. *Manual therapy.* **20**(1), pp.176-182.
- Li, J. et al. 2015. Unilateral total hip replacement patients with symptomatic leg length inequality have abnormal hip biomechanics during walking. *Clinical Biomechanics.* **30**(5), pp.513-519.
- Li, J. et al. 2014. Hip contact forces in asymptomatic total hip replacement patients differ from normal healthy individuals: implications for preclinical testing. *Clinical Biomechanics.* **29**(7), pp.747-751.
- Lipshitz, H. et al. 1980. In vitro studies of the wear of articular cartilage—III. The wear characteristics of chemically modified articular cartilage when worn against a highly polished characterized stainless steel surface. *Journal of biomechanics.* **13**(5), pp.423-436.
- Lipshitz, H. and Glimcher, M. 1975. In vitro wear of articular cartilage. *The Journal of bone and joint surgery. American volume.* **57**(4), pp.527-534.
- Lipshitz, H. and Glimcher, M.N.J. 1976. Changes in the hexosamine content and swelling ratio of articular cartilage as functions of depth from the surface. *The Journal of bone and joint surgery. American volume.* **58**(8), pp.1149-1153.
- Liu, F. et al. 2006. Importance of head diameter, clearance, and cup wall thickness in elastohydrodynamic lubrication analysis of metal-on-metal hip resurfacing prostheses. *Proceedings of the Institution of Mechanical Engineers, Part H: Journal of Engineering in Medicine.* **220**(6), pp.695-704.
- Liu, Y. et al. 2017. Recent progress in cartilage tissue engineering—our experience and future directions. *Engineering.* **3**(1), pp.28-35.

- Livermore, J. et al. 1990. Effect of femoral head size on wear of the polyethylene acetabular component. *The Journal of bone and joint surgery. American volume.* **72**(4), pp.518-528.
- Lombardi Jr, A.V. et al. 2000. An in vivo determination of total hip arthroplasty pistoning during activity. *The Journal of Arthroplasty.* **15**(6), pp.702-709.
- Lu, X. et al. 2006. The Stribeck curve: experimental results and theoretical prediction. *Journal of tribology.* **128**(4), pp.789-794.
- Lund et al. 2019. AnyPyTools: A Python package for reproducible research with the AnyBody Modeling System. *Journal of Open Source Software.* **4**(33), p1108.
- Lunn, D.E. et al. 2019. Hip kinematics and kinetics in total hip replacement patients stratified by age and functional capacity. *Journal of Biomechanics.*
- Lunn, D.E. et al. 2016. Basic biomechanics of the hip. *Orthopaedics and Trauma.* **30**(3), pp.239-246.
- Lynn, S.K. and Noffal, G.J. 2012. Lower extremity biomechanics during a regular and counterbalanced squat. *The Journal of Strength & Conditioning Research.* **26**(9), pp.2417-2425.
- Macdonald, S.J. et al. 2003. Metal-on-metal versus polyethylene in hip arthroplasty: a randomized clinical trial. *Clinical Orthopaedics and Related Research®.* **406**(1), pp.282-296.
- Mahoney, O.M. 1990. Unsatisfactory results with a ceramic total hip prosthesis. *The Journal of bone and joint surgery. American volume.* **72**(5), pp.663-671.
- Mak, M. et al. 2002. Effect of microseparation on contact mechanics in ceramic-on-ceramic hip joint replacements. *Proceedings of the Institution of Mechanical Engineers, Part H: Journal of Engineering in Medicine.* **216**(6), pp.403-408.
- Maldonado, D.R. et al. 2018. Fresh Femoral Head Osteochondral Allograft Transplantation for Treating Osteochondritis Dissecans of the Femoral Head. *Arthroscopy techniques.* **7**(4), pp.e331-e335.
- Manders, C. et al. 2008. Validation of musculoskeletal gait simulation for use in investigation of total hip replacement. *Journal of Biomechanics.* **41**, pS488.
- Masonis, J.L. and Bourne, R.B. 2002. Surgical approach, abductor function, and total hip arthroplasty dislocation. *Clinical Orthopaedics and Related Research (1976-2007).* **405**, pp.46-53.
- Mathieson, A. 2000. NICE issues guidance on hips. *The Journal of Perioperative Practice.* **10**(6), p285.
- Matthies, A. et al. 2011. Retrieval analysis of 240 metal-on-metal hip components, comparing modular total hip replacement with hip resurfacing. *The Journal of bone and joint surgery. British volume.* **93**(3), pp.307-314.
- McConnell, T.H. and Hull, K.L. 2011. *Human form human function: Essentials of anatomy and physiology.* 1st ed. Baltimore, MD: Lippincott Williams & Wilkins.
- McCrary, J.L. et al. 2001. Vertical ground reaction forces: objective measures of gait following hip arthroplasty. *Gait & posture.* **14**(2), pp.104-109.
- McGrory, B.J. et al. 1995. Participation in sports after hip and knee arthroplasty: review of literature and survey of surgeon preferences. In: *Mayo Clinic Proceedings:* Elsevier, pp.342-348.

- McKee, G. 1970. 10 Development of Total Prosthetic Replacement of the Hip. *Clinical Orthopaedics and Related Research*®. **72**, pp.85-103.
- Meftah, M. et al. 2013. A novel method for accurate and reproducible functional cup positioning in total hip arthroplasty. *The Journal of arthroplasty*. **28**(7), pp.1200-1205.
- Meira, E.P. and Zeni, J. 2014. Sports participation following total hip arthroplasty. *International journal of sports physical therapy*. **9**(6), p839.
- Mellon, S. et al. 2011. The effect of motion patterns on edge-loading of metal-on-metal hip resurfacing. *Medical engineering & physics*. **33**(10), pp.1212-1220.
- Meneghini, R.M. et al. 2006. Muscle damage during MIS total hip arthroplasty: Smith-Peterson versus posterior approach. *Clinical Orthopaedics and Related Research*®. **453**, pp.293-298.
- Moisio, K.C. et al. 2003. Normalization of joint moments during gait: a comparison of two techniques. *Journal of Biomechanics*. **36**, pp.599-603.
- Mollon, B. et al. 2013. The clinical status of cartilage tissue regeneration in humans. *Osteoarthritis and cartilage*. **21**(12), pp.1824-1833.
- Moretti, V.M. and Post, Z.D. 2017. Surgical approaches for total hip arthroplasty. *Indian journal of orthopaedics*. **51**(4), p368.
- Morlock, M. et al. 2001. Duration and frequency of every day activities in total hip patients. *Journal of biomechanics*. **34**(7), pp.873-881.
- Mow, V. and Ateshian, G. 1997. In *Lubrication and Wear of Diarthrodial Joints: Basic Orthopaedic Biomechanics*; Mow, VC; Hayes, WC, Eds. Lippincott-Raven, Philadelphia.
- Mow, V.C. et al. 1993. Biomechanics of diarthrodial joints: a review of twenty years of progress. *Journal of biomechanical engineering*. **115**(4B), pp.460-467.
- Mulholland, S.J. and Wyss, U.P. 2001. Activities of daily living in non-Western cultures: range of motion requirements for hip and knee joint implants. *International Journal of Rehabilitation Research*. **24**(3), pp.191-198.
- Müller, M. et al. 2011. Randomized controlled trial of abductor muscle damage in relation to the surgical approach for primary total hip replacement: minimally invasive anterolateral versus modified direct lateral approach. *Archives of orthopaedic and trauma surgery*. **131**(2), pp.179-189.
- Murray, M. et al. 1975. Kinesiology after McKee-Farrar total hip replacement. A two-year follow-up of one hundred cases. *The Journal of bone and joint surgery. American volume*. **57**(3), pp.337-342.
- Murray, M. et al. 1972. Kinesiologic Measurements of Functional Performance Before and After Mckee-farrar Total Hip Replacement: A Study Of Thirty Patients With Rheumatoid Arthritis, Osteoarthritis, Or Avascular Necrosis Of The Femoral Head. *JBJS*. **54**(2), pp.237-256.
- Nadzadi, M.E. et al. 2003. Kinematics, kinetics, and finite element analysis of commonplace maneuvers at risk for total hip dislocation. *Journal of biomechanics*. **36**(4), pp.577-591.
- Nagura, T. et al. 2002. Mechanical loads at the knee joint during deep flexion. *Journal of Orthopaedic Research*. **20**(4), pp.881-886.

- Nevelos, J. et al. 2001. Comparative analysis of two different types of alumina-alumina hip prosthesis retrieved for aseptic loosening. *The Journal of bone and joint surgery. British volume.* **83**(4), pp.598-603.
- NHS. 2019. *Hip replacement.* [Online]. Available from: <https://www.nhs.uk/conditions/hip-replacement/>.
- NICE. 2002. *The clinical effectiveness and cost effectiveness of metal on metal hip resurfacing.* [Online]. [Accessed 26 October 2016]. Available from: <http://guidance.nice.org.uk/TA44>.
- Nigg, B.M. et al. 1999. *Biomechanics of the musculo-skeletal system.* Wiley New York.
- NJR. 2018. *National Joint Registry Centre.* [Online]. [Accessed 26 October 2016]. Available from: www.njrcentre.org.uk.
- O'Connor, D.O. et al. 1996. In vitro measurement of strain in the bone cement surrounding the femoral component of total hip replacements during simulated gait and stair-climbing. *Journal of orthopaedic research.* **14**(5), pp.769-777.
- O'Connor, J.D. et al. 2018. Long-term hip loading in unilateral total hip replacement patients is no different between limbs or compared to healthy controls at similar walking speeds. *Journal of biomechanics.* **80**, pp.8-15.
- Oladeji, L.O. et al. 2018. Large fresh osteochondral allografts for the hip: growing the evidence. *HIP International.* **28**(3), pp.284-290.
- Oonishi, H. et al. 2004. Alumina hip joints characterized by run-in wear and steady-state wear to 14 million cycles in hip-simulator model. *Journal of Biomedical Materials Research Part A: An Official Journal of The Society for Biomaterials, The Japanese Society for Biomaterials, and The Australian Society for Biomaterials and the Korean Society for Biomaterials.* **70**(4), pp.523-532.
- Oonishi, H. et al. 1998. Retrieved total hip prostheses. Part I: the effects of cup thickness, head sizes and fusion defects on wear. *Journal of Materials Science: Materials in Medicine.* **9**(7), pp.393-401.
- Paul, J. 1966. Paper 8: forces transmitted by joints in the human body. In: *Proceedings of the Institution of Mechanical Engineers, Conference Proceedings:* SAGE Publications Sage UK: London, England, pp.8-15.
- Pearsall, D. and Costigan, P. 1999. The effect of segment parameter error on gait analysis results. *Gait & Posture.* **9**(3), pp.173-183.
- Perron, M. et al. 2003. Assessing advanced locomotor recovery after total hip arthroplasty with the timed stair test. *Clinical rehabilitation.* **17**(7), pp.780-786.
- Perron, M. et al. 2000. Three-dimensional gait analysis in women with a total hip arthroplasty. *Clinical Biomechanics.* **15**(7), pp.504-515.
- Peters, A. et al. 2010. Quantification of soft tissue artifact in lower limb human motion analysis: a systematic review. *Gait & posture.* **31**(1), pp.1-8.
- Pfirschmann, C.W. et al. 2005. Abductor tendons and muscles assessed at MR imaging after total hip arthroplasty in asymptomatic and symptomatic patients. *Radiology.* **235**(3), pp.969-976.
- Prosser, G.H. et al. 2010. Outcome of primary resurfacing hip replacement: evaluation of risk factors for early revision: 12,093 replacements from the Australian Joint Registry. *Acta orthopaedica.* **81**(1), pp.66-71.

- Queen, R.M. et al. 2013. Stair ascending and descending in hip resurfacing and large head total hip arthroplasty patients. *The Journal of arthroplasty*. **28**(4), pp.684-689.
- Radin, E.L. and Paul, I.L. 1971. Response of joints to impact loading. I. In vitro wear. *Arthritis & Rheumatism: Official Journal of the American College of Rheumatology*. **14**(3), pp.356-362.
- Ramamurti, B.S. et al. 1996. Loci of movement of selected points on the femoral head during normal gait: three-dimensional computer simulation. *The Journal of arthroplasty*. **11**(7), pp.845-852.
- Riberto, M. et al. 2013. Setting up a human motion analysis laboratory: camera positioning for kinematic recording of gait. *Int J Phys Med Rehabil*. **1**(131), p2.
- Ritter, M.A. and Meding, J.B. 1987. Total hip arthroplasty. Can the patient play sports again? *Orthopedics*. **10**, pp.1447-52.
- Ritter, M.A. et al. 1983. Correlation of prosthetic femoral head size and/or design with longevity of total hip arthroplasty. *Clinical orthopaedics and related research*. (176), pp.252-257.
- Robertson, G. et al. 2013. *Research methods in biomechanics, 2E*. Human Kinetics.
- Roebroeck, M. et al. 1994. Biomechanics and muscular activity during sit-to-stand transfer. *Clinical Biomechanics*. **9**(4), pp.235-244.
- Rydell, N.W. 1966. Forces acting on the femoral head-prosthesis: a study on strain gauge supplied prostheses in living persons. *Acta Orthopaedica Scandinavica*. **37**(sup88), pp.1-132.
- Saikko, V. 2014. In vitro wear simulation on the RandomPOD wear testing system as a screening method for bearing materials intended for total knee arthroplasty. *Journal of biomechanics*. **47**(11), pp.2774-2778.
- Saikko, V. and Calonijs, O. 2002. Slide track analysis of the relative motion between femoral head and acetabular cup in walking and in hip simulators. *Journal of Biomechanics*. **35**(4), pp.455-464.
- Saikko, V. et al. 2003. Effect of extent of motion and type of load on the wear of polyethylene in a biaxial hip simulator. *Journal of Biomedical Materials Research Part B: Applied Biomaterials: An Official Journal of The Society for Biomaterials, The Japanese Society for Biomaterials, and The Australian Society for Biomaterials and the Korean Society for Biomaterials*. **65**(1), pp.186-192.
- Saikko, V.O. 1996. A three-axis hip joint simulator for wear and friction studies on total hip prostheses. *Proceedings of the Institution of Mechanical Engineers, Part H: Journal of Engineering in Medicine*. **210**(3), pp.175-185.
- Schache, A.G. et al. 2001. The effect of differing Cardan angle sequences on three dimensional lumbo-pelvic angular kinematics during running. *Medical engineering & physics*. **23**(7), pp.495-503.
- Scheerlinck, T. 2014. Cup positioning in total hip arthroplasty. *Acta Orthop Belg*. **80**(03), pp.336-347.
- Schmalzried, T.P. 2012. Patient activity and hip wear. In: *Seminars in Arthroplasty*: Elsevier, pp.193-196.
- Schmalzried, T.P. et al. 1996. Long-duration metal-on-metal total hip arthroplasties with low wear of the articulating surfaces. *The Journal of arthroplasty*. **11**(3), pp.322-331.

- Schmalzried, T.P. et al. 2000. Wear is a function of use, not time. *Clinical Orthopaedics and Related Research (1976-2007)*. **381**, pp.36-46.
- Schmalzried, T.P. et al. 1998. Quantitative assessment of walking activity after total hip or knee replacement. *JBJS*. **80**(1), pp.54-9.
- Schmidt, M. et al. 1996. Cobalt chromium molybdenum metal combination for modular hip prostheses. *Clinical Orthopaedics and Related Research®*. **329**, pp.S35-S47.
- Schoenfeld, B.J. 2010. Squatting kinematics and kinetics and their application to exercise performance. *The Journal of Strength & Conditioning Research*. **24**(12), pp.3497-3506.
- Scholes, S. and Unsworth, A. 2000. Comparison of friction and lubrication of different hip prostheses. *Proceedings of the Institution of Mechanical Engineers, Part H: Journal of Engineering in Medicine*. **214**(1), pp.49-57.
- Schreven, S. et al. 2015. Optimising filtering parameters for a 3D motion analysis system. *Journal of Electromyography and Kinesiology*. **25**(5), pp.808-814.
- Schwachmeyer, V. et al. 2013. In vivo hip joint loading during post-operative physiotherapeutic exercises. *PLoS One*. **8**(10), pe77807.
- Seagrave, K.G. et al. 2017. Acetabular cup position and risk of dislocation in primary total hip arthroplasty: a systematic review of the literature. *Acta orthopaedica*. **88**(1), pp.10-17.
- Sechriest II, V.F. et al. 2007. Activity level in young patients with primary total hip arthroplasty: a 5-year minimum follow-up. *The Journal of arthroplasty*. **22**(1), pp.39-47.
- Sedel, L. et al. 1990. Alumina-on-alumina hip replacement. Results and survivorship in young patients. *The Journal of bone and joint surgery. British volume*. **72**(4), pp.658-663.
- Selbie, W.S. et al. 2014. Three-dimensional kinetics. *Research methods in biomechanics*. pp.151-176.
- Shaju, K. et al. 2005. The 22-mm vs the 32-mm femoral head in cemented primary hip arthroplasty: long-term clinical and radiological follow-up study. *The Journal of arthroplasty*. **20**(7), pp.903-908.
- Shon, W.Y. et al. 2005. Impingement in total hip arthroplasty: a study of retrieved acetabular components. *The Journal of arthroplasty*. **20**(4), pp.427-435.
- Sieber, H.-P. et al. 1999. Analysis of 118 second-generation metal-on-metal retrieved hip implants. *The Journal of bone and joint surgery. British volume*. **81**(1), pp.46-50.
- Silva, M. et al. 2002. Average patient walking activity approaches 2 million cycles per year: pedometers under-record walking activity. *The Journal of arthroplasty*. **17**(6), pp.693-697.
- Simon, S.R. 2004. Quantification of human motion: gait analysis—benefits and limitations to its application to clinical problems. *Journal of biomechanics*. **37**(12), pp.1869-1880.
- Sinclair, J. et al. 2012. Influence of the helical and six available Cardan sequences on 3D ankle joint kinematic parameters. *Sports Biomechanics*. **11**(3), pp.430-437.
- Skaggs, D.L. et al. 2000. Variability in gait analysis interpretation. *Journal of Pediatric Orthopaedics*. **20**(6), pp.759-764.

- Smith, A.J. et al. 2012. Failure rates of stemmed metal-on-metal hip replacements: analysis of data from the National Joint Registry of England and Wales. *The Lancet*. **379**(9822), pp.1199-1204.
- Smith, S. et al. 2001. The effect of femoral head diameter upon lubrication and wear of metal-on-metal total hip replacements. *Proceedings of the Institution of Mechanical Engineers, Part H: Journal of Engineering in Medicine*. **215**(2), pp.161-170.
- Smith, S. and Unsworth, A. 2000. Simplified motion and loading compared to physiological motion and loading in a hip joint simulator. *Proceedings of the Institution of Mechanical Engineers, Part H: Journal of Engineering in Medicine*. **214**(3), pp.233-238.
- Smith, S. and Unsworth, A. 2001. A five-station hip joint simulator. *Proceedings of the Institution of Mechanical Engineers, Part H: Journal of Engineering in Medicine*. **215**(1), pp.61-64.
- Stagni, R. et al. 2000. Effects of hip joint centre mislocation on gait analysis results. *Journal of biomechanics*. **33**(11), pp.1479-1487.
- Stansfield, B. et al. 2003. Direct comparison of calculated hip joint contact forces with those measured using instrumented implants. An evaluation of a three-dimensional mathematical model of the lower limb. *Journal of biomechanics*. **36**(7), pp.929-936.
- Stewart, T. 2010. Tribology of artificial joints. *Orthopaedics and Trauma*. **24**(6), pp.435-440.
- Stewart, T. et al. 1997. Friction of composite cushion bearings for total knee joint replacements under adverse lubrication conditions. *Proceedings of the Institution of Mechanical Engineers, Part H: Journal of Engineering in Medicine*. **211**(6), pp.451-465.
- Stolk, J. et al. 2002. Stair climbing is more detrimental to the cement in hip replacement than walking. *Clinical Orthopaedics and Related Research*[®]. **405**, pp.294-305.
- Sum, J. et al. 1998. Effects of normalization on joint moments during level walking. *Gait & Posture*. **7**, p184.
- Swanson, E.A. et al. 2009. Activity recommendations after total hip and knee arthroplasty: a survey of the American Association for Hip and Knee Surgeons. *The Journal of arthroplasty*. **24**(6), pp.120-126.
- Sychterz, C.J. et al. 1999. Analysis of temporal wear patterns of porous-coated acetabular components: distinguishing between true wear and so-called bedding-in. *JBJS*. **81**(6), pp.821-830.
- Talis, V. et al. 2008. Asymmetric leg loading during sit-to-stand, walking and quiet standing in patients after unilateral total hip replacement surgery. *Clinical Biomechanics*. **23**(4), pp.424-433.
- Temple, J. 2004. Total hip replacement. *Nursing Standard (through 2013)*. **19**(3), p44.
- Thier, S. et al. 2017. Arthroscopic autologous chondrocyte implantation in the hip for the treatment of full-thickness cartilage defects: A case series of 29 patients and review of the literature. *SICOT-J*. **3**.

- Tirico, L.E. et al. 2018. Modern Osteochondral Allograft Transplantation: The “Gold Standard” for Femoral Condyle Cartilage Repair? *Orthopaedic journal of sports medicine*. **6**(3_suppl), p2325967118S00004.
- Turell, M. et al. 2003. Quantification of the effect of cross-path motion on the wear rate of ultra-high molecular weight polyethylene. *Wear*. **255**(7-12), pp.1034-1039.
- Underwood, R.J. et al. 2012. Edge loading in metal-on-metal hips: low clearance is a new risk factor. *Proceedings of the Institution of Mechanical Engineers, Part H: Journal of Engineering in Medicine*. **226**(3), pp.217-226.
- van Arkel, R.J. et al. 2013. Hip abduction can prevent posterior edge loading of hip replacements. *Journal of Orthopaedic Research*. **31**(8), pp.1172-1179.
- Van der Weegen, W. et al. 2011. Survival of metal-on-metal hip resurfacing arthroplasty: a systematic review of the literature. *The Journal of bone and joint surgery. British volume*. **93**(3), pp.298-306.
- VanLaanen, J.B. 2013. *Validation of a cross-shear model for ultra-high molecular weight polyethylene (UHMWPE) wear*. Master of Science thesis, Colorado School of Mines.
- Vassiliou, K. et al. 2007. Laboratory studies on the tribology of hard bearing hip prostheses: ceramic on ceramic and metal on metal. *Proceedings of the Institution of Mechanical Engineers, Part H: Journal of Engineering in Medicine*. **221**(1), pp.11-20.
- Vaughan-Graham, J. et al. 2019. Transitions sit to stand and stand to sit in persons post-stroke: Path of centre of mass, pelvic and limb loading—A pilot study. *Clinical Biomechanics*. **61**, pp.22-30.
- Visuri, T. and Honkanen, R. 1978. The influence of total hip replacement on selected activities of daily living and on the use of domestic aid. *Scandinavian journal of rehabilitation medicine*. **10**(4), pp.221-225.
- Visuri, T. and Honkanen, R. 1980. Total hip replacement: its influence on spontaneous recreation exercise habits. *Arch Phys Med Rehabil*. **61**(7), pp.325-8.
- Walter, W.L. et al. 2004. Edge loading in third generation alumina ceramic-on-ceramic bearings: Stripe wear1. *The Journal of arthroplasty*. **19**(4), pp.402-413.
- Wang, A. 2001. A unified theory of wear for ultra-high molecular weight polyethylene in multi-directional sliding. *Wear*. **248**(1-2), pp.38-47.
- Wang, A. et al. 1998. Lubrication and wear of ultra-high molecular weight polyethylene in total joint replacements. *Tribology International*. **31**(1-3), pp.17-33.
- Wang, A. et al. 1997b. The significance of nonlinear motion in the wear screening of orthopaedic implant materials. *Journal of Testing and Evaluation*. **25**(2), pp.239-245.
- Wang, A. et al. 1996. Mechanistic and morphological origins of ultra-high molecular weight polyethylene wear debris in total joint replacement prostheses. *Proceedings of the Institution of Mechanical Engineers, Part H: Journal of Engineering in Medicine*. **210**(3), pp.141-155.
- Wang, A. et al. 1997a. Orientation softening in the deformation and wear of ultra-high molecular weight polyethylene. *Wear*. **203**, pp.230-241.
- Wang, Y. et al. 2006. Development of a set of stribeck curves for conformal contacts of rough surfaces. *Tribology Transactions*. **49**(4), pp.526-535.

- Wannop, J.W. et al. 2012. Normalization of ground reaction forces, joint moments, and free moments in human locomotion. *Journal of Applied Biomechanics*. **28**(6), pp.665-76.
- Wehner, T. et al. 2009. Internal loads in the human tibia during gait. *Clinical Biomechanics*. **24**(3), pp.299-302.
- Widhalm, R. et al. 1990. Is there greater danger of sports injury or osteoporosis caused by inactivity in patients with hip prosthesis? Sequelae for long-term stability of prosthesis anchorage. *Zeitschrift fur Orthopadie und ihre Grenzgebiete*. **128**(2), pp.139-143.
- Winter, D.A. 1984. Kinematic and kinetic patterns in human gait: variability and compensating effects. *Human movement science*. **3**(1-2), pp.51-76.
- Winter, D.A. 2009. *Biomechanics and motor control of human movement*. John Wiley & Sons.
- Wylde, V. et al. 2008. Return to sport after joint replacement. *The Journal of bone and joint surgery. British volume*. **90**(7), pp.920-923.
- Yoshida, H. et al. 2006. Three-dimensional dynamic hip contact area and pressure distribution during activities of daily living. *Journal of biomechanics*. **39**(11), pp.1996-2004.
- Yu, B. et al. 1999. Estimate of the optimum cutoff frequency for the Butterworth low-pass digital filter. *Journal of Applied Biomechanics*. **15**(3), pp.318-329.
- Yusuf, H.R. et al. 1996. Leisure-time physical activity among older adults: United States, 1990. *Archives of internal medicine*. **156**(12), pp.1321-1326.
- Zhou, Y. et al. 1997. Start up and steady state friction of alumina against alumina. *Wear*. **210**(1-2), pp.112-119.
- Zywiell, M.G. et al. 2011. State of the art in hard-on-hard bearings: how did we get here and what have we achieved? *Expert review of medical devices*. **8**(2), pp.187-207.

10. Appendix

Within this section questionnaires, graphs and scripts are included. Questionnaires were used when determining which activities to include within the study and when achieving ethical approval. Graphs are not directly linked to the overall conclusions drawn from the project, but provide a wider view of the data set and provide context to some of the more relevant findings. Scripts relate to the automated computational calculations within the methodology. These provide the reader with more detail on some of the processes involved in the biomechanical calculations (Visual3D), multi-body modelling (AnyBody) and batch processing (Python) involved in the study.

10.1. Joint Replacement and Physical Activity Questionnaire

Have you been treated with a joint replacement?

Yes

If *Yes*, please continue.

Are you 18 or over?

Yes

If *Yes*, please continue.

No

If *No*, thank you for your time, but you *do not* have to complete the rest of this form.

No

If *No*, thank you for your time, but you *do not* have to complete the rest of this form.

Do you suffer/have any of the following movement disorders:

Parkinson's disease

Multiple Sclerosis

Vestibular disorder

Other: _____

Background details on you:

Are you: Male/Female

How old are you today:

How much do you weigh:

How tall are you:

Occupation:

Which joint(s) have you had replacements for?

- | | |
|---|--|
| <input type="checkbox"/> Right ankle | <input type="checkbox"/> Left ankle |
| <input type="checkbox"/> Right knee | <input type="checkbox"/> Left knee |
| <input type="checkbox"/> Right hip | <input type="checkbox"/> Left hip |
| <input type="checkbox"/> Right elbow | <input type="checkbox"/> Left elbow |
| <input type="checkbox"/> Right shoulder | <input type="checkbox"/> Left shoulder |

Please provide your name and address (or email) ONLY if you wish us to contact you with the results from this questionnaire:

Name:

Email:

Questions relating to the replacement:

What type of replacement do you have?

- Total
- Partial
- Don't know
- Other

Please specify if other: _____

How long have you had the replacement(s) for?

Have you had a revision surgery?

Questions relating to physical activity:

How many hours a week, on average, would you engage in physical activity *before* the joint replacement?

Moderate intensity activity: (Eg. Brisk walking/gardening)

Vigorous intensity activity: (Eg. Running/fast cycling)

How many hours, on average, do you *currently* engage in physical activity (with the replacement)?

Moderate intensity activity: (Eg. Brisk walking/gardening)

Vigorous intensity activity: (Eg. Running/fast cycling)

Do you believe that the joint replacement(s) impact your physical activity:

- Positively
- Negatively
- Not at all

Select the recreational activities you engage in and the amount of time per week. If you don't know the time per week spent doing the activity, leave the 'time per week' parts blank.

Activity	Hours per week
<input type="checkbox"/> Bowling	_____
<input type="checkbox"/> Cycling	_____
<input type="checkbox"/> Dancing	_____
<input type="checkbox"/> Do-it-yourself (DIY)	_____
<input type="checkbox"/> Gardening	_____
<input type="checkbox"/> Golf	_____
<input type="checkbox"/> Hiking	_____
<input type="checkbox"/> Praying	_____
<input type="checkbox"/> Rowing	_____
<input type="checkbox"/> Speed walking	_____
<input type="checkbox"/> Swimming	_____
<input type="checkbox"/> Tennis	_____
<input type="checkbox"/> Other	_____

Please specify if other:

Select the corresponding activities which you engage in, but may not be confident completing.

- Cycling
- Dancing
- Do-it-yourself (DIY)
- Gardening
- Golf
- Hiking
- Praying
- Rowing
- Speed walking
- Swimming
- Tennis
- Other

Please specify if other: _____

Select the daily household/transport activities that you engage in and whether you feel confident completing them.

Task

Confident

- | | | |
|--------------------------|-----------------------------------|--------------------------|
| <input type="checkbox"/> | Getting into bed | <input type="checkbox"/> |
| <input type="checkbox"/> | Getting out of bed | <input type="checkbox"/> |
| <input type="checkbox"/> | Getting into the bath | <input type="checkbox"/> |
| <input type="checkbox"/> | Getting out of the bath | <input type="checkbox"/> |
| <input type="checkbox"/> | Getting into a car | <input type="checkbox"/> |
| <input type="checkbox"/> | Getting out of a car | <input type="checkbox"/> |
| <input type="checkbox"/> | Walking up steps/stairs | <input type="checkbox"/> |
| <input type="checkbox"/> | Walking down steps/ stairs | <input type="checkbox"/> |
| <input type="checkbox"/> | Walking uphill | <input type="checkbox"/> |
| <input type="checkbox"/> | Walking downhill | <input type="checkbox"/> |
| <input type="checkbox"/> | Walking on uneven ground | <input type="checkbox"/> |
| <input type="checkbox"/> | Sitting down (from a chair/bench) | <input type="checkbox"/> |
| <input type="checkbox"/> | Standing up (from a chair/bench) | <input type="checkbox"/> |
| <input type="checkbox"/> | Sitting down (from a soft sofa) | <input type="checkbox"/> |
| <input type="checkbox"/> | Standing up (from a soft sofa) | <input type="checkbox"/> |
| <input type="checkbox"/> | Other | <input type="checkbox"/> |

Please specify if you feel unconfident completing other daily activities:

Select the movement patterns which you may be not be confident completing.

- Sitting

- Rising
- Lying down
- Standing up
- Stepping down
- Stepping up
- Bending down
- Reaching up
- Reaching down
- Kneeling
- Twisting at the hip

This is the end of the questionnaire.

If you have any queries, please feel free to contact the lead researcher on:

Sp11rbl@leeds.ac.uk

Please return the questionnaire to your group coordinator when possible.

Thank you for your time and effort.

10.2.Ethics Documentation

10.2.1. Recruitment Poster

Institute of Medical & Biological Engineering
UNIVERSITY OF LEEDS

Participants required for a study investigating human motion

Are you:

Healthy and injury free?

Aged over 18?

What activities are appropriate after a hip replacement? We are looking to recruit healthy participants to complete a number of daily tasks to determine this.

In our lab at the University of Leeds you will be asked to complete common activities such as sitting/standing and walking uphill. Reflective markers will be placed on the body whilst motion is analysed with 13 cameras. One data collection session lasting approximately 2 hours will be required.

Results will provide information about loading of the hip during each activity. This will influence both physiotherapy and pre-clinical testing for hip replacements. Please note: subject recruitment will finish **1/12/17**

If you would be interested in taking part or want to know more about this study please contact: Robin Layton at sp11rbl@leeds.ac.uk.

University ethics committee reference number: MEEC 16-021

Robin Layton sp11rbl@leeds.ac.uk	Robin Layton sp11rbl@leeds.ac.uk	Robin Layton sp11rbl@leeds.ac.uk	Robin Layton sp11rbl@leeds.ac.uk	Robin Layton sp11rbl@leeds.ac.uk	Robin Layton sp11rbl@leeds.ac.uk	Robin Layton sp11rbl@leeds.ac.uk	Robin Layton sp11rbl@leeds.ac.uk
--	--	--	--	--	--	--	--

Figure 184. The recruitment poster for healthy participants to be involved in the movement analysis data collection.

10.2.3. Participant Information

Research Project investigating activities of daily living.

INFORMATION FOR PARTICIPANTS

Introduction

We are inviting you to take part in a research study. Before you decide whether or not you would like to take part, it is important for you to understand the purpose of the research and what it will involve. Please ask us if you would like more information or if there is anything that is unclear. The decision to take part in this study is entirely yours and you should not feel under any pressure to participate.

Purpose of the study

Success following a total hip replacement has been shown to decrease for younger, more active patients. The main purpose of this research is to better understand whether common activities might be a risk to the longevity of a total hip replacement. Following analysis, this study aims to determine the appropriateness of each activity following a hip replacement. Findings will also be relevant to the conditions of pre-clinical testing of hip prostheses.

Am I a suitable participant for this study?

The only limits to participation in the study are that you are generally healthy, have had no injuries in the past 6 months and that you are over the age of 18. It is important for participants to have 'normal' locomotion and no pre-existing condition which may influence walking technique. A health questionnaire will be completed prior to data collection.

Is there any pressure to take part?

There is no pressure to take part and you can withdraw from the study at any time during the collection of the data. Data will not be used for two weeks following the collection; during this time you may request that the data is destroyed without reason.

What will happen if I take part?

You will be invited to attend the biomechanics Laboratory at the University of Leeds at a time convenient to you. The session will last approximately 2 hours.

If you agree to participate you will be asked to perform and repeat a number of common daily activities including: sitting/standing, stair negotiation, lunging and squatting. Your motion will be recorded during tasks using video and specialist motion tracking equipment. The forces exerted between your foot and the floor will also be measured. The recording of motion will require you to wear cycling shorts (provided), a sports t-shirt for females and no top for males. Small reflective

markers placed on anatomical landmarks on body. The location of these markers will be recorded by the motion analysis system in 3D. Height and weight will also be measured. This data will then undergo further analysis to assess the forces occurring at the hip joint for each activity. This will allow us to understand the forces and motions we might expect a total hip replacement to experience.

What do I have to do?

You will be asked to bring with you your everyday shoes and a sports t-shirt. A consent form will need to be completed prior to the start of data collection. Small, lightweight reflective markers will be attached to your legs with sticky tape and these will be used to measure your motion whilst you complete the activities. You will be asked to wear cycling shorts as this limits the movement of markers in relation to the skin. A screening questionnaire will need to be completed to ensure that you have no allergies to any of the materials used. The sticky tape is an adhesive, any allergy to this would mean that you cannot complete the data collection.

What are the possible benefits of taking part in this study?

There are no direct benefits to you resulting from the research however the objective of the research is to improve the function of individuals with a total hip replacement in the medium and long term.

What happens if something goes wrong?

As with all research using human subjects, there are some risks but these are similar to those you would experience doing these activities in your day to day life. You will be asked to complete a health questionnaire to ensure that you are fit enough to undertake the tests and you may withdraw at any time. A member of staff who is first aid trained will always be present. Please note that the University of Leeds is liable only if negligent.

Will data and information about me be kept confidential?


We will ask you to complete a health questionnaire to ensure that you are fit enough to participate in the study but this will be kept safe and separate from the information obtained during the test. You will not be identifiable from the other data obtained during the tests. We will be taking video recordings of the test procedures but these will be stored on a secure computer and only the researchers involved in the study will have access to these. These recordings will not be available for public viewing except if required for research reporting and review purposes. In this case steps will be taken to ensure that participant details are completely confidential. For context, the camera system will record the markers and no real image is therefore obtained. All participation and associated data will be anonymised.

What will happen to the results of the study?

The results from the study will be used to improve the understanding surrounding the appropriateness of activities for individuals following a total hip replacement. Findings will progress our understanding of the mechanisms of wear for a hip replacement and may influence the conditions of pre-clinical testing of devices in the future. Some of the results will appear in

published papers and presented at scientific meetings. You will not be identified in any of these papers or presentations.

10.2.4. Screening Questionnaire and Consent Form


 UNIVERSITY OF LEEDS

Screening Questionnaire

Please read the following questions very carefully and answer each one honestly by deleting as applicable.


1	Has your doctor ever said that you have a heart condition <u>and</u> that you should only do physical activity recommended by a doctor?	Yes/No
2	Do you feel pain in your chest when you do physical activity?	Yes/No
3	In the past month, have you had chest pain when you were not doing physical activity?	Yes/No
4	Has your doctor ever said that you have high blood pressure?	Yes/No
5	Does exercise cause you to feel dizzy or faint or do you ever lose consciousness?	Yes/No
6	Do you ever have nausea when you exercise?	Yes/No
7	Do you ever feel short of breath when you exercise?	Yes/No
8	Do you have any bone, joint, or muscular problem(s) that could be made worse by exercising?	Yes/No
9	Do you have any joint replacements?	Yes/No
10	Is your doctor currently prescribing drugs for you?	Yes/No
11	Do you smoke?	Yes/No
12	Do you drink excessive amounts of alcohol on a regular basis?	Yes/No
13	Do you know of any other reason why you should not do vigorous physical activity?	Yes/No

I have read, understood and completed the questionnaire to the best of knowledge

Name _____

Signature _____

Date _____


 UNIVERSITY OF LEEDS

Institute of Medical and Biological Engineering
 Ethics Ref No: MEEC 16-021 Date awarded: 12.05.17

Subject Consent Form

Title: Understanding Movement and its Influence on the Tribology of Human Joints

Please delete as applicable

1	I have read the Information for Participants sheet.	Yes/No
2	I agree to having reflective markers placed on my body during data collection	Yes/No
3	I am happy for video recordings to be used for research reporting and review purposes and understand that my participation/ data will be anonymised.	Yes/No
4	I have had the opportunity to ask questions and discuss the research study.	Yes/No
5	I am satisfied with the answers to my questions.	Yes/No
6	I have received enough information about this study.	Yes/No
7	I understand that I am free to withdraw from the study up to two weeks after data collection without giving reason and without affecting my future care.	Yes/No
8	I agree for the data collected from me to be used alongside other data collected and in relevant future research.	Yes/No

Signature _____ Date ___/___/___

Name (block capitals) _____

Signature of person taking consent _____ Date ___/___/___

Name (block capitals) _____

Figure 185. Screening questionnaire and consent form that were completed by participants prior to data collection.

10.2.5. Risk Assessment Details

University of Leeds - Faculty of Biological Sciences
RISK ASSESSMENT FORM

RISK ASSESSMENT DETAILS		DEGREE OF RISK	RISK RATING MATRIX																																																							
School	Biomedical Sciences	<table border="1" style="width: 100%; border-collapse: collapse;"> <thead> <tr> <th colspan="2" style="text-align: center;">LIKELIHOOD (L)</th> </tr> </thead> <tbody> <tr><td>5</td><td>Inevitable</td></tr> <tr><td>4</td><td>Highly Likely</td></tr> <tr><td>3</td><td>Possible</td></tr> <tr><td>2</td><td>Unlikely</td></tr> <tr style="background-color: #f08080;"><td>1</td><td>Remote Possibility</td></tr> </tbody> </table>	LIKELIHOOD (L)		5	Inevitable	4	Highly Likely	3	Possible	2	Unlikely	1	Remote Possibility	<table border="1" style="width: 100%; border-collapse: collapse;"> <thead> <tr> <th colspan="2"></th> <th colspan="5" style="text-align: center;">SEVERITY</th> </tr> <tr> <th rowspan="5" style="writing-mode: vertical-rl; transform: rotate(180deg);">LIKELIHOOD</th> <th>1</th> <th>2</th> <th>3</th> <th>4</th> <th>5</th> </tr> </thead> <tbody> <tr><td>1</td><td>1</td><td>2</td><td>3</td><td>4</td><td>5</td></tr> <tr><td>2</td><td>2</td><td>4</td><td>6</td><td>8</td><td>10</td></tr> <tr><td>3</td><td>3</td><td>6</td><td>9</td><td>16</td><td>15</td></tr> <tr><td>4</td><td>4</td><td>8</td><td>12</td><td>16</td><td>20</td></tr> <tr><td>5</td><td>5</td><td>10</td><td>15</td><td>20</td><td>25</td></tr> </tbody> </table>			SEVERITY					LIKELIHOOD	1	2	3	4	5	1	1	2	3	4	5	2	2	4	6	8	10	3	3	6	9	16	15	4	4	8	12	16	20	5	5	10	15	20	25
LIKELIHOOD (L)																																																										
5	Inevitable																																																									
4	Highly Likely																																																									
3	Possible																																																									
2	Unlikely																																																									
1	Remote Possibility																																																									
		SEVERITY																																																								
LIKELIHOOD	1	2	3	4	5																																																					
	1	1	2	3	4	5																																																				
	2	2	4	6	8	10																																																				
	3	3	6	9	16	15																																																				
	4	4	8	12	16	20																																																				
5	5	10	15	20	25																																																					
Building	LC Miall																																																									
Risk Assessment Title	Understanding Movement and its Influence on the Tribology of Human Joints																																																									
Risk Assessment Log Reference																																																										
Date	March 2017																																																									
Name of Assessors	Brendan McDermott																																																									
Manager Responsible	Neil Messenger																																																									
Location	Biomechanics Laboratory, Level 4 LC Miall, University of Leeds																																																									
Details of Activity	Biomechanical analysis of activities of daily living for healthy subjects																																																									
Other assessments which might also be required, <input checked="" type="checkbox"/> if needed: • Manual Handling <input type="checkbox"/> REF • COSHH <input type="checkbox"/> REF • Personal Protective Equipment (PPE) <input type="checkbox"/> REF • Noise <input type="checkbox"/> REF • Other <input type="checkbox"/> REF		<table border="1" style="width: 100%; border-collapse: collapse;"> <thead> <tr> <th colspan="2" style="text-align: center;">SEVERITY (S)</th> </tr> </thead> <tbody> <tr><td>5</td><td>Very High - Multiple Deaths</td></tr> <tr style="background-color: #f08080;"><td>4</td><td>High - Death, serious injury, permanent disability</td></tr> <tr><td>3</td><td>Moderate - RIDDOR over 3 days</td></tr> <tr style="background-color: #f08080;"><td>2</td><td>Slight - First Aid treatment</td></tr> <tr><td>1</td><td>Nil - Very Minor</td></tr> </tbody> </table>	SEVERITY (S)		5	Very High - Multiple Deaths	4	High - Death, serious injury, permanent disability	3	Moderate - RIDDOR over 3 days	2	Slight - First Aid treatment	1	Nil - Very Minor	<table border="1" style="width: 100%; border-collapse: collapse;"> <thead> <tr> <th colspan="2" style="text-align: center;">PERSONS AT RISK</th> </tr> </thead> <tbody> <tr> <td colspan="2" style="text-align: center;">PERSONS AT RISK</td> </tr> <tr style="background-color: #f08080;"><td colspan="2">Employees</td></tr> <tr><td colspan="2">Students</td></tr> <tr><td colspan="2">Clients</td></tr> <tr><td colspan="2">Contractors</td></tr> <tr style="background-color: #f08080;"><td colspan="2">Members of the public</td></tr> <tr><td colspan="2">Work Experience students</td></tr> <tr><td colspan="2">Other Persons</td></tr> </tbody> </table>	PERSONS AT RISK		PERSONS AT RISK		Employees		Students		Clients		Contractors		Members of the public		Work Experience students		Other Persons																										
SEVERITY (S)																																																										
5	Very High - Multiple Deaths																																																									
4	High - Death, serious injury, permanent disability																																																									
3	Moderate - RIDDOR over 3 days																																																									
2	Slight - First Aid treatment																																																									
1	Nil - Very Minor																																																									
PERSONS AT RISK																																																										
PERSONS AT RISK																																																										
Employees																																																										
Students																																																										
Clients																																																										
Contractors																																																										
Members of the public																																																										
Work Experience students																																																										
Other Persons																																																										
REVIEW DATES		<table border="1" style="width: 100%; border-collapse: collapse;"> <thead> <tr> <th style="width: 30%;">RISK RATING SCORE</th> <th style="width: 70%;">ACTION</th> </tr> </thead> <tbody> <tr style="background-color: #f08080;"><td>1 - 4</td><td>Broadly Acceptable - No action required</td></tr> <tr style="background-color: #f08080;"><td>5 - 9</td><td>Moderate - Reduce risks if reasonably practicable</td></tr> <tr><td>10 -15</td><td>High Risk - Priority Action to be undertaken</td></tr> <tr style="background-color: #f08080;"><td>16 -25</td><td>Unacceptable - Action must be taken IMMEDIATELY</td></tr> </tbody> </table>	RISK RATING SCORE	ACTION	1 - 4	Broadly Acceptable - No action required	5 - 9	Moderate - Reduce risks if reasonably practicable	10 -15	High Risk - Priority Action to be undertaken	16 -25	Unacceptable - Action must be taken IMMEDIATELY																																														
RISK RATING SCORE	ACTION																																																									
1 - 4	Broadly Acceptable - No action required																																																									
5 - 9	Moderate - Reduce risks if reasonably practicable																																																									
10 -15	High Risk - Priority Action to be undertaken																																																									
16 -25	Unacceptable - Action must be taken IMMEDIATELY																																																									

Figure 186. Summary of the risk assessment for data collection within the movement analysis laboratory.

10.3. Python Macro Script

```
1 from anypytools.abctools import AnyPyProcess
2 app = AnyPyProcess()
3
4 #Run kinematic optimization and inverse dynamics in Anybody
5 #Export hip reaction forces
6
7 macrolist = [['load "MoCap_LowerBody.main_S1.any" -def MotionAndParameterOptimizationModel="1" -def InverseDynamicModel="0" -def TrialNumber ="1"',
8              'operation Main.RunMotionAndParameterOptimizationSequence',
9              'run',
10             'load "MoCap_LowerBody.main_S1.any" -def MotionAndParameterOptimizationModel="0" -def InverseDynamicModel="1" -def TrialNumber ="1"',
11             'operation Main.InverseDynamicAnalysisSequence',
12             'run',
13             'classoperation Main.Studies.InverseDynamicStudy.Output.BodyModel.SelectedOutput.Right.Leg.JointReactionForce.Hip_MediolateralForce "Dump"',
14             'classoperation Main.Studies.InverseDynamicStudy.Output.BodyModel.SelectedOutput.Right.Leg.JointReactionForce.Hip_ProximoDistalForce "Dump"',
15             'classoperation Main.Studies.InverseDynamicStudy.Output.BodyModel.SelectedOutput.Right.Leg.JointReactionForce.Hip_AnteroPosteriorForce "Dump"',
16             'exit']]
17
18 output = app.start_macro(macrolist)
19
20 #Write to a .txt file
21
22 outfile = open("Hip reaction forces out.txt",'w')
23 outstr = str(output)
24
25 #Remove empty lines
26 newoutstr = outstr.replace("\n","")
27
28 #Replace commas with a comma and new line
29
30 newoutstr2 = newoutstr.replace(","," , \n")
31 outfile.write(str(newoutstr2))
32 outfile.close()
33
```

Figure 187. AnyBody Macro written within the Python add on, AnyPyTools. The macro runs the kinematic optimisation and inverse dynamics for a given C3D file (MoCap_LowerBody.main_S1 in this case). MedioLateral, ProximoDistal and AnteroPosterior hip reaction forces are exported to Python (‘dumped’). The data was then written to a text file and formatted to remove unwanted empty lines and commas.

10.4.Sliding Velocity and Acceleration Graphs

Within this section, sliding displacement, velocity and acceleration is presented for a further three femoral head points, for each activity (in addition to Point 7 shown in section 4.4.16.). The femoral head points occupy three different locations on the femoral head, ensuring that the data is not mirrored (Medial (-) Lateral (+); Anterior (+) Posterior (-); Proximal (-) Distal (+)) (mm). Resulted points were 1 (0, -14, 0) (most posterior point), 11 (-14, 0, 0) (most medial point) and 17 (7, 0, 12) (same distal positioning as point 7, but located laterally on the medial-lateral axis).

10.4.1. Walk

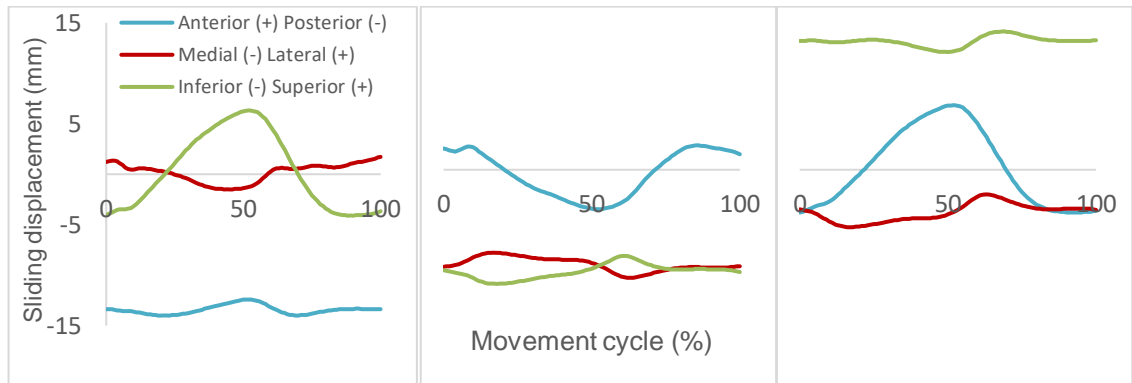


Figure 188. Sliding displacement shown in each axis for a mean walk. From left to right, femoral head points 1 (0, -14, 0), 11 (-14, 0, 0) and 17 (7, 0, 12) are shown.

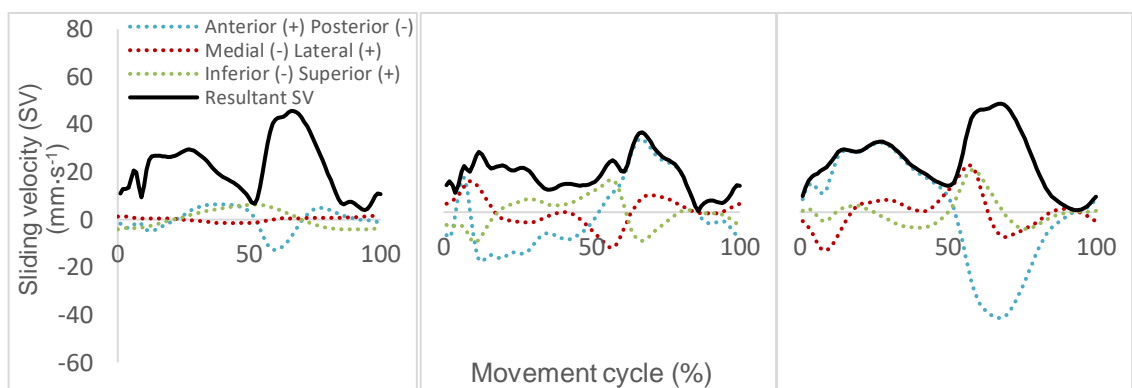


Figure 189. Sliding velocity shown in each axis for a mean walk. Resultant sliding velocity is shown in black. From left to right, femoral head points 1 (0, -14, 0), 11 (-14, 0, 0) and 17 (7, 0, 12) are shown.

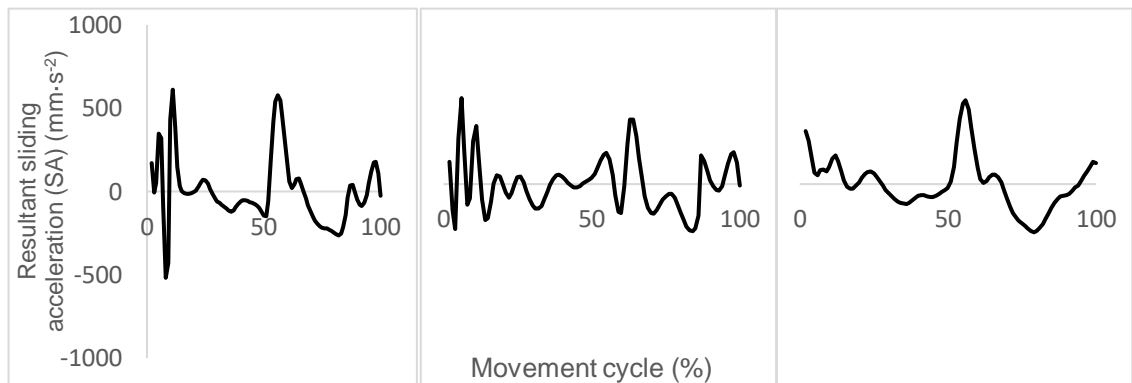


Figure 190. Sliding acceleration shown for a mean walk. From left to right, femoral head points 1 (0, -14, 0), 11 (-14, 0, 0) and 17 (7, 0, 12) are shown.

10.4.2. Walk Turn

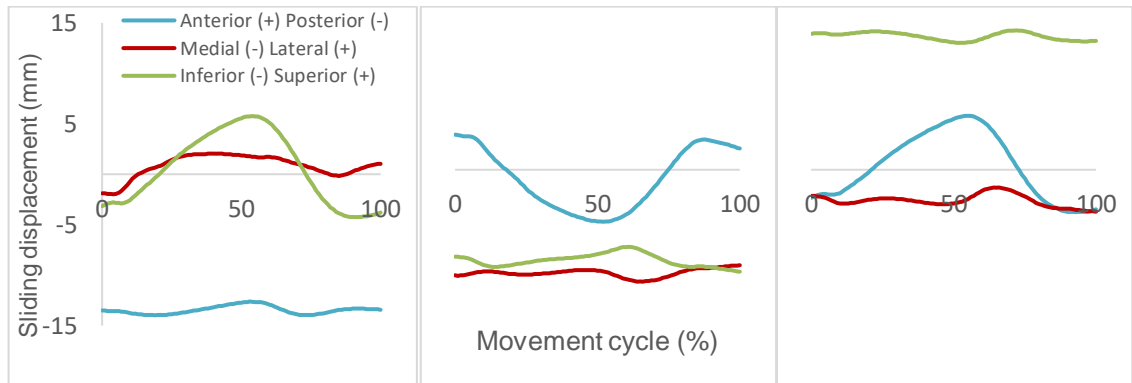


Figure 191. Sliding displacement shown in each axis for a mean walk turn. From left to right, femoral head points 1 (0, -14, 0), 11 (-14, 0, 0) and 17 (7, 0, 12) are shown.

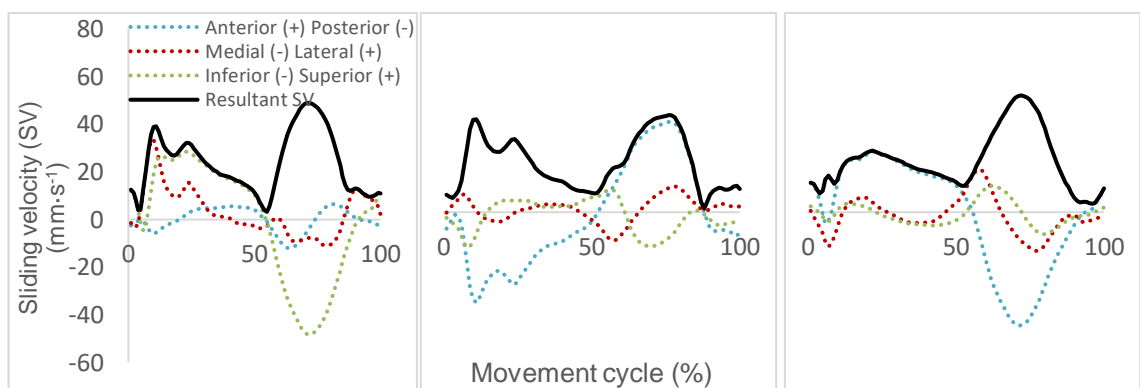


Figure 192. Sliding velocity shown in each axis for a mean walk turn. Resultant sliding velocity is shown in black. From left to right, femoral head points 1 (0, -14, 0), 11 (-14, 0, 0) and 17 (7, 0, 12) are shown.

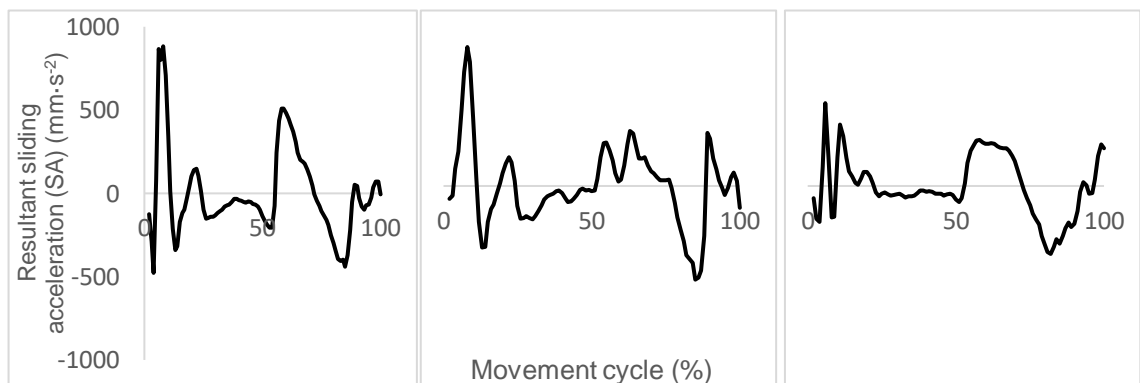


Figure 193. Sliding acceleration shown for a mean walk turn. From left to right, femoral head points 1 (0, -14, 0), 11 (-14, 0, 0) and 17 (7, 0, 12) are shown.

10.4.3. Incline Walk

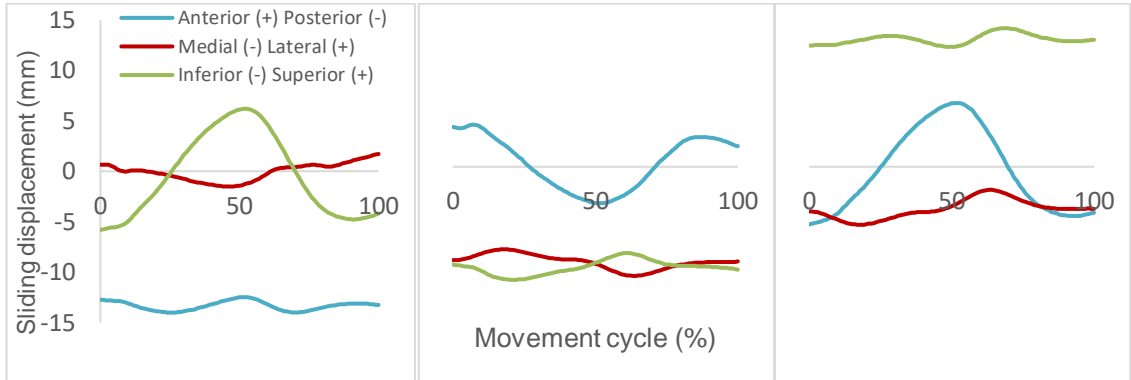


Figure 194. Sliding displacement shown in each axis for a mean incline walk. From left to right, femoral head points 1 (0, -14, 0), 11 (-14, 0, 0) and 17 (7, 0, 12) are shown.

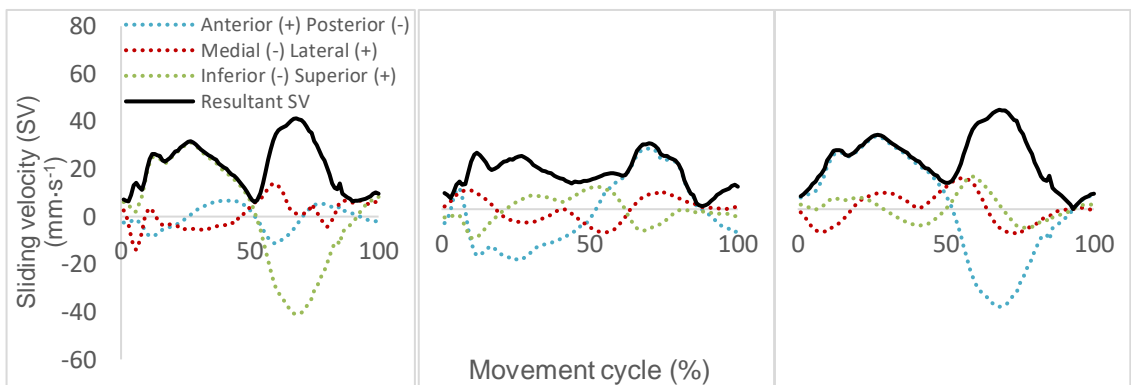


Figure 195. Sliding velocity shown in each axis for a mean incline walk. Resultant sliding velocity is shown in black. From left to right, femoral head points 1 (0, -14, 0), 11 (-14, 0, 0) and 17 (7, 0, 12) are shown.

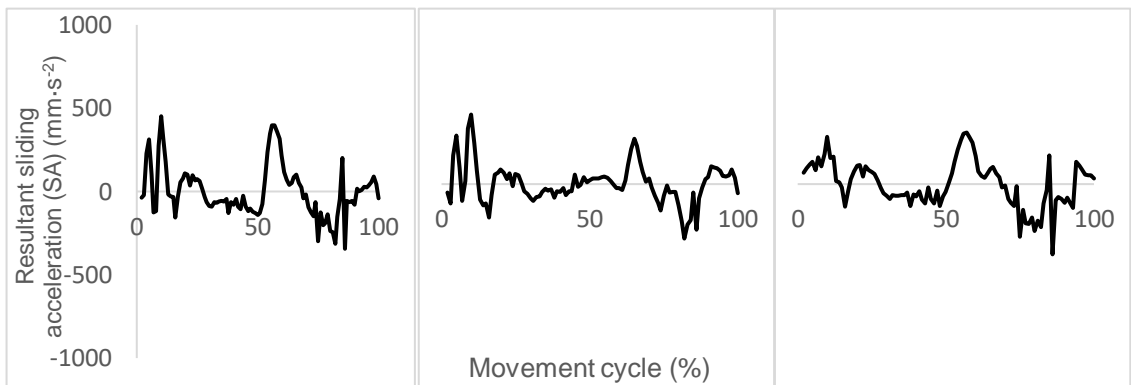


Figure 196. Sliding acceleration shown for a mean incline walk. From left to right, femoral head points 1 (0, -14, 0), 11 (-14, 0, 0) and 17 (7, 0, 12) are shown.

10.4.4. Decline Walk

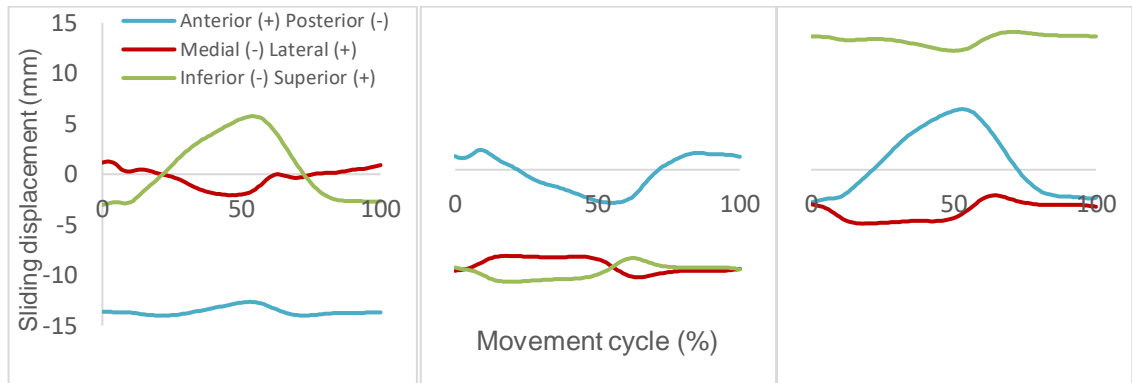


Figure 197. Sliding displacement shown in each axis for a mean decline walk. From left to right, femoral head points 1 (0, -14, 0), 11 (-14, 0, 0) and 17 (7, 0, 12) are shown.

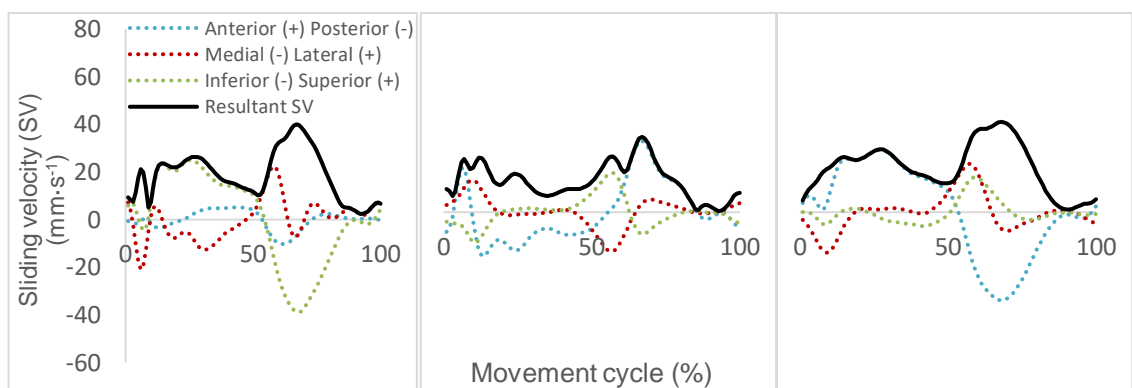


Figure 198. Sliding velocity shown in each axis for a mean decline walk. Resultant sliding velocity is shown in black. From left to right, femoral head points 1 (0, -14, 0), 11 (-14, 0, 0) and 17 (7, 0, 12) are shown.

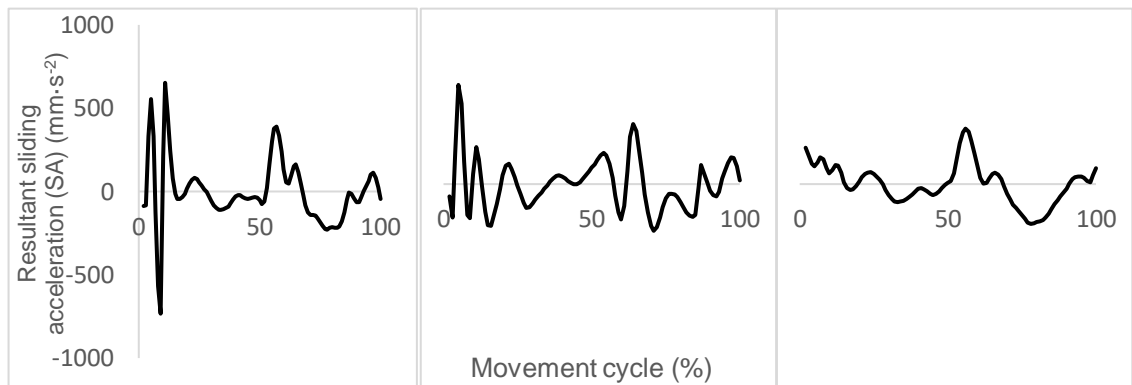


Figure 199. Sliding acceleration shown for a mean decline walk. From left to right, femoral head points 1 (0, -14, 0), 11 (-14, 0, 0) and 17 (7, 0, 12) are shown.

10.4.5. Stand to Sit

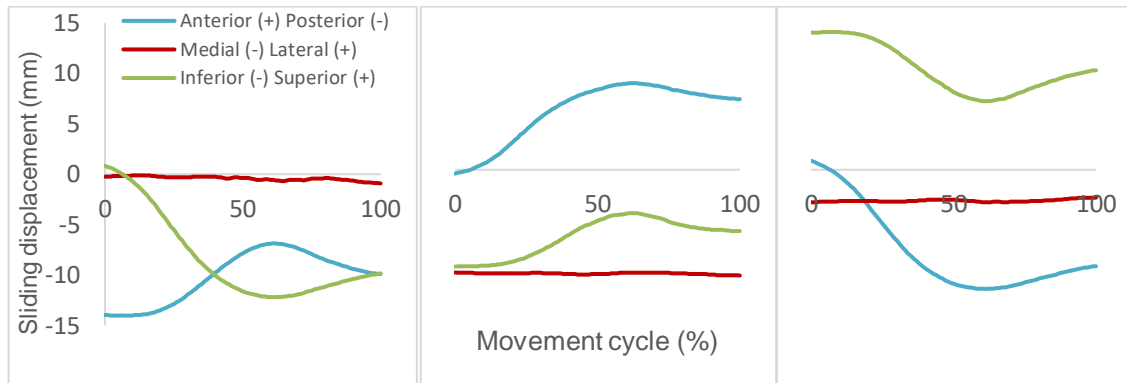


Figure 200. Sliding displacement shown in each axis for a mean stand to sit. From left to right, femoral head points 1 (0, -14, 0), 11 (-14, 0, 0) and 17 (7, 0, 12) are shown.

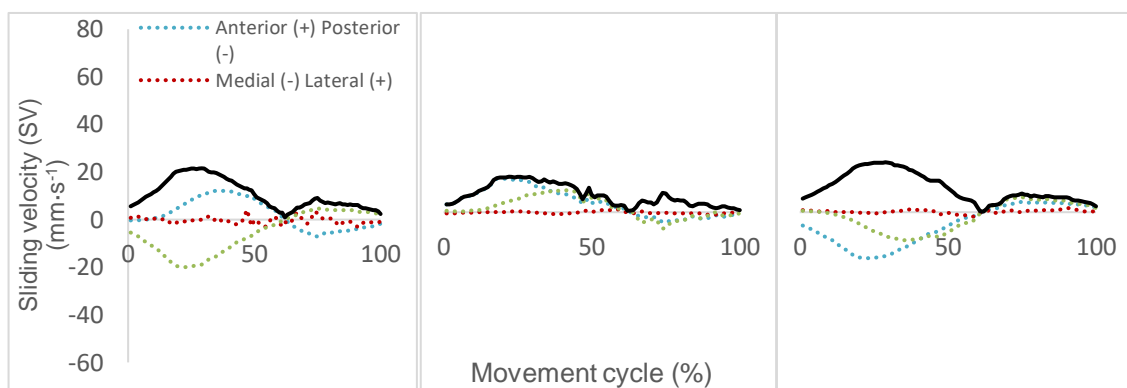


Figure 201. Sliding velocity shown in each axis for a mean stand to sit. Resultant sliding velocity is shown in black. From left to right, femoral head points 1 (0, -14, 0), 11 (-14, 0, 0) and 17 (7, 0, 12) are shown.

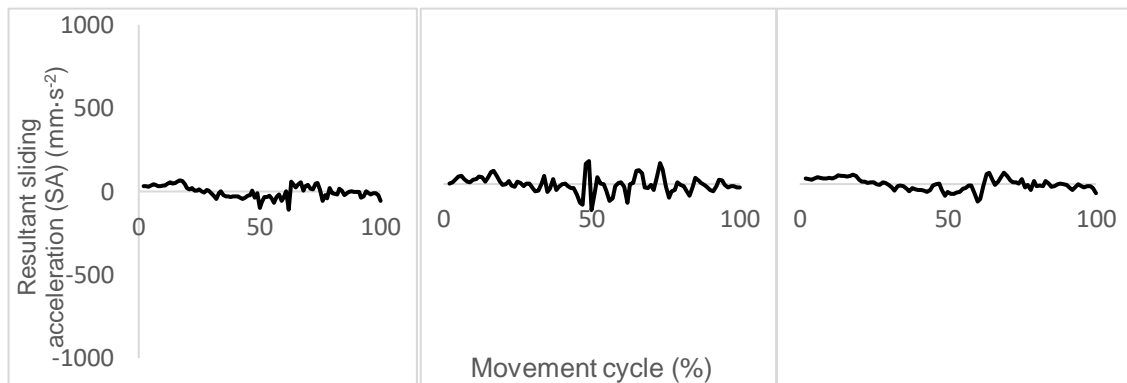


Figure 202. Sliding acceleration shown for a mean stand to sit. From left to right, femoral head points 1 (0, -14, 0), 11 (-14, 0, 0) and 17 (7, 0, 12) are shown.

10.4.6. Sit to Stand

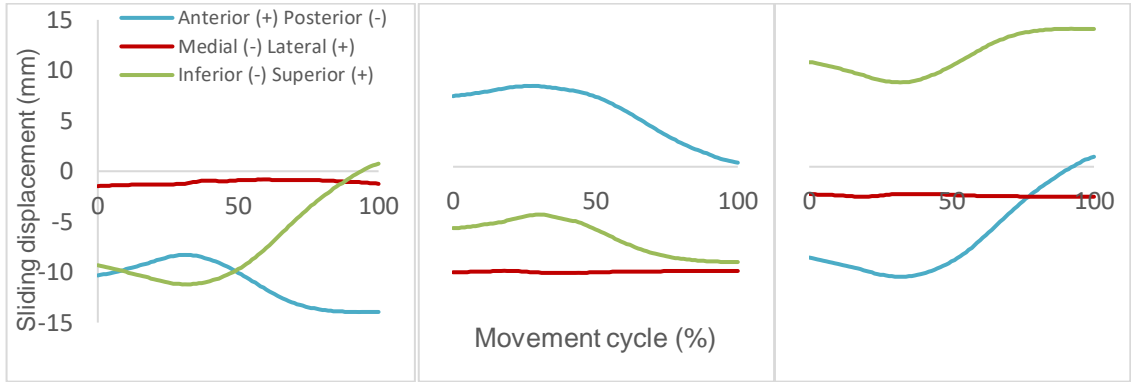


Figure 203. Sliding displacement shown in each axis for a mean sit to stand. From left to right, femoral head points 1 (0, -14, 0), 11 (-14, 0, 0) and 17 (7, 0, 12) are shown.

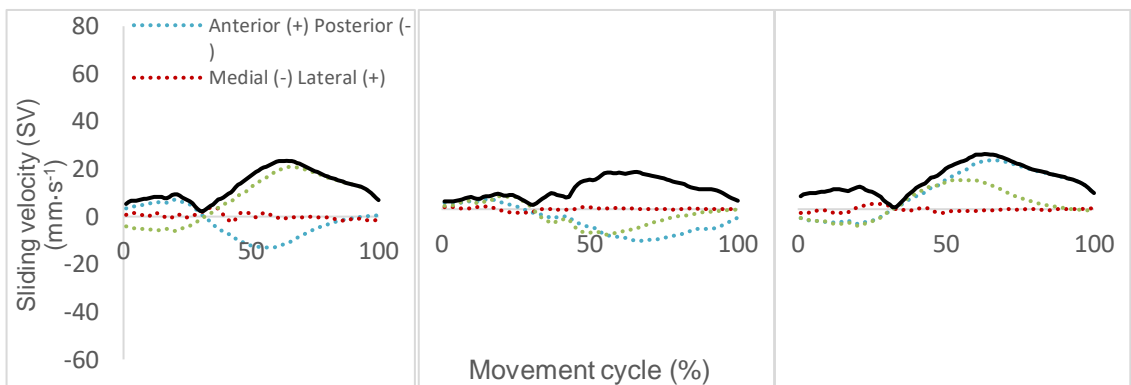


Figure 204. Sliding velocity shown in each axis for a mean sit to stand. Resultant sliding velocity is shown in black. From left to right, femoral head points 1 (0, -14, 0), 11 (-14, 0, 0) and 17 (7, 0, 12) are shown.

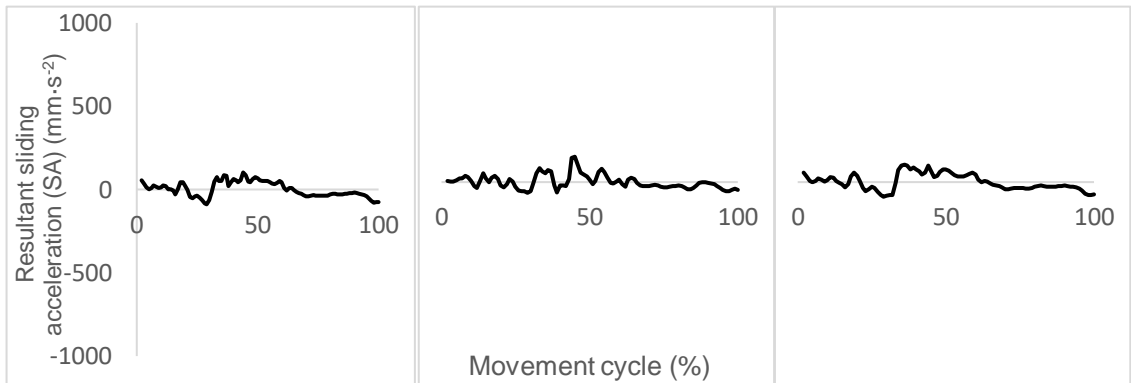


Figure 205. Sliding acceleration shown for a mean sit to stand. From left to right, femoral head points 1 (0, -14, 0), 11 (-14, 0, 0) and 17 (7, 0, 12) are shown.

10.4.7. Sit Cross Legged

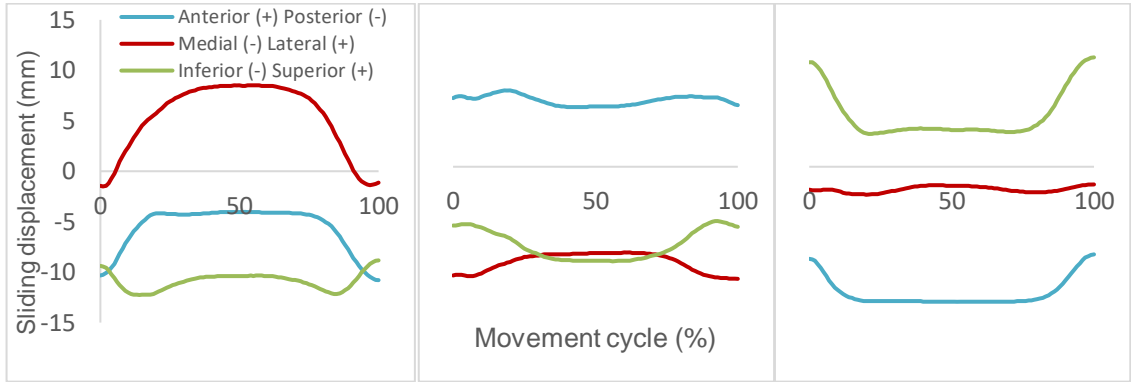


Figure 206. Sliding displacement shown in each axis for a mean sit cross legged. From left to right, femoral head points 1 (0, -14, 0), 11 (-14, 0, 0) and 17 (7, 0, 12) are shown.

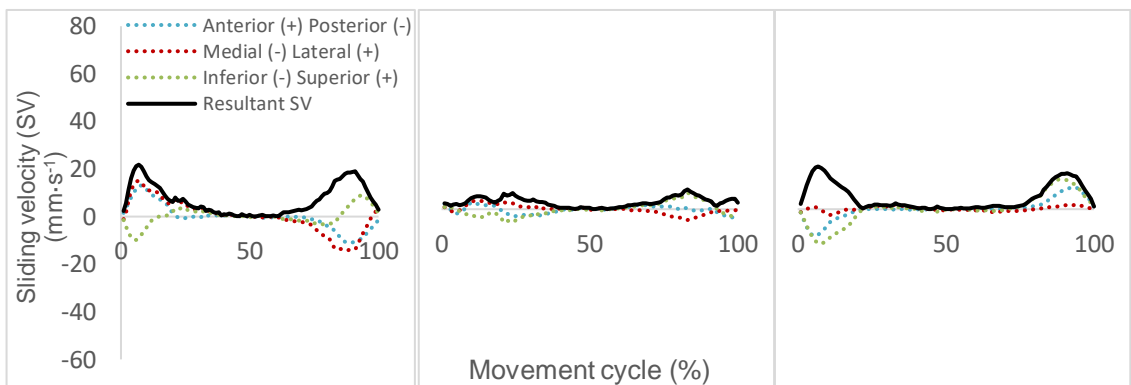


Figure 207. Sliding velocity shown in each axis for a mean sit cross legged. Resultant sliding velocity is shown in black. From left to right, femoral head points 1 (0, -14, 0), 11 (-14, 0, 0) and 17 (7, 0, 12) are shown.

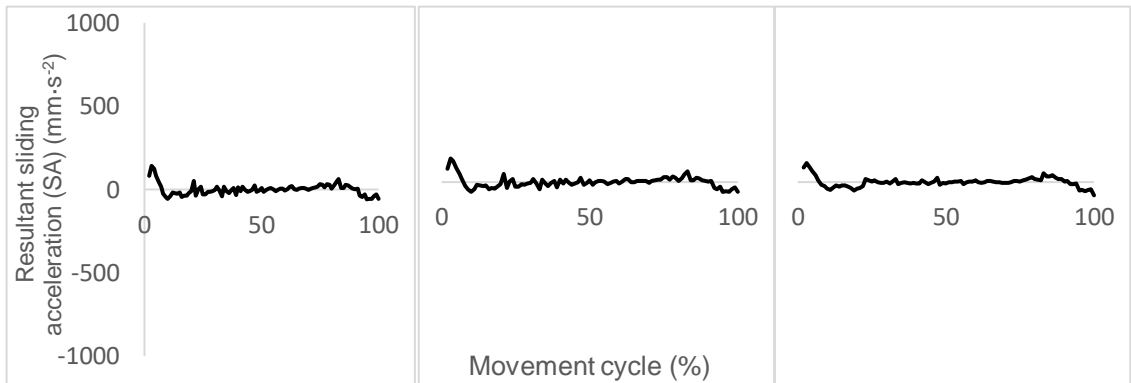


Figure 208. Sliding acceleration shown for a mean sit cross legged. From left to right, femoral head points 1 (0, -14, 0), 11 (-14, 0, 0) and 17 (7, 0, 12) are shown.

10.4.8. Squat

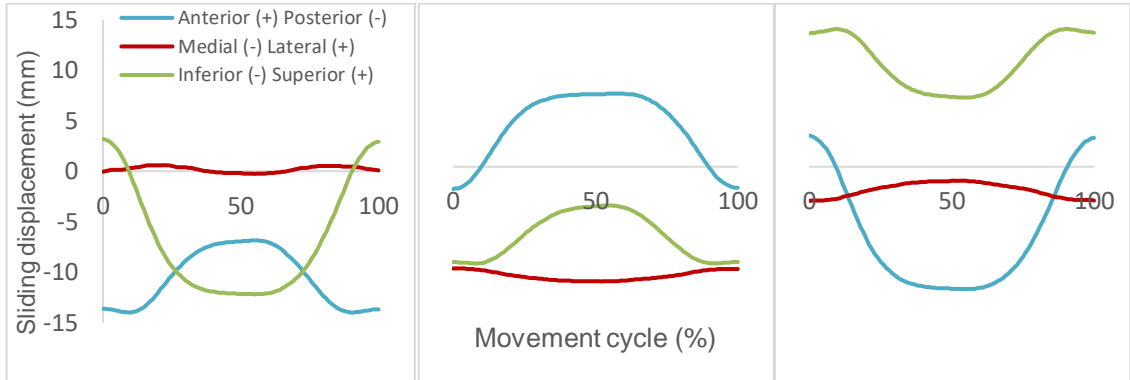


Figure 209. Sliding displacement shown in each axis for a mean squat. From left to right, femoral head points 1 (0, -14, 0), 11 (-14, 0, 0) and 17 (7, 0, 12) are shown.

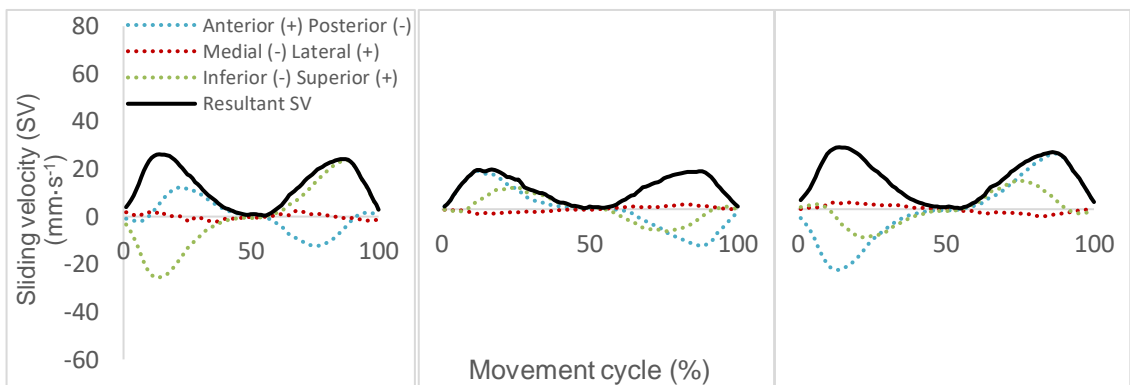


Figure 210. Sliding velocity shown in each axis for a mean squat. Resultant sliding velocity is shown in black. From left to right, femoral head points 1 (0, -14, 0), 11 (-14, 0, 0) and 17 (7, 0, 12) are shown.

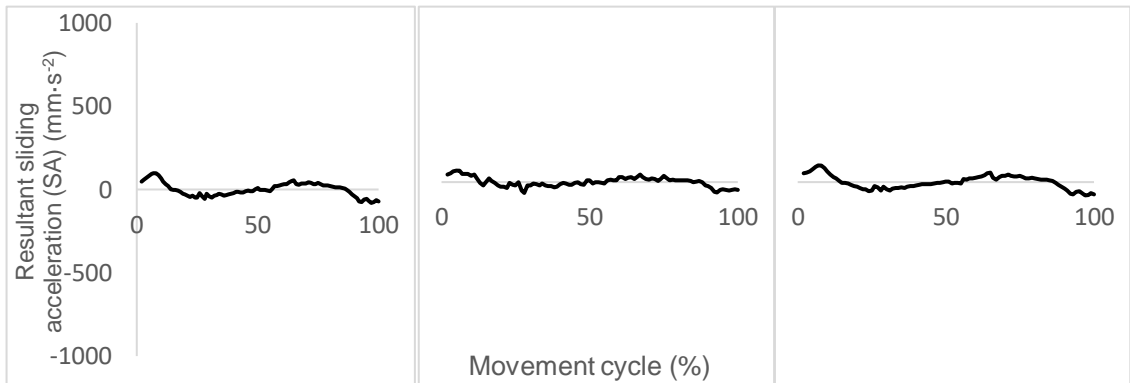


Figure 211. Sliding acceleration shown for a mean squat. From left to right, femoral head points 1 (0, -14, 0), 11 (-14, 0, 0) and 17 (7, 0, 12) are shown.

10.4.9. Stand Reach

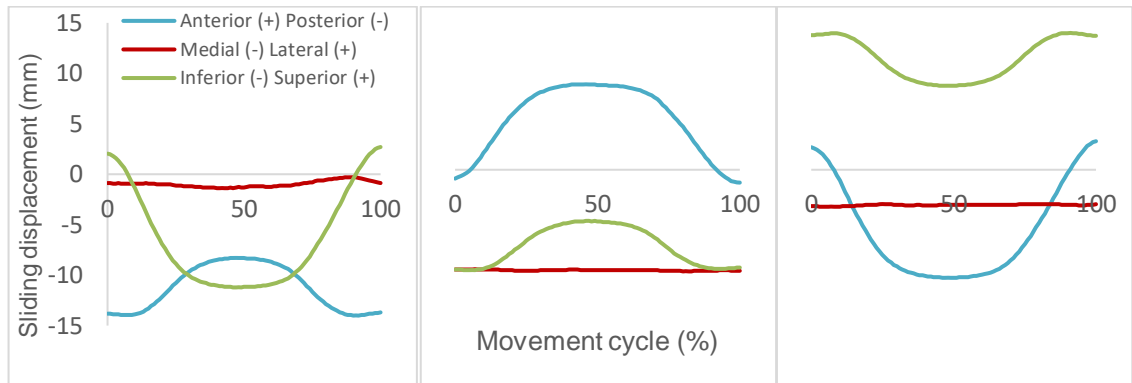


Figure 212. Sliding displacement shown in each axis for a mean stand reach. From left to right, femoral head points 1 (0, -14, 0), 11 (-14, 0, 0) and 17 (7, 0, 12) are shown.

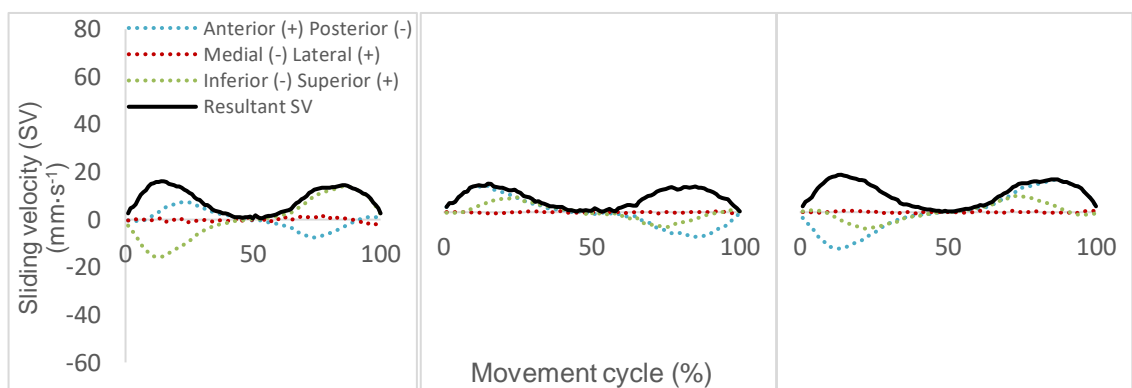


Figure 213. Sliding velocity shown in each axis for a mean stand reach. Resultant sliding velocity is shown in black. From left to right, femoral head points 1 (0, -14, 0), 11 (-14, 0, 0) and 17 (7, 0, 12) are shown.

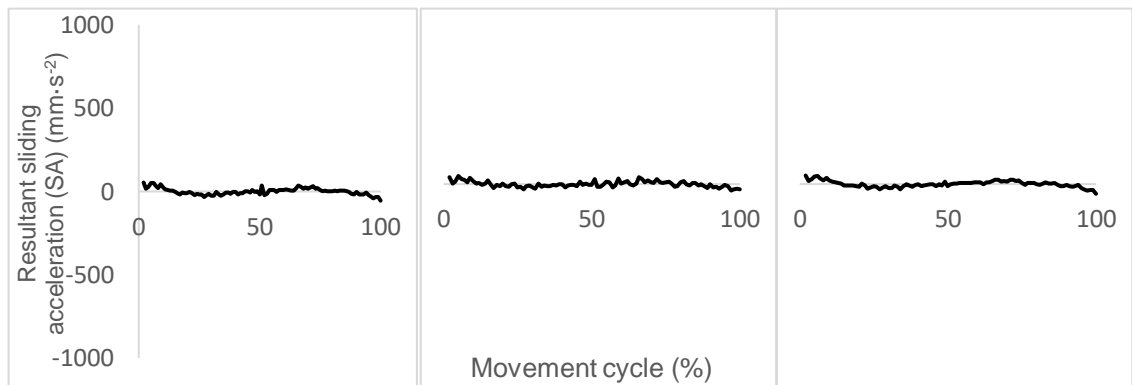


Figure 214. Sliding acceleration shown for a mean stand reach. From left to right, femoral head points 1 (0, -14, 0), 11 (-14, 0, 0) and 17 (7, 0, 12) are shown.

10.4.10. Kneel Reach

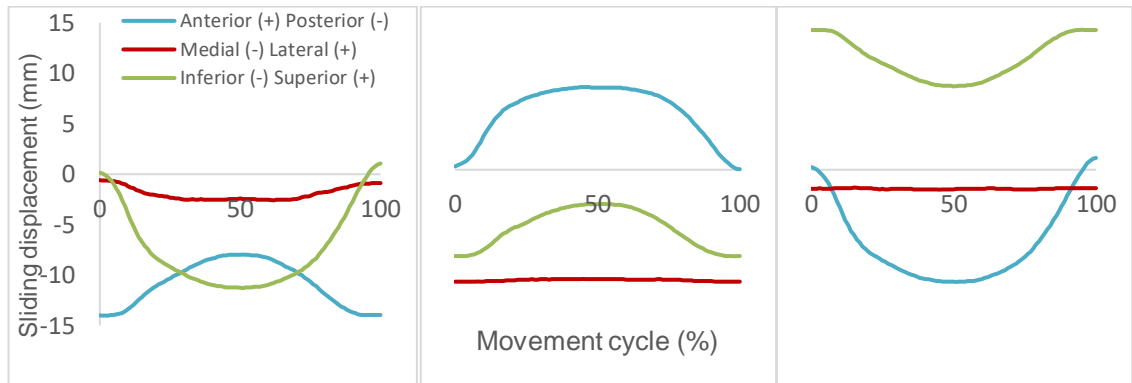


Figure 215. Sliding displacement shown in each axis for a mean kneel reach. From left to right, femoral head points 1 (0, -14, 0), 11 (-14, 0, 0) and 17 (7, 0, 12) are shown.

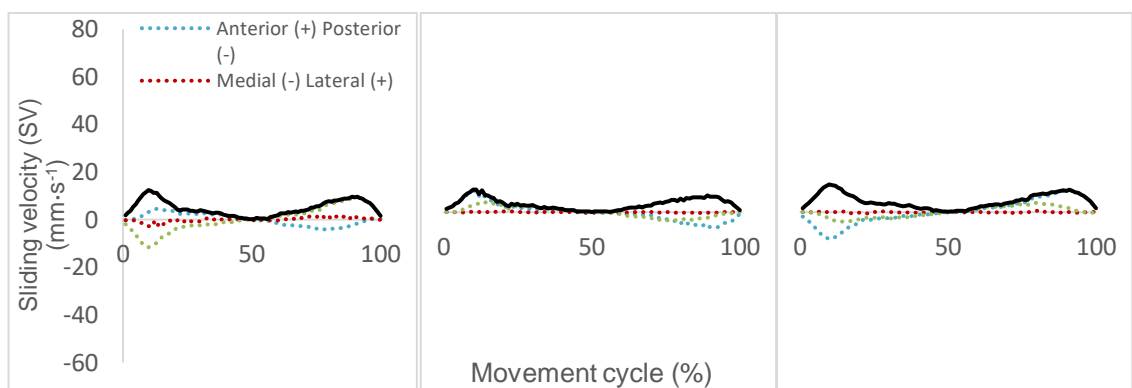


Figure 216. Sliding velocity shown in each axis for a mean kneel reach. Resultant sliding velocity is shown in black. From left to right, femoral head points 1 (0, -14, 0), 11 (-14, 0, 0) and 17 (7, 0, 12) are shown.

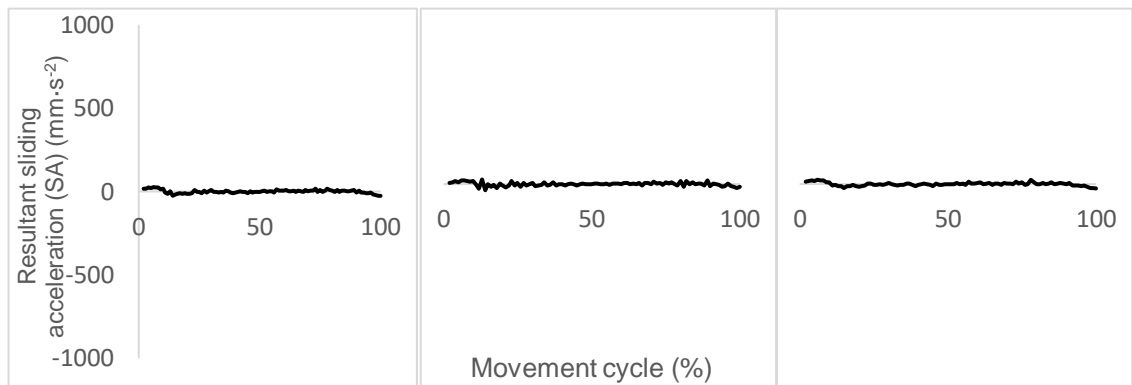


Figure 217. Sliding acceleration shown for a mean kneel reach. From left to right, femoral head points 1 (0, -14, 0), 11 (-14, 0, 0) and 17 (7, 0, 12) are shown.

10.4.11. Lunge

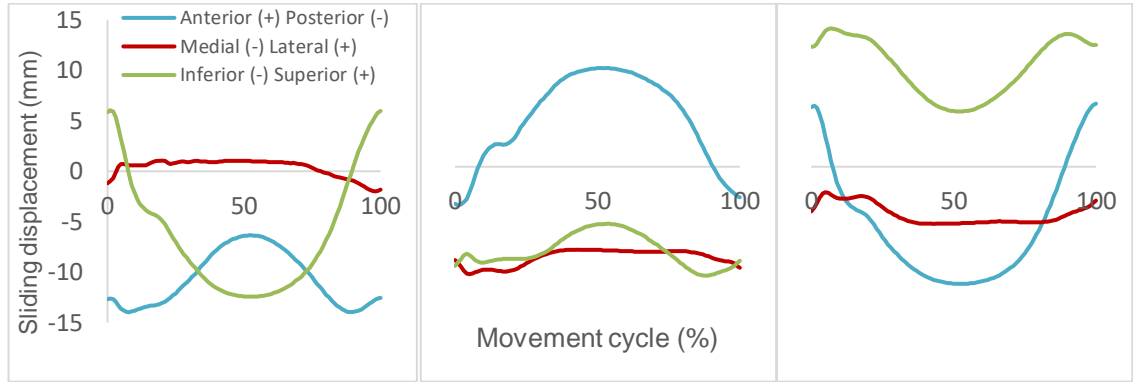


Figure 218. Sliding displacement shown in each axis for a mean lunge. From left to right, femoral head points 1 (0, -14, 0), 11 (-14, 0, 0) and 17 (7, 0, 12) are shown.

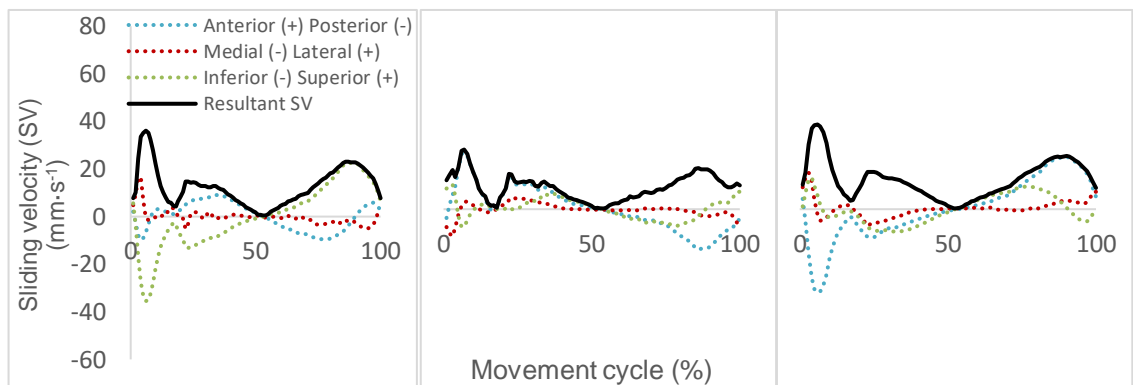


Figure 219. Sliding velocity shown in each axis for a mean lunge. Resultant sliding velocity is shown in black. From left to right, femoral head points 1 (0, -14, 0), 11 (-14, 0, 0) and 17 (7, 0, 12) are shown.

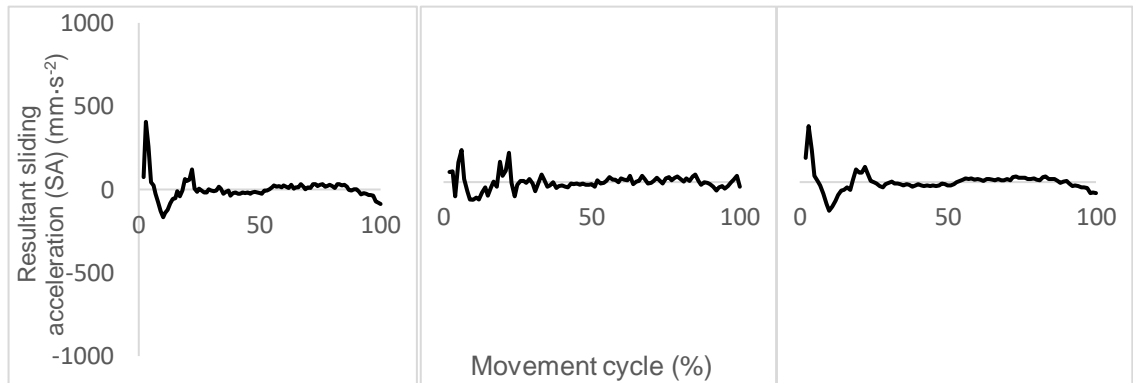


Figure 220. Sliding acceleration shown for a mean lunge. From left to right, femoral head points 1 (0, -14, 0), 11 (-14, 0, 0) and 17 (7, 0, 12) are shown.

10.4.12. Golf Swing

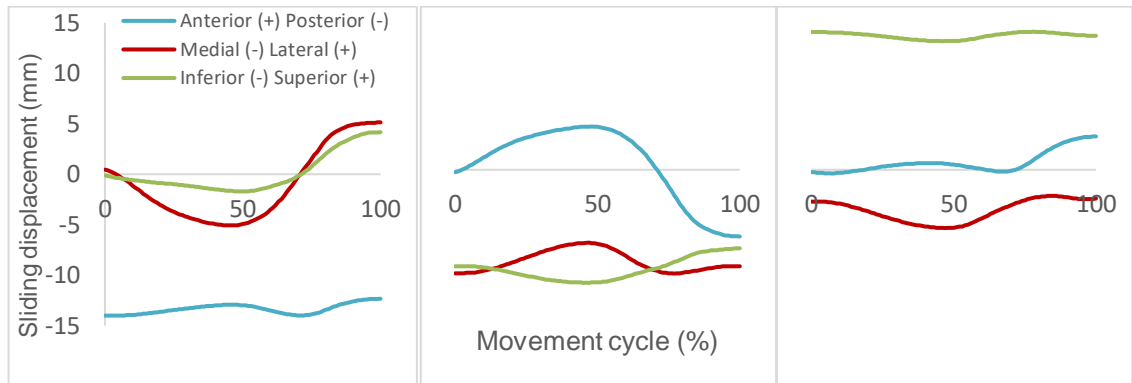


Figure 221. Sliding displacement shown in each axis for a mean golf swing. From left to right, femoral head points 1 (0, -14, 0), 11 (-14, 0, 0) and 17 (7, 0, 12) are shown.

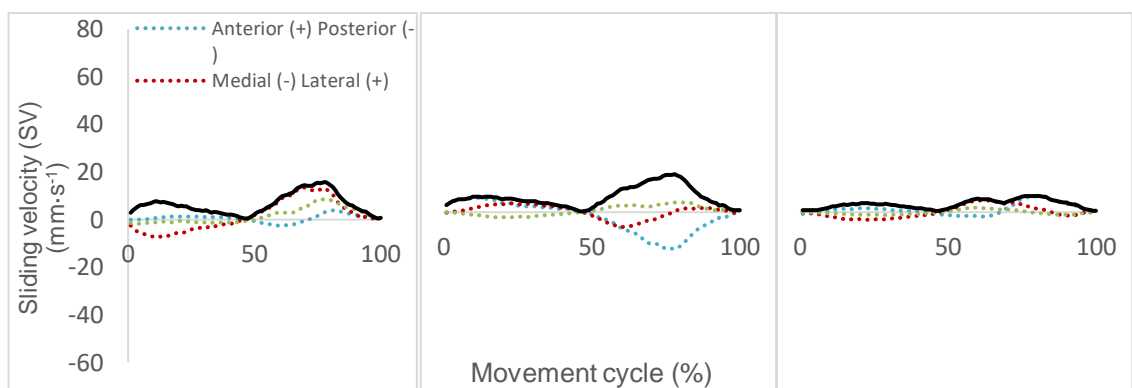


Figure 222. Sliding velocity shown in each axis for a mean golf swing. Resultant sliding velocity is shown in black. From left to right, femoral head points 1 (0, -14, 0), 11 (-14, 0, 0) and 17 (7, 0, 12) are shown.

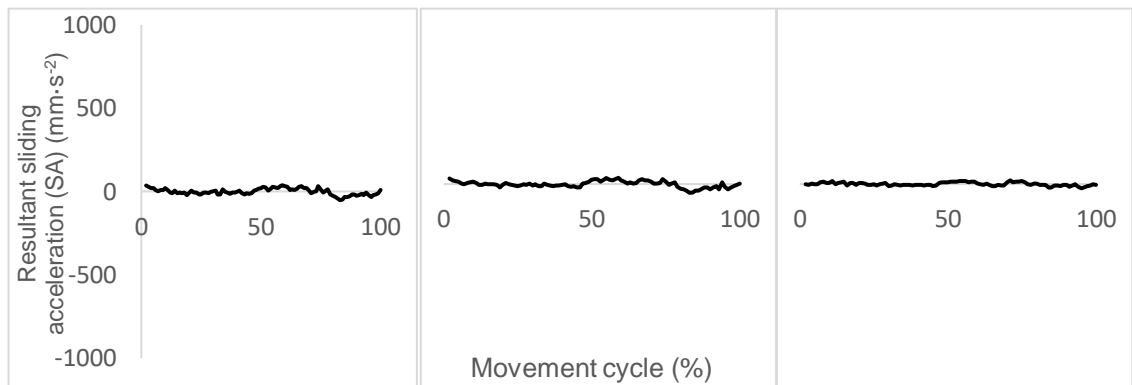


Figure 223. Sliding acceleration shown for a mean golf swing. From left to right, femoral head points 1 (0, -14, 0), 11 (-14, 0, 0) and 17 (7, 0, 12) are shown.

10.4.13. Cycle

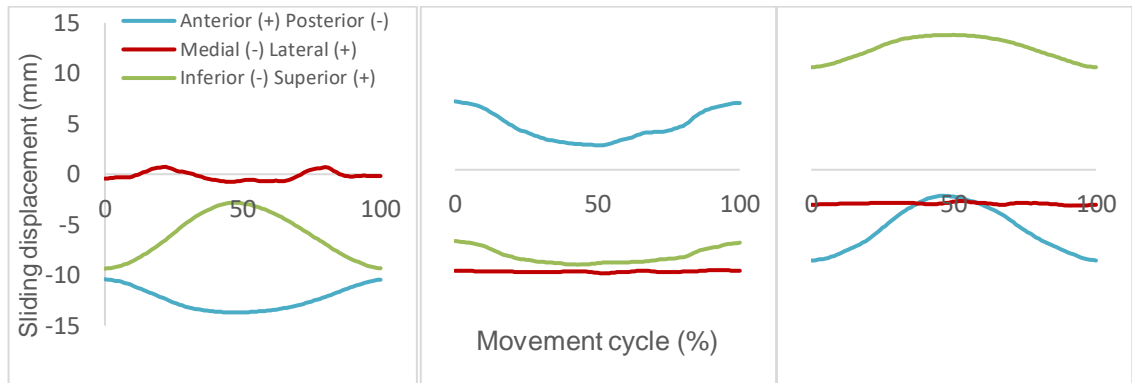


Figure 224. Sliding displacement shown in each axis for a mean cycle. From left to right, femoral head points 1 (0, -14, 0), 11 (-14, 0, 0) and 17 (7, 0, 12) are shown.

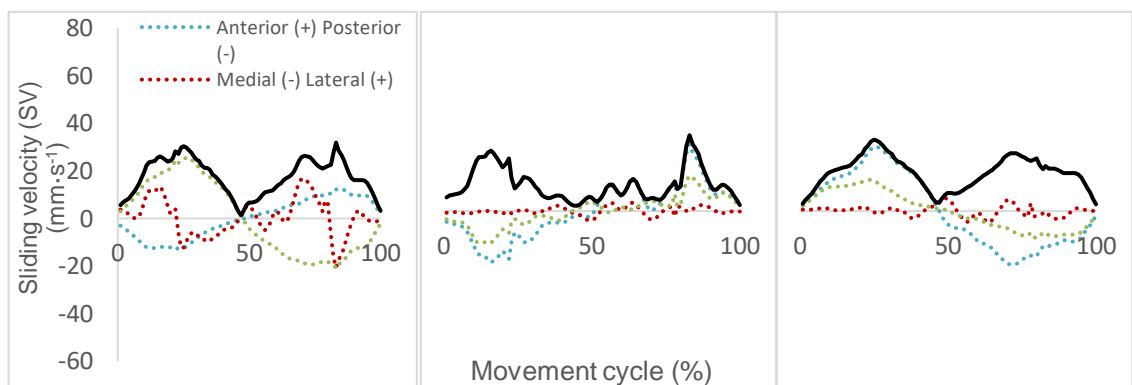


Figure 225. Sliding velocity shown in each axis for a mean cycle. Resultant sliding velocity is shown in black. From left to right, femoral head points 1 (0, -14, 0), 11 (-14, 0, 0) and 17 (7, 0, 12) are shown.

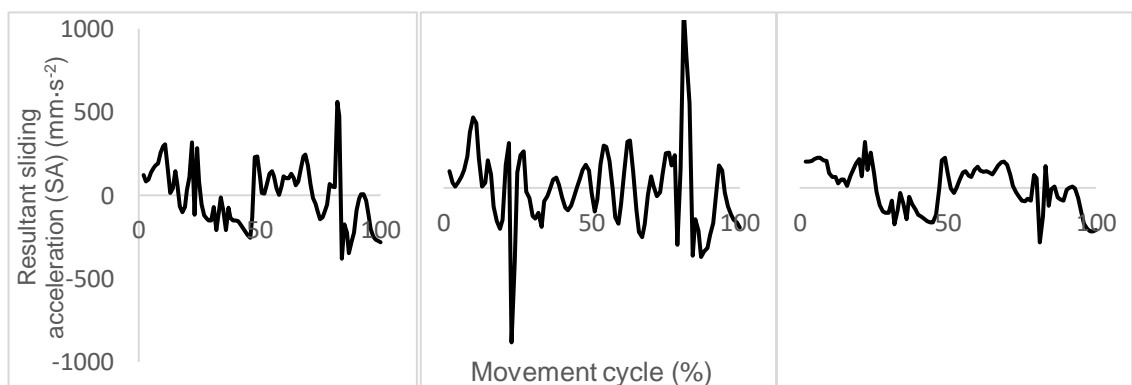


Figure 226. Sliding acceleration shown for a mean cycle. From left to right, femoral head points 1 (0, -14, 0), 11 (-14, 0, 0) and 17 (7, 0, 12) are shown.

10.5. Hip Reaction Force, Sliding Velocity and Sliding Acceleration Scatter Plots

Within this Appendix section, hip reaction force (HRF) is plotted against sliding velocity (SV) and sliding acceleration (SA). The sliding conditions relate to the motion path located at Point 7 on the femoral head (*Medial, Anterior, Distal*; 0 mm, 7 mm, 12 mm). Walk, walk turn, sit to stand, lunge, golf swing and Leeds Prosim input data are shown in section 5.7. to provide a visualisation during the discussion. The remaining activities (stand to sit, squat, stand reach and kneel reach) are presented below. It is worth noting that incline walk, decline walk, sit cross legged and cycle are not shown as the HRFs were not calculated.

10.5.1. Stand to Sit

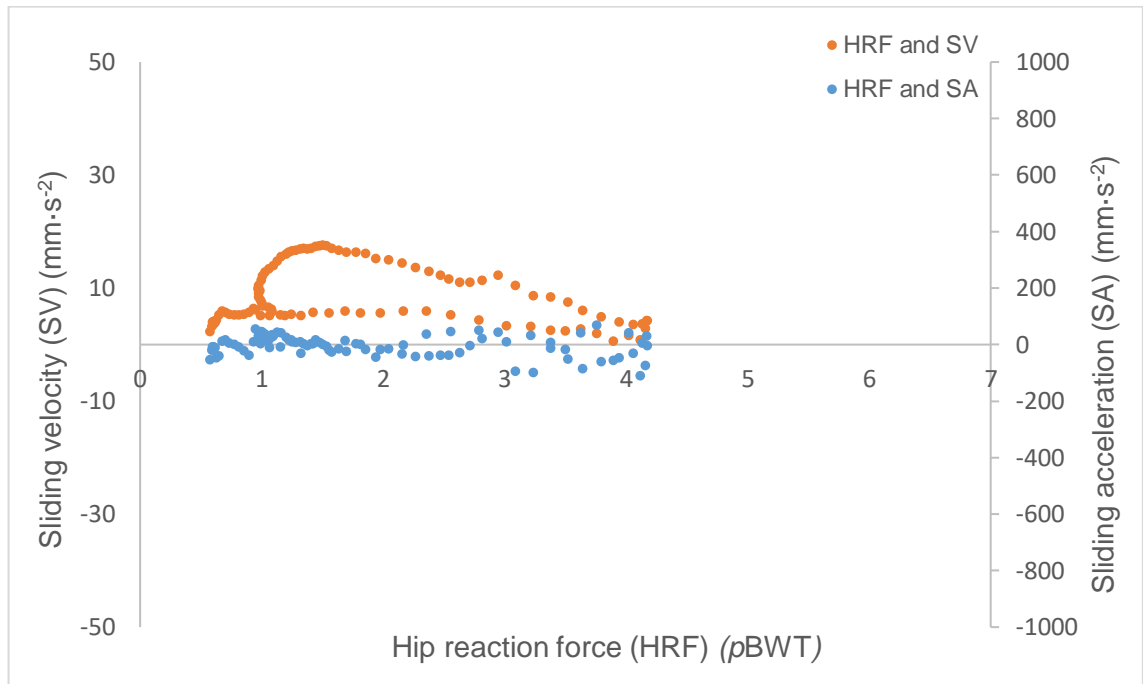


Figure 227. Hip reaction force (proportional to body weight or pBWT) is shown alongside the corresponding sliding velocity and sliding acceleration for a stand to sit motion path. The motion path is located at femoral head ‘point 7’ (Medial, Anterior, Distal; 0 mm, 7 mm, 12 mm).

10.5.2. Squat

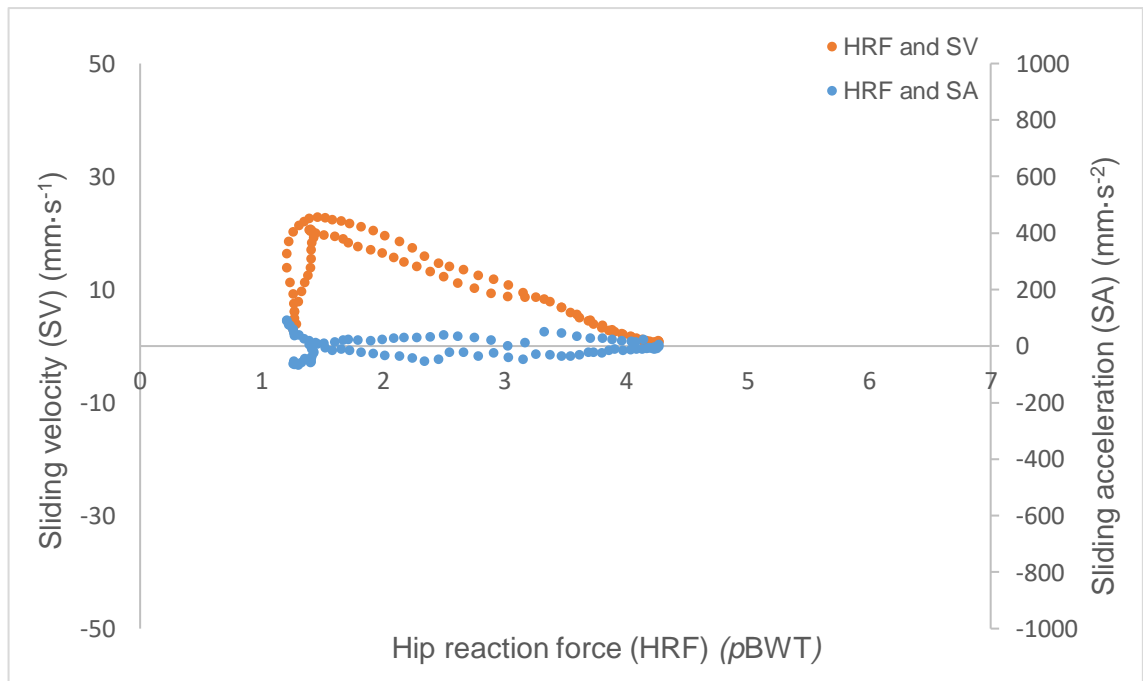


Figure 228. Hip reaction force (proportional to body weight or pBWT) is shown alongside the corresponding sliding velocity and sliding acceleration for a squat motion path. The motion path is located at femoral head ‘point 7’ (Medial, Anterior, Distal; 0 mm, 7 mm, 12 mm).

10.5.3. Stand Reach



Figure 229. Hip reaction force (proportional to body weight or *pBWT*) is shown alongside the corresponding sliding velocity and sliding acceleration for a stand reach motion path. The motion path is located at femoral head ‘point 7’ (*Medial, Anterior, Distal*; 0 mm, 7 mm, 12 mm).

10.5.4. Kneel Reach

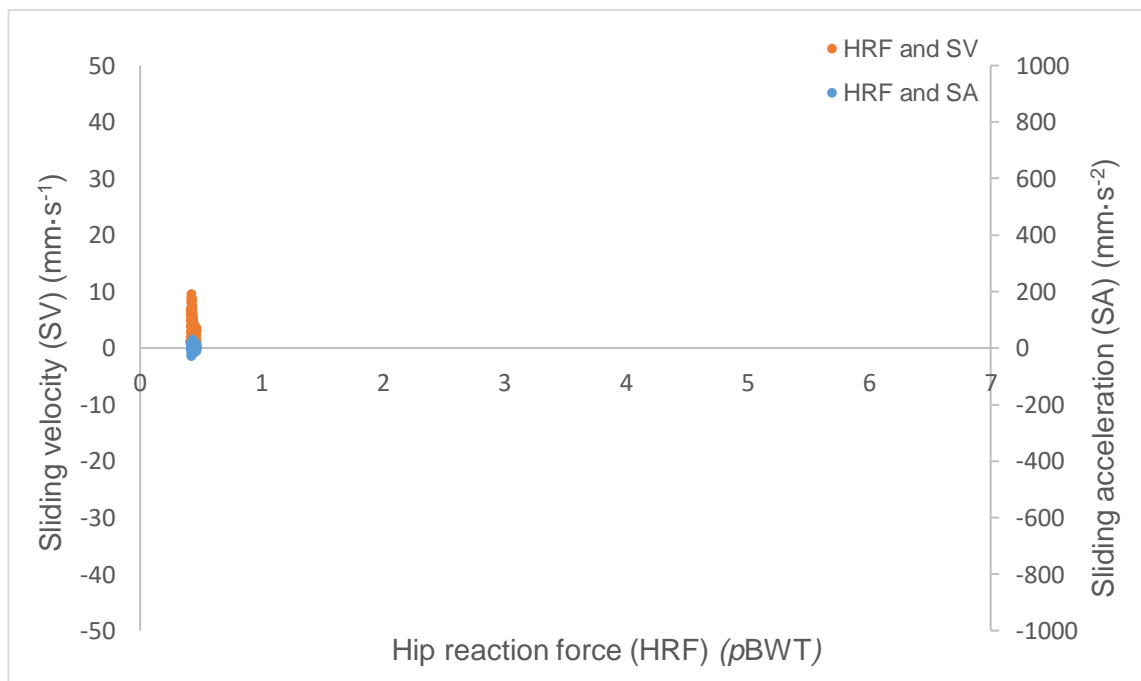


Figure 230. Hip reaction force (proportional to body weight or *pBWT*) is shown alongside the corresponding sliding velocity and sliding acceleration for a kneel reach motion path. The motion path is located at femoral head ‘point 7’ (*Medial, Anterior, Distal*; 0 mm, 7 mm, 12 mm).

10.6. Ground Reaction Forces and Hip Moments

The following section presents and discusses the mean vertical ground reaction force (vGRF) and hip moments for each of the thirteen activities. Figures 231 to 248 show the vGRF (proportional to body weight or $pBWT$) and hip moments alongside standard deviations (SD). Table 24 displays the peak vGRF, mean SD and peak SD for each activity.

Hip joint moments are reported about three axes (X: flexion-extension; Y: abduction-adduction; Z: internal-external rotation). Standard deviations (SDs) are also resulted for activities. Peak joint moments and standard deviations are resulted in Table 25. The incline/decline walk, sit cross legged and cycling data was not included in this section, as ground reaction force data could not be collected.

10.6.1. Walk

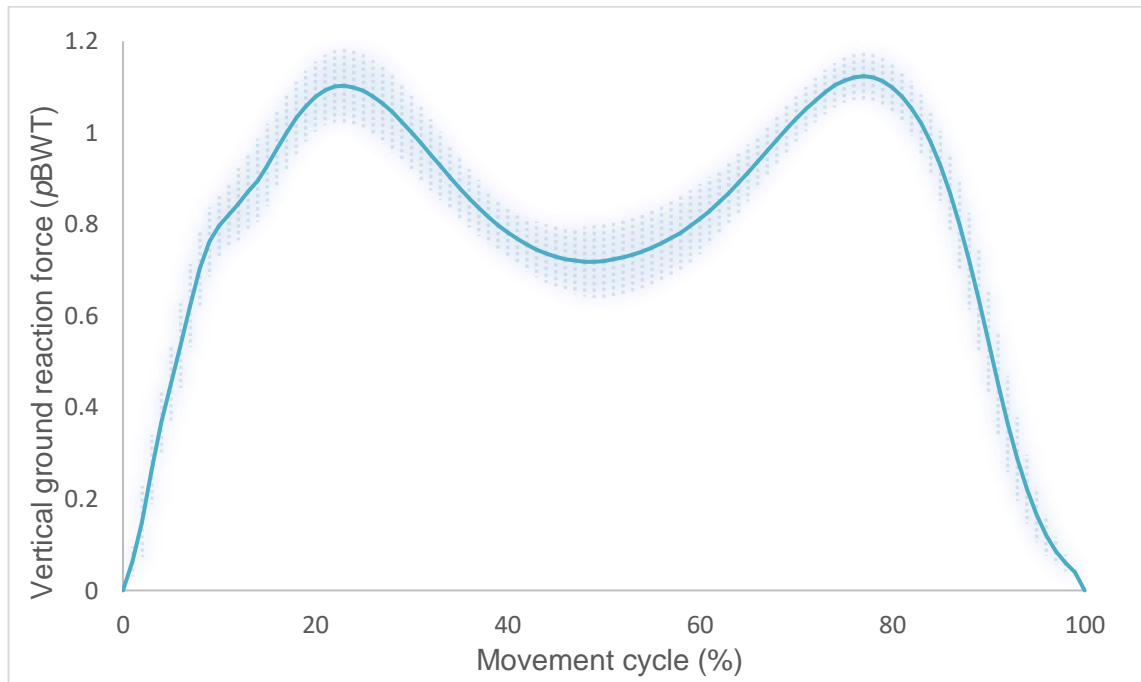


Figure 231. Mean right foot, vertical ground reaction force during one gait cycle for a level walk, proportional to body weight (*pBWT*). Standard deviation above and below the mean are shown as shaded error bars ($n=17$).

A sharp increase in the *vGRF* was observed at initial contact, during walking (Figure 231). A smoothed impact transient can be observed within the curve, at $\approx 10\%$ of the gait cycle. Two peaks occurred during walking, with a ‘valley’ seen between the two at mid-stance (mid-stance *vGRF*: 0.7 *pBWT*). The first peak occurred at weight acceptance and the second peak was observed during the propulsive phase of gait (both 1.1 *pBWT*). Variation was lowest at initial-contact and toe-off. However, consistent variation could be observed when the lower limb was fully loaded, with a mean standard deviation (SD) of ± 0.07 *pBWT*.

The first peak represents weight acceptance, whereas the second peak represents the propulsive phase of gait (Jacobs et al., 1972; Winter, 2009). Existing literature suggests that walking *vGRF* data for a healthy population, will peak between 0.9 and 1.2 *pBWT* (Chao et al., 1983; Hamill et al., 1984; Hamill and Knutzen, 2006; Herzog et al., 1989; Keller et al., 1996). This range was further validated by results within the current study.

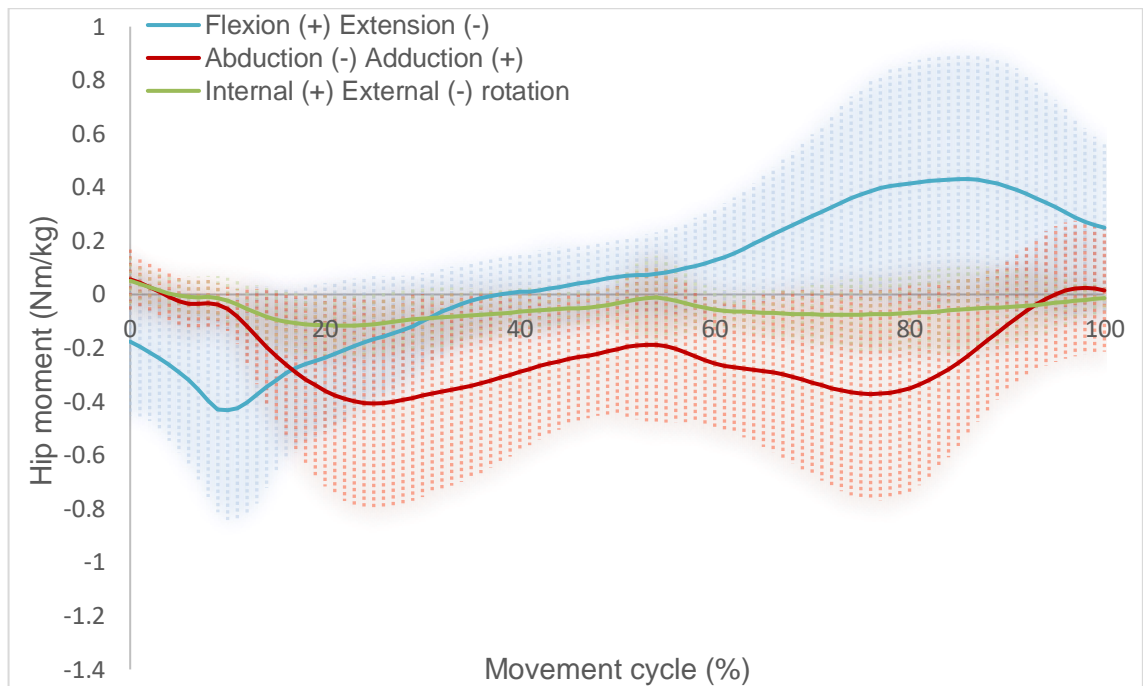


Figure 232. Mean right hip moment during one gait cycle for a level walk. Standard deviation above and below the mean are shown as shaded error bars (n=17).

At initial contact and during the majority of the stance phase, the hip displayed an extensor moment (peak extension moment: 0.4 Nm/kg) (Figure 232). The hip moment becomes flexed from approximately mid-stance and throughout the early swing phase (peak flexor moment: 0.4 Nm/kg). The flexion moment the decreased during the late swing phase, in preparation for initial contact. Mean SD was ± 0.3 Nm/kg, however variation was larger at the two peaks (flexor peak = ± 0.4 Nm/kg; extensor peak = ± 0.5 Nm/kg). From initial contact, the hip showed a net abductor moment throughout the majority of the gait cycle. Two abductor peaks were observed (both 0.4 Nm/kg). During the swing phase, the abduction moment decreased, eventually returning to a neutral joint moment. Average abductor SD was ± 0.3 Nm/kg. The hip showed a net external rotation moment throughout the movement cycle, however this was minimal, peaking twice at 0.1 Nm/kg. The SD was consistent throughout and averaged at ± 0.1 Nm/kg.

The initial extension moment during occurred as the lower limb was loaded (Figure 232). During late stance, hip extension was decelerated via hip flexors. Hip flexors then shortened to produce power, enabling the body to propel forwards and initiate the swing phase (peak flexion: 0.4 Nm/kg) (Hamill and Knutzen, 2006; Winter, 1984). The hip is thought to exhibit the highest variability, compared to other lower limb joint moments, during locomotion (Hamill and Knutzen, 2006). Mean peak extension moments have been found to range from 0.3 to 1.0 Nm/kg during the loading phase, with flexion

moments ranging from 0.4 to 0.9 Nm/kg during propulsion (Hamill and Knutzen, 2006; Lewis and Sahrman, 2015; O'Connor et al., 2018). This variation is important to consider when replicating realistic loading of both a THR and tissue engineered cartilage substitution.

10.6.2. Walk Turn

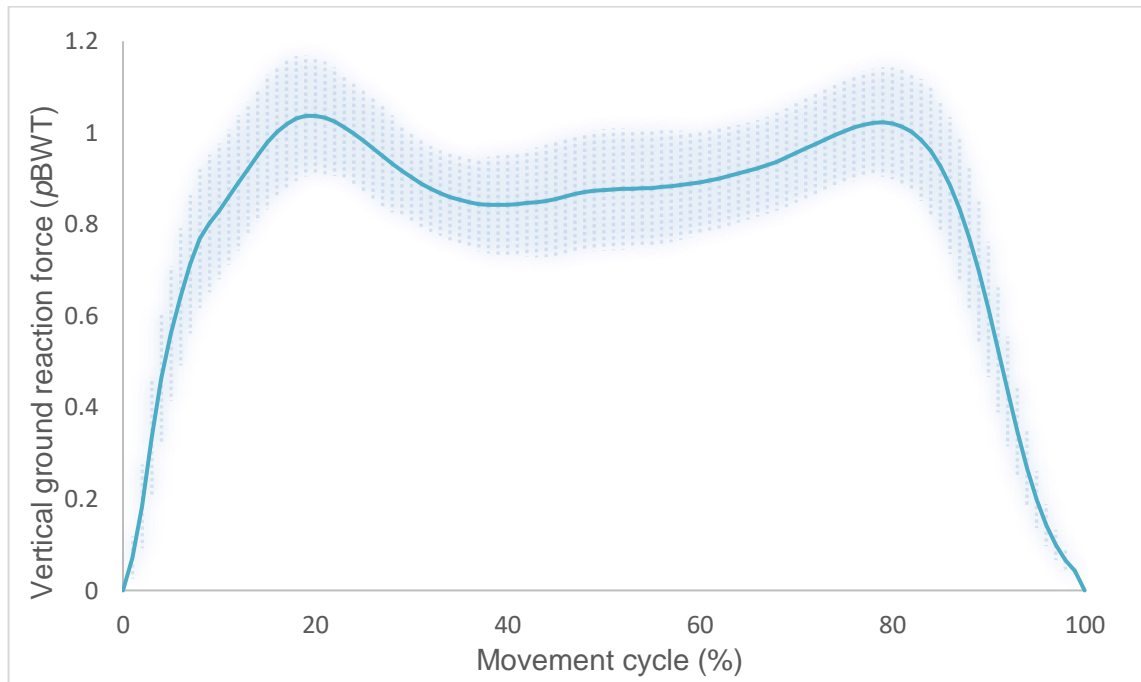


Figure 233. Mean right foot, vertical ground reaction force during one gait cycle for a walk turn, proportional to body weight (*pBWT*). Standard deviation above and below the mean are shown as shaded error bars ($n=17$).

Mean force data, for the walk turn, showed a similar trend to the normal walk. Two peaks were observed, each rising to 1.0 *pBWT* (Figure 233). The ‘valley’ typically seen with walking data, was less obvious for the walk turn, reaching a magnitude of 0.9 *pBWT* at mid-stance. The SD was noticeably lower than the straight forward walk, averaging at ± 0.1 *pBWT*.

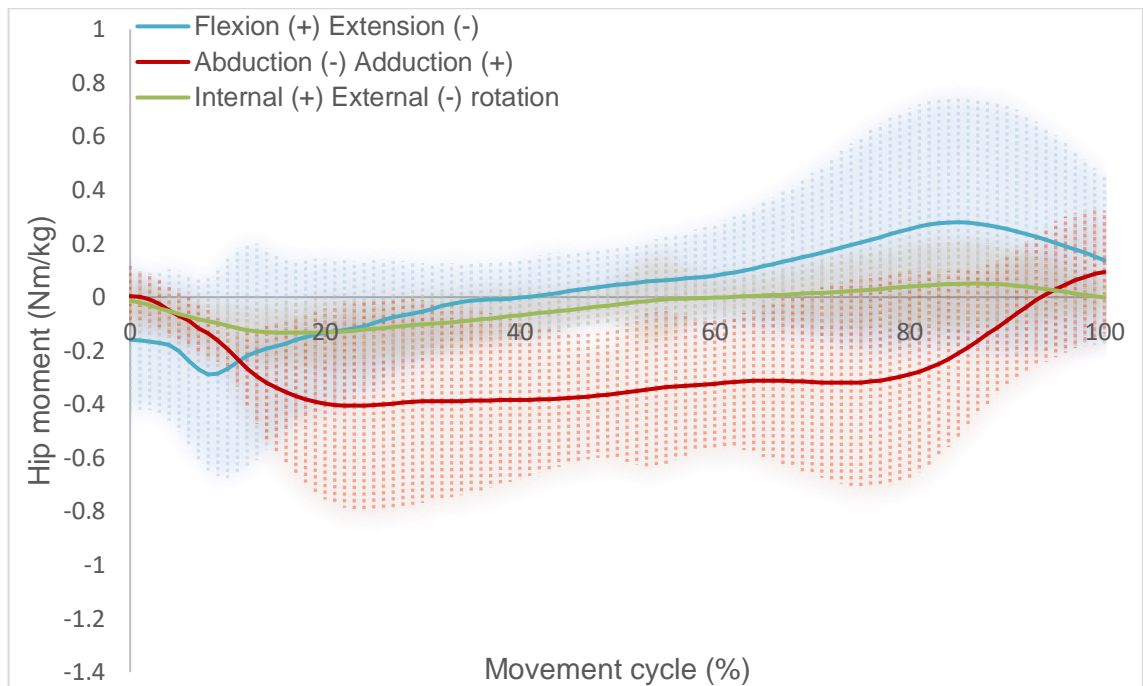


Figure 234. Mean right hip moment during one gait cycle for a walk turn. Standard deviation above and below the mean are shown as shaded error bars (n=18).

Similar to the straight walk, walk turn initially displayed a hip extensor moment at weight acceptance (0.3 Nm/kg) and moved to a peak flexor moment during the swing phase (0.3 Nm/kg) (Figure 234). Average SD was ± 0.3 Nm/kg and was largest at the two peaks (extensor peak: ± 0.4 Nm/kg; flexor peak: ± 0.5 Nm/kg). A net abductor moment was observed throughout the gait cycle, peaking at 0.4 Nm/kg (mean SD: ± 0.3 Nm/kg). The hip showed an external rotation moment during the breaking phase of gait and an internal rotation moment during the propulsion phase (when accelerating off the right foot). The SD was consistent throughout the movement, averaging at $0.1 \pm$ Nm/kg.

The only notable difference between the walk and walk turn, was a slightly reduced magnitude, both at flexor (0.1 Nm/kg decrease) and extensor (0.1 Nm/kg decrease) peaks (Figure 234). This seems reasonable, given the slight reduction in v GRF. Although v GRF and hip moments are similar for the two walking tasks, it is likely that hip reaction forces will show differences (particularly when considering the discrepancy between hip kinematics at heel strike). Kinetic analysis of the walk turn are lacking within the literature, further emphasising the importance of analysing the biomechanics of this common movement.

10.6.3. Stand to Sit and Sit to Stand

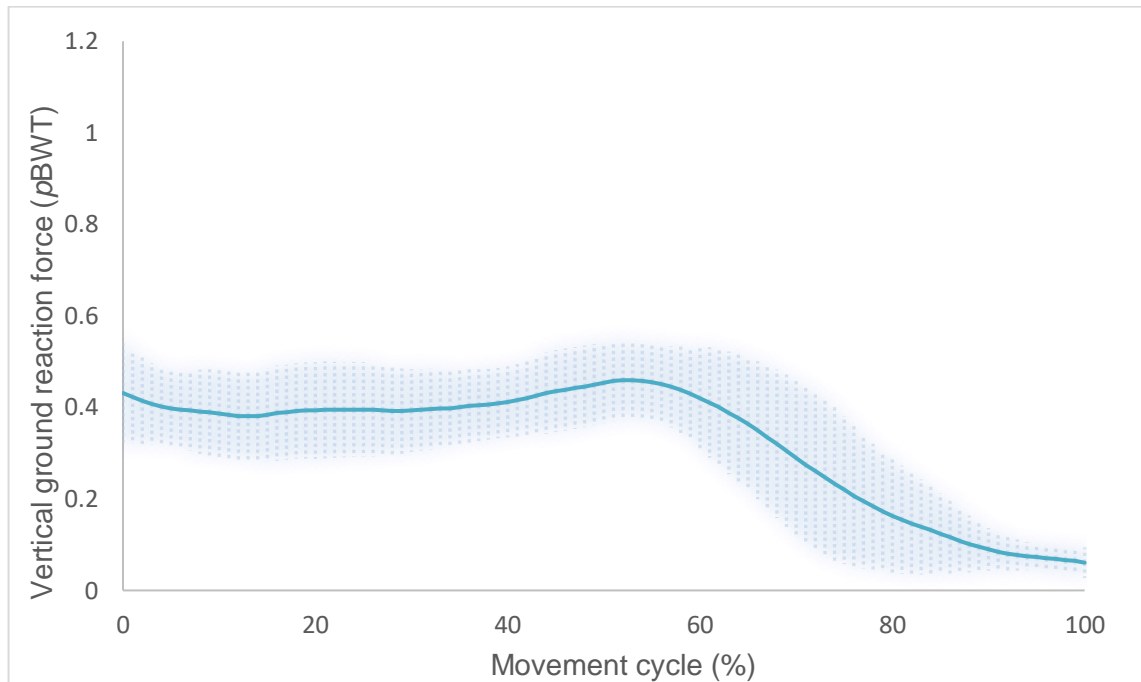


Figure 235. Mean right foot, vertical ground reaction force during one movement cycle for a stand to sit, proportional to body weight (*pBWT*) (chair height: 47 cm). Standard deviations above and below the mean are shown as shaded error bars ($n=8$).

When stood in a static position, mean $vGRF$ was 0.4 *pBWT* (Figure 235). The magnitude decreased at the point of contact with the chair ($\approx 60\%$ of the cycle). Force decreased to a minimum of <0.1 *pBWT* when sat down. Average SD was ± 0.1 *pBWT*, however the variation was close to zero when sat down on the chair. Variation was relatively high at the point where individuals made contact with the stool (peak SD was ± 0.2 *pBWT*). Given that the magnitude of force was low during this contact period (<0.4 *pBWT*), the SD reached up to 130% of the mean $vGRF$.

It is reasonable to suggest that stand to sit (StSi) $vGRF$ will be higher (similar to values at the top end of the SD), when the movement time is slower and the lower limb is unloaded slowly. Sitting down more quickly may increase impact at contact with the seat, whilst reducing the force transmitted through the joints during descent (as there is a lower requirement for muscles at the hip to counteract the motion). These two distinct techniques (fast and slow decent) may be the reason for high variation at this point.

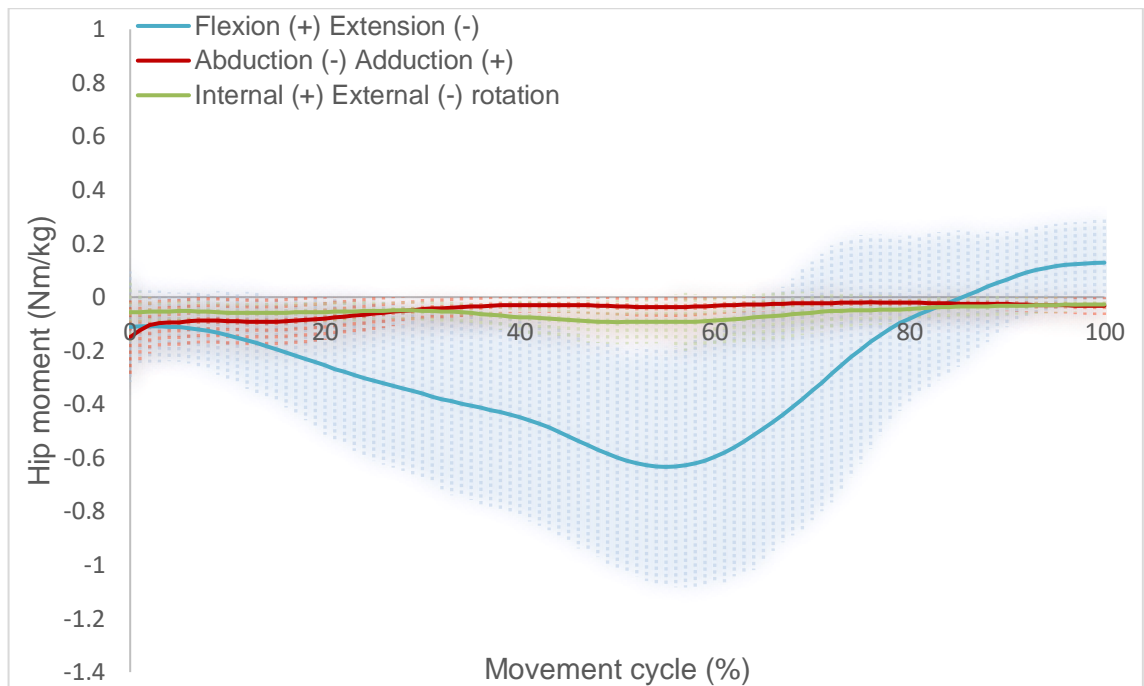


Figure 236. Mean right hip moment during one movement cycle for a stand to sit (chair height: 47 cm). Standard deviation above and below the mean are shown as shaded error bars (n=8).

When standing, a slight hip extension moment was seen at static standing. As the individual lowered down to the chair, a hip extension moment was observed, peaking prior to contact with the seat (0.6 Nm/kg) (Figure 236). Once in contact with the chair, hip extension was counteracted by a flexor moment, as the hip angle extended. A flexor moment of 0.1 Nm/kg was observed when sitting, at the end of the movement. Both abduction and external rotation moments were low (<0.1 Nm/kg) throughout the movement, highlighting the linear nature of this activity.

Average SDs were ± 0.3 Nm/kg (flexion-extension), ± 0.1 Nm/kg (abduction-adduction) and ± 0.1 Nm/kg (internal-external rotation). Variation increased during the phase in which the hip extension moment was decreasing (prior to a position of balanced sitting) (peak extension variation: ± 0.5 Nm/kg). Similar to the vGRF, the F-E moment SD peaked when in contact with the chair. This peak variation equated to $\pm 120\%$ of the mean F-E moment.

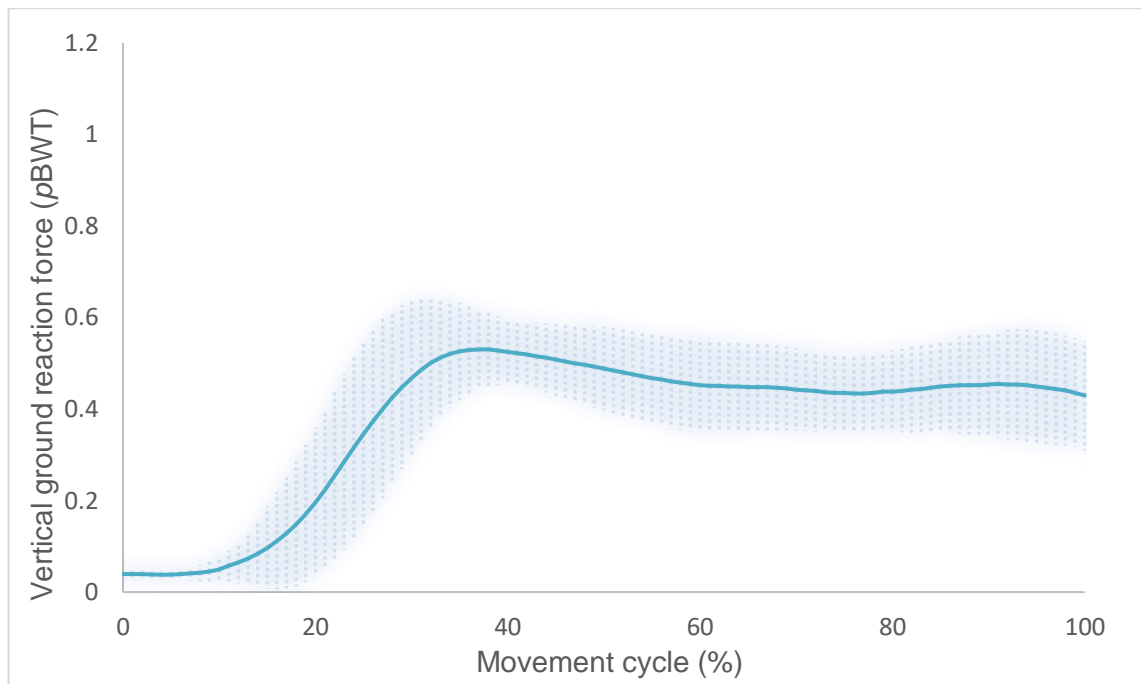


Figure 237. Mean right foot, vertical ground reaction force during one movement cycle for a sit to stand, proportional to body weight (*p*BWT) (chair height: 47 cm). Standard deviation above and below the mean are shown as shaded error bars (n=8).

Mean force was <0.1 *p*BWT when sat down and increased to 0.5 *p*BWT when stood up (Figure 237). Similar to the stand to sit, average SD was ± 0.1 *p*BWT. The SD was close to zero when seated, but reached a peak of ± 0.2 *p*BWT during the dynamic motion of standing up. This variation may have occurred due to variation in the time taken to lift off the seat by subjects.

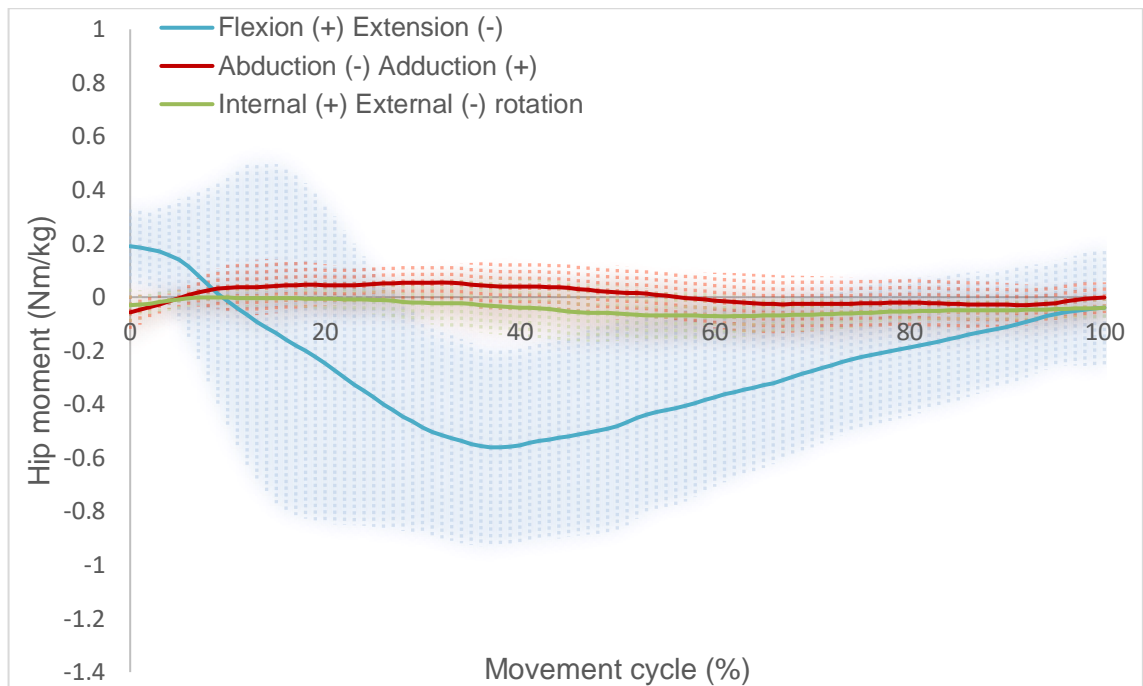


Figure 238. Mean right hip moment during one movement cycle for a sit to stand (chair height: 47 cm). Standard deviation above and below the mean are shown as shaded error bars (n=8).

From a seated position, a hip extension moment was observed, peaking at 0.6 Nm/kg (Figure 238). This period corresponded to an increasing hip extension angle, which allowed the body to ascend from the chair. Mid-way through standing up, the hip extension moment decreased and the hip adopted a neutral standing position. Mean variation mirrored that of the stand to sit (flexion-extension: ± 0.3 Nm/kg; abduction-adduction ± 0.1 Nm/kg; internal-external rotation ± 0.1 Nm/kg). The SD was increased during the phase in which individuals experienced a decreasing flexion moment at the hip (prior to a position of balanced standing).

Although vGRF showed similar magnitudes for StSi and SiSt, the former produced a larger flexor moment when standing (+0.1 Nm/kg) and a slightly increased peak SD (increase of ± 0.1 Nm/kg). However, minor differences were observed between both vBWT and hip moments for StSi and SiSt.

Existing literature has reported net hip moments during standing and sitting. StSi peak net joint moments were reported as 0.3 Nm/kg by Bergmann, who used instrumented hip implants to collect data from THR patients (Bergmann et al., 2001). This is lower than the 0.5 Nm/kg reported in the current study, possibly due to low functionality of the patients (Figure 238). Within the same study, Bergmann assessed net hip moments during a SiSt (Bergmann et al., 2001). Similar to the current study, Bergmann reported a larger

peak net moment during SiST, compared to StSi. Given that v GRFs were 0.5 p BWT for both StSi and SiSt, the increased moment seen when standing up is likely due to an increased moment arm, caused by differences in the kinematics.

More recently, Lamontagne et al. (2012) showed peak extension moments of 0.5 Nm/kg (THR patients) and 0.7 Nm/kg (healthy control) for both a StSi and SiSt. The 0.6 Nm/kg peak extension moment seen in the current study (for both StSi and SiSt) is closely matched to results within the literature.

10.6.4. Squat

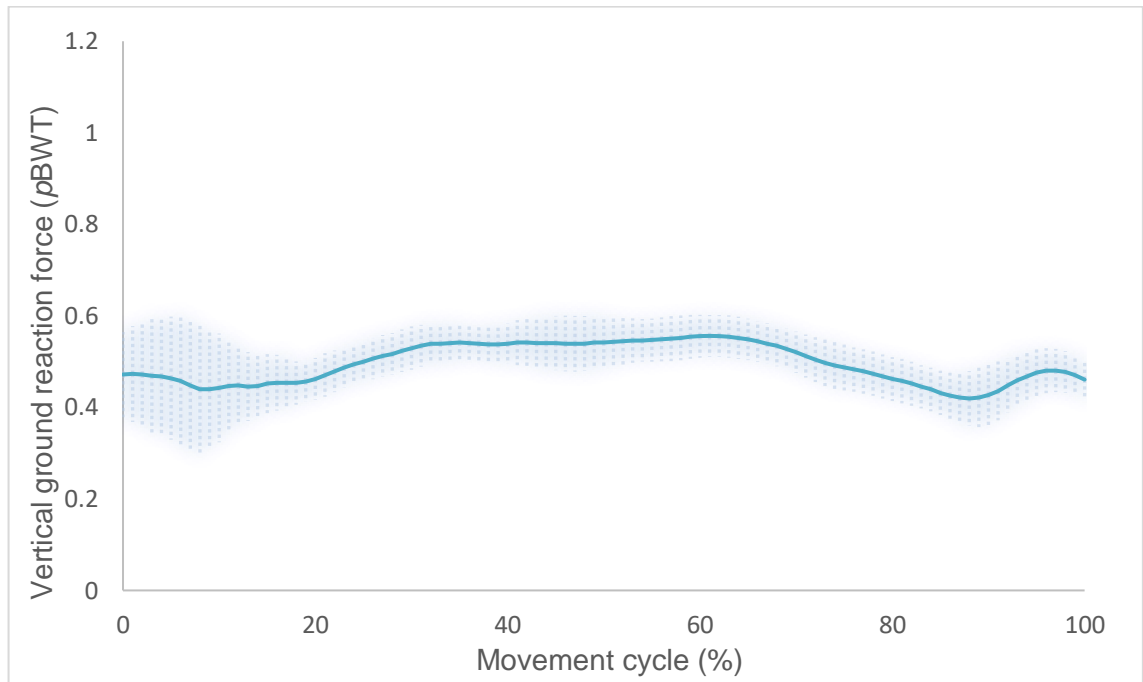


Figure 239. Mean right foot, vertical ground reaction force during one movement cycle for a squat, proportional to body weight (*pBWT*). Standard deviation above and below the mean are shown as shaded error bars ($n=11$).

The squat showed little fluctuation in vGRF and peaked at 0.6 *pBWT*. Variation was generally low, although the beginning of the movement (0-15%) resulted a larger SD than the average (± 0.11 compared to ± 0.06 *pBWT*) (Figure 239).

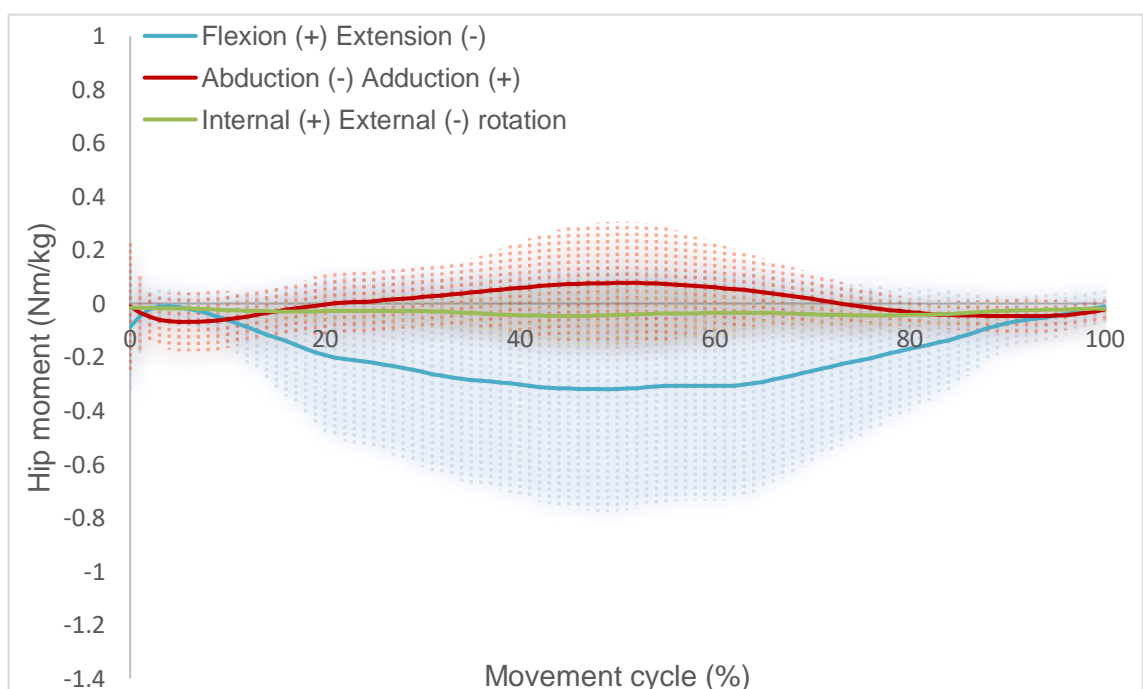


Figure 240. Mean right hip moment during one movement cycle for a squat. Standard deviation above and below the mean are shown as shaded error bars (n=11).

The hip extension moment increased from initiation of the squat, to the lowest point of the movement (peak extension moment: 0.3 Nm/kg) (Figure 240). From this point, a flexion moment was observed up to a neutral, standing position. A net adduction moment occurred during the dynamic movement of the squat, peaking at 0.1 Nm/kg. The mean hip rotation moment remained neutral throughout. Mean SD for the flexion-extension moment was ± 0.3 Nm/kg and peaked at ± 0.5 Nm/kg, at the lowest point of the squat ($\approx 50\%$ of the cycle). Given that peak extension variation occurred at the peak extension moment (0.3 Nm/kg), the SD at this point was over $\pm 150\%$. Average abduction-adduction SD was ± 0.1 Nm/kg, peaking at $\approx 50\%$ of the cycle (± 0.2 Nm/kg).

Existing literature supports the suggestion in the current study, that maximal moments will occur at the bottom of the squat (Nagura et al., 2002). It has also been suggested that extensor moments increase with squat depth, possibly explaining the high variation in extension moments seen during the activity (Schoenfeld, 2010). Previous analysis of squat hip extension moments, resulted peak extension moments of 0.6 pBWT (± 0.3 Nm/kg) (Lynn and Noffal, 2012). The discrepancy in extension moment peaks, between the current study and the literature, is likely due to the use of held dumbbells and potentially deeper squats ($+20^\circ$ F-E ROM) (Lynn and Noffal, 2012; Schoenfeld, 2010).

10.6.5. Stand Reach

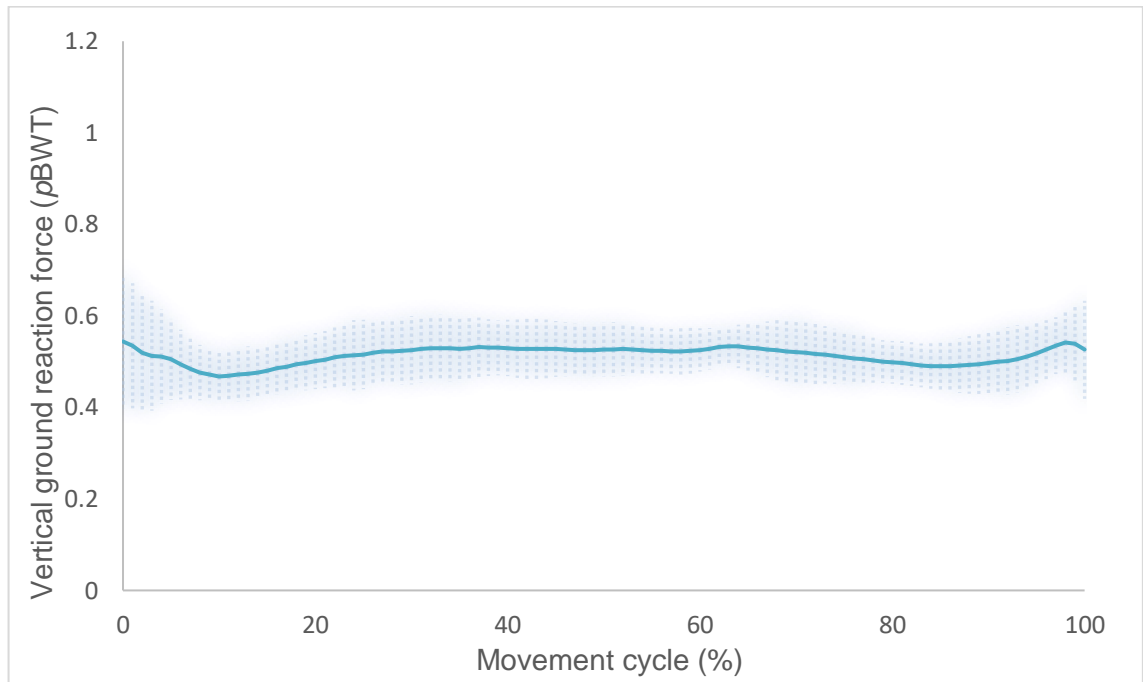


Figure 241. Mean right foot, vertical ground reaction force during one movement cycle for standing and reaching down to the floor, proportional to body weight (*pBWT*). Standard deviation above and below the mean are shown as shaded error bars ($n=12$).

Stand reach force remained stable throughout the movement, with slight increases at the beginning and end of the movement (mean: 0.5 *pBWT*). The SD average was ± 0.1 *pBWT* (Figure 241).

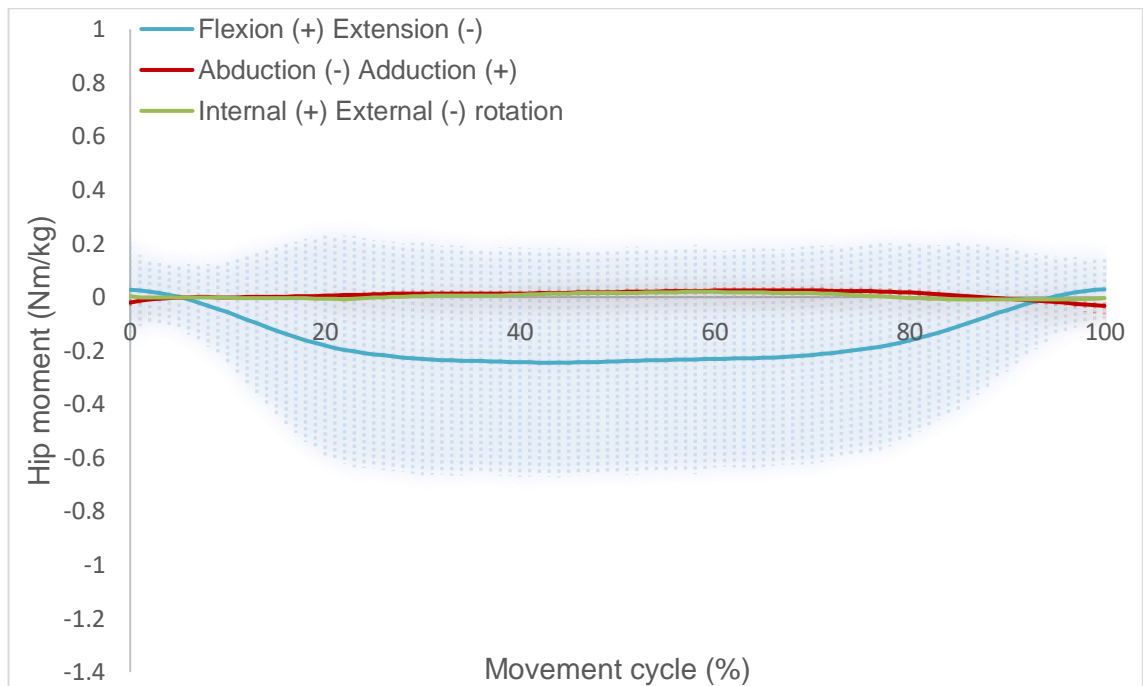


Figure 242. Mean right hip moment during one movement cycle for standing and reaching down to the floor. Standard deviation above and below the mean are shown as shaded error bars (n=12).

A peak hip extension moment of 0.2 Nm/kg was observed, with a mean SD of ± 0.3 Nm/kg. Both abduction-adduction and internal-external moments remained at ≈ 0 Nm/kg throughout (Figure 242). Mean SDs were ± 0.3 Nm/kg, ± 0.1 Nm/kg and ± 0.1 Nm/kg for flexion-extension, abduction-adduction and internal-external rotation moments, respectively. Flexion-extension variability was increased, in relation to the mean, during the dynamic phase of the task and reached a peak of ± 0.4 Nm/kg.

Although the peak extension moments for stand reach was comparable to other high flexion activities, the relative peak SD (occurring at peak extension) was the highest of all activities ($\pm 200\%$). This high SD may have occurred due to differences in hip flexibility between subjects.

10.6.6. Kneel Reach

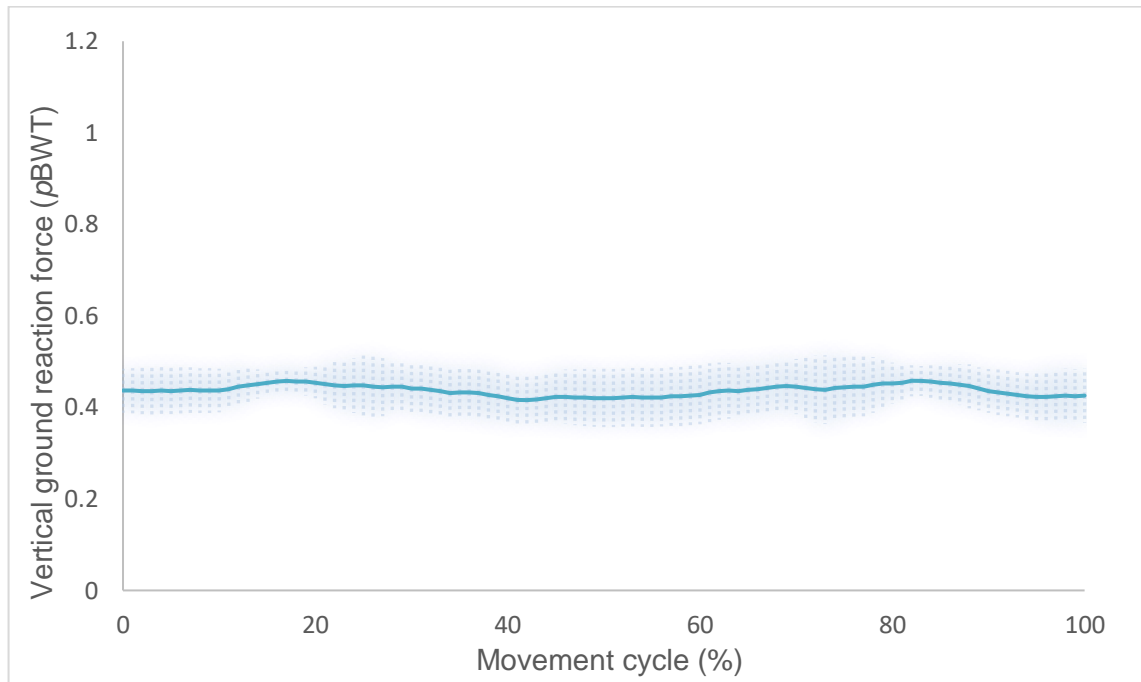


Figure 243. Mean right foot, vertical ground reaction force during one movement cycle for kneeling and reaching forwards, proportional to body weight (*p*BWT). Standard deviation above and below the mean are shown as shaded error bars (*n*=13).

Vertical force showed little change throughout the movement, averaging at 0.4 *p*BWT (mean SD: ± 0.1). Kneel reach showed the same peak *v*GRF (0.5 *p*BWT) as stand reach (Figure 243).

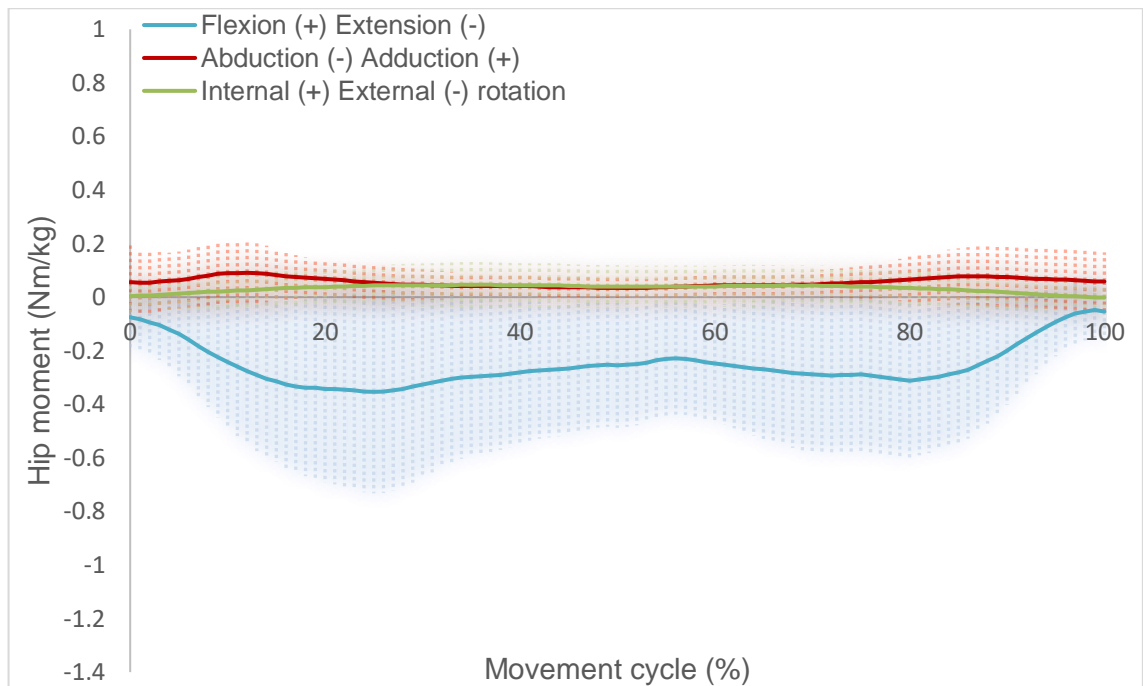


Figure 244. Mean right hip moment during one movement cycle for kneeling and reaching forwards. Standard deviation above and below the mean are shown as shaded error bars (n=10).

An extension moment was observed during hip flexion and peaked at $\approx 20\%$ of the kneel reach (0.4 Nm/kg) (Figure 244). A brief decrease in the extension moment was observed at 55% of the movement. The extension moment then decreased back to 0 Nm/kg , as the hip extended back to the original, kneeling position ($80\text{-}100\%$ of the movement). Average SDs were ± 0.3 , ± 0.1 and $\pm 0.1 \text{ Nm/kg}$ for flexion-extension, abduction-adduction and rotation moments, respectively. The flexion-extension moment showed a marked increase in variation when the hip flexed into the reaching position ($20\text{-}30\%$ of the cycle), peaking at $\pm 0.4 \text{ Nm/kg}$. Peak variation, occurring at peak extension, was equivalent to $\pm 100\%$. This variation may have been caused by variation in hip flexibility between subjects.

10.6.7. Lunge

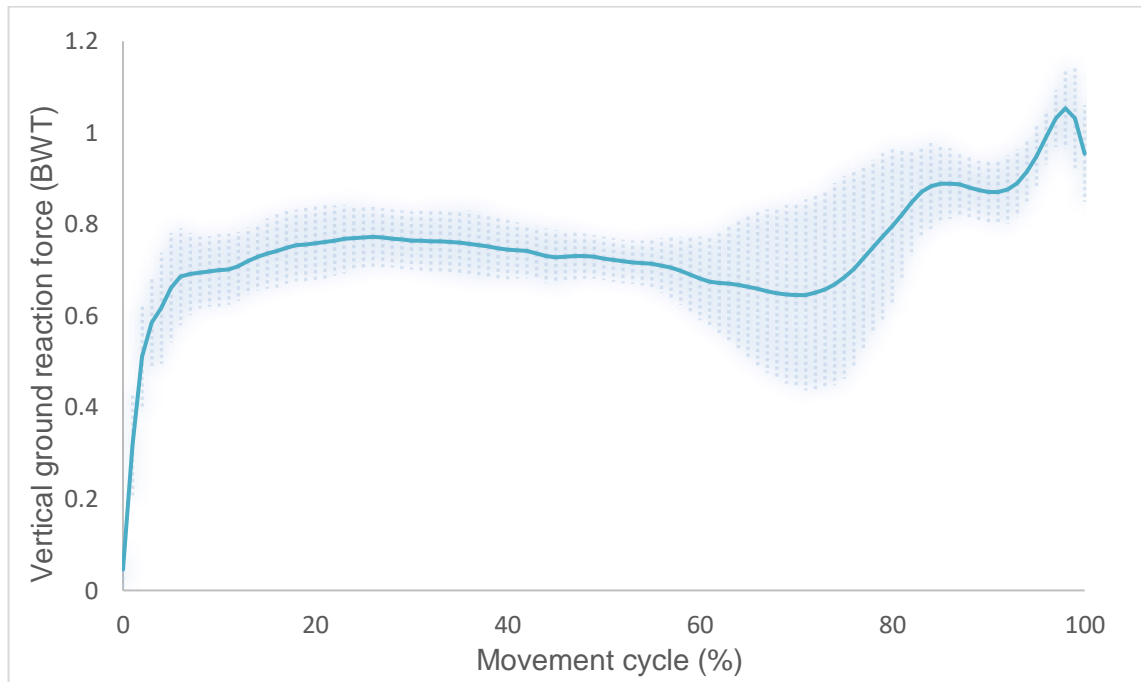


Figure 245. Mean right vertical ground reaction force during one movement cycle for a right footed lunge, proportional to body weight (BWT). Standard deviation above and below the mean are shown as shaded error bars (n=17).

At initial contact, v GRF increased dramatically (Figure 245). During mid-stance, as the individual moved down into a lunge, the force remained between 0.8 and 0.7 p BWT. At the deepest point of the lunge (70% of the force data) v GRF was 0.6 p BWT. Force then increased as the heel lifted and the body was propelled up and out of the lunge position (peaking at 0.9 p BWT). A final period of propulsion, saw the v GRF increase to 1 p BWT, before toe-off. Average SD was ± 0.1 p BWT, however the variation was largest when the individual propelled up and out of the lunge (60-85%) (± 0.2 p BWT).

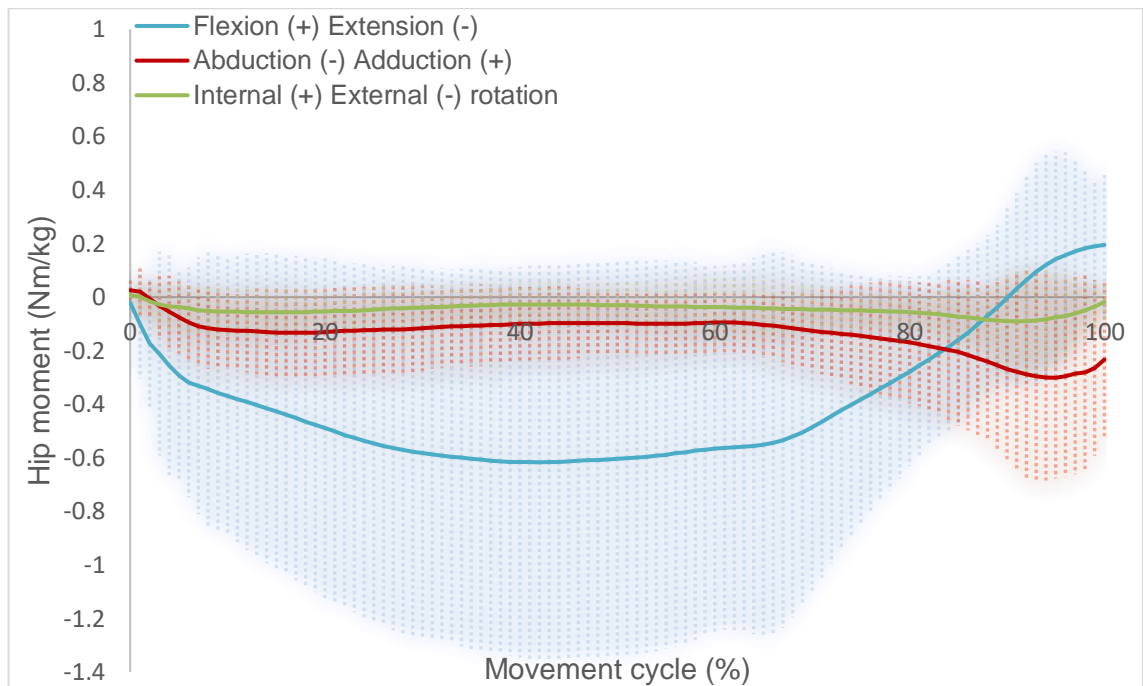


Figure 246. Mean right hip moment during one movement cycle for a right footed lunge. Standard deviation above and below the mean are shown as shaded error bars (n=13).

At initial contact, the hip exhibited an extension moment period that peaked when the lunge manoeuvre was at its lowest point ($\approx 50\%$) (0.6 Nm/kg) (Figure 246). From this point, a flexion moment was observed during the propulsion phase of the lunge. A net abduction moment was observed throughout the movement, with a peak of 0.3 Nm/kg occurring at 95% of the cycle (toe-off). A small net external hip moment occurred throughout the movement. Average SDs were $\pm 0.6 \text{ Nm/kg}$, $\pm 0.2 \text{ Nm/kg}$ and $\pm 0.1 \text{ Nm/kg}$ for flexion-extension, abduction-adduction and internal-external rotation moments, respectively. Flexion-extension variability peaked at 50% of the cycle (at the lowest point of the lunge) ($\pm 0.7 \text{ Nm/kg}$). Abduction-adduction ($\pm 0.4 \text{ Nm/kg}$) and internal-external rotation ($\pm 0.2 \text{ Nm/kg}$) moments both peaked at the point of toe-off ($\approx 95\%$ of the cycle).

Flanagan et al. (2004) assessed a forward lunge in elderly, healthy individuals. The peak extensor moment was double that of the current study (1.3 Nm/kg) (Flanagan et al., 2004). In another study, assessing a badminton lunge, 1.2 Nm/kg peak hip net moments were observed (Kuntze et al., 2010). The higher hip moments seen in the literature are likely due to the completion of faster and potentially more dynamic lunges, than in the current study. This highlights that kinetic values seen in the current study may be increased for some individuals, given that the lunge can be completed at different intensities. It has been suggested that badminton players, who regularly lunge, may be able to avoid excessive loading through manipulating their technique. Individuals who are

inexperienced at lunging, yet complete the task dynamically, may therefore be at a higher risk of excessive hip loading (Lees and Hurley, 1995). This is another factor to consider, when analysing hip loading during the lunge.

10.6.8. Golf Swing

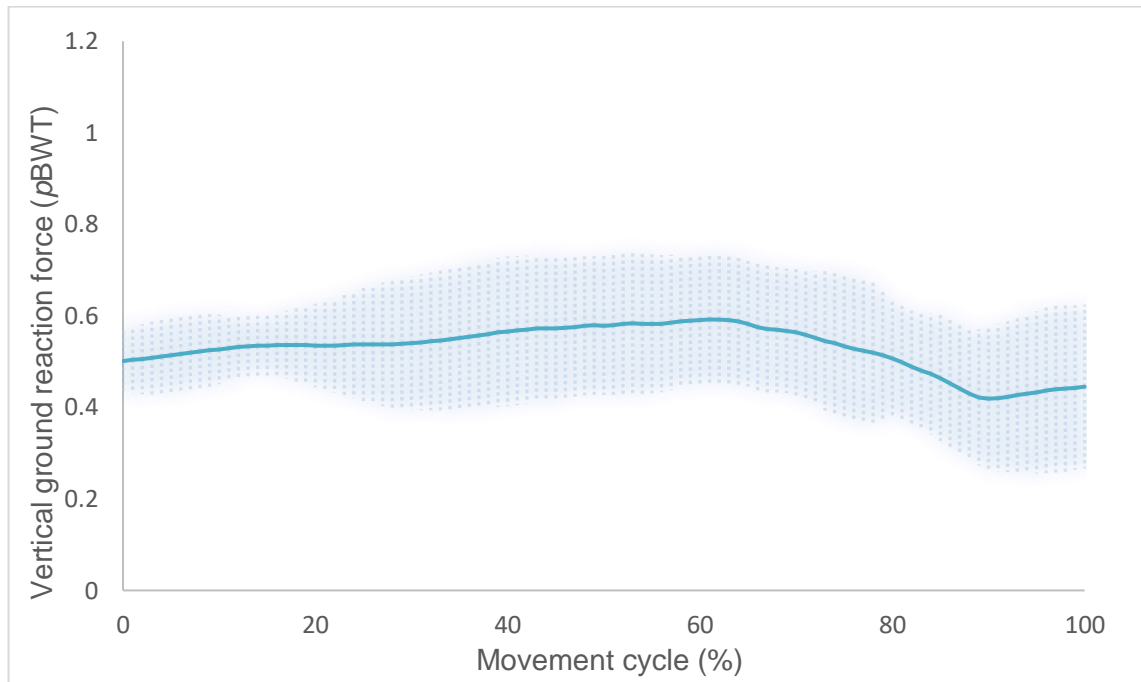


Figure 247. Mean right foot, vertical ground reaction force during one movement cycle for a golf swing, proportional to body weight (*pBWT*). Standard deviation above and below the mean are shown as shaded error bars ($n=18$).

Mean $vGRF$ increased from 0.5 to 0.6 *pBWT* during the backswing and downswing (Figure 247). During the follow through, force decreased to a minimum of 0.4 *pBWT*. The SD averaged out at ± 0.1 *pBWT* and was increased to ± 0.2 *pBWT* at certain points in the swing. The change in force magnitude occurred due to the shifting of weight from the back foot (during the backswing and downswing) to the front foot (during the follow through). From this force trace, peak loading appears to have occurred at the point of impact with the ball ($\approx 60\%$ of the movement).

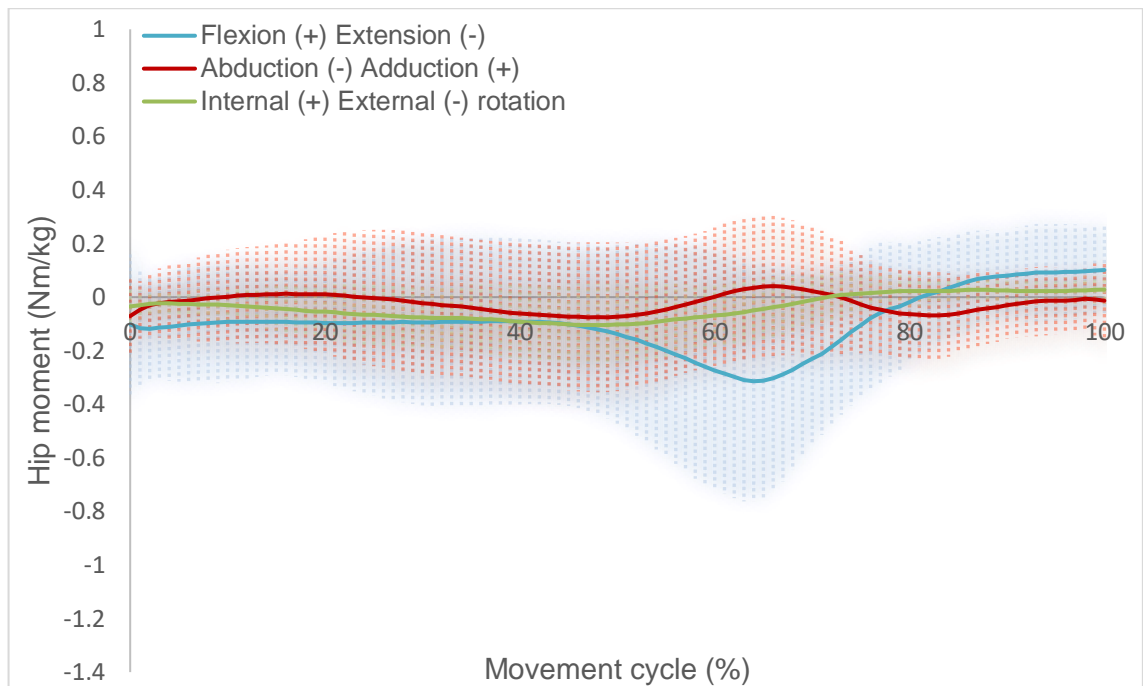


Figure 248. Mean right hip moment during one movement cycle for a golf swing. Standard deviation above and below the mean are shown as shaded error bars (n=16).

The hip extension moment remained at 0.1 Nm/kg throughout the back swing ($\approx 0-50\%$ of the golf swing) and demonstrated an increased extension moment during the down swing ($\approx 50-70\%$) (peaking at 0.3 Nm/kg) (Figure 248). The hip extension moment decreased from the bottom of the down swing and during the follow through. The flexion moment reached a peak of 0.1 Nm/kg and plateaued at the top of the follow through. Mean variation for flexion-extension, abduction-adduction and internal-external rotation moments were ± 0.3 , ± 0.2 and ± 0.1 Nm/kg, respectively. The flexion-extension SD peaked during the down swing (± 0.4 Nm/kg). Golf swing F-E moments showed a maximum SD at peak hip extension ($\pm 160\%$ of the peak). This highlights the variation in sagittal plane hip moments, during the swing.

Biomechanical analyses of the hip during a golf swing is limited. It has been shown, however, that the trail leg (also analysed in this study) is loaded during the backswing and transfers weight onto the front foot during the downswing (Hume et al., 2005). This transfer of force, between feet, allows a player to influence the club-head velocity at impact (Hume et al., 2005). Therefore, vGRF and lower limb moments might be expected to vary depending on the skill of the individual. Current research into joint moments has generally focused on the foot and knee rather than the hip. The vGRF range for golfers, however, has been reported at 1.6 - 2 pBWT (Hume et al., 2005). This increased loading

(compared to static standing) is due to the shifting of weight from the back foot during the backswing, to the front foot during impact and the follow through. Values are unsurprisingly higher than magnitudes for the non-golfers in the current study and suggests that considerably higher hip forces might be expected for a population of regular golfers.

10.6.9. Peak Forces

Peak ν GRF is presented in Table 24 and highlights differences in lower limb loading for activities. The standard deviation (SD) (inter-subject variation) is a method for quantifying variation between subjects. Both the average and peak SD are presented within this section in order to identify whether the variation fluctuated throughout the movement cycle.

Table 24. Peak vertical ground reaction forces (ν GRF), average and mean standard deviations (SD) for common daily activities. Data is normalised to proportion of body weight.

	Peak νGRF	Average SD	Peak SD
Walk	1.1	± 0.1	± 0.1
Walk turn	1.0	± 0.1	± 0.2
Stand to sit	0.5	± 0.1	± 0.2
Sit to stand	0.5	± 0.1	± 0.2
Squat	0.6	± 0.1	± 0.1
Stand reach	0.5	± 0.1	± 0.1
Kneel reach	0.5	± 0.1	± 0.1
Lunge	1.1	± 0.1	± 0.2
Golf swing	0.6	± 0.1	± 0.2

Peak vertical ground reaction forces ranged from 0.5 to 1.1 proportional to body weight (p BWT) (Table 24). The walk and lunge showed the highest ground reaction force, both at 1.1 p BWT. Variation was equal to or below ± 0.2 p BWT for all activities, suggesting low levels of inter-subject variation.

Peak flexion-extension joint moments are resulted in Table 25, as this was the dominant moment of force acting at the hip for the majority of activities. Highlighting maximum values allows for an overview of the different net turning forces, occurring for activities at the hip. Mean and maximum standard deviations (SDs) provide a quantification of the variation between subjects, both at peak points and as an average across the movement cycle.

Table 25. Peak hip joint moments (flexion-extension) and average and mean standard deviations for common daily activities. Data is normalised to body weight (Nm/kg). Maximum values, between activities, are highlighted in bold.

	Peak joint moment (Nm/kg)		Standard deviation (\pm Nm/kg)	
	Flexion	Extension	Mean	Max
Walk	0.4	0.4	0.3	0.5
Walk turn	0.3	0.3	0.3	0.5
Stand to sit	0.1	0.6	0.3	0.5
Sit to stand	0.2	0.6	0.3	0.6
Squat	0	0.3	0.3	0.5
Stand reach	0	0.2	0.3	0.4
Kneel reach	0	0.4	0.3	0.4
Lunge	0.2	0.6	0.6	0.7
Golf swing	0.1	0.3	0.3	0.5

When considering flexion-extension moments (Table 25), the walk resulted the largest flexion moment (0.4 Nm/kg), closely followed by the walk turn (0.3 Nm/kg). Stand to sit, sit to stand and lunge showed the largest hip extension moments (all 0.6 Nm/kg). Mean SDs were ± 0.3 Nm/kg for all activities, other than the lunge (± 0.6 Nm/kg). Peak SDs varied across activities, with the lunge showing the largest peak variation (± 0.7 Nm/kg).

10.6.10. Discussion

Peak v GRF was ≈ 1.0 p BWT for activities that had periods with one foot in contact with the ground (walking tasks and lunge). Those with both feet on the ground throughout, saw values of ≈ 0.5 p BWT (as body weight was balanced between legs). Average v GRF variation was low during walking tasks and the lunge ($\approx \pm 10\%$ of the peak). This variation rose to $\approx \pm 20\%$ of the peak in activities with both feet on the ground throughout (possibly due to variation in the balancing of force between limbs).

Walking tasks saw similar flexion (0.3 to 0.4 Nm/kg) and extension (0.3 to 0.4 Nm/kg) moment peaks. Other activities saw considerably higher hip extensor moments, due to higher levels of hip angular flexion. Extension moments were highest for SiSt, StSi and lunge (0.6 Nm/kg). Joint moment variation was high across all activities, with peak SDs over $\pm 100\%$ of the moment peak, for 10 of the 11 activities. Given that v GRF showed small SDs, high variation in joint moments highlights the difference in kinematics between individuals. Ultimately, this suggests differences in technique (ROM and angular velocity) between individuals. The cause of this may be due to flexibility, strength or skill level (previous practice).

10.6.11. Conclusion

Vertical ground reaction forces provide a reasonable assessment of the load an individual will experience throughout each activity. Ground reaction forces influenced both hip moments and hip reaction forces. Hip moments provide important information regarding the net contribution of muscles at the hip, to enable a balance of the body position (and torque acting at a hip prosthesis). This might be expected to show similar trends to hip reaction force magnitudes. The high variation identified in v GRF and sagittal plane hip moments, for many of the activities, may lead to similar variations in localised hip reaction forces. Understanding kinetic data, alongside hip kinematics, is crucial for understanding the wear of both THR and tissue engineered cartilage.